Multi-scale structural study of the Betic metamorphic complexes integrated with petrological and geochronological data

Alejandro Ruiz Fuentes

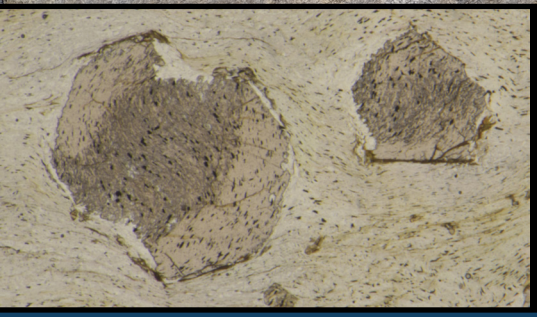

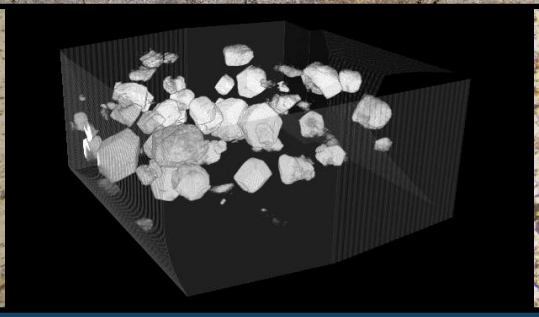

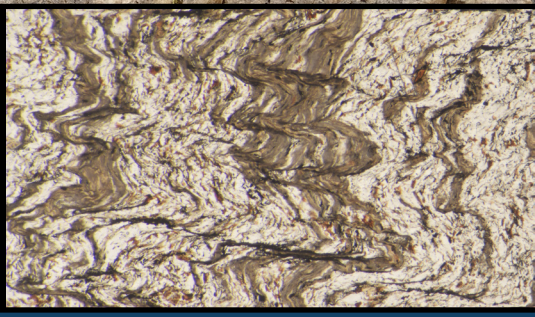

Ph.D. Thesis 2023

Supervised by Domingo Aerden

UNIVERSIDAD DE GRANADA

Programa Doctorado
Ciencias de la Tierra

UNIVERSIDAD DE GRANADA

Departamento de Geodinámica

Programa Doctorado
Ciencias de la Tierra

Multi-scale structural study of the Betic metamorphic complexes integrated with petrological and geochronological data

Memoria de Tesis Doctoral presentada por D. Alejandro Ruiz Fuentes para optar al grado de Doctor por la Universidad de Granada.

Granada,

Fdo. Alejandro Ruiz Fuentes

Vº Bº del Director

Fdo. Domingo Aerden

Editor: Universidad de Granada. Tesis Doctorales
Autor: Alejandro Ruiz Fuentes
ISBN: 978-84-1195-075-6
URI: https://hdl.handle.net/10481/85102

The doctoral candidate D. Alejandro Ruiz Fuentes and the thesis supervisor Prof. Domingo Aerden:

Guarantee, by signing this doctoral thesis, that the work has been done by the doctoral candidate under the direction of the thesis supervisor and, as far as our knowledge reaches, in the performance of the work, the rights of other authors to be cited (when their results or publications have been used) have been respected.

Granada, July 2023

Thesis supervisor	Doctoral candidate
Signed: Domingo Aerden	Signed: Alejandro Ruiz Fuentes

Agradecimientos

Me gustaría dedicar estas líneas a expresar mi agradecimiento a aquellas personas que han contribuido directa o indirectamente a la realización de esta tesis doctoral, y a aquellas que me han acompañado durante el proceso.

En primer lugar quiero agradecer a mi director de tesis Domingo Aerden el constante trabajo de seguimiento llevado a cabo durante los años de realización de esta tesis, y su entera disponibilidad para prestar apoyo en las tareas que han ido surgiendo. Agradezco la confianza que depositó en mí al inicio y durante el desarrollo de este proyecto, así como transferirme su pasión por la geología estructural y la tectónica.

A Jesús Galindo Zaldívar agradezco su labor como tutor y su ayuda con multitud de trámites burocráticos. Asimismo, agradezco su apoyo financiero continuo a lo largo de todos los años que ha durado esta tesis, sin el cual la realización de la misma no habría sido posible.

Doy las gracias a Michel Corsini y Jean-Marc Lardeaux por hacer posible mi estancia en la Université Côte d'Azur, por sus valiosas enseñanzas sobre múltiples aspectos de la petrología metamórfica y por su ayuda con la parte petrológica y geocronológica de esta tesis. Agradezco también a Delphine Bosch y Olivier Bruguier recibirme en la Université de Montpellier y su colaboración y apoyo en la obtención de datos geocronológicos y termobarométricos. A Philippe Münch de la Université de Montpellier agradezco su colaboración para la obtención de las edades Ar/Ar.

También quiero dar las gracias al Departamento de Geodinámica de la Universidad de Granada por ofrecer los medios necesarios para la realización de la tesis, y por la ayuda prestada por sus miembros siempre que ha sido necesario.

Varias personas de la Universidad de Granada han contribuido a la obtención de los datos utilizados en esta tesis. Entre ellos cabe destacar a Ángel Perandrés Villegas del Departamento de Geodinámica, quien realizó las láminas delgadas, agradezco su disponibilidad y paciencia durante todo el proceso. He de expresar también mi gratitud a Fátima Linares Ordóñez del CIC por su plena disposición y buen hacer en todo lo relativo a la utilización del Microtomógrafo de Rayos-X. También doy las gracias a Miguel Ángel Hidalgo Laguna del CIC por transmitir su ayuda y valiosa experiencia durante la realización de análisis en la Microsonda electrónica. Gracias a Eva María Marín Martín del Departamento de Mineralogía y Petrología por su ayuda y consejos respecto a la utilización del laboratorio de molienda de rocas.

Agradezco a José Benavente Herrera, Coordinador del Programa de Doctorado de Ciencias de la Tierra, su ayuda con diversos trámites burocráticos relacionados con la tesis, así como en lo concerniente a las tareas de la Comisión de Garantía Interna del programa.

Debo mencionar también a Agustín Martín Algarra del Departamento de Estratigrafía y Paleontología, con quien he podido trabajar durante el desarrollo de esta tesis. Su amplio conocimiento y las discusiones que he mantenido con él acerca de la estratigrafía y tectónica de la Cordillera Bética han contribuido a mejorar la calidad de este trabajo.

Gracias también a Ángel Puga Bernabéu del Departamento de Estratigrafía y Paleontología, quien me ofreció su apoyo y confianza al comienzo de mi carrera investigadora y me dio las pautas a seguir para iniciarme en este mundo, por lo que es en parte responsable de que haya alcanzado este objetivo.

En el ámbito más personal me gustaría acordarme de mis compañeros, algunos doctorandos y otros ya doctores. Quiero dar las gracias especialmente a Víctor, Olmo, Cristina, Cristina, Ángela y Lourdes, con los que he compartido momentos desde el inicio de la tesis. También quiero mencionar a los becarios que han ido llegando más tarde, Asier, Mayte, Marcos, Roberto y Paula. A todos ellos les agradezco los buenos momentos pasados y el apoyo moral recibido.

También me gustaría dar las gracias a mis padres y hermanas por el apoyo y ánimo recibidos durante la realización de este proyecto.

Por último, me gustaría expresar mi especial reconocimiento a Ángela, quien constantemente me motivó a realizar el trabajo de la mejor manera posible, cuya compañía en numerosas jornadas de campo hizo dicha tarea mucho más agradable, y cuyo cariño y comprensión me han ayudado a sobrellevar los momentos más difíciles.

Esta tesis doctoral ha sido posible gracias a un contrato de Formación de Profesorado Universitario (FPU17/01874) otorgado por el Gobierno de España, una ayuda para movilidad internacional financiada por la Universidad de Granada, los medios materiales del Departamento de Geodinámica de la Universidad de Granada y del grupo de investigación RNM-148 (Junta de Andalucía), y los proyectos de investigación CGL2016-80687-R y PID2022-136678NB-I00 AEI/FEDER del Gobierno de España, y P18-RT-3275 y B-RNM-301-UGR18 de la Junta de Andalucía.

Abstract

The Betic Cordillera in southern Spain records a complex Alpine tectonic evolution derived from the Africa-Iberia convergence and the westward drift of the Alborán Domain. Several aspects concerning the tectonic processes that operated during the development of this mountain belt are still a matter of debate. In order to contribute to a better understanding of these processes, a regional-scale microstructural study of porphyroblast inclusion trails has been performed in the metamorphic complexes of the cordillera. The new data have been combined with metamorphic and geochronological data and outcrop-scale structural observations in order to integrate them in the regional tectonic framework.

Inclusion trail data have been collected using 3D images obtained by scanning rock samples using the X-ray Computed microtomography (XCT) technique. This technique allows measuring the orientation of microstructural elements directly in each porphyroblast present in the sample, which supposes a major improvement with respect to traditional methods based on integration of observations made in differently oriented thin sections. A very detailed characterization of porphyroblast inclusion trails, size and shape has been performed in two samples to evaluate the suitable mechanism of porphyroblast growth, being the non-rotation model favoured by the obtained results.

In the Nevado-Filábride Complex, 5 samples have been analysed through XCT to complement previous data of porphyroblast inclusion trails in the complex, which were mainly determined with thin section methods. The results confirm the presence of three sets of Foliation Intersection/Inflection Axes (FIA) oriented WNW-ESE, ENE-WSW and NNW-SSE in previously poorly studied areas of the complex. Several sets of foliations and crenulation cleavages have been studied at outcrop-scale to investigate the subdivision and internal structure of the complex on which no consensus exists. Subhorizontal high-strain zones located towards the lower part of the complex have been identified that postdate upright folding of the main foliation. These shear zones usually coincide with the boundaries of the previously defined Veleta-Mulhacén or Ragua-Calar Alto units, supporting the differentiation of these units, but a profound revision of their map-scale geometry is necessary.

In the Alpujárride Complex, porphyroblast inclusion trails have been characterized through XCT and thin sections in 60 oriented samples widely distributed throughout the western and central part of the complex. Three FIA sets have been demonstrated in these rocks with similar orientations and temporal relationships (WNW-ESE, ENE-WSW and NNW-SSE) as in the Nevado-Filábride. These FIA developed mainly during the prograde evolution of the complex, but the ENE-WSW set was repeated during a late-metamorphic stage following partial exhumation of the complex. Several generations of late-metamorphic crenulation cleavages have been distinguished and interpreted to reflect alternations of contraction and extension.

The regional consistency of FIA orientations in the Internal Zones and evidence for generalized subvertical and subhorizontal preferred orientations of inclusion trails shown in this thesis coincide with similar observations reported previously in other mountain belts. So far, this data has only found explanation in terms of the micro-partitioning of deformation around rigid objects, which allow them to maintain rotationally stable positions during bulk non-coaxial deformation. Crustal shortening directions indicated by the three successive FIA sets distinguished in this thesis according to this 'non-rotational' model coincide well with Paleogene-Neogene vectors of Africa-Iberia convergence and simultaneous westward displacement of the Alborán Domain. This provides an additional argument in favour of the possibility that early tectonic fabrics are preserved with their original orientations by porphyroblasts.

The metamorphic conditions (7-9.5 kbar and 600-680 ºC) and age (21-18.5 Ma) of the main foliation in the Alpujárride Complex, which developed or reequilibrated during decompression, have been determined and agree well with previously published data. Microstructural evidences indicate that the WNW-ESE and NNW-SSE FIA sets developed before this foliation, although the NNW-SSE set might have been partially coeval with it. The repeated generation of ENE-WSW FIAs after NNW-SSE FIAs is confirmed by an age of 17.5 Ma obtained for monazite inclusions in garnets. This age coincides with the beginning of continental collision between the Internal and External Zones of the cordillera. In the Nevado-Filábride, a maximum age of 14.5 Ma has been obtained for a garnet porphyroblast hosting an ENE-WSW FIA and confirms a repetition of this set also in this complex.

The similar orientations and temporal relationships of FIAs in both complexes suggest an equivalent kinematic evolution despite different paleogeographic positions and later exhumation of the Nevado-Filábrides. All these results demonstrate the potential of a new methodology for reconstructing the tectonic evolution of orogenic belts, whose principle ingredient is the integration of porphyroblast inclusion trails data with petrology, geochronology and outcrop-scale structural observations.

Resumen

La Cordillera Bética, situada en el sur de España, registra una compleja evolución tectónica Alpina derivada de la convergencia entre África e Iberia y el desplazamiento hacia el oeste del Dominio de Alborán. Varios aspectos relativos a los procesos tectónicos que han actuado durante el desarrollo de este cinturón montañoso son todavía cuestiones debatidas. Para contribuir a un mejor entendimiento de estos procesos, se ha realizado un estudio microestructural a escala regional de foliaciones internas de porfiroblastos en los complejos metamórficos de la cordillera. Los nuevos datos han sido combinados con datos metamórficos y geocronológicos y con observaciones estructurales a escala de afloramiento para integrarlos en el contexto tectónico regional.

Los datos de foliaciones internas han sido obtenidos usando imágenes 3D adquiridas mediante la técnica de microtomografía computerizada de rayos-X (XCT). Esta técnica permite medir la orientación de elementos microestructurales directamente en cada porfiroblasto presente en la muestra, lo que supone una gran mejora respecto a métodos tradicionales basados en la integración de observaciones hechas en láminas delgadas con diferente orientación. Una caracterización muy detallada de foliaciones internas, tamaño y forma de porfiroblastos se ha realizado en dos muestras para evaluar el mecanismo de crecimiento de porfiroblastos más probable, siendo el modelo de no-rotación favorecido por los resultados obtenidos.

En el Complejo Nevado-Filábride, 5 muestras han sido analizadas mediante XCT para complementar datos previos de foliaciones internas de porfiroblastos en el complejo, que fueron principalmente determinados con métodos de láminas delgadas. Los resultados confirman la presencia de tres sets de Ejes de Intersección/Inflexión de Foliación (FIA) orientados WNW-ESE, ENE-WSW y NNW-SSE en áreas del complejo escasamente estudiadas con anterioridad. Varios sets de foliaciones y clivajes de crenulación han sido estudiados a escala de afloramiento para investigar la subdivisión y estructura interna del complejo, respecto a lo cual no hay consenso. Zonas de alta deformación subhorizontales localizadas hacia la parte baja del complejo han sido identificadas y se desarrollan con posterioridad a un plegamiento vertical de la foliación principal. Estas zonas de cizalla normalmente coinciden con los límites de las unidades Veleta-Mulhacén o Ragua-Calar Alto, definidas previamente, apoyando la diferenciación de estas unidades, aunque una profunda revisión de su cartografía es necesaria.

En el Complejo Alpujárride, las foliaciones internas de porfiroblastos han sido caracterizadas con XCT y láminas delgadas en 60 muestras orientadas ampliamente distribuidas en los sectores occidental y central del complejo. Tres sets de FIA han sido obtenidos en estas rocas, con orientaciones y relaciones temporales similares (WNW-ESE, ENE-WSW y NNW-SSE) a las del Nevado-Filábride. Estos FIA se desarrollaron principalmente durante la evolución metamórfica prograda del complejo, pero el set ENE-WSW se repitió durante una etapa tardimetamórfica después de la exhumación parcial del complejo. Varias generaciones de clivajes de crenulación tardimetamórficos han sido

distinguidas e interpretadas como resultado de alternancias de eventos contractivos y extensionales.

La consistencia regional de las orientaciones de FIA en las Zonas Internas, y evidencias de una generalizada orientación preferente subvertical y subhorizontal de las foliaciones internas, coinciden con observaciones similares hechas previamente en otros cinturones montañosos. Estos datos solo han sido explicados en términos de micro-partición de la deformación alrededor de objetos rígidos, lo que les permite mantener posiciones estables durante una generalizada deformación no-coaxial. Las direcciones de acortamiento cortical indicadas por los tres sucesivos sets de FIA distinguidos en esta tesis de acuerdo con este modelo no-rotacional, coinciden con los vectores de convergencia entre África e Iberia durante el Paleógeno-Neógeno, y el simultáneo desplazamiento hacia el oeste del Dominio de Alborán. Esto proporciona un argumento adicional en favor de la posibilidad de que fábricas tectónicas tempranas sean preservadas con su orientación original en los porfiroblastos.

Las condiciones metamórficas (7-9.5 kbar y 600-680 ºC) y edad (21-18.5 Ma) de la foliación principal en el Complejo Alpujárride, que se desarrolló o reequilibró durante la descompresión, han sido determinadas y coinciden con datos previamente publicados. Evidencias microestructurales indican que los sets de FIA WNW-ESE y NNW-SSE se desarrollaron con anterioridad a esta foliación, aunque el set NNW-SSE podría haber sido parcialmente coetáneo a esta. La generación repetida de FIAs ENE-WSW después del NNW-SSE se confirma con una edad de 17.5 Ma obtenida para inclusiones de monacita en granates. Esta edad coincide con el comienzo de la colisión continental entre las Zonas Internas y Externas de la cordillera. En el Nevado-Filábride, una edad máxima de 14.5 Ma ha sido obtenida para un porfiroblasto de granate que incluye un FIA ENE-WSW y confirma la repetición de este set también en este complejo.

La similitud en las orientaciones y relaciones temporales de FIAs en ambos complejos sugieren una evolución cinemática equivalente a pesar de sus diferentes posiciones paleogeográficas y posterior exhumación del Nevado-Filábride. Todos estos resultados demuestran el potencial de una nueva metodología para reconstruir la evolución tectónica de cinturones orogénicos, cuyo principal ingrediente es la integración de datos de foliaciones internas de porfiroblastos con petrología, geocronología y observaciones estructurales a escala de afloramiento.

CONTENTS

Part I

Part II

Part III

Part I

1. Introduction.

2. The Betic Cordillera.

3. Methodology.

1. Introduction

1.1. Scope and motivation of the thesis

Our knowledge regarding the orogenic evolution of the Betic Cordillera has been notably increased since early studies dealing with its essential architecture and subdivision (e.g. Bertrand and Kilian, 1889; Brouwer, 1926; Blumenthal, 1927; van Bemmelen, 1927; Fallot et al., 1960; Nijhuis, 1964; Egeler and Simon, 1969; Puga et al., 1974). Nevertheless, several issues remain unresolved concerning the internal structure of the principle nappe complexes (e.g. Martínez-Martínez et al., 2002; Gómez-Pugnaire et al., 2012; Tubía et al., 2013; Sanz de Galdeano, 2017), the role of extension vs. contraction (e.g. Balanyá et al., 1997; Orozco et al., 1998; Simancas, 2018; Williams and Platt, 2018), kinematics of deformation (e.g. Jabaloy et al., 1993; Porkoláb et al., 2022), detailed metamorphic evolution (e.g. Booth-Rea et al., 2015; Santamaría-López et al., 2019), or the relationship between metamorphism and radiometric ages (e.g. Platt et al., 2006; Li and Massonne, 2018). The long persistence of these questions highlights the need to explore new research approaches and techniques. Against this background, this Ph.D. Thesis focuses attention on a little explored yet rich archive of geological history represented by metamorphic porphyroblasts in the Betic-Rif orogen. Several state-of-the-art analytical techniques are applied to characterize the 3D morphology, orientation and petrological features of porphyroblast inclusion trails in oriented rock samples.

1.2. Porphyroblast inclusion trails and orogenesis

The mechanical behaviour of porphyroblasts during deformation has been intensely debated in the last decades. The debate has mainly focused on the kinematic significance of straight, sigmoidal or spiral-shaped inclusion trails that record a relative rotation between the porphyroblast and the matrix. Initially, such microstructures were assumed to record shearing-induced porphyroblast rotation (Fig. 1.1) (e.g. Zwart, 1960; Rosenfeld, 1970; Passchier et al., 1992). This model was, however, challenged by Bell (1985), Bell et al. (1986, 1992) or Bell and Johnson (1989), who argued that porphyroblasts generally nucleate and grow within microlithon domains where they maintain static orientations with respect to bulk kinematic axes (Fig. 1.1 and 1.2). Inclusion-trail curvature in this model is the result of folding/crenulation of the matrix foliation instead of porphyroblast rotation.

Numerical modelling has not allowed resolving the question as both rotational and non-rotational behaviour can be reproduced depending on the precise starting assumptions and deformation regimes considered (e.g. ten Grotenhuis et al., 2002; Fay et al., 2008; Bons et al., 2009; Sanislav, 2010; Griera et al., 2013). Detailed study of the geometry and orientation of inclusion-trails across meso- and macro-scale folds has also

led to mixed conclusions including major porphyroblast rotation (e.g. Zwart and Oele, 1966; Powell and MacQueen, 1976; Visser and Mancktelow, 1992; Busa and Gray, 1992), limited porphyroblast rotation (e.g. Timms, 2003) or no porphyroblast rotation (e.g. Forde and Bell, 1993; Bell and Forde, 1995; Bell and Hickey, 1997; Hickey and Bell, 1999; Aerden et al., 2010).

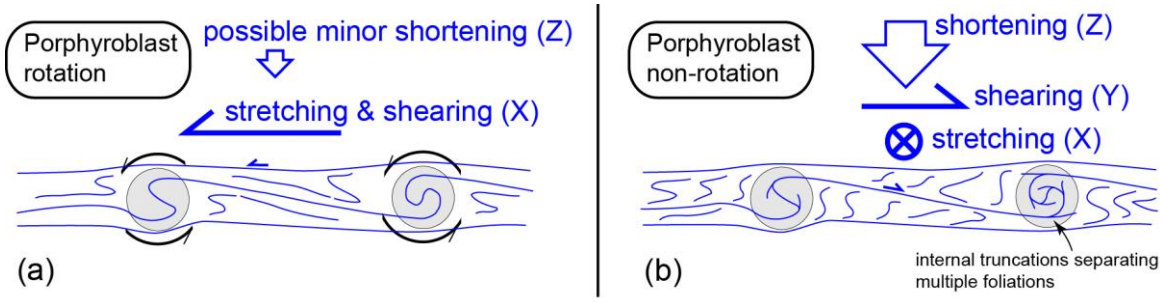

Fig. 1.1. Sketch illustrating rotational versus non-rotational interpretations of spiral-shaped inclusion trails (modified from Aerden et al., 2021). (a) Progressive (sub-)simple shear causing porphyroblast rotation in the direction of the maximum stretching axes (X). Clockwise inclusion-trail curvature indicates sinistral shearing. (b) In the non-rotational model spiral inclusion trails represent multiple sequentially overgrown crenulation cleavages formed by alternating subhorizontal and subvertical bulk shortening. Clockwise inclusion trail curvature indicates dextral shearing components associated with all shortening events, and the FIA can be parallel to the maximum stretching direction.

However, inclusion-trail orientations have increasingly been found to have remarkably consistent orientations on a regional scale and this clearly favours limited or no porphyroblast rotation, regardless the underlying causes. This has been shown both for simple, relatively straight inclusion trails (e.g. Fyson, 1980; Johnson, 1992; Aerden, 1995; Evins, 2005) as well as more complex inclusion trail patterns including the classic snowball garnet texture (e.g. Hayward, 1992; Bell et al., 1998; Cihan and Parsons, 2005; Sayab, 2005; Shah et al., 2011; Bell and Sapkota, 2012). Particularly relevant microstructural elements in these studies are the axes of inclusion-trail curvature or of inclusion-trail intersection in the case of porphyroblasts that overgrew two or more foliations showing truncational relationship. Such axes, known as Foliation Intersection- or Inflection Axes ("FIA"; Bell et al., 1995; Kim and Sanislav, 2017) represent a first-order kinematic indicator in rotational- and non-rotational porphyroblast models. In the first case, FIAs can be assumed to form normal to the shearing direction, whereas in the second case they should have formed normal to directions of bulk shortening. Therefore, given a large enough number of FIA data in a sufficiently large region, these microstructures have the potential to provide valuable information about the direction of large-scale tectonic transport or crustal shortening within an orogen. Note, however, that both models make different predictions about the sense of shear (tectonic transport), the degree of coaxiality of deformation and the number of deformation phases involved as summarized in Fig. 1.1.

Until recently, the standard technique for measuring FIAs consisted in studying sets of radial thin sections cut at regular angular intervals of a sample and recording the predominant asymmetry (i.e. curvature sense) of inclusion trails in each section

(Hayward, 1990; Bell et al., 1995). This allows the average trend and plunge of FIAs to be constrained with a precision that depends on the number and angular spacing of the thin sections used. However, application of this method can be problematic in rocks containing a mixture of two or more FIA sets with different orientations, or where FIAs are defined by roughly equal proportions of inclusion trails with opposite curvature senses (Aerden and Ruiz-Fuentes, 2020).

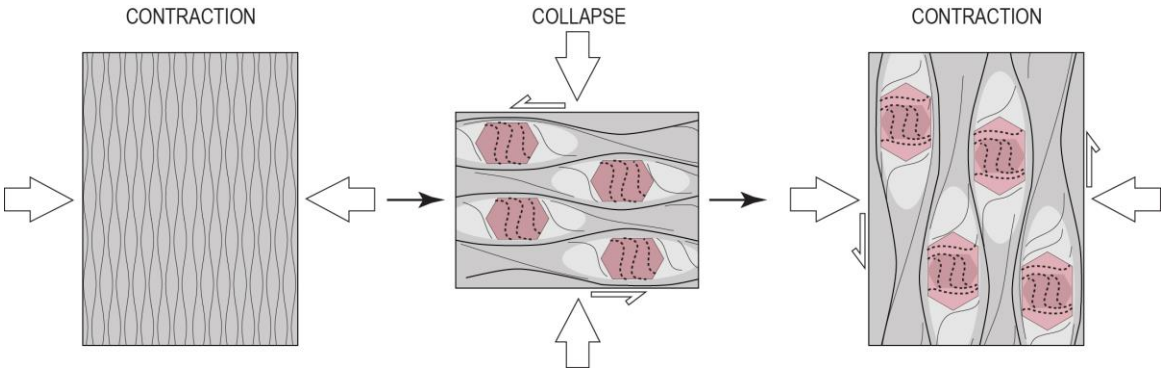

Fig. 1.2. Conceptual model showing the development of sigmoidal and spiral-shaped inclusion trails as predicted by the non-rotational model (modified from Aerden et al., 2022). Porphyroblasts nucleate and grow in microlithon domains and overgrow actively developing crenulations. Growth ceases when new cleavage planes intensify against porphyroblast rims. Spiral-shaped inclusion trails require a minimum of two successive crenulation events resulting from alternating crustal shortening and gravitational collapse.

The recent development of X-ray Computed Tomography (XCT) as a tool for micro-structural analysis of metamorphic rocks in 3D (e.g. Huddlestone-Holmes and Ketcham, 2005, 2010; Sayab et al., 2015) has greatly improved the objectiveness and precision of FIA data as it allows to measure FIAs of individual porphyroblasts and to assess their distribution and spread in a sample. This also eliminates the need of interpretative correlation of inclusion-trails between different porphyroblasts and thin sections, which in the case of complex inclusion trails can be a factor of uncertainty. A drawback of the technique is that the sharpness or definition of inclusion trails in XCT images is generally lower as in thin section, particularly in the case of very fine-grained graphitic inclusion trails, and that mineral phases with similar X-ray attenuation coefficients cannot be distinguished. Therefore, the technique is best used in combination with optical microscopy.

Regional-scale studies of FIA have commonly revealed the existence of several FIA sets with specific preferred orientations, from which a chronology of deformation episodes was established. Relative timing criteria include FIAs that change orientation from the core to the rim of single porphyroblasts, or the association of particular FIA sets with specific metamorphic minerals. Orogens where this methodology has been successfully applied include:

- The Alps (Bell et al., 1995).
- The Appalachians (Bell et al., 1998; Bell and Kim, 2004; Ham and Bell, 2004; Yeh and Bell, 2004; Rich, 2006; Sanislav, 2011).

- The Mount Isa Inlier of NE Australia (Mares, 1998; Kim and Bell, 2005; Sayab, 2005, 2008; Abu Sharib and Bell, 2011).
- The Georgetown Inlier of NE Australia (Cihan and Parsons, 2005).
- The Greenvale Province of NE Australia (Ali, 2010).
- The Kimberley Province of NW Australia (Bell and Mares, 1999).
- The Iberian Massif (Aerden, 2004)
- The French Armorican Massif (Aerden et al., 2021).
- The Bohemian Massif (Skrzypek et al., 2011).
- The Korean peninsula (Kim and Jung, 2010; Kim and Ree, 2013).
- The Himalaya (Shah et al., 2011; Bell and Sapkota, 2012; Sayab et al., 2016).
- The Rocky Mountains (Cao and Fletcher, 2012).
- The Betic Cordillera (Aerden et al., 2013).

Some of these studies have linked FIA data to radiometric metamorphic ages from monazite grains showing distinct textural relationships with garnet porphyroblasts (Bell and Welch, 2002; Cihan et al., 2006; Ali, 2010; Sanislav, 2011; Cao and Fletcher, 2012; Abu Sharib and Sanislav, 2013; Quentin de Gromard, 2013) or from garnet porphyroblasts themselves (Aerden et al. 2022).

1.3. Objectives

The main objective of this Ph.D. Thesis is to contribute to a better understanding of the tectonic evolution of the Betic Cordillera by integrating the information provided by porphyroblast inclusion trails in the regional tectonic framework. This includes the development of a methodology or workflow that allows inclusion trails to be routinely measured with the XCT technique on a regional scale. This data also provides a test for competing genetic models of sigmoidal/spiral-shaped inclusion trails (Aerden and Ruiz-Fuentes, 2020, Chapter 4).

Aerden and Sayab (2008) and Aerden et al. (2013) already studied the geometry and orientation of inclusion-trails in about 100 Nevado-Filábride samples, which were mostly collected in the western Sierra Nevada. However, they used relatively imprecise methods that extract 3D information from (2D) measurements made in differently oriented thin sections of single samples. The use of XCT in previously studied and new samples from the Nevado-Filábride Complex can help to better interpret the previous data and to check the homogeneity of the microstructural features in poorly explored areas of the complex (Appendix 10.2). Besides, in order to appropriately integrate this data into the tectonic evolution of the complex, a detailed study dealing with the structural relationships of multiple sets of foliations at regional scale is necessary, which has been done in several areas from Sierra Nevada and Sierra de los Filabres (Fig. 1.3; Ruiz-Fuentes and Aerden, 2018, Chapter 5; Chapter 6).

Aerden et al. (2022) published a large set of inclusion-trail data acquired with XCT and a series of Sm/Nd garnet ages, which revealed the existence of several sets of inclusion trails in the Betic-Rif orogen, each having a specific and regionally consistent

trend. Most of this data was collected in the Sebtide (Rif Mountains) and Nevado-Filábride complexes, whereas the Alpujárride remained under-represented in spite of being the largest of the three complexes in terms of total outcrop area. The scarceness of inclusion-trail data from the Alpujárride Complex motivated further study as part of this thesis. Inclusion trails were studied in the western and central sectors of the complex (partially included in Aerden et al., 2022), and complemented with detailed analyses of outcrop-scale deformation structures and fabrics in the same areas (Fig. 1.3; Ruiz-Fuentes and Aerden, 2023, Chapter 7).

In order to appropriately integrate macro- and micro-structural data in the tectonic framework of the Betic Cordillera, constraints on the timing and metamorphic conditions of the different deformation phases and inclusion-trail sets already recognized by Aerden et al. (2022) and Ruiz-Fuentes and Aerden (2023) are necessary, for which a petrological and geochronological study has been performed in selected samples (Fig. 1.3; Chapter 8).

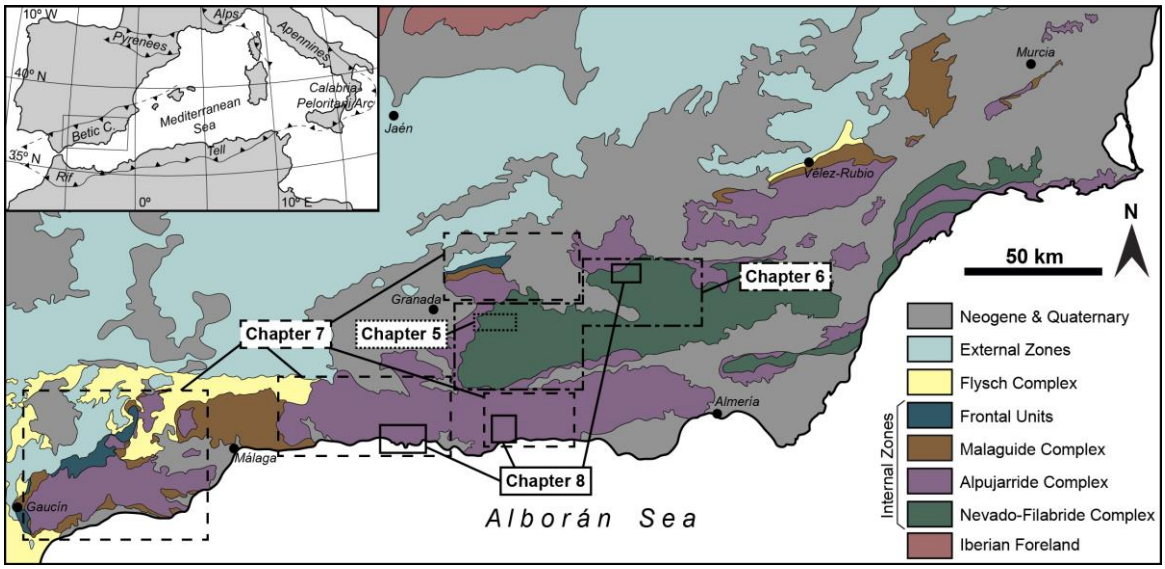

Fig. 1.3. Geological map of the Betic Cordillera. The squares indicate the areas studied in the chapters 5 to 8 of this Thesis. Chapter 4 has an essentially conceptual approach and only two samples have been studied, only one of them from the Betic Cordillera, so their locations have not been indicated.

1.4. Structure of the Ph.D. Thesis

This work is presented as a compendium of publications in agreement with the University of Granada guidelines, so the original structure and content of the published papers are maintained. The Ph.D. is divided in the following sections:

Part I presents the main issues addressed on the Ph.D. Thesis, the geological setting of the studied area and the applied methodologies.

- **Chapter 1. Introduction.** The use of porphyroblast inclusion trails to unravel tectonic histories. Objectives and structure of the Ph.D. Thesis.
- **Chapter 2. The Betic Cordillera.** Geological setting of the Betic Cordillera.

- **Chapter 3. Methodology.** Brief description of the methodologies used during the Ph.D. Thesis.

Part II contains the main results of the Ph.D. Thesis in the shape of published papers or manuscripts prepared for future submission.

- **Chapter 4. X-ray computed micro-tomography of spiral garnets: A new test of how they form.** 3D analysis of inclusion trails and shape of garnet porphyroblasts in two samples through X-ray Computed Tomography.
- **Chapter 5. Transposition of foliations and superposition of lineations during polyphase deformation in the Nevado-Filabride complex: tectonic implications.** Structural study focused on an area of the Nevado-Filábride Complex where different generations of foliations and lineations are superposed, complemented with microstructural data from porphyroblast inclusion trails.
- **Chapter 6. Structural analysis along four transects through the Nevado-Filábride Complex and implications for its internal structure.** Structural study along several transects of different sectors of the Nevado-Filábride Complex.
- **Chapter 7. Deciphering western Mediterranean kinematics using metamorphic porphyroblasts from the Alpujárride Complex (Betic Cordillera).** Micro- and macro-structural study of porphyroblast inclusion trails and late metamorphic structures in the western and central sectors of the Alpujárride Complex.
- **Chapter 8. Linking deformation, metamorphism and geochronology to constrain the tectonic evolution of the western Mediterranean.** Integration of microstructural, petrological and geochronological data to constrain the age and P-T conditions of several deformation episodes in the Betic Cordillera.

Part III contains the main conclusions of this work and additional data.

- **Chapter 9. Conclusions.** Main conclusions and forthcoming research derived from this work.
- **Chapter 10. Appendix.** Supporting information.

2. The Betic Cordillera

2.1. General features

The Betic Cordillera in southern Spain is located at the northern branch of the Gibraltar Arc, which constitutes the western end of the peri-Mediterranean Alpine orogenic system. The Rif Cordillera in northern Morocco is the southern continuation of the Betic Cordillera on the other side of the Gibraltar strait. The Gibraltar Arc is the result of a complex tectonic evolution controlled by the convergence between Iberia and Africa and the westward movement of the allochthonous Alborán Domain. The latter is derived from a continental terrane known as AlKaPeCa (Bouillin et al., 1986) or Mesomediterranean Terrane (Guerrera et al., 1993), whose original position, essentially east of Iberia, is debated (see review in Guerrera et al., 2021).

The Betic Cordillera is divided in three main domains, the External Zones, the Flysch Complex (or Campo de Gibraltar Complex), and the Internal Zones. The External Zones, divided in the Prebetic and Subbetic Domains, are mainly composed by Mesozoic and Cenozoic sedimentary rocks corresponding to shallow and deep marine environments of the South Iberian paleomargin (García-Hernández et al., 1980; Vera, 2004). Subvolcanic rocks (mainly dolerites) appear intruded in Triassic sediments (Puga et al., 1989; Morata, 1993), and volcanic rocks (mainly basaltic pillow lavas) of Jurassic to Cretaceous age are interbedded in the Subbetic sedimentary sequence (Puga et al., 1989; Portugal-Ferreira et al., 1995; Molina et al., 1998). The Flysch Complex includes Cretaceous to lower Miocene turbiditic deposits whose source area was the Alborán Domain (Mauretanian units) and the African continent (Massylian units) (e.g. Didon et al., 1973; Guerrera et al., 1993, 2012; Jabaloy-Sánchez et al., 2019). The Internal Zones are mainly composed of a stack of tectonically bounded metamorphic units which on ascending order are the Nevado-Filábride (Egeler, 1963), Alpujárride (van Bemmelen, 1927) and Maláguide (Blumenthal, 1927; Durand-Delga, 1964) complexes. Detached sedimentary covers of Triassic to Lower Miocene age from the two upper complexes are located at the front of the Internal Zones, and constitute the Frontal Units (Jabaloy-Sánchez et al., 2019). The Alpujárride and Maláguide complexes correspond to the allochtonous Alborán Domain, while the whole Nevado-Filábride, or at least its lower part, is considered part of the subducted South Iberian paleomargin (e.g. Guerrera et al., 1993; Platt et al., 2006; Puga et al., 2011; Gómez-Pugnaire et al., 2012; Rodríguez-Cañero et al., 2018). Poorly preserved small synorogenic basins developed in the early to middle Miocene, followed by deposition of thick upper Miocene sediments in wide intramontane basins (e.g. Sanz de Galdeano and Vera, 1992; Braga et al., 2003; Jabaloy-Sánchez et al., 2019). Calc-alkaline, shoshonitic, lamproitic and basaltic volcanic rocks of middle Miocene to Plio-

Pleistocene age appear in the eastern part of the cordillera (e.g. Turner et al., 1999; Duggen et al., 2004).

Paleogene orogenic activity in the Internal Zones is recorded by metamorphic ages (Platt et al., 2005; Homonnay et al., 2018; Aerden et al., 2022; Bessière et al., 2022; Poulaki et al., 2023) but the geodynamic context is poorly constrained. In the early Miocene, a westward moving Alborán Domain started to collide with the South Iberian paleomargin and to deform the External Zones and Flysch Complex into a thin-skinned fold-and-thrust belt rooted in Triassic clayey and evaporitic materials (e.g. Guezou et al., 1991; Crespo-Blanc and Campos, 2001; Platt et al., 2003a; Luján et al., 2006; Crespo-Blanc, 2007). The Flysch Complex was thrusted over the External Zones, but also back-thrusted over the Internal Zones at several points (e.g. Rodríguez-Fernández, 1982; Martín-Algarra, 1987; Geel and Roep, 1998; Martín-Algarra et al., 2009b) in the vicinity of the Internal-External Zones Boundary (IEZB). The IEZB itself can either be a thrust placing the Internal Zones over the External Zones (e.g. Martín-Algarra et al., 2009b), or a strike-slip fault zone (e.g. Sanz de Galdeano and López-Garrido, 2012), or a back-thrust placing the External Zones onto the Internal Zones (e.g. Lonergan et al., 1994; Jabaloy-Sánchez et al., 2007). Towards the central-western part of the cordillera, the northern limit of the Alpine front of the Subbetic Domain is gravitationally dismantled in the form of km-scale olistostromes emplaced onto, and later covered by, sediments of the southern margin of the Guadalquivir basin (e.g. Vera, 2004; Rodríguez-Fernández et al., 2013; Martínez del Olmo, 2019). Contrastingly, in the central-eastern sector, deformation is progressively attenuated towards the northern limit of the Alpine front of the Prebetic Domain (e.g. Dabrio and López-Garrido, 1970; Guezou et al., 1991), where it is adjacent to undeformed Triassic rocks of the Tabular Cover of the Iberian Massif (e.g. Gil et al., 1987; Pérez-López and Pérez-Valera, 2007).

2.2. The Internal Zones

Pre-Alpine (Variscan) deformation structures are well preserved in the Paleozoic basement of the Maláguide Complex (Foucault and Paquet, 1971; Balanyá, 1991; Cuevas et al., 2001; Martín-Algarra et al., 2009b; Ruiz-Fuentes et al., 2022), but in the two lower complexes only relics of pre-Alpine tectonism are preserved due to a much stronger Alpine overprint (e.g. Puga et al., 1975; Puga and Díaz de Federico, 1976; Argles et al., 1999; Zeck and Williams, 2001; Acosta-Vigil et al., 2014; Massonne, 2014; Ruiz-Cruz and Sanz de Galdeano, 2014; Sánchez-Navas et al., 2012, 2014, 2016, 2017).

The Alpujárride and Nevado-Filábride complexes are bounded by a subhorizontal detachment originally interpreted as a thrust (e.g. Egeler and Simon 1969), but later reinterpreted as extensional (Jabaloy et al., 1993; Martínez-Martínez et al., 2002). However, the contact places older rocks (e.g. Permian phyllites) of the Alpujárride complex over younger rocks (i.e. Mesozoic marbles) of the Nevado-Filábride sequence (Poulaki and Stockli, 2022 and references therein) implying an original thrust contact, which was either reactivated or cut at a low angle during late-orogenic extension.

The nature of the contact between the Maláguide and Alpujárride complexes depends on the area where it crops out. In the vicinity of the IEZB, for example near Gaucín, in the Sierra Arana, or Sierra Espuña, the contact is transitional typically involving a series of thrust sheets made of Palaeozoic-Triassic rocks of no clear attribution. These slices, called Alpujárride-Maláguide Transitional/Intermediate Units (Sanz de Galdeano et al., 1995a, 2001) or Epimetamorphic Maláguide Units (Roep and Mac Gillavry, 1962; Martín-Algarra, 1987, Navas-Parejo, 2012) can appear thrusted over Triassic carbonates of the Lower- or Intermediate Alpujárrides. At other locations, where the Maláguide Complex overlies Upper Alpujárride Units (e.g. Los Reales nappe at Fuengirola, or the Benamocarra Unit east of Málaga), the contact is difficult to pinpoint because of similar characteristics of the basal metapelites of the former (Morales Fm.) and underlying Alpujárride schists. To solve this problem, Boulin (1970), Aldaya et al. (1979) and Elorza and García-Dueñas (1981) interpret an intermediate Benamocarra Unit with transitional characteristics. In the area of Fuengirola, Tubía and Navarro-Vilá (1984) and Tubía (1988) situate the Alpujárride-Maláguide boundary immediately below a specific level of Maláguide metapelites with post-kinematic garnet and andalusite porphyroblasts (Tubía and Navarro-Vilá, 1984; Tubía, 1988).

The oldest unconformable deposits on top of the Internal Zones are Burdigalian in age (Rodríguez-Fernández, 1982; Martín-Algarra, 1987; Aguado et al., 1990; Alonso-Chaves and Rodríguez-Vidal, 1998) and make up the Viñuela Group. These sediments predate the Iberia-Alborán collision since they are back-thrusted by the Flysch Complex (Rodríguez-Fernández, 1982; Martín-Algarra, 1987; Jabaloy-Sánchez et al., 2019) that formerly separated both continental domains.

2.2.1. Nevado-Filábride Complex

2.2.1.1. Lithological succession and subdivision

Early workers in the Nevado-Filábride Complex (e.g. Brouwer, 1926; van Bemmelen, 1927; Fallot et al., 1960; Egeler, 1963) already distinguished a relatively homogeneous lower unit called Kristalline Schiefer (crystalline schists) (Brouwer, 1926) and a more heterogeneous upper unit called Mischungszone (mixed zone) (Brouwer, 1926). This initial subdivision was refined and renamed by Puga et al. (1974, 2002) as the Veleta- and Mulhacén nappes/complexes, first in the Sierra Nevada area and later extended to the Sierra de los Filabres. These authors further subdivide the Mulhacén complex into the Caldera-, Ophiolite- and Sabinas- units (in ascending order) apart from certain levels of calcareous breccia (Soportújar formation) interpreted as intra-orogenic sediments. In the Sierra de los Filabres, several local subdivisions have been proposed (e.g. Nijhuis, 1964; Kampschuur, 1975; Linthout and Vissers, 1979; de Jong and Bakker, 1991; Zevenhuizen, 2022). These were correlated and/or grouped by García-Dueñas et al. (1987) into a lower Calar Alto unit and upper Bédar-Macael unit that together would constitute the Mulhacén complex. Martínez-Martínez et al. (2002) presented a significantly revised map interpretation of the Veleta-Mulhacén contact in the Sierra Nevada with respect to the previous 1:50,000 Spanish geological map, and renamed the Veleta nappe as Ragua unit

since they consider the 3396 m high Veleta peak itself to be composed of Calar Alto rocks. Several authors have argued that the Nevado-Filábride sequence is essentially stratigraphic and does not contain major internal tectonic contacts (Galindo-Zaldivar et al., 1989; Jabaloy et al., 1993; Gómez-Pugnaire et al., 2000, 2004, 2012; Sanz de Galdeano and López-Garrido, 2016a; Santamaría-López and Sanz de Galdeano, 2018; Santamaría-López et al., 2019).

The Nevado-Filábride lithostratigraphic sequence consists of a thick lower succession of Paleozoic (Lafuste and Pavillon, 1976; Laborda-López et al., 2015; Jabaloy-Sánchez et al., 2018; Poulaki and Stockli, 2022) graphite schists and dark quartzites locally interbedded with graphitic marbles, which all together constitute the Veleta- or Ragua unit. Similar graphite schists are also present in the Mulhacén nappe but these contain characteristic cm- to dm-sized pseudomorphed porphyroblasts of pre-Alpine origin (Puga et al., 1975; Puga and Díaz de Federico, 1976). These rocks are overlain by a Permo-Triassic to Jurassic series of light coloured quartzites and schists with a metaconglomerate level at the base (Tahal Fm.), calc-schists, metaevaporite levels, graphite schists and marbles (Tendero et al., 1993; Jabaloy-Sánchez et al., 2018; Poulaki and Stockli, 2022). Lenses of sheared ultra-mafic rocks, eclogites and amphibolites of Jurassic igneous origin (Puga et al., 2011), and felsic gneisses of late-Paleozoic age (Priem et al., 1966; Andriessen et al., 1991; Nieto et al., 2000; Gómez-Pugnaire et al., 2000, 2004, 2012; Martínez-Martínez et al., 2010) appear throughout the Nevado-Filábride sequence but concentrated in the Mulhacén unit. Along the Alpujárride detachment and at some deeper levels, lenses of calcareous breccias (rauhwacke) are found, originally called “Konglomeratische mergel” (Brouwer, 1926), containing clasts of underlying Nevado-Filábride rocks. Their presence along a major detachment is consistent with a tectonic/cataclastic origin (e.g. Brouwer, 1926; Leine, 1968; Martínez-Martínez, 1986a, 2007; Galindo-Zaldívar, 1990), although a sedimentary origin has also been considered (Puga et al., 1996; Orozco et al., 1999).

2.2.1.2. Tectono-metamorphic evolution

The deformation sequence in the Nevado-Filábrides is debated. The main foliation transposes an older fabric that developed under eclogite to amphibolite facies conditions (Fig. 2.1; Bakker et al., 1989; Augier et al., 2005a, 2005b; Booth-Rea et al., 2015; Jabaloy-Sánchez et al., 2015). The main foliation appears itself crenulated and locally transposed under greenschist facies conditions (Fig. 2.1; Bakker et al., 1989; González-Casado et al., 1995; Augier et al., 2005a, 2005b; Behr and Platt, 2012; Booth-Rea et al., 2015; Jabaloy-Sánchez et al., 2015). Some authors distinguish several crenulation- and folding phases post-dating the main foliation (e.g. Bakker et al., 1989; de Jong, 1993; Aerden and Sayab, 2008), while others do not apply such distinctions (e.g. Galindo-Zaldivar et al., 1989; Jabaloy et al., 1993; Augier et al., 2005c; Booth-Rea et al., 2015). The latest fabrics are ductile-brittle S-C structures associated to the activity of extensional detachments (e.g. Jabaloy et al., 1993; Augier et al., 2005c), still followed by large-wavelength folding (Jabaloy et al., 1993; Martínez-Martínez et al., 2002) and low-angle faulting locally placing Nevado-Filábride rocks on top of the Alpujárride Complex (Voet,

1964; Langenberg, 1973; Orozco et al., 1999). Regarding the distribution of strain within the complex, some authors interpret a progressive upwards strain gradient towards the Alpujárride Complex (Galindo-Zaldivar et al., 1989; Jabaloy et al., 1993), whereas others interpret several wide shear zones within the complex coinciding with the boundaries between inferred tectonic units (García-Dueñas et al., 1988; Martínez-Martínez et al., 1995, 2002; Augier et al., 2005c; Martínez-Martínez, 2007; Behr and Platt, 2012; Booth-Rea et al., 2015).

Kinematic interpretations of the main foliations are quite variable ranging from top-to-the-ENE (Campos et al., 1986; Orozco, 1986), –E followed by –NW (Martínez-Martínez, 1986b), –NW to –WSW (García-Dueñas et al., 1987), –W to –SW (Jabaloy et al., 1993; González-Casado et al., 1995; Augier et al., 2005c; Martínez-Martínez, 2007), –SSW followed by –WSW (Behr and Platt, 2012), or –NNW followed by –W (Porkoláb et al., 2022). A more complex (polyphase) tectonic evolution involving several changes in the direction crustal shortening direction has been deduced from porphyroblast inclusion trails (Aerden et al., 2013; Aerden et al., 2022).

The Nevado-Filábride Complex experienced early eclogite- and blueschist-facies metamorphism but extensively re-equilibrated under amphibolite- and greenschist- facies conditions. In general, the metamorphic grade increases towards the upper part of the complex. The precise metamorphic trajectory of the complex and its timing are controversial as can be appreciated from the variable P-T-t paths of previous authors shown in Fig. 2.1. Most authors interpret a single metamorphic loop but some envisage two loops, the first of which would have reached higher pressures (Puga et al., 2000; Li and Massonne, 2018). P-T-t paths differ notably regarding the thermal history during decompression/exhumation with proposals ranging from nearly isothermal (Augier et al., 2005a, 2005b; Ruiz-Cruz et al., 2015; Li and Massonne, 2018 for their first loop), cooling (Gómez-Pugnaire et al., 1994; Puga et al., 2000; Behr and Platt, 2012), heating (Gómez-Pugnaire and Fernández-Soler, 1987; Santamaría-López et al., 2019), or cooling followed by re-heating (Bakker et al., 1989; Booth-Rea et al., 2015). The precise timing of metamorphic events also remains debated in view of a large spread of Eocene to Middle-Miocene radiometric ages, which are summarized in Fig. 2.2 (Monié et al., 1991; Augier et al., 2005a; Puga et al., 2005; Platt et al., 2006; Kirchner et al., 2016; Li and Massonne, 2018; Aerden et al., 2022; Porkoláb et al., 2022; Poulaki et al., 2023).

2.2.2. Alpujárride Complex

2.2.2.1. Lithological succession and subdivision

The typical lithostratigraphic sequence of the Alpujárride Complex comprises a Paleozoic basement consisting of migmatites and gneisses overlain by graphite schists and quartzites. The sedimentary cover of this basement includes light-coloured schists, quartzites and phyllites of Permo-Triassic age (Esteban et al., 2023) and Triassic carbonates (e.g. Kozur et al., 1974; Braga and Martín, 1987). However, this succession presents specific peculiarities and variations in different tectonic units as seen below.

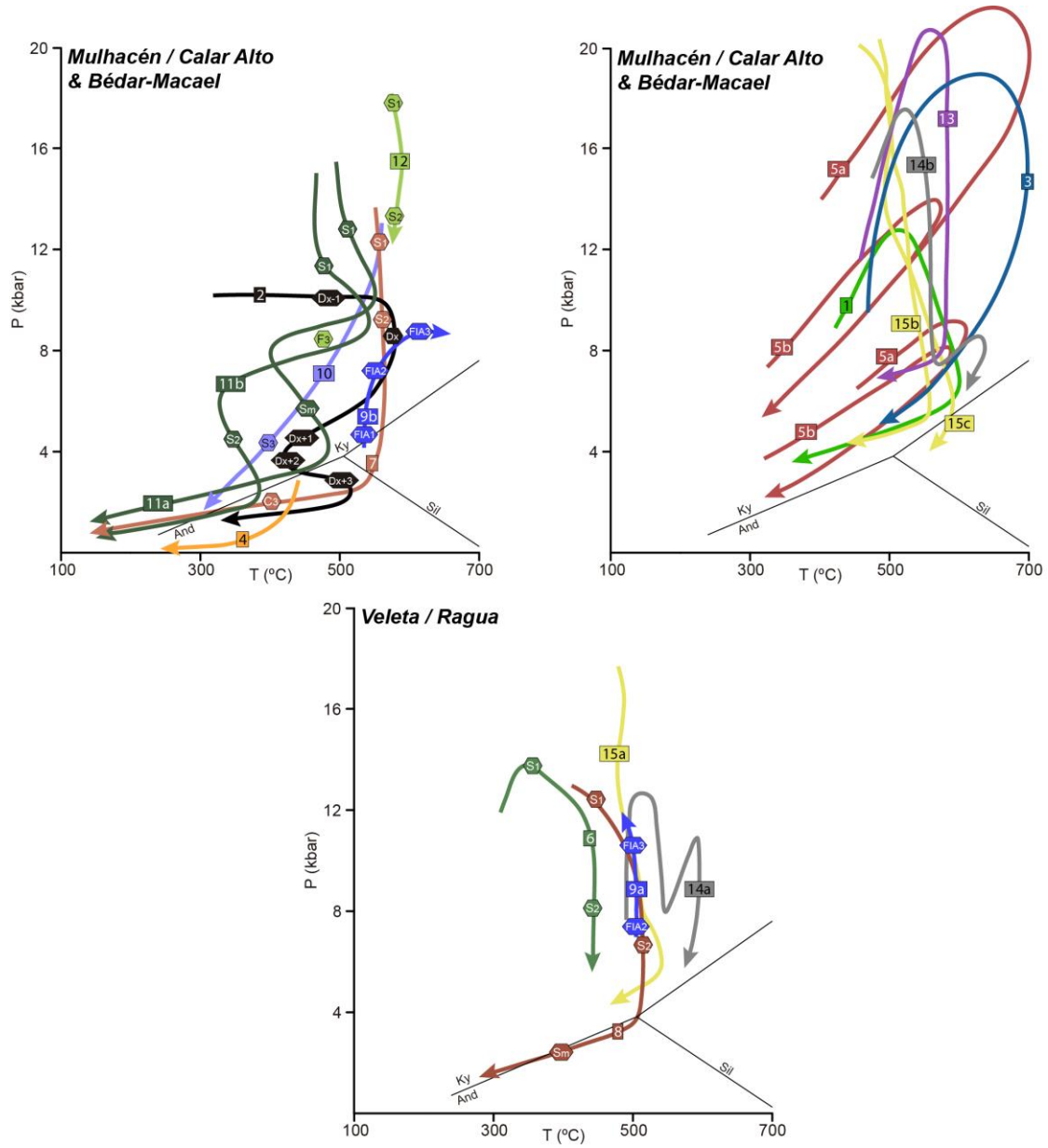

Fig. 2.1. P-T-t paths of the different tectonic units of the Nevado-Filábride Complex. The paths of the Mulhacén/Calar Alto and Bédar-Macael units have been represented in different diagrams in function of the existence or not of deformation constraints. The hexagons indicate the position of the deformation phase interpreted by the authors. While the hexagons are located in an average position for clarity, the original authors may have interpreted a larger area for the deformation phase. (1) metabasites, Sª de Baza (Gómez-Pugnaire and Fernández-Soler, 1987); (2) Mulhacén nappe, eastern Sª de los Filabres (Bakker et al., 1989); (3) metaevaporites, Cóbdar area (Gómez-Pugnaire et al., 1994); (4) quartz segregations, Dos Picos shear zone (González-Casado et al., 1995); (5) eclogites and amphibolites, a: Lugros and b:Cóbdar areas (Puga et al., 2000); (6) metapelites, eastern Sª Nevada (Booth-Rea et al., 2003); (7) metapelites, Sª de los Filabres (Augier et al., 2005a); (8) metapelites, Sª Nevada and Sª de los Filabres (Augier et al., 2005b); (9) metapelites from a: Veleta, b: Ophiolite unit, Sª Nevada and Sª de Baza (Aerden et al., 2013); (10) Mulhacén nappe, Sª Alhamilla (Behr and Platt, 2012); (11) metapelites from a: Calar Alto base, b: Calar Alto top, eastern Sª Nevada and Sª de los Filabres (Booth-Rea et al., 2015); (12) Tahal schist, eastern Sª Nevada (Jabaloy-Sánchez et al., 2015); (13) schists, gneisses and eclogites, western Sª Nevada (Ruiz-Cruz et al., 2015); (14) metapelites from a: Ragua, b: Calar Alto, western Sª Nevada (Li and Massonne, 2018); (15) metapelites from a: Ragua, b: Calar Alto, c: Bédar-Macael, western and central Sª Nevada (Santamaría-López et al., 2019).

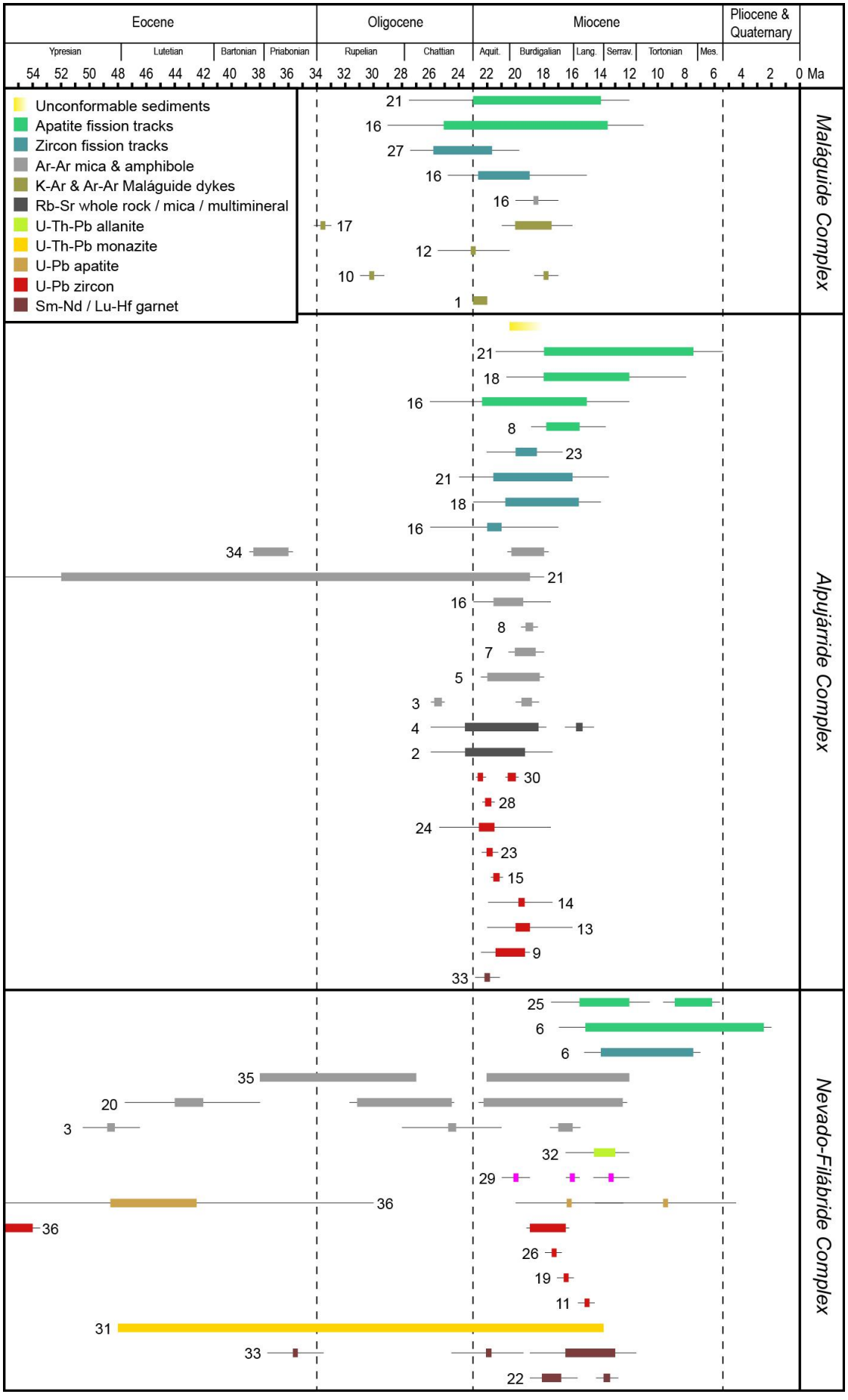
Eocene
Oligocene
Miocene
Pliocene & Quaternary
Ypresian
Lutetian
Bartonian
Priabonian
Rupelian
Chattian
Aquit.
Burdigalian
Lang.
Serrav.
Tortonian
Mes.
54 52 50 48 46 44 42 40 38 36 34 32 30 28 26 24 22 20 18 16 14 12 10 8 6 4 2 0 Ma
Unconformable sediments
Apatite fission tracks
Zircon fission tracks
Ar-Ar mica & amphibole
K-Ar & Ar-Ar Maláguide dykes
Rb-Sr whole rock / mica / multimineral
U-Th-Pb allanite
U-Th-Pb monazite
U-Pb apatite
U-Pb zircon
Sm-Nd / Lu-Hf garnet
Maláguide Complex
Alpujárride Complex
Nevado-Filábride Complex

Fig. 2.2 (previous page). Radiometric ages obtained in the Internal Zones from Eocene to Quaternary: (1) Torres-Roldán et al., 1986; (2) Zeck et al., 1989; (3) Monié et al., 1991; (4) Zeck et al., 1992; (5) Monié et al., 1994; (6) Johnson et al., 1997; (7) Platt et al., 1998; (8) Sosson et al., 1998; (9) Platt and Whitehouse, 1999; (10) Turner et al., 1999; (11) Lopez Sánchez-Vizcaíno et al., 2001; (12) Platzman et al., 2000; (13) Sánchez-Rodríguez and Gebauer, 2000; (14) Zeck and Williams, 2001; (15) Whitehouse and Platt, 2003; (16) Platt et al., 2003b; (17) Duggen et al., 2004; (18) Esteban et al., 2004; (19) Gómez-Pugnaire et al., 2004; (20) Augier et al., 2005a; (21) Platt et al., 2005; (22) Platt et al., 2006; (23) Esteban et al., 2007; (24) Esteban et al., 2011; (25) Vázquez et al., 2011; (26) Gómez-Pugnaire et al., 2012; (27) Esteban et al., 2013; (28) Sánchez-Navas et al., 2014; (29) Kirchner et al., 2016; (30) Frasca et al., 2017; (31) Li and Massonne, 2018; (32) Santamaría-López et al., 2019; (33) Aerden et al., 2022; (34) Bessière et al., 2022; (35) Porkoláb et al., 2022; (36) Poulaki et al., 2023. Ages of unconformable sediments from: González Donoso et al., 1982; Aguado et al., 1990; Comas et al., 1992; Alonso-Chaves and Rodríguez-Vidal, 1998; Rodríguez-Fernández et al., 1999.

The Alpujárride Complex is generally considered to be formed by a stack of lithotectonic units, but no consensus exists regarding the exact boundaries between these units (e.g. García-Dueñas and Navarro-Vilá, 1976 and Sanz de Galdeano et al., 1995a north of Sierra Nevada), their relative tectonic positions (e.g. peridotites of Sierra Alpujata and Sierra Bermeja with respect to adjacent Guadaiza and Ojén nappes, Tubía and Cuevas, 1986; Esteban et al., 2008; Mazzoli and Martín-Algarra, 2011; Sanz de Galdeano and López Garrido, 2016b; Sanz de Galdeano, 2017), spatial correlation (e.g. Aldaya et al., 1979; Simancas and Campos, 1993; Azañón et al., 1994; Sanz de Galdeano and López-Garrido, 2003) and even their true existence (Williams and Platt, 2017, 2018). Lithotectonic units were originally defined in restricted areas, and later correlated across the complex in ways that vary in detail (e.g. Aldaya et al., 1979; Azañón et al., 1994; Sanz de Galdeano and López-Garrido, 2003) but coincide regarding the distinction of three main (Lower-, Intermediate- and Upper-) Alpujárride units (Tubía et al., 1992; Martín-Algarra et al., 2004).

The Lower Alpujárride units (Fig. 2.3) include the locally defined Lújar-Gádor-, Escalate- (Azañón et al., 1994), and the Lújar-, Cástaras-, Alcázar- (Aldaya, 1969), Víboras- (Gallegos, 1975), Padules- or La Mora units (Sanz de Galdeano et al., 1995a, b). These units are mainly composed of Permo-Triassic phyllites and Triassic carbonates, although younger strata (Jurassic to Oligocene) are also found in the La Mora unit (Durand-Delga and Magné, 1961; García-Dueñas and Navarro-Vilá, 1976; Sanz de Galdeano et al., 1995b).

The Intermediate Alpujárride units (Fig. 2.3) include the Tejeda- (Aldaya et al., 1979), Herradura- (Avidad and García-Dueñas, 1972), Trevenque- (Gallegos, 1975), Blanquizares- (Sanz de Galdeano et al., 1995a), Guadaiza-, Ojén- (Navarro-Vilá and Tubía, 1983) or Yunquera- (Dürr, 1967) nappes/units. The Ojén nappe contains amphibolites and eclogites with Jurassic protolith ages (Tubía and Gil-Ibarguchi, 1991; Sánchez-Rodríguez and Gebauer, 2000). In the Guadaiza and Ojén nappes, migmatites and mylonites in the upper part of the unit dated at 22 Ma have been related to emplacement of the overlying Ronda peridotites of the Upper Alpujárride Los Reales nappe (Tubía and Cuevas, 1986; Tubía, 1988; Tubía et al., 1997; Esteban et al., 2011).

The base of the Guadaiza nappe is composed of pre-Alpine migmatites (Istán migmatites: Tubía, 1988: Esteban et al., 2008; Acosta-Vigil et al., 2014).

The Upper Alpujárride units (Fig. 2.3) comprise, amongst others, the Adra- (Aldaya, 1969), La Plata- (García-Dueñas and Navarro-Vilá, 1976), Hernán Valle- (Comas et al., 1979), Guájares- (Avidad and García-Dueñas, 1972), Sayalonga- (Aldaya et al., 1979), or Los Reales- (Navarro-Vilá and Tubía, 1983) nappes/units. The Los Reales nappe in the western Betics includes a basal peridotite slab overlain by a crustal section which comprises in ascending order: a Paleozoic basement with granulites (also known as kinzigites), migmatites, high-grade gneisses, medium-grade graphite schists and quartzites, whereas the generally lower-grade Permo-Triassic sequence is less well-represented as in the Lower and Intermediate units.

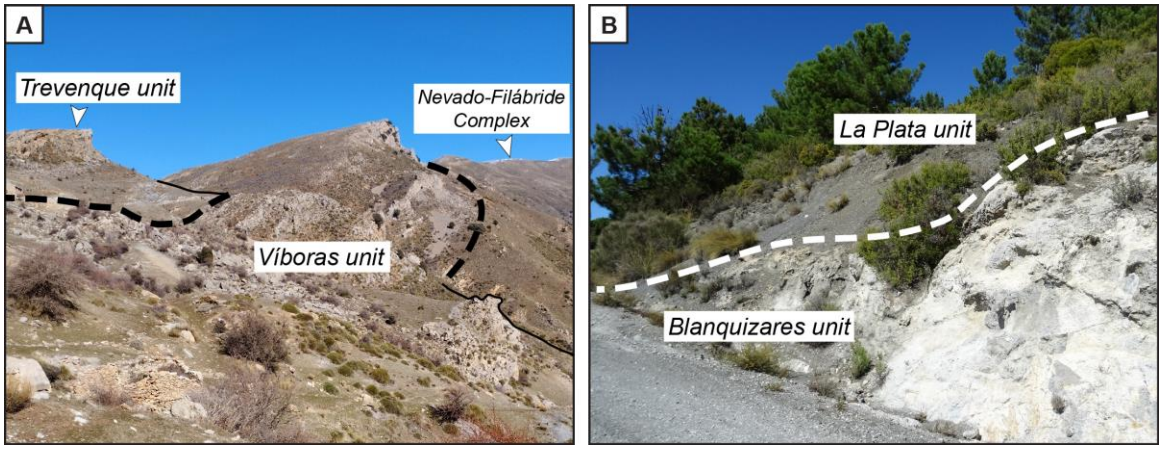

Fig. 2.3. Superposition of tectonic units on the Alpujárride Complex. Dashed lines indicate the tectonic contacts. A) Phyllites and carbonates of the Trevenque unit (Intermediate Alp.) overlie carbonates of the Víboras unit (Lower Alp.). B) Graphite schists of the La Plata unit (Upper Alp.) rest on top of carbonates of the Blanquizares unit (Intermediate Alp.).

2.2.2.2. Tectono-metamorphic evolution

The early Alpine tectonic evolution is characterized by subduction-related HP/LT and HP metamorphism (Fig. 2.4) locally reaching eclogite facies conditions (e.g. Tubía and Gil-Ibarguchi, 1991; Azañón and Goffé, 1997; Balanyá et al., 1997; Sánchez-Rodríguez and Gebauer, 2000; Azañón and Crespo-Blanc, 2000; Booth-Rea et al., 2002a, 2005). Although the corresponding deformation is traditionally labelled "D_1", recent microstructural analysis of "S_1" inclusion trails indicates a complex polyphase deformation history preceding S_2 (Aerden et al., 2022), which is also the object of this thesis. The timing of peak-pressure conditions is still debated with interpretations ranging from Eocene (Platt et al., 2005; Bessière et al., 2022) based on Ar-Ar mica ages, to late-Oligocene or even Early Miocene based on monazite and zircon ages in high-grade rocks (Sánchez-Rodríguez and Gebauer, 2000; Massonne, 2014).

Decompression during D_2 deformation (Fig. 2.4) was accompanied by sillimanite growth in the higher-grade rocks (e.g. Cuevas, 1989b; Balanyá et al., 1997; Azañón et al., 1998; Williams and Platt, 2017) and the development of a pervasive S_2 foliation that

commonly is the main foliation in outcrop. Associated structures include small-scale isoclinal folds, crenulation- and mineral-lineations, and large-scale folds in the Sierra de Lújar (Simancas, 2018). Radiometric dating through U-Pb on zircon rims (Platt and Whitehouse, 1999; Zeck and Williams, 2001; Whitehouse and Platt, 2003; Esteban et al., 2007), Rb-Sr on whole rock and micas (Zeck et al., 1989; Zeck et al., 1992) and Ar-Ar on micas (Monié et al., 1991, 1994; Sosson et al., 1998; Platt et al., 1998, 2003b, 2005; Bessière et al., 2022) indicate and early Miocene age (22-18Ma) of D_2 and the associated high-temperature metamorphism.

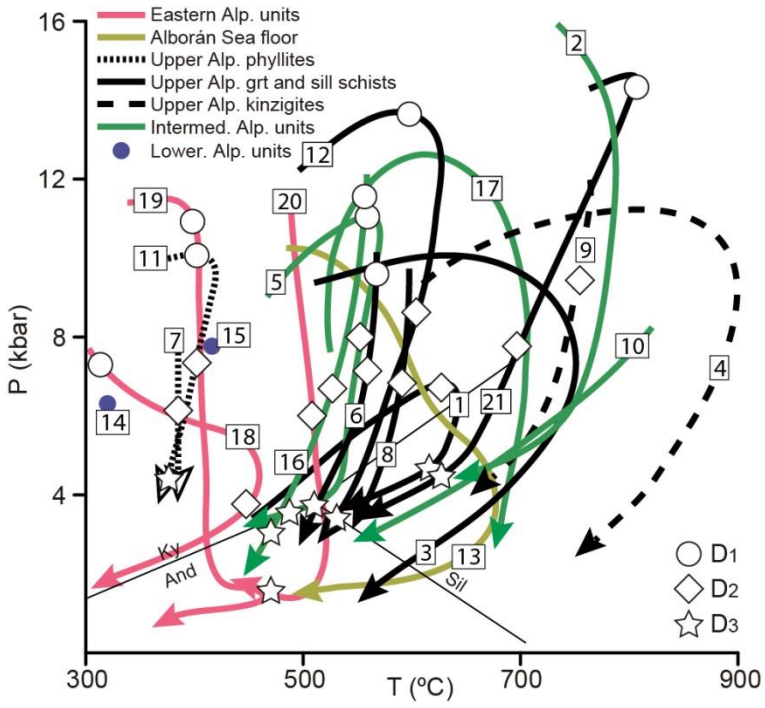

Fig. 2.4. P-T-t paths and P-T estimations for several units of the Alpujárride Complex. Stars, diamonds and circles represent the interpreted position of each deformation phase: (1) Adra nappe (Cuevas, 1989b); (2) Eclogites, Ojén nappe (Tubía and Gil-Ibarguchi, 1991); (3) sillimanite schists, Los Reales nappe near Fuengirola (Tubía, 1994); (4) kinzigites, Los Reales nappe near Fuengirola (Tubía, 1994); (5) light coloured schists, Tejeda unit (Azañón and Alonso-Chaves, 1996); (6) garnet schists, Adra nappe (Azañón et al., 1997); (7) phyllites, Jubrique unit (Balanyá et al., 1997); (8) sillimanite schists, Jubrique unit (Balanyá et al., 1997); (9) kinzigites, Jubrique unit (Balanyá et al., 1997); (10) quartz-feldspathic mylonites, Ojén nappe (Tubía et al., 1997); (11) phyllites, Salobreña unit (Azañón et al., 1998); (12) sillimanite schists, Salobreña unit (Azañón et al., 1998); (13) metamorphic rocks from the Alborán Sea floor (Soto and Platt, 1999); (14) phyllites, Lújar-Gádor unit (Azañón and Crespo-Blanc, 2000); (15) phyllites, Escalate unit (Azañón and Crespo-Blanc, 2000); (16) light coloured schists, Herradura unit (Azañón and Crespo-Blanc, 2000); (17) Yunquera unit (Esteban et al., 2005); (18) Almanzora unit (Booth-Rea et al., 2005); (19) fine-grained schists of the Variegato unit (Booth-Rea et al., 2005); (20) garnet graphite schists of the Variegato unit (Booth-Rea et al., 2005); (21) Bentomiz unit, Torrox area (Alonso-Chaves and Orozco, 2007).

The kinematics of D_2 as interpreted by different authors in different areas from lineations and shear-sense criteria vary considerably including top-to-the-N in Sierra de las Estancias (Akkerman et al., 1980); top-to-the-NE in the eastern Alpujárrides (Tubía et al., 1992); top-to-the-N/ENE in the Contraviesa area (Azañón et al., 1997); coaxial flattening in the Jubrique area (Balanyá et al., 1997); top-to-the-NE/N for the Almuñécar

and Contraviesa areas (Rossetti et al., 2005); top-to-the-ENE in the Almuñécar area (Williams and Platt, 2017); top-to-the-NE for both Almuñécar and Contraviesa areas (Simancas, 2018); top-to-the-E in the western Betics, and a swing from top-to-the-ESE in Torrox to top-to-the-ENE in Almuñécar (Williams and Platt, 2018). These interpretations require critical revision as they are based on broad orientation maxima and significant local variations are ignored. For this reason Azañón and Crespo-Blanc (2000) and Alonso-Chaves and Orozco (2007) did not interpret the kinematic axes of D_2. A more fundamental problem is that the large majority of kinematic interpretations are based on the unproven assumption that stretching lineations resulted from shearing rather than relatively coaxial deformation as discussed by Aerden et al. (2022).

The retrograde metamorphic evolution of the Alpujárride Complex is characterized by andalusite growth (Fig. 2.4) (e.g. Cuevas, 1989b; Balanyá et al., 1997; Azañón et al., 1998; Williams and Platt, 2017) associated with the development of major recumbent folds (D_3), whose geometry and origin by extension or compression have been debated since several decades (e.g. Tubía et al., 1992, 1993; Simancas and Campos, 1993; Balanyá et al., 1993, 1997, 1998; Azañón et al., 1997; Orozco et al., 1998; Platt, 1998; Azañón and Crespo-Blanc, 2000; Orozco et al., 2004; Williams and Platt, 2017, 2018; Simancas, 2018).

In the Jubrique area, Balanyá et al. (1997) recognized a crenulation cleavage associated with flattening. In the Fuengirola area, Tubía et al. (1993) and Tubía (1994) describe post-D_2 SC structures and shear zones with ESE stretching lineations attributed to crustal extension or transtension prior to top-to-the-ENE thrust emplacement of the peridotites. In the Torrox area, Alonso-Chaves and Orozco (2007, 2012) recognize the presence of a sub-horizontal crenulation cleavage associated with recumbent folds with highly variable orientations and interpreted them as extensional. Around Almuñécar, Simancas and Campos (1993) and Simancas (2018) describe numerous NNW-vergent recumbent folds which they interpreted as compressional. Azañón et al. (1998) attribute S_3 crenulation cleavage and associated ENE-WSW to E-W trending folds to compression, but in the same area Williams and Platt (2017, 2018) interpret an extensional origin of these structures. In the Contraviesa area, Cuevas (1991) reported several mylonitic high-strain zones within the Adra nappe, and attributed them to D_3 top-to-the-NE thrusting. Simancas and Campos (1993), however, interpreted these thrusts as post-D_3 semi-brittle structures with N-directed transport. Azañón et al. (1997) interpreted the lithological changes which Cuevas (1991) and Simancas and Campos (1993) related to thrusting, to a late set of low-angle normal faults. Nevertheless, Cuevas (1991), Simancas and Campos (1993) and Azañón et al. (1997) all agreed on a contractional origin of D_3 folds, as Rossetti et al. (2005) did in the Contraviesa and Almuñécar areas. In contrast, Orozco et al. (1998, 2004, 2017) proposed and extensional origin of D_3 folds. Post-metamorphic low-angle faults (D_4) affect the entire Alpujárride Complex and are also susceptible to discussion of whether they are thrusts or low-angle normal faults (e.g. Cuevas et al., 1986; Cuevas, 1991; Simancas and Campos, 1993; Crespo-Blanc et al., 1994; Crespo-Blanc, 1995; Azañón and Crespo-Blanc, 2000; Simancas, 2018).

2.2.3. Maláguide Complex

The Maláguide Complex is composed of Paleozoic marine sediments, continental Triassic redbeds, and a Jurassic to Lower Miocene marine series. It records both Variscan and Alpine tectonic events (Foucault and Paquet, 1971; Felder, 1981; Balanyá, 1991; Cuevas et al., 2001; Martín-Algarra et al., 2009b, 2019; Ruiz-Fuentes et al., 2022). Pre-Alpine features are relatively well-preserved given the weak Alpine metamorphic overprint. Two pre-Alpine deformation events have been described in several areas where detailed studies have been performed, near Gaucín (Balanyá, 1991), Ardales (Martín-Algarra et al., 2009b) Montes de Málaga (Cuevas et al., 2001, Martín-Algarra et al., 2019) and NE of Granada (Ruiz-Fuentes et al., 2022).

During the Alpine evolution, several deformation events affected the complex. An initial contractional event generated an intra-Maláguide thrust stack leading to the superposition of the Maláguide on top of the Alpujárride Complex, and differentiation of the main Alpine Maláguide units (e.g. Roep and Mac Gillavry, 1962: Casolidad, Cerro Colorado, Castillones and Salud units; Martín-Martín and Martín-Algarra, 1997: Morrón de Totana and Perona units; Booth-Rea et al., 2004: Lower- and Higher-Maláguide units; Martín-Algarra et al., 2009a: Ardales-Mojón and Castillejos-Turón units; Navas-Parejo, 2012 and Ruiz-Fuentes et al., 2022: Epimetamorphic, Lower and Upper Maláguide units). A slaty cleavage and NW- to N-directed thrusts developed during this episode (e.g. Lonergan, 1993; Martín-Martín and Martín-Algarra, 1997; Booth-Rea et al., 2004; Fernández-Fernández et al., 2007; Martín-Rojas et al., 2007; Ruiz-Fuentes et al., 2022), whose age is debated as Eocene (Lonergan, 1993; Fernández-Fernández et al., 2007) or Oligocene (Martín-Martín and Martín-Algarra, 1997; Martín-Rojas et al., 2007). Following the first contractional event, some authors interpret an extensional episode (Booth-Rea et al., 2004; Fernández-Fernández et al., 2007; Esteban et al., 2013) while others recognize renewed thrusting (Lonergan, 1993; Martín-Martín and Martín-Algarra, 1997; Martín-Rojas et al., 2007) in the Oligocene-Lower Miocene.

Associated to the collision of the Internal Zones with the South Iberian palaeomargin, south-vergent structures (Sanz de Galdeano et al., 1995a; Fernández-Fernández et al., 2007; Ruiz-Fuentes et al., 2022) developed in the Maláguide Complex in the northeastern Betic Cordillera, where the IEZB is a SSE/SE-directed backthrust (Lonergan et al., 1994; Jabaloy-Sánchez et al., 2007) developed during the Lower-Middle Miocene (Martín-Algarra, 1987; Lonergan et al., 1994; Sanz de Galdeano et al., 1995a; Martín-Martín et al., 1996; Fernández-Fernández et al., 2007).

Strike-slip faults accommodating the westward displacements of the Internal Zones during the Middle Miocene developed within and also delimit the Maláguide Complex in areas close to the IEZB (Balanyá, 1984; Sanz de Galdeano and López-Garrido, 2016c; Ruiz-Fuentes et al., 2022). These structures were still followed by Upper Miocene SW-directed normal faults and extensional detachments (Booth-Rea et al., 2002b, 2004; Ruiz-Fuentes et al., 2022).

3. Methodology

3.1. Field work

Detailed structural analysis of outcrop-scale structures was performed at the areas indicated in Fig. 1.3. The orientations of foliations, crenulation cleavages, axial planes of folds, fold axes and lineations were systematically measured and combined in several regional-scale structural cross sections. Field work was complemented with study of about 200 oriented samples, most of which contain garnet-, staurolite-, plagioclase- and/or andalusite porphyroblasts. The FIA of these porphyroblasts were measured using thin sections and XCT scans following the procedures detailed below. Outcrops with well-developed porphyroblast inclusion trails specified in some previous works (e.g. Cuevas, 1989a; Williams and Platt, 2018) were specifically targeted.

3.2. Sample processing

In the laboratory, each sample is first re-oriented in a sand-box. Subsequently, a horizontal marker line is drawn around the samples with the aid of a thin rigid board and a permanent marker pen or white-paint pen. The next step is drawing a second line around the sample representing its intersection with a vertical N-S striking plane and an arrow indicating north. The marked-up sample is then cut with a diamond saw (Fig. 3.1a) in order to obtain one or several precisely oriented rectangular blocks to make thin-sections of.

Samples lacking porphyroblasts were studied in two perpendicular thin sections, one parallel and one perpendicular to the main linear structures of the rock (fold axes and/or lineations) and both perpendicular to the main cleavage. Porphyroblastic samples were initially studied in one horizontal thin section with a north-arrow marked on it. This first section allowed assessing the type and quality of inclusion trails, and also to measure their strike in case of relatively straight inclusion trails. Strike data were represented in moving-average rose diagrams made with the program MARD (Munro and Blenkinsop, 2012). The further procedure was decided for each sample based on the dominant porphyroblast mineral and the type of inclusion trails as follows:

- Samples with garnets containing well-developed quartz-rich inclusion trails were selected for XCT analysis. Quartz inclusions offer a good X-ray attenuation contrast with respect to the hosting garnet, so they are well visible in XCT scans (Fig. 3.1c, d). The method used to measure their orientation in 3D is detailed in section 3.3. Generally, the same thin section block that was used to make the horizontal thin section was scanned.

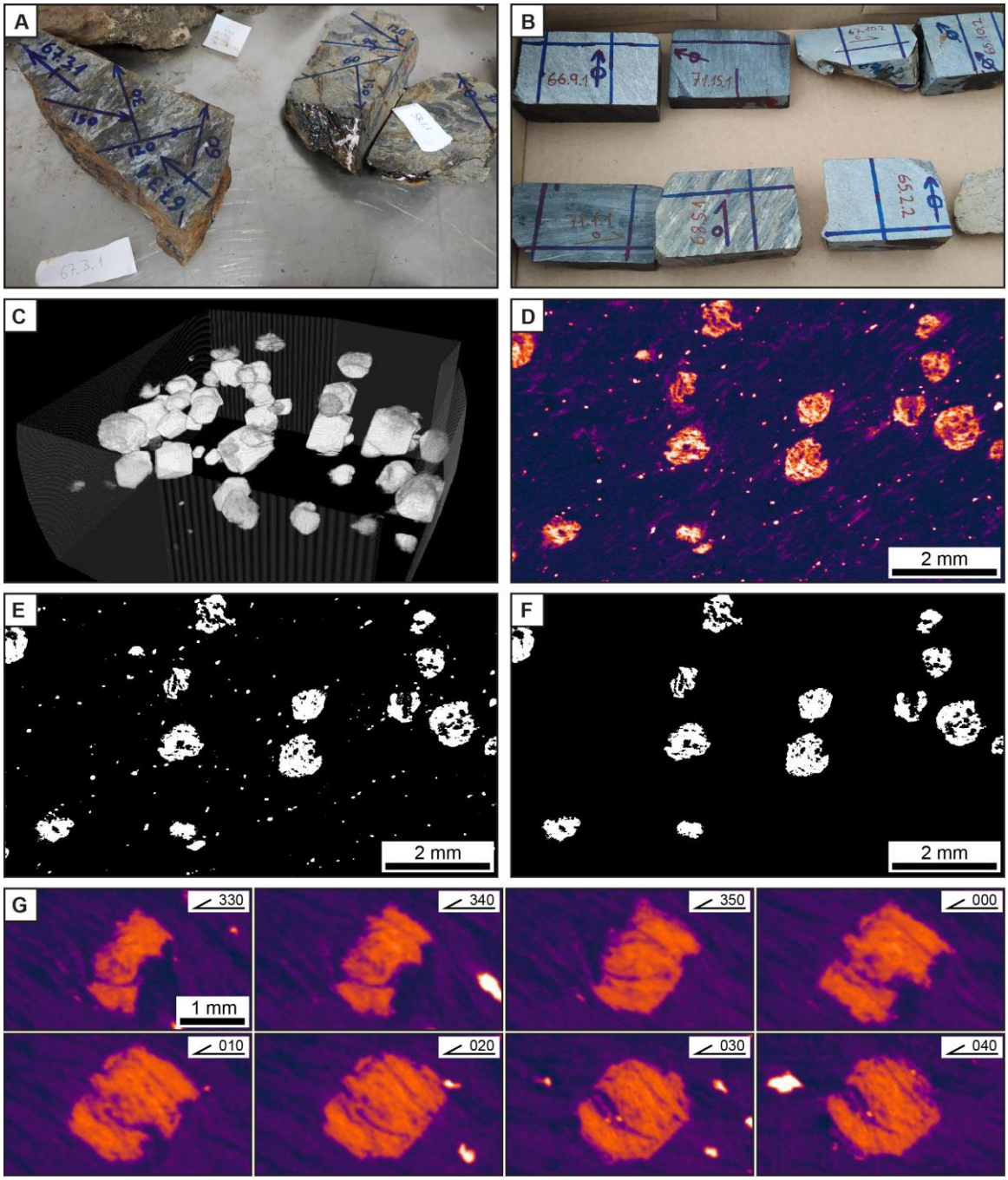

Fig. 3.1. A) Samples marked for cutting a radial set of vertical thin sections. B) Cm-sized blocks from thin sections marked for further cutting in order to obtain a block of optimal size for XCT analysis as a function of garnet size. C) 3D view of an XCT scan, white elements are garnets. D) Slice through an XCT scan where several garnets are visible due to high X-ray attenuation with respect to the matrix. E) Same image as D binarized through segmentation of a specific range of X-ray attenuation values. F) Same image as E after segmenting by size to remove small particles. G) Garnet visualized through differently oriented radial virtual sections. Asymmetry of inclusion trails changes between sections oriented N-000 and N-020 which constrains the direction of its FIA.

- Samples with garnets hosting inclusion trails mainly made of fine graphite, and samples containing staurolite, plagioclase or andalusite porphyroblasts with well-developed inclusion trails were analysed in sets of six vertical thin sections cut at 30º intervals striking N-000, N-030, N-060, N-090, N-120 and N-150. An average

FIA trend was determined from these thin-sections following the technique of Hayward (1990; Fig. 3.2). This technique is based on the principle that the asymmetry of inclusion trails (S or Z) observed in thin section depends on the viewing direction and on the angle between the FIA and the thin-section plane. For a constant viewing direction, the asymmetry of inclusion trails in a radial set of thin sections will switch where the FIA passes between two neighbouring thin sections. Therefore, a set of five thin sections spaced 30° allows determining an average FIAs with a theoretical precision of ±15°. Samples analysed with this method were not chosen for XCT analysis since fine grained graphite inclusions are poorly visible in XCT scans, whereas porphyroblastic minerals other than garnet have a much lower X-ray attenuation contrast with respect to the matrix and their mineral inclusions making them also less suitable for XCT.

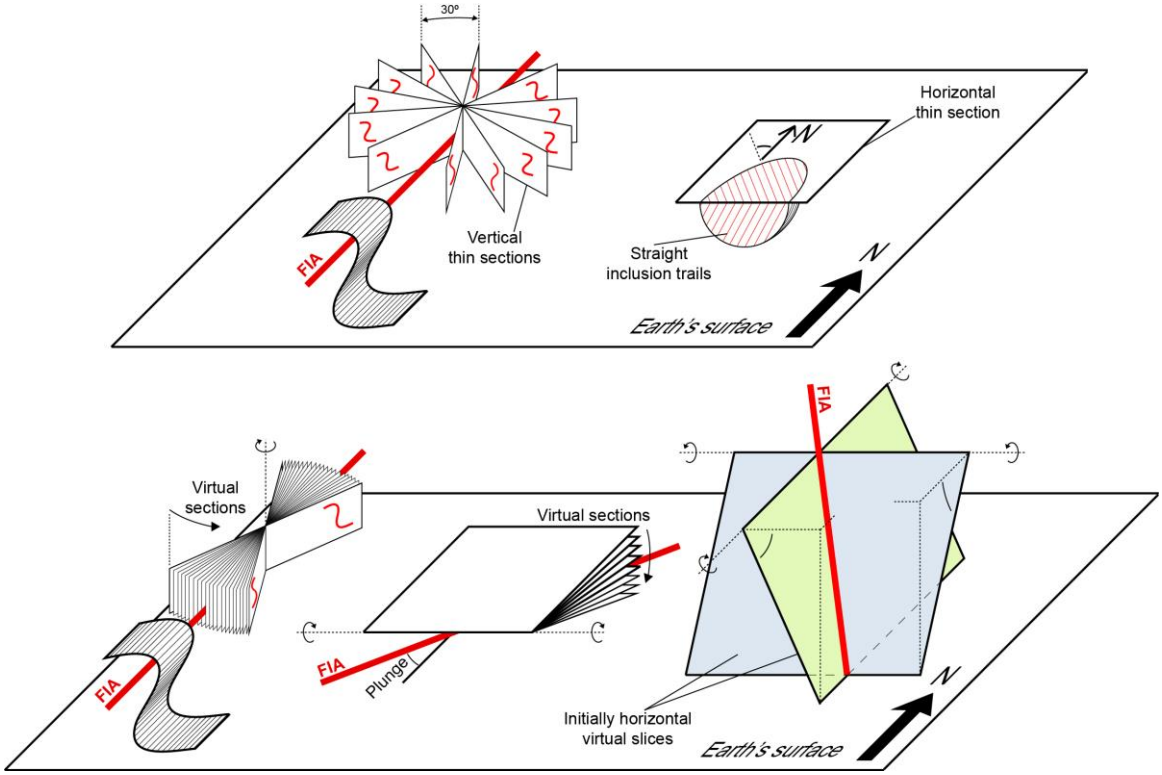

Fig. 3.2. Upper part: technique first proposed by Hayward (1990) for determine the average FIA trend in a sample using a radial set of vertical thin sections. Determining the average FIA plunge requires cutting a second radial set of thin-sections about an axes oriented normal to the FIA trend, but this was not done for this study. Lower part: analogous technique for measuring the 3D orientation (trend and plunge) of FIAs in individual porphyroblasts visualized in XCT scans. The precision of this method is much greater as virtual sections can interactively be rotated back and forward by 1° intervals.

After the microstructural investigation, several garnetiferous samples were selected for thermobarometric and geochronological analysis in an attempt to constrain the P-T conditions and age of different FIA sets recognized regionally. These samples were chosen based on the following criteria:

- All garnets in the sample, or at least the large majority, belong to the same FIA set so that petrological and geochronological data can be linked to that particular FIA

set. In the Nevado-Filábride Complex, however, few samples match this criterion. Therefore, a big sample was selected hosting a numerous garnets with well-developed inclusion trails whose FIAs had all been measured and found to belong to three main sets. A thin section was then cut at a precisely planned location to intersect several garnet porphyroblasts representative of those three FIA sets.

- The garnets must be relatively big to maximize the possibility of finding inclusions of datable minerals inside.
- The samples have relatively simple mineral parageneses of clear Alpine attribution, and/or can be presumed to have a Permo-Triassic sedimentary age. This, to avoid the presence of possible pre-Alpine features.

3.3. XCT analysis

X-ray Computed microtomography is a non-destructive technique that produces high-resolution 3D images composed of voxels (the equivalent of pixels in 2D images). Each voxel has a value which represents the X-ray attenuation of the material at that location (e.g. Cnudde and Boone, 2013; Hanna and Ketcham, 2017). The sample of interest is placed between an X-ray source and a detector. X-rays passing through the rotating object interact with different minerals and structures within the object, leading to variations in their attenuation (absorption and scattering). Multiple projections of the object are acquired by incrementally rotating the object for obtaining X-ray images from different angles. The acquired 2D X-ray images are then processed to generate a 3D volume representing X-ray attenuation in the form of an image stack.

The scanned rock fragments were usually the same blocks from which thin sections had been made. However, blocks containing numerous small garnets were usually trimmed down in order to increase the scanning resolution while still counting with a large number of garnets in the scanned volume. Thus, the block size was decided in order to maximize the scanned volume with a suitable resolution which could be scanned within a reasonable period of time (usually 4 hours). For garnets of approximately 3 mm diameter, a resolution of 18-20 µm is enough to adequately visualize their inclusion trails in the XCT scan and this allows to scan the entire thin-section block. Very small garnets in some of ours samples (approximately 0.5 mm diameter) required a scanning resolution of approximately 5 µm and, consequently, a reduction of the block to approximately 1 cm^3. An orientation arrow made of metal wire was glued to each block to aid later reorientation of the generated tiff image stack. Reorientation was done in such a way as to align the x-y and z- axes of the image stack with geographic coordinate axes (E-W, N-S, and vertical respectively). Microstructural elements can from then on be directly measured in the scan doing a kind of sub-mm- to cm-scale "field work".

The selected blocks were scanned in the Centro de Instrumentación Científica, University of Granada, using an Xradia 510 VERSA ZEISS microtomograph at 140 kV and 1201-3201 projections. The digital image stacks were processed and analysed with the open-source Fiji distribution (Schindelin et al., 2012) of the software ImageJ

(Schneider et al., 2012). Since the original image stacks were too large for efficient processing using a standard desktop computer, they were converted from 16-bit to 8-bit. Portions of the stack with no data (air), or parts of the sample devoid of garnets, were eliminated to further reduce the file size and facilitate digital image analysis. In order to correctly determine the number of FIAs in a sample and to avoid accidental repetition of the same garnet analysis, a list was created first of all garnets and their centre coordinates. This was done through the following steps:

- Since garnets have high X-ray attenuation values, voxels with such features were segmented from the rest of the sample using the Threshold tool (Fig. 3.1e).
- Small particles with high X-ray attenuation values were eliminated using the 3D Simple Segmentation tool (3D plugin; Ollion et al., 2013) which allows segmentation by particle size (Fig. 3.1f).
- The centre coordinates of remaining garnet porphyroblasts were obtained with the Particle Analyser tool (BoneJ plugin; Doube et al., 2010).

Once all garnets have been located, the microstructural analysis can be performed. Garnet shapes and shape orientations were quantified through calculation of best-fit ellipsoids with the Particle Analyser tool (Doube et al., 2010), or more specifically, with the 3D Ellipsoid Fitting tool (Ollion et al., 2013). The principle axes of best-fit ellipsoids are given as vector components, then converted in an Excel worksheet to trend and plunge data for plotting in stereograms and contouring.

Measuring a FIA starts with extracting from the image stack a small volume only containing the garnet of interest using the Make Substack tool. The extracted volume is then analysed with the Volume Viewer plugin, which allows visualization of virtual slices of any orientation. The trend of the FIA preserved within the garnet is then determined analogous as when using radial sets of vertical thin sections (Hayward, 1990), by varying the strike of a vertical slice passing through the garnet centre and recording where the asymmetry of the inclusion trails switches. Since the strike of the vertical slice can be changed by increments of 1°, FIA trends can be determined with high precision, only being limited by the quality and definition of inclusion trails (Fig. 3.1g, 3.2). The typical error of a FIA trend determined in this way is estimated to be ±5° to ±15°. After the FIA trend is determined, its plunge is obtained with a similar precision by rotating a virtual slice around a horizontal axis lying normal to the FIA trend.

Very steeply plunging FIAs (>60°), however, cannot be easily measured following the above procedure, because such FIA always lie close to any vertical section regardless of its strike and this makes it difficult to recognize the asymmetry switch. In such cases, an alternative approach was used consisting in rotating a virtual slice first about one horizontal axes, and then about a second horizontal axes oriented normal to the first one (for example, N-S and then E-W). In this way, two planes can be identified, namely, the ones across which the inclusion-trail asymmetry switched both containing the FIA. Therefore the intersection line of these planes is the FIA (Fig. 3.2).

The orientations of fold- or crenulation axes observed in the matrix were also measured by recording the x, y, z coordinates of two or more points located along the same axis and converting this data to trend and plunge using simple trigonometry.

3.4. Electron Probe Microanalyses

Chemical compositions of minerals were obtained by Electron Probe Microanalyses (EPMA). The analyses have been performed in the Centro de Instrumentación Científica, University of Granada, using two microprobes:

- CAMECA SX100 (20 kV accelerating voltage, 20 nA beam current, 5 µm beam diameter; standards: albite (Na), periclase (Mg), SiO_2 (Si), Al_2O_3 (Al), Fe_2O_3 (Fe), ZnS (Zn), $MnTiO_3$ (Mn), diopside (Ca), TiO_2 (Ti), sanidine (K), SO_4Ba (Ba))
- JEOL JXA-iSP100 (20 kV accelerating voltage, 20 nA beam current, 5 µm beam diameter; standards: $MnTiO_3$ (Mn), Fe_2O_3 (Fe), Cr_2O_3 (Cr), orthoclase (K), wollastonite (Ca), $MnTiO_3$ (Ti), albite (Na), Al_2O_3 (Al), wollastonite (Si), MgO (Mg))

The location of point-analyses were chosen based on petrographic study of thin sections using an optical microscope, aimed at performing thermobarometry and identifying compositional differences between garnets belonging to different FIA sets that were identified through the micro-structural analysis. Point-analyses include both isolated minerals and profiles through garnet porphyroblasts in order to reveal chemical zoning patterns. Thin sections were first optically scanned at a resolution of 1200 pixels per inch and point-analyses were digitized on these scans. At the beginning of each microprobe session, three arbitrary reference points lying far apart in the polished thin-section were located in the thin section scan as well as the live microprobe image. The coordinates of these three points in both images allowed to instantly converting the coordinates of all points digitized on the optically scanned image to the coordinate frame used by the microprobe. From then on, coordinates can be entered on the computer screen to rapidly move the beam spot to the point of interest without need to manually search for it. The final position of the analyses was manually fine-tuned using the live visualizing system of the microprobe (optical for the CAMECA, backscattered electrons image for the JEOL) to avoid polishing defects and grain boundaries.

3.5. P-T estimations

3.5.1. Thermobarometry

Thermobarometry consists on the estimation of temperature and pressure conditions under which rocks or minerals formed or equilibrated from mineral assemblages and chemical compositions of rocks and minerals. It is primarily based on the free energy (Gibbs energy) minimization principle ($\Delta G=0$). Gibbs energy can be expressed in terms of enthalpy (ΔH), entropy (ΔS), volume (ΔV) and equilibrium constant (see details in Spear, 1993 or Vernon and Clarke, 2008). ΔH, ΔS and ΔV are known from experimental

calibrations, and the equilibrium constant is obtained from the compositions of minerals in equilibrium from the sample of interest. From these data, different calibrations for determined geothermobarometers are proposed (see review in Spear, 1993).

Good geothermometers are characterized by high ΔH and low ΔV, which occurs in exchange reactions (ionic exchange of components with similar ionic radii between coexisting minerals), so they are used to estimate temperatures. Good geobarometers are characterized by low ΔH and high ΔV. Net-transfer reactions (reactions where phases are produced and consumed) fulfil these requirements and are used as geobarometers. Solubility of trace elements in certain mineral phases is also used to derive geothermobarometers.

Some exchange thermometers were used to estimate the temperature of metamorphism in our samples. The Garnet-Biotite thermometer was applied with the calibrations of Ferry and Spear (1978), Dasgupta et al. (1991) and Bhattacharya et al. (1992). The Garnet-Staurolite thermometer was also used following the calibration of Perchuk (1991). Garnet-Chloritoid (Perchuk, 1991) and Garnet-Ilmenite (Pownceby et al., 1987, 1991) exchange thermometers were also applied although unrealistic results were obtained, so they were not taken into account. In the case of the Garnet-Ilmenite thermometer, probably due to the very low Mn content (Pownceby et al., 1987) in both garnets and ilmenites present in the analysed samples. The net-transfer reaction involving Garnet-Plagioclase-Muscovite-Biotite was used as geobarometer according to the calibration of Ghent and Stout (1981). P-T estimations have been calculated using the GPT spreadsheet of Reche and Martínez (1996). The Zr-in-Rutile geothermometer, based on the solibility of Zr in rutile, was also used with the calibrations of Zack et al. (2004), Ferry and Watson (2007) and Tomkins et al. (2007).

3.5.2. Thermodynamic modelling

Equilibrium assemblage diagrams were calculated with the software Theriak-Domino (de Capitani and Petrakakis, 2010) which predicts stable mineral assemblages based on the principle of Gibbs free energy minimization. Equilibrium assemblage diagrams are calculated for determined bulk rock compositions. Whole rock major elements were determined through X-ray fluorescence (XRF) in the Centro de Instrumentación Científica, University of Granada. These diagrams show the variable stable mineral assemblages which can develop in the analysed sample in function of the specific pressure and temperature conditions, which allow estimating the P-T conditions of metamorphism from mineralogical observations.

3.6. Ar-Ar geochronology

The micaschist samples used for thermobarometry and fulfilling the microstructural criteria regarding FIA outlined in the last paragraph of section 3.2 contain a well-developed principle matrix foliation that was dated using the $^{40}Ar/^{39}Ar$ method. The samples were processed in order to obtain single grains. The separation of datable

minerals was performed at the Géoazur Laboratory (France), according to the following procedure:

- Samples were crushed with the aid of a hammer and a mortar.
- Crushed samples were sieved to isolate the fraction of rock in the order of 200-300 µm.
- The samples were cleaned with water and an ultrasonic cleaner in order to eliminate smaller particles adhered to the sieved fraction.
- The cleaned samples were dried in a laboratory oven.
- White mica, biotite and amphibole grains were finally selected from the dried samples with the aid of a microscope.

Samples were irradiated in the Triga Mark II nuclear reactor of Pavia (Italy), and Ar analyses were performed at Géosciences Montpellier Laboratory (France). These processes are detailed in section 10.5.

3.7. U-Th-Pb geochronology

The main objective was to obtain radiometric ages from datable minerals included within garnets in order to constrain their ages and hence the age of the FIA included in the garnets. This work was performed in the University of Montpellier and included several steps.

Firstly, datable minerals (monazite, xenotime, zircon or rutile) were searched in the selected thick sections (ca. 50 µm) using a Scanning Electron Microscope (SEM) according to the following procedure:

- SEM coordinates of three reference points located in three corners of the thick sections were noted.
- Minerals containing elements with a high atomic number, and therefore prone to U-Th-Pb dating, were identified in the thick sections as they show high luminescence in backscattered electron (BSE) images.
- Energy-dispersive X-ray spectroscopy (EDS) analyses were performed in the high-luminescent minerals to check their composition, and if suitable for radiometric dating, their coordinates were noted.

The chosen minerals were in-situ analysed through laser-ablation inductively coupled plasma-mass spectrometry (LA-ICP-MS). The reference points initially located in the SEM were searched in the LA-ICP-MS in order to convert the SEM coordinates of the points of analysis to LA-ICP-MS coordinates. The analyses of monazite and xenotime were calibrated with the standards Manangotry (Poitrasson et al., 2000) and Moacyr (Seydoux-Guillaume et al., 2002). The obtained data were processed with the software Glitter (van Achterberg et al., 2001), and the final results were plotted in Tera-Wasserburg diagrams made with Isoplot/Ex (Ludwig, 2003).

References Part I

Abu Sharib, A.S.A.A., Bell, T.H., 2011. Radical changes in bulk shortening directions during orogenesis: significance for progressive development of regional folds and thrusts. Precambrian Research. 188, 1–20. https://doi.org/10.1016/j.precamres.2011.03.008

Abu Sharib, A.S.A.A., Sanislav, I.V., 2013. Polymetamorphism accompanied switching in horizontal shortening during Isan Orogeny: Example from the Eastern Fold Belt, Mount Isa Inlier, Australia. Tectonophysics 587, 146-167. https://doi.org/10.1016/j.tecto.2012.06.051

Acosta-Vigil, A., Rubatto, D., Bartoli, O., Cesare, B., Meli, S., Pedrera, A., Azor, A., Tajčmanová, L., 2014. Age of anatexis in the crustal footwall of the Ronda peridotites, S Spain. Lithos 210-211, 147-167. https://doi.org/10.1016/j.lithos.2014.08.018

Aerden, D.G.A.M., 1995. Porphyroblast non-rotation during crustal extension in the Variscan Lys-Caillaouas Massif, Pyrenees. Journal of Structural Geology 17, 709-725. https://doi.org/10.1016/0191-8141(94)00090-M

Aerden, D.G.A.M., 2004. Correlating deformation in Variscan NW-Iberia using porphyroblasts; implications for the Ibero-Armorican Arc. Journal of Structural Geology 26, 177-196. https://doi.org/10.1016/S0191-8141(03)00070-1

Aerden, D.G.A.M., Sayab, M., 2008. From Adria- to Africa-driven orogenesis: evidence from porphyroblasts in the betic Cordillera, Spain. Journal of Structural Geology 30, 1272–1287. https://doi.org/10.1016/j.jsg.2008.06.009

Aerden, D.G.A.M., Ruiz-Fuentes, A., 2020. X-ray computed micro-tomography of spiral garnets: A new test of how they form. Journal of Structural Geology 136, 104054. https://doi.org/10.1016/j.jsg.2020.104054

Aerden, D.G.A.M., Sayab, M., Bouybaouene, M.L., 2010. Conjugate-shear folding: A model for the relationships between foliations, folds and shear zones. Journal of Structural Geology 32, 1030-1045. https://doi.org/10.1016/j.jsg.2010.06.010

Aerden, D.G.A.M., Bell, T.H., Puga, E., Sayab, M., Lozano, J.A., Díaz de Federico, A., 2013. Multi-stage mountain building vs. relative plate motions in the Betic Cordillera deduced from integrated microstructural and petrological analysis of porphyroblast inclusion trails. Tectonophysics 587, 188-206. https://doi.org/10.1016/j.tecto.2012.11.025

Aerden, D.G.A.M., Ruiz-Fuentes, A., Sayab, M., Forde, A., 2021. Kinematics of subduction in the Ibero-Armorican arc constrained by 3D microstructural analysis of garnet and pseudomorphed lawsonite porphyroblasts from Île de Groix (Variscan belt). Solid Earth 12, 971-992. https://doi.org/10.5194/se-12-971-2021

Aerden, D.G.A.M., Farrell, T.P., Baxter, E.F., Stewart, E.M., Ruiz-Fuentes, A., Bouybaouene, M., 2022. Refined tectonic evolution of the Betic-Rif orogen through integrated 3-D microstructural analysis and Sm-Nd dating of garnet porphyroblasts. Tectonics 41, e2022TC007366. https://doi.org/10.1029/2022TC007366

Aguado, R., Feinberg, H., Durand-Delga, M., Martín-Algarra, A., Esteras, M., Didon, J., 1990. Nuevos datos sobre la edad de las formaciones miocenas transgresivas sobre las Zonas

Internas béticas: La formación de San Pedro de Alcántara (provincia de Málaga). Revista de la Sociedad Geológica de España 3, 79-85.

Akkerman, J.H., Maier, G., Simon, O.J., 1980. On the geology of the Alpujarride complex in the western Sierra de las Estancias (Betic Cordilleras, SE Spain). Geologie en Mijnbouw 59 (4), 363-374.

Aldaya, F., 1969. Los mantos Alpujárrides al Sur de Sierra Nevada (zona bética, provincia de Granada.). Acta Geológica Hispánica IV (5), 126-130.

Aldaya, F., García-Dueñas, V., Navarro-Vilá, F., 1979. Los Mantos Alpujárrides del tercio central de las Cordilleras Béticas. Ensayo de correlación tectónica de los Alpujárrides. Acta Geológica Hispánica 14, 154-166.

Ali, A., 2010. The tectono-metamorphic evolution of the Balcooma Metamorphic Group, north-eastern Australia: a multidisciplinary approach. Journal of Metamorphic Geology 28, 397–422. https://doi.org/10.1111/j.1525-1314.2010.00871.x

Alonso-Chaves, F.M., Rodriguez-Vidal, J., 1998. Subsidence tectonique et sédimentation synrift associée au rifting du domaine d'Alboran au Miocène inférieur (Chaîne bétique, Espagne). Comptes Rendus de l'Académie des Sciences – Series IIA – Earth and Planetary Science 326, 51-56. https://doi.org/10.1016/S1251-8050(97)83203-X

Alonso-Chaves, F.M., Orozco, M., 2007. Evolución tectónica de las Sierras de Tejeda y Almijara: Colapso extensional y exhumación de áreas metamórficas en el Dominio de Alborán (Cordilleras Béticas). Revista de la Sociedad Geológica de España 20 (3-4), 211-228.

Alonso-Chaves, F.M., Orozco, M., 2012. El Complejo Alpujárride de La Axarquía: Zonas de cizalla dúctiles a escala cortical y pliegues recumbentes asociados. Geogaceta 52, 5-8.

Andriessen, P.A.M., Hebeda, E.H., Simon, O.J., Verschure, R.H., 1991. Tourmaline K-Ar ages compared to other radiometric dating systems in Alpine anatectic leucosomes and metamorphic rocks (Cyclades and southern Spain). Chemical Geology 91, 33-48. https://doi.org/10.1016/0009-2541(91)90014-I

Argles, T.W., Prince, C.I., Foster, G.L., Vance, D., 1999. New garnets for old? Cautionary tales from young mountain belts. Earth and Planetary Science Letters 172, 301-309. https://doi.org/10.1016/S0012-821X(99)00209-5

Augier, R., Agard, P., Monié, P., Jolivet, L., Robin, C., Booth-Rea, G., 2005a. Exhumation, doming and slab retreat in the Betic Cordillera (SE Spain): in situ 40Ar/39Ar ages and P-T-d-t paths for the Nevado-Filabride complex. Journal of Metamorphic Geology 23, 357-381. https://doi.org/10.1111/j.1525-1314.2005.00581.x

Augier, R., Booth-Rea, G., Agard, P., Martínez-Martínez, J.M., Jolivet, L., Azañón, J.M., 2005b. Exhumation constraints for the lower Nevado-Filabride Complex (Betic Cordillera, SE Spain): a Raman thermometry and Tweequ multiequilibrium thermobarometry approach. Bulletin de la Société Géologique de France 176, 403-416. https://doi.org/10.2113/176.5.403

Augier, R., Jolivet, L., Robin, C., 2005c. Late Orogenic doming in the eastern Betic Cordilleras: Final exhumation of the Nevado-Filabride complex and its relation to basin genesis. Tectonics 24, TC4003. https://doi.org/10.1029/2004TC001687

Avidad, J., García-Dueñas, V., 1972. Mapa de la Hoja nº 1055 (Motril). Mapa Geológico de España E. 1:50.000. Segunda Serie (MAGNA), Primera edición. IGME.

Azañón, J.M., Alonso-Chaves, F.M., 1996. Alpine tectono-metamorphic evolution of the Tejeda Unit, an extensionally dismembered Alpujarride Nappe (Western Betics). Comptes Rendus de l'Académie des Sciences de Paris 322, 47-54.

Azañón, J.M., Goffé, B., 1997. Ferro- and magnesiocarpholite assemblages as record of high-P, low-T metamorphism in the Central Alpujarrides, Betic Cordillera (SE Spain). European Journal of Mineralogy 9, 1035-1051.

Azañón, J.M., Crespo-Blanc, A., 2000. Exhumation during a continental collision inferred from the tectonometamorphic evolution of the Alpujarride Complex in the central Betics (Alboran Domain, SE Spain). Tectonics 19 (3), 549-565. https://doi.org/10.1029/2000TC900005

Azañón, J.M., García-Dueñas, V., Martínez-Martínez, J.M., Crespo-Blanc, A., 1994. Alpujarride tectonic sheets in the central Betics and similar eastern allochthonous units (SE Spain). Comptes Rendus de l'Académie des Sciences de Paris 318, 667-674.

Azañón, J.M., Crespo-Blanc, A., García-Dueñas, V., 1997. Continental collision, crustal thinning and nappe forming during the pre-Miocene evolution of the Alpujarride Complex (Alboran Domain, Betics). Journal of Structural Geology 19 (8), 1055-1071. https://doi.org/10.1016/S0191-8141(97)00031-X

Azañón, J.M., García-Dueñas, V., Goffé, B., 1998. Exhumation of high-pressure metapelites and coeval crustal extension in the Alpujarride complex (Betic Cordillera). Tectonophysics 285, 231-252. https://doi.org/10.1016/S0040-1951(97)00273-4

Bakker, H.E., de Jong, K., Helmers, H., Biermann, C., 1989. The geodynamic evolution of the Internal Zone of the Betic Cordilleras (south-east Spain): a model based on structural analysis and geothermobarometry. Journal of Metamorphic Geology 7, 359-381. https://doi.org/10.1111/j.1525-1314.1989.tb00603.x

Balanyá, J.C., 1984. El Complejo Dorsaliano al Este de Granada: Relaciones estructurales con la Zona Bética y el Subbético Interno. I Congreso Español de Geología, 3, 169-175.

Balanyá, J.C., 1991. Estructura del Dominio de Alboran en la parte norte del Arco de Gibraltar. PhD Thesis, Universidad de Granada. https://digibug.ugr.es/handle/10481/50668

Balanyá, J.C., Azañón, J.M., Sánchez-Gómez, M., García-Dueñas, V., 1993. Pervasive ductile extensión, isothermal decompression and thinning of the Jubrique unit in the Paleogene (Alpujarride Complex, western Betics Spain). Comptes Rendus de l'Académie des Sciences de Paris 316, 1595-1601.

Balanyá, J.C., García-Dueñas, V., Azañón, J.M., Sánchez-Gómez, M., 1997. Alternating contractional and extensional events in the Alpujarride nappes of the Alboran Domain (Betics, Gibraltar Arc). Tectonics 16, 226-238. https://doi.org/10.1029/96TC03871

Balanyá, J.C., García-Dueñas, V., Azañón, J.M., Sánchez-Gómez, M., 1998. Reply to "Comment on 'Alternating contractional and extensional events in the Alpujarride nappes of the Alboran Domain (Betics, Gibraltar Arc)'". Tectonics 17 (6), 977-981. https://doi.org/10.1029/1998TC900006

Behr, W.M., Platt, J.P., 2012. Kinematic and thermal evolution during two-stage exhumation of a Mediterranean subduction complex. Tectonics 31, TC4025. https://doi.org/10.1029/2012TC003121

Bell, T.H., 1985. Deformation partitioning and porphyroblast rotation in metamorphic rocks: a radical interpretation. Journal of Metamorphic Geology 3, 109-118. https://doi.org/10.1111/j.1525-1314.1985.tb00309.x

Bell, T.H., Johnson, S.E., 1989. Porphyroblast inclusion trails: the key to orogenesis. Journal of Metamorphic Geology 7, 279-310. https://doi.org/10.1111/j.1525-1314.1989.tb00598.x

Bell, T.H., Forde, A., 1995. On the significance of foliation patterns preserved around folds by mineral overgrowth. Tectonophysics 246, 171-181. https://doi.org/10.1016/0040-1951(94)00263-9

Bell, T.H., Hickey, K.A., 1997. Distribution of pre-folding linear indicators of movement direction around the Spring Hill Synform, Vermont: significance for mechanism of folding in this portion of the Appalachians. Tectonophysics 274, 275-294. https://doi.org/10.1016/S0040-1951(97)00008-5

Bell, T.H., Mares, V.M., 1999. Correlating deformation and metamorphism around orogenic arcs. American Mineralogist 84, 1727-1740. https://doi.org/10.2138/am-1999-11-1203

Bell, T.H., Welch, P.W., 2002. Prolonged Acadian orogenesis: Revelations from foliation intersection axis (FIA) controlled monazite dating of foliations in porphyroblasts and matrix. American Journal of Science 302, 549-581. https://doi.org/10.2475/ajs.302.7.549

Bell, T.H., Kim, H.S., 2004. Preservation of Acadian deformation and metamorphism through intense Alleghanian shearing. Journal of Structural Geology 26, 1591- 1613. https://doi.org/10.1016/j.jsg.2004.01.006

Bell, T.H., Sapkota, J., 2012. Episodic gravitational collapse and migration of the mountain chain during orogenic roll-on in the Himalayas. Journal of Metamorphic Geology 30, 651-666. https://doi.org/10.1111/j.1525-1314.2012.00992.x

Bell, T.H., Rubenach, M.J., Fleming, P.D., 1986. Porphyroblast nucleation, growth and dissolution in regional metamorphic rocks as a function of deformation partitioning during foliation development. Journal of Metamorphic Geology 4, 37-67. https://doi.org/10.1111/j.1525-1314.1986.tb00337.x

Bell, T.H., Johnson, S.E., Davis, B., Forde, A., Hayward, N., Wilkins, C., 1992. Porphyroblast inclusion-trail orientation data: eppure non son girate! Journal of Metamorphic Geology 10, 295-307. https://doi.org/10.1111/j.1525-1314.1992.tb00084.x

Bell, T.H., Forde, A., Wang, J., 1995. A new indicator of movement direction during orogenesis: measurement technique and application to the Alps. Terra Nova 7, 500-508. https://doi.org/10.1111/j.1365-3121.1995.tb00551.x

Bell, T.H., Hickey, K.A., Upton, G.J.G., 1998. Distinguishing and correlating multiple phases of metamorphism across a multiply deformed region using the axes of spiral, staircase, and sigmoidal inclusion trails in garnet. Journal of Metamorphic Geology 16, 767–794. https://doi.org/10.1111/j.1525-1314.1998.00170.x

Bertrand, M., Kilian, W., 1889. Études sur les terrains secondaires et tertiaires dans les Provinces de Grenade et de Malaga. Mémoires à l'académie des sciences de l'institut de France 30, 377-582.

Bessière, E., Scaillet, S., Augier, R., Jolivet, L., Azañón, J.M., Booth-Rea, G., Romagny, A., Duval, F., 2022. 40Ar/39Ar Age Constraints on HP/LT Metamorphism in Extensively Overprinted Units: The Example of the Alpujárride Subduction Complex (Betic Cordillera, Spain). Tectonics 41, e2021TC006889. https://doi.org/10.1029/2021TC006889

Bhattacharya, A., Mohanty, L., Maji, A., Sen, S.K., Raith, M., 1992. Non-ideal mixing in the phlogopite-annite binary: constraints from experimental data on Mg-Fe partitioning and a reformulation of the biotite-garnet geothermometer. Contrib Mineral Petrol 111, 87-93. https://doi.org/10.1007/BF00296580

Blumenthal, M., 1927. Versuch einer tektonischen Gliederung der betischen Cordilleren von Centra- und Südwest-Andalusien. Eclogae Geologicae Helvetiae 20, 487-532.

Bons, P.D., Jessell, M.W., Griera, A., 2009. Porphyroblast rotation versus nonrotation: Conflict resolution!: Comment. Geology 37, e182. https://doi.org/10.1130/G25131C.1

Booth-Rea, G., Azañón, J.M., Goffé, B., Vidal, O., Martínez-Martínez, J.M., 2002a. High-pressure, low-temperature metamorphism in Alpujarride Units of southeastern Betics (Spain). Comptes Rendus Geosciences 334, 857-865. https://doi.org/10.1016/S1631-0713(02)01787-X

Booth-Rea, G., García-Dueñas, V., Azañón, J.M., 2002b. Extensional attenuation of the Malaguide and Alpujarride thrust sheets in a segment of the Alboran basin folded during the Tortonian (Lorca area, Eastern Betics). Comptes Rendus Geoscience 334, 557-563. https://doi.org/10.1016/S1631-0713(02)01794-7

Booth-Rea, G., Azañón, J.M., Martínez-Martínez, J.M., 2003. Metamorfismo de AP/BT en metapelitas de la unidad de Ragua (complejo Nevado-Filábride, Cordillera Bética). Resultados termo-barométricos del estudio de equilibrios locales. Geogaceta 34, 87-90.

Booth-Rea, G., Azañón, J.M., García-Dueñas, V., 2004. Extensional tectonics in the northeastern Betics (SE Spain): case study of extension in a multilayered upper crust with contrasting rheologies. Journal of Structural Geology 26, 2039-2058. https://doi.org/10.1016/j.jsg.2004.04.005

Booth-Rea, G., Azañón, J.M., Martínez-Martínez, J.M., Vidal, O., García-Dueñas, V., 2005. Contrasting structural and P-T evolution of tectonic units in the southeastern Betics: Key for understanding the exhumation of the Alboran Domain HP/LT crustal rocks (western Mediterranean). Tectonics 24, TC2009 https://doi.org/10.1029/2004TC001640.

Booth-Rea, G., Martínez-Martínez, J.M., Giaconia, F., 2015. Continental subduction, intracrustal shortening, and coeval upper-crustal extension: P-T evolution of subducted south Iberian paleomargin metapelites (Betics, SE Spain). Tectonophysics 663, 122-139. https://doi.org/10.1016/j.tecto.2015.08.036

Bouillin, J.P., Durand Delga, M., Olivier, P., 1986. Betic-Rifain and Tyrrhenian Arcs: distinctive features, genesis and development stages, in: Wezel, F.C., (Ed.), The origin of arcs, Amsterdam, Elsevier, p. 281–304.

Boulin, J., 1970. Les zones internes des Cordilleres Bétiques de Málaga à Motril. Ann. Hebert et Haug. Trav. Lab. Géol. Fac. Sc. Paris, 10, 239 p.

Braga, J.C., Martín, J.M., 1987. Distribucion de las algas dasycladaceas en el Trias Alpujarride. Cuadernos Geología Ibérica 11, 475-489.

Braga, J.C., Martín, J.M., Quesada, C., 2003. Patterns and average rates of late Neogene-Recent uplift of the Betic Cordillera, SE Spain. Geomorphology 50, 3-26. https://doi.org/10.1016/S0169-555X(02)00205-2

Brouwer, H.A., 1926. Zur Geologie der Sierra Nevada. Geologische Rundschau 17, 118-137. https://doi.org/10.1007/BF01801854

Busa, M.D., Gray, N.H., 1992. Rotated staurolite porphyroblasts in the Littleton Schist at Bolton, Connecticut, USA. Journal of Metamorphic Geology 10, 627-636. https://doi.org/10.1111/j.1525-1314.1992.tb00111.x

Campos, J., García-Dueñas, V., González Lodeiro, F., Orozco, M., 1986. La zona de cizalla del contacto entre el grupo de mantos del Mulhacén y la unidad del Veleta (Sierra Nevada y Sierra de los Filabres, Andalucía). Geogaceta 1, 15-17.

Cao, H., Fletcher, C., 2012. FIA trends along the Precambrian Rocky Mountains: a new approach to timing continental docking. Journal of Metamorphic Geology 30, 639-650. https://doi.org/10.1111/j.1525-1314.2012.00994.x

Cihan, M., Parsons, A., 2005. The use of porphyroblasts to resolve the history of macro- scale structures: an example from the Robertson River Metamorphics, North-Eastern Australia. Journal of Structural Geology 27, 1027–1045. https://doi.org/10.1016/j.jsg.2005.02.004

Cihan, M., Evins, P., Lisowiec, N., Blake, K., 2006. Time constraints on deformation and metamorphism from EPMA dating of monazite in the Proterozoic Robertson River Metamorphics, NE Australia. Precambrian Research 145, 1-23. https://doi.org/10.1016/j.precamres.2005.11.009

Cnudde, V., Boone, M.N., 2013. High-resolution X-ray computed tomography in geosciences: A review of the current technology and applications. Earth-Science Reviews 123, 1-17. https://doi.org/10.1016/j.earscirev.2013.04.003

Comas, M.C., Delgado, F., Vera, J.A., 1979. Mapa y memoria de la Hoja nº 993 (Benalúa de Guadix). Mapa Geológico de España E. 1:50.000. Segunda Serie (MAGNA), Primera edición. IGME.

Comas, M.C., García-Dueñas, V., Jurado, M.J., 1992. Neogene tectonic evolution of the Alboran Sea from MCS data. Geo-Marine Letters 12, 157-164. https://doi.org/10.1007/BF02084927

Crespo-Blanc, A., 1995. Interference pattern of extensional fault systems: a case study of the Miocene rifting of the Alboran basement (North of Sierra Nevada, Betic Chain). Journal of Structural Geology 17, 1559-1569. https://doi.org/10.1016/0191-8141(95)E0044-D

Crespo-Blanc, A., 2007. Superimposed folding and oblique structures in the palaeomargin-derived units of the Central Betics (SW Spain). Journal of the Geological Society, London 164, 621-636. https://doi.org/10.1144/0016-76492006-084

Crespo-Blanc, A., Campos, J., 2001. Structure and kinematics of the South Iberian paleomargin and its relationship with the Flysch Trough units: extensional tectonics within the Gibraltar Arc fold-and-thrust belt (western Betics). Journal of Structural Geology 23, 1615-1630. https://doi.org/10.1016/S0191-8141(01)00012-8

Crespo-Blanc, A., Orozco, M., García-Dueñas, V., 1994. Extension versus compression during the Miocene tectonic evolution of the Betic chain. Late folding of normal fault systems. Tectonics 13, 78-88. https://doi.org/10.1029/93TC02231

Cuevas, J., 1989a. Microtectónica y metamorfismo de los Alpujárrides del tercio central de las Cordilleras Béticas (entre Motril y Adra). Parte I: Litología y estructuras asociadas a D1, D2 y D3. Boletín Geológico y Minero 100 (4), 497-540.

Cuevas, J., 1989b. Microtectónica y metamorfismo de los Mantos Alpujárrides del tercio central de las Cordilleras Béticas (entre Motril y Adra). Parte II: Las Zonas Miloníticas. Boletín Geológico y Minero 100 (5), 719-766.

Cuevas, J., 1991. Internal structure of the Adra Nappe (Alpujarride Complex, Betics, Spain). Tectonophysics 200, 199-212. https://doi.org/10.1016/0040-1951(91)90015-K

Cuevas, J., Aldaya, F., Navarro-Vilá, F., Tubía, J.M., 1986. Caractérisation de deux étapes de charriage principales dans les nappes Alpujarrides centrales (Cordillères Bétiques, Espagne). Comptes Rendus de l'Académie des Sciences de Paris 302, 1177-1180.

Cuevas, J., Navarro-Vilá, F., Tubía, J.M., 2001. Evolución estructural poliorogénica del Complejo Maláguide (Cordilleras Béticas). Boletín Geológico y Minero 11, 47-58.

Dabrio, C.J., López-Garrido, A.C., 1970. Estructura en escamas del sector noroccidental de la Sierra de Cazorla (Zona Prebetica) y del borde de la depresión del Guadalquivir (provincia de Jaen). Cuad. Geol Univ. Granada 1, 149-157.

Dasgupta, S., Sengupta, P., Guha, D., Fukuoka, M., 1991. A refined garnet – biotite Fe – Mg Exchange geothermometer and its application in amphibolites and granulites. Contrib Mineral Petrol 109, 130-137. https://doi.org/10.1007/BF00687206

de Capitani, C., Petrakakis, K., 2010. The computation of equilibrium assemblage diagrams with Theriak/Domino software. American Mineralogist 95, 1006-1016. https://doi.org/10.2138/am.2010.3354

de Jong, K., 1993. Redefinition of the deformation scheme of the Mulhacen Complex and implications for the relative timing of the overthrusting of the Alpujarride Complex in the Betic Zone (SE Spain). Geologie en Mijnbouw 71, 317-326.

de Jong, K., Bakker, H., 1991. The Mulhacen and Alpujarride Complex in the eastern Sierra de los Filabres, SE Spain: Litho-stratigraphy. Geologie en Mijnbouw 70, 93-103.

Didon, J., Durand-Delga, M., Kornprobst, J., 1973. Homologies géologiques entre les deux rives du détroit de Gibraltar. Bulletin de la Société Géologique de France S7-XV, 77-105. https://doi.org/10.2113/gssgfbull.S7-XV.2.77

Doube, M., Klosowski, M.M., Arganda-Carreras, I., Cordelières, F.P., Dougherty, R.P., Jackson, J.S., Schmid, B., Hutchinson, J.R., Shefelbine, S.J., 2010. BoneJ: Free and extensible bone image analysis in ImageJ. Bone 47, 1076-1079. https://doi.org/10.1016/j.bone.2010.08.023

Duggen, S., Hoernle, K., van den Bogaard, P., Harris, C., 2004. Magmatic evolution of the Alboran region: the role of subduction in forming the western Mediterranean and causing the Messinian Salinity Crisis. Earth and Planetary Science Letters 218, 91–108. https://doi.org/10.1016/S0012-821X(03)00632-0

Durand-Delga, M., 1964. Essai sur la structure des domaines émergés autour de la Méditerranée occidentale. Geologische Rundschau 53, 534-535. https://doi.org/10.1007/BF02054550

Durand-Delga, M., Magné, J., 1961. Présence d'Oligocène supérieur sous le front des nappes alpujarrides au Nord-Est de Grenade (Andalousie): Comptes rendus de l'Académie de Sciences de Paris 252, 559-561.

Dürr, S.H., 1967. Geologie der Serrania de Ronda und ihrer südwestlichen ausläufer (Andalusien). Geol. Rom. 6, 1-73.

Egeler, C.G., 1963. On the tectonics of the eastern Betic cordilleras (SE Spain). Geologische Rundschau 53, 260-269. https://doi.org/10.1007/BF02040750

Egeler, C.G., Simon, O.J., 1969. Orogenic evolution of the Betic Zone (Betic Cordilleras, Spain) with emphasis on the nappe structures. Geologie en Mijnbouw 48, 296-305.

Elorza, J.J., García-Dueñas, V., 1981. Mapa y memoria de la Hoja nº 1054 (Vélez-Málaga). Mapa Geológico de España E. 1:50.000. Segunda Serie (MAGNA), Primera edición. IGME.

Esteban, J.J., Sánchez-Rodríguez, L., Seward, D., Cuevas, J., Tubía, J.M., 2004. The late thermal history of the Ronda area, southern Spain. Tectonophysics 389, 81-92. https://doi.org/10.1016/j.tecto.2004.07.050

Esteban, J.J., Cuevas, J., Tubía, J.M., Gil Ibarguchi, J.I., Seward, D., 2005. Metamorfismo, exhumación y termocronología de la unidad de Yunquera (Alpujárrides occidentales, Cordilleras Béticas). Revista de la Sociedad Geológica de España 18, 61-74.

Esteban, J.J., Cuevas, J., Tubía, J.M., Liati, A., Seward, D., Gebauer, D., 2007. Timing and origin of zircon-bearing chlorite schists in the Ronda peridotites (Betic Cordilleras, Southern Spain). Lithos 99, 121-135. https://doi.org/10.1016/j.lithos.2007.06.006

Esteban, J.J., Cuevas, J., Vegas, N., Tubía, J.M., 2008. Deformation and kinematics in a melt-bearing shear zone from the Western Betic Cordilleras (Southern Spain). Journal of Structural Geology 30, 380-393. https://doi.org/10.1016/j.jsg.2007.11.010

Esteban, J.J., Cuevas, J., Tubía, J.M., Sergeev, S., Larionov, A., 2011. A revised Aquitanian age for the emplacement of the Ronda peridotites (Betic Cordilleras, southern Spain). Geological Magazine 148, 183-187. https://doi.org/10.1017/S0016756810000737

Esteban, J.J., Tubía, J.M., Cuevas, J., Seward, D., Larionov, A., Sergeev, S., Navarro-Vilá, F., 2013. Insights into extensional events in the Betic Cordilleras, southern Spain: New fission-track and U-Pb SHRIMP analyses. Tectonophysics 603, 179-188. https://doi.org/10.1016/j.tecto.2013.05.027

Esteban, J.J., Cuevas, J., Tubía, J.M., 2023. Provenance Analysis of the Ojén Nappe and Its Implication for the Geodynamic History (Alpujárride Complex, Betic Cordilleras, Spain). Minerals 13, 569. https://doi.org/10.3390/min13040569

Evins, P.M., 2005. A 3D study of aligned porphyroblast inclusion trails across shear zones and folds. Journal of Structural Geology 27, 1300-1314. https://doi.org/10.1016/j.jsg.2004.08.003

Fallot, P., Faure-Muret, A., Fontboté, J.M., Solé, L., 1960. Estudios sobre las series de Sierra Nevada y de la llamada Mischungszone. Boletín del Instituto Geológico y Minero de España 71, 347-557.

Fay, C., Bell, T.H., Hobbs, B.E., 2008. Porphyroblast rotation versus nonrotation: Conflict resolution! Geology 36, 307-310. https://doi.org/10.1130/G24499A.1

Felder, T.H., 1981. Les Malaguides de la Serranía de Ronda et leurs relations aux autres unités de zones internes des Cordillères bétiques (Espagne méridionale). Eclogae geologicae Helvetiae 74, 161-173.

Fernández-Fernández, E.M., Jabaloy-Sánchez, A., Nieto, F., González-Lodeiro, F., 2007. Structure of the Maláguide Complex near Vélez Rubio (Eastern Betic Cordillera, SE Spain). Tectonics 26, TC4008 https://doi.org/10.1029/2006TC002019.

Ferry, J.M., Spear, F.S., 1978. Experimental Calibration of the Partitioning of Fe and Mg Between Biotite and Garnet. Contrib Mineral Petrol 66, 113-117. https://doi.org/10.1007/BF00372150

Ferry, J.M., Watson, E.B., 2007. New thermodynamic models and revised calibrations for the Ti-in-zircon and Zr-in-rutile thermometers. Contrib Mineral Petrol 154, 429-437. https://doi.org/10.1007/s00410-007-0201-0

Forde, A., Bell, T.H., 1993. The rotation of garnet porphyroblasts around a single fold, Lukmanier Pass, Central Alps: Discussion. Journal of Structural Geology 15, 1365-1368. https://doi.org/10.1016/0191-8141(93)90110-V

Foucault, A., Paquet, J., 1971. Sur l'importance d'une tectogenèse hercynienne dans la région des Cordillères Bétiques (Sud de la Sierra Arana, Province de Grenade, Espagne). Comptes Rendus de l'Académie des Sciences de Paris 272, 2756-2758.

Frasca, G., Gueydan, F., Poujol, M., Brun, J.P., Parat, F., Monié, P., Pichat, A., Mazier, S., 2017. Fast switch from extensional exhumation to thrusting of the Ronda Peridotites (South Spain). Terra Nova 29, 117-126. https://doi.org/10.1111/ter.12255

Fyson, W.K., 1980. Fold fabrics and emplacement of an Archean granitoid pluton, Cleft Lake, Northwest Territories. Can. J. of Earth Sc., 17. 325-332. https://doi.org/10.1139/e80-032

Galindo-Zaldivar, J., 1990. Geometría y Cinemática de las Deformaciones Neógenas en Sierra Nevada (Cordilleras Béticas). PhD Thesis, Universidad de Granada. https://digibug.ugr.es/handle/10481/37526

Galindo-Zaldivar, J., González-Lodeiro, F., Jabaloy, A., 1989. Progressive extensional shear structures in a detachment contact in the Western Sierra Nevada (Betic Cordilleras, Spain). Geodinamica Acta 3, 73-85. https://doi.org/10.1080/09853111.1989.11105175

Gallegos, J.A., 1975. Los Alpujárrides al W de Sierra Nevada. PhD Thesis, Universidad de Granada.

García-Dueñas, V., Navarro-Vilá, F., 1976. Alpujarrides, Malaguides et autres unités allochtones au Nord de la Sierra Nevada (Cordillères Bétiques, Andalousie). Bulletin de la Société Géologique de France 7-XVIII-3, 641-648. https://doi.org/10.2113/gssgfbull.S7-XVIII.3.641

García-Dueñas, V., Martínez-Martínez, J.M., Orozco, M., Martín Ramos, D., 1987. El sentido de desplazamiento de los Mantos Nevado-Filábrides. Geogaceta 3, 11-13.

García-Dueñas, V., Martínez-Martínez, J.M., Orozco, M., Soto, J.I., 1988. Plis-nappes, cisaillements syn- à post-métamorphiques et cisaillements ductiles-fragiles en distension dans les Nevado-Filabrides (Cordillères bétiques, Espagne). Comptes Rendus de l'Académie des Sciences de Paris 307 (Série II), 1389-1395.

García-Hernández, M., Lopez-Garrido, A.C., Rivas, P., Sanz de Galdeano, C., Vera, J.A., 1980. Mesozoic palaeogeographic evolution of the External Zones of the Betic Cordillera. Geologie en Mijnbouw 59, 155-168.

Geel, T., Roep, T.B., 1998. Oligocene to middle Miocene basin development in the Eastern Betic Cordilleras, SE Spain (Vélez Rubio Corridor – Espuña): reflections of West Mediterranean plate-tectonic reorganizations. Basin Research 10, 325-343. https://doi.org/10.1046/j.1365-2117.1998.00068.x

Ghent, E.D., Stout, M.Z., 1981. Geobarometry and Geothermometry of Plagioclase-Biotite-Garnet-Muscovite Assemblages. Contrib Mineral Petrol 76, 92-97. https://doi.org/10.1007/BF00373688

Gil, A., Fernández, J., López-Garrido, A.C., 1987. Evolución de facies en el Trias de la Zona Prebética y borde de la meseta transversal Orcera-Puente Génave (Prov. Jaén). Cuadernos Geología Ibérica 11, 403-420.

Gómez-Pugnaire, M.T., Fernández-Soler, J.M., 1987. High-pressure metamorphism in metabasites from the Betic Cordilleras (S.E. Spain) and its evolution during the Alpine orogeny. Contrib Mineral Petrol 95, 231-244.

Gómez-Pugnaire, M.T., Franz, G., López Sánchez-Vizcaíno, V., 1994. Retrograde formation of NaCl-scapolite in high pressure metaevaporites from the Cordilleras Béticas (Spain). Contrib Mineral Petrol 116, 448-461. https://doi.org/10.1007/BF00310911

Gómez-Pugnaire, M.T., Braga, J.C., Martín, J.M., Sassi, F.P., Del Moro, A., 2000. Regional implications of a Palaeozoic age for the Nevado-Filábride Cover of the Betic Cordillera, Spain. Schweizerische Mineralogische und Petrographische Mitteilungen 80, 45-52.

Gómez-Pugnaire, M.T., Galindo-Zaldívar, J., Rubatto, D., González-Lodeiro, F., López Sánchez-Vizcaíno, V., Jabaloy, A., 2004. A reinterpretation of the Nevado-Filábride and Alpujárride Complexes (Betic Cordillera): field, petrography and U-Pb ages from orthogneisses (western Sierra Nevada, S Spain). Schweizerische Mineralogische und Petrographische Mitteilungen 84, 303-322.

Gómez-Pugnaire, M.T., Rubatto, D., Fernández-Soler, J.M., Jabaloy, A., López-Sánchez-Vizcaíno, V., González-Lodeiro, F., Galindo-Zaldívar, J., Padrón-Navarta, J.A., 2012. Late Variscan magmatism in the Nevado-Filábride Complex: U-Pb geochronologic evidence for the pre-Mesozoic nature of the deepest Betic complex (SE Spain). Lithos 146-147, 93-111. https://doi.org/10.1016/j.lithos.2012.03.027

González-Casado, J.M., Casquet, C., Martínez-Martínez, J.M., García-Dueñas, V., 1995. Retrograde evolution of quartz segregations from the Dos Picos shear zone in the Nevado-Filabride Complex (Betic chains, Spain). Evidence from fluid inclusions and quartz c-axis fabrics. Geol. Rundsch. 84, 175-186. https://doi.org/10.1007/BF00192249

González Donoso, J.M., Linares, D., Molina, E., Serrano, F., Vera, J.A., 1982. Sobre la edad de la Formación de La Viñuela (Cordilleras Béticas, provincia de Málaga). Boletín de la Real Sociedad Española de Historia Natural (Sección Geológica) 80, 255-275.

Griera, A., Llorens, M.G., Gomez-Rivas, E., Bons, P.D., Jessel, M.W., Evans, L.A., Lebensohn, R., 2013. Numerical modelling of porphyroclast and porphyroblast rotation in anisotropic rocks. Tectonophysics 587, 4–29. https://doi.org/10.1016/j.tecto.2012.10.008

Guerrera, F., Martín-Algarra, A., Perrone, V., 1993. Late Oligocene-Miocene syn-/-late-orogenic successions in Western and Central Mediterranean chains from the Betic Cordillera to the Southern Apennines. Terra Nova 5, 525-544. https://doi.org/10.1111/j.1365-3121.1993.tb00302.x

Guerrera, F., Martín-Algarra, A., Martín-Martín, M., 2012. Tectono-sedimentary evolution of the 'Numidian Formation' and Lateral Facies (southern branch of the western Tethys): constraints for central-western Mediterranean geodynamics. Terra Nova 24, 34-41. https://doi.org/10.1111/j.1365-3121.2011.01034.x

Guerrera, F., Martín-Martín, M., Tramontana, M., 2021. Evolutionary geological models of the central-western peri-Mediterranean chains: a review. International Geology Review 63, 65-86 https://doi.org/10.1080/00206814.2019.1706056

Guezou, J.C., Frizon de Lamotte, D., Coulon, M., Morel, J.L., 1991. Structure and kinematics of the Prebetic nappe complex (southern Spain): definition of a «Betic Floor Thrust» and implications in the Betic-Rif orocline. Annales Tectonicae 5, 32-48.

Ham, A.P., Bell, T.H., 2004. Recycling of foliations during folding. Journal of Structural Geology 26, 1989-2009. https://doi.org/10.1016/j.jsg.2004.04.003

Hanna, R.D., Ketcham, R.A., 2017. X-ray computed tomography of planetary materials: A primer and review of recent studies. Chemie der Erde 77, 547-572. https://doi.org/10.1016/j.chemer.2017.01.006

Hayward, N., 1990. Determination of early fold axis orientations in multiply deformed rocks using porphyroblast inclusion trails. Tectonophysics 179, 353-369. https://doi.org/10.1016/0040-1951(90)90301-N

Hayward, N., 1992. Microstructural analysis of the classical spiral garnet porphyroblasts of south-east Vermont - evidence for non-rotation. Journal of Metamorphic Geology 10(4), 567–587. https://doi.org/10.1111/j.1525-1314.1992.tb00106.x

Hickey, K.A., Bell, T.H., 1999. Behaviour of rigid objects during deformation and metamorphism: a test using schists from the Bolton syncline, Connecticut, USA. Journal of Metamorphic Geology 17, 211-228. https://doi.org/10.1046/j.1525-1314.1999.00192.x

Homonnay, E., Corsini, M., Lardeaux, J.M., Romagny, A., Münch, P., Bosch, D., Cenki-Tok, B., Ouazzani-Touhami, M., 2018. Miocene crustal extension following thrust tectonic in the Lower Sebtides units (internal Rif, Ceuta Peninsula, Spain): Implication for the geodynamic evolution of the Alboran domain. Tectonophysics 722, 507-535. https://doi.org/10.1016/j.tecto.2017.11.028

Huddlestone-Holmes, C.R., Ketcham, R.A., 2005. Getting the inside story: using computed X-ray tomography to study inclusion trails in garnet porphyroblasts. American Mineralogist 90, ea1-ea17. https://doi.org/10.2138/am.2005.1840

Huddlestone-Holmes, C.R., Ketcham, R.A., 2010. An X-ray computed tomography study of inclusion trail orientations in multiple porphyroblasts from a single sample. Tectonophysics 480, 305–320. https://doi.org/10.1016/j.tecto.2009.10.021

Jabaloy, A., Galindo-Zaldivar, J., Gonzalez-Lodeiro, F., 1993. The Alpujarride-Nevado- Filabride extensional shear zone, Betic Cordillera, SE Spain. Journal of Structural Geology 15, 552–569. https://doi.org/10.1016/0191-8141(93)90148-4

Jabaloy-Sánchez, A., Fernández-Fernández, E., González-Lodeiro, F., 2007. A cross section of the eastern Betic Cordillera (SE Spain) according field data and a seismic reflection profile. Tectonophysics 433, 97-126. https://doi.org/10.1016/j.tecto.2006.11.004

Jabaloy-Sánchez, A., Gómez-Pugnaire, M.T., Padrón-Navarta, J.A., López Sánchez-Vizcaíno, V., Garrido, C.J., 2015. Subduction- and exhumation-related structures preserved in metaserpentinites and associated metasediments from the Nevado-Filábride Complex (Betic Cordillera, SE Spain). Tectonophysics 644-645, 40-57. https://doi.org/10.1016/j.tecto.2014.12.022

Jabaloy-Sánchez, A., Talavera, C., Gómez-Pugnaire, M.T., López-Sánchez-Vizcaíno, V., Vázquez-Vílchez, M., Rodríguez-Peces, M.J., Evans, N.J., 2018. U-Pb ages of detrital zircons from the Internal Betics: A key to deciphering palaeogeographic provenance and tectono-stratigraphic evolution. Lithos 318-319, 244-266. https://doi.org/10.1016/j.lithos.2018.07.026

Jabaloy Sánchez, A., Martín-Algarra, A., Padrón-Navarta, J.A., Martín-Martín, M., Gómez-Pugnaire, M.T., López Sánchez-Vizcaíno, V., Garrido, C.J., 2019. Lithological Successions of the Internal Zones and Flysch Trough Units of the Betic Chain, in: Quesada, C., Oliveira, J.T., (Eds.), The Geology of Iberia: A Geodynamic Approach, Vol. 3, Ch. 8, p. 377-432 (Alpine Cycle, Vergés, J., Kullber, J.C., Volume Coordinators), Regional Geology Reviews. https://doi.org/10.1007/978-3-030-11295-0_8

Johnson, C., Harbury, N., Hurford, A.J., 1997. The role of extension in the Miocene denudation of the Nevado-Filábride Complex, Betic Cordillera (SE Spain). Tectonics 16, 189-204. https://doi.org/10.1029/96TC03289

Johnson, S.E., 1992. Sequential porphyroblast growth during progressive deformation and low-P high-T (LPHT) metamorphism, Cooma Complex, Australia: The use of microstructural analysis to better understand deformation and metamorphic histories. Tectonophysics 214, 311-339. https://doi.org/10.1016/0040-1951(92)90204-J

Kampschuur, W., 1975. Data on thrusting and metamorphism in the eastern Sierra de los Filabres: higher Nevado-Filabride units and the glaucophanitic greenschist facies. Tectonophysics 27, 57-81. https://doi.org/10.1016/0040-1951(75)90048-7

Kim, H.S., Bell, T.H., 2005. Combining compositional zoning and foliation intersection axes (FIAs) in garnet to quantitatively determine early P-T-t paths in multiply deformed and metamorphosed schists: north central Massachusetts, USA. Contrib. Mineral. Petrol. 149, 141-163. https://doi.org/10.1007/s00410-004-0640-9

Kim, H.S., Jung, W.S., 2010. The use of garnet porphyroblasts to resolve the metamorphic pressure-temperature-deformation (P-T-d) path: An example from the Imjingang belts, South Korea. Geosciences Journal 14, 111-126. DOI 10.1007/s12303-010-0012-6

Kim, H.S., Ree, J.H., 2013. Permo-Triassic changes in bulk crustal shortening direction during deformation and metamorphism of the Taebaeksan Basin, South Korea using foliation intersection/inflection axes: Implications for tectonic movement at the eastern margin of Eurasia during the Songrim (Indosinian) orogeny. Tectonophysics 587, 133-145. https://doi.org/10.1016/j.tecto.2012.08.033

Kim, H.S., Sanislav, I.V., 2017. Foliation intersection/inflection axes within porphyroblasts (FIAs): a review of advanced applications and significance. Geosciences Journal 21, 1013-1032. https://doi.org/10.1007/s12303-017-0047-z

Kirchner, K.L., Behr, W.M., Loewy, S., Stockli, D.F., 2016. Early Miocene subduction in the western Mediterranean: Constraints from Rb-Sr multimineral isochron geochronology. Geochemistry, Geophysics, Geosystems 17, 1842-1860. https://doi.org/10.1002/2015GC006208

Kozur, H., Kampschuur, W., Mulder-Blanken, C.W.H., Simon, O.J., 1974. Contribution to the Triassic ostracode faunas of the Betic Zone (southern Spain). Scripta Geol. 23, 1-56.

Laborda-López, C., Aguirre, J., Donovan, S.K., 2015. Surviving metamorphism: taphonomy of fossil assemblages in marble and calc-silicate schist. Palaios 30, 668-679. https://doi.org/10.2110/palo.2015.013

Lafuste, M.L.J., Pavillon, M.J., 1976. Mise en evidence d'Eifélien daté au sein des terrains métamorphiques des zones internes des Cordillères bétiques. Intérêt de ce nouveau repére stratigraphique. Comptes Rendus de l'Académie des Sciences de Paris, Série II 283, 1015-1018.

Langenberg, C.W., 1973. Gravitational gliding in the northern Sierra de los Filabres (SE Spain). Geologie en Mijnbouw 52, 187-192.

Leine, L., 1968. Rauhwackes in the Betic Cordilleras, Spain: Nomenclature, description and genesis of weathered carbonate breccias of tectonic origin. PhD Thesis, Univ. Amsterdam.

Li, B., Massonne, H.J., 2018. Two Tertiary metamorphic events recognized in high-pressure metapelites of the Nevado-Filábride Complex (Betic Cordillera, S Spain). Journal of Metamorphic Geology 36, 603-630. https://doi.org/10.1111/jmg.12312

Linthout, K., Vissers, R.L.M., 1979. On the classification of tectonic units in the Nevado-Filabride Complex of the northern Sierra de los Filabres, Betic Cordilleras, SE Spain. Geologie en Mijnbouw 58, 49-56.

Lonergan, L., 1993. Timing and kinematics of deformation in the Malaguide Complex, Internal Zone of the Betic Cordillera, Southeast Spain. Tectonics 12, 460-476. https://doi.org/10.1029/92TC02507

Lonergan, L., Platt, J.P., Gallagher, L., 1994. The Internal-External Zone Boundary in the eastern Betic Cordillera, SE Spain. Journal of Structural Geology 16, 175-188. https://doi.org/10.1016/0191-8141(94)90103-1

López Sánchez-Vizcaíno, V., Rubatto, D., Gómez-Pugnaire, M.T., Trommsdorff, V., Müntener, O., 2001. Middle Miocene high-pressure metamorphism and fast exhumation of the Nevado-Filábride Complex, SE Spain. Terra Nova 13, 327-332. https://doi.org/10.1046/j.1365-3121.2001.00354.x

Ludwig, K.R., 2003. Mathematical–Statistical Treatment of Data and Errors for 230Th/U Geochronology. Reviews in Mineralogy and Geochemistry 52, 631–656. https://doi.org/10.2113/0520631

Luján, M., Crespo-Blanc, A., Balanyá, J.C., 2006. The Flysch Trough thrust imbricate (Betic Cordillera): A key element of the Gibraltar Arc orogenic wedge. Tectonics 25, TC6001. https://doi.org/10.1029/2005TC001910

Mares, V.M., 1998. Structural development of the Soldiers Cap Group in the Eastern Fold Belt of the Mt Isa Inlier: A succession of horizontal and vertical deformation events and large-scale shearing. Australian Journal of Earth Sciences 45, 373-387. https://doi.org/10.1080/08120099808728398

Martín-Algarra, A., 1987. Evolución geológica alpina del contacto entre las Zonas Internas y las Zonas Externas de la Cordillera Bética. PhD Thesis, Universidad de Granada, 1171 p. https://digibug.ugr.es/handle/10481/75699

Martín-Algarra, A., Crespo-Blanc, A., Delgado, F., Estévez, A., González-Lodeiro, F., Orozco, M., Sánchez-Gómez, M., Sanz de Galdeano, C., García-Dueñas, V., 2004. Complejo

Alpujárride. Estructura. Rasgos generales, in: Vera, J.A., (Ed.) Geología de España. SGE-IGME Madrid, 416-417.

Martín-Algarra, A., Mazzoli, S., Perrone, V., Rodríguez-Cañero, R., Navas-Parejo, P., 2009a. Variscan Tectonics in the Malaguide Complex (Betic Cordillera, Southern Spain): Stratigraphic and Structural Alpine versus Pre-Alpine Constraints from the Ardales Area (Province of Málaga). I. Stratigraphy. The Journal of Geology 117, 241-262. https://doi.org/10.1086/597364

Martín-Algarra, A., Mazzoli, S., Perrone, V., Rodríguez-Cañero, R., 2009b. Variscan Tectonics in the Malaguide Complex (Betic Cordillera, Southern Spain): Stratigraphic and Structural Alpine versus Pre-Alpine Constraints from the Ardales Area (Province of Málaga). II. Structure. The Journal of Geology 117, 263-284. https://doi.org/10.1086/597365

Martín-Algarra, A., García-Casco, A., Gómez-Pugnaire, M.T., Jabaloy-Sánchez, A., Laborda-López, C., López Sánchez-Vizcaíno, V., Mazzoli, S., Navas-Parejo, P., Perrone, V., Rodríguez-Cañero, R., Sánchez-Navas, A., 2019. Paleozoic Basement and Pre-Alpine History of the Betic Cordillera, in: Quesada, C., Oliveira, J.T., (Eds.), The Geology of Iberia: A Geodynamic Approach, Vol. 2, Ch. 9, p. 261–305. Regional Geology Reviews. https://doi.org/10.1007/978-3-030-10519-8_9

Martín-Martín, M., Martín-Algarra, A., 1997. La estructura del área de Sierra Espuña (contacto Zonas Internas-Externas, sector oriental de la Cordillera Bética). Estudios Geológicos 53, 237-248.

Martín-Martín, M., El Mamoune, B., Martín-Algarra, A., Martín-Pérez, J.A., 1996. The Internal-External Zone Boundary in the Eastern Betic Cordillera, SE Spain: Discussion. Journal of Structural Geology 18, 523-524.

Martín-Rojas, I., Estévez, A., Martín-Martín, M., Delgado, F., García-Tortosa, F.J., 2007. New data from Orihuela and Callosa Mountains (Betic Internal Zone, Alicante, SE Spain). Implications for the "Almágride Complex" controversy. Journal of Iberian Geology 33 (2), 311-318.

Martínez del Olmo, W., 2019. El complejo olistostrómico del Mioceno de la Cuenca del Río Guadalquivir (SO de España). Revista de la Sociedad Geológica de España 32, 3-16.

Martínez-Martínez, J.M., 1986a. Evolución tectono-metamórfica del complejo Nevado-Filábride en el sector de unión entre Sierra Nevada y Sierra de los Filabres (Cordilleras Béticas). Cuad. Geol. Univ. Granada 13, 1-194.

Martínez-Martínez, J.M., 1986b. Fabricas y texturas miloniticas. Cinematica de las traslaciones en el Complejo Nevado-Filabride (Cordilleras Beticas, España). Estudios Geológicos 42, 291–300.

Martínez-Martínez, J.M., 2007. Coexistencia de zonas de cizalla dúctil de extensión y de acortamiento en el domo de Sierra Nevada, Béticas (SE de España). Revista de la Sociedad Geológica de España 20, 229-245.

Martínez-Martínez, J.M., Soto, J.I., Balanyá, J.C., 1995. Large scale structures in the Nevado-Filabride Complex and crustal seismic fabrics of the deep seismic reflection profile ESCI-Béticas2. Revista de la Sociedad Geológica de España 8, 477-489.

Martínez-Martínez, J.M., Soto, J.I., Balanyá, J.C., 2002. Orthogonal folding of extensional detachments: Structure and origin of the Sierra Nevada elongated dome (Betics, SE Spain). Tectonics 21, 1012. https://doi.org/10.1029/2001TC001283

Martínez-Martínez, J.M., Torres-Ruiz, J., Pesquera, A., Gil-Crespo, P.P., 2010. Geological relationships and U-Pb zircon and 40Ar/39Ar tourmaline geochronology of gneisses and tourmalinites from the Nevado-Filabride complex (western Sierra Nevada, Spain): Tectonic implications. Lithos 119, 238-250. https://doi.org/10.1016/j.lithos.2010.07.002

Massonne, H.J., 2014. Wealth of P-T-t information in medium-high grade metapelites: Example from the Jubrique Unit of the Betic Cordillera, S Spain. Lithos 208-209, 137-157. https://doi.org/10.1016/j.lithos.2014.08.027

Mazzoli, S., Martín-Algarra, A., 2011. Deformation partitioning during transpressional emplacement of a "mantle extrusion wedge": the Ronda peridotites, western Betic Cordillera, Spain. Journal of the Geological Society, London 168, 373–382. https://doi.org/10.1144/0016-76492010-126

Molina, J.M., Vera, J.A., de Gea, G., 1998. Vulcanismo submarino del Santoniense en el Subbetico: datación con nannofósiles e interpretación (Formación Capas Rojas, Alamedilla, provincia de Granada). Estudios Geológicos 54, 191-197.

Monié, P., Galindo-Zaldivar, J., González-Lodeiro, F., Goffe, B., Jabaloy, A., 1991. 40Ar/39Ar geochronology of Alpine tectonism in the Betic Cordilleras (southern Spain). Journal of the Geological Society 148, 289-297. https://doi.org/10.1144/gsjgs.148.2.0289

Monié, P., Torres-Roldán, R.L., García-Casco, A., 1994. Cooling and exhumation of the Western Betic Cordilleras, 40Ar/39Ar thermochronological constraints on a collapsed terrane. Tectonophysics 238, 353-379. https://doi.org/10.1016/0040-1951(94)90064-7

Morata, D., 1993. Petrología y geoquímica de las ofitas de las Zonas Externas de las Cordilleras Béticas. PhD Thesis, Universidad de Granada. https://digibug.ugr.es/handle/10481/54267

Munro, M.A., Blenkinsop, T.G., 2012. MARD-A moving average rose diagram application for the geosciences. Computers & Geosciences 49, 112-120. https://doi.org/10.1016/j.cageo.2012.07.012

Navarro-Vilá, F., Tubía, J.M., 1983. Essai d'une nouvelle différenciation des Nappes Alpujarrides dans le secteur occidental des Cordillères Bétiques (Andalousie, Espagne). Comptes Rendus de l'Académie des Sciences de Paris 296, 111-114.

Navas-Parejo, P., 2012. Paleozoic Stratigraphy and Palaeogeography of the Malaguide Complex (Betic Cordillera) and other Western Mediterranean related domains (Calabria-Peloritani Terrane). PhD Thesis, Universidad de Granada. https://digibug.ugr.es/handle/10481/23780

Nieto, J.M., Puga, E., Díaz de Federico, A., 2000. Late Variscan pyroclastic rocks from the Mulhacén Complex (Betic Cordillera, Spain). In: Leyrit, H., Montenat, Ch (Eds.),

Volcaniclastic Rocks, from Magmas to Sediments. Gordon and Breach Science Publishers, 217–224.

Nijhuis, H.J., 1964. On the stratigraphy of the Nevado-Filabride units as exposed in the eastern Sierra de los Filabres (SE Spain). Geologie en Mijnbouw 43, 321-325.

Ollion, J., Cochennec, J., Loll, F., Escude, C., Boudier, T., 2013. TANGO: a generic tool for high-throughput 3D image analysis for studying nuclear organization. Bioinformatics 29, 1840–1841. DOI: 10.1093/bioinformatics/btt276

Orozco, M., 1986. Fábrica de cuarzo y cabalgamientos hacia el ENE en Sierra Nevada y Sierra de los Filabres (Cordilleras Béticas). Geogaceta 1, 40-41.

Orozco, M., Alonso-Chaves, F.M., Nieto, F., 1998. Development of large north-facing folds and their relation to crustal extension in the Alboran domain (Alpujarras region, Betic Cordilleras, Spain). Tectonophysics 298, 271-295. https://doi.org/10.1016/S0040-1951(98)00188-7

Orozco, M., Molina, J.M., Crespo-Blanc, A., Alonso-Chaves, F.M., 1999. Palaeokarst and rauhwacke development, mountain uplift and subaerial sliding of tectonic sheets (northern Sierra de los Filabres, Betic Cordilleras, Spain). Geologie en Mijnbouw 78, 103-117.

Orozco, M., Álvarez-Valero, A.M., Alonso-Chaves, F.M., Platt, J.P., 2004. Internal structure of a collapsed terrain The Lújar syncline and its significance for the fold- and sheet-structure of the Alborán Domain (Betic Cordilleras, Spain). Tectonophysics 385, 85-104. https://doi.org/10.1016/j.tecto.2004.04.025

Orozco, M., Alonso-Chaves, F.M., Platt, J.P., 2017. Late extensional shear zones and associated recumbent folds in the Alpujarride subduction complex, Betic Cordillera, southern Spain. Geologica Acta 15, 51-66. DOI: 10.1344/GeologicaActa2017.15.1.5

Passchier, C.W., Trouw, R.A.J., Zwart, H.J., Vissers, R.L.M., 1992. Porphyroblast rotation: eppur si muove? Journal of Metamorphic Geology 10, 283-294. https://doi.org/10.1111/j.1525-1314.1992.tb00083.x

Perchuk, L.L., 1991. Derivation of a thermodynamically consistent set of geothermometers and geobarometers for metamorphic and magmatic rocks, in: Perchuk, L.L. (Ed.), Progress in Metamorphic and Magmatic Petrology, p. 93-111. Cambridge University Press.

Pérez-López, A., Pérez-Valera, F., 2007. Palaeogeography, facies and nomenclature of the Triassic units in the different domains of the Betic Cordillera (S Spain). Palaeogeography, Palaeoclimatology, Palaeoecology 254, 606-626. https://doi.org/10.1016/j.palaeo.2007.07.012

Platt, J.P., 1998. Comment on "Alternating contractional and extensional events in the Alpujarride nappes of the Alboran Domain (Betics, Gibraltar Arc)" by Juan C. Balanyá et al. Tectonics 17 (6), 973-976. https://doi.org/10.1029/1998TC900005

Platt, J.P., Whitehouse, M.J., 1999. Early Miocene high-temperature metamorphism and rapid exhumation in the Betic Cordillera (Spain): evidence from U-Pb zircon ages. Earth and Planetary Science Letters 171, 591-605. https://doi.org/10.1016/S0012-821X(99)00176-4

Platt, J.P., Soto, J.I., Whitehouse, M.J., Hurford, A.J., Kelley, S.P., 1998. Thermal evolution, rate of exhumation, and tectonic significance of metamorphic rocks from the floor of the Alboran

extensional basin, western Mediterranean. Tectonics 17, 671-689. https://doi.org/10.1029/98TC02204

Platt, J.P., Allerton, S., Kirker, A., Mandeville, C., Mayfield, A., Platzman, E.S., Rimi, A., 2003a. The ultimate arc: Differential displacement, oroclinal bending, and vertical axis rotation in the External Betic-Rif arc. Tectonics 22, 1017. https://doi.org/10.1029/2001TC001321

Platt, J.P., Argles, T.W., Carter, A., Kelley, S.P., Whitehouse, M.J., Lonergan, L., 2003b. Exhumation of the Ronda peridotite and its crustal envelope: constraints from thermal modelling of a P-T-time array. Journal of the Geological Society 160, 655-676. https://doi.org/10.1144/0016-764902-108

Platt, J.P., Kelley, S.P., Carter, A., Orozco, M., 2005. Timing of tectonic events in the Alpujarride Complex, Betic Cordillera, southern Spain. Journal of the Geological Society, London 162, 451-462. https://doi.org/10.1144/0016-764903-039

Platt, J.P., Anczkiewicz, R., Soto, J.I., Kelley, S.P., Thirlwall, M., 2006. Early Miocene continental subduction and rapid exhumation in the western Mediterranean. Geology 34, 981-984. https://doi.org/10.1130/G22801A.1

Platzman, E., Platt, J.P., Kelly, S.P., Allerton, S., 2000. Large clockwise rotation in an extensional allochthon, Alboran Domain (southern Spain). Journal of the Geological Society London 157, 1187–1197. https://doi.org/10.1144/jgs.157.6.1187

Poitrasson, F., Chenery, S., Shepherd, T.J., 2000. Electron microprobe and LA-ICP-MS study of monazite hydrothermal alteration: Implications for U-Th-Pb geochronology and nuclear ceramics. Geochim. Cosmochim. Acta 64, 3283–3297.

Porkoláb, K., Matenco, L., Hupkes, J., Willingshofer, E., Wijbrans, J., van Schrojenstein Lantman, H., van Hinsbergen, D.J.J., 2022. Tectonic evolution of the Nevado-Filábride Complex (Sierra de los Filabres, Southeastern Spain): Insights from new structural and geochronological data. Tectonics 41, e2021TC006922. https://doi.org/10.1029/2021TC006922

Portugal-Ferreira, M., Morata, D., Puga, E., Demant, A., Aguirre, L., 1995. Evolución geoquímica y temporal del magmatismo básico Mesozoico en las Zonas Externas de las Cordilleras Béticas. Estudios Geológicos 51, 109-118.

Poulaki, E.M., Stockli, D.F., 2022. The paleotectonic evolution of the western Mediterranean: provenance insights from the internal Betics, southern Spain. Frontiers in Earth Science 10, 929502. https://doi.org/10.3389/feart.2022.929502

Poulaki, E.M., Stockli, D.F., Shuck, B.D., 2023. Pre-Subduction Architecture Controls Coherent Underplating During Subduction and Exhumation (Nevado-Filábride Complex, Southern Spain). Geochemistry, Geophysics, Geosystems 24, e2022GC010802. https://doi.org/10.1029/2022GC010802

Powell, D., MacQueen, J.A., 1976. Relationships between garnet shape, rotational inclusion fabrics and strain in some Moine metamorphic rocks of Skye, Scotland. Tectonophysics 35, 391-402. https://doi.org/10.1016/0040-1951(76)90077-9

Pownceby, M.I., Wall, V.J., O'Neill, H.S.C., 1987. Fe-Mn partitioning between garnet and ilmenite: experimental calibration and applications. Contrib Mineral Petrol 97, 116-126. https://doi.org/10.1007/BF00375219

Pownceby, M.I., Wall, V.J., O'Neill, H.S.C., 1991. An experimental study of the effect of Ca upon garnet-ilmenite Fe-Mn exchange equilibria. American Mineralogist 76, 1580-1588.

Priem, H.N.A., Boelrijk, N.A.I.M., Hebeda, E.H., Verschure, R.H., 1966. Isotopic age determinations on tourmaline granite-gneisses and a metagranite in the eastern Betic Cordilleras (south-eastern Sierra de los Filabres), S.E. Spain. Geologie en Mijnbouw 45, 184-187.

Puga, E., Díaz de Federico, A., 1976. Pre-Alpine metamorphism in the Sierra Nevada Complex (Betic Cordillera Spain). Cuadernos de Geología de la Universidad de Granada 7, 161-171.

Puga, E., Díaz de Federico, A., Fontbote, J.M., 1974. Sobre la individualización y sistematización de las unidades profundas de la Zona Bética. Estudios Geológicos 30, 543-548

Puga, E., Fontboté, J.M., Martín-Vivaldi, J.L., 1975. Kyanite Pseudomorphs after Andalusite in Polymetamorphic Rocks of the Sierra Nevada (Betic Cordillera, Southern Spain). Schweiz. Mineral. Petrogr. Mitt. 55, 227-241.

Puga, E., Portugal, M., Díaz de Federico, A., Bargossi, G.M., Morten, L., 1989. The evolution of the magmatism in the external zones of the Betic Cordilleras during the Mesozoic. Geodinamica Acta 3, 253-266. https://doi.org/10.1080/09853111.1989.11105191

Puga, E., Nieto, J.M., Díaz de Federico, A., Portugal, M., Reyes, E., 1996. The intra-orogenic Soportújar Formation of the Mulhacén Complex: Evidence for the polycyclic character of the Alpine orogeny in the Betic Cordilleras. Eclogae Geologicae Helvetiae 89, 129-162.

Puga, E., Nieto, J.M., Díaz de Federico, A., 2000. Contrasting P-T paths in eclogites of the Betic ophiolitic association, Mulhacén complex, southeastern Spain. The Canadian Mineralogist 38, 1137-1161. https://doi.org/10.2113/gscanmin.38.5.1137

Puga, E., Díaz de Federico, A., Nieto, J.M., 2002. Tectonostratigraphic subdivisión and petrological characterisation of the deepest complexes of the Betic zone: a review. Geodinamica Acta 15, 23-43. https://doi.org/10.1080/09853111.2002.10510737

Puga, E., Fanning, C.M., Nieto, J.M., Díaz de Federico, A., 2005. Recrystallization textures in zircon generated by ocean-floor and eclogite-facies metamorphism: a cathodoluminiscence and U-Pb SHRIMP study, with constraints from REE elements. The Canadian Mineralogist 43, 183-202. https://doi.org/10.2113/gscanmin.43.1.183

Puga, E., Fanning, M., Díaz de Federico, A., Nieto, J.M., Beccaluva, L., Bianchini, G., Díaz Puga, M.A., 2011. Petrology, geochemistry and U-Pb geochronology of the Betic Ophiolites: Inferences for Pangaea break-up and birth of the westernmost Tethys Ocean. Lithos 124, 255-272. https://doi.org/10.1016/j.lithos.2011.01.002

Quentin de Gromard, R., 2013. The significance of E-W structural trends for the Alice Springs Orogeny in the Charters Towers Province, North Queensland. Tectonophysics 587, 168-187. https://doi.org/10.1016/j.tecto.2012.09.002

Reche, J., Martínez, F.J., 1996. GPT: An excel spreadsheet for thermobarometric calculations in metapelitic rocks. Computers & Geosciences 22, 775-784. https://doi.org/10.1016/0098-3004(96)00007-6

Rich, B.H., 2006. Permian bulk shortening in the Narragansett Basin of southeastern New Englan, USA. Journal of Structural Geology 28, 682-694. https://doi.org/10.1016/j.jsg.2006.01.003

Rodríguez-Cañero, R., Jabaloy-Sánchez, A., Navas-Parejo, P., Martín-Algarra, A., 2018. Linking Palaeozoic palaeogeography of the Betic Cordillera to the Variscan Iberian Massif: new insight through the first conodonts of the Nevado-Filábride Complex. International Journal of Earth Sciences 107, 1791-1806. https://doi.org/10.1007/s00531-017-1572-8

Rodríguez-Fernández, J., 1982. El Mioceno del sector central de las Cordilleras Béticas. PhD Thesis, University of Granada, 224 p. https://digibug.ugr.es/handle/10481/32561

Rodríguez-Fernández, J., Comas, M.C., Soria, J., Martín-Pérez, J.A., Soto, J.I., 1999. The sedimentary record of the Alboran basin: An attempt at sedimentary sequence correlation and subsidence analysis, in: Zahn, R., Comas, M.C., and Klaus, A. (eds), Proceedings of the Ocean Drilling Program, Scientific Results, Vol. 161, p. 69–76.

Rodríguez-Fernández, J., Roldán, F.J., Azañón, J.M., García-Cortés, A., 2013. El colapso gravitacional del frente orogénico alpino en el Dominio Subbético durante el Mioceno medio-superior: El Complejo Extensional Subbético. Boletín Geológico y Minero 124, 477-504.

Roep, T.B., Mac Gillavry, H.J., 1962. Preliminary note on the presence of distinct tectonic units in the Betic of Málaga of the Vélez Rubio region (SE Spain). Geologie en Mijnbow 41, 423-429.

Rosenfeld, J.L., 1970. Rotated garnets in metamorphic rocks. Geological Society of America Special Paper, 129, 105.

Rossetti, F., Faccenna, C., Crespo-Blanc, A., 2005. Structural and kinematic constraints to the exhumation of the Alpujarride Complex (Central Betic Cordillera, Spain). Journal of Structural Geology 27, 199-216. https://doi.org/10.1016/j.jsg.2004.10.008

Ruiz Cruz, M.D., Sanz de Galdeano, C., 2014. Garnet variety and zircon ages in UHP meta-sedimentary rocks from the Jubrique zone (Alpujárride Complex, Betic Cordillera, Spain): evidence for a pre-Alpine emplacement of the Ronda peridotite. International Geology Review 56, 845-868. https://doi.org/10.1080/00206814.2014.904759

Ruiz-Cruz, M.D., Sanz de Galdeano, C., Santamaría, A., 2015. Petrology and thermobarometric estimates for metasediments, orthogneisses, and eclogites from the Nevado-Filábride complex in the western Sierra Nevada (Betic Cordillera, Spain). The Canadian Mineralogist 53, 1083-1107. https://doi.org/10.3749/canmin.1500037

Ruiz-Fuentes, A., Aerden, D.G.A.M., 2018. Transposition of foliations and superposition of lineations during polyphase deformation in the Nevado-Filabride complex: tectonic implications. International Journal of Earth Sciences 107, 1975-1988. https://doi.org/10.1007/s00531-017-1582-6

Ruiz-Fuentes, A., Aerden, D.G.A.M., 2023. Deciphering western Mediterranean kinematics using metamorphic porphyroblasts from the Alpujárride Complex (Betic Cordillera). Journal of Structural Geology 168, 104823. https://doi.org/10.1016/j.jsg.2023.104823

Ruiz-Fuentes, A., Cabrera-Porras, A., Martín-Algarra, A., 2022. Structural record of polyorogenic pre-Alpine and Alpine deformations within a major thrust nappe close to a suture zone (Internal-External Zones Boundary of the central Betic Cordillera, S Spain). International Geology Review https://doi.org/10.1080/00206814.2022.2129472

Sánchez-Navas, A., Oliveira-Barbosa, R.C., García-Casco, A., Martín-Algarra, A., 2012. Transformation of Andalusite to Kyanite in the Alpujarride Complex (Betic Cordillera, Southern Spain): Geologic Implications. The Journal of Geology 120, 557-574. https://doi.org/10.1086/666944

Sánchez-Navas, A., García-Casco, A., Martín-Algarra, A., 2014. Pre-Alpine discordant granitic dikes in the metamorphic core of the Betic Cordillera: tectonic implications. Terra Nova 26, 477-486. https://doi.org/10.1111/ter.12123

Sánchez-Navas, A., Macaione, E., Oliveira-Barbosa, R.C., Messina, A., Martín-Algarra, A., 2016. Transformation of kyanite to andalusite in the Benamocarra Unit (Betic Cordillera, S. Spain). Kinetics and petrological significance. European Journal of Mineralogy 28, 337-353. https://doi.org/10.1127/ejm/2016/0028-2518

Sánchez-Navas, A., García-Casco, A., Mazzoli, S., Martín-Algarra, A., 2017. Polymetamorphism in the Alpujarride Complex, Betic Cordillera, South Spain. The Journal of Geology 125, 637-657. https://doi.org/10.1086/693862

Sánchez-Rodriguez, L., Gebauer, D., 2000. Mesozoic formation of pyroxenites and gabbros in the Ronda area (southern Spain), followed by Early Miocene subduction metamorphism and emplacement into the middle crust: U-Pb sensitive high-resolution ion microprobe dating of zircon. Tectonophysics 316, 19-44. https://doi.org/10.1016/S0040-1951(99)00256-5

Sanislav, I.V., 2010. Porphyroblast rotation and strain localization: Debate settled!: Comment. Geology 38(4), e204. https://doi.org/10.1130/G30522C.1

Sanislav, I.V., 2011. A long-lived metamorphic history in the contact aureole of the Mooselookmeguntic pluton revealed by in situ dating of monazite grains preserved as inclusions in staurolite porphyroblasts. Journal of Metamorphic Geology 29, 251-273. https://doi.org/10.1111/j.1525-1314.2010.00916.x

Santamaría-López, A., Sanz de Galdeano, C., 2018. SHRIMP U-Pb detrital zircon dating to check subdivisions in metamorphic complexes: a case of study in the Nevado-Filábride complex (Betic Cordillera, Spain). International Journal of Earth Sciences 107, 2539-2552. https://doi.org/10.1007/s00531-018-1613-y

Santamaría-López, A., Lanari, P., Sanz de Galdeano, C., 2019. Deciphering the tectono-metamorphic evolution of the Nevado-Filábride complex (Betic Cordillera, Spain) – A petrochronological study. Tectonophysics 767, 128158. https://doi.org/10.1016/j.tecto.2019.06.028

Sanz de Galdeano, C., 2017. Implication of the geology of the Guadaiza and Verde valleys (Malaga Province, Betic Cordillera) on the position of the Ronda peridotites and the structure of the Alpujárride Complex. Boletín Geológico y Minero 128, 989-1006.

Sanz de Galdeano, C., Vera, J.A., 1992. Stratigraphic record and palaeogeographical context of the Neogene basins in the Betic Cordillera, Spain. Basin Research 4, 21-36. https://doi.org/10.1111/j.1365-2117.1992.tb00040.x

Sanz de Galdeano, C., López-Garrido, A.C., 2003. Revisión de las unidades Alpujárrides de las sierras de Tejeda, Almijara y Guájares (sector central de la Zona Interna Bética, provincias de Granada y Málaga). Revista de la Sociedad Geológica de España 16, 135-149.

Sanz de Galdeano, C., López-Garrido, A.C., 2012. The Torcal de Antequera, an example of a structure formed by a large scale dextral transcurrent system. Estudios Geológicos 68 (2), 189-202.

Sanz de Galdeano, C., López-Garrido, A., 2016a. The nevado-filábride complex in the western part of Sierra de los Filabres (Betic Internal Zone), structure and lithologic succession. Boletín Geológico y Minero 127, 823-836. DOI: 10.21701/bolgeomin.127.4.005

Sanz de Galdeano, C., López Garrido, A.C., 2016b. Geometry of the contact of the peridotites of Sierra Alpujata with the Sierra Blanca succession (Alpujarride Complex, Betic Internal Zone). Geogaceta 60, 7-10.

Sanz de Galdeano, C., López-Garrido, A.C., 2016c. Transcurrencia y mélange tectónica en el área de Sierra Arana (Cordillera Bética, NE de Granada). Estudios Geológicos 72(2), e055 http://dx.doi.org/10.3989/egeol.42468.415

Sanz de Galdeano, C., Delgado, F., López-Garrido, A.C., 1995a. Estructura del Alpujárride y del Maláguide al NW de Sierra Nevada (Cordillera Bética). Revista de la Sociedad Geológica de España 8, 239-250.

Sanz de Galdeano, C., Delgado, F., López-Garrido, A.C., Martín-Algarra, A., 1995b. Appartenance alpujarride proposée de l'unité de La Mora au NE de Grenade (Cordillère bétique, Espagne). Comptes Rendus de l'Academie des Sciences de Paris 321, 893-900.

Sanz de Galdeano, C., Andreo, B., García-Tortosa, F.J., López-Garrido, A.C., 2001. The Triassic palaeogeographic transition between the Alpujarride and Malaguide complexes. Betic-Rif Internal Zone (S Spain, N Morocco). Palaeogeography, Palaeoclimatology, Palaeoecology 167, 157-173. https://doi.org/10.1016/S0031-0182(00)00236-4

Sayab, M., 2005. Microstructural evidence for N-S shortening in the Mount Isa Inlier (NW Queensland, Australia): the preservation of early W-E-trending foliations in porphyroblasts revealed by independent 3D measurement techniques. Journal of Structural Geology 27, 1445-1468. https://doi.org/10.1016/j.jsg.2005.01.013

Sayab, M., 2008. Correlating multiple deformation events across the Mesoproterozoic NE Australia using foliation intersection axes (FIA) preserved within porphyroblasts. Gondwana Research 13, 331-351. https://doi.org/10.1016/j.gr.2007.09.003

Sayab, M., Suuronen, J.P., Hölttä, P., Aerden, D., Lahtinen, R., Kallonen, A.P., 2015. High-resolution X-ray computed microtomography: A holistic approach to metamorphic fabric analyses. Geology 43, 55-58. https://doi.org/10.1130/G36250.1

Sayab, M., Shah, S.Z., Aerden, D., 2016. Metamorphic record of the NW Himalayan orogeny between the Indian plate-Kohistan Ladakh Arc and Asia: Revelations from foliation intersection axis (FIA) controlled P-T-t-d paths. Tectonophysics 671, 110-126. https://doi.org/10.1016/j.tecto.2015.12.032

Schindelin, J., Arganda-Carreras, I., Frise, E., Kaynig, V., Longair, M., Pietzsch, T., Preibisch, S., Rueden, C., Saalfeld, S., Schmid, B., Tinevez, J.Y., White, D.J., Hartenstein, V., Eliceiri, K., Tomancak, P., Cardona, A., 2012. Fiji: an open-source platform for biological-image analysis. Nature Methods 9, 676–682. https://doi.org/10.1038/nmeth.2019

Schneider, C.A., Rasband, W.S., Eliceri, K.W., 2012. NIH Image to ImageJ: 25 years of image analysis. Nature Methods 9, 671–675. https://doi.org/10.1038/nmeth.2089

Seydoux-Guillaume, A.M., Paquette, J.L., Wiedenbeck, M., Montel, J.M., Heinrich, W., 2002. Experimental resetting of the U–Th–Pb systems in monazite. Chemical Geology 191, 165-181. https://doi.org/10.1016/S0009-2541(02)00155-9

Shah, S.Z., Sayab, M., Aerden, D., Asif Khan M., 2011. Foliation intersection axes preserved in garnet porphyroblasts from the Swat area, NW Himalaya: A record of successive crustal shortening directions between the Indian plate and Kohistan-Ladakh Island Arc. Tectonophysics 509, 14-32. https://doi.org/10.1016/j.tecto.2011.05.010

Simancas, J.F., 2018. A reappraisal of the Alpine structure of the Alpujárride Complex in the Betic Cordillera: Interplay of shortening and extension in the westernmost Mediterranean. Journal of Structural Geology 115, 231-242. https://doi.org/10.1016/j.jsg.2018.08.001

Simancas, J.F., Campos, J., 1993. Compresión NNW-SSE tardi a postmetamórfica y extensión subordinada en el Complejo Alpujárride (Dominio de Alborán, Orógeno Bético). Revista de la Sociedad Geológica de España 6, 23-35.

Skrzypek, E., Schulmann, K., Stípská, P., Chopin, F., Lehmann, J., Lexa, O., Haloda, J., 2011. Tectono-metamorphic history recorded in garnet porphyroblasts: insights from thermodynamic modelling and electron backscatter diffraction análisis of inclusion trails. Journal of Metamorphic Geology 29, 473-496. https://doi.org/10.1111/j.1525-1314.2010.00925.x

Sosson, M., Morillon, A.C., Bourgois, J., Féraud, G., Poupeau, G., Saint-Marc, P., 1998. Late exhumation stages of the Alpujarride Complex (western Betic Cordilleras, Spain): new thermochronological and structural data on Los Reales and Ojen nappes. Tectonophysics 285, 253-273. https://doi.org/10.1016/S0040-1951(97)00274-6

Soto, J.I., Platt, J.P., 1999. Petrological and Structural Evolution of High-Grade Metamorphic Rocks from the Floor of the Alboran Sea Basin, Western Mediterranean. Journal of Petrology 40, 21-60. https://doi.org/10.1093/petroj/40.1.21

Spear, F.S., 1993. Metamorphic Phase Equilibria and Pressure-Temperature-Time Paths. Monograph. Washington, D.C.: Mineralogical Society of America

Tendero, J.A., Martín-Algarra, A., Puga, E., Díaz de Federico, A., 1993. Lithostratigraphie des métasédiments de l'association ophiolitique Nevado-Filabride (SE Espagne) et mise en évidence d'objets ankéritiques évoquant des foraminifères planctoniques du Crétacé : conséquences paléogéographiques. Comptes Rendus de l'Académie des Sciences de Paris 316, 1115-1122.

ten Grotenhuis, S.M., Passchier, C.W., Bons, P.D., 2002. The influence of strain localisation on the rotation behaviour of rigid objects in experimental shear zones. Journal of Structural Geology 24, 485–499. https://doi.org/10.1016/S0191-8141(01)00072-4

Timms, N.E., 2003. Garnet porphyroblast timing and behaviour during fold evolution: implications from a 3-D geometric analysis of a hand-sample scale fold in a schist. Journal of Metamorphic Geology 21, 853-873. https://doi.org/10.1046/j.1525-1314.2003.00487.x

Tomkins, H.S., Powell, R., Ellis, D.J., 2007. The pressure dependence of the zirconium-in-rutile thermometer. Journal of Metamorphic Geology 25, 703-713. https://doi.org/10.1111/j.1525-1314.2007.00724.x

Torres-Roldán, R.L., Poli, G., Peccerillo, A., 1986. An Early Miocene arc-tholeiitic magmatic dike event from the Alboran Sea – Evidence for precollisional subduction and back-arc crustal extension in the westernmost Mediterranean. Geologische Rundschau 75, 219-234. https://doi.org/10.1007/BF01770190

Tubía, J.M., 1988. Estructura de los Alpujárrides occidentales: Cinemática y condiciones de emplazamiento de las peridotitas de Ronda. Parte I: Características litológicas. Boletín Geológico y Minero 99(II), 165-212.

Tubía, J.M., 1994. The Ronda peridotites (Los Reales nappe): an example of the relationship between lithospheric thickening by oblique tectonics and late extensional deformation within the Betic Cordillera (Spain). Tectonophysics 238, 381-398. https://doi.org/10.1016/0040-1951(94)90065-5

Tubía, J.M., Navarro-Vilá, F., 1984. Criterios para la diferenciación entre los esquistos de grado medio del Complejo Maláguide y del Manto de Los Reales al W de Málaga. La posición del contacto de corrimiento. El borde Mediterráneo Español, Granada, 33-34.

Tubía, J.M., Cuevas, J., 1986. High-temperature emplacement of the Los Reales peridotite nappe (Betic Cordillera, Spain). Journal of Structural Geology 8, 473-482. https://doi.org/10.1016/0191-8141(86)90064-7

Tubía, J.M., Gil-Ibarguchi, J.I., 1991. Eclogites of the Ojén nappe: a record of subduction in the Alpujárride complex (Betic Cordilleras, southern Spain). Journal of the Geological Society, London 148, 801-804. https://doi.org/10.1144/gsjgs.148.5.0801

Tubía, J.M., Cuevas, J., Navarro-Vilá, F., Álvarez, F., Aldaya, F., 1992. Tectonic evolution of the Alpujárride Complex (Betic Cordillera, southern Spain). Journal of Structural Geology 14 (2), 193-203. https://doi.org/10.1016/0191-8141(92)90056-3

Tubía, J.M., Navarro-Vilá, F., Cuevas, J., 1993. The Maláguide-Los Reales Nappe: an example of crustal thinning related to the emplacement of the Ronda peridotites (Betic Cordillera). Physics

of the Earth and Planetary Interiors 78, 343-354. https://doi.org/10.1016/0031-9201(93)90165-6

Tubía, J.M., Cuevas, J., Gil Ibarguchi, J.I., 1997. Sequential development of the metamorphic aureole beneath the Ronda peridotites and its bearing on the tectonic evolution of the Betic Cordillera. Tectonophysics 279, 227-252. https://doi.org/10.1016/S0040-1951(97)00124-8

Tubía, J.M., Cuevas, J., Esteban, J.J., 2013. Localization of deformation and kinematic shift during the hot emplacement of the Ronda peridotites (Betic Cordilleras, southern Spain). Journal of Structural Geology 50, 148-160. https://doi.org/10.1016/j.jsg.2012.06.010

Turner, S.P., Platt, J.P., George, R.M.M., Kelley, S.P., Pearson, D.G., Nowell, G.M., 1999. Magmatism Associated with Orogenic Collapse of the Betic-Alboran Domain, SE Spain. Journal of Petrology 40, 1011-1036. https://doi.org/10.1093/petroj/40.6.1011

van Achterberg, E., Ryan, C.G., Jackson, S.E., Griffin, W.L., 2001. Data reduction software for LA-ICP-MS: appendix, in: Sylvester, P.J. (Ed.), Laser Ablation-ICP-Mass Spectrometry in the Earth Sciences: Principles and Applications. In: Short Course Ser., Mineral. Assoc. Can., vol.29, Ottawa, Ontario, Canada, pp. 239–243.

van Bemmelen, R.W., 1927. Bijdrage tot de geologie der betische ketens in de provincie Granada. Thesis Delft.

Vázquez, M., Jabaloy, A., Barbero, L., Stuart, F.M., 2011. Deciphering tectonic- and erosion-driven exhumation of the Nevado-Filábride Complex (Betic Cordillera, Southern Spain) by low temperature thermochronology. Terra Nova 23, 257-263. https://doi.org/10.1111/j.1365-3121.2011.01007.x

Vera, J.A., editor, 2004. Geología de España, IGME-SGE.

Vernon, R.H., Clarke, G.L., 2008. Principles of metamorphic petrology. Cambridge University Press, New York.

Visser, P., Mancktelow, N.S., 1992. The rotation of garnet porphyroblasts around a single fold, Lukmanier Pass, Central Alps. Journal of Structural Geology 14, 1193-1202. https://doi.org/10.1016/0191-8141(92)90069-9

Voet, H.W., 1964. Evidence of “late” alpine overthrusting, in the region NW of Líjar, Sierra de los Filabres (SE Spain). Geologie en Mijnbouw 43, 10-15.

Whitehouse, M.J., Platt, J.P., 2003. Dating high-grade metamorphism—constraints from rare-earth elements in zircon and garnet. Contrib Mineral Petrol 145, 61-74. https://doi.org/10.1007/s00410-002-0432-z

Williams, J.R., Platt, J.P., 2017. Superposed and refolded metamorphic isograds and superposed directions of shear during late orogenic extension in the Alborán Domain, southern Spain. Tectonics 36, 756-786. https://doi.org/10.1002/2016TC004358

Williams, J.R., Platt, J.P., 2018. A new structural and kinematic framework for the Alborán Domain (Betic-Rif arc, western Mediterranean orogenic system). Journal of the Geological Society 175, 465-496. https://doi.org/10.1144/jgs2017-086

Yeh, M.W., Bell, T.H., 2004. Significance of dextral reactivation of an E-W transfer fault in the formation of the Pennsylvania orocline, central Appalachians. Tectonics 23, TC5009. https://doi.org/10.1029/2003TC001593

Zack, T., Moraes, R., Kronz, A., 2004. Temperature dependence of Zr in rutile: empirical calibration of a rutile thermometer. Contrib Mineral Petrol 148, 471-488. https://doi.org/10.1007/s00410-004-0617-8

Zeck, H.P., Williams, I.S., 2001. Hercynian Metamorphism in Nappe Core Complexes of the Alpine Betic-Rif Belt, Western Mediterranean—a SHRIMP Zircon Study. Journal of Petrology 42, 1373-1385. https://doi.org/10.1093/petrology/42.7.1373

Zeck, H.P., Albat, F., Hansen, B.T., Torres-Roldán, R.L., García-Casco, A., Martín-Algarra, A., 1989. A 21 ± 2 Ma age for the termination of the ductile Alpine deformation in the internal zone of the Betic Cordilleras, South Spain. Tectonophysics 169, 215-220. https://doi.org/10.1016/0040-1951(89)90196-0

Zeck, H.P., Monié, P., Villa, I.M., Hansen, B.T., 1992. Very high rates of cooling and uplift in the Alpine belt of the Betic Cordilleras, southern Spain. Geology 20, 79-82. https://doi.org/10.1130/0091-7613(1992)020<0079:VHROCA>2.3.CO;2

Zevenhuizen, W.A., 2022. Lithostratigraphy and structure of the Macael marbles (Betic zone, Spain). Boletín Geológico y Minero 133, 195-223. http://dx.doi.org/10.21701/bolgeomin/133.2/009

Zwart, H.J., 1960. The chronological succession of folding and metamorphism in the Central Pyrenees. Geologische Rundschau, 50, 203–218. https://doi.org/10.1007/bf01786838

Zwart, H.J., Oele, J.A., 1966. Rotated magnetite crystals from the Rocroi massif (Ardennes). Geologie en Mijnbouw 45, 70-74.

Part II

4. X-ray computed micro-tomography of spiral garnets: A new test of how they form.

5. Transposition of foliations and superposition of lineations during polyphase deformation in the Nevado-Filabride complex: tectonic implications.

6. Structural analysis along four transects through the Nevado-Filábride Complex and implications for its internal structure.

7. Deciphering western Mediterranean kinematics using metamorphic porphyroblasts from the Alpujárride Complex (Betic Cordillera).

8. Linking deformation, metamorphism and geochronology to constrain the tectonic evolution of the western Mediterranean.

4. X-ray computed micro-tomography of spiral garnets: A new test of how they form

Domingo G.A.M. Aerden[1,2], Alejandro Ruiz-Fuentes[1]

[1] *Departamento de Geodinámica, Universidad de Granada, Av. Fuentenueva, 18071, Granada, Spain*

[2] *Instituto Andaluz de Ciencias de la Tierra, CSIC/Universidad de Granada, Av. de las Palmeras 4, 18100, Armilla, Granada, Spain*

Published on: Journal of Structural Geology, v. 136 (2020), 104054
https://doi.org/10.1016/j.jsg.2020.104054
JCR Impact Factor: 3.571 (2020)

Abstract

Garnet porphyroblasts with spiral shaped inclusion trails of two micaschist samples have been investigated with X-ray computed tomography. For each garnet crystal, the orientation of its internal Foliation Intersection/Inflexion Axes (FIA) was measured, its volume and shape orientation, the latter via calculation of best-fit ellipsoids. Additionally, image analysis of inclusion trails was performed in slices passing through garnet centres oriented normal to FIA. Our data demonstrate subvertical and subhorizontal preferred orientations of the inclusion trails and of the porphyroblast crystals themselves in both samples. This supports a genetic model in which garnets periodically overgrew a succession of vertical and horizontal foliations during alternating crustal shortening and gravitational collapse without significantly rotating. The fact that both samples come from areas previously identified as regional shear zones supports the idea that porphyroblasts are able to maintain stable positions even in such environments. Our study exemplifies the strength of X-ray computed micro-tomography compared to previous techniques based on serial thin sections for distinguishing multiple FIA sets present in single samples.

Keywords: Spiral garnet, Non-rotation, X-ray computed microtomography, Porphyroblast

4.1. Introduction

Spiral shaped inclusion trails were long thought to form by shearing-induced porphyroblast rotation (Rosenfeld, 1970) until an alternative model was proposed envisaging overgrowth of multiple suborthogonal crenulation-cleavages by non-rotating porphyroblasts (Bell and Johnson, 1989; Bell et al., 1992; Stallard and Hickey, 2001; Bell and Fay, 2016). Important implications of the new model were: (i) an opposite shear sense as deduced previously from the sense of inclusion-trail curvature, (ii) polyphase deformation histories where previously a single shearing event was concluded, and (iii) that axes of apparent porphyroblast rotation referred to as 'FIA' in the literature (Foliation Intersection- or Inflexion Axes; e.g. Bell et al., 1995) record crustal shortening normal to their trend alternating with gravitational collapse stages (e.g. Bell et al., 1995). Then new methods were developed to measure FIAs using sets of differently oriented thin sections of single samples (Hayward, 1990; Bell et al., 1995; Aerden, 2003) whose application systematically revealed the presence of multiple sets of FIA in metamorphic belts with regionally consistent trends, as well as vertical and horizontal preferred orientations of inclusion trails (e.g. Aerden, 1994, 1995; 1998, 2004; Bell et al., 1998; Jung et al., 1999; Cihan and Parsons, 2005; Sayab, 2005; Ali, 2010; Abu Sharib and Bell, 2011; Shah et al., 2011; Bell and Sapkota, 2012; Aerden et al., 2013). In spite of this evidence, the idea that porphyroblasts generally do not rotate, not even in shear zones, continued to raise doubts because of the conflict with analogue and numerical models of rotating objects in non-coaxial flow. On the other hand, it has been increasingly recognized that the behaviour of natural porphyroblast-matrix systems is more complex as these models suggest, due to factors such as matrix anisotropy (Griera et al., 2013; Ran et al., 2019), object-matrix slip (ten Grotenhuis et al., 2002; Johnson, 2008), pure-shear components (Bell, 1985), non-steady state deformation (Fay et al., 2008), and metamorphic reactions (Wintch and Yeh, 2013). Consequently, some researchers have proposed that spiral-shaped inclusion trails might develop by rotation or non-rotation depending on the vorticity of deformation and tectonic setting (Passchier and Trouw, 2005; Robyr et al., 2009).

Concerns have also been raised regarding the objectivity of inclusion-trail data supporting the non-model rotation (Paterson and Vernon, 2001; Stallard et al., 2003; Jiang and Williams, 2005). The collection of such data admittedly involves some degree of interpretation, and increasingly so with greater complexity of the inclusion trails. Moreover, the methods used so far for measuring FIAs are statistical in nature. They characterize the preferred orientation of inclusion trails in 3D based on (2D) orientation data from differently oriented thin sections, but cannot reveal the internal structure of individual porphyroblasts. X-ray computed tomography now makes this possible and therefore offers an opportunity for testing different genetic models of inclusion trails.

Huddlestone-Holmes and Ketcham (2005, 2010) were the first to measure the FIAs of a large number of porphyroblasts in a single sample using XCT to evaluate their spread and test the rotation versus the non-rotation model. The data strongly favoured non-rotation, although the authors admitted that a more conclusive test would be provided by

inclusion trails showing larger curvature than the ones studied. Robyr et al. (2007, 2009) studied several spiral garnets from the Alps using a combination of XCT and EBSD. They favoured the classic snowball model, except for a final growth stage that would have taken place under relatively coaxial conditions. However, this interpretation was based mainly on regional tectonic considerations, not on quantitative orientation data for the inclusion-trails.

In this paper, we present XCT data for numerous spiral-garnets in two micaschist samples collected from different regional shear zones in the Iberian Central System (Variscan orogen) and Betic Cordillera (Alpine orogen). The volume, shape-orientation, FIA, and inclusion-trail patterns of these porphyroblasts have been analysed in detail and unequivocally favour an origin without significant porphyroblast rotation.

4.2. Geological context of the samples

Sample 49.10 (Lat. 41.24174, Long. -3.44406) is a garnet-staurolite-biotite schist from the Variscan Iberian Massif taken from the upper part of the so called Berzosa shear zone (Capote et al., 1977) in the Iberian Central System. This several km thick structure formed in the Carboniferous and separates greenschist facies Ordovician to Devonian metapelites and quartzites in the hangingwall from high grade Cambro-Ordovician orthogneises and schists in the footwall. Different kinematic interpretations have been proposed including top-to-the east ductile thrusting (Macaya et al., 1991), top-to-the SE extensional shearing (Escuder-Viruete et al., 1998), or top-to-the SE thrusting followed by reversed top to the NW extensional shearing (Rubio Pascual et al., 2016). The main shear zone foliation (S_2 in the cited works) presumably formed subhorizontal or gently dipping when it overprinted km-scale east-verging F1 folds that are still the dominant regional-scale structures in the hangingwall unit. Later D_3 folding about N-S axes steepened or even overturned the shear zone associated with 'backthrusting' (Macaya et al., 1991) and produced a locally intense S_3 crenulation cleavage. Rubio Pascual et al. (2016) determined metamorphicconditions of 625 ºC/9.5 kbar for a similar garnet-staurolite schist (their sample 2) collected from the same area and structural position.

Sample 46.8 (Lat. -2.82784º, Long. 37.30270º) is a garnet-kyanite-chloritoid schist from the high-pressure/low-temperature Nevado-Filabride complex (NFC) of the Betic Cordillera. This complex represents the south-eastern Iberian paleomargin subducted to about 50 km depth during the Alpine orogeny and exhumed in the late Miocene (Puga et al., 2017). The uppermost ca. 500 m of the NFC is commonly interpreted as a ductile shear zone with dominantly westward tectonic transport. However, multiple generations of differently oriented folds, crenulations and Foliation Intersection Axes (FIA) in porphyroblasts record a more complex polyphase deformation history whose tectonic significance has been the subject of recent and ongoing research (Aerden and Sayab, 2008; Behr et al., 2012; Aerden et al., 2013; Ruiz-Fuentes and Aerden, 2018). The sample was taken from an outcrop in the western Sierra de los Filabres located about 100 m structurally below the hangingwall detachment of the NFC with the overlying Alpujarride complex. It is part of a band of light-coloured relatively coarse-grained schists that hosts

up to hectometer scale mafic and ultramafic boudins and has been interpreted as a dismembered ophiolite (Aerden et al., 2013; Puga et al., 2017).

4.3. The samples in thin section

Sample 49.10 contains garnet porphyroblasts with an average size of 3 mm and more numerous 0.5–5 mm sized staurolite porphyroblasts, both with well developed inclusion trails, as well as some biotite porphyroblasts with poorly developed inclusion trails. The matrix minerals biotite, quartz and muscovite, define the macroscopic foliation, which is oriented 070/63 (dip-azimuth/dip) in the sample, and lineation oriented 155/30. Inclusion trails within garnet typically curve 90º–180º, whereas those of staurolite are commonly straight and never curve more than 90º, consistent with later nucleation of this mineral. This is witnessed in some other samples from the Berzosa shear zone, not considered in this work, containing large staurolite crystals that include garnet. Initially, 6 vertical thin sections plus a horizontal one were studied of sample 49.10 and allowed us to constrain the average trend of garnet FIAs between N030 and N060 using the asymmetry technique of Hayward (1990). Fig. 4.1 shows representative microstructures in a thin section oriented at a high angle to this average FIA trend. A sequence of 4 foliations is interpreted in anticipation of the final conclusions of this paper about how the inclusion trails formed.

Our Nevado-Filabride sample contains garnet porphyroblasts with more variable sizes between 2 and 12 mm. All of them contain spiral shaped inclusion trails curving up to 270º defined by quartz plus minor amounts of rutile, ilmenite, chloritoid, phengite and kyanite. Small kyanite porphyroblasts in the matrix and sometimes included in garnet rims, plus plagioclase porphyroblasts with simple inclusion trails that probably grew after garnet growth had ceased are also present in the rock (Fig. 4.2). The matrix foliation is mainly defined by quartz and phengitic white mica. It dips on average 60ºN and locally appears tightly folded with steep axial planes and E-W trending axes. Because of the large size reached by garnet porphyroblasts in the sample, a radial set of vertical polished slabs instead of thin sections was prepared on which the inclusion trail patterns of the larger garnets are clearly visible and allowed to constrain their average FIA trend of N075 ± 015 using the technique of Hayward (1990). A vertical thin section was then prepared normal to the FIA (Fig. 4.2) in which 5 foliations can be interpreted assuming the non-rotational origin of the spiral garnets concluded later in this paper.

4.4. X-ray computed tomography and image analysis techniques

X-ray computed tomography (XCT) scans were performed at the Geological Survey of Finland with a BHGE phoenix v|tome|x industrial system (240 kV/320 W). The scanned volume in sample 46.8 measures 2024 (X) x 1874 (Y) x 2022 (Z) voxels with a voxel size of 30.2 μm. Because of the smaller size of garnets in sample 49.10, a smaller volume (1444 x 768 x 2023 voxels) was scanned but with a higher resolution of 26.1 μm.

Orientation arrows made of copper wire were previously stuck on the samples and appear brightly in the scan (i.e. strong X-ray attenuation).

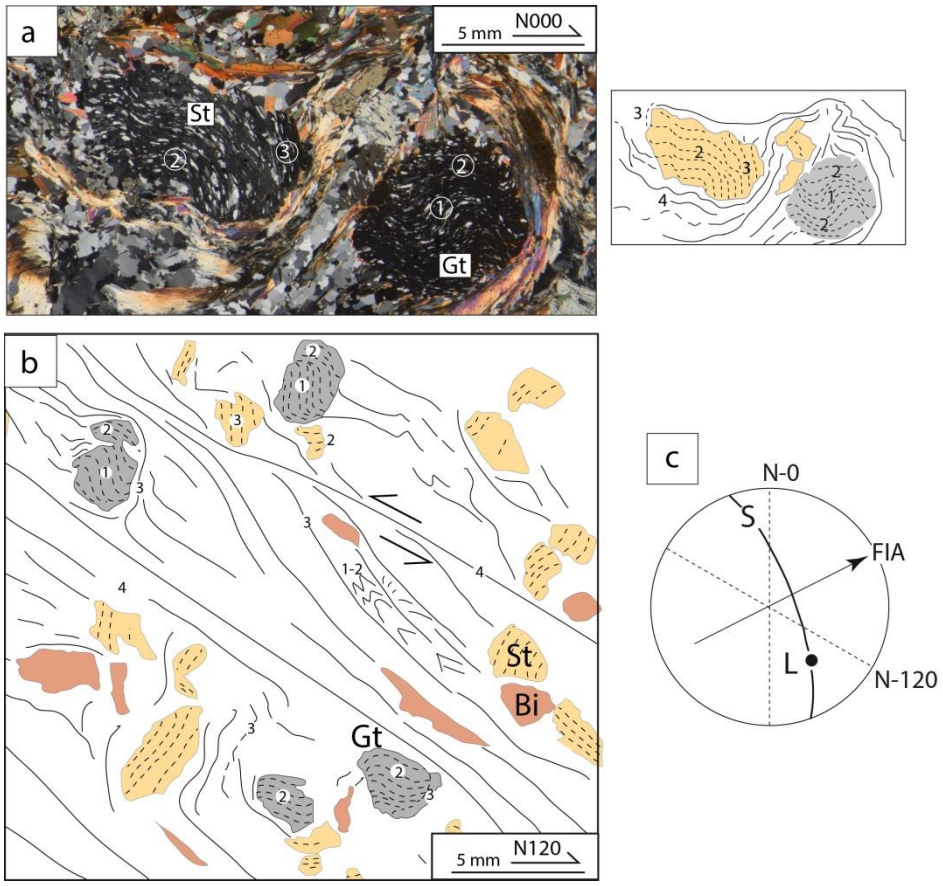

Fig. 4.1. (a) Garnet (Gt) and staurolite (St) porphyroblasts in the N-S striking vertical thin section of sample 49.10 and accompanying microstructural sketch. (b) Line tracing of part of the N-120 striking vertical thin section of sample 49.10 containing garnet (grey), staurolite (yellow) and biotite (brown red) porphyroblasts. Inclusion trails and matrix foliations can be interpreted as a succession of 4 foliations numbered accordingly. Note opposite curvature sense of inclusion trails in (a) and (b) because of a N-060 trending FIA in this sample. This geometric effect forms the basis of Hayward's (1990) FIA technique. (d) Stereoplot showing the orientation of the macroscopic cleavage (S) and lineation (L) measured in outcrop, the thin section planes of (a) and (b), and the average FIA trend. (For interpretation of the references to colour in this figure legend, the reader is referred to the Web version of this article.)

XCT scans were processed and analysed using the Fiji distribution (Schindelin et al., 2012) of the open-source image processing software ImageJ (Schneider et al., 2012), which includes the 3D plugin suite of Ollion et al. (2013). Inclusion trails in the studied garnets are mostly composed of quartz and stand out clearly in the XCT scans due to a high contrast in X-ray attenuation relative to garnet. Staurolite porphyroblasts in sample 49.10 were not studied in detail because they appear with less well-defined boundaries and less clear inclusion-trails in the scan. The scans were first converted from 16-bit to 8-bit grey scale to reduce the file size 50% without losing important information, but allowing more efficient computer processing. The scans were reoriented in such a way that the viewing direction is down on a horizontal plane with North pointing upward on the computer screen.

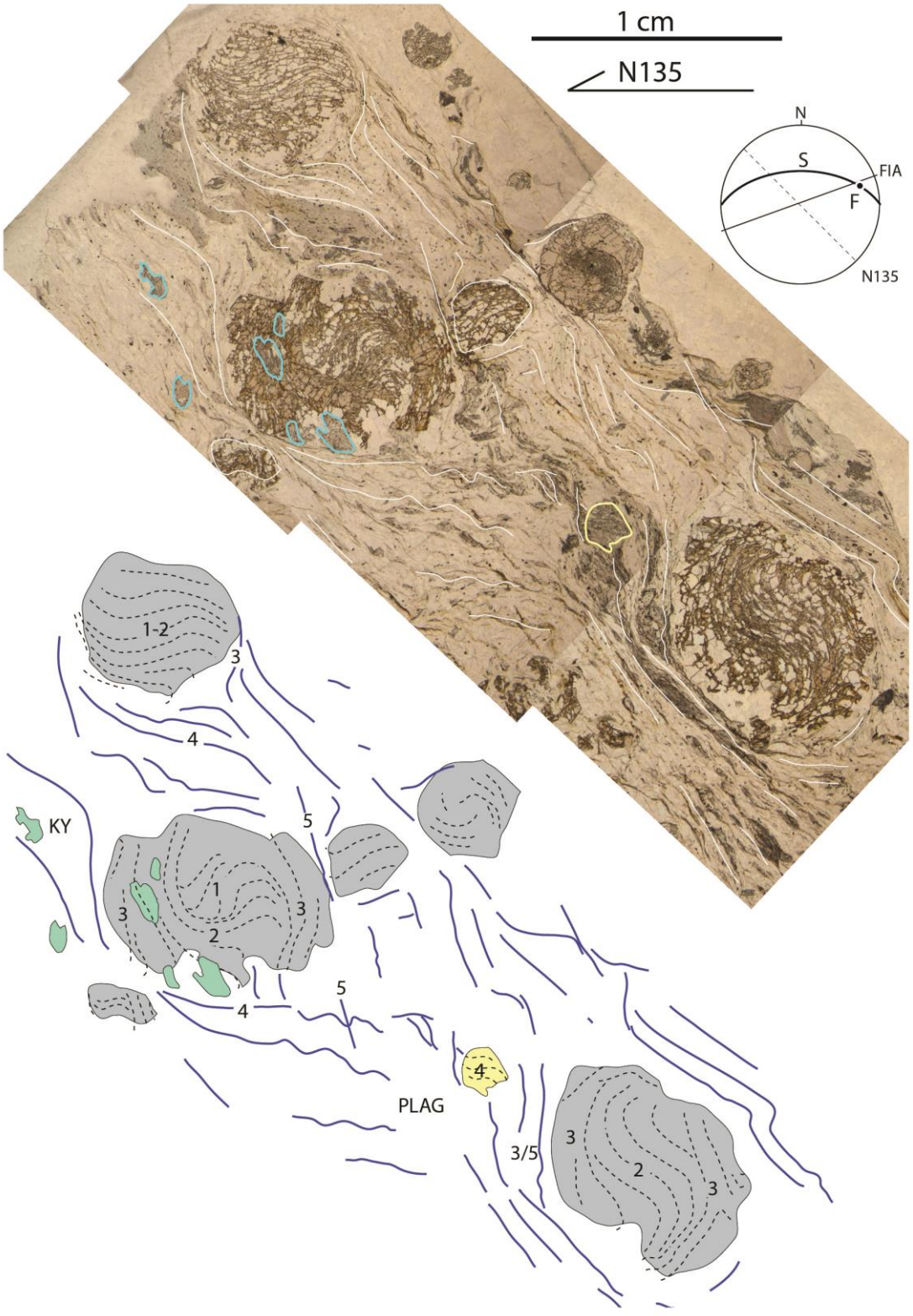

Fig. 4.2. Photograph and microstructural interpretation of a N-135 (NW-SE) striking vertical thin section of sample 46.8 containing several large garnet porphyroblasts plus smaller kyanite and plagioclase porphyroblasts. Kyanite is included in the outer zone of garnet but plagioclase postdates garnet. A succession of five foliations can be interpreted in anticipation of the non-rotational model for spiral inclusion trails concluded in this paper. The stereoplot shows the foliation (S) and the axis (F) of an upright fold measured in the outcrop, the average FIA trend of larger garnets as measured from a radial set of polished slabs, and the thin section plane (stipple line).

Garnets were segmented with the standard 'Threshold' tool, combined with the plugin '3D Simple Segmentation' in order to eliminate particles smaller than garnet porphyroblasts but with similar X-ray attenuation (mostly opaque minerals). Garnets located at the edges of the sample were manually eliminated as they are not entire grains. Adjacent garnets in contact with each other were separated by manually eliminating the linking voxels to avoid the software treating them as single porphyroblasts. A few more coalesced garnet pairs were eliminated from the analysis.

Garnets volumes were measured with the plugin '3D Geometrical Measure'. Their shape anisotropy was characterized with '3D Ellipsoid Fitting' after selecting garnets based on volume size with '3D Simple Segmentation'. The ellipsoid data include centre coordinates, length and orientation of X, Y, and Z axes in Cartesian coordinates. The latter were converted to trend/plunge data and represented in stereoplots.

The ellipsoid-centre coordinates of each garnet allowed locating them in the 3D scan to measure their FIAs with the plugin 'Volume Viewer', in a way analogous to the thin-section based technique of Hayward (1990) and as previously done by Huddlestone-Holmes and Ketcham (2005), using virtual XCT slices. The procedure involves interactively rotating a vertical slice passing through the garnet centre around a vertical axis, and recording the strike range over which the inclusion-trail curvature sense switches. The FIA plunge can then be determined by interactively rotating an initially horizontal slice around a horizontal axis oriented normal to the FIA trend. The accuracy of FIA trends and plunges determined this way depends somewhat on the size and definition of inclusion trails but lies around ±10º. All measured FIA were represented in a transparent 3D model created with '3D Viewer' and plotted in stereograms. All microstructural data can be found in tabulated form in the electronic supplement of this article.

Finally, inclusion trails were studied in central slices oriented normal to their FIA which show their true cross-sectional geometry without cut effects. The best-developed inclusion trails were manually traced in Adobe Illustrator with dashed lines. The orientations of all individual dashes were then automatically measured with the 'Analyze Particle' function of ImageJ to assess their degree of preferred orientation.

4.5. Results

4.5.1. Sample 49.10

The scanned volume of sample 49.10 corresponds to the same matchbox sized block from which the vertical N090 striking thin section was made (Fig. 4.3). Thus, one side of the scan coincides nearly with that thin section, which is useful for checking mineral compositions and microstructural details. Following the procedures outlined in the previous section, the FIAs of 40 garnets contained in this volume were measured and represented in a stereoplot (Fig. 4.4a). The plot shows the FIA clustering about a mean direction of 070/20. Best-fit ellipsoids for the same 40 garnet porphyroblasts have an

average X/Z ratio of 1.64 ± 0.25 (σ). The long axes (X) exhibit bimodal, subvertical and subhorizontal preferred orientations in a stereoplot, approximately normal to the FIA maximum (Fig. 4.4a). The short axes (Z) show a larger dispersion roughly parallel to FIAs.

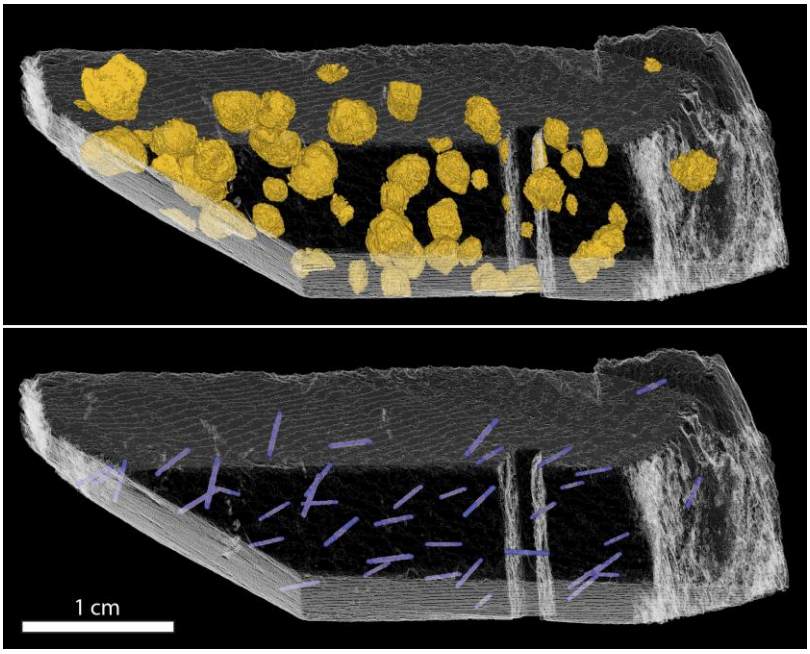

Fig. 4.3. XCT image of the scanned block of sample 49.10 rendered in 3D to show the position of the 40 porphyroblasts analysed. The FIA preserved in these porphyroblasts are shown separately with blue lines. (For interpretation of the references to colour in this figure legend, the reader is referred to the Web version of this article.)

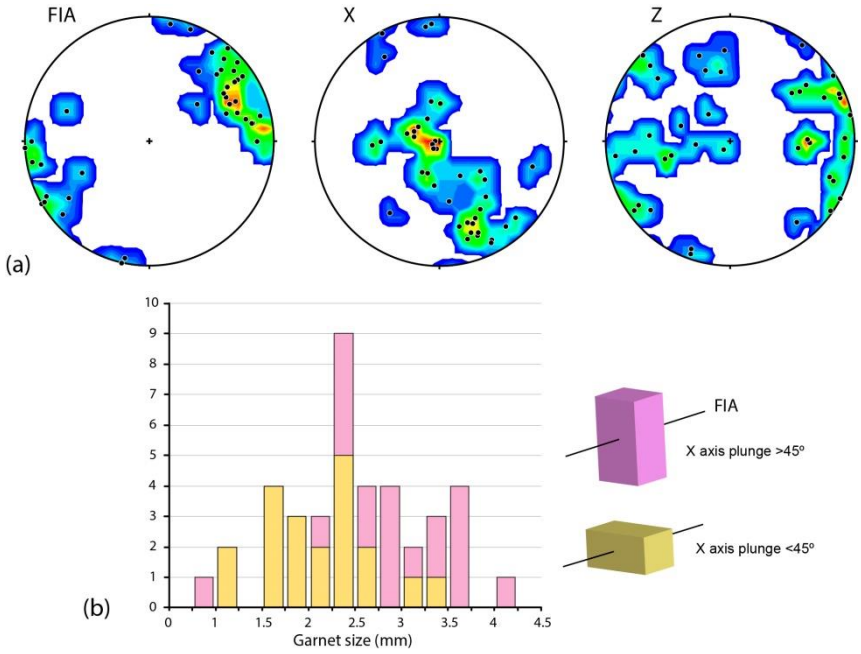

Fig. 4.4. XCT data for sample 49.10. (a) Shows from left to right contoured equal-area stereograms of FIAs, long axes (X) of porphyroblast crystals and short axes (Z). (b) Histogram showing the size distributions of porphyroblasts with steeply dipping long axes (≥45º) versus gently dipping (<45º). Steeply dipping porphyroblasts are on average larger.

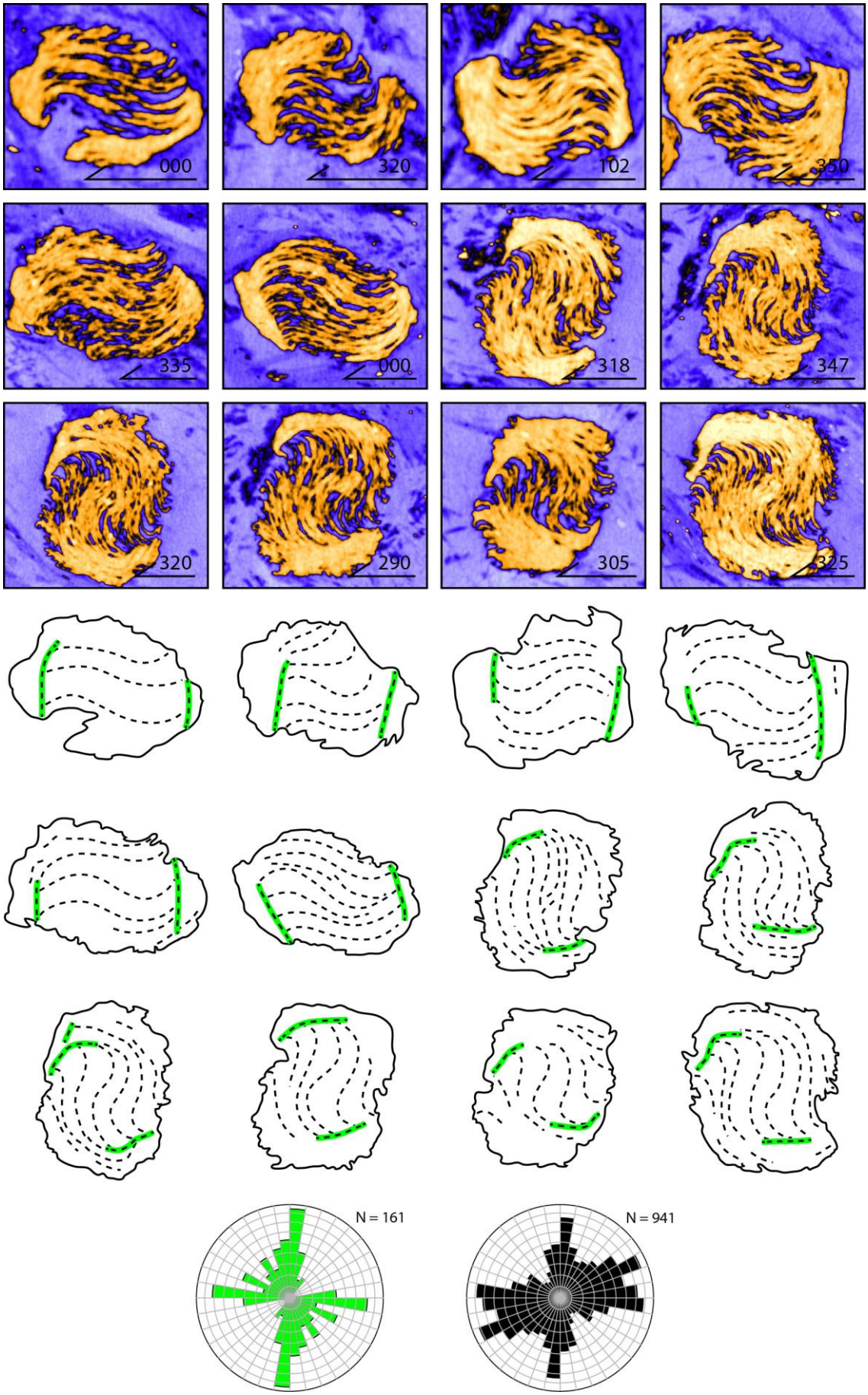
000
320
102
350
335
000
318
347
320
290
305
325
N = 161
N = 941

Fig. 4.5 (previous page). Central XCT slices through selected porphyroblasts of sample 49.10 and dashed line drawings. Inclusion-trail truncations are marked with a green background line. The rose diagrams plots the result of automatic orientation analysis of all individual dashes making up the line drawings. It demonstrates the preferred vertical and horizontal orientations of the inclusion trails and associated truncations. (For interpretation of the references to colour in this figure legend, the reader is referred to the Web version of this article.)

Detailed study of the XCT scan and of the 7 thin sections revealed that the elongate shapes of garnet crystals is related to inclusion-poor garnet overgrowths or caps located on opposite sides of inclusion-rich cores. Two groups of garnets can be distinguished based on their different average size and different mean elongation direction. The first group is characterized by subhorizontal garnet caps that grew above and below porphyroblast cores thereby producing an overall vertical to steeply dipping elongation. These garnets are on average larger (Fig. 4.4b) as those of the second group, which have subvertical caps and truncations situated on the left and right of garnet cores and hence causing subhorizontal elongation. Automated orientation analysis of inclusion-trail patterns in slices oriented normal to their FIA (Fig. 4.5) further demonstrates that not only the garnet crystals have preferred vertical and horizontal orientations, but also their inclusion trails and associated truncation surfaces.

4.5.2. Sample 46.8

Seventy-seven garnets were identified in the scanned volume of sample 46.8 (Fig. 4.6). Thirteen were too small to determine a FIA or had poorly developed inclusion trails. One garnet yielded 2 different FIAs preserved in the core and the rim, thus a total of 65 FIAs were measured. The majority of these FIA have gentle plunges and trend between N240 and N300 (Fig. 4.7a) subparallel to the axes of the earlier mentioned scarce folds observed in the outcrop. However, the FIAs exhibit much greater dispersion as in sample 49.10 and some have very steep plunges. Several lines of evidence indicate that this large spread is due to the presence of not one, but multiple generations of spiral garnets in the sample with distinctive FIA trends:

1- A rose diagram for the 65 FIAs exhibits a remarkably similar distribution of trends as a rose diagram for 82 average FIAs measured by Aerden et al. (2013) and Ruiz-Fuentes and Aerden (2018) for 68 samples from different locations in the NFC (Fig. 4.7b). Based on various relative timing criteria, these workers deduced a succession of 5 FIA sets referred to as FIA set 1 to 5, although the oldest FIA (FIA set 1) is somewhat uncertain. We performed Watson's U^2 test for homogeneity of two samples (e.g. Jammalamadaka and SenGupta, 2001) to check the statistical significance of the observed similarity of the two rose diagrams using the package 'circular' (Agostinelli and Lund, 2017) in the open-source statistics software "R". The test provides a measure of the likeliness that two samples (i.e. data sets) were drawn from the same parent population, which is the Null hypothesis of the test (H_0). The P-value returned for our data is 0.29, which means that if H_0 is true, then the probability of getting the observed (small) mismatch between the rose diagrams is 29%. A P-value of 0.05 (confidence level of 95%) is conventionally taken as the

threshold for rejecting H_0, so our much larger P-value allows the conclusion that the observed match is statistically highly significant.

2- A strong correlation exists between FIA trend and garnet size (Fig. 4.7c). This is particularly clear for FIAs defining the N110 (FIA set 2) and N165 (FIA set 4) trend maxima, which are only preserved in relatively small garnets. Conversely, larger garnet (≥6 mm diameter) exclusively have E-W to N060 trending FIA (FIA set 3 and 5; Fig. 4.7c) consistent with the average FIA of N075 ± 10 that we initially determined from the radial polished slabs.

3- The curvature sense of inclusion trails defining FIA set 2 (N120) and set 3 (N080) are consistently clockwise viewing west, but those associated with FIA sets 4 (N165) and 5 (N045) are defined by roughly equal amounts of inclusion trails with opposite curvature sense (Fig. 4.7d). The latter suggests that deformation was relatively coaxial during the formation of the two younger FIA sets as discussed in section 7.2.

4- A single garnet porphyroblast was found apparently preserving a N090 trending FIA in its core and a N165 FIA in the rim (Fig. 4.8), consistent with the relative timing of FIA sets 3 (E-W trending) and 4 (NNW-SSE trending).

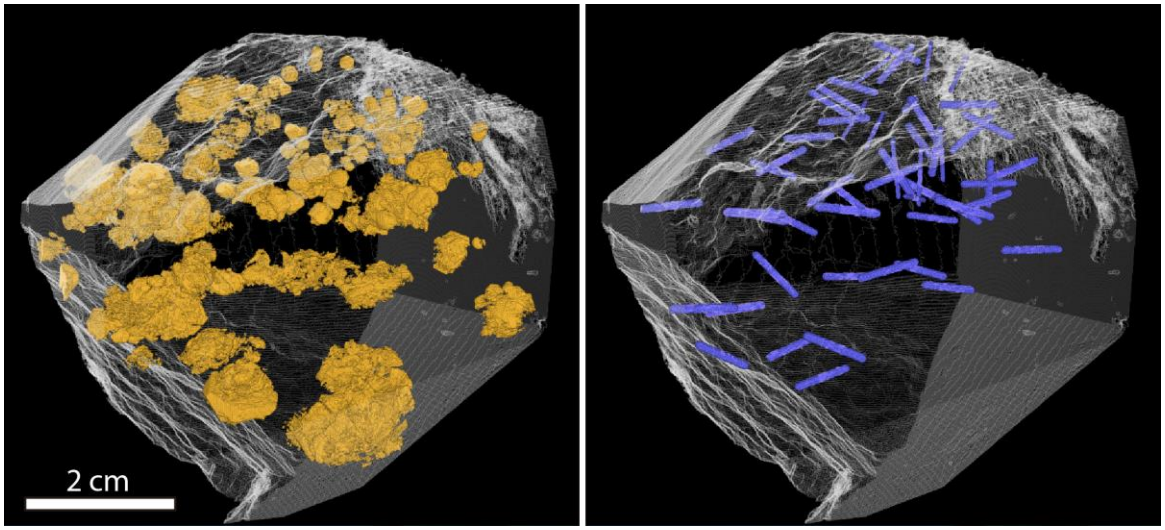

Fig. 4.6. XCT image of the scanned block of sample 46.8 rendered in 3D to show the position of the porphyroblasts that were analysed. FIA orientations are shown separately with blue lines. (For interpretation of the references to colour in this figure legend, the reader is referred to the Web version of this article.)

The porphyroblast shape data for sample 46.8 indicate an average X/Z ratio of 1.8 (±0.6; standard deviation) with X predominantly subhorizontal, subparallel to FIAs (Fig. 4.7a). Note that this is contrary to the situation in sample 49.10 where FIAs are mostly perpendicular to X. Porphyroblast short axes (Z) show a bimodal distribution with a vertical maximum and a more smeared out, moderately to gently south plunging maximum. Image analysis of inclusion trails viewed in slices through porphyroblast centres oriented normal to their FIA demonstrates that not only the porphyroblast crystals, but also their inclusion-trail patterns have bimodal vertical-horizontal preferred orientations (Fig. 4.9) as earlier also shown in sample 49.10.

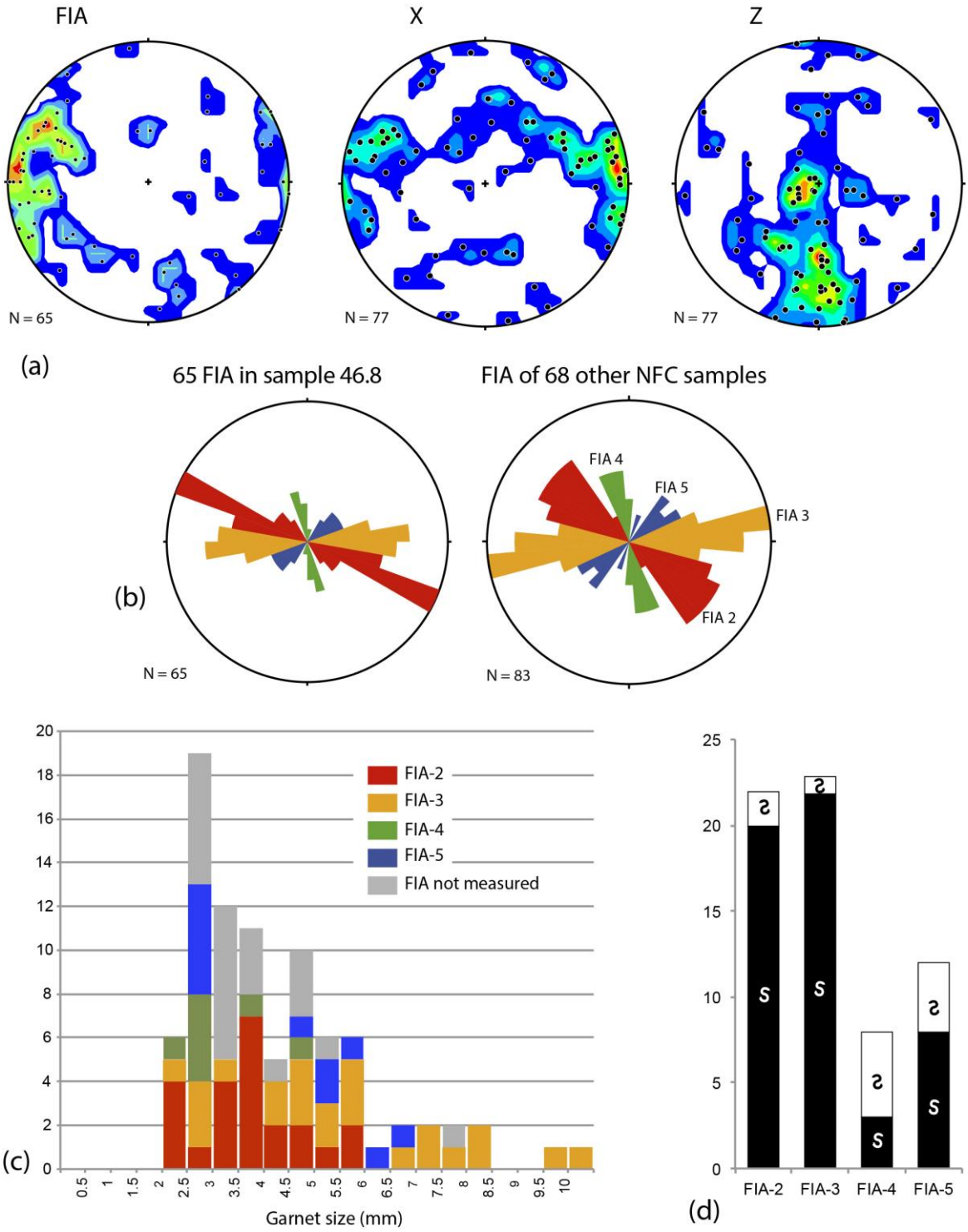

Fig. 4.7. XCT data for sample 46.8. (a) Shows from left to right contoured equal-area stereoplots for FIAs, long axes (X) of garnet porphyroblasts and short axes (Z). (b) Rose diagrams showing the distribution of FIA trends in sample 46.8 (left) and the trends of 82 average FIAs previously determined in 68 samples of the NFC and interpreted as representing a succession of 5 FIA sets (FIA set 1 to 5). The similarity of both diagrams supports our interpretation that sample 46.8 hosts multiple garnet generations and FIA sets. (c) Histogram showing the relationships between garnet size and FIA trend. FIA-2 and FIA-4 are only preserved in smaller porphyroblasts, whereas FIA-3 and FIA-5 are also hosted in larger garnets. (d) Histogram for the number of porphyroblasts in each FIA set with clockwise or anticlockwise inclusion trail curvature viewing SW, W or NW. FIA2 and FIA3 have a consistent curvature sense, but not FIA4 and FIA5.

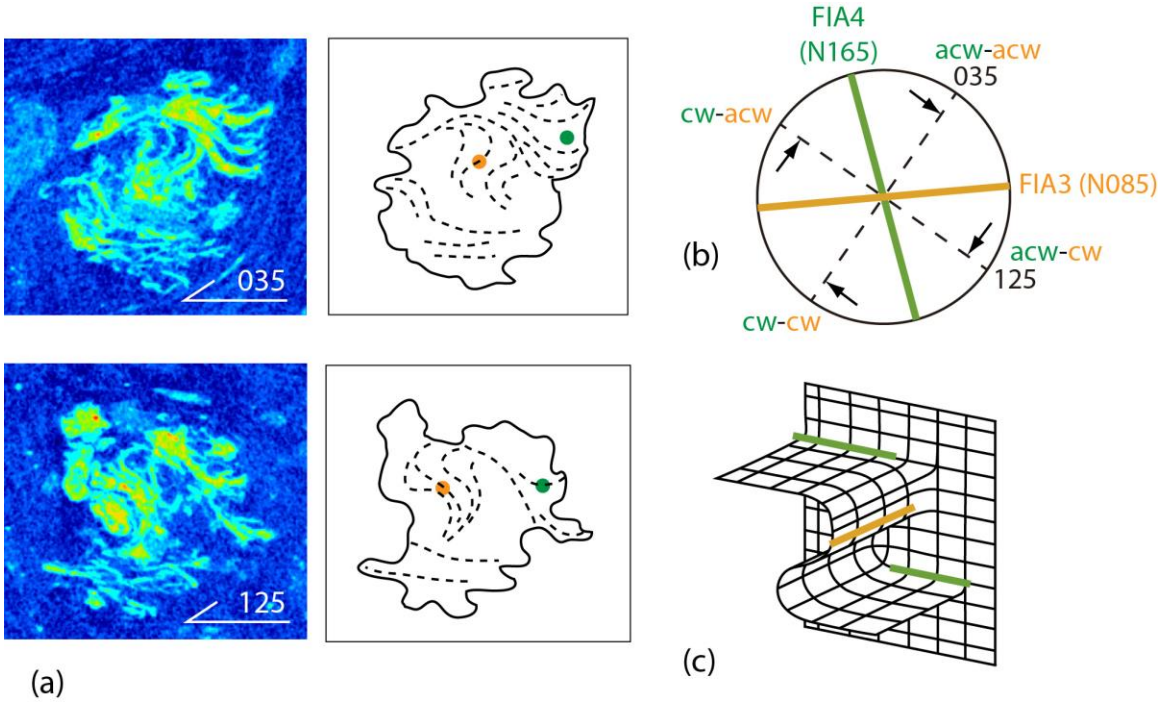

Fig. 4.8. (a) Two vertical XCT slices through a porphyroblast that preserves 2 different FIAs in the core and the rim. The N-125 striking slice shows a reversal of the curvature sense of inclusion trails from anticlockwise (acw) in the core to clockwise (cw) in the rim, but in the N-035 striking slice it is consistently anticlockwise. Study of additional slices striking around the compass allowed determination of an older N-085 FIA and younger N-165 FIA. (b) Stereogram indicating the curvature sense and reversal observed in vertical slices depending on their strike relative to core and rim FIAs. Small black arrows indicate the viewing direction. (c) Conceptual model of the 2 FIAs determined for the porphyroblast shown in (a).

4.6. Interpretation

4.6.1. Sample 49.10

The microstructural data for sample 49.10 lead us to interpret three pulses of garnet growth punctuated by the development of an equal number of crenulation-cleavages (Stallard and Hickey, 2001) as illustrated in Fig. 4.10a. Garnets first nucleated when a subhorizontal crenulation cleavage (S_2) started to develop and included sigmoidal or weakly crenulated inclusion trails of an earlier S_1. Growth ceased when S_2 intensified and compositionally differentiated against porphyroblast margins. A subsequent subvertical foliation (S_3) triggered a new pulse of garnet growth in the form of inclusion-poor caps above and below pre-existing porphyroblasts, and also as newly nucleated porphyroblasts in D_3 crenulation hinges. The latter include sigmoidal inclusion trails of S_2. Growth stopped again when S_3 differentiated against garnet edges. The formation of a third subhorizontal crenulation cleavage (S_4) finally caused inclusion-poor garnet caps to develop on both sides of syn-D_3 garnet cores, and as minor extensions of pre-existing syn D_c caps.

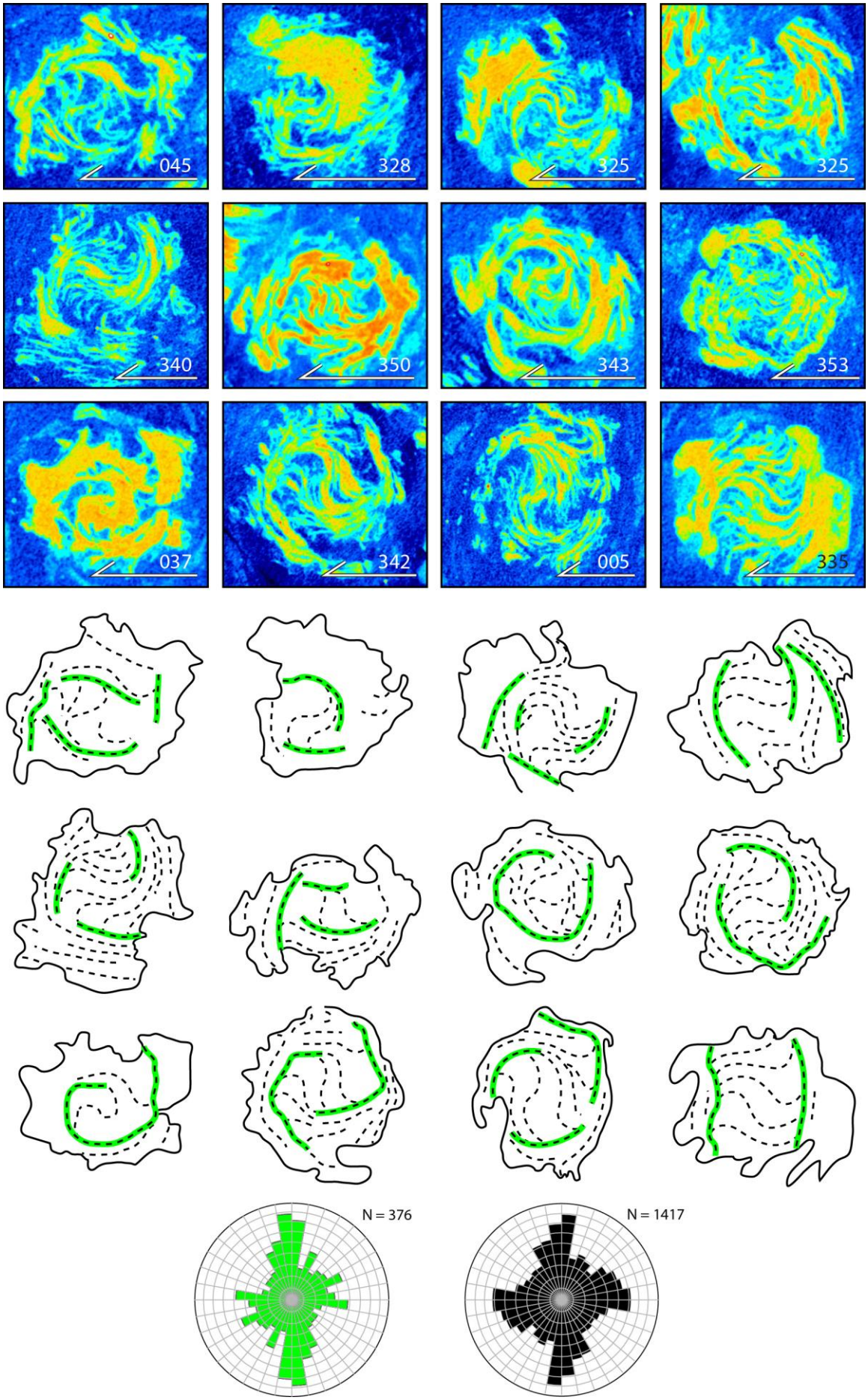
045
328
325
325
340
350
343
353
037
342
005
335
N = 376
N = 1417

Fig. 4.9 (previous page). Central slices through selected porphyroblasts of sample 46.8 and dashed line drawings. Truncations are marked with a green background line. Rose diagrams plot the result of automated orientation analysis of all individual dashes making up the line tracings using ImageJ. It demonstrates preferred vertical and horizontal orientations of the inclusion trails and associated truncations. (For interpretation of the references to colour in this figure legend, the reader is referred to the Web version of this article.)

The peculiar small-circle distribution of FIAs observed in the stereogram of Fig. 4.4a is suggestive of late (post-garnet) rotations of porphyroblasts about a horizontal N065 trending axes that dispersed originally subparallel FIAs. This possibility can be discarded, though, because such rotations would not have allowed the preservation of strong subvertical and subhorizontal preferred orientations of the inclusion trails. We propose instead that the small-circle distribution reflects the anastomosing (non-planar) geometry of successive crenulation-cleavages overgrown by garnet resulting in variably oriented intersection axes between these cleavages.

4.6.2. Sample 46.8

Similar vertical/horizontal preferred orientations of inclusion trails in sample 46.8 as in sample 49.10 suggest a similar FIA formation mechanism without significant porphyroblast rotation. However, the presence of 4 different FIA sets in this sample implies that this mechanism repeated itself 4 times. If this is correct, then the consistently clockwise curvature sense (viewing west) of inclusion trails associated with FIA set 2 and 3 were produced by alternating crustal shortening with a component of south-side up shearing on vertical foliations and gravitational collapse with a component of top-to-the-north horizontal shearing (Bell and Johnson, 1989). In contrast, inconsistent curvature senses of inclusion trails associated with FIA sets 4 and 5 suggest that later deformations were relatively coaxial and partitioned into domains with opposite shear sense. A particularly striking example is shown in Fig. 4.11a where two neighbouring spiral garnets with NNW-SSE FIAs curve in opposite directions. This can be explained assuming that these porphyroblasts formed in opposite limbs of a microfold and of a subsequent re-fold (Fig. 4.11b). The FIAs with steep plunges in sample 46.8 are inferred to have formed where a subvertical crenulation cleavage locally overprinted and intersected a previous steeply dipping cleavage with different strike belonging to an earlier FIA set.

The fact that porphyroblast long axes (X) and FIA are broadly parallel in sample 46.8 (Fig. 4.7a) suggests that porphyroblasts grew in low-strain lenses with prolate shapes aligned with crenulation and fold axes. This is consistent with the fact that stretching lineations are almost everywhere parallel to fold axes throughout the NFC. However, rather than having resulted from progressive reorientation of fold axes in simple shear (i.e. sheath folds), our inclusion-trail data suggest that folds and crenulations formed immediately with their axes parallel to the maximum stretching axes, because they deformed foliation initially lay in the XZ plane of the instantaneous strain ellipsoid (e.g. Aerden, 1998; Xypolias et al., 2013). In contrast, the fact that maximum porphyroblast shape elongation axes in sample 49.10 are mainly perpendicular to FIAs suggests that

crenulation axes in this sample formed perpendicular to the X- and parallel to Y-axis of the instantaneous strain ellipsoid there. This scenario is consistent with the reported abundance of curvilinear D_1 and D_2 fold axes in the sample area (Macaya et al., 1991) presumably due to differential reorientation of fold axes towards X.

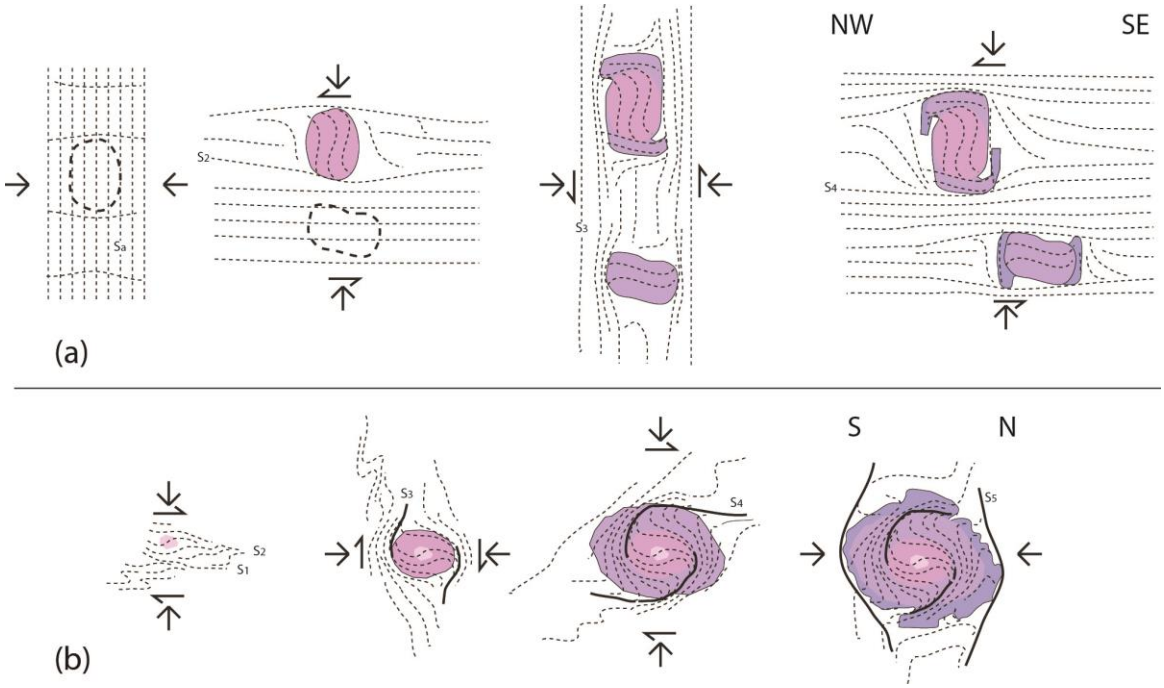

Fig. 4.10. (a) Genetic model for the development of inclusion trails with vertical and horizontal preferred orientations in sample 49.10. Episodic porphyroblast growth is punctuated by a succession of vertical (S_1 and S_3) and horizontal (S_2 and S_4) crenulation cleavages. See text for further explanation. (b) Similar non-rotational interpretation of a large garnet porphyroblast from the same outcrop as sample 46.8 studied and dated by Farrell et al. (2019) (and manucript in preparation).

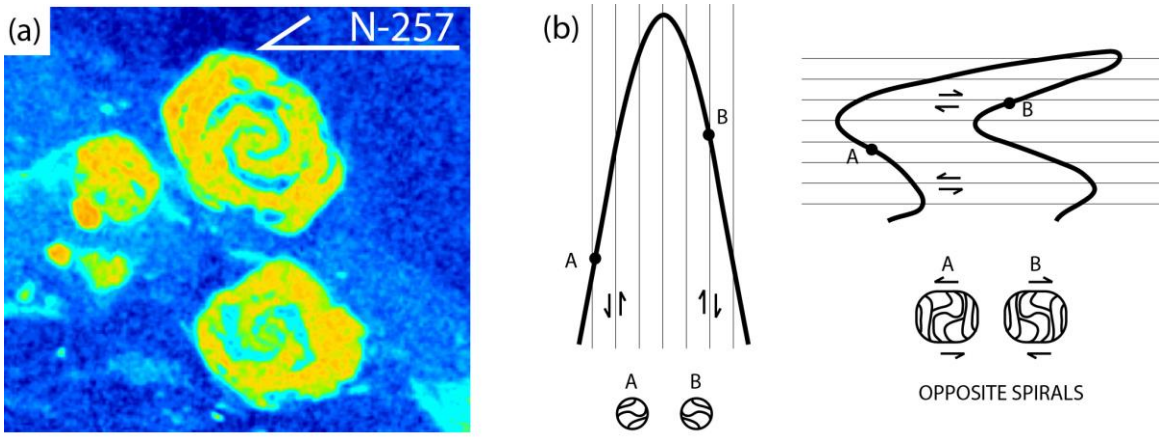

Fig. 4.11. (a) XCT slice through 2 adjacent spiral garnets subperpendicular to their NNW trending FIAs (FIA set 4). (b) Conceptual model of how the inclusion-trails in (a) might have formed in opposite fold limbs with opposite shear senses during two consecutive folding events.

4.7. Discussion

4.7.1. Complex foliation successions versus simple macroscopic structures

The main matrix cleavage in both samples has been generally called "S_2" in the literature and its inclusion trails "S_1". However, the polyphase nature of "S_1" demonstrated herein implies that neither S_1 nor S_2 represent single (extensional or compressive) orogenic events with simple kinematics. Indeed, Rubio Pascual et al. (2016), Martínez-Martínez (1986) and Behr and Platt (2013) recognized that the 'main foliation' was active during at least 2 successive shearing events, before still being overprinted by sets of later crenulation cleavages and folds. Our 3D analysis of inclusion trails in sample 49.10 has shown that the main cleavage is probably a mixture of no less than 4 foliations that defining a single FIA set with NE-SW trend. Consistent anticlockwise curvature of these trails (viewing NE) can be inferred to record alternating SE-up shearing along vertical foliations and top-to-the NW shearing on horizontal ones. Nine other samples from different locations in the Berzosa shear studied by Aerden (unpublished data) show the same dominant anticlockwise curvature sense suggesting that this reflects regional-scale kinematics.

Our interpretation of four different FIA sets in sample 46.8 implies a succession of at least 9 foliations, since each set of spiral garnets would have required a minimum of 2 new foliations (Fig. 4.9). Assuming the classic rotational model for some or all of these FIA sets allows to significantly reduce the number of foliations needed, but at the cost of leaving unexplained 2 important aspects of our data. Firstly, the predominantly subhorizontal plunges of all 4 FIA sets, inconsistent with significant reorientation of earlier FIA trends during the formation of younger ones. For example, porphyroblast rotations associated with N-S trending FIA set 4 should affected the plunges of E-W trending FIA 2 and 3. Secondly, the rotational model is at odds with vertical-horizontal preferred orientations of inclusion trails not only in the samples studied herein, but also consistently found in other samples of the NFC (Aerden et al., 2013; their Fig. 4b) and in metamorphic belts around the world (e.g. Aerden, 1995, 1998; 2004; Hayward, 1992; Bell and Sapkota, 2012).

The proposed FIA model raises the question, though, why no evidence is found for so many foliations and fold generations in outcrop or how this microstructural complexity can be reconciled with relatively simple macroscopic structures. Indeed, the maximum number of deformation phases that can be distinguished in any outcrop of the NFC is 4: the main foliation (S_2), relics of an overprinted previous foliation (S_1), and 1 or 2 younger crenulation cleavages. The paradox of complex foliation succession recorded by porphyroblasts versus simple matrix fabrics was previously addressed by Adshead-Bell and Bell (1999), Paterson and Vernon (2001), and Ham and Bell (2004) who proposed 2 complementary explanations. Firstly, not every foliation that becomes trapped in a porphyroblast necessarily developed pervasively or is associated with large bulk strains. For this reason, the P-T conditions of a sample do not necessarily change much between successive foliation forming events. In other words, the orthogonal foliation successions

preserved by porphyroblasts record temporary permutations between the principle stresses not necessarily all associated with large regional displacements. Secondly, the development of new cleavage planes is commonly restricted to the margins of rigid porphyroblasts and other competent bodies, either due to strain localization where bulk strain is relatively low, or due to reactivation of a pre-existing foliation where bulk deformation is intense (e.g. Aerden, 1994, 1995; Ham and Bell, 2004; Bell and Bruce, 2006). Repeated reactivation of the same foliation in different stress fields may also explain the variable shear-senses and lineation directions associated with "S_2" in the Nevado-Filabride Complex (Jabaloy et al., 1993; Aerden and Sayab, 2008).

Farrell et al. (2019, and article in preparation) recently dated with the Sm-Nd method different growth zones of 3 large garnets with approximately E-W trending FIAs in a similar sample as 46.8 taken a few meters away from it from the same outcrop. The growth history of one of these garnets, modelled in Fig. 4.10b, is interpreted to have involved the sequential development of 3 crenulation cleavages. The radiometric ages indicate that these garnets and the 3 overgrown foliations formed in less than 1 million year, between 14 and 13 Ma. Previous radiometric ages for the NFC, however, indicate a much longer period of metamorphism dating back at least to ca. 20 Ma (Platt et al., 2006) and probably earlier (Li and Massonne, 2018), during which numerous foliations developed grouped in 4 or possibly 5 (depending on whether FIA 1 is eventually confirmed or not) FIA sets.

4.7.2. Significance of inconsistent inclusion-trail curvature sense

It is not uncommon to observe inclusion trails that have opposite curvature senses in the same thin section. Distinguishing the different possible underlying causes requires knowledge of the spatial orientation of the FIA that can only be obtained via study of multiple, differently oriented thin sections and/or XCT. We will now briefly discuss three possible causes responsible for inconsistent inclusion trail curvature in single thin sections.

1- Where a thin section is cut parallel to the average orientation of FIAs in a sample, and where those FIAs belong to a single set with a single orientation maximum, inconsistent curvature senses arise as a cut effect due to the spread of individual FIAs about the mean. Hayward (1990) showed that individual FIA typically deviate up to 20º from the average FIA in spiral garnets, and suggested that this results from the wrapping of foliation planes around porphyroblasts, influenced by the orientation of straight crystal faces, before being included in a new growth stage. In this case, thin sections making an angle greater than 20º with the average FIA will show consistent inclusion-trail curvature senses.
2- Inclusion trails with true opposite curvature sense (i.e. not a cut effect) but belonging to a single FIA set will show this in thin-sections of any orientation. This situation is expected where relatively coaxial deformation produced crenulations with opposite asymmetry in a sample that were overgrown by porphyroblasts.

3- The presence of 2 or more FIA sets in a sample gives rise to complex inclusion trail patterns with inconsistent curvature sense. Resolving these FIA sets and establishing their relative timing is in principle possible using sets of radial thin sections by focusing attention on those inclusion trails that show a reversal of their curvature sense from core to rim of single porphyroblasts (Bell et al., 1995). However, this only works well where several conditions are simultaneously met: (i) The sample contains sufficient porphyroblasts preserving a different FIAs in cores and rims, instead being hosted in separate porphyroblasts. (ii) Each FIA set individually is defined by inclusion trails that have consistent curvature sense. (iii) None of the FIA have steep or subvertical plunges. Significantly, Aerden et al. (2013) were able to determine separate core versus rim FIAs in only one samples out of a total of 68 studied, suggesting that the above conditions are rarely met in the NFC. Five of their samples yielded multiple FIAs thanks to their inclusion in different porphyroblast minerals, and in a few more samples allowed to infer multiple FIAs based on the results of calculating best-fit planes for the inclusion trails.

4.8. Conclusions

Application of the XCT technique has allowed us to accurately measure the FIAs, sizes and shapes of a large number of spiral garnets present in 2 micaschist samples from 2 regional shear zones. The principle advantage of XCT over thin-section based methods for measuring FIAs is that it eliminates the need to interpret how inclusion trails correlate between different porphyroblasts and thin sections. This is particularly problematic where these microstructures exhibit inconsistent curvature sense in the same thin section. By establishing relationships between FIA trend, porphyroblast size and shape, and inclusion trail curvature sense, XCT allows the distinction of multiple porphyroblast generations where this would not have been possible using thin sections alone. Although XCT reduces the number of thin sections needed for studying metamorphic rocks in 3D, its limited resolution (depending on the volume studied) and the difficulty to distinguish mineral phases with similar X-ray attenuation coefficients, make that the method should be ideally combined with microstructural analysis of thin sections cut with orientations chosen based on the 3D data (e.g. perpendicular to FIA). Our study illustrates how inclusion trails can provide a holistic record of complex tectonic histories that contrasts with simple 2D models inferred from study of thin sections mainly cut parallel to the matrix lineation and based on the assumption that FIAs are perpendicular to that lineation.

Our XCT data confirm earlier reported vertical and horizontal alignment of inclusion trails in different mountain belts (e.g. Hayward, 1992; Aerden, 2004; Bell and Sapkota, 2012; Aerden et al., 2013), which demonstrate a lack of porphyroblast rotation. Since both our samples were taken from regional shear zones, it may be concluded that porphyroblasts are able to maintain stable positions even where the matrix around them is sheared. This is made possible by the partitioning of deformation into shortening and shearing components as numerically modelled by Fay et al. (2008). However, more

research is necessary to discover how this mechanism emerges from the fundamental properties and processes of metamorphic rocks such as anisotropy, pressure solution, polymineralic compositions, and metamorphic reactions.

Author statement

Conceptualization: Aerden Methodology: Aerden 50%; Ruiz Fuentes 50% Formal analysis: Aerden 50%; Ruiz Fuentes 50% Investigation: Aerden 25%; Ruiz Fuentes 75% Writing original draft, Review & Editing: Aerden 75%, Ruiz Fuentes 25% Visualization: Aerden 50%; Ruiz Fuentes 50%

Declaration of competing interest

The authors declare that they have no known competing financial interests or personal relationships that could have appeared to influence the work reported in this paper.

Acknowledgements

We thank Mohammad Sayab for performing the X-ray scans of both samples at the Geological Survey of Finland with financial support of Academy of Finland RAMI infrastructure project (#293109). We thank Ioan Sanislav and an anonymous reviewer for helpful comments and Joao Hippertt for his editorial work. We thank Claudio Agostinelli and Eduardo García Portugués for help with Watson U^2 test. The first author also wishes to thank Ramón Capote and Sonia Sánchez Martínez for our field trip to the Berzosa shear zone in 1999 when sample 49.10 was collected. This research was supported by projects CGL2016-80687-R AEI/FEDER of the Spanish government, project RNM148 of the regional government of Andalusia, and a Ph.D. scholarship awarded to A. Ruiz-Fuentes (FPU17/01874) by the Spanish Ministerio de Educación, Cultura y Deporte.

Appendix A. Supplementary data

Supplementary data to this article can be found online at https://doi.org/10.1016/j.jsg.2020.104054.

References

Abu Sharib, A.S.A.A., Bell, T.H., 2011. Radical changes in bulk shortening directions during orogenesis: significance for progressive development of regional folds and thrusts. Precambrian Res. 188, 1–20.

Adshead-Bell, N.S., Bell, T.H., 1999. The progressive development of a macroscopic upright fold pair during five near-orthogonal foliation-producing events: complex microstructures versus a simple macrostructure. Tectonophysics 306, 121–147.

Aerden, D.G.A.M., 1994. Kinematics of orogenic collapse in the Variscan Pyrenees deduced from microstructures in porphyroblastic rocks from the Lys–Caillaouas Massif. Tectonophysics 236, 139–160.

Aerden, D.G.A.M., 1995. Porphyroblast non-rotation during crustal extension in the Variscan Pyrenees. J. Struct. Geol. 17, 709–726.

Aerden, D.G.A.M., 1998. Tectonic evolution of the Montagne Noire and a possible orogenic model for syn-collisional exhumation of deep rocks, Hercynian belt, France. Tectonics 17, 62–79.

Aerden, D.G.A.M., 2003. Preferred orientation of planar microstructures determined via statistical best-fit of measured intersection-lines: the "FitPitch" computer program. J. Struct. Geol. 25, 923–934.

Aerden, D.G.A.M., 2004. Correlating deformations in the Iberian Massif (Variscan belt) using porphyroblasts; implications for the development of the Ibero-Armorican Arc. J. Struct. Geol. 26, 177–196.

Aerden, D.G.A.M., Sayab, M., 2008. From Adria- to Africa-driven orogenesis: evidence from porphyroblasts in the betic Cordillera, Spain. J. Struct. Geol. 30, 1272–1287.

Aerden, D.G.A.M., Bell, T.H., Puga, E., Sayab, M., Lozano, J.A., Díaz de Federico, A., 2013. Multi-stage mountain building vs. Relative plate motions in the Betic Cordillera deduced from integrated microstructural and petrological analysis of porphyroblast inclusion trails. Tectonophysics 587, 188–206.

Agostinelli, C., Lund, U., 2017. R package 'circular': circular Statistics (version 0.4-93). https://r-forge.r-project.org/projects/circular/.

Ali, A., 2010. The tectono-metamorphic evolution of the Balcooma Metamorphic Group, north-eastern Australia: a multidisciplinary approach. J. Metamorph. Geol. 28, 397–422.

Behr, W.M., Platt, J.P., 2012. Kinematic and thermal evolution during two-stage exhumation of a Mediterranean subduction complex. Tectonics 31. https://doi.org/ 10.1029/2012TC003121. TC4025.

Behr, W.M., Platt, J.P., 2013. Rheological evolution of a Mediterranean subduction complex. J. Struct. Geol. 54, 136–155.

Bell, T.H., Johnson, S.E., 1989. Porphyroblast inclusion trails: the key to orogenesis. J. Metamorph. Geol. 7, 279–310.

Bell, T.H., 1985. Deformation partitioning and porphyroblast rotation in metamorphic rocks: A radical reinterpretation. J. Metamorph. Geol. 3, 109–118. https://doi.org/ 10.1111/j.1525-1314.1985.tb00309.x.

Bell, T.H., Bruce, M.D., 2006. The internal inclusion trail geometries preserved within a first phase of porphyroblast growth. J. Struct. Geol. 28, 236–252.

Bell, T.H., Sapkota, J., 2012. Episodic gravitational collapse and migration of the mountain chain during orogenic roll-on in the Himalayas. J. Metamorph. Geol. 30, 651–666.

Bell, T.H., Fay, C., 2016. Holistic microstructural techniques reveal synchronous and alternating andalusite and staurolite growth during three tectonic events resulted from shifting partitioning of growth vs deformation. Lithos 262, 699–712.

Bell, T.H., Johnson, S.E., Davis, B., Forde, A., Hayward, N., Wilkins, C., 1992. Porphyroblast inclusion-trail orientation data: eppure non son girate! J. Metamorph. Geol. 10, 295–307.

Bell, T.H., Forde, A., Wang, J., 1995. A new indicator of movement direction during orogenesis - measurement technique and application to the Alps. Terra. Nova 7, 500–508.

Bell, T.H., Hickey, K.A., Upton, G.J.G., 1998. Distinguishing and correlating multiple phases of metamorphism accross a multiply deformed region using the axes of spiral, staircase, and sigmoidally curved inclusion trails in garnet. J. Metamorph. Geol. 16, 767–794.

Capote, R., Fernandez-Casals, M.J., González-Lodeiro, F., lglesias Ponce de Leon, M., 1977. El limite entre las zonas Astur Occidental Leonesa y Galaico-Castellana en el Sistema Central. Bol. Geol. Min. 88, 517–520.

Cihan, M., Parsons, A., 2005. The use of porphyroblasts to resolve the history of macro- scale structures: an example from the Robertson River Metamorphics, North-Eastern Australia. J. Struct. Geol. 27, 1027–1045.

Escuder Viruete, J., Hernaiz Huerta, P.P., Valverde Vaquero, P., Rodrıíguez Fernandez, R., Dunning, G., 1998. Variscan syncollisional extension in the Iberian Massif: structural, metamorphic and geochronological evidence from the Somosierra sector of the Sierra de Guadarrama (central Iberian zone, Spain). Tectonophysics 290, 87–109.

Farrell, T., Aerden, D., Baxter, E., 2019. A rapid pulse of garnet growth and deformation in the betic Cordillera, Spain revealed from zoned Sm-Nd geochronology of spiral garnets (Abstract). Goldschmidt Abstr. 956, 2019.

Fay, C., Bell, T.H., Hobbs, B.E., 2008. Porphyroblast rotation versus nonrotation: Conflict resolution! Geology 36, 307–310.

Griera, A., Llorens, M.G., Gomez-Rivas, E., Bons, P.D., Jessel, M.W., Evans, L.A., Lebensohn, R., 2013. Numerical modelling of porphyroclast and porphyroblast rotation in anisotropic rocks. Tectonophysics 587, 4–29.

Ham, A.P., Bell, T.H., 2004. Recycling of foliations during folding. J. Struct. Geol. 26, 1989–2009.

Hayward, N., 1990. Determination of early fold axis orientations in multiply deformed rocks using porphyroblast inclusion trails. Tectonophysics 179, 353–369.

Hayward, N., 1992. Microstructural analysis of the classical spiral garnet porphyroblasts of south-east Vermont: evidence for non-rotation. J. Metamorph. Geol. 10, 567–587.

Huddlestone-Holmes, C.R., Ketcham, R.A., 2005. Getting the inside story: using computed X-ray tomography to study inclusion trails in garnet porphyroblasts. Am. Mineral. 90 https://doi.org/10.2138/am.2005.1840.

Huddlestone-Holmes, C.R., Ketcham, R.A., 2010. An X-ray computed tomography study of inclusion trail orientations in multiple porphyroblasts from a single sample. Tectonophysics 480, 305–320.

Jabaloy, A., Galindo-Zaldivar, J., Gonzalez-Lodeiro, F., 1993. The Alpujarride-Nevado- Filabride extensional shear zone, Betic Cordillera, SE Spain. J. Struct. Geol. 15, 552–569.

Jammalamadaka, S.R., SenGupta, A., 2001. Topics in Circular Statistics, Section 7.5. World Scientific Press, Singapore.

Jiang, D.Z., Williams, P.F., 2005. Reply to the comments by Domingo Aerden on "Reference frame, angular momentum, and porphyroblast rotation". J. Struct. Geol. 27, 1134–1137.

Johnson, S.E., 2008. The effects of strain localisation on rigid-object kinematics. In: Bons, P.D., Jessel, M.W., Koehn, D. (Eds.), Microdynamics Simulation. Springer, pp. 246–252.

Jung, W.S., Ree, J.H., Park, Y., 1999. Non-rotation of garnet porphyroblasts and 3D inclusion trail data: an example from the Imjingang belt, South Korea. Tectonophysics 307, 381–395.

Li, B., Massonne, H.J., 2018. Two tertiary metamorphic events recognized in high- pressure metapelites of the Nevado-Filabride complex (betic Cordillera, S Spain). J. Metamorph. Geol. 36, 603–630.

Macaya, J., Gonzalez-Lodeiro, F., Martínez-Catalán, J.R., Álvarez, F., 1991. Continuous deformation, ductile thrusting and backfolding of cover and basement in the Sierra de Guadarrama, Hercynian orogen of central Spain. Tectonophysics 191, 291–309.

Martínez-Martínez, J.M., 1986. Fabricas y texturas miloniticas. Cinematica de las traslaciones en el Complejo Nevado-Filabride (Cordilleras Beticas, Espan~a). Estud. Geol. 42, 291–300.

Ollion, J., Cochennec, J., Loll, F., Escude, C., Boudier, T., 2013. TANGO: a generic tool for high-throughput 3D image analysis for studying nuclear organization. Bioinformatics 29, 1840–1841.

Passchier, C.W., Trouw, R.A.J., 2005. Microtectonics. Springer, Berlin, Heidelberg, New York.

Paterson, S.R., Vernon, R.H., 2001. Inclusion trail patterns in porphyroblasts from the Foothills Terrane, California: a record of orogenesis or local strain heterogeneity? J. Metamorph. Geol. 19, 351–372.

Platt, J.P., Anczkiewicz, R., Soto, J.I., Kelley, S.P., Thirlwall, M, 2006. Early Miocene continental subduction and rapid exhumation in the western Mediterranean. Geology 34, 981–984. https://doi.org/10.1002/2015GC006208.

Puga, E., Díaz de Federico, A., Fanning, M., Nieto, J.M., Rodríguez Martínez-Conde, J.A., Díaz Puga, M.A., Lozano, J.A., Bianchini, G., Natali, C., Beccaluva, L., 2017. The Betic ophiolites and the Mesozoic evolution of the western Tethys. Geosciences 7, 31. https://doi.org/10.3390/geosciences7020031, 2017.

Ran, H., de Riese, T., Llorens, M.G., Finch, M.A., Evans, L.A., Gomez-Rivas, E., Griera, A., Jessell, M.W., Lebensohn, R.A., Piazolo, S., Bons, P.D., 2019. Time for anisotropy: the significance of mechanical anisotropy for the development of deformation structures. J. Struct. Geol. 125, 41–47.

Robyr, M., Vonlanthen, P., Baumgartner, L.P., Grobety, B., 2007. Growth mechanism of snowball garnets from the Lukmanier Pass area (Central Alps, Switzerland): a combined μCT/EPMA/EBSD study. Terra. Nova 19, 240–244.

Robyr, M., Carlson, W.D., Passchier, C., Vonlanthen, P., 2009. Microstructural, chemical and textural records during growth of snowball garnet. J. Metamorph. Geol. 27, 423–437.

Rosenfeld, J.L., 1970. Rotated garnets in metamorphic rocks. Geol. Soc. Am. Spec. Pap. 129, 102.

Rubio Pascual, F.J., Lopez-Carmona, A., Arenas, R., 2016. Thickening vs. extension in the Variscan belt: P-T modelling in the Central Iberian autochthon. Tectonophysics 681, 144–158.

Ruiz-Fuentes, A., Aerden, D.G.A.M., 2018. Transposition of foliations and superposition of lineations during polyphase deformation in the Nevado-Filabride complex: tectonic implications. Int. J. Earth Sci. 107, 1975–1988.

Sayab, M., 2005. Microstructural evidence for N–S shortening in the Mount Isa Inlier (NW Queensland, Australia): the preservation of early W–E-trending foliations in porphyroblasts revealed by independent 3D measurement techniques. J. Struct. Geol. 27, 1445–1468.

Schindelin, J., Arganda-Carreras, I., Frise, E., Kaynig, V., Longair, M., Pietzsch, T., Preibisch, S., Rueden, C., Saalfeld, S., Schmid, B., Tinevez, J.Y., White, D.J., Hartenstein, V., Eliceiri, K., Tomancak, P., Cardona, A., 2012. Fiji: an open-source platform for biological-image analysis. Nat. Methods 9, 676–682.

Schneider, C.A., Rasband, W.S., Eliceri, K.W., 2012. NIH Image to ImageJ: 25 years of image analysis. Nat. Methods 9, 671–675.

Shah, S.Z., Sayab, M., Aerden, D., Asif Khan, M., 2011. Foliation intersection axes preserved in garnet porphyroblasts from the Swat area, NW Himalaya: a record of successive crustal shortening directions between the Indian plate and Kohistan- Ladakh Island Arc. Tectonophysics 509, 14–32.

Stallard, A., Hickey, K., 2001. Shear zone vs folding origin for spiral inclusion trails in the Canton Schist. J. Struct. Geol. 23, 1845–1864.

Stallard, A.R., Hickey, K.A., Upton, G.J., 2003. Measurement and correlation of microstructures: the case of foliation intersection axes. J. Metamorph. Geol. 21, 241–252.

ten Grotenhuis, S.M., Passchier, C.W., Bons, P.D., 2002. The influence of strain localisation on the rotation behaviour of rigid objects in experimental shear zones. J. Struct. Geol. 24, 485–499.

Wintsch, R.P., Yeh, M.W., 2013. Oscillating brittle and viscous behavior through the earthquake cycle in the Red River Shear Zone: monitoring flips between reaction and textural softening and hardening. Tectonophysics 587, 46–62.

Xypolias, P., Chatzaras, V., Beane, R., Papadopoulou, S., 2013. Heterogeneous constrictional deformation in a ductile shear zone resulting from the transposition of a lineation-parallel fold. J. Struct. Geol. 52, 44–59.

5. Transposition of foliations and superposition of lineations during polyphase deformation in the Nevado-Filabride complex: tectonic implications

Alejandro Ruiz-Fuentes[1], Domingo G.A.M. Aerden[1,2]

[1] *Departamento de Geodinámica, Universidad de Granada, Av. Fuentenueva, 18071, Granada, Spain*

[2] *Instituto Andaluz de Ciencias de la Tierra, CSIC/Universidad de Granada, Av. de las Palmeras 4, 18100, Armilla, Granada, Spain*

Published on: International Journal of Earth Sciences, v. 107 (2018), 1975–1988
https://doi.org/10.1007/s00531-017-1582-6
JCR Impact Factor: 2.295 (2018)

Abstract

Detailed structural analysis in a ca. 80 km^2 area of the western Nevado-Filabride complex (Betic Cordillera) reveals a heterogeneous internal structure characterized by multiple cross-cutting foliations and lineations that locally transpose earlier ones. The large-scale geometry of these fabrics conflicts with continuous westward to south-westward tectonic transport related to thrusting or crustal extension, and mismatches a previously inferred extensional detachment in the area. Multiple crenulation lineations can be distinguished in the field and correlated with five Foliation Intersection Axes (FIA1-5) preserved in garnet and plagioclase porphyroblasts of the western Sierra Nevada. These indicate crustal shortening in different directions associated with vertical foliation development and intermitted stages of gravitational collapse producing horizontal foliations. The large spread of lineation- and fold-axes trends in the Nevado-Filabride complex results from the mixed presence of multiple generations of these structures whose distinction is critical for tectonic models. The five principle FIA trends remarkably match successive vectors of relative Africa-Iberia plate motion since the Eocene, suggesting that deformation of the Nevado-Filabride took place during this period, although peak metamorphism in at least some of its parts was reached as late as the Middle Miocene.

Keywords: Transposition, Deformation partitioning, Inclusion trails, Betic Cordillera, Nevado-Filabride complex

5.1. Introduction

Polyphase deformation and its partitioning at different scales (Bell, 1985; Carreras et al., 2013) commonly creates complex structures in metamorphic rocks difficult to decipher and interpret. A particular fabric that is dominant in one outcrop can either be completely transposed in another outcrop or might not even have developed there (e.g. Bishop, 1971; Lagoeiro et al., 2003; Webber et al., 2008; Ulrich et al., 2011). In central sectors of the Nevado-Filabride complex (NFC), Aerden and Sayab (2008) and Aerden et al. (2013) showed the main schistosity folded into large-scale antiforms and synforms, which are in turn overprinted by a sub-horizontal crenulation cleavage associated with the Nevado-Filabride/Alpujarride detachment (NFAD). The latter was still weakly folded in different directions creating an elongate open dome-shaped tectonic window. These authors noted that lineation- and fold trends vary spatially and temporally throughout the NFC, something not considered in models proposing continuous top-to-W or -SW ductile shear on a simple 'main cleavage' related to thrusting (Puga et al., 2017), extension (Jabaloy et al., 1993; Augier et al., 2005), thrusting followed by extension (Martínez-Martínez et al., 2002), or simultaneous thrusting and extension (Booth-Rea et al., 2015). These different interpretations reflect insufficient structural data and conflicting maps of different authors, in particular regarding the number and location of internal tectonic contacts within the NFC. As a contribution towards the resolution of these questions, we performed structural analysis in a ca. 80 km^2 area of the western Sierra Nevada supported with microstructural analysis of oriented samples. Since the study area is composed mainly of a monotonous sequence of graphite schists and quartzites that do not lend themselves to detailed lithological mapping, we concentrate on the structure as defined by different variably dipping tectonic foliations, associated lineations and folds, and their relationship with previously inferred tectonic contacts.

5.2. Geological setting

The Betic Cordillera is the southernmost mountain range of the Iberian Peninsula that, together with the Rif mountains in north Africa, constitute the western termination of the Alpine orogenic belt in the Mediterranean. It formed due to progressive collision of the Alboran Domain or microplate with the south Iberian paleomargin since the Eocene (Platt et al., 2013) or earlier (Puga et al., 2017), the former traditionally interpreted as being composed of three stacked complexes, from bottom to top: the Nevado-Filabride, Alpujarride and Malaguide complexes. However, recent evidence for a Middle Miocene age of HP metamorphism in the NFC (López-Sánchez-Vizcaíno et al., 2001; Gómez-Pugnaire et al., 2004; Platt et al., 2006; Kirchner et al., 2016), and affinities between gneiss bodies in this complex with late Variscan granitoids of the Iberian Massif (Gómez-Pugnaire et al., 2012) support the hypothesis that this complex represents the subducted south Iberian paleomargin (Platt et al., 2006).

The NFC (Fig. 5.1) and Alpujarride complex record subduction-related high-pressure metamorphism, followed by retrogression in greenschist to amphibolite facies conditions,

which in the case of the Alpujarride Complex, was followed by significant reheating that has been linked to the Miocene extension in the Mediterranean basin and the exhumation of peridotite massifs (Platt et al., 2003). The Malaguide complex only has low-grade metamorphism and record Hercynian and Alpine deformation (Cuevas et al., 2001). These three complexes were thrust during the Miocene (Platt et al., 2013) over Mesozoic cover sequences of the so called Frontal Units and External Zones (Fig. 5.1), which in the Gibraltar Arc are separated by Paleogene Flysch sediments.

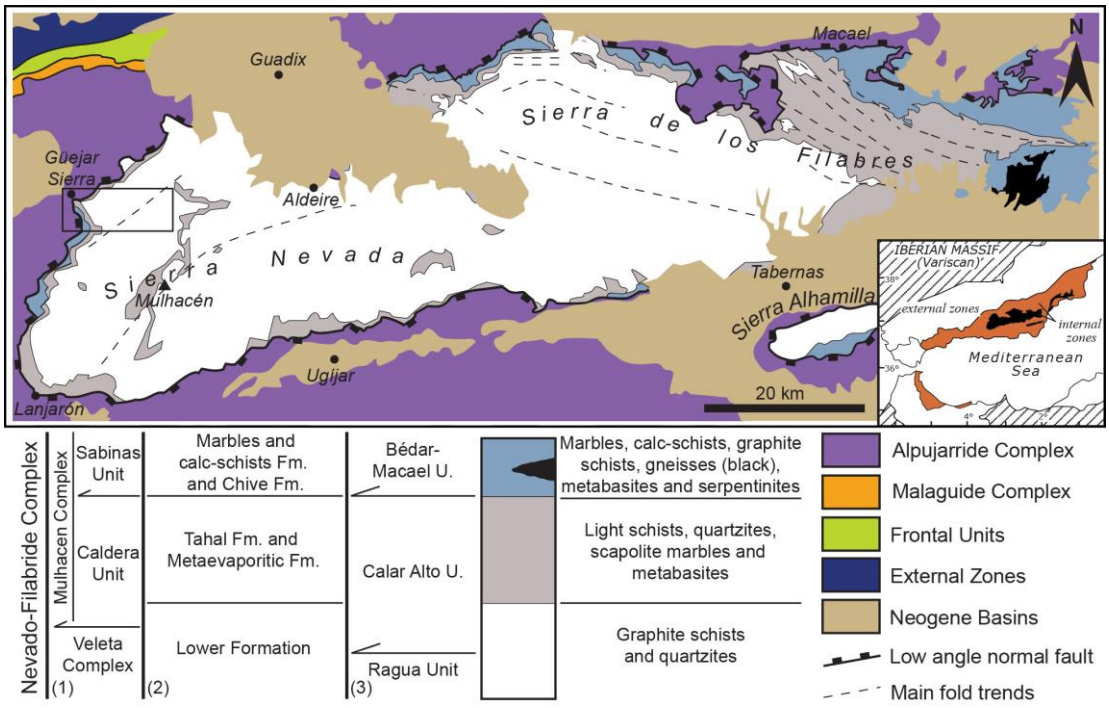

Fig. 5.1. Geological map showing the distribution of lithologies in the Nevado-Filabride complex and the subdivisions proposed by: (1) Puga et al., 2002; (2) Gómez-Pugnaire et al., 2012; (3) Martínez-Martínez et al., 2002. The box shows the location of the studied area.

The lithostratigraphic columns of the two lower metamorphic complexes resemble a thick series of Palaeozoic dark schists (Lafuste and Pavillon, 1976; Gómez-Pugnaire et al., 1982; Laborda-López et al., 2015) and quartzites at the base, overlain by light schists, feldspathic quartzites or phyllites, still followed by marbles that in the Alpujarride complex have been dated as Middle Triassic (Fallot et al., 1954). Following the recognition of large-scale extension in the Neogene evolution of the Betic Zone and Alboran Sea (e.g. Platt et al., 1983; Aldaya et al., 1984; García-Dueñas et al., 1988; Platt and Vissers, 1989; Comas et al., 1992), the contact between both complexes was reinterpreted as an extensional detachment, or as thrusts later reactivated as such, along which the NFC was finally exhumed in the Late Miocene (Johnson et al., 1997; Vázquez et al., 2011).

5.3. Tectonic subdivision and age of the NFC

Díaz de Federico et al. (1978) distinguished a series of internal thrust units and grouped these in a lower Veleta complex and upper Mulhacen complex. The latter was subdivided further in two continental units, the Caldera and Sabinas units, separated by a

dismembered ophiolite marked by cm to km-scale amphibolite-, eclogite- and serpentinite boudins derived from Jurassic igneous protoliths (Hebeda et al., 1980; Puga et al., 2005; 2011, 2017) in a matrix of light micaschists and calc-schists.

Martínez-Martínez et al. (2002) agree with a thrust contact between the Caldera and Sabinas units, but move the Mulhacen-Veleta contact to a much deeper level and reinterpret it as a low-angle extensional detachment in western Sierra Nevada, the so called Filabres detachment. Towards the east, the contact is thought to gradually cut upward through the NFC pile until joining the Nevado-Filabride—Alpujarride detachment. Based on a correlation with tectonic units defined in the eastern Sierra de los Filabres (García-Dueñas et al., 1988), they renamed tectonic units in the Sierra Nevada as Ragua (lower part of Veleta complex), Calar-Alto (upper part of Veleta complex plus Caldera unit), and Bédar-Macael (Sabinas unit).

Other workers (Galindo-Zaldívar, 1993; Jabaloy et al., 1993; Gómez-Pugnaire et al., 2012; Sanz de Galdeano and López-Garrido, 2016; Sanz de Galdeano et al., 2016) consider the NFC a single unit and attribute local litho-stratigraphic repetitions to isoclinal folding. Due to the presence of gneiss bodies derived from late-Variscan granites in the upper light schists and marbles traditionally considered Permo-Triassic (as in the Alpujarride Complex), plus skarn-like rocks thought to have formed by contact metamorphism with the gneiss protoliths, they propose a pre-Permian age of the entire NFC. The metabasite and serpentinite bodies are considered to represent igneous intrusions in thinned continental crust.

5.4. Deformation sequence in the NFC

Deformation sequences recognized by different authors in various parts of the NFC complex differ significantly in number and orientation of deformation phases. Aerden and Sayab (2008) proposed their correlation as D_1 to D_5, where D_1 corresponds to a completely transposed relic foliation (S_1) preserved in microlithons of S_2 and as inclusion trails in garnet porphyroblasts. D_2 generated a penetrative crenulation cleavage or schistosity parallel to the bedding (S_0) associated with 100 m to km-scale isoclinal folds also called “planar-linear fabric” (Jabaloy et al., 1993; Jabaloy-Sánchez et al., 2015). A third phase (D_3) deformed S_2 into upright folds associated with a sub-vertical crenulation cleavage (S_3) whose strike changes from NW-SE in the eastern Sierra de los Filabres to NE-SW in Sierra Nevada. Based on a detailed study of porphyroblast inclusion trails, Aerden et al. (2013) proposed that D_3 in fact comprises different foliations which they termed D_{3a}, D_{3b} and D_{3c}. D_4 is associated with the Nevado-Filabride—Alpujárride contact, concentrated in a several hundred m thick zone following this contact and characterized by a sub-horizontal crenulation cleavage, shear-band cleavage (S_4), and quartz and carbonate mylonites in the uppermost levels. The last movement stages on this contact created brittle carbonate fault rocks derived from the NFC. This major tectonic boundary and the associated D_4 fabrics were still weakly folded by late- to post-Miocene folds variably trending N-S, NE-SW or E-W. In our study area, a similar deformation sequence can be recognized as described below.

5.5. Structural sequence in the study area

5.5.1. Foliations

The dominant foliation in the study (Fig. 5.2 and Fig. 5.3) corresponds mostly to a composite S_1-S_2 fabric associated with isoclinally folded and transposed quartz veins (Fig. 5.4a, c, d, f). The orientation of this foliation is relatively consistent dipping moderately NE to N, except in subarea F (Fig. 5.2), where it has an opposite dip towards the S or SE. Due to limited outcrop, we could not determine whether this local change is due to D_3 or D_4 folding (see further below), and even do not discard a 100 meter-scale landslide as a possible cause.

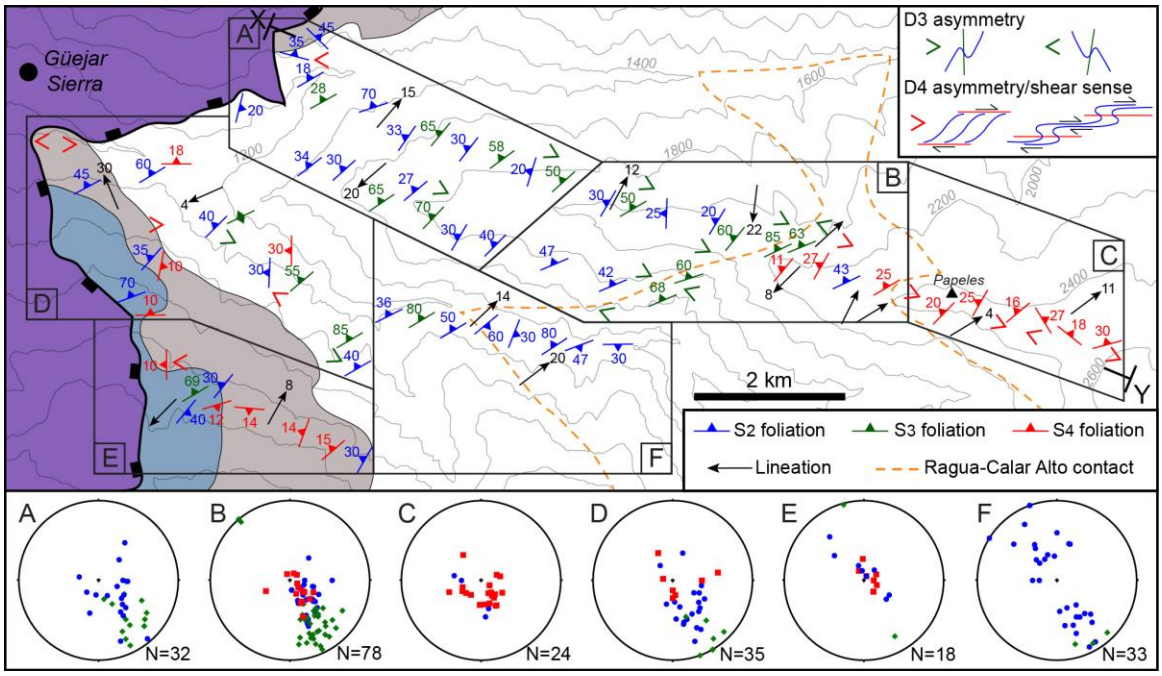

Fig. 5.2. Geological map of the box of Fig. 5.1 with representative measures of each foliation. The totality of measures is represented by area in stereograms.

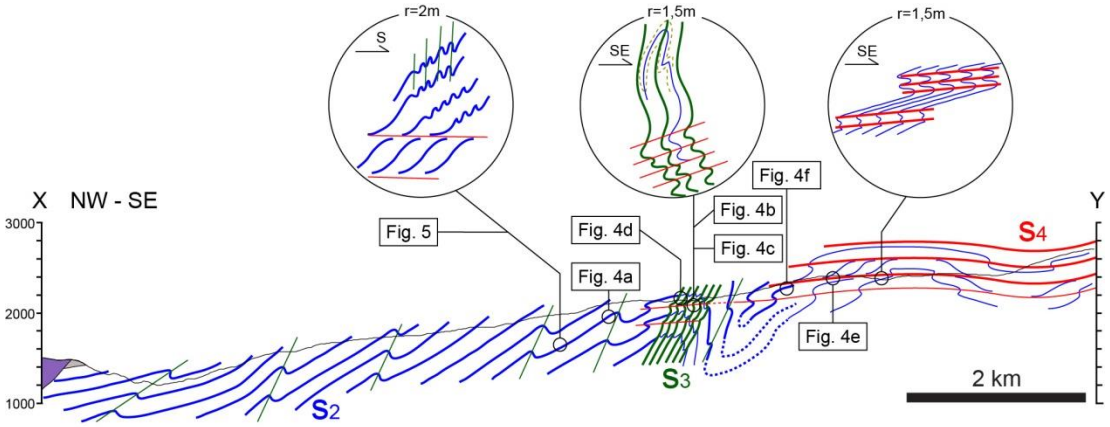

Fig. 5.3. Structural cross section from X to Y as marked in Fig. 5.2. The boxes show the location of images of Fig. 5.4 and 5.5. The circles show local observations in areas where the main foliation is S_2, S_3 or S_4.

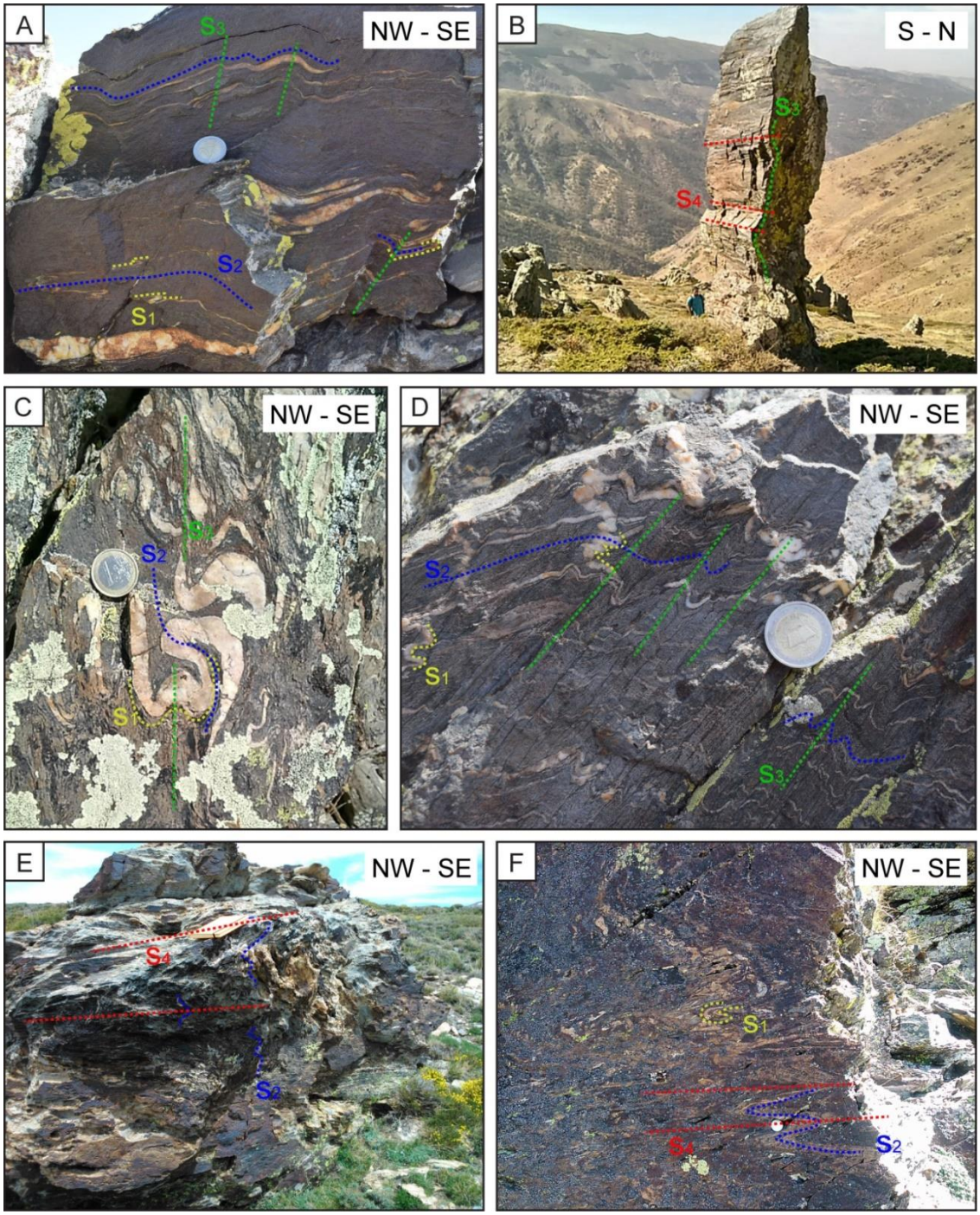

Fig. 5.4. Outcrop observations. a S_2 in quartz-schists folding quartz veins refolded by S_3. b Vertical S_3 in quartzite weakly crenulated by S_4. c Quartz vein representing S_1 folded by S_2 and S_3 with the latter being the main foliation in outcrop. d S_3 in psammitic layers within the zone of transposition of S_2. S_3 is the main foliation here. e Outcrop in which sub-horizontal S_4 is the main foliation and isoclinally folds S_2. f Psammitic layers with S_4 folding S_2, which in turn folds early quartz veins representing S_1.

Outcrops in the western part of the study area (Fig. 5.2) commonly show S_2 folded by cm- to dm-scale folds whose axial planes dip more steeply towards NW and are associated with a sub-vertical crenulation cleavage (S_3) (Fig. 5.4a and Fig. 5.5). In a several 100 m wide zone in the middle to eastern part of the map (Fig. 5.2 subarea B), the intensity of S_3 increases notably to the point of becoming the main cleavage that fully transposes S_2 by isoclinal folding (Fig. 5.4b, c, d). This transposition is particularly clear

in some metapsammitic layers due to a coarse spacing of S_3 cleavage planes. The asymmetry or vergence of small-scale D_3 folds is opposite in this zone as in the area west of it, implying that the transposition zone coincides with a large-scale D_3 fold-limb. In the light schists and marbles of subareas D and E, as well as a few meters below these two rock types, S_2 and S_3 cannot be clearly differentiated in the field due to increased intensity of sub-horizontal S_4.

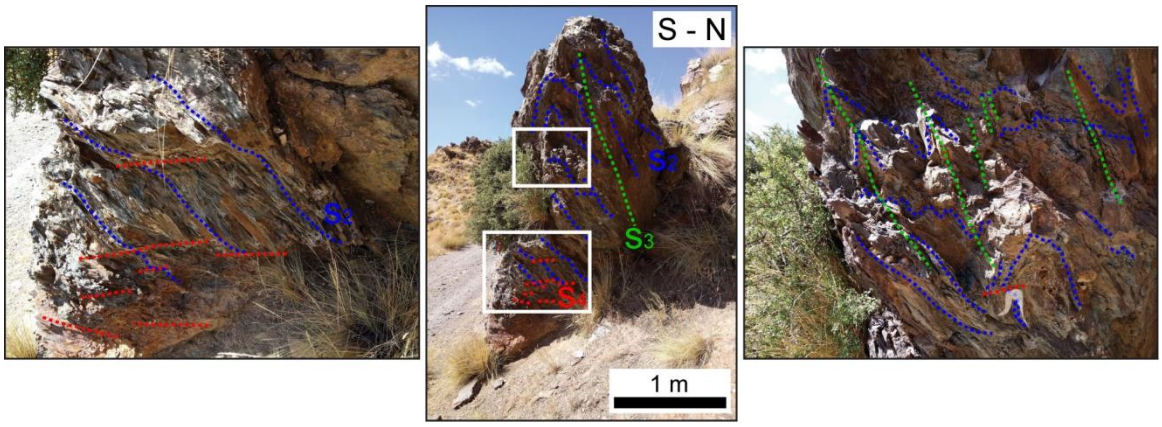

Fig. 5.5. S_2-S_3-S_4 relationships in an outcrop whose location is marked in Fig. 5.3.

D_4 structures comprise crenulation- and shear band cleavages that generally dip lower than 30º with variable strikes (Fig. 5.2 and 5.3). Where these structures overprint a steeply dipping to vertical previous foliation, a 'normal' crenulation cleavage is developed with open to tight D_4 folds (Fig. 5.4e, f), but where S_4 forms a low angle with the pre-existing foliations 'extensional' crenulations formed (Fig. 5.5) called pseudo S-C fabrics by Aerden and Sayab (2008). Thus, the development of 'normal' or 'extensional' crenulations probably depended on two factors: the initial orientation of the pre-existing foliation and the intensity and vorticity of local D_4 strain. In the western part of our map (Fig. 5.2), above approximately 1800 m, S_4 is developed, in light schists, as a widely spaced sub-horizontal extensional crenulation cleavage (Fig. 5.6a) or normal crenulation cleavage that indicate an apparent top to the SE shear sense.

In the eastern part of our cross-section above approximately 2400 m altitude, S_4 constitutes the main macroscopic foliation in outcrop and transposes all previous fabrics (Fig. 5.4e, f). Switching asymmetries (i.e. vergence) of D_4 crenulations, minor folds and pseudo-SC fabrics are best attributed to pre-existing D_3 folds vertically flattened and sheared by D_4 (Fig. 5.3), as we did not find evidence for large-scale D_4 folding. Similar D_3-D_4 fold interference patterns were previously described in central sectors of the NFC by Aerden and Sayab (2008) and are also known from other orogens (Dirks et al., 1997; Aerden, 1998; Ham and Bell, 2004; Fossen, 2016). In the vicinity of the outcropping Nevado-Filabride—Alpujarride contact in subarea D, two sets of shear bands with opposite shear-sense were observed (Fig. 5.6b). The more steeply dipping set occasionally cuts the gently dipping one (Fig. 5.6c), but we did not observe a reverse relationship. Due to scarce observations and very variable strikes of the steep shear bands we are not certain if they perhaps represent conjugate sets (Platt and Vissers, 1980) or if they postdate S_4.

5.5.2. Lineations

The lineations we observed in the field are crenulation or intersection lineations (Fig. 5.7a, b, c). Even where we initially perceived a finely spaced lineation in a thick quartzite bed in the immediate footwall of the Filabres detachment of Martínez-Martínez et al. (2002) as a mineral stretching lineation, later study of thin sections showed that it is caused by the intersection of S_2 and S_3 (Fig. 5.7d, e, f). Lineations trends in the Veleta complex define a N060 maximum, consistent with the great-circle distribution of foliation poles (Fig. 5.8a). In the Mulhacen complex, lineations have a somewhat larger spread with a main N050 maximum and smaller N065 maximum (Fig. 5.8b). Foliation poles in the Mulhacen complex show a significantly greater spread as in the Veleta complex (Fig. 5.8) suggesting more complex internal structures. In several outcrops, we observed a younger NE-SW trending lineation overprinting older NNE-SSW or E-W trending ones (Fig. 5.7b and c). This relative timing (Fig. 5.8c) suggests that the N050-N060 maximum in the stereograms correspond to the youngest and dominant lineation, and that the large dispersion of the data reflects the presence of older lineations that can only be locally distinguished.

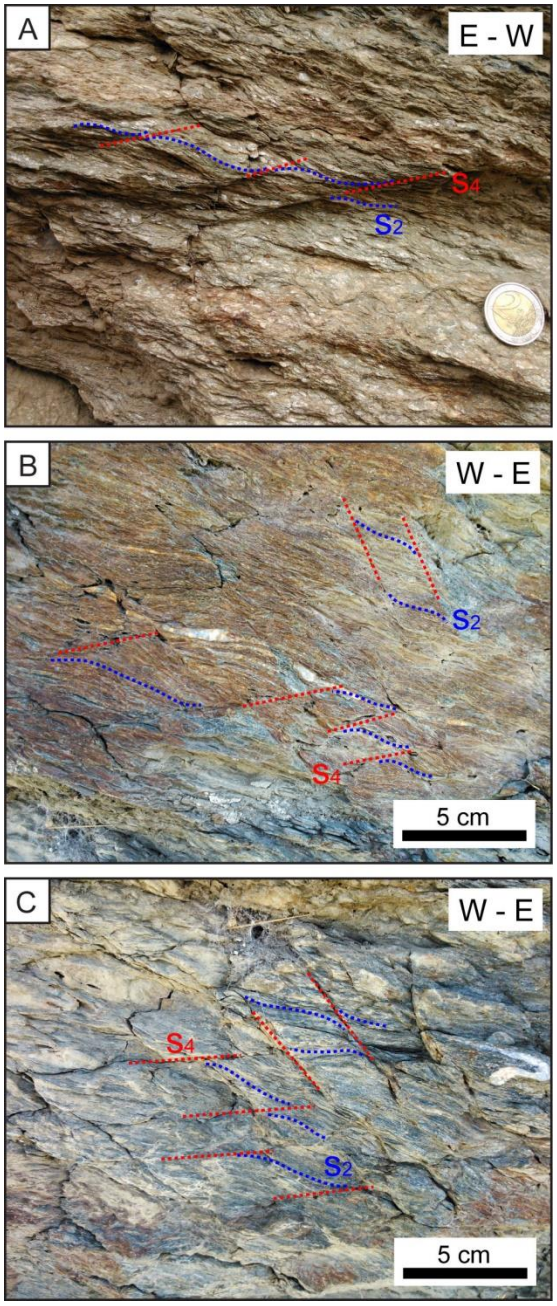

Fig. 5.6. Outcrop images of shear band cleavage. a Light schists with shear band cleavage with a top-to-the east asymmetry. b Two sets of shear band cleavage showing opposite asymmetry. c The sub-vertical set cuts the other set.

5.5.3. Foliation Intersection Axes in porphyroblasts

The use of porphyroblast inclusion trails as indicators of polyphase deformation histories received a major impulse after Bell (1985) and Bell and Johnson (1989) showed that sigmoid and spiral-shaped inclusion-trails generally form by overgrowth of crenulations rather than by porphyroblast rotation as assumed earlier. Their 'non-rotation' model has been confirmed in numerous metamorphic belts, where systematic measurement of inclusion trail orientations revealed their remarkable regional consistency (e.g. Aerden et al., 2013 and references cited therein).

Increasing importance has been given in these studies to crenulation or microfold axes preserved in porphyroblasts, known as Foliation Intersection or Inflexion Axes (FIA). The non-rotation model predicts that FIA should develop perpendicular to the direction of crustal shortening, so the presence of multiple FIA sets in a region is believed to track changes in this direction through time (e.g. Bell et al., 1995; Aerden, 2004; Shah et al., 2011; Bell and Sapkota, 2012; Sayab et al., 2016).

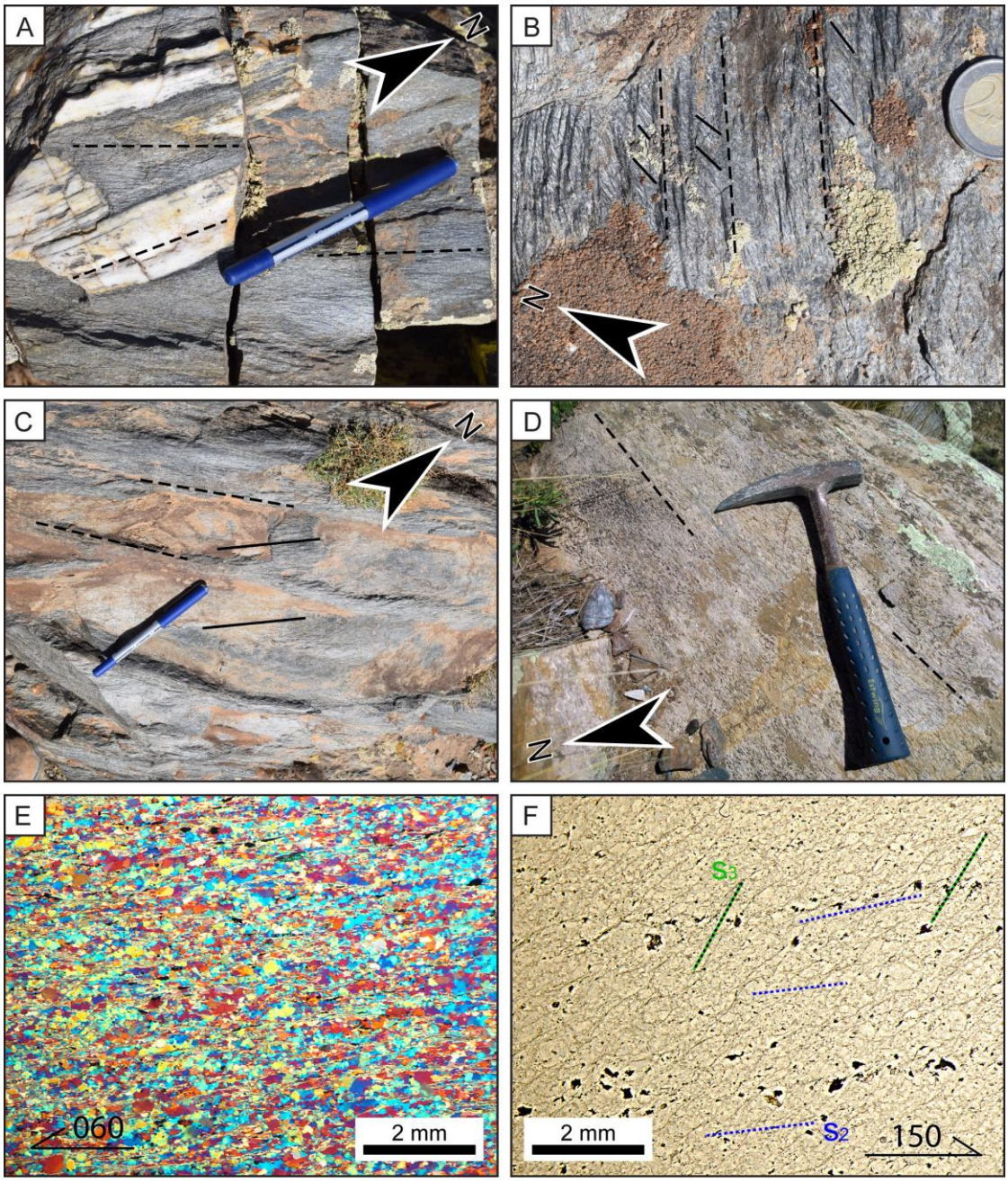

Fig. 5.7. Outcrop and microscopic examples of the lineations found in the field. a Graphite schist with quartz veins where different lineations are seen in the quartz layers and in the micaschist. b Micaschists where two lineations are found and one set is clearly younger. c Another example of a micaschist where temporal relationships between lineation sets are found. d Quartzite that shows an apparent stretching lineation in the field that in fact results from the intersection of two cleavage planes. e Vertical thin section parallel to the lineation of d where there is no evidence of elongated crystals or aggregates. The gypsum plate reveals no crystallographic preferred orientation. f Vertical thin section cut perpendicular to the lineation of the quartzite in d in which two foliations are seen.

Aerden et al. (2013) distinguished 4 FIA sets in the Nevado-Filabride complex (FIA-1 to FIA-4) whose trends were tentatively correlated with successive vectors of relative Africa-Iberia convergence from the Eocene till ca. 15Ma. The majority of these FIAs come from the western Sierra Nevada and 11 are from our study area (Fig. 5.2). In order to study the relationships between these FIA and the structures recognized in the field, we studied inclusion trails in 7 samples precisely oriented with respect to the north and the horizontal plane. FIAs in these samples were determined in the same way as Aerden et al. (2013) using two complementary techniques, namely, (1) the asymmetry technique of Bell et al. (1995), which constrains a FIA trend based on the curvature sense of inclusion trails observed in radial sets of vertical thin sections, and (2) the FitPitch program (Aerden, 2003), which calculated best-fit planes (representing included foliations) for pitch angles of inclusion trails measured in the same sets of radial sections plus an extra horizontal thin section. The newly determined FIA are: N090 ± 15 (sample AR2), N060 ± 15 (sample AR3 and AR5), N120 ± 15 (sample AR4), N075 ± 15 (sample AR9), N080 ± 5 (sample 46.8.1), N067 ± 11 (sample 49.5.1). These FIA trends are shown in the rose diagram of Fig. 5.9 together with those determined by Aerden et al. (2013).

5.6. Discussion

5.6.1. Relationship between lineations and strain

Crenulation and fold axes in the NFC have been previously stated to be mostly parallel to the principle extension direction or stretching lineation, although oblique relationships between lineations and folds have also been described. Most workers have interpreted these lineations as indicators of tectonic transport on flat lying foliations associated with thrusts or extensional detachments. Some of them attribute the parallelism between fold axes and maximum extension direction to a constrictional regime (Galindo-Zaldívar, 1993; Jabaloy et al., 1993) possibly related to 'lateral escape' or extrusion (Aerden, 1998, 2004; Mukherjee, 2013a). Others assume that fold axes have been progressively rotated into the direction of tectonic transport (Martínez-Martínez et al., 2002; Augier et al., 2005; Martínez-Martínez, 2007), although evidence for this model is limited to scarce non-cylindrical folds that can also be interpreted as fold-interference structures (Soto, 1991). However, none of these interpretations provide a detailed explanation of the large variation of lineation directions in the NFC (cf. Aerden and Sayab, 2008), conflicting shear-sense indicators and polyphase character of deformation.

In our experience, the apparent stretching lineations commonly result from the intersection at a low-angle of two foliations, which commonly creates a strong mineral lineation on one of the foliation surfaces, particularly in the form of aligned phyllosilicate traces. These linear fabrics do not necessarily imply strong stretching or shearing parallel to that lineation. In the upper marble formation, e.g., moderate boudinage in two perpendicular directions indicates a flattening type of strain ($K<1$) and is associated with a late intersection lineation parallel to the intermediate (Y) axes of the strain ellipsoid. Vissers (1981) performed strain analysis on a deformed conglomerate and also found an oblate shape of the strain ellipsoid. However, Soto et al. (1990) found a prolate strain

ellipsoid in a deformed metagranite in the eastern NFC. Quartz fabrics associated with the main foliation (S_{1-2}) have also been occasionally interpreted as indicating an important component of pure-shear or flattening (Platt and Behrmann, 1986; Jabaloy et al., 1993).

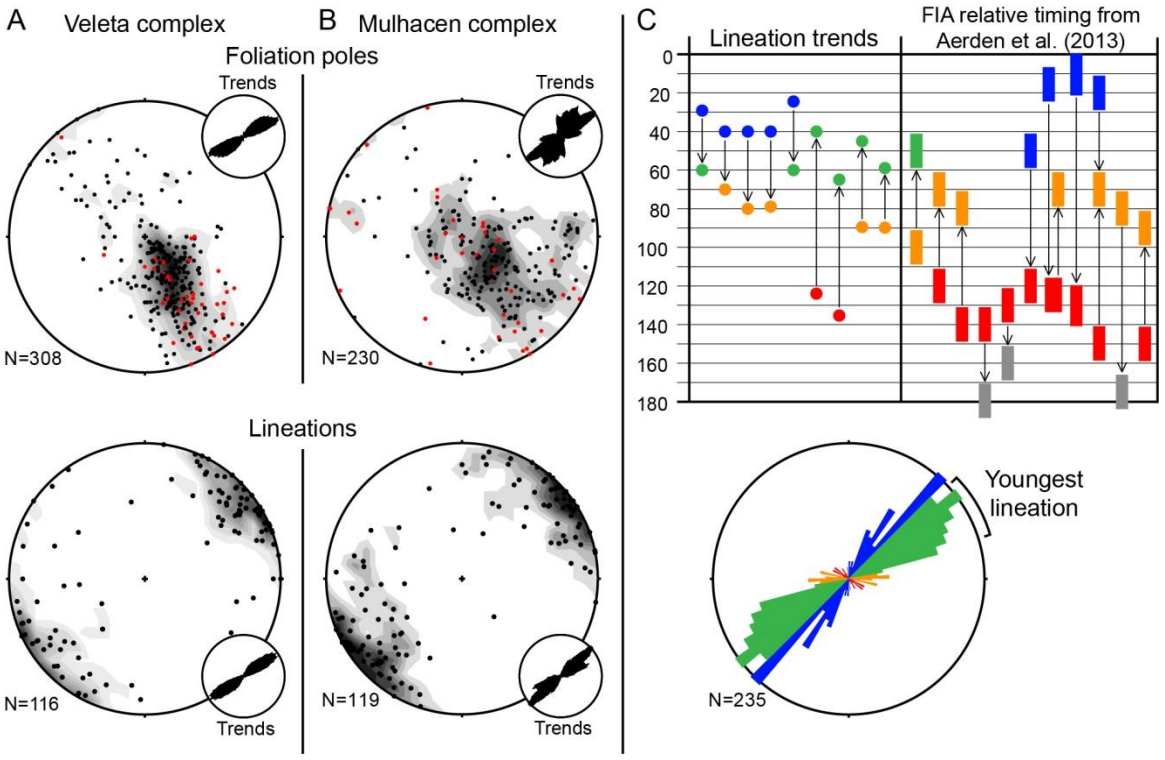

Fig. 5.8. Foliation poles (black dots for main schistosity; red dots for crenulation cleavages) and lineations from a Veleta complex and b Mulhacen complex. Main and crenulation foliations are differentiated in foliation poles stereograms. c Temporal relationships between different sets of lineations compared with FIA data from Aerden et al. (2013) and lineations assigned to FIA sets. Arrows point to the youngest lineation or FIA set.

5.6.2. Tectonic interpretation of lineations and FIA

Fig. 5.9a plots 82 FIA from the Nevado-Filabride complex. 60 of these were measured with the asymmetry technique and 22 with FitPitch. 16 FIAs plunging > 45° are omitted and not represented in the rose diagram, because they result from the intersection of two steeply dipping best-fit planes and therefore do not accurately reflect crustal shortening directions. The rose diagram exhibits two principle maxima at N080 and N120 plus two weaker and narrower ones at N165 and N065. The principle maxima represent the second and third generation FIA of Aerden et al. (2013; FIA-2 and -3). The relative timing of FIA was based on (1) different orientations (assumed sub-parallel to FIAs) of inclusion trails in garnet core versus rims observed in horizontal thin sections, (2) different FIAs obtained for garnet core versus rims with the asymmetry technique, and (3) different FIA trends for different minerals (plagioclase, chloritoid, garnet) whose relative timing is known independently. FIA-1 has NNE-SSW to NE-SW trend but is under-represented in the rose diagram. It was concluded mainly from the generally NE-SW strike of inclusion trails in garnet cores in the Mulhacen nappe, and of simple straight inclusion trails in small garnets of the Veleta complex.

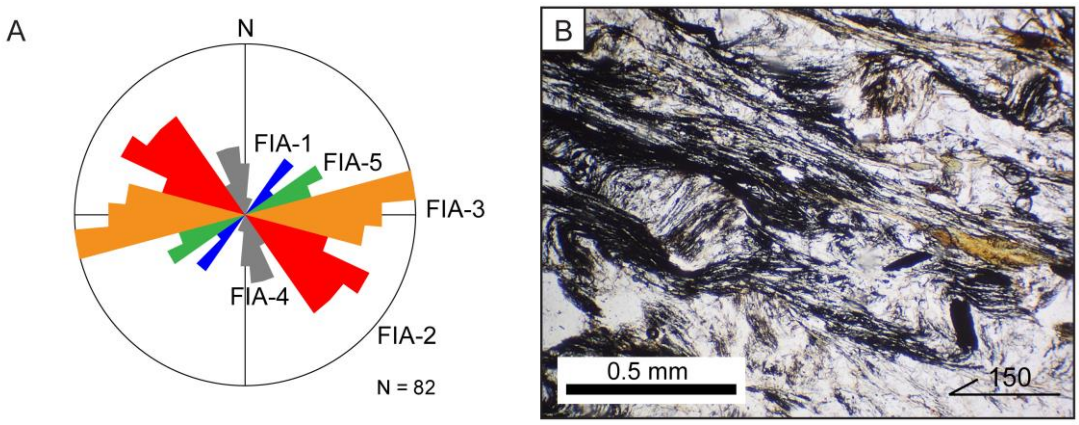

Fig. 5.9. a Rose diagram showing FIA trends. b Plagioclase porphyroblasts in sample AR5 showing continuity of their inclusion trails with the crenulated schistosity in the matrix.

All new FIAs except the one in sample AR5 can be matched to the 4 FIA trends recognized by Aerden et al. (2013). The N060 FIA of sample AR5, however, cannot be assigned to FIA-1 in spite of a similar trend. The reason is that this FIA is continuous with similarly oriented crenulation axes in the matrix (Fig. 5.9b) and therefore formed late. It is included in small plagioclase porphyroblasts known to generally postdate garnet growth in the NFC (Gómez-Pugnaire and Fernández-Soler, 1987; De Jong, 1993; Aerden et al., 2013). Interestingly, Aerden et al. (2013) found in one of their samples (A144) also collected from our study area, a N050 trending FIA in plagioclase porphyroblasts as well, and a N095 FIA in older garnet porphyroblasts. Since the relative timing of these 2 FIA did not allow interpretation as FIA-1 followed by FIA-3, respectively, they discussed the possibility of a younger fifth FIA repeating the trend of FIA-1, but in the end suggested that the sample might have been reorientated by late brittle deformation (Sanz de Galdeano and López-Garrido, 2016). This explanation looses credibility in the light of our new evidence for a young N060 FIA so we conclude that FIA-5 does indeed exist and is associated with the trend maximum of lineations measured in the field. The older lineations with different trends that we locally observed may be related to FIA-1, -2 and -3 (Fig. 5.8c). Significantly, the trend of FIA-5 is approximately normal to the NNW-SSE vector of relative Africa-Iberia motion since about 15Ma (e.g. Sanz de Galdeano and Alfaro, 2004; Galindo-Zaldívar et al., 2015; Martínez-Martos et al., 2017) and therefore allow to extend the proposed correlation of FIA trends with plate motions forward.

5.6.3. Assessment of the Ragua-Calar Alto contact

As mentioned above, Martínez-Martínez et al. (2002) proposed a new tectonic contact within the original Veleta complex (Fig. 5.10a) and correlated the rocks below and above it with the Ragua- and Calar-Alto units, respectively. The latter had been previously defined by García-Dueñas et al. (1988) in the Sierra de los Filabres. They interpret the Veleta-Mulhacen boundary stratigraphic and thus include the Caldera unit in the Calar-Alto unit. In the Sierra de los Filabres, the Ragua-Calar Alto boundary is considered to be a several 100 m wide ductile thrust zone, the Dos Picos shear zone (García-Dueñas et al., 1988; González-Casado et al., 1995; Martínez-Martínez, 2007). In the western Sierra Nevada, though, the contact between these units is interpreted as a younger extensional

detachment (Filabres detachment). Towards the east the Filabres detachment is inferred to cut up through the stratigraphy until joining the NFAD in central sectors of the Nevado-Filabride tectonic window (Martínez-Martínez et al., 2002). This geometry implies strong thinning of the Mulhacen nappe both from the west and east towards this central area (Fig. 5.10a). By contrast, the tectonic contacts of Puga et al. (2002) (Fig. 5.10b) or a lack of internal contacts (Gómez-Pugnaire et al., 2012) (Fig. 5.1) implies only progressive westward thinning caused by the NFAD alone.

In the western Sierra Nevada, the Ragua unit is mapped as several tectonic windows controlled by interference of open E-W and NNE-SSW trending folds (Martínez-Martínez et al., 2002). These would fall under the D_5 structures here. The largest of these windows is partially included in our study area (Fig. 5.2). The stated recognition criteria for the contact included: (i) decimetric to metric bands of fault rocks with NE-SW trending striations, (ii) shear bands and extensional crenulation cleavage indicating top-to-the west shear sense (Martínez-Martínez et al., 2002), and (iii) different dip angles of the main foliation in its footwall and hanging wall, interpreted as a hanging-wall ramp / footwall flat geometry (Martínez-Martínez, 2007; his Fig. 3). However, our field data do not corroborate these criteria in the study area, and raise problems regarding its map trace. On the northern slope of the Genil valley, the contact has been placed at top of a ca. 20 m thick quartzite layer that contains a penetrative intersection lineation that can be easily mistaken in the field for a stretching lineation (Fig. 5.7d). We did not find brittle fault rocks or mylonites in the vicinity of the map trace of the contact. Shear bands occur throughout most of our study area but do not particularly intensify towards the map trace, but rather near the original Veleta-Mulhacen boundary of Puga et al. (2002). Moreover, shear bands predominantly show a top-to-SE shear in the dark schists, and show inconsistent apparent shear-senses as have also been reported in other terrains (e.g. Ham and Bell, 2004; Mukherjee and Koyi, 2010; Mukherjee, 2013b) (Fig. 5.2). Finally, our orientation data do not confirm different dip angles of the main foliation above and below the contact, but suggest a similar ca. 35° dip towards NW.

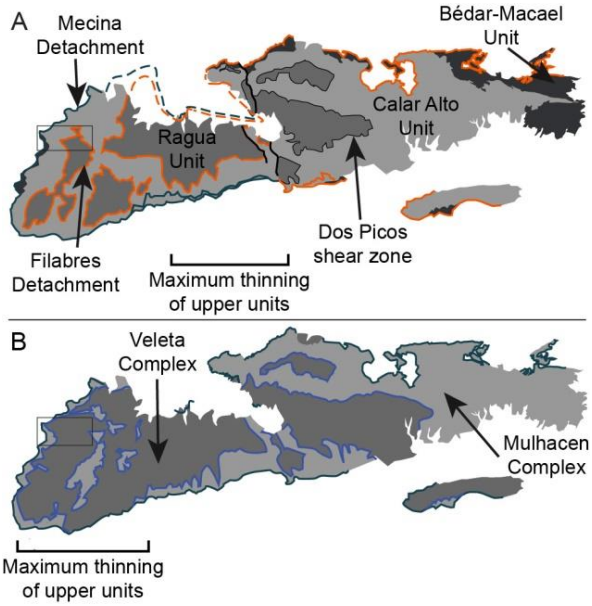

Fig. 5.10. Tectonic subdivision of the NFC proposed by a Martínez-Martínez et al. (2002) and b Puga et al. (2002). Location of maximum thinning of upper units is different in both proposals. Note that tectonic contacts in these maps do not coincide with the lithological boundaries in Fig. 5.1. Boxes show the location of Fig. 5.2.

The map trace of the contact combined with a rugged topography in the study area allowed us to model the orientation of the contact along its map trace. We performed this analysis with the aid of the SK2 Excel macro of Blenkinsop (2012), which allows 3D

visualization of virtual planes as well as their intersection with the topography in Google Earth (Fig. 5.11a). The plane orientations that best reproduce the contact´s trace (Figs. 5.11a, b) define an open antiform trending NNE-SSW with fold-limb dips of not > 15° on both sides. The main foliation above and below the contact dips generally steeper between 30 to 50° (Fig. 5.11b) implying a cross-cutting contact. On the northern slope of the Genil valley the contact's trace is sub-parallel to the cleavage trace due to similar apparent dip angles, but on the southern valley slope and east of San Juan stream, foliation traces run perpendicular to the supposed detachment and evidence the cross-cutting nature of the contact, incompatible with a footwall flat. Similar cross-cutting arises north of Vadillo River, at 2400 m altitude, where the foliation continues dipping NW in spite of having crossed the axial trace of the open antiform. Only several km further east does the foliation gradually changes its strike towards WNW-ESE.

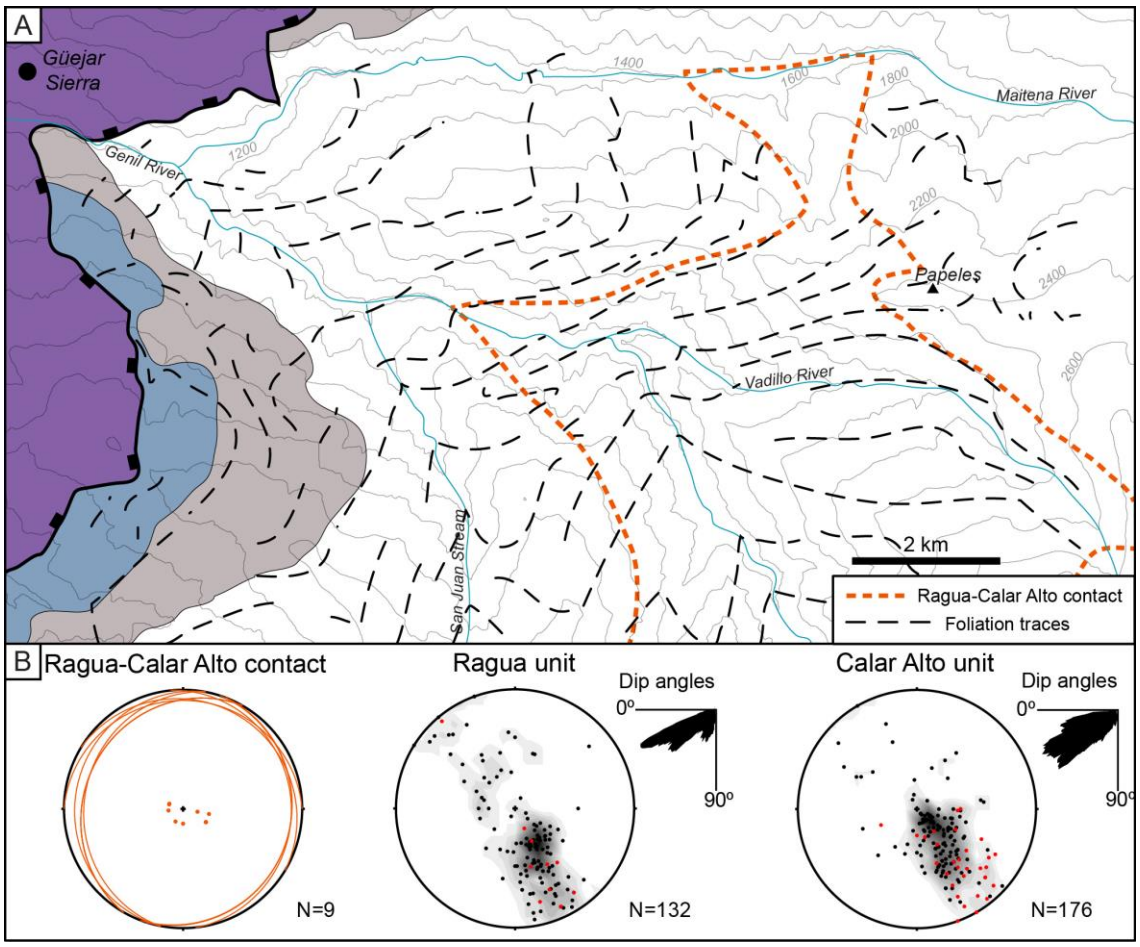

Fig. 5.11. a Foliation traces map showing oblique relationships between the Ragua-Calar Alto contact and the foliation trace in several areas. b Simulated planes which would reproduce the contact trace (orange dots and great circles) and foliation poles for the Ragua and Calar Alto units (black dots for main schistosity; red dots for crenulation cleavages).

Thus, the mapped trace of the contact implies a late sub-horizontal contact that sharply cuts steeper dipping foliations that are a mixture of S_2 and S_3. Such a contact should be easily detectable in the field, but since we did not find any evidence for it in the field we suggest it does not exist in the study area.

5.6.4. Assessment of the Mulhacen-Veleta contact

The Veleta-Mulhacen contact in westernmost Sierra Nevada coincides with the lithological contact between graphite rich dark schists containing small garnets and light schists containing larger sized garnets (Figs. 5.2, 5.10b). The Mulhacen complex also includes graphite schists, which are differentiated from those belonging to Veleta complex based on differences in metamorphic mineral content (Puga, 1976; Puga et al., 2002). The fact that structural data from the Mulhacen complex are much more variable as those in the Veleta complex suggests a more complex fold structure in the former that might support a contact between both nappes. In addition, the trace of the contact roughly follows the main foliation in its hanging wall, but appears to locally cut the foliation in its footwall (Fig. 5.11a). We also highlighted the upwards intensification of S_4 towards the Nevado-Filabride—Alpujarride contact which could be associated with major displacements accommodated by this zone. Thus, various indirect indications exist in favour of the contact, although no definitive ones. Further investigation in adjacent areas of the complex will help clarify this question in the future.

5.6.5. Core complex models

We have shown that the main cleavage in outcrop is not everywhere the same foliation, contrary to what would be expected if the NFC is an extensional metamorphic core complex. The very large westward displacement of the Alpujarride Complex over the NFC implied by such a model (Martínez-Martínez et al., 2002) is questionable considering the lack of a westward metamorphic gradient. Such a model does neither account for the polyphase structure and large dispersion of linear structural indicators in the NFC (Aerden et al., 2013, their Fig. 3). Detailed analysis of these structures and porphyroblast inclusion trails indicates a far more complex kinematic evolution involving bulk crustal shortening in different directions alternating with transitory stages of gravitational collapse (Aerden and Sayab, 2008; Aerden et al., 2013). Of these, the Miocene crustal extension was probably the latest and strongest phase of gravitational collapse followed by renewed contraction since the Late Miocene (Sanz de Galdeano and Alfaro, 2004; Galindo-Zaldívar et al., 2015; Martínez-Martos et al., 2017).

Acknowledgements

We thank Soumyajit Mukherjee for his review and editorial guidance, which greatly helped clarify the manuscript. We also thank Ángel Perandrés Villegas for excellent quality thin-sections he made for this study. The research was funded by grants from the Spanish government (CGL2016-80687-R AEI/FEDER) and regional government of Andalusia (RNM148).

References

Aerden, D.G.A.M., 1998. Tectonic evolution of the Montagne Noire and a possible orogenic model for syncollisional exhumation of deep rocks, Variscan belt, France. Tectonics 17, 62-79.

Aerden, D.G.A.M., 2003. Preferred orientation of planar microstructures determined via statistical best-fit of measured intersection-lines: the “FitPitch” computer program. J. Struct. Geol. 25, 923-934.

Aerden, D.G.A.M., 2004. Correlating deformation in Variscan NW-Iberia using porphyroblasts: implications for the Ibero-Armorican Arc. J. Struct. Geol. 26, 177-196.

Aerden, D.G.A.M., Sayab, M., 2008. From Adria- to Africa-driven orogenesis: evidence from porphyroblasts in the Betic Cordillera, Spain. J. Struct. Geol. 30, 1272–1287.

Aerden, D.G.A.M., Bell, T.H., Puga, E., Sayab, M., Lozano, J.A., Díaz de Federico, A., 2013. Multi-stage mountain building vs. Relative plate motions in the Betic Cordillera deduced from integrated microstructural and petrological analysis of porphyroblast inclusion trails. Tectonophysics 587, 188-206.

Aldaya, F., Campos, J., García-Dueñas, V., González-Lodeiro, F., Orozco, M., 1984. El contacto Alpujárrides/Nevado-Filábrides en la vertiente Meridional de Sierra Nevada. Implicaciones Tectónicas. In: El Borde mediterráneo español: evolución del orógeno bético y geodinámica de las depresiones Neógenas, Granada, pp 18-20.

Augier, R., Jolivet, L., Robin, C., 2005. Late Orogenic doming in the eastern Betic Cordilleras: Final exhumation of the Nevado-Filabride complex and its relation to basin genesis. Tectonics 24, TC4003. https://doi.org/10.1029/2004TC001687

Bell, T.H., 1985. Deformation partitioning and porphyroblast rotation in metamorphic rocks: a radical interpretation. J. Metamorph. Geol. 3, 109-118.

Bell, T.H., Johnson, S.E., 1989. Porphyroblast inclusion trails: the key to orogenesis. J. Metamorph. Geol. 7, 279-310.

Bell, T.H., Sapkota, J., 2012. Episodic gravitational collapse and migration of the mountain chain during orogenic roll-on in the Himalayas. J. Metamorph. Geol. 30, 651-666.

Bell, T.H., Forde, A., Wang, J., 1995. A new indicator of movement direction during orogenesis: measurement technique and application to the Alps. Terra Nova 7, 500-508.

Bishop, D.G., 1972. Transposition structures associated with cleavage formation in the Otago schists. N.Z. J. Geol. Geophys. 15, 360-371.

Blenkinsop, T.G., 2012. Visualizing structural geology: From Excel to Google Earth. Comput. Geosci. 45, 52-56.

Booth-Rea, G., Martínez-Martínez, J.M., Giaconia, F., 2015. Continental subduction, intracrustal shortening, and coeval upper-crustal extension: P-T evolution of subducted south Iberian paleomargin metapelites (Betics, SE Spain). Tectonophysics 663, 122-139.

Carreras, J., Cosgrove, J.W., Druguet, E., 2013. Strain partitioning in banded and/or anisotropic rocks: Implications for inferring tectonic regimes. J. Struct. Geol. 50, 7-21.

Comas, M.C., García-Dueñas, V., Jurado, M.J., 1992. Neogene Tectonic Evolution of the Alboran Sea from MCS Data. Geo. Mar. Lett. 12, 157-164.

Cuevas, J., Navarro-Vilá, F., Tubía, J.M., 2001. Evolución estructural poliorogénica del Complejo Maláguide (Cordilleras Béticas). Boletín Geológico y Minero 112, 47-58.

De Jong, K., 1993. Redefinition of the deformation scheme of the Mulhacen Complex and implications for the relative timing of the overthrusting of the Alpujarride Complex in the Betic Zone (SE Spain). Geol Mijnbouw 71, 317-326.

Díaz de Federico, A., Puga, E., Burgos, J., Gallegos, J.A., Sanz de Galdeano, C., 1978. Mapa geológico de la Hoja nº 1027 (Güejar Sierra).Mapa Geológico de España E. 1:50.000. Segunda Serie (MAGNA), Primera edición. IGME.

Dirks, P.H.G.M., Zhang, J.S., Passchier, C.W., 1997. Exhumation of high-pressure granulites and the role of lower crustal advection in the North China Craton near Datong. J. Struct. Geol. 19, 1343-1358.

Fallot, P., Solé-Sabaris, L., Lemoine, M., 1954. Observations sur le Trias bétique et ses algues calcaires. Mem. Com. Inst. Geol. Prov. Barcelona 2, 23-60.

Fossen, H., 2016. Structural Geology. Cambridge University Press, Cambridge.

Galindo-Zaldívar, J., 1993. Geometría de las Deformaciones Neógenas en Sierra Nevada (Cordilleras Béticas). PhD Thesis, Universidad de Granada.

Galindo-Zaldívar, J., Gil, A.J., Sanz de Galdeano, C., Lacy, M.C., García-Armenteros, J.A., Ruano, P., Ruiz, A.M., Martínez-Martos, M., Alfaro, P., 2015. Active shallow extension in central and eastern Betic Cordillera from CGPS data. Tectonophysics 663, 290-301.

García-Dueñas, V., Martínez-Martínez, J.M., Orozco, M., Soto, J.I., 1988. Plis-nappes, cisaillements syn- à post-métamorphiques et cisaillements ductiles-fragiles en distension dans les Nevado-Filabrides (Cordillères bétiques, Espagne). Comptes Rendus de l'Académie des Sciences de Paris 307 (Série II), 1389-1395.

Gómez-Pugnaire, M.T., Fernández-Soler, J.M., 1987. High-pressure metamorphism in metabasites from the Betic Cordilleras (S.E. Spain) and its evolution during the Alpine orogeny. Contrib. Mineral. Petrol. 95, 231-244.

Gómez-Pugnaire, M.T., Chacón, J., Mitrofanov, F., Timofeev, V., 1982. First report on pre-Cambrian rocks in the graphite-bearing series of the Nevado-Filábride Complex (Betic Cordilleras, Spain). Neues Jahrbuch für Geologie und Palaeontologie Monatshefte 3, 176-180.

Gómez-Pugnaire, M.T., Galindo-Zaldívar, J., Rubatto, D., González-Lodeiro, F., López-Sánchez-Vizcaíno, V., Jabaloy, A., 2004. A reinterpretation of the Nevado-Filabride and Alpujárride Complexes (Betic Cordillera): field, petrography and U-Pb ages from orthogneisses (western Sierra Nevada, S Spain). Schweiz Mineral Petrog Mitt 84, 303-322.

Gómez-Pugnaire, M.T., Rubatto, D., Fernández-Soler, J.M., Jabaloy-Sanchez, A., López-Sánchez-Vizcaino, V., Gonzalez-Lodeiro, F., Galindo-Zaldivar, J., Padron-Navarta, J.A. 2012. Late Variscan magmatism in the Nevado–Filabride Complex: U-Pb geochronologic evidence for the pre-Mesozoic nature of the deepest Betic complex (SE Spain). Lithos 146, 93-111.

González-Casado, J.M., Casquet, C., Martínez-Martínez, J.M., García-Dueñas, V., 1995. Retrograde evolution of quartz segregations from the Dos Picos shear zone in the Nevado-

Filábride Complex (Betic chains, Spain). Evidence from fluid inclusions and quartz c-axis fabrics. Geol. Rundsch. 84, 175-186.

Ham, A.P., Bell, T.H., 2004. Recycling of foliations during folding. J. Struct. Geol. 26, 1989-2009.

Hebeda, E.H., Boelrijk, N.A.I.M., Priem, H.N.A., Verdurmen, E.A.T., Verschure, R.H., Simon, O.J., 1980. Excess radiogenic Ar and undisturbed Rb-Sr systems in basic intrusives subjected to Alpine metamorphism in southeastern Spain. Earth Planet. Sci. Lett. 47, 81-90.

Jabaloy, A., Galindo-Zaldívar, J., González-Lodeiro, F., 1993. The Alpujárride–Nevado–Filábride extensional shear zone, Betic Cordillera, SE Spain. J. Struct. Geol. 15, 555–569.

Jabaloy-Sánchez, A., Gómez-Pugnaire, M.T., Padrón-Navarta, J.A., López Sánchez-Vizcaíno, V., Garrido, C.J., 2015. Subduction- and exhumation-related structures preserved in metaserpentinites and associated metasediments from the Nevado-Filábride Complex (Betic Cordillera, SE Spain). Tectonophysics 644-645, 40-57.

Johnson, C., Harbury, N., Hurford, A.J., 1997. The role of extension in the Miocene denudation of the Nevado-Filábride Complex, Betic Cordillera (SE Spain). Tectonics 16, 189-204.

Kirchner, K.L., Behr, W.M., Loewy, S., Stockli, D.F., 2016. Early Miocene subduction in the western Mediterranean: Constraints from Rb-Sr multimineral isochron geochronology. Geochem. Geophys. Geosyst. 17, 1842-1860.

Laborda-López, C., Aguirre, J., Donovan, S.K., 2015. Surviving metamorphism: taphonomy of fossil assemblages in marble and calc-silicate schist. Palaios 30, 668-679.

Lafuste, M.L.J., Pavillon, M.J., 1976. Mise en evidence d'Eifélien daté au sein des terrains métamorphiques des zones internes des Cordillères bétiques. Intérêt de ce nouveau repére stratigraphique. Comptes Rendus de l'Académie des Sciences de Paris, Série II 283, 1015-1018.

Lagoeiro, L., Hippertt, J., Lana, C., 2003. Deformation partitioning during folding and transposition of quartz layers. Tectonophysics 361, 171-186.

López-Sánchez-Vizcaíno, V., Rubatto, D., Gómez-Pugnaire, M.T., Trommsdorff, V., Müntener, O., 2001. Middle Miocene high-pressure metamorphism and fast exhumation of the Nevado–Filábride complex, SE Spain. Terra Nova 13, 327–332.

Martínez-Martínez, J.M., 2007. Coexistencia de zonas de cizalla dúctil de extensión y de acortamiento en el domo de Sierra Nevada, Béticas (SE de España). Rev. Soc. Geol. Esp. 20, 229–245.

Martínez-Martínez, J.M., Soto, J.I., Balanyá, J.C., 2002. Orthogonal folding of extensional detachments: structure and origin of the Sierra Nevada elongated dome (Betics, SE Spain). Tectonics 21 http://dx.doi.org/10.1029/2001TC001283.

Martínez-Martos, M., Galindo-Zaldívar, J., Martínez-Moreno, F.J., Calvo-Rayo, R., Sanz de Galdeano, C., 2017. Superposition of tectonic structures leading elongated intramontane basin: the Alhabia basin (Internal Zones, Betic Cordillera). Int. J. Earth Sci. 106, 2461-2471.

Mukherjee, S., 2013a. Channel flow extrusion model to constrain dynamic viscosity and Prandtl number of the Higher Himalayan Shear Zone. Int. J. Earth Sci. 102, 1811-1835.

Mukherjee, S., 2013b. Deformation Microstructures in Rocks. Springer Geochemistry/Mineralogy, Berlin.

Mukherjee, S., Koyi, H.A., 2010. Higher Himalayan Shear Zone, Zanskar Indian Himalaya: microstructural studies and extrusion mechanism by a combination of simple shear and channel flow. Int. J. Earth Sci. 99, 1083-1110.

Platt, J.P., Behrmann, J.H., 1986. Structures and fabrics in a crustal-scale shear zone, Betic Cordillera, SE Spain. J. Struct. Geol. 8, 15-33.

Platt, J.P., Vissers, R.L.M., 1980. Extensional structures in anisotropic rocks. J. Struct. Geol. 2, 397-410.

Platt, J.P., Vissers, R.L.M., 1989. Extensional collapse of thickened continental lithosphere: A working hypothesis for the Alboran Sea and Gibraltar Arc. Geology 5, 540-543.

Platt, J.P., Anczkiewicz, R., Soto, J.I., Kelley, S.P., Thirlwall, M., 2006. Early Miocene continental subduction and rapid exhumation in the western Mediterranean. Geology 34, 981–984.

Platt, J.P., Argles, T.W., Carter, A., Kelley, S.P., Whitehouse, M.J., Lonergan, L., 2003. Exhumation of the Ronda peridotite and its crustal envelope: constraints from thermal modelling a PT-time array. J. Geol. Soc. Lond. 160, 655-677.

Platt, J.P., Behr, W.M., Johanesen, K., Williams, J.R., 2013. The Betic-Rif Arc and Its Orogenic Hinterland: A Review. Annu. Rev. Earth. Planet. Sci. 41, 313-357.

Platt, J.P., Van der Eeckhout, B., Janzen, E., Konert, G., Simon, O.J., Weijermars, R., 1983. The structure and tectonic evolution of the Aguilón foldnappe, Sierra Alhamilla, Betic Cordilleras, SE Spain. J. Struct. Geol. 5, 519-535.

Puga, E., 1976. Investigaciones petrológicas en Sierra Nevada Occidental. PhD Thesis, Universidad de Granada.

Puga, E., Díaz de Federico, A., Fanning, M., Nieto, J.M., Rodríguez Martínez-Conde, J.A., Díaz Puga, M.A., Lozano, J.A., Bianchini, G., Natali, C., Beccaluva, L., 2017. The Betic Ophiolites and the Mesozoic Evolution of the Western Tethys. Geosciences 7, 31 doi:10.3390/geosciences7020031.

Puga, E., Díaz de Federico, A., Nieto, J.M., 2002. Tectonostratigraphic subdivision and petrological characterisation of the deepest complexes of the Betic zone: a review. Geodin, Acta 15, 23-43.

Puga, E., Fanning, M., Díaz de Federico, A., Nieto, J.M., Beccaluva, L., Bianchini, G., Díaz Puga, M.A., 2011. Petrology, geochemistry and U-Pb geochronology of the Betic Ophiolites: Inferences for Pangaea break-up and birth of the westernmost Tethys Ocean. Lithos 124, 255-272.

Puga, E., Fanning, C.M., Nieto, J.M., Díaz de Federico, A., 2005. Recrystallization textures in zircón generated by ocean-floor and eclogite-facies metamorphism: a cathodoluminiscence and U-Pb SHRIMP study with constraints from REE elements. Canadian Mineralogist 43, 183-202.

Sanz de Galdeano, C., Alfaro, P., 2004. Tectonic significance of the present relief of the Betic Cordillera. Geomorphology 63, 175-190.

Sanz de Galdeano, C., López-Garrido, A.C., 2016. The nevado-filabride complex in the western part of Sierra de los Filabres (Betic Internal Zone), structure and lithologic succession. Boletín Geológico y Minero, 127 (4), 823-836.

Sanz de Galdeano, C., López-Garrido, A.C., Santamaría-López, A., 2016. Major scale structure of the marbles situated between Cóbdar and Macael (Nevado-Filábride Complex, Betic Cordillera, Almería province Spain), and general stratigraphic arrangement. Rev. Soc. Geol. Esp. 29 (2), 107-116.

Sayab, M., Shah, S.Z., Aerden, D., 2016. Metamorphic record of the NW Himalayan orogeny between the Indian plate-Kohistan Ladakh Arc and Asia: Revelations from foliation intersection axis (FIA) controlled P-T-t-d paths. Tectonophysics 671, 110-126.

Shah, S.Z., Sayab, M., Aerden, D., Asif Khan, M., 2011. Foliation intersection axes preserved in garnet porphyroblasts from the Swat area, NW Himalaya: A record of successive crustal shortening directions between the Indian plate and Kohistan-Ladakh Island Arc. Tectonophysics 509, 14-32.

Soto, J.I., 1991. Estructura y evolución metamórfica del complejo Nevado-Filábride en la terminación oriental de la Sierra de los Filabres (Cordilleras Béticas). PhD Thesis, Universidad de Granada.

Soto, J.I., García-Dueñas, V., Martínez-Martínez, J.M., 1990. Valor de la deformación dúctil asimétrica en el ortogneis de Lubrín (Manto de Bédar-Macael, Complejo Nevado-Filábride, Béticas). Geogaceta 7, 92-94.

Ulrich, S., Konopásek, J., Jerábek, P., Tajcmanová, L., 2011. Transposition of structures in the Neoproterozoic Kaoko Belt (NW Namibia) and their absolute timing. Int. J. Earth Sci. 100, 415-429.

Vázquez, M., Jabaloy, A., Barbero, L., Stuart, F.M., 2011. Deciphering tectonic- and erosion driven exhumation of the Nevado–Filábride Complex (Betic Cordillera, Southern Spain) by low temperature thermochronology. Terra Nova 23, 257-263. http://dx.doi.org/10.1111/j.1365-3121.2011.01007.x.

Vissers, R.L.M., 1981. A structural study of the central Sierra de los Filabres (Betic Zone, SE Spain), with emphasis on deformational processes and their relation to the alpine metamorphism. PhD Thesis, University of Amsterdam.

Webber, C.E., Little, T., Newman, J., Tikoff, B., 2008. Fabric superposition in upper mantle peridotite, Red Hills, New Zealand. J. Struct. Geol. 30, 1412-1428.

6. Structural analysis along four transects through the Nevado-Filábride Complex and implications for its internal structure

Alejandro Ruiz-Fuentes[1]

[1] *Departamento de Geodinámica, Universidad de Granada, Av. Fuentenueva, 18071, Granada, Spain*

Manuscript in preparation

Abstract

Structural analysis has been performed along four regional-scale transects through the Nevado-Filábride Complex. Three main fold-generations have been recognized along these sections associated with 3 cleavages, which postdate an earlier deformation history recorded by porphyroblast inclusion trails. The principle cleavage in the complex (S_2) is locally folded and crenulated with upright axial planes (D_3). These structures are in turn deformed in gently-dipping or subhorizontal high-strain zones (D_4) associated with the Nevado-Filábride/Alpujárride contact but also present at deeper structural levels coinciding in part with earlier proposed tectonic contacts. An early origin of internal contacts as thrusts is proposed followed by modification of these contacts by D_4 shear zones.

Keywords: Nevado Filábride Complex, Betic Cordillera, Alpine orogeny, Overprinted foliations

6.1. Introduction

Reconstructing the tectonic evolution of mountain belts requires integration of multidisciplinary data in a plate-tectonic framework. Accurate descriptions of the structure and microstructure of metamorphic rocks in the cores of orogens is a prerequisite for correct interpretation of petrological, geochemical and geophysical data. Within the Betic Cordillera of southern Spain, the Nevado-Filábride Complex occupies the deepest outcropping structural levels and records a complicated polyphase deformation history. Several competing tectono-metamorphic models have been proposed for the complex mainly based on petrological and geochronological data (e.g. Puga et al., 2000; López Sánchez-Vizcaíno et al., 2001; Platt et al., 2006; Booth-Rea et al., 2015; Kirchner et al., 2016; Li and Massonne, 2018; Porkoláb et al., 2022) but assuming highly simplified and idealized kinematics. The internal subdivision of the complex also continues to be a fundamental question after several decades (e.g. Kampschuur, 1975; Linthout and Vissers, 1979; de Jong and Bakker, 1991; de Jong, 1993a; Jabaloy et al., 1993; Gómez-Pugnaire et al., 2000, 2012; Martínez-Martínez et al., 2002; Augier et al., 2005c; Aerden and Sayab, 2008; Zevenhuizen, 2022). In order to further assess the presence and geometry of proposed tectonic contacts, structural analysis has been undertaken along four transects through western and central areas of the main Nevado-Filábride tectonic window. Two generations of late- metamorphic folds and associated fabrics have been recognized (D_3 and D_4) that formed during exhumation and represent the latest stages of ductile deformation. Several D_4 high-strain zones are identified transposing older structures. Their coincidence with contacts proposed by earlier workers supports the existence of these contacts.

6.2. Geological setting

6.2.1. The Betic Cordillera

The Betic-Rif orogenic system of southern Spain and northern Morocco (Fig. 6.1) constitutes the western extremity of the Alpine Mediterranean chains. It formed as a consequence of subduction and continental collision driven by Africa-Iberia convergence and west-directed emplacement of allochthonous units during Paleogene and Neogene times onto the Iberian margin. The Betic Cordillera is classically subdivided in three domains: i) the External Zones, mainly composed of Mesozoic sedimentary rocks deformed into a fold-and-thrust belt, which represents the former South Iberian paleomargin; ii) the Flysch Complex, made up of more distal basinal deposits; iii) the Internal Zones composed of three stacked metamorphic complexes, named Nevado-Filábride, Alpujárride and Maláguide from bottom to top. The two upper complexes are allochthonous units and were originally located east or northeast of their current position (Bouillin et al., 1986; Guerrera et al., 1993, 2021), and at least the lower part of the Nevado-Filábrides is usually considered to represent a portion of South Iberian crust (Guerrera et al., 1993; Platt et al., 2006; Puga et al., 2011; Gómez-Pugnaire et al., 2012;

Rodríguez-Cañero et al., 2018) subducted under the Alpujárride and Maláguide complexes.

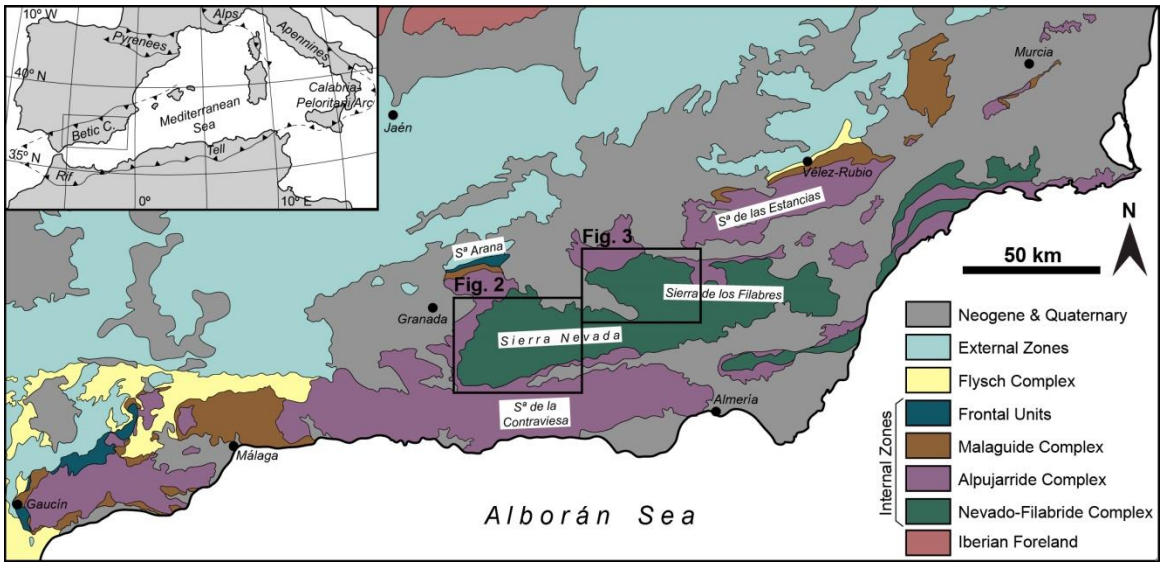

Fig. 6.1. Geological map of the Internal Zones of the Betic Cordillera (modified from Ruiz-Fuentes and Aerden, 2023). Squares indicate the areas encompassed by maps of Figs. 6.2 and 6.3.

The Alpujárride Complex experienced high pressure metamorphism in the Paleogene (Tubía and Gil-Ibarguchi, 1991; Azañón and Goffé, 1997; Platt et al., 2005; Bessière et al., 2022) related to the emplacement of the overlying Maláguide Complex. Continental collision between the Internal allochthonous units and the External Zones occurred during the late Burdigalian (Martín-Algarra, 1987; Martín-Martín et al., 1996) leading to destruction of the Flysch basin and development of the external fold-and-thrust belt. Retro-vergent structures associated to the continental collision appear along the Internal-External Zones Boundary (IEZB) from the western to the eastern part of the cordillera (e.g. Martín-Algarra, 1987; Balanyá, 1991; Lonergan et al., 1994; Sanz de Galdeano et al., 1995; Fernández-Fernández et al., 2007; Ruiz-Fuentes et al., 2022). The Nevado-Filábride Complex experienced early blueschist- to eclogite-facies metamorphism followed by decompression and reequilibration in the greenschist- to amphibolite facies, but P-T-t trajectories vary considerably in detail among authors. Metamorphic ages range from Eocene to Middle-Miocene (Augier et al., 2005a; Platt et al., 2006; Kirchner et al., 2016; Aerden et al., 2022; Porkoláb et al., 2022; Poulaki et al., 2023).

6.2.2. Lithological succession and internal structure of the Nevado Filábride Complex

The Nevado-Filábride Complex is composed of Paleozoic (e.g. Laborda-López et al., 2015; Rodríguez-Cañero et al., 2018) graphite schists and quartzites locally intercalated with graphitic marbles, overlain by a Permo-Mesozoic (Tendero et al., 1993; Jabaloy-Sánchez et al., 2018; Poulaki and Stockli, 2022) sequence of quartzites, light coloured schists, calcschists, meta-evaporites and marbles. Paleozoic gneisses (e.g. Gómez-Pugnaire et al., 2004, 2012; Martínez-Martínez et al., 2010), serpentinite lenses and

Jurassic mafic rocks (Puga et al., 2011) appear intercalated along the whole sequence and especially towards the upper part of the complex.

Different map interpretations have been presented dividing the complex in several tectonic subunits (Puga et al., 1974, 2002; García-Dueñas et al., 1988a; Martínez-Martínez et al., 1995, 2002; Poulaki et al., 2023) or considering the whole complex as a single unit (Galindo-Zaldivar et al., 1989; Jabaloy et al., 1993; Gómez-Pugnaire et al., 2004, 2012; Sanz de Galdeano and López-Garrido, 2016; Santamaría-López and Sanz de Galdeano, 2018; Santamaría-López et al., 2019). The maps of Figs. 6.2 and 6.3, depict the subdivision of Puga et al. (2002) and the boundary between the Ragua and Calar Alto units of Martínez-Martínez et al. (2002). Following early works (e.g. Brouwer, 1926; Fallot et al., 1961), Puga et al. (1974, 2002) distinguished a lower Veleta- and upper Mulhacén nappes/complexes in the Sierra Nevada range, which occupies the western portion of the ca. 100 km long Nevado-Filábride tectonic window (Fig. 6.1). The Veleta complex is composed of a thick sequence of graphite schists and quartzites. The Mulhacén complex comprises similar graphite schists which can contain pre-Alpine cm- to dm-sized relic pseudomorphed porphyroblasts (Puga et al., 1975) overlain by a Permo-Mesozoic cover sequence. Puga et al., (1974, 1996, 2002) divided the Mulhacén complex further into the Caldera, Ophiolitic and Sabinas units in ascending order, each unit being separated by the Soportújar Fm., interpreted by them as an intra-orogenic formation, but mostly considered of tectonic/cataclastic origin associated with detachments by later workers. Martínez-Martínez et al. (2002), presented a map showing the Veleta-Mulhacén contact at a much deeper structural level within the original Veleta nappe, and consequently renamed this nappe as Ragua unit.

The main foliation observed in outcrop in the Nevado-Filábride (usually called S_2) is associated with tight to isoclinal (F_2) folds. Relics of a previous fabric (S_1) are locally visible in outcrop. S_2 is affected by at least two crenulation cleavages that developed during late-metamorphic stages at relatively low pressure (Bakker et al. 1989; González-Casado et al., 1995; Augier et al., 2005a; Behr and Platt, 2012; Booth-Rea et al., 2015; Jabaloy-Sánchez et al., 2015). Note, however, that not all cited works differentiate the two crenulation cleavages. Shear bands or S-C structures are also common and appear concentrated near the Nevado-Filábride-Alpujárride detachment and other late shear zones within the Nevado-Filábride. They are affected by late upright folds created during compression since the late-Tortonian that controls much of the current topography of anticlinal sierras and synclinal basins.

Some authors envisage a progressive upward increase of strain in the Nevado-Filábride Complex towards the contact with the Alpujárride Complex (Galindo-Zaldivar et al., 1989; Jabaloy et al., 1993), whereas others interpret multiple strain gradients also associated with internal tectonic contacts (García-Dueñas et al., 1988a; Martínez-Martínez et al., 1995, 2002; Augier et al., 2005c; Martínez-Martínez, 2007; Behr and Platt, 2012; Booth-Rea et al., 2015). Ruiz-Fuentes and Aerden (2018) showed that strain associated with two sets of crenulation cleavage (their S_3 and S_4) is heterogeneous and locally causes transposition of S_2. Inclusion-trails of garnet porphyroblasts in the complex

record a polyphase deformation history that probably took place from Eocene to middle Miocene times (Aerden et al., 2013, 2022).

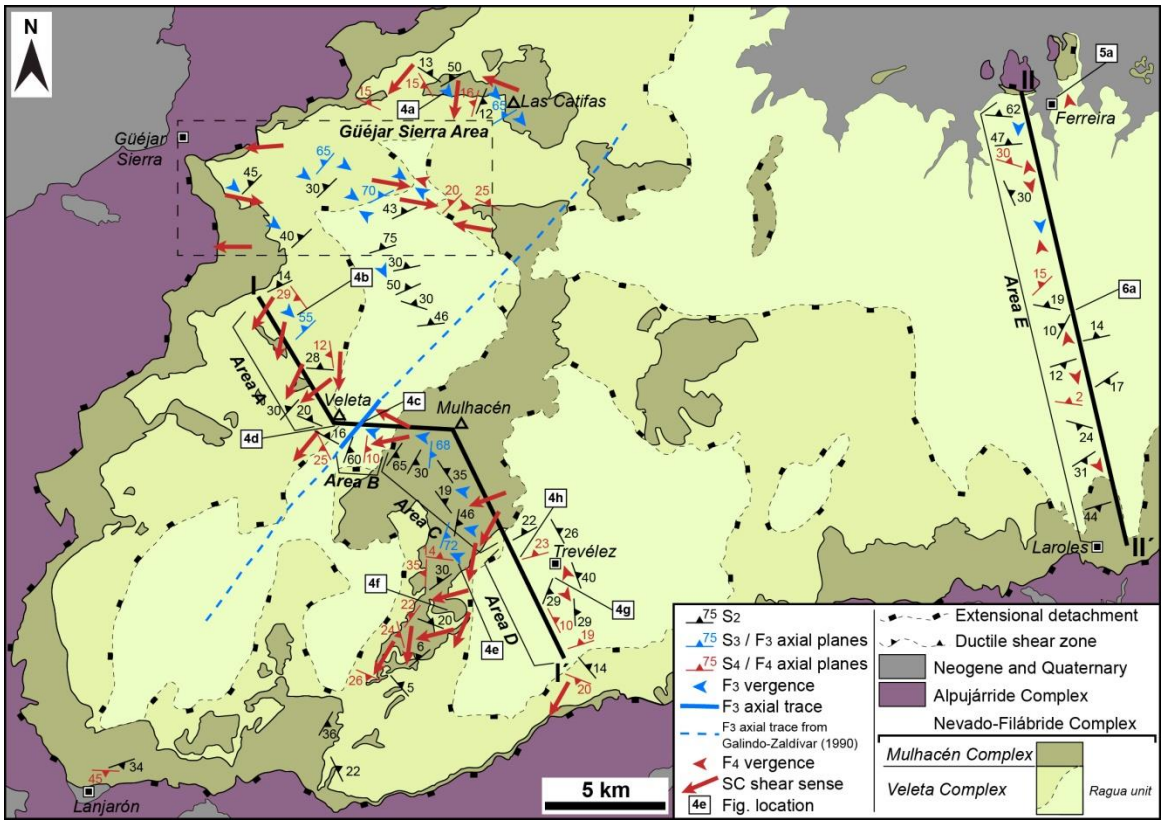

Fig. 6.2. Geological map of the western and central Sierra Nevada. The map shows the original Veleta-Mulhacén subdivision (Puga et al., 2002). The contact between the Ragua and Calar Alto units (Martínez-Martínez et al., 2002) is also shown. The upper part of Veleta and the Mulhacén complex are included in the Calar Alto and Bédar-Macael units of Martínez-Martínez et al. (2002). Locations of images of Figs. 6.4 and 6.5 and cross sections of Fig. 6.7 are indicated.

6.3. Structural analysis

The main regional foliation (S_2) is affected by at least two deformation phases with contrasting orientations called D_3 and D_4 (Figs. 6.4, 6.5 and 6.6). Both deformations generated crenulation cleavage that locally transpose S_2 and then become the main cleavage in outcrop. This implies that the main foliation in one outcrop cannot be automatically assumed to be the same generation as the main foliation in another outcrop. D_3 created upright folds with S_3 crenulation cleavage, whereas D_4 is associated with folds with subhorizontal axial planes and S_4 crenulation cleavage. Overprinting relationships between D_3 and D_4 structures can be directly observed in some outcrops (Fig. 6.4a) (see also Ruiz-Fuentes and Aerden, 2018). S_4 probably formed coeval with S-C structures as they are spatially linked and have similar flat-lying orientations (Fig. 6.6 and 6.7). Moreover, S-C structures indicating opposite shear senses are relatively common and suggest a major component of sub-vertical shortening. Therefore, it seems that the only difference between S_4 and S-C structures is the average angle between spaced shear bands or cleavage planes and a pre-existing cleavage, as a function of the initial orientation of

the latter and the intensity of D_4 strain. Note that this view is consistent with models envisaging a component of shearing parallel to crenulation-cleavage planes (e.g. Tanner, 2016) as opposed to shortening and volume loss only (e.g. Gray and Durney, 1979). The geometry and distribution of these structures was studied in detail along four cross sections, two in the western-central Sierra Nevada and two in the Sierra de los Filabres.

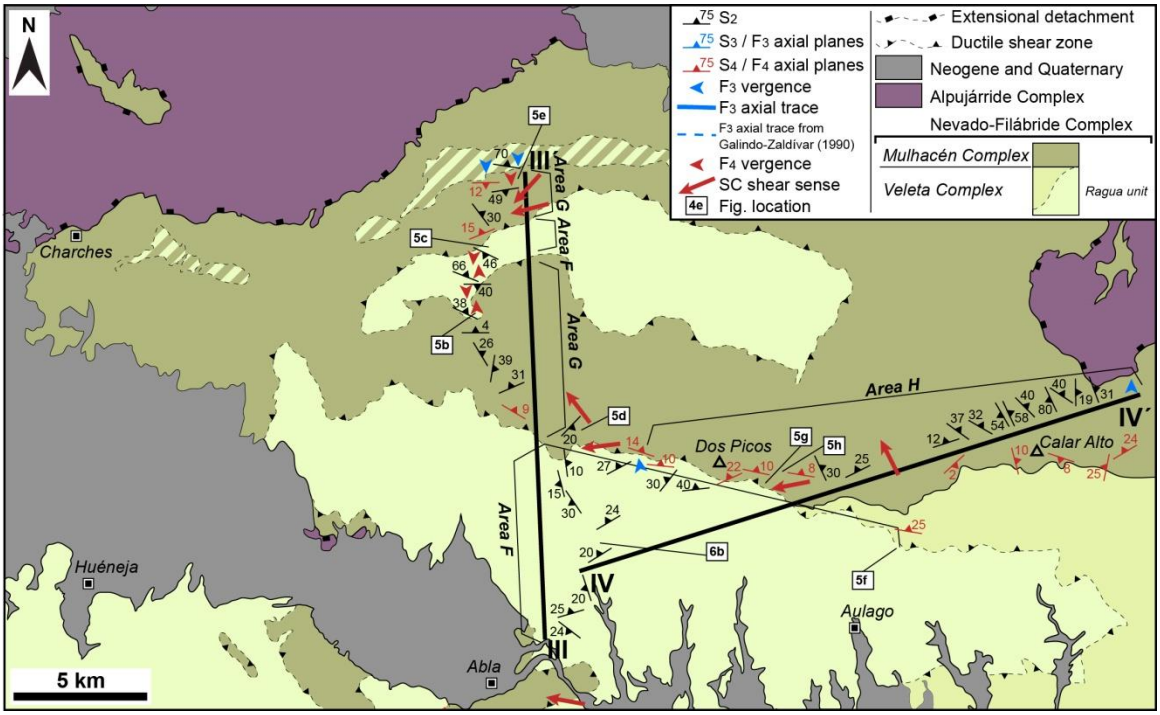

Fig. 6.3. Geological map of the western Sierra de los Filabres. The map shows the original Veleta-Mulhacén subdivision (Puga et al., 2002). The contact between the Ragua and Calar Alto units (Martínez-Martínez et al., 2002) is also shown. The upper part of Veleta and the Mulhacén complex are included in the Calar Alto and Bédar-Macael units of Martínez-Martínez et al. (2002). Striped areas are considered as Mulhacén or Ragua. Locations of images of Fig. 6.5 and cross sections of Fig. 6.7 are indicated.

6.3.1. Sierra Nevada Area

In Area A of cross-section I-I' (western Sierra Nevada) S_2 dips gently N to NNW (Fig. 6.6), F_3 folds are SE vergent similar as in the Güéjar Sierra area (Fig. 6.4b, 6.7), and crenulation or mineral lineations have NE-SW trends. S-C structures show a top-to-the-SW –SSW sense of shear with the C planes dipping more gently towards the WSW as S-planes. This situation contrasts with data from the Güéjar Sierra area where asymmetries indicate both top-to-the-W and top-to-the-E on opposite sides of D_3 folds (Ruiz-Fuentes and Aerden, 2018). Also in the Las Catifas area, top-to-the-SW and top-to-the-WNW senses are both found.

In Area B (section I-I'), S_2 changes (Fig. 6.6 and 6.7) from NW dipping near Veleta peak to ESE dipping further east due to a major F_3 anticline. Minor F_3 folds and crenulations are symmetrical in the hinge region with near-vertical axial planes and NNE-SSW trends (Fig. 6.4c and 6.7). In the eastern limb of the anticline, F_3 parasitic folds are

WNW-vergent (Fig. 6.7) and C planes become E-dipping. S-C structures are particularly well developed in an area near the Veleta peak (Fig. 6.4d) coinciding with the Ragua-Calar Alto detachment of Martínez-Martínez et al. (2002). S-C structures in the eastern limb of the F_3 anticline indicate a top-to-the-W- to NW sense of shear.

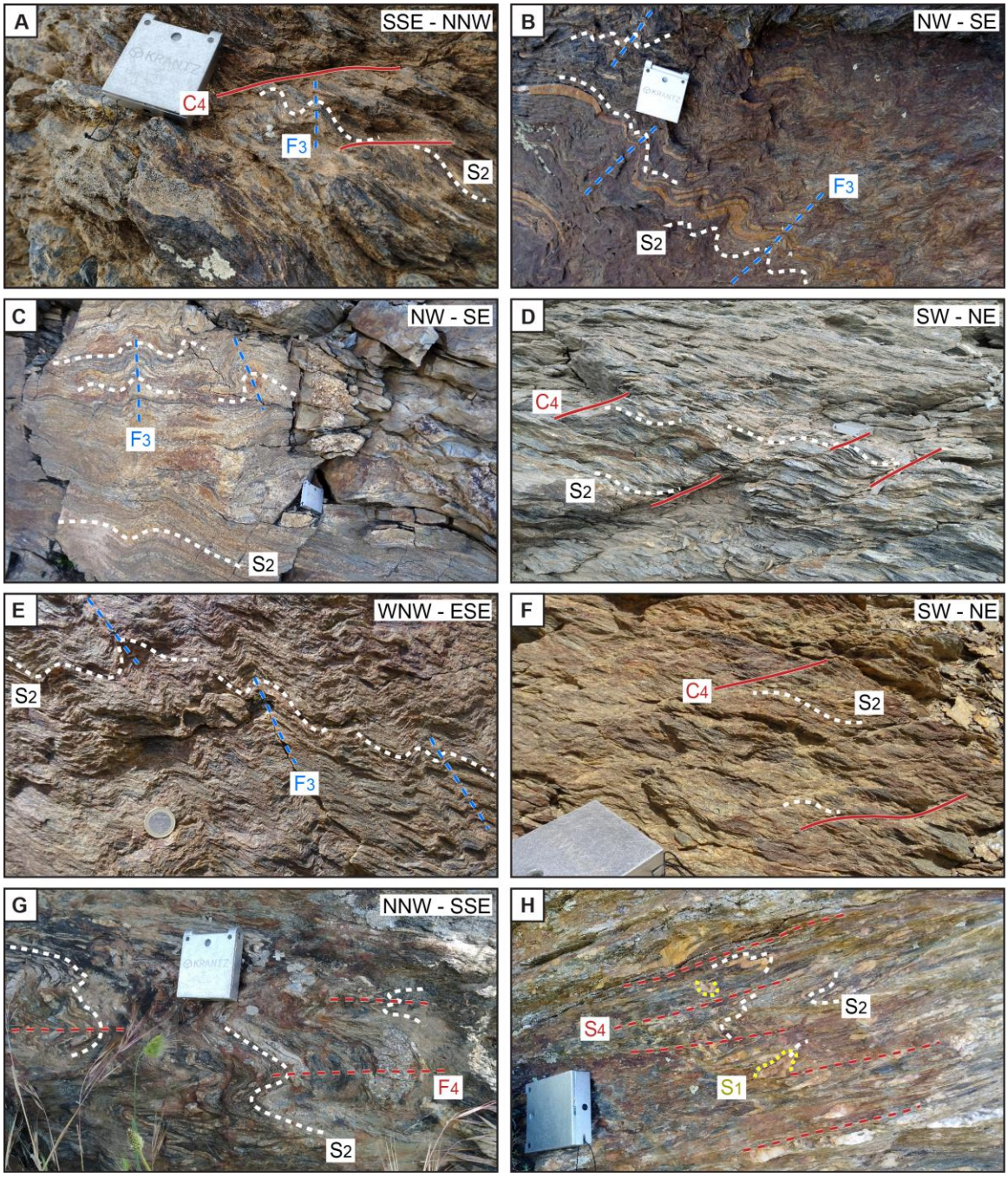

Fig. 6.4. Outcrop images of western Sierra Nevada. A) F_3 folds cut by C planes associated to D_4. B) F_3 folds with SE vergence in Area A. C) Symmetric and NW-vergent F_3 folds east of the Veleta peak. D) D_4 S-C structures developed at the base of the Veleta peak. E) WNW-vergent F_3 folds in Area C. F) D_4 S-C structures developed towards the Veleta-Mulhacén/Ragua-Calar Alto contact. G) F_4 folds in the Veleta/Ragua unit SE of Trevélez. H) Intensely developed S_4 in the Veleta/Ragua unit west of Trevélez in the vicinity of the contact with the Mulhacén/Calar Alto unit. S_2 is completely transposed by S_4.

In Area C (section I-I'), S_2 generally dips E although it is locally affected by open WNW- to W-vergent F_3 folds (Fig. 6.4e and 6.7). C planes mainly dip gently W (Fig. 6.7) and become particularly abundant in the vicinity of the Veleta-Mulhacén (or Ragua-Calar Alto) contact west of Trevélez (Fig. 6.4f). In contrast, where the Veleta-Mulhacén (or Ragua-Calar Alto) contact is best exposed, about halfway between Veleta and Mulhacén peaks, it is parallel to S_2 and no S-C structures are observed. Crenulation and mineral lineations have similar orientations as in areas A and B here. The asymmetry of S-C structures roughly indicates a top-to-the-SW sense of shear, although shows significant variation between neighbouring outcrops.

In Area D (section I-I'), S_2 has a similar attitude as in Area C (Fig. 6.6). No F_3 folds were found in this area but F_4 folds are abundant (Fig. 6.4g) with gentle N-NE-dipping axial planes and NE-SW-trending axes. F_4 folds become tight to isoclinal on approach of the Veleta-Mulhacén contact where S_4 transposes S_2 and becomes the main cleavage (Fig. 6.4h). Crenulation lineations mainly have NE-SW orientations similar as in the above described areas.

In Area E (section II-II'), S_2 generally dips N in the northern part of the section, but towards the S in the southern half thus defining an open antiform (Fig. 6.6 and 6.7). F_4 folds have gently N-dipping axial planes and are preferentially developed in the northern part of the section where they cause transposition of S_2. The vergence of F_4 folds (Fig. 6.7) is variable in the northern part, although northward vergences prevail (Fig. 6.5a). In the southern part, the vergence is dominantly towards the south (Fig. 6.7). Orientations of crenulation and mineral lineations are variable.

6.3.2. Sierra de los Filabres Area

In Areas F, G and H (sections III-III' and IV-IV'), S_2 has highly variable orientations (Fig. 6.6) and is locally overprinted by an intense, subhorizontal S_4. In the Veleta/Ragua unit (Area F), F_4 folds are found mostly near the limit with the Mulhacén/Calar Alto unit (Fig. 6.7). Opposite asymmetries of F_4 folds (Fig. 6.5b and c) in the northern part of section III-III' are interpreted to reflect the presence of F_3 folds (Fig. 6.7). This is supported by opposite asymmetries of local F_3 folds found in the northern and central-southern part of the sierra. In the southern part of the section, gentle upright folds are also present but the lack of F_4 structures does not allow then to be unambiguously assigned to D_3. They could also correspond to late post-D_4 folds.

In the Mulhacén/Calar Alto unit (Areas G and H), S_4 is intensely developed at the base of this unit (Fig. 6.7) where it transposes S_2 (Fig. 6.5g). This D_4 high-strain zone is several hundred meters thick and affects both the Mulhacén/Calar Alto as well as the uppermost part of the Veleta/Ragua unit. It exhibits abundant S-C structures (Fig. 6.5d and h) predominantly indicating top-to-the-W shearing, but orthogonal top-to-the-NW and –SW shear senses are found in the central and northern part of the area (Fig. 6.3), respectively. Outside the transposition zone, S_2 is affected by open to tight F_4 folds with subhorizontal axial planes associated with S_4 crenulation cleavages (Fig. 6.5e and f).

Crenulation and mineral lineations trends are mainly E-W in Area G, but highly variable in Area H ranging from E-W to NW-SE.

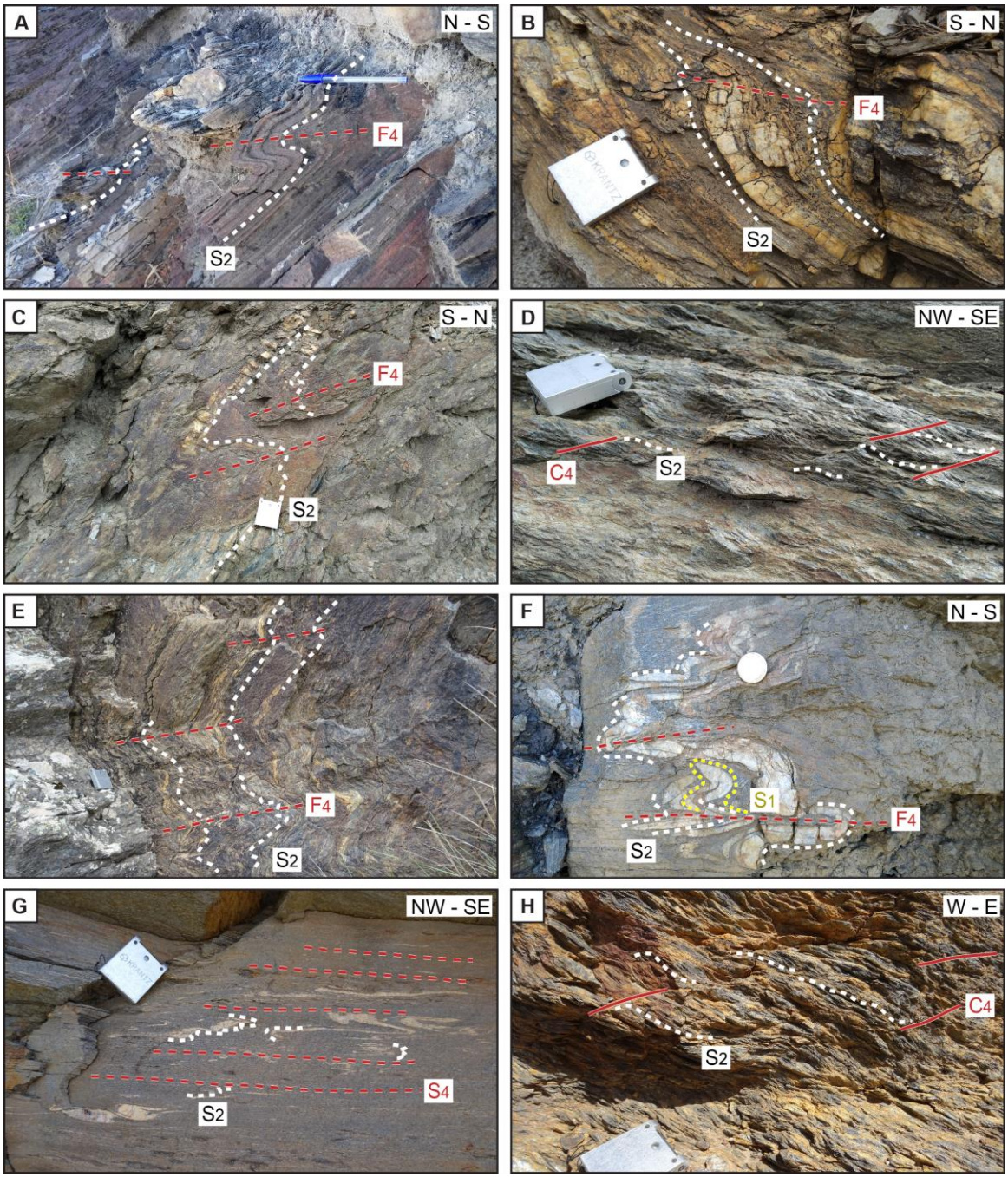

Fig. 6.5. Outcrop images from central Sierra Nevada and western Sierra de los Filabres. A) F_4 folds developed near Ferreira. B) F_4 folds located at the southern part of the Veleta/Ragua tectonic window. C) F_4 folds located at the northern part of the Veleta/Ragua tectonic window. Note the opposite asymmetry of F_4 folds and the opposite dip direction of S_2. D) D_4 S-C structures developed at the Veleta-Mulhacén/Ragua-Calar Alto contact. E) Relatively open F_4 folds developed structurally overlying the zone of S-C structures development. F) D_2-D_4 fold interference in the Veleta/Ragua unit. G) Intensely developed S_4 in the Veleta-Mulhacén/Ragua-Calar Alto contact east of the Dos Picos summit. S_2 is completely transposed by S_4. H) D_4 S-C structures developed near the Veleta-Mulhacén/Ragua-Calar Alto contact in a zone of intensely developed D_4 structures.

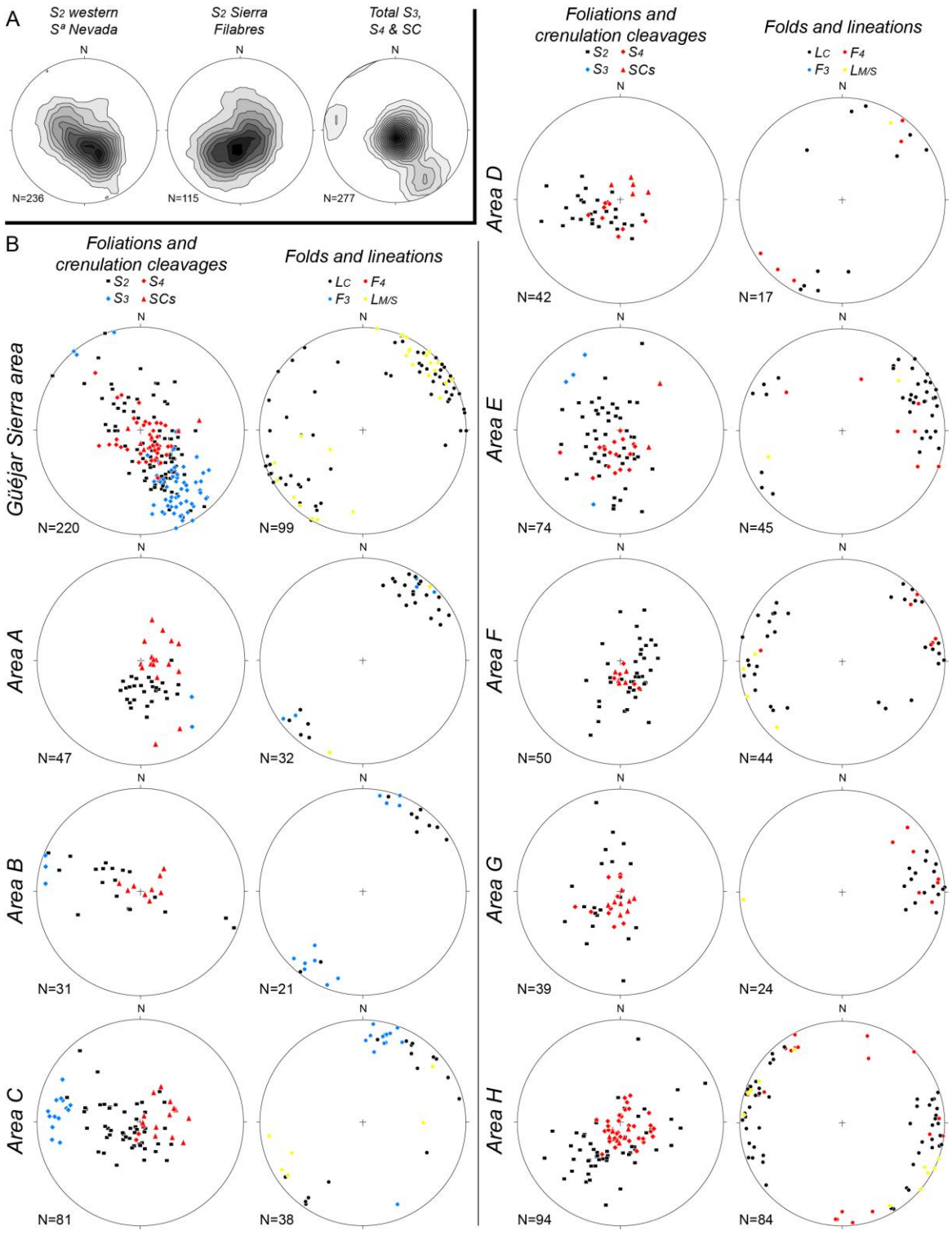

Fig. 6.6. Equal-area and lower-hemisphere projections of structures. Projections were made with Stereonet software (Allmendinger et al., 2013). A) Contour diagrams of S_2 in Sierra Nevada and Sierra de los Filabres, and crenulation cleavages, axial planes and shear surfaces of D_3 and D_4 structures in both areas. B) Planar and linear structures are represented in function of their location in the areas indicated in Figs. 6.2 and 6.3. Data of S-Cs correspond to C planes. Data from the Güéjar Sierra area has been taken from Ruiz-Fuentes and Aerden (2018).

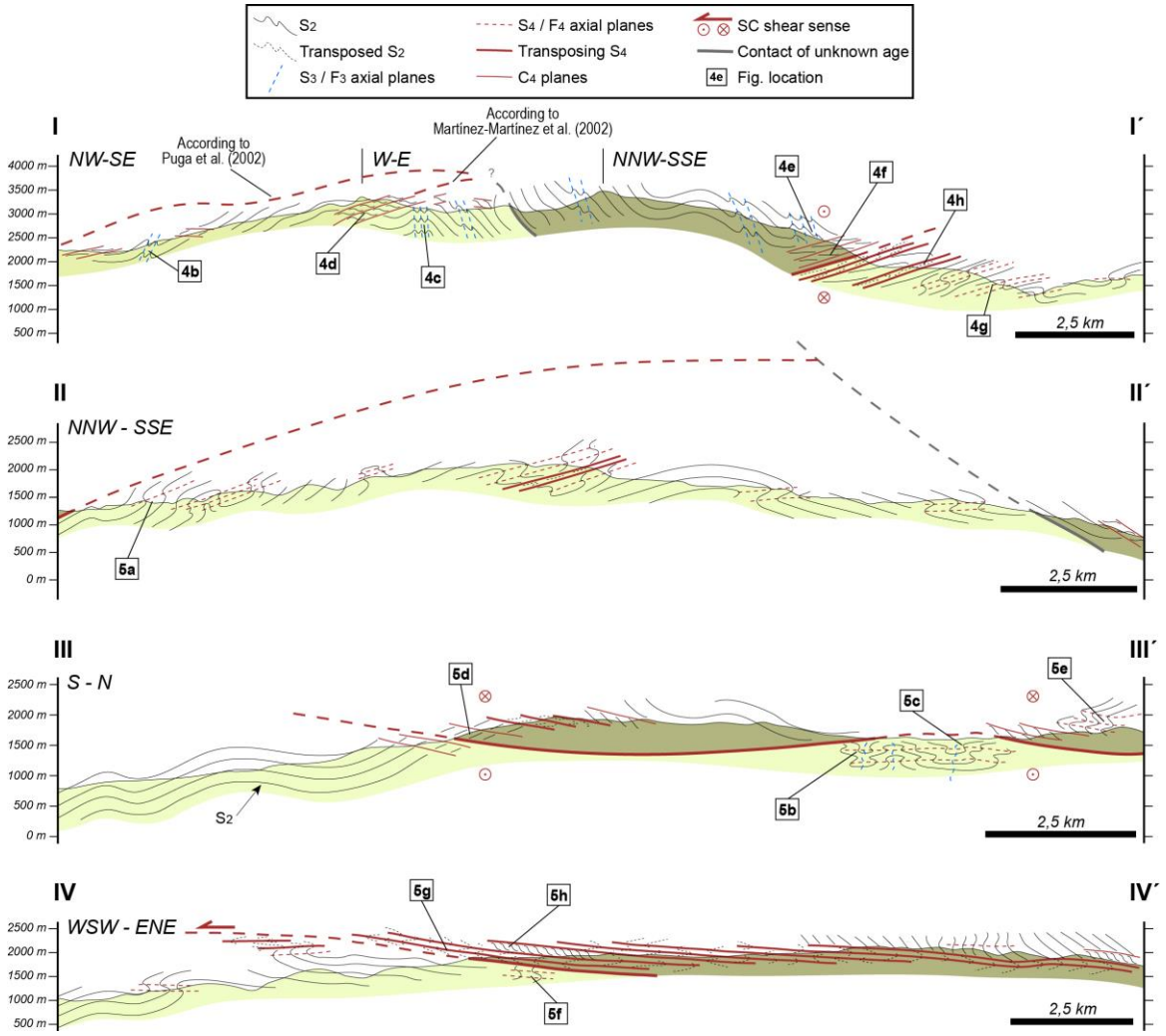

Fig. 6.7. Cross sections in western (I-I') and central (II-II') Sierra Nevada and in western Sierra de los Filabres (III-III' and IV-IV'). White numbers in black squares indicate the location of pictures of Figs. 6.4 and 6.5.

6.4. Discussion

6.4.1. Veleta-Mulhacén / Ragua-Calar Alto contact

Although D_4 structures may be found throughout the Nevado-Filábride Complex, they appear concentrated in zones that coincide with the Veleta-Mulhacén and Ragua-Calar Alto contacts and near the contact with the Alpujárride Complex. This heterogeneous character of D_4 structures supports the existence of tectonic units in the complex (Puga et al., 1974, 2002; Campos et al., 1986; García-Dueñas et al., 1988a; Martínez-Martínez et al., 1995, 2002), particularly in its lower part, instead of a single continuous lithostratigraphic sequence (e.g. Jabaloy et al., 1993; Gómez-Pugnaire et al., 2004; Sanz de Galdeano and López-Garrido, 2016; Santamaría-López and Sanz de Galdeano, 2018). Internal tectonic contacts are also supported by a temperature gap across the Ragua-Calar Alto contact (Augier et al., 2005b), the presence of distinctive cm- to dm-sized pre-Alpine metamorphic minerals in the Mulhacén/Calar Alto unit, but not found in the Veleta succession (Puga et al., 1975; Puga and Díaz de Federico, 1976; García-Dueñas et al.,

1988b; Gómez-Pugnaire and Franz, 1988; Martín-Algarra et al., 2019), and the superposition of older rocks onto younger ones (e.g. Martínez-Martínez et al., 2010; Jabaloy-Sánchez et al., 2018; Poulaki et al., 2023).

In the western Sierra Nevada, a shear zone characterized by a high concentration of S-C structures (Fig. 6.4c and 6.7) but lacking S_4 crenulation cleavage is present at the base of the Veleta peak where Martínez-Martínez et al. (2002) place their Ragua-Calar Alto boundary. However, the lithologies on both sides of the shear zone are similar leaving open the alternative possibility that the shear zone is developed within the Veleta complex instead of bounding it. Ruiz-Fuentes and Aerden (2018) pointed out certain geometric problems with the map trace of the proposed contact further north in the Güéjar Sierra area, when taking into account the topography and structural data.

South of Trevélez, Poulaki et al. (2023) found similar maximum depositional ages (their samples 19SSN01, 18SSN15 and 19SSN03) on both sides of the Ragua-Calar Alto contact, but falling within the single Veleta unit of Puga et al. (2002) and hence supporting the latter.

In the Güéjar Sierra area, Ruiz-Fuentes and Aerden (2018) preferred the Veleta-Mulhacén contact rather than the Ragua-Calar Alto contact because of the above mentioned geometric inconsistencies. North of this area, on the other hand, near Las Catifas peak, I have found dm-sized andalusite pseudomorphs of unambiguous Mulhacén/Calar Alto attribution (e.g. Puga et al., 1975; García-Dueñas et al., 1988b) in an area mapped as Veleta (García-Dueñas and Navarro-Vilá, 1980). This supports the proposal of Martínez-Martínez et al. (2002) that, at least in this area, the Veleta-Mulhacén contact is located at a deeper level. Ruiz-Fuentes and Aerden (2018) found a rather abrupt intensification of D_4 deformation at the Veleta-Mulhacen contact previously mapped in the eastern part of the Güéjar Sierra area, but not in the western part of the same area. D_4 structures reappear at the SW sector of this area but it is unclear if they are related to the Veleta-Mulhacen contact, the Nevado-Filábride—Alpujárride contact or both.

Between the Veleta and Mulhacén peaks, the contact is clearly exposed separating graphite schists of the Veleta/Ragua unit and graphite schists containing mafic intercalations of the Mulhacén/Calar Alto unit. A very steeply east-dipping attitude can be deduced for a relatively large portion of the contact from its map trace (Díaz de Federico et al., 1978) and suggests that it is subparallel to S_2 rather than D_4 structures as the latter are generally subhorizontal (Fig. 6.6). This suggests that the D_4 high-strain zones recognized at the base of the Veleta peak and west of Trevélez modify or cut an older (thrust) contact which formed parallel to S_2. In this case these zones may represent different shear zones developed at different structural levels instead of a single one as envisaged by Martínez-Martínez et al., (2002). An early thrust origin of the Veleta-Mulhacén contact followed by folding of the contact and subsequent reactivation or modification was already proposed by de Jong (1993a; his D_2^{Vel}, D_3^{Vel}, and D_4^{Vel} deformation phases).

6.4.2. Inherited structures

The morphology of the Sierra Nevada and Sierra de los Filabres elongate ranges is determined by late Miocene-Pliocene open antiforms and synforms with E-W trends (Jabaloy et al., 1993; Martínez-Martínez et al., 2002). These structures only cause modest variations in the orientation of D_4 contacts, whereas the main foliation (S_2) exhibits a much more complex and tighter D_3 folding (Fig. 6.6). F_3 folds control the asymmetry/vergence of subsequent F_4 folds and S-C fabrics which changes between opposite fold limbs (see sections I-I', II-II', and the northern part of section III-III'). The asymmetries of D_3 and D_4 structures are also systematically opposite to each other within the same D_3 fold limb. These relationships result from vertical shortening (gravitational collapse) of upright antiforms and synforms (e.g. Dirks et al., 1997; Aerden, 1994, 1998; Bell et al., 2003; Ham and Bell, 2004; Aerden and Sayab, 2008; Fossen, 2016; Aerden et al., 2021). Vissers (1981) already noticed that the Nevado-Filabride/Alpujarride contact cuts large-scale (F_3) folds with moderately to steeply north-dipping axial planes in the north of his study area, which he also labelled F_3. De Jong (1993a, 1993b) also recognized, in the eastern Sierra de los Filabres, km-scale folds cross-cut by bands of mylonitic foliation associated to the Veleta-Mulhacén and Nevado-Filábride—Alpujárride contacts, equivalent to our D_4 structures. Of special interest is a major NE-SW trending anticline deforming S_2 whose axial trace passes between Veleta and Mulhacén peaks. This fold is associated with a change in vergence of minor D_3 folds as already recognized by Galindo-Zaldivar et al. (1989) and Jabaloy et al. (1993) and predates the Nevado-Filábride—Alpujárride contact, instead of folding it as was interpreted by Martínez-Martínez et al., (2002).

F_3 folds are also responsible for variable orientations of intersection lines between S- and C- planes as these depend on the local orientation S_2 (the 'S' plane) has when they were overprinted by C-planes. In this respect, it is important to note that S-C structures in the Nevado-Filábride are the product of polyphase deformation and should not be confused with similar structures produced during a single deformation as explicitly distinguished by Lister and Snoke (1984). It is not uncommon to find S-C intersections with totally different orientations in nearby outcrops, or indicating opposite shear senses (e.g. in the Güéjar Sierra area). Nevertheless, top-to-the-SW or –W shear sense appears to be the most common and likely reflect the regional tectonic transport direction during D_4. As the direction of tectonic transport during D_4 was subparallel to the axes of D_3 folds, D_4 shear zones did not cause major displacements of these pre-existing structures. This may explain the fact that the trace of the major F_3 anticline in the western Sierra Nevada (Galindo-Zaldivar et al., 1989; Galindo-Zaldivar, 1990; Jabaloy et al., 1993), does not appear to be displaced, neither by the Veleta-Mulhacén contact nor the Ragua-Calar Alto contact. However, the axial trace of these structures has been only loosely defined by vergence changes of small-scale F_3 folds along a limited number of outcrops and has not been mapped yet in detail.

Interestingly, structures with similar orientation and vergence as the F_3 folds in the westernmost Sierra Nevada (SE-vergent) also appear further north in the vicinity of the

IEZB associated with south-directed back-thrusts (e.g. García-Dueñas and Navarro-Vilá, 1976; Sanz de Galdeano et al., 1995; Ruiz-Fuentes et al., 2022; Ruiz-Fuentes and Aerden, 2023). Although these structures formed earlier than D_3 in the late Burdigalian (see following section), their southward propagation could have later produced D_3 folds in the Nevado-Filábride, followed by exhumation during D_4 in the Serravalian-Tortonian.

6.4.3. Timing of deformation

Garnets in the Nevado-Filábride Complex grew during the development of multiple "S_1" foliations transposed by S_2 and still during the development of S_2 itself at temperatures of 500-600ºC (e.g. Behr and Platt, 2012; Aerden et al., 2013; Booth-Rea et al., 2015; Jabaloy-Sánchez et al., 2015; Li and Massonne, 2018). Since temperatures during D_3 and D_4 have been estimated as 300-500 ºC (González-Casado et al., 1995; Augier et al., 2005a, 2005b; Behr and Platt, 2012; Booth-Rea et al., 2015; Jabaloy-Sánchez et al., 2015), it follows that these events post-date the youngest garnet ages obtained in the Nevado-Filábride, which lie around 13 Ma (Platt et al., 2006; Santamaría-López et al., 2019; Aerden et al., 2022), and allanite ages linked to high-temperature/low-pressure of 13-15 Ma (Santamaría-López et al., 2019). D_3 and D_4 must have been relatively short-lived events as the Nevado-Filábride Complex reached near-surface temperatures at 12 ± 1 Ma and 9-8 Ma in the eastern Sierra de los Filabres and western Sierra Nevada, respectively, according to fission-track data (Johnson et al., 1997).

6.5. Conclusions

Gently dipping high-strain zones characterized by intensely developed S_4 crenulation cleavage and associated S-C structures have been identified within the Nevado-Filábride Complex and support the existence of late-metamorphic tectonic contacts within the lower part of the complex. A component of vertical shortening within these high-strain zones superposed on pre-existing upright D_3 folds produced "christmas-tree"-like fold-interference geometries characterized by opposite vergences of D_3 and D_4 parasitic folds and crenulations on the same F_3 fold limb. These D_4 zones seem to coincide with earlier proposed contacts between the Veleta-Mulhacén or Ragua and Calar Alto units. In the western Sierra Nevada, however, in the area between Mulhacén and Veleta peaks, this contact dips steeply parallel to the S_2 cleavage whereas D_4 structures are absent. This suggests that the contact formed during D_2 and was later cut and displaced by D_4 shear zones/contacts.

Acknowledgements

This research is part of a Ph.D. project of ARF financed by an FPU grant from the Spanish Ministry of Education, Culture and Sports (FPU17/01874). Research was funded by Spanish government grant CGL2016-80687-R AEI/FEDER, and Junta de Andalucía Projects P18-RT-3275 (AGORA), B-RNM-301-UGR18 (PAPEL) and RNM148.

References

Aerden, D.G.A.M., 1994. Kinematics of orogenic collapse in the Variscan Pyrenees deduced from microstructures in porphyroblastic rocks from the Lys-Caillaouas massif. Tectonophysics 238, 139-160. https://doi.org/10.1016/0040-1951(94)90053-1

Aerden, D.G.A.M., 1998. Tectonic evolution of the Montagne Noire and a possible orogenic model for syncollisional exhumation of deep rocks, Variscan belt, France. Tectonics 17, 62-79. https://doi.org/10.1029/97TC02342

Aerden, D., Sayab, M., 2008. From Adria- to Africa-driven orogenesis: Evidence from porphyroblasts in the Betic Cordillera, Spain. Journal of Structural Geology 30, 1272-1287. https://doi.org/10.1016/j.jsg.2008.06.009

Aerden, D.G.A.M., Bell, T.H., Puga, E., Sayab, M., Lozano, J.A., Díaz de Federico, A., 2013. Multi-stage mountain building vs. relative plate motions in the Betic Cordillera deduced from integrated microstructural and petrological analysis of porphyroblast inclusion trails. Tectonophysics 587, 188-206. https://doi.org/10.1016/j.tecto.2012.11.025

Aerden, D.G.A.M., Ruiz-Fuentes, A., Sayab, M., Forde, A., 2021. Kinematics of subduction in the Ibero-Armorican arc constrained by 3D microstructural analysis of garnet and pseudomorphed lawsonite porphyroblasts from Île de Groix (Variscan belt). Solid Earth 12, 971-992. https://doi.org/10.5194/se-12-971-2021

Aerden, D.G.A.M., Farrell, T.P., Baxter, E.F., Stewart, E.M., Ruiz-Fuentes, A., Bouybaouene, M., 2022. Refined tectonic evolution of the Betic-Rif orogen through integrated 3-D microstructural analysis and Sm-Nd dating of garnet porphyroblasts. Tectonics 41, e2022TC007366. https://doi.org/10.1029/2022TC007366

Allmendinger, R. W., Cardozo, N. C., Fisher, D., 2013. Structural Geology Algorithms: Vectors & Tensors. Cambridge, England, Cambridge University Press, 289 pp.

Augier, R., Agard, P., Monié, P., Jolivet, L., Robin, C., Booth-Rea, G., 2005a. Exhumation, doming and slab retreat in the Betic Cordillera (SE Spain): in situ 40Ar/39Ar ages and P-T-d-t paths for the Nevado-Filabride complex. Journal of Metamorphic Geology 23, 357-381. https://doi.org/10.1111/j.1525-1314.2005.00581.x

Augier, R., Booth-Rea, G., Agard, P., Martínez-Martínez, J.M., Jolivet, L., Azañón, J.M., 2005b. Exhumation constraints for the lower Nevado-Filabride Complex (Betic Cordillera, SE Spain): a Raman thermometry and Tweequ multiequilibrium thermobarometry approach. Bulletin de la Société Géologique de France 176, 403-416. https://doi.org/10.2113/176.5.403

Augier, R., Jolivet, L., Robin, C., 2005c. Late Orogenic doming in the eastern Betic Cordilleras: Final exhumation of the Nevado-Filabride complex and its relation to basin genesis. Tectonics 24, TC4003. https://doi.org/10.1029/2004TC001687

Azañón, J.M., Goffé, B., 1997. Ferro- and magnesiocarpholite assemblages as record of high-P, low-T metamorphism in the Central Alpujarrides, Betic Cordillera (SE Spain). European Journal of Mineralogy 9, 1035-1051.

Bakker, H.E., de Jong, K., Helmers, H., Biermann, C., 1989. The geodynamic evolution of the Internal Zone of the Betic Cordilleras (south-east Spain): a model based on structural analysis and geothermobarometry. Journal of Metamorphic Geology 7, 359-381. https://doi.org/10.1111/j.1525-1314.1989.tb00603.x

Balanyá, J.C., 1991. Estructura del Dominio de Alboran en la parte norte del Arco de Gibraltar. PhD Thesis, Universidad de Granada. https://digibug.ugr.es/handle/10481/50668

Behr, W.M., Platt, J.P., 2012. Kinematic and thermal evolution during two-stage exhumation of a Mediterranean subduction complex. Tectonics 31, TC4025. https://doi.org/10.1029/2012TC003121

Bell, T.H., Ham, A.P., Hickey, K.A., 2003. Early formed regional antiforms and synforms that fold younger matrix schistosities: their effect on sites of mineral growth. Tectonophysics 367, 253-278. https://doi.org/10.1016/S0040-1951(03)00126-4

Bessière, E., Scaillet, S., Augier, R., Jolivet, L., Azañón, J.M., Booth-Rea, G., Romagny, A., Duval, F., 2022. 40Ar/39Ar Age Constraints on HP/LT Metamorphism in Extensively Overprinted Units: The Example of the Alpujárride Subduction Complex (Betic Cordillera, Spain). Tectonics 41, e2021TC006889. https://doi.org/10.1029/2021TC006889

Booth-Rea, G., Martínez-Martínez, J.M., Giaconia, F., 2015. Continental subduction, intracrustal shortening, and coeval upper-crustal extensión: P-T evolution of subducted south Iberian paleomargin metapelites (Betics, SE Spain). Tectonophysics 663, 122-139. https://doi.org/10.1016/j.tecto.2015.08.036

Bouillin, J.P., Durand Delga, M., Olivier, P., 1986. Betic-Rifain and Tyrrhenian Arcs: distinctive features, genesis and development stages, in: Wezel, F.C., (Ed.), The origin of arcs, Amsterdam, Elsevier, p. 281–304.

Brouwer, H.A., 1926. Zur Geologie der Sierra Nevada. Geologische Rundschau 17, 118-137. https://doi.org/10.1007/BF01801854

Campos, J., García-Dueñas, V., González Lodeiro, F., Orozco, M., 1986. La zona de cizalla del contacto entre el grupo de mantos del Mulhacén y la unidad del Veleta (Sierra Nevada y Sierra de los Filabres, Andalucía). Geogaceta 1, 15-17.

de Jong, K., 1993a. The tectono-metamorphic evolution of the Veleta Complex and the development of the contact with the Mulhacen Complex (Betic Zone, SE Spain). Geologie en Mijnbouw 71, 227-237.

de Jong, K., 1993b. Redefinition of the deformation scheme of the Mulhacen Complex and implications for the relative timing of the overthrusting of the Alpujarride Complex in the Betic Zone (SE Spain). Geologie en Mijnbouw 71, 317-326.

de Jong, K., Bakker, H., 1991. The Mulhacen and Alpujarride Complex in the eastern Sierra de los Filabres, SE Spain: Litho-stratigraphy. Geologie en Mijnbouw 70, 93-103.

Díaz de Federico, A., Puga, E., Burgos, J., Gallegos, J.A., Sanz de Galdeano, C., 1978. Mapa geológico de la Hoja nº 1027 (Güejar Sierra): Mapa Geológico de España E. 1:50.000. Segunda Serie (MAGNA), Primera edición. IGME.

Dirks, P.H.G.M., Zhang, J.S., Passchier, C.W., 1997. Exhumation of high-pressure granulites and the role of lower crustal advection in the North China Craton near Datong. Journal of Structural Geology 19, 1343-1358. https://doi.org/10.1016/S0191-8141(97)00044-8

Fallot, P., Faure-Muret, A., Fontboté, J.M., Solé, L., 1961. Estudios sobre las series de Sierra Nevada y de la llamada Mischungszone. Boletín del Instituto Geológico y Minero de España 71, 347-557.

Fernández-Fernández, E.M., Jabaloy-Sánchez, A., Nieto, F., González-Lodeiro, F., 2007. Structure of the Maláguide Complex near Vélez Rubio (Eastern Betic Cordillera, SE Spain). Tectonics 26, TC4008 https://doi.org/10.1029/2006TC002019.

Fossen, H., 2016. Structural geology. Cambridge University Press, Cambridge.

Galindo-Zaldivar, J., 1990. Geometría y Cinemática de las Deformaciones Neógenas en Sierra Nevada (Cordilleras Béticas). PhD Thesis, Universidad de Granada. https://digibug.ugr.es/handle/10481/37526

Galindo-Zaldivar, J., González-Lodeiro, F., Jabaloy, A., 1989. Progressive extensional shear structures in a detachment contact in the Western Sierra Nevada (Betic Cordilleras, Spain). Geodinamica Acta 3, 73-85. https://doi.org/10.1080/09853111.1989.11105175

García-Dueñas, V., Navarro-Vilá, F., 1976. Alpujarrides, Malaguides et autres unités allochtones au Nord de la Sierra Nevada (Cordillères Bétiques, Andalousie). Bulletin de la Société Géologique de France 7-XVIII-3, 641-648. https://doi.org/10.2113/gssgfbull.S7-XVIII.3.641

García-Dueñas, V., Navarro-Vilá, F., 1980. Memoria de la Hoja n° 1010 (La Peza): Mapa Geológico de España E. 1:50.000. Segunda Serie (MAGNA), Primera edición. IGME.

García-Dueñas, V., Martínez-Martínez, J.M., Orozco, M., Soto, J.I., 1988a. Plis-nappes, cisaillements syn- à post-métamorphiques et cisaillements ductiles-fragiles en distensión dans les Nevado-Filabrides (Cordillères bétiques, Espagne). Comptes Rendus de l'Académie des Sciences de Paris 307, 1389-1395.

García-Dueñas, V., Martínez-Martínez, J.M., Soto, J.I., 1988b. Los Nevado-Filabrides, una pila de pliegue-mantos separados por zonas de cizalla. Simposio sobre: Cinturones orogénicos. SGE, 17-26.

Gómez-Pugnaire, M.T., Franz, G., 1988. Metamorphic evolution of the Palaeozoic series of the Betic Cordillera (Nevado-Filabride complex, SE Spain) and its relationship with the alpine orogeny. Geologische Rundschau 77, 619-640. https://doi.org/10.1007/BF01830174

Gómez-Pugnaire, M.T., Braga, J.C., Martín, J.M., Sassi, F.P., Del Moro, A., 2000. Regional implications of a Palaeozoic age for the Nevado-Filábride Cover of the Betic Cordillera, Spain. Schweizerische Mineralogische und Petrographische Mitteilungen 80, 45-52.

Gómez-Pugnaire, M.T., Galindo-Zaldívar, J., Rubatto, D., González-Lodeiro, F., López Sánchez-Vizcaíno, V., Jabaloy, A., 2004. A reinterpretation of the Nevado-Filábride and Alpujárride Complexes (Betic Cordillera): field, petrography and U-Pb ages from orthogneisses (western Sierra Nevada, S Spain). Schweizerische Mineralogische und Petrographische Mitteilungen 84, 303-322.

Gómez-Pugnaire, M.T., Rubatto, D., Fernández-Soler, J.M., Jabaloy, A., López-Sánchez-Vizcaíno, V., González-Lodeiro, F., Galindo-Zaldívar, J., Padrón-Navarta, J.A., 2012. Late Variscan magmatism in the Nevado-Filábride Complex: U-Pb geochronologic evidence for the pre-Mesozoic nature of the deepest Betic complex (SE Spain). Lithos 146-147, 93-111. https://doi.org/10.1016/j.lithos.2012.03.027

González-Casado, J.M., Casquet, C., Martínez-Martínez, J.M., García-Dueñas, V., 1995. Retrograde evolution of quartz segregations from the Dos Picos shear zone in the Nevado-Filabride Complex (Betic chains, Spain). Evidence from fluid inclusions and quartz c-axis fabrics. Geol. Rundsch. 84, 175-186. https://doi.org/10.1007/BF00192249

Gray, D.R., Durney, D.W., 1979. Investigations on the mechanical significance of crenulation cleavage. Tectonophysics 58, 35-79. https://doi.org/10.1016/0040-1951(79)90321-4

Guerrera, F., Martín-Algarra, A., Perrone, V., 1993. Late Oligocene-Miocene syn-/-late-orogenic successions in Western and Central Mediterranean chains from the Betic Cordillera to the Southern Apennines. Terra Nova 5, 525-544. https://doi.org/10.1111/j.1365-3121.1993.tb00302.x

Guerrera, F., Martín-Martín, M., Tramontana, M., 2021. Evolutionary geological models of the central-western peri-Mediterranean chains: a review. International Geology Review 63, 65-86 https://doi.org/10.1080/00206814.2019.1706056

Ham, A.P., Bell, T.H., 2004. Recycling of foliations during folding. Journal of Structural Geology 26, 1989-2009. https://doi.org/10.1016/j.jsg.2004.04.003

Jabaloy, A., Galindo-Zaldívar, J., González-Lodeiro, F., 1993. The Alpujárride—Nevado-Filábride extensional shear zone, Betic Cordillera, SE Spain. Journal of Structural Geology 15, 555-569. https://doi.org/10.1016/0191-8141(93)90148-4

Jabaloy-Sánchez, A., Gómez-Pugnaire, M.T., Padrón-Navarta, J.A., López Sánchez-Vizcaíno, V., Garrido, C.J., 2015. Subduction- and exhumation-related structures preserved in metaserpentinites and associated metasediments from the Nevado-Filábride Complex (Betic Cordillera, SE Spain). Tectonophysics 644-645, 40-57. https://doi.org/10.1016/j.tecto.2014.12.022

Jabaloy-Sánchez, A., Talavera, C., Gómez-Pugnaire, M.T., López-Sánchez-Vizcaíno, V., Vázquez-Vílchez, M., Rodríguez-Peces, M.J., Evans, N.J., 2018. U-Pb ages of detrital zircons from the Internal Betics: A key to deciphering palaeogeographic provenance and tectono-stratigraphic evolution. Lithos 318-319, 244-266. https://doi.org/10.1016/j.lithos.2018.07.026

Johnson, C., Harbury, N., Hurford, A.J., 1997. The role of extension in the Miocene denudation of the Nevado-Filábride Complex, Betic Cordillera (SE Spain). Tectonics 16, 189-204. https://doi.org/10.1029/96TC03289

Kampschuur, W., 1975. Data on thrusting and metamorphism in the eastern Sierra de los Filabres: higher Nevado-Filabride units and the glaucophanitic greenschist facies. Tectonophysics 27, 57-81. https://doi.org/10.1016/0040-1951(75)90048-7

Kirchner, K.L., Behr, W.M., Loewy, S., Stockli, D.F., 2016. Early Miocene subduction in the western Mediterranean: Constraints from Rb-Sr multimineral isochron geochronology.

Geochemistry, Geophysics, Geosystems 17, 1842-1860. https://doi.org/10.1002/2015GC006208

Laborda-López, C., Aguirre, J., Donovan, S.K., 2015. Surviving metamorphism: taphonomy of fossil assemblages in marble and calc-silicate schist. Palaios 30, 668-679. https://doi.org/10.2110/palo.2015.013

Li, B., Massonne, H.J., 2018. Two Tertiary metamorphic events recognized in high-pressure metapelites of the Nevado-Filábride Complex (Betic Cordillera, S Spain). Journal of Metamorphic Geology 36, 603-630. https://doi.org/10.1111/jmg.12312

Linthout, K., Vissers, R.L.M., 1979. On the classification of tectonic units in the Nevado-Filabride Complex of the northern Sierra de los Filabres, Betic Cordilleras, SE Spain. Geologie en Mijnbouw 58, 49-56.

Lister, G.S., Snoke, A.W., 1984. S-C Mylonites. Journal of Structural Geology 6, 617-638. https://doi.org/10.1016/0191-8141(84)90001-4

Lonergan, L., Platt, J.P., Gallagher, L., 1994. The Internal-External Zone Boundary in the eastern Betic Cordillera, SE Spain. Journal of Structural Geology 16, 175-188. https://doi.org/10.1016/0191-8141(94)90103-1

López Sánchez-Vizcaíno, V., Rubatto, D., Gómez-Pugnaire, M.T., Trommsdorff, V., Müntener, O., 2001. Middle Miocene high-pressure metamorphism and fast exhumation of the Nevado-Filábride Complex, SE Spain. Terra Nova 13, 327-332. https://doi.org/10.1046/j.1365-3121.2001.00354.x

Martín-Algarra, A., 1987. Evolución geológica alpina del contacto entre las Zonas Internas y las Zonas Externas de la Cordillera Bética. PhD Thesis, Universidad de Granada, 1171 p. https://digibug.ugr.es/handle/10481/75699

Martín-Algarra, A., García-Casco, A., Gómez-Pugnaire, M.T., Jabaloy-Sánchez, A., Laborda-López, C., López Sánchez-Vizcaíno, V., Mazzoli, S., Navas-Parejo, P., Perrone, V., Rodríguez-Cañero, R., Sánchez-Navas, A., 2019. Paleozoic Basement and Pre-Alpine History of the Betic Cordillera, in: Quesada, C., Oliveira, J.T., (Eds.), The Geology of Iberia: A Geodynamic Approach, Vol. 2, Ch. 9, p. 261–305. Regional Geology Reviews. https://doi.org/10.1007/978-3-030-10519-8_9

Martín-Martín, M., El Mamoune, B., Martín-Algarra, A., Martín-Pérez, J.A., 1996. The Internal-External Zone Boundary in the Eastern Betic Cordillera, SE Spain: Discussion. Journal of Structural Geology 18, 523-524.

Martínez-Martínez, J.M., 2007. Coexistencia de zonas de cizalla dúctil de extensión y de acortamiento en el domo de Sierra Nevada, Béticas (SE de España). Revista de la Sociedad Geológica de España 20, 229-245.

Martínez-Martínez, J.M., Soto, J.I., Balanyá, J.C., 1995. Large scale structures in the Nevado-Filabride Complex and crustal seismic fabrics of the deep seismic reflection profile ESCI-Béticas2. Revista de la Sociedad Geológica de España 8, 477-489.

Martínez-Martínez, J.M., Soto, J.I., Balanyá, J.C., 2002. Orthogonal folding of extensional detachments: Structure and origin of the Sierra Nevada elongated dome (Betics, SE Spain). Tectonics 21, 1012. https://doi.org/10.1029/2001TC001283

Martínez-Martínez, J.M., Torres-Ruiz, J., Pesquera, A., Gil-Crespo, P.P., 2010. Geological relationships and U-Pb zircon and 40Ar/39Ar tourmaline geochronology of gneisses and tourmalinites from the Nevado-Filabride complex (western Sierra Nevada, Spain): Tectonic implications. Lithos 119, 238-250. https://doi.org/10.1016/j.lithos.2010.07.002

Platt, J.P., Kelley, S.P., Carter, A., Orozco, M., 2005. Timing of tectonic events in the Alpujarride Complex, Betic Cordillera, southern Spain. Journal of the Geological Society, London 162, 451-462. https://doi.org/10.1144/0016-764903-039

Platt, J.P., Anczkiewicz, R., Soto, J.I., Kelley, S.P., Thirlwall, M., 2006. Early Miocene continental subduction and rapid exhumation in the western Mediterranean. Geology 34, 981-984. https://doi.org/10.1130/G22801A.1

Porkoláb, K., Matenco, L., Hupkes, J., Willingshofer, E., Wijbrans, J., van Schrojenstein Lantman, H., van Hinsbergen, D.J.J., 2022. Tectonic evolution of the Nevado-Filábride Complex (Sierra de los Filabres, Southeastern Spain): Insights from new structural and geochronological data. Tectonics 41, e2021TC006922. https://doi.org/10.1029/2021TC006922

Poulaki, E.M., Stockli, D.F., 2022. The paleotectonic evolution of the western Mediterranean: provenance insights from the internal Betics, southern Spain. Frontiers in Earth Science 10, 929502. https://doi.org/10.3389/feart.2022.929502

Poulaki, E.M., Stockli, D.F., Shuck, B.D., 2023. Pre-Subduction Architecture Controls Coherent Underplating During Subduction and Exhumation (Nevado-Filábride Complex, Southern Spain). Geochemistry, Geophysics, Geosystems 24, e2022GC010802. https://doi.org/10.1029/2022GC010802

Puga, E., Díaz de Federico, A., 1976. Pre-Alpine metamorphism in the Sierra Nevada Complex (Betic Cordillera Spain). Cuadernos de Geología de la Universidad de Granada 7, 161-171.

Puga, E., Díaz de Federico, A., Fontbote, J.M., 1974. Sobre la individualización y sistematización de las unidades profundas de la Zona Bética. Estudios Geológicos 30, 543-548

Puga, E., Fontboté, J.M., Martín-Vivaldi, J.L., 1975. Kyanite Pseudomorphs after Andalusite in Polymetamorphic Rocks of the Sierra Nevada (Betic Cordillera, Southern Spain). Schweiz. Mineral. Petrogr. Mitt. 55, 227-241.

Puga, E., Nieto, J.M., Díaz de Federico, A., Portugal, M., Reyes, E., 1996. The intra-orogenic Soportújar Formation of the Mulhacén Complex: Evidence for the polycyclic character of the Alpine orogeny in the Betic Cordilleras. Eclogae Geologicae Helvetiae 89, 129-162.

Puga, E., Nieto, J.M., Díaz de Federico, A., 2000. Contrasting P-T paths in eclogites of the Betic ophiolitic association, Mulhacén complex, southeastern Spain. The Canadian Mineralogist 38, 1137-1161. https://doi.org/10.2113/gscanmin.38.5.1137

Puga, E., Díaz de Federico, A., Nieto, J.M., 2002. Tectonostratigraphic subdivisión and petrological characterisation of the deepest complexes of the Betic zone: a review. Geodinamica Acta 15, 23-43. https://doi.org/10.1080/09853111.2002.10510737

Puga, E., Fanning, M., Díaz de Federico, A., Nieto, J.M., Beccaluva, L., Bianchini, G., Díaz Puga, M.A., 2011. Petrology, geochemistry and U-Pb geochronology of the Betic Ophiolites: Inferences for Pangaea break-up and birth of the westernmost Tethys Ocean. Lithos 124, 255-272. https://doi.org/10.1016/j.lithos.2011.01.002

Rodríguez-Cañero, R., Jabaloy-Sánchez, A., Navas-Parejo, P., Martín-Algarra, A., 2018. Linking Palaeozoic palaeogeography of the Betic Cordillera to the Variscan Iberian Massif: new insight through the first conodonts of the Nevado-Filábride Complex. International Journal of Earth Sciences 107, 1791-1806. https://doi.org/10.1007/s00531-017-1572-8

Ruiz-Fuentes, A., Aerden, D.G.A.M., 2018. Transposition of foliations and superposition of lineations during polyphase deformation in the Nevado-Filabride complex: tectonic implications. International Journal of Earth Sciences 107, 1975-1988. https://doi.org/10.1007/s00531-017-1582-6

Ruiz-Fuentes, A., Aerden, D.G.A.M., 2023. Deciphering western Mediterranean kinematics using metamorphic porphyroblasts from the Alpujárride Complex (Betic Cordillera). Journal of Structural Geology 168, 104823. https://doi.org/10.1016/j.jsg.2023.104823

Ruiz-Fuentes, A., Cabrera-Porras, A., Martín-Algarra, A., 2022. Structural record of polyorogenic pre-Alpine and Alpine deformations within a major thrust nappe close to a suture zone (Internal-External Zones Boundary of the central Betic Cordillera, S Spain). International Geology Review https://doi.org/10.1080/00206814.2022.2129472

Santamaría-López, A., Sanz de Galdeano, C., 2018. SHRIMP U-Pb detrital zircon dating to check subdivisions in metamorphic complexes: a case of study in the Nevado-Filábride complex (Betic Cordillera, Spain). International Journal of Earth Sciences 107, 2539-2552. https://doi.org/10.1007/s00531-018-1613-y

Santamaría-López, A., Lanari, P., Sanz de Galdeano, C., 2019. Deciphering the tectono-metamorphic evolution of the Nevado-Filábride complex (Betic Cordillera, Spain) – A petrochronological study. Tectonophysics 767, 128158. https://doi.org/10.1016/j.tecto.2019.06.028

Sanz de Galdeano, C., López-Garrido, A., 2016. The nevado-filábride complex in the western part of Sierra de los Filabres (Betic Internal Zone), structure and lithologic succession. Boletín Geológico y Minero 127, 823-836. DOI: 10.21701/bolgeomin.127.4.005

Sanz de Galdeano, C., Delgado, F., López-Garrido, A.C., 1995. Estructura del Alpujárride y del Maláguide al NW de Sierra Nevada (Cordillera Bética). Revista de la Sociedad Geológica de España 8, 239-250.

Tanner, P.W.G., 2016. A new model for the formation of a spaced crenulation (shear band) cleavage in the Dalradian rocks of the Tay Nappe, SW Highlands, Scotland. Journal of Structural Geology 84, 120-141. https://doi.org/10.1016/j.jsg.2015.11.007

Tendero, J.A., Martín-Algarra, A., Puga, E., Díaz de Federico, A., 1993. Lithostratigraphie des métasédiments de l'association ophiolitique Nevado-Filabride (SE Espagne) et mise en évidence d'objets ankéritiques évoquant des foraminifères planctoniques du Crétacé : conséquences paléogéographiques. Comptes Rendus de l'Académie des Sciences de Paris 316, 1115-1122.

Tubía, J.M., Gil-Ibarguchi, J.I., 1991. Eclogites of the Ojén nappe: a record of subduction in the Alpujárride complex (Betic Cordilleras, southern Spain). Journal of the Geological Society, London 148, 801-804. https://doi.org/10.1144/gsjgs.148.5.0801

Vissers, R.L.M., 1981. A structural study of the central Sierra de los Filabres (Betic Zone, SE Spain) with emphasis on deformational processes and their relation to the Alpine metamorphism. PhD Thesis, University of Amsterdam.

Zevenhuizen, W.A., 2022. Lithostratigraphy and structure of the Macael marbles (Betic zone, Spain). Boletín Geológico y Minero 133, 195-223. http://dx.doi.org/10.21701/bolgeomin/133.2/009

7. Deciphering western Mediterranean kinematics using metamorphic porphyroblasts from the Alpujárride Complex (Betic Cordillera)

Alejandro Ruiz-Fuentes[1], Domingo G.A.M. Aerden[1,2]

[1] *Departamento de Geodinámica, Universidad de Granada, Av. Fuentenueva, 18071, Granada, Spain*

[2] *Instituto Andaluz de Ciencias de la Tierra, CSIC/Universidad de Granada, Av. de las Palmeras 4, 18100, Armilla, Granada, Spain*

Published on: Journal of Structural Geology, v. 168 (2023), 104823
https://doi.org/10.1016/j.jsg.2023.104823
JCR Impact Factor: 3.366 (2021)

Abstract

3D microstructural analysis of porphyroblast inclusion trails using X-ray Computed Tomography is integrated with analysis of field structures to unravel the Alpine deformation history of the Alpujárride Complex, which constitutes the partially submerged metamorphic core of the Gibraltar Arc. Prograde metamorphism in the complex has been traditionally linked to a 'D_1' event witnessed by inclusion trails in garnet porphyroblasts. Orientation data for these microstructures reveal three age groups with differently oriented axes of inclusion-trail curvature (known as FIA). The successive development of FIAs trending WNW-ESE, ENE-WSW and NNW-SSE is shown and correlated with the Paleogene-Neogene relative plate-motion paths of Africa, Iberia and the Alborán Domain as known from paleomagnetic data. During the late-metamorphic evolution of the Alpujárride Complex, after garnet growth had ceased, two steeply dipping crenulation cleavages and associated folds with roughly suborthogonal N-S and E-W trends developed, in addition to two subhorizontal ones. Inclusion trails are also found to exhibit a general preference for subvertical and subhorizontal orientations, suggesting a protracted orogenic evolution characterized by multiple stress permutations causing alternations of crustal shortening and gravitational collapse.

Keywords: Alpujárride complex, Betic cordillera, Alpine orogeny, Foliation intersection axes, X-ray computed tomography

7.1. Introduction

In the Alpujárride Complex of the Betic Cordillera, a succession of at least three tectonic foliations and associated fold sets has been recognized but no consensus has been reached on their tectonic significance (extension, compression, transpression, etc.) and kinematics (see review in e.g. Williams and Platt, 2017; Jabaloy-Sánchez et al., 2019a). These structures are predated by one or several foliations that are only preserved as inclusion trails within garnet porphyroblasts. The latter grew during prograde metamorphism, whereas the main external fabrics formed during decompression. This study focuses on the geometry and preferred orientations of these relic microstructures using oriented thin sections and X-ray computed microtomography (XCT) in 60 samples that span about 200 km distance in E-W direction. This microstructural work is integrated with conventional analysis of structural relationships in outcrop along various transects.

The principle difficulty for interpreting the tectonic significance of relic foliations has traditionally been that their original orientation was uncertain. In recent decades, however, remarkably consistent orientations of inclusion trails found in numerous mountain belts suggest that they preserve the original orientations in which they formed due to a general lack of porphyroblast rotation (e.g. Fyson, 1980; Bell et al., 1992; Hayward, 1992; Aerden, 1995, 1998, 2004; Bell and Forde, 1995; Bell and Welch, 2002; Stallard and Hickey, 2001; Bell et al., 2003; Ham and Bell, 2004; Sayab, 2005; Cihan et al., 2006; Sanislav, 2010; Sanislav and Bell, 2011; Shah et al., 2011; Skrzypek et al., 2011; Bell and Sapkota, 2012; Abu Sharib and Sanislav, 2013; Aerden et al., 2010, 2013, 2021, 2022; Sayab et al., 2016). Inclusion trail data in these studies have consequently allowed extending tectonic reconstructions further back in time and in more detail. Of particular interest are the orientations of so called Foliation Intersection- or Inflexion-Axes (Bell et al., 1995), abbreviated as FIA (equivalent to relative porphyroblast-matrix rotation axes) as they are thought to form normal to the direction of tectonic transport or crustal shortening. Aerden et al. (2022) recently presented a collection of ca. 350 FIA data from the Betic-Rif orogen and showed that they cluster in three sets with distinctive trends (WNW-ESE, NE-SW, and NNW-SSE). Relative timing criteria and Sm–Nd garnet dating supported the sequential formation of the three FIA sets, from the Late Eocene to the Early Miocene, oriented normal to (changing) relative plate-motion vectors between Africa, Iberia and the Alborán Domain. Most of Aerden et al.'s data, however, were collected in the Nevado-Filábride and Sebtide complexes with only 47 individual FIAs coming from the Alpujárride Complex, despite its much larger total outcrop area compared to the other two complexes. In this paper, we present 647 new individual plus 25 average FIAs for the Alpujárride Complex and document their relationships with polyphase structures and fabrics recognizable in the field. This evidence confirms the existence of three FIA sets in the Betic-Rif orogen and supports their relationship with orogen dynamics and the Tertiary paleogeographic evolution of the Western Mediterranean region.

7.2. Geological setting

7.2.1. The Betic Cordillera

The Betic Cordillera (Fig. 7.1) of southern Spain is situated at the western termination of the Mediterranean Alpine system and constitutes the northern branch of the Gibraltar Arc. Its 'Internal Zones' comprise a stack of metamorphic complexes arranged, from bottom to top, as the Nevado-Filábride, Alpujárride and Maláguide complexes. The first is generally considered part of subducted and exhumed South-Iberian crust (Platt et al., 2006; Gómez-Pugnaire et al., 2012; Rodríguez-Cañero et al., 2018), whereas the Alpujárride and Maláguide complexes jointly constitute the so called 'Alborán Domain' which constitutes the core of the Gibraltar Arc and crops out also in the Rif mountains of northern Morocco. The equivalent units of the Alpujárride and Maláguide complexes are called Sebtide complex and Ghomaride complex there. The Alborán domain is derived from a continental fragment known as AlKaPeCa (Bouillin, 1986) or Mesomediterranean Microplate (Guerrera et al., 1993) originally situated east or south-east of Iberia (see review in Guerrera et al., 2021). Westward drift of the Alborán Domain, independent of continuous N–S to NW-SE-changing Iberia-Africa convergence, led to its eventual collision with the South Iberian paleomargin and the development of an external fold-and-thrust belt in Mesozoic and Cenozoic sedimentary rocks of shelf and basin environments corresponding to the present External Zones and Flysch Units (or Campo de Gibraltar Complex), respectively. Cover sediments of the Alborán Domain appear at the front of the Internal Zones as several tectonic slices known as the Frontal Units (or Dorsale Calcaire). These are overthrusted by the Alpujárride-Maláguide stack, but also partially backthrusted onto these complexes (Jabaloy-Sánchez et al., 2019b).

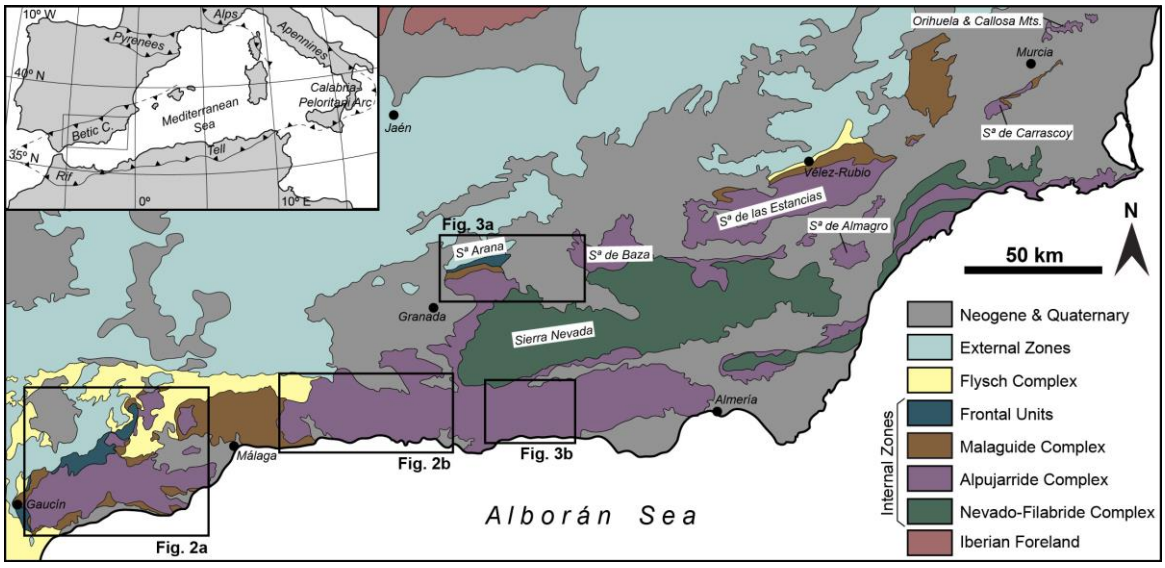

Fig. 7.1. Geological map of the Internal Zones of the Betic Cordillera, which as the more detailed maps of Figs. 7.2 and 7.3 are based on IGME MAGNA 1/50 000 map series.

Pre-Alpine structures in the Paleozoic basements of the three complexes are only well preserved in the low-grade to non-metamorphic Maláguide Complex (e.g. Foucault and

Paquet, 1971; Balanyá, 1991; Cuevas et al., 2001; Martín-Algarra et al., 2009; Ruiz-Fuentes et al., 2022). In the Alpujárride and Nevado-Filábride complexes, their recognition is complicated by intense Alpine deformation and metamorphism, but nevertheless evidenced by geochronological and petrological data (e.g. Puga and Díaz de Federico, 1976; Sánchez-Navas et al., 2012, 2014, 2017; Acosta-Vigil et al., 2014; Massonne, 2014; Sanz de Galdeano and Ruiz Cruz, 2016).

The Maláguide Complex is only affected by Alpine metamorphism in its lower part, which reached sub-greenschist facies conditions (Nieto et al., 1994; Ruiz Cruz et al., 2005). The Alpujárride Complex underwent high-pressure/low-temperature (HP/LT) metamorphism in the Eocene (Platt et al., 2005; Bessière et al., 2022) followed by progressive heating during the Oligocene and exhumation in the Miocene (Aguado et al., 1990; Crespo-Blanc et al., 1994; Sosson et al., 1998; Sánchez-Rodríguez and Gebauer, 2000; Esteban et al., 2004; Massonne, 2014). Exhumation of the complex was synchronous with HP metamorphism in the Nevado-Filábride Complex (López Sánchez-Vizcaíno et al., 2001; Platt et al., 2006; Kirchner et al., 2016), which was exhumed in the late Miocene (Johnson et al., 1997). Recent geochronological and petrological evidence, however, indicates that the Nevado-Filábrides may have experienced an earlier HP metamorphic event in the Eocene, synchronous with that of the Alpujárride Complex (Augier et al., 2005; Li and Massonne, 2018; Porkoláb et al., 2022; Aerden et al., 2022).

7.2.2. Alpujárride Complex

The Alpujárride Complex has been traditionally subdivided in a large number of nappe units defined and named in restricted study areas (e.g. Los Reales nappe (Tubía, 1988), Sayalonga unit (Aldaya et al., 1979), Murtas nappe (Aldaya, 1969), La Plata nappe (García-Dueñas and Navarro-Vilá, 1976), etc.). Attempts to regionally correlate these units resulted in partially discrepant proposals (see Sanz de Galdeano and López-Garrido, 2003 for a review). In the Central and eastern Betics, Azañón et al. (1994) distinguished five units called, from bottom to top, the Lújar-, Escalate-, Herradura-, Salobreña- and Adra units. Tubía et al. (1992), Sanz de Galdeano and López-Garrido (2003) and Martín-Algarra et al. (2004) proposed three main units, identified as the Lower-, Intermediate- and Upper Units. The latter subdivision is followed in this paper.

The Lower Alpujárride units are composed of Permo-Triassic phyllites and marbles that preserve relics of blueschist-facies metamorphism dated late-Eocene (Azañón and Crespo-Blanc, 2000; Bessière et al., 2022). The Intermediate and Upper units include a portion of Paleozoic basement composed of high-to medium grade migmatites, gneisses and graphite schists overlain by Permo-Triassic light-colored schists and quartzites, phyllites and marbles. In the Western Betics, the Intermediate unit hosts rare eclogite lenses with Jurassic protolith ages (Tubía and Gil-Ibarguchi, 1991; Sánchez-Rodríguez and Gebauer, 2000), whereas the Upper unit (Los Reales nappe) contains a several kilometer thick peridotite slab (Ronda peridotites) at the base of the crustal sequence.

In the Montes de Málaga and Fuengirola areas, the boundary between the Upper Alpujárride units and the Maláguide complex has proven difficult to identify because of similar lithologies and metamorphic grades on both sides. In the Montes de Málaga, an extra 'Benamocarra unit' has been defined with transitional characteristics (e.g. Estévez González and Chamón Cobos, 1978; Aldaya et al., 1979; Elorza and García-Dueñas, 1981). Tubía and Navarro-Vilá (1984) and Tubía (1988) placed the contact at the base of a level of brownish schists containing post-kinematic andalusite and garnet porphyroblasts.

Most structural research in the Alpujárride Complex considers four main deformation phases (D_1-D_4), the first of which corresponds to relics of a HP/LT foliation (S_1) preserved within garnet porphyroblasts and microlithons of the main S_2 regional cleavage (e.g. Azañón and Goffé, 1997; Booth-Rea et al., 2002). The latter is associated with small-scale tight-to isoclinal F_2 folds, except for a possible km-scale structure interpreted in the Sierra de Lujar (Simancas, 2018). In general, however, regional-scale folds have been classified as D_3 structures associated with S_3 crenulation cleavage. They mostly have N- to NW-vergence except in a zone close to the boundary with the External Zones, where an opposite vergence is observed as discussed later. The above succession of ductile structures and fabrics are cut by a series of low-angle detachment faults and shear bands (D_4) with top-to-the-North movement.

D_1 is generally attributed to approximately N–S directed Africa-Eurasia convergence, subduction and crustal shortening in the Eocene to Oligocene, but its precise kinematics (polarity of subduction) has remained uncertain. D_2 has been variably interpreted in terms of extensional exhumation along a low-angle crustal shear zone (Azañón et al., 1997; Balanyá et al., 1997; Azañón and Crespo-Blanc, 2000; Alonso-Chaves and Orozco, 2007; Williams and Platt, 2017, 2018; Simancas, 2018), or transpressional exhumation along a sinistral NE-trending steep shear zone (Tubía et al., 1992; Rossetti et al., 2005). D_3 structures have been alternatively attributed to top-to-the-N/NE crustal extension (Orozco et al., 1998, 2004; Platt, 1998) or thrusting (Cuevas, 1991; Tubía et al., 1992; Simancas and Campos, 1993; Balanyá et al., 1993, 1997, 1998; Azañón et al., 1997; Azañón and Crespo-Blanc, 2000; Simancas, 2018). No agreement exists either on the extensional or thrust character of late D_4 faults (Cuevas et al., 1986; Cuevas, 1991; Simancas and Campos, 1993; Crespo-Blanc et al., 1994; Azañón and Crespo-Blanc, 2000; Simancas, 2018).

7.3. Structural relationships in outcrop

Orientation data for crenulation-cleavages collected throughout the Alpujárride Complex (Figs. 7.2 and 7.3) display a bimodal distribution of steep and shallow dips, which reflects the existence of at least two different age sets exhibiting overprinting relationships in outcrop (Figs. 7.4–7.6). In order to avoid confusion and maintain the traditional denomination of crenulation cleavage in the Alpujárride Complex as "S_3", we will further refer to both sets as S_{3V} (steep to subvertical dips, ~60-90º) and S_{3H} (gentle to subhorizontal dips, ~ 0-30º), but note that we interpret a different timing for them. Studied

lineations are mainly crenulation lineations, which are usually parallel to intersection and mineral lineations when found in nearby outcrops.

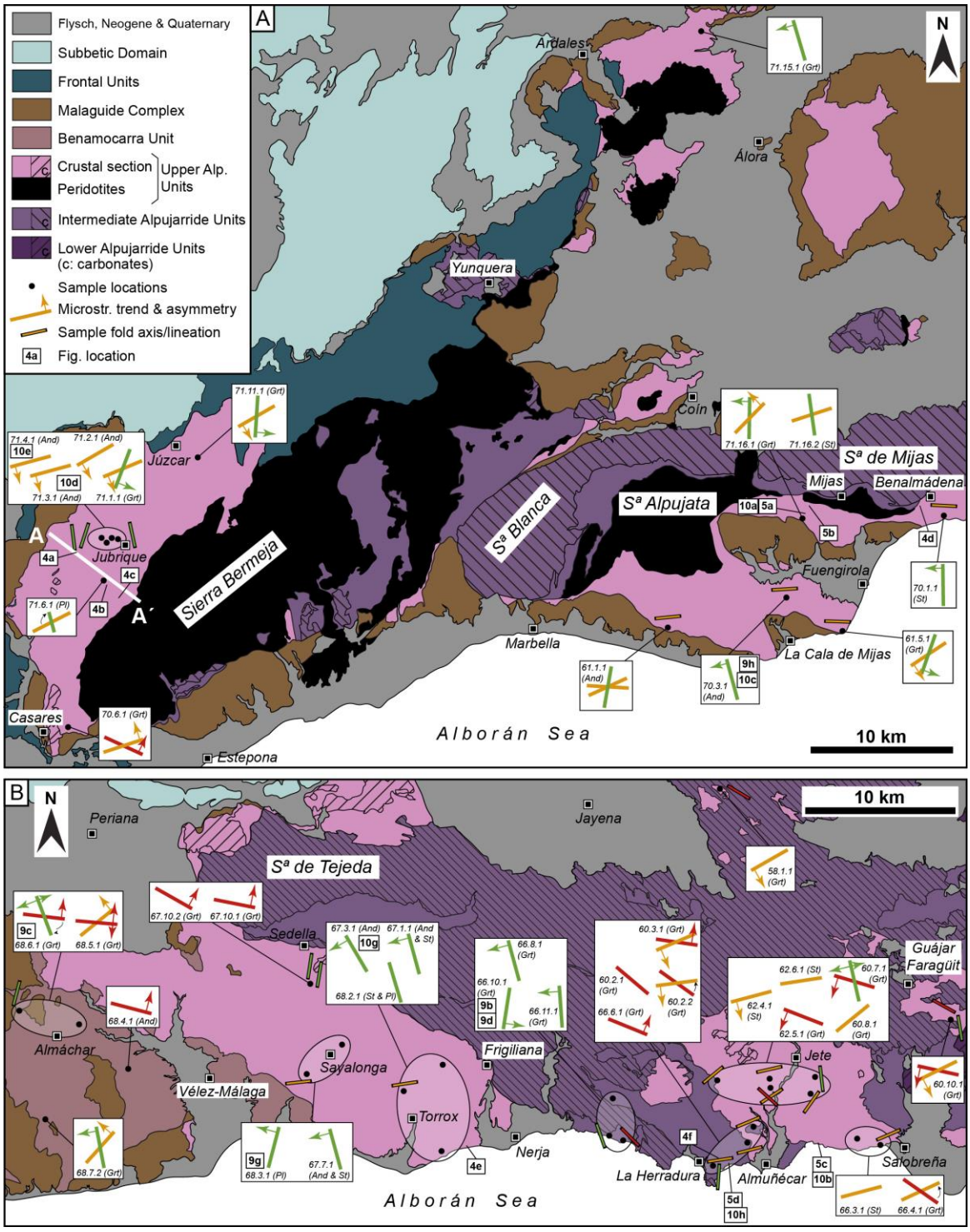

Fig. 7.2. Geological maps of the Jubrique-Fuengirola (A) and Torrox-Almuñécar (B) areas showing the location of cross sections, outcrop and microstructural images (Figure numbers in small boxes), average microstructural trends indicated with red, orange and green bars corresponding to the three trend ranges defined in Fig. 7.11, and tectonic transport directions (thin arrows) deduced from inclusion-trail asymmetries. (For interpretation of the references to color in this figure legend, the reader is referred to the Web version of this article.)

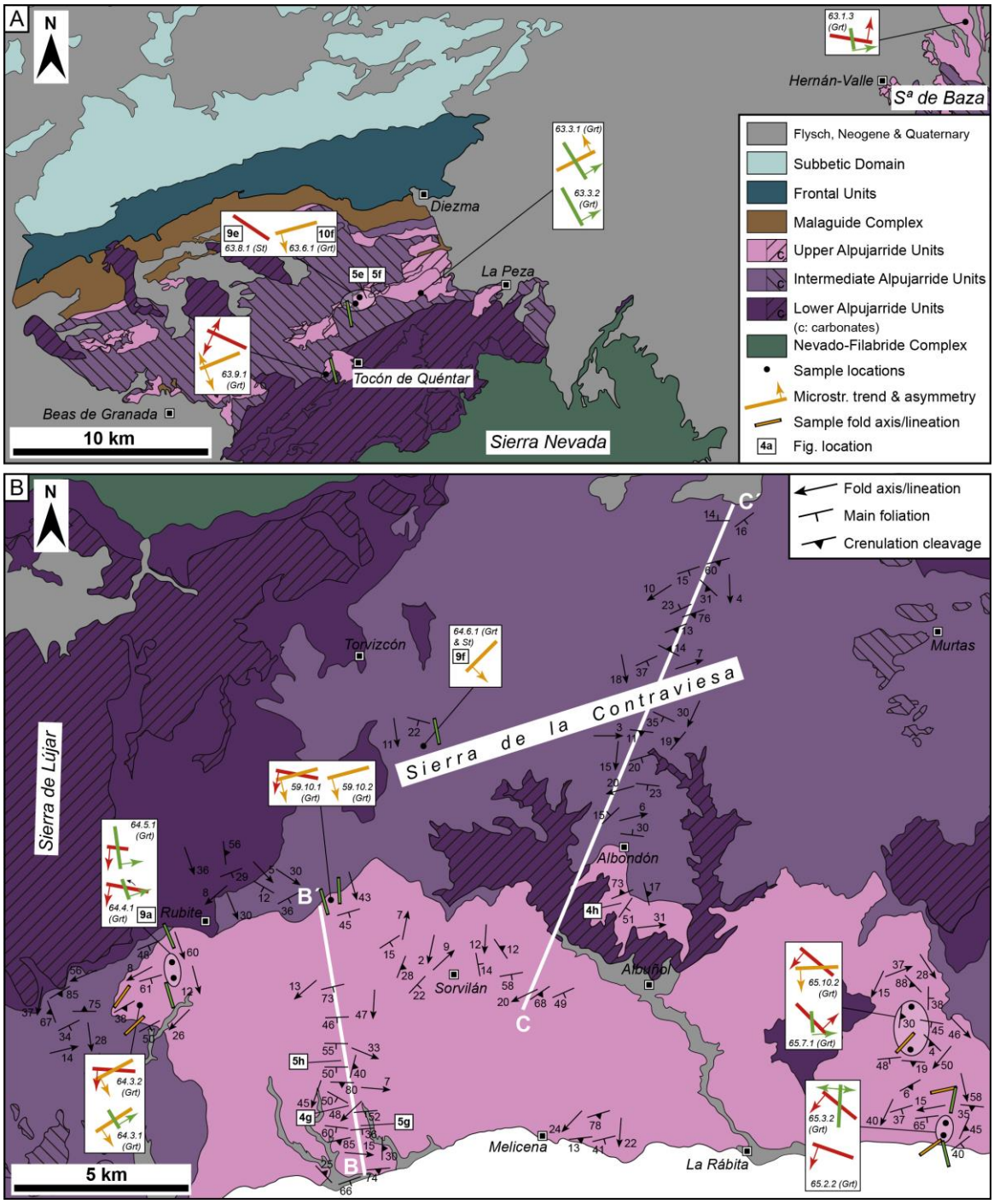

Fig. 7.3. Geological maps of the Tocón de Quéntar (A) and Contraviesa (B) areas showing the location of cross sections, outcrop and microstructural images (Figure numbers in small boxes), average microstructural trends indicated with red, orange and green bars corresponding to the three trend ranges defined in Fig. 7.11, and the directions of tectonic transport (thin arrows) deduced from inclusion-trail asymmetries. Map 'A' is partially based on Sanz de Galdeano et al. (1995). (For interpretation of the references to color in this figure legend, the reader is referred to the Web version of this article.)

7.3.1. Jubrique area

In the Jubrique area (Fig. 7.2a), S_2 is strongly overprinted or fully transposed by a gently west-dipping S_{3H} (Fig. 7.4a, b, c, 7.7 and 7.8) associated with synkinematic andalusite porphyroblasts. S_2 generally dips slightly steeper NW to WSW, but locally in opposite (E) direction, especially in the lower part of the schists and quartzites and in the underlying gneisses. S_{3H} reaches its maximum intensity in the middle part of the schist-quartzite succession. Fold- and crenulation axes have NNESSW to NNW-SSE trends, but a younger set of E-W-trending kink-like folds was identified in the upper part of the succession.

7.3.2. Fuengirola area

In the Fuengirola area (south-east of the Sierra Alpujata peridotites; Fig. 7.2a) S_2 is variably overprinted by either an S_{3V} or S_{3H} (Figs. 7.4, 7.5 and 7.7). South of Sierra Alpujata, S_{3H} is well developed and associated with gently E-dipping shear planes and tight to isoclinal F_{3H} folds with E-W trends. Andalusite porphyroblasts grew synchronous with this foliation and postdate an earlier sillimanite-bearing schistosity (S_2). South of Benalmádena, S_{3H} is more widely spaced and associated with relatively open folds (Fig. 7.4d).

Between Mijas and Fuengirola (Fig. 7.2a), two principle sets of S_{3V} and S_{3H} crenulation cleavages were found although their relative timing could not be determined in this area. The first strikes NNW-SSE associated with (Fig. 7.5a and b) ENE-vergent folds. An additional weaker set of E-W trending folds is also present, which become increasingly important in the Torrox and Almuñécar areas further east (see sections 3.3 and 3.4). In the Contraviesa area, overprinting relationships between E-W and N–S folds (see section 3.6) suggest a later timing of the first. Between La Cala de Mijas and Fuengirola and near Benalmádena, S_{3V} is weaker although F_{3V} folds with NNW-SSE trends are still abundant. From there moving westward, the intensity of S_{3V} diminishes further until, near the eastern boundary of the Sierra Alpujata peridotites, it disappears completely.

7.3.3. Torrox area

The Torrox area (Fig. 7.2b) is characterized by a pervasive S_{3H} transposing S_2 (Fig. 7.4e) in the lower part of the micaschists above the Torrox orthogneiss body. In higher levels, S_{3H} is weaker or absent but F_{3H} folds are locally still prominent. A large number of orientation data for folds and lineations collected by Alonso-Chaves and Orozco (2012) complemented with our own data (Fig. 7.7) indicate a broadly bimodal trend distribution with a strong E-W maximum and a more dispersed NNW-SSE maximum. Note that fold axes and lineations measured in the Fuengirola area (Fig. 7.7), although less numerous, exhibit a similar bimodal distribution (section 3.2).

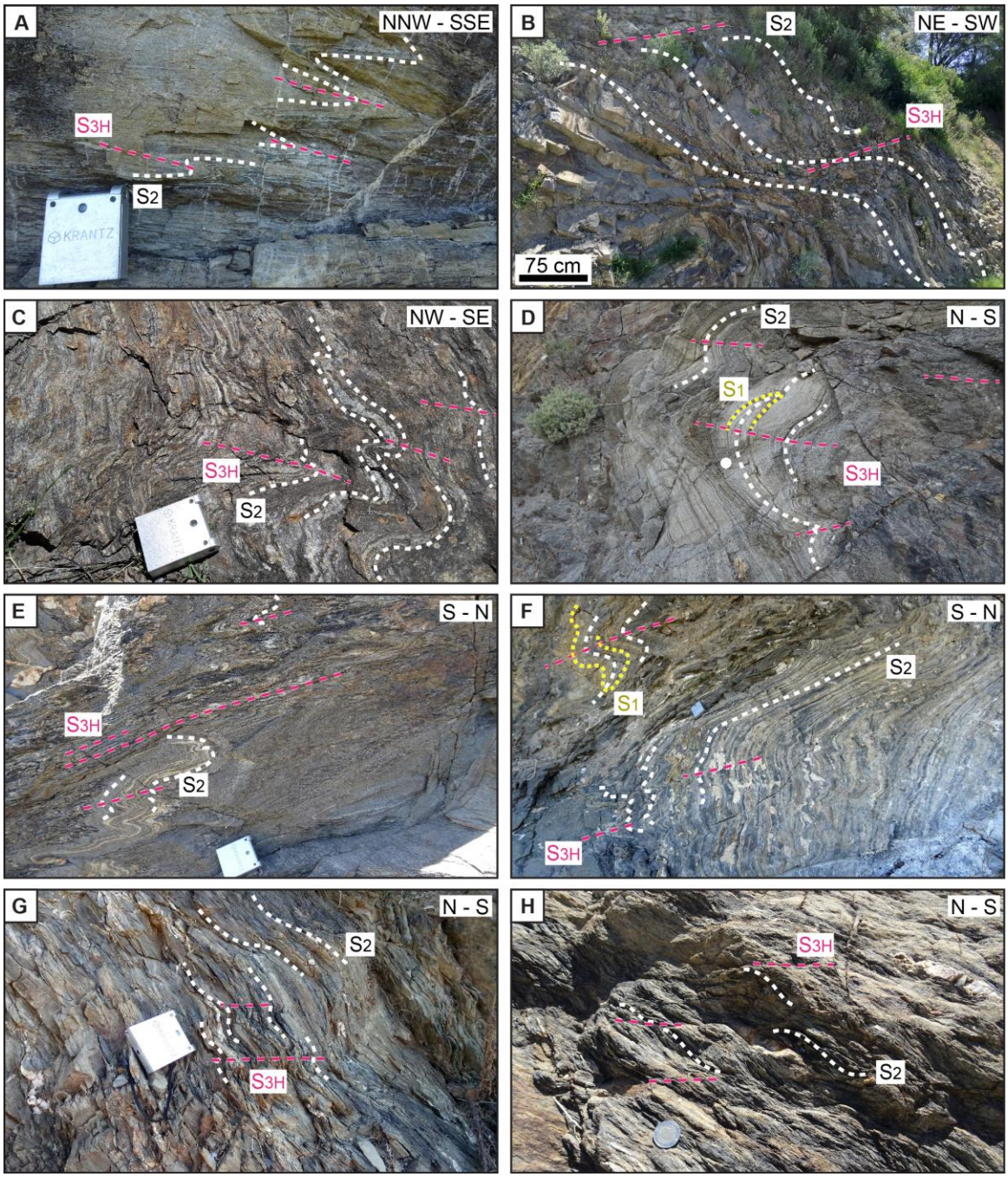

Fig. 7.4. Outcrop images of S_{3H}. A) Intensely developed S_{3H} in quartzites situated near the middle of the Jubrique schist-quartzite formation. B) Widely spaced shear bands in the lower levels of the same formation. C) F_{3H} folds in gneisses of the Jubrique Fm. D) Folds associated with S_{3H} in the Benalmádena area. E) S_{3H} near Torrox transposing S_2 in a pelitic layer above a less deformed psammitic layer showing F_{3H} folds. F) Interference of F_2 and F_{3H} folds near La Herradura. G) Coeval D_{3H} folds and shear bands in the Contraviesa area. H) Subhorizontal shear bands south of Albondón genetically related to S_{3H}.

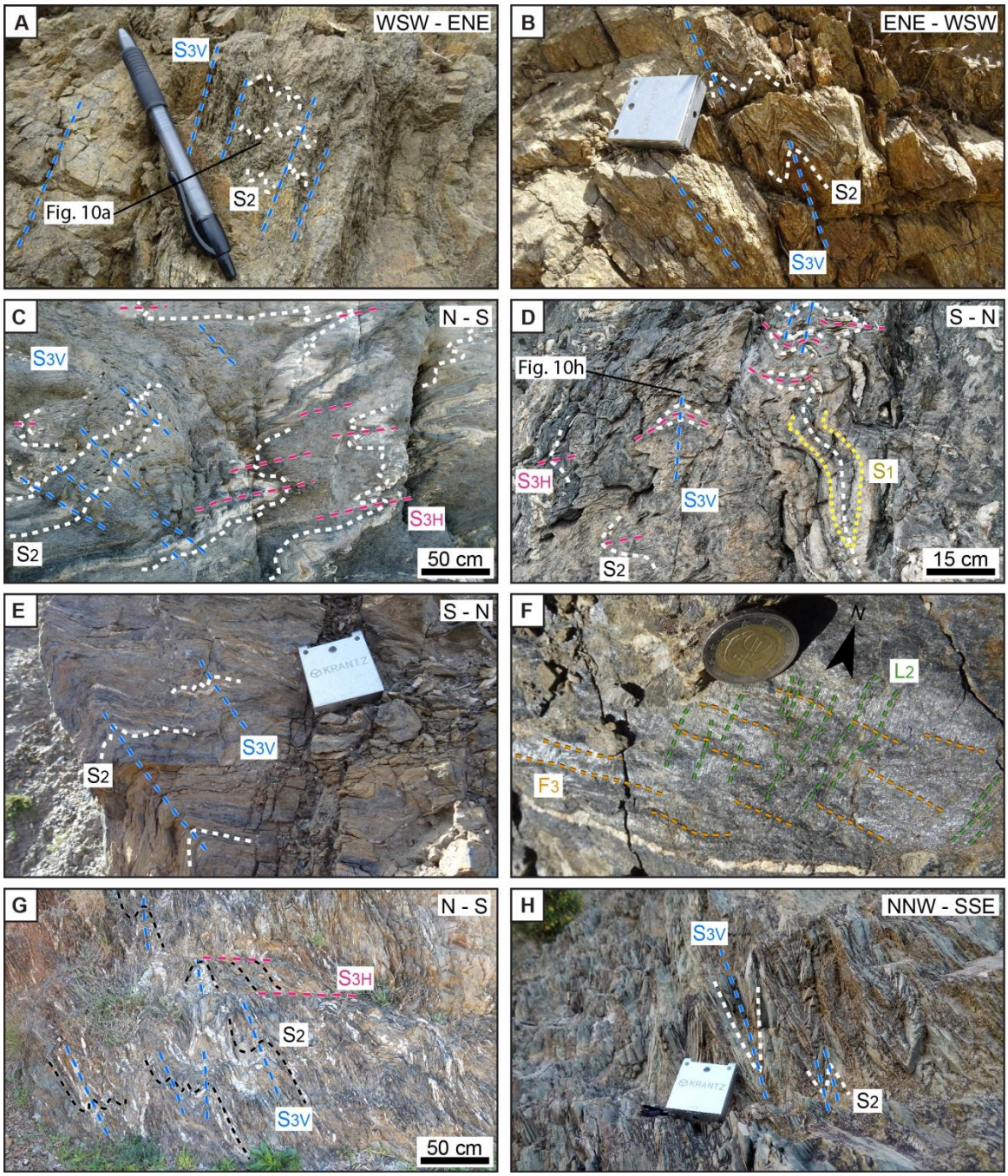

Fig. 7.5. Outcrop images of S_{3V}. A) S_{3V} is intensely developed and becomes the main foliation in outcrop south of Mijas. Fig. 7.10a shows a microscope image of the S_{3V} crenulations. B) Intensely folded gneisses south of Mijas. C) S_{3V} overprinting D_{3H} folds east of Almuñécar. Fig. 7.10b shows a microscopic image of the same outcrop. D) Fold interference in amphibolites of the Herradura nappe west of Almuñécar with S_{3V} overprinting S_{3H}, in turn overprinting an F_2 fold. Fig. 7.10h shows a microscope image of the same outcrop. E) South-vergent D_{3V} folds north of Tocón de Quéntar. F) N–S L_2 overprinted by E-W F_{3V} folds north of Tocón de Quéntar. G) D_{3V} folds cut by D_{3H} shear bands in the Contraviesa area. H) S_{3V} partially transposing S_2 in the Contraviesa area.

7.3.4. Almuñécar area

In the Almuñécar area (Fig. 7.2b), S_{3H} is generally less intense as in the Torrox area but still locally transposes S_2. F_{3H} folds (Fig. 7.4f) have ENE-WSW to E-W trends and inconsistent vergences. An L_3 lineation is visible in outcrop parallel to fold axes. In the southernmost part of the area, between La Herradura and Salobreña, a steeply dipping widely spaced crenulation cleavage (S_{3V}) with ENE-WSW strike and northward vergence was observed to overprint S_{3H} (Fig. 7.5c and d).

7.3.5. Tocón de Quéntar – Sierra de Baza area

In the Tocón de Quéntar area (Fig. 7.3a), micaschist outcrops are scarce and correspond to small weathered klippe located on top of carbonate rocks by means of low angle faults probably related to the D_4 low-angle faults and shear bands in the Contraviesa area. The main foliation is overprinted by a spaced S_{3V} crenulation cleavage associated with ENE-WSW- to NE-SW trending folds (Fig. 7.5e and f, 7.7). Interestingly, the vergence of these folds is southward (Fig. 7.5e), opposite to that observed in the Contraviesa area. Orientation data for pre-D_3 folds and lineations suggest two sets of structures with NNW-SSE versus NW-SE to WNW-ESE trends.

7.3.6. Contraviesa area

In the Contraviesa area (Fig. 7.3b), S_2 dips moderately to steeply south (Fig. 7.7) and is overprinted with variable intensity by WSW-ENE striking S_{3V} or S_{3H} (Fig. 7.5g, h, 7.8b, c). As previously described by Cuevas (1991), S_{3V} is particularly well developed in the Upper Alpujárride unit (Adra nappe) cropping out in the south of the Contraviesa area. Within the Intermediate Alpujárride unit (Murtas nappe) further north, S_{3V} becomes scarcer as D_{3H} structures make their appearance (Fig. 7.8). The latter correspond to south-verging tight to open folds with subhorizontal axial planes and top-to-the north shear bands and faults which postdate D_{3V} structures (Fig. 7.4g, h and 7.5g). F_2 folds and L_2 lineation have variable plunges and plunge directions, ranging from SE to SW, and define a broad N–S maximum (Fig. 7.7). Plunge directions of F_{3V} and F_{3H} folds show an even larger spread from E to S to W with a weak E-W maximum. In several outcrops an E-W to NE-SW striking S_{3V} was observed deforming an older steeply WSW dipping foliation, and resulting in very steeply SW plunging fold- and crenulation axes. This is consistent with structural data of Azañón et al. (1997) from the eastern Sierra de la Contraviesa, which also show early NNE-SSW trending lineation and folds (their 'L_2') overprinted by ENE-WSW trending folds (their 'F_3'). Thus, the weakly bimodal distribution of D_2 and D_3 linear structures in the Contraviesa area probably reflects the superposition of ENE-WSW structures over older N–S ones. Note that equivalent structural data for the Tocón, Torrox and Fuengirola areas all exhibit similar bimodal trends (Fig. 7.7).

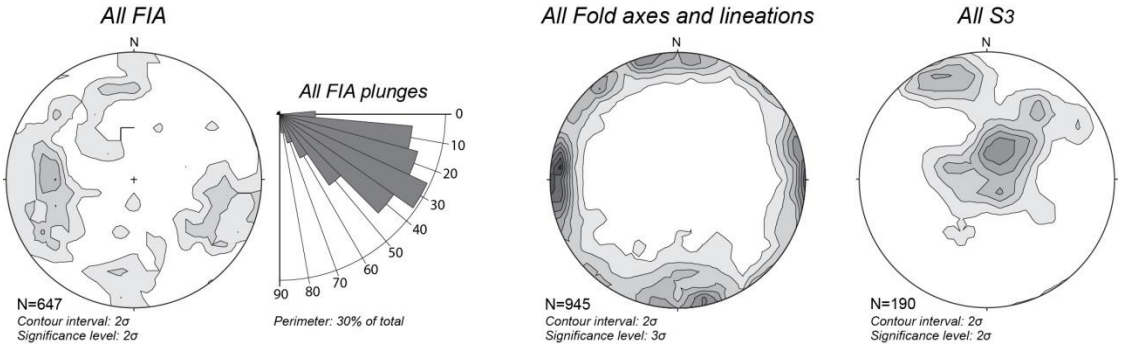

Fig. 7.6. Equal-area and lower-hemisphere projections for: total porphyroblast FIAs measured in all areas, all fold axes and lineations shown separately for different areas in Fig. 7.7, and a similar compilation of poles to all crenulation cleavages shown in Fig. 7.7. All equal-area projections were made with the program 'Stereonet' by Allmendinger et al. (2013) and use Kamb contours with contour interval and significance level set to 2 or 3σ (see figure).

7.4. Microstructural analysis

7.4.1. Microstructural approach

A total of 140 samples of medium-to high-grade metapelites containing garnet, staurolite, plagioclase and/or andalusite porphyroblasts (Figs. 7.9 and 7.10) were studied in thin section to analyze mineral relationships and to select appropriate samples for further microstructural analysis in additional differently oriented thin sections and X-ray computed micro-tomographies (XCT) (see XCT method on Supplementary Material 10.3.1). Section 10.3.2 (Supplementary material) lists the 60 selected samples, their locations and corresponding nappe units. Fig. 7.11a shows the general relationships between the principle index minerals in these rocks and the traditionally distinguished deformation phases. Sillimanite is a good marker of the high-temperature stage in high-grade rocks linked to the D_2 event. Andalusite mainly grew during D_3 (Cuevas, 1989; Azañón et al., 1998; Williams and Platt 2017), although we actually recognized three different types of andalusite porphyroblasts: (i) small equidimensional crystals with well-developed straight to sigmoidal inclusion trails indicating syn-D_3 growth (Fig. 7.10c, d and e), (ii) up to several cm long post-kinematic crystals overgrowing all matrix fabrics (Fig. 7.10f), and (iii) large crystals usually devoid of inclusion trails which appear broken, stretched (Fig. 7.10g) and partially replaced by fine-grained quartz-mica aggregates. The third type possibly corresponds to the pre-Alpine andalusite crystals reported by Sánchez-Navas et al. (2012) in the vicinity of the Torrox orthogneiss.

Whilst garnet porphyroblasts in our samples of Permo-Triassic metasediments can only be Alpine, those in Paleozoic dark schists could, in principle, also be Variscan. Nevertheless, an Alpine origin in both rock types is considered likely because (i) evidence for Variscan garnet growth has previously only been found in high-grade gneisses not studied herein, (ii) inclusion trails of garnets in samples from cover and basement rocks have similar orientations as shown further, and (iii) Sm–Nd ages of garnets in five Paleozoic schist samples from the Alpujárride- and Sebtide complexes are all Alpine (Farrell, 2019; Aerden et al., 2022).

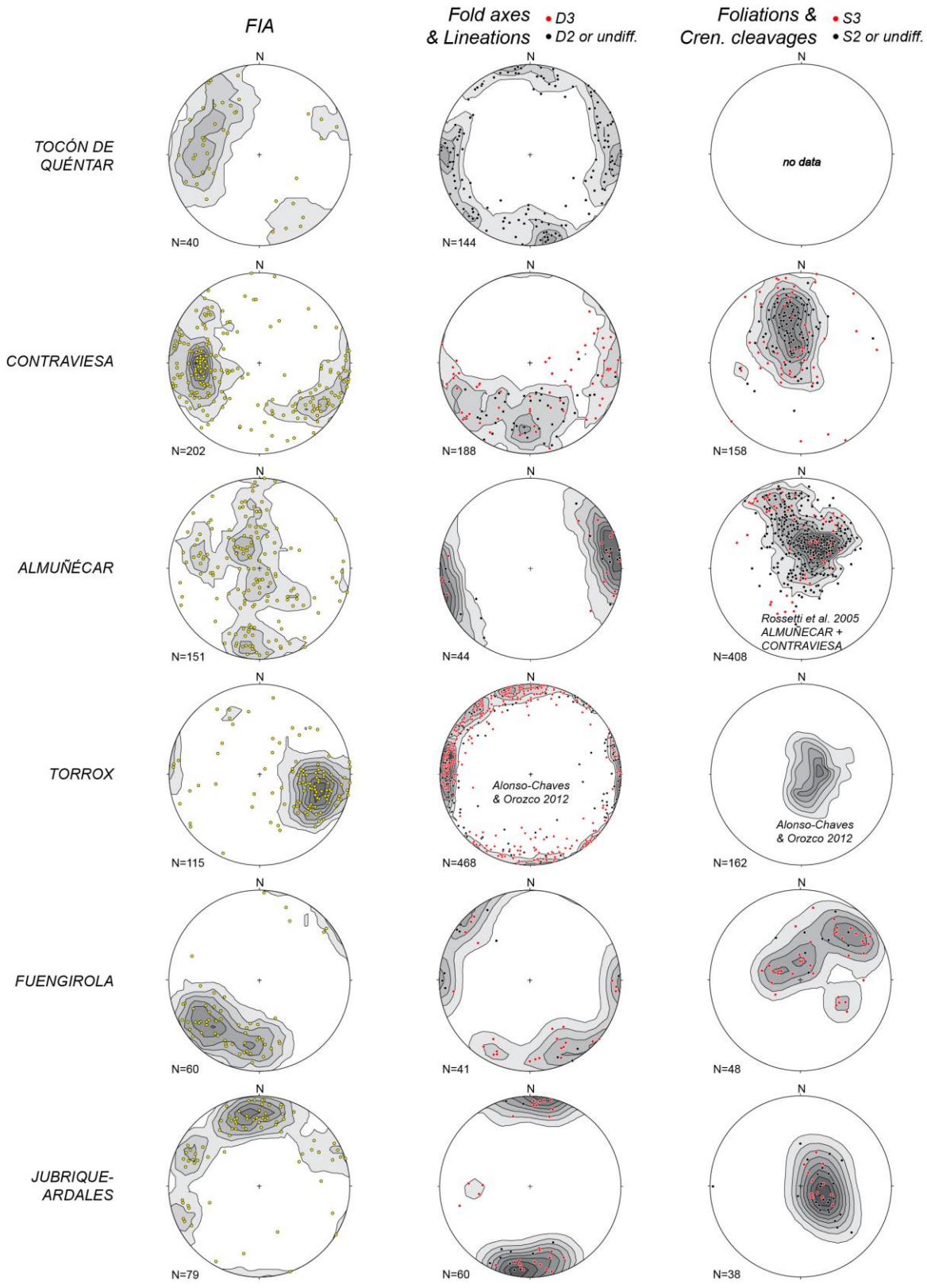

Fig. 7.7. Equal-area and lower-hemisphere projections for: porphyroblast FIAs measured in different areas, F_2/L_2 (black dots) and F_3/L_3 (red dots) fold axes and associated lineations measured in outcrop, and poles to the main foliation (S_2; black dots) and superposed crenulation cleavages (S_3; red dots). All equal-area projections were made with the program 'Stereonet' by Allmendinger et al. (2013) and use Kamb contours with both contour interval and significance level set to 2σ.

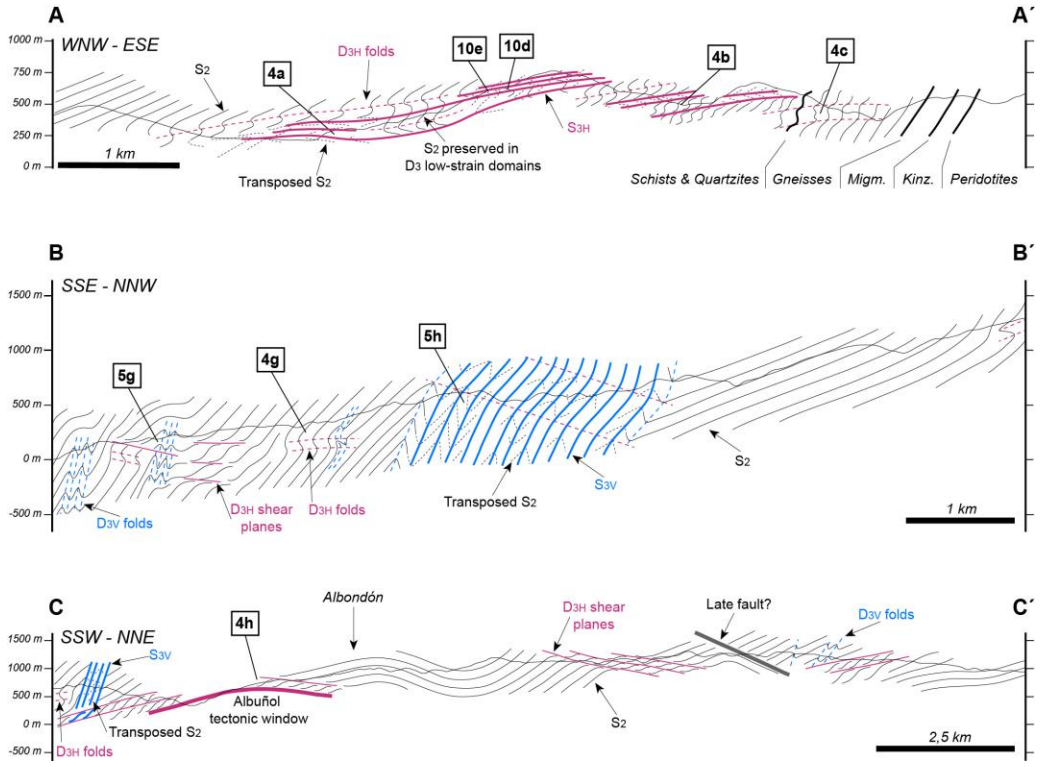

Fig. 7.8. Cross sections of the Jubrique (A-A′) and Contraviesa (B–B′ and C–C′) areas. White numbers in black squares correspond to Figure numbers.

The studied porphyroblasts host straight to weakly sigmoidal to spiral-shaped inclusion trails composed of quartz, graphite and/or opaque minerals (Figs. 7.9 and 7.10), although inclusion trails-free porphyroblasts are also common. Samples were initially studied in horizontal thin sections (regardless of the orientation of the matrix foliation and lineation), because of the advantage that the strike of relatively straight inclusion trails can be directly measured on such sections. Samples were classified in three groups. A first group of 36 samples contains garnet porphyroblasts with well-developed sigmoidal or spiral inclusions whose FIA can be readily measured in XCT scans. Some of these samples also contain planar inclusion trails whose orientations were also measured. A second group of 15 samples contains asymmetrically curved inclusion trails, but either less well developed in garnet porphyroblasts or well developed but hosted by other porphyroblastic minerals (andalusite, plagioclase, staurolite), which are less apt for XCT analysis because of a lower X-ray attenuation contrast with their mineral inclusions and the matrix. These samples were studied using the radial thin-sectioning technique of Hayward (1990) and Bell et al. (1995) by which the average orientation of porphyroblast FIAs in a sample can be determined. As we cut six vertical thin sections for each sample, our average FIAs are constrained to 30º trend ranges. A third group of 9 samples only contains porphyroblasts with relatively straight inclusion trails, whose strikes were measured in the initially cut horizontal thin sections. Microstructural data obtained from XCT scans and thin sections are presented in contoured equal-area projections made with 'Stereonet' (Allmendinger et al., 2013) and in moving-average rose diagrams, respectively, for each sample. The rose diagrams were made with the program 'MARD' (Munro and Blenkinsop, 2012). Due to space limitations, these diagrams are provided as

supplementary data together with a table summarizing the mean microstructural orientation in each sample (Supplementary Material 10.3.3, 10.3.4 and 10.3.5).

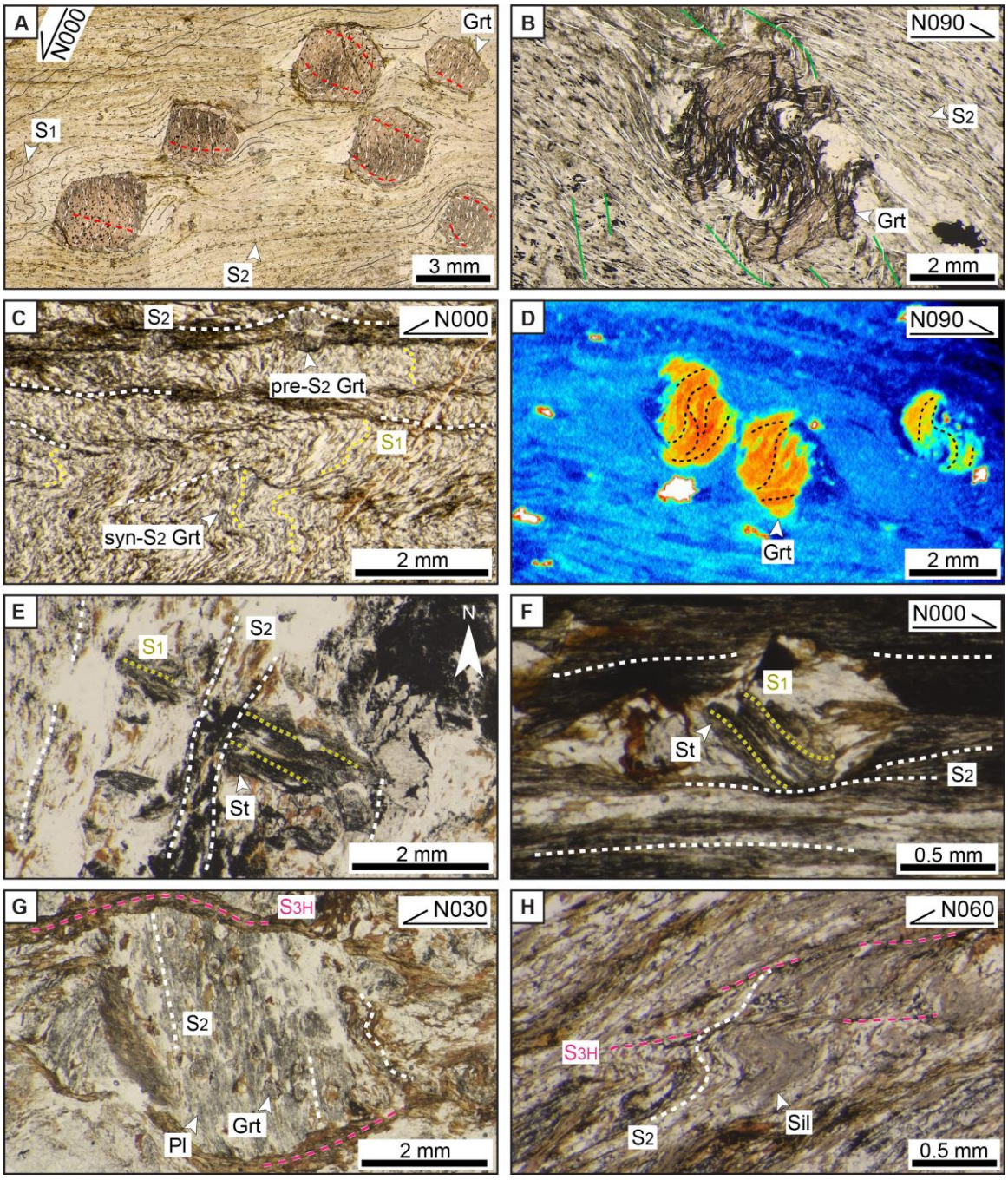

Fig. 7.9. Microstructural images (taken under plane polarized light except D which is an XCT image; half arrows indicate the upward direction together with the normal direction indicating the horizontal, geographic direction with numbers). A) Garnets with sigmoidal inclusion trails. The S_2 foliation and relics of S_1 are visible in the matrix. B) Garnet with sigmoidal inclusion trails with internal truncations. C) Syn-S_2 garnets of the Benamocarra unit in microlithons of an incipient S_2 foliation. D) XCT image of garnets hosting spiral shaped inclusion trails. Same sample as in B for comparison. E) Staurolite porphyroblasts whose straight inclusion trails are wrapped by S_2 (plain view, north is indicated by the arrow). F) Staurolite porphyroblast with weakly sigmoidal inclusion trails. G) Plagioclase with straight inclusion trails including tiny garnet porphyroblasts. H) S_{3H} folding sillimanite associated with S_2 in the Fuengirola area. Note local shear-band character of S_{3H}.

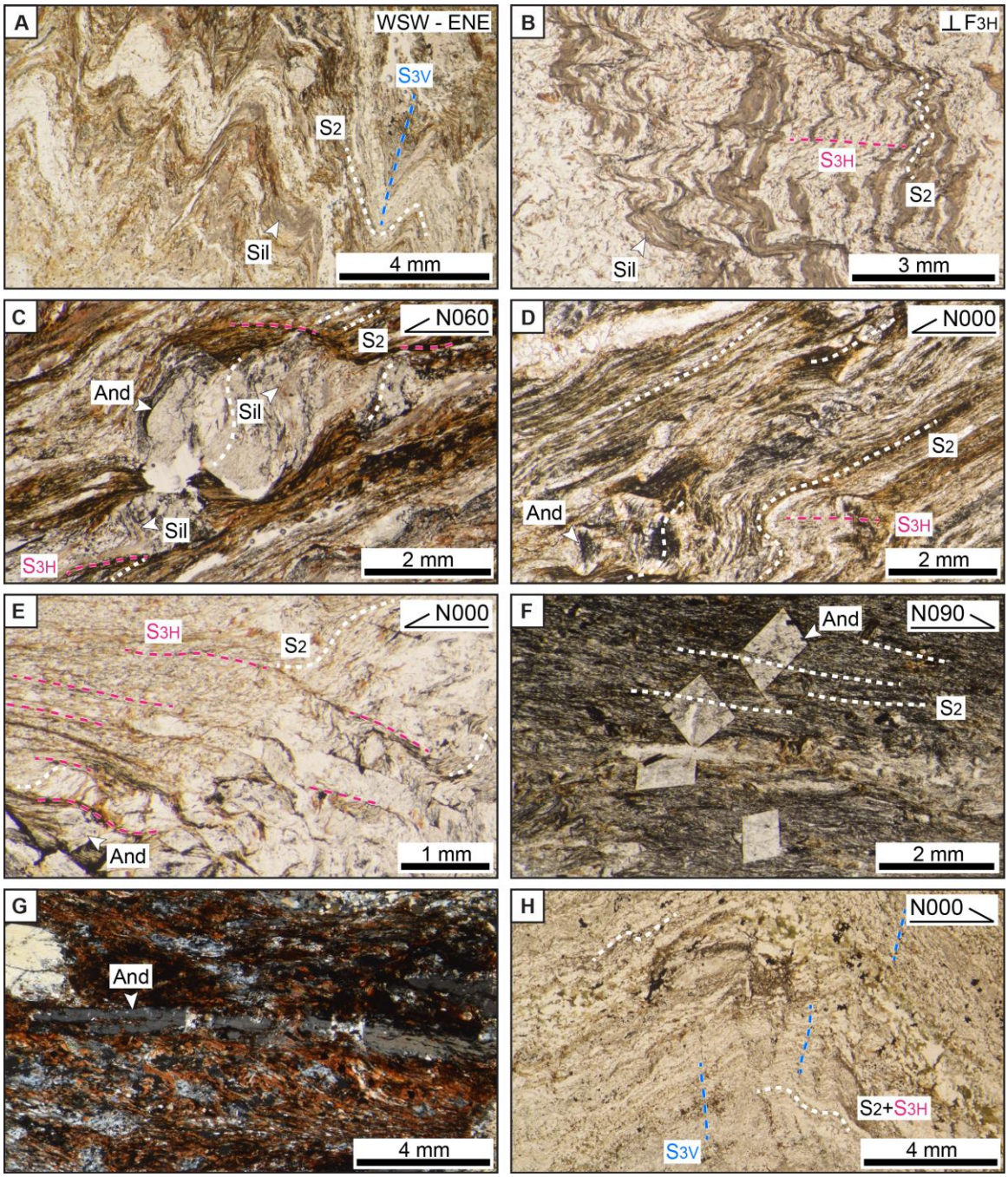

Fig. 7.10. Microstructural images (taken under plane polarized (A, B, C, D, E, F, H) or cross polarized light (G); half arrows indicate the upward direction together with the normal direction indicating the horizontal, geographic direction with numbers). A) Detail of outcrop image of Fig. 7.5a. Sillimanite is folded by S_{3V}. B) Detail of outcrop image of Fig. 7.5c. S_{3H} crenulates a sillimanite-bearing S_2. C) Syn-D_{3H} andalusite porphyroblasts include sillimanite-bearing S_2. D) Syn-D_{3H} andalusite porphyroblasts of the Jubrique area. E) S_{3H} partially transposes S_2 and is associated with andalusite growth. Jubrique area. F) Post-kinematic andalusite porphyroblasts of the Tocón de Quéntar area. G) Stretched andalusite porphyroblast adjacent to the Torrox gneiss which might be Variscan. H) Incipient S_{3V} affects S_2 and S_{3H} in the outcrop of Fig. 7.5d.

7.4.2. Relative timing criteria and microstructural sequence

Mean microstructural trends defined by FIAs and/or inclusion-trail strikes are plotted in rose diagrams for all porphyroblastic minerals collectively (Fig. 7.11b) and also separately for garnet versus plagioclase, andalusite and staurolite porphyroblasts (Fig. 7.11c). Three sets of microstructures are visible in these plots that define NNW-SSE (green), ENE-WSW (orange) and WNW-ESE (red) orientation maxima. Note that, whereas all three sets are present in garnet porphyroblasts, andalusite, staurolite and plagioclase porphyroblasts almost exclusively contain the NNW-SSE and ENE-WSW sets.

Relative timing criteria for microstructures with different trends include: (1) porphyroblasts with differently oriented FIAs in the core versus the rim (Fig. 7.12a and b), (2) porphyroblasts containing inclusion trails with different strikes in the core versus rim (Fig. 7.12c), (3) weakly crenulated inclusion trails whose axial planes can be taken as the direction of an incipient foliation (Fig. 7.12d), (4) inclusion trails hosted in garnet versus staurolite and andalusite, since the latter formed later (e.g. Balanyá et al., 1997; Azañón et al., 1997; Williams and Platt, 2017), (5) crenulation lineations in the matrix versus FIAs.

Fig. 7.11e summarizes timing relationships found in our samples following the above criteria. Mean microstructural trends are represented with red, orange or green symbols depending on their association with the WNW-ESE, ENE-WSW or NNW-SSE modal maxima in the rose diagram of Fig. 7.11b. In the case of a mean microstructural trend falling within the overlap zones between two trend groups its assignment to one of these groups was based on relative timing criteria with other microstructural trends in the sample or in nearby samples. The trends of matrix crenulations and fold axes measured in samples or their outcrops are also represented (star and triangle symbols).

Mutual relative-timing criteria between inclusion trails in porphyroblasts (five samples) suggest that WNW-ESE FIAs (red) formed first, followed by ENE-WSW FIAs (orange) and finally NNW-SSE ones (green). This succession is supported by the fact that matrix lineations and folds mainly have ’green’ and ’orange’ trends and that ’red’ FIAs almost exclusively occur within garnet porphyroblasts (Fig. 7.11c), whereas the two younger FIA sets are found equally in garnet, staurolite, andalusite and plagioclase porphyroblasts. One sample (63.8.1) contains a ’red’ FIA hosted by staurolite, which probably grew synchronous with garnets in other samples.

Sample 68.4.1, however, paradoxically contains a ’red’ FIA included by late (syn-D_{3H}) andalusite porphyroblasts post-dating garnet growth. Two possible explanations are (1) that these andalusites grew in a zone where ’red’ structural trends were preserved due to the partitioning of later deformations around it, or (2) grew in a pre-existing plunging fold which can create FIAs oblique to the shortening direction (see Fig. 5e of Aerden et al., 2022). Another contradictory relationship was found in sample 66.11.1, where garnets with ’green’ FIAs are surrounded by L_2 lineation and F_2 folds oriented within the ’red’

trend range (133/05). The proximity of this direction to the overlap zone with the 'green' trend range and the fact that neighboring sample 66.10.1 hosts similar matrix structures but trending slightly more NNW-SSE within the 'green' trend range suggests that 66.11.1 is an outlier and in fact belongs to the 'green' trend group. All other relative timing criteria between FIAs versus L_2 and F_2 folds are consistent with the sequence of 'red', 'orange' and 'green' microfabrics.

Relative timing relationships between FIAs and L_3 lineations and F_3 folds imply a repetition of 'orange' fabrics after 'green' ones. This follows from nine samples containing E-W to NE-SW trending L_3/F_3 surrounding inclusion trails with 'green' FIAs or strikes (Fig. 7.11e). Furthermore, syn-D_3 andalusite porphyroblasts preserve both 'green' and 'orange' FIAs that necessarily post-date all garnet FIAs and S_2. Indeed, both S_{3H} and S_{3V} matrix crenulations deform sillimanite fibers associated with S_2 (Figs. 7.9h, 7.10a, 7.10b, 7.10c and 7.11a; Cuevas 1989; Azañón et al., 1998; Williams and Platt 2017).

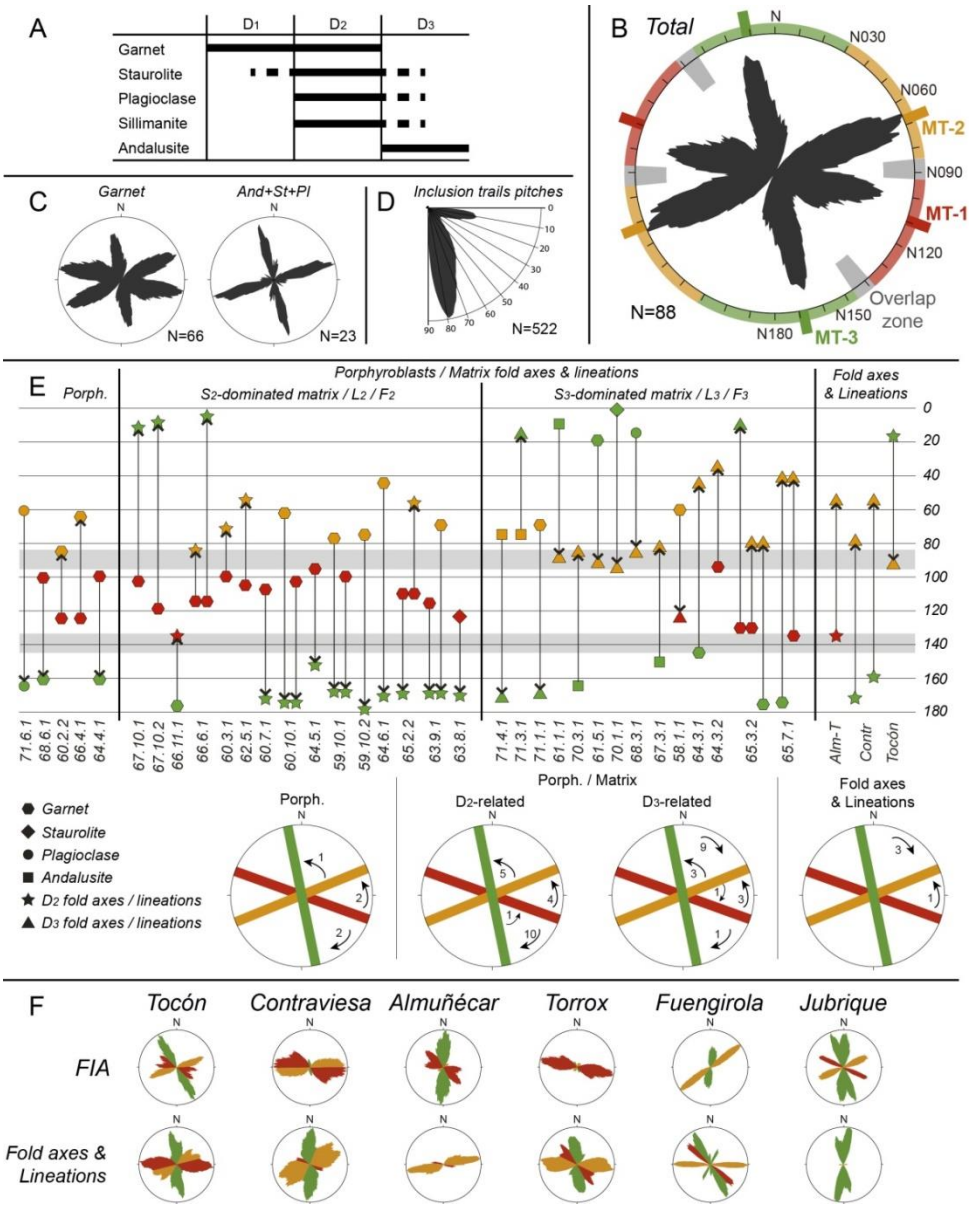

Fig. 7.11 (previous page). A) Summary of relationships between mineral growth and deformation phases. B) Rose diagram compiling all mean FIA trends and inclusion-trail strikes listed in section 10.3.5. Three microstructural trends (MT-1, MT-2 and MT-3) are indicated associated with modal maxima at N070, N110, N170 and trend ranges N140–N090, N090–N030, N140–N210. Structures falling within these trend ranges are colored red, orange and green, respectively, in E and F. C) Same data separated for garnets versus andalusite, staurolite and plagioclase. D) Summary of inclusion trail pitches measured in sections oriented normal to FIA in samples containing a single or very dominant FIA set. Data from individual samples can be found in section 10.3.6. E) Temporal relationships between (micro)structures with different trends in individual samples based on inclusion-trail geometry alone (core-rim relationships, truncational relationships, crenulated inclusion trails), inclusion trails versus crenulation- and fold axes in the matrix (S_2 and S_3 dominated), and overprinting relationships between fold axes and lineations mutually. Arrows point from older to younger elements and are summarized by four circular diagrams, where numbers indicate how many times each temporal relationship is found. F) Rose diagrams for FIAs, fold axes and lineations plotted in Fig. 7.7 and color-coded according to the three trend ranges defined in B. (For interpretation of the references to color in this figure legend, the reader is referred to the Web version of this article.)

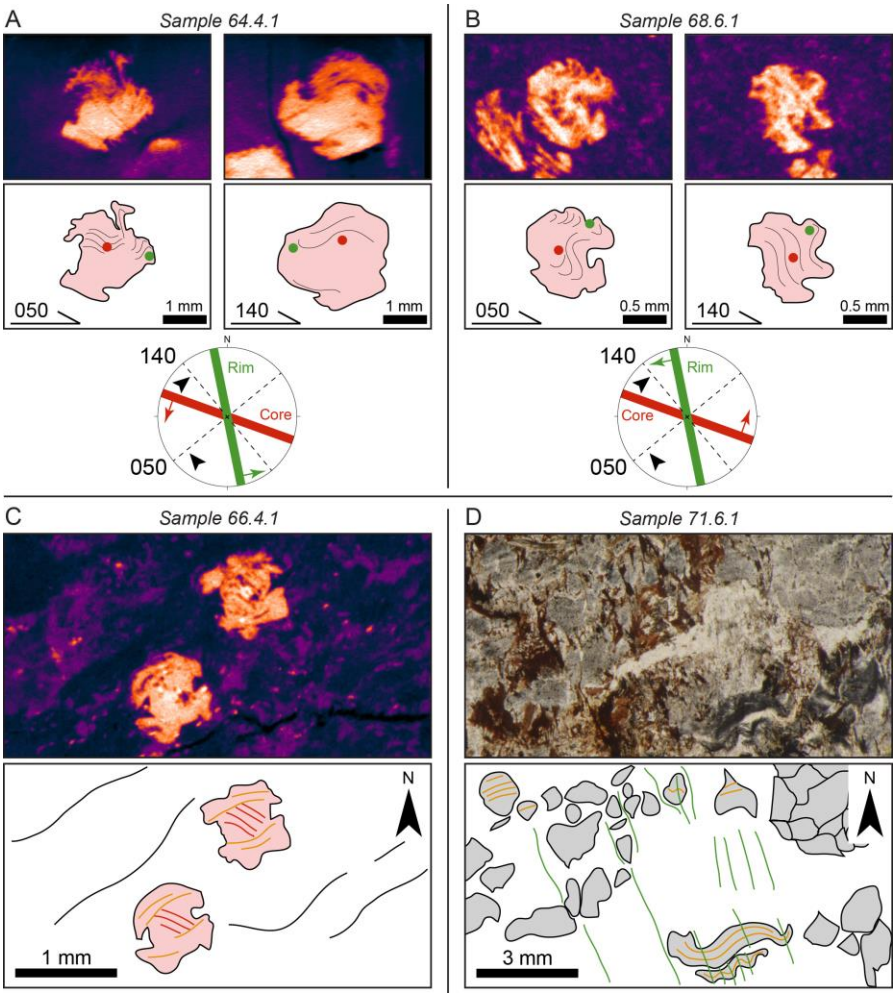

Fig. 7.12. Examples of temporal relationships between microstructural trends indicated by different FIAs (A and B; XCT images; half arrows indicate the upward direction together with the normal direction indicating the horizontal, geographic direction with numbers), different inclusion-trail strikes (C; XCT image; plain view, north is indicated by the arrow) in core versus rims of garnets, or by weakly crenulated inclusion trails (D; microphotograph, plane polarized light; plain view, north is indicated by the arrow) in plagioclase. The microstructural trends are color-coded according to the three trend ranges defined in Figure 7.11b.

7.4.3. Regional distribution of microstructural trends

FIAs, lineations and fold axes in our samples and their outcrops are shown in the maps of Figs. 7.2 and 7.3 with red, orange or green trend bars. The curvature sense or asymmetry of sigmoidal to spiral-shaped inclusion trails is symbolized in these maps with small arrows drawn normal to FIA trend bars. These arrows are opposite to the direction of tectonic transport that would be traditionally deduced from the asymmetry of inclusion-trails, assuming a 'rotational' origin, but point in the correct direction according to the non-rotational interpretation (Bell and Johnson, 1989) favored in this paper (see section 5.1). For ease of discussion, inclusion-trail asymmetries are therefore specified in terms of tectonic transport directions predicted by the 'non-rotational' model. That is, a clockwise sigmoid or spiral corresponds to top-to-the right tectonic transport.

Different FIA sets are heterogeneously distributed in the Alpujárride complex. In the Western Betics (Fig. 7.2a) only 'green' and 'orange' FIAs have been found in 14 samples with the exception of sample 70.6.1, which contains both 'orange' and 'red' FIAs. Particularly noteworthy is the consistency of FIA orientations in the Fuengirola and Jubrique areas despite very different trends of matrix lineations and fold axes in both regions (E-W to SE-NW versus N–S, respectively). In the Almuñécar-Torrox area (Fig. 7.2b), significant differences can be noticed between the data from samples collected west and east of Nerja. West of this town, garnets mainly preserve 'red' and 'green' FIAs, whereas east of it all three FIAs are roughly equally represented and this is further maintained to the east in the Tocón de Quéntar and Contraviesa areas (Fig. 7.3a and b).

7.5. Interpretation and discussion

7.5.1. Formation mechanism of inclusion trails

Consistent inclusion-trail orientations in metamorphic belts (see Introduction) have been mostly explained in terms of a model envisaging porphyroblast nucleation and growth within actively developing microlithon domains without much porphyroblast rotation (Bell, 1985; Fay et al., 2008; Bell and Fay 2016). According to this model, sigmoidal and spiral-shaped inclusion trails form by overgrowth of one or multiple crenulations. Furthermore, preferred subvertical and subhorizontal orientations of inclusion trails documented in different orogens (Bell et al., 1992; Hayward, 1992; Johnson, 1992; Aerden, 1994, 1995, 1998, 2004; Mares, 1998; Sayab, 2005; Shah et al., 2011; Bell and Sapkota, 2012; Aerden et al., 2013; Aerden and Ruiz-Fuentes, 2020) are inferred to reflect alternations of crustal shortening and transient gravitational collapse stages. FIAs resulting from this process should have subhorizontal plunges and trends normal to the crustal shortening direction.

Several general features of our microstructural data, and similar ones described by Aerden et al. (2022, their Fig. 6) support the above summarized 'non-rotational' model in the Betic-Rif orogen and its predictions:

- Our FIAs have mainly sub-horizontal to gentle plunges regardless of their trend or timing (Fig. 7.6). If they had formed by shearing-induced porphyroblast rotation, then it is difficult to explain why older FIAs were not reoriented and steepened during the development of younger ones.
- Dip angles of internal foliations measured in porphyroblast cores show a bimodal distribution with strong preferences for steep or flat lying (Figs. 7.11d and 7.13 and section 10.3.6). Axial planes and truncations associated with more complex inclusion-trail patterns exhibit similar flat-steep patterns (Fig. 7.13).
- FIA trends have consistent orientations in samples and areas where matrix structures and fabrics have totally different orientations (Fig. 7.2a).
- The shear sense indicated by asymmetric pressure shadows of porphyroblasts often conflicts with the sense of inclusion-trail curvature if porphyroblast rotation is assumed (Fig. 7.14).

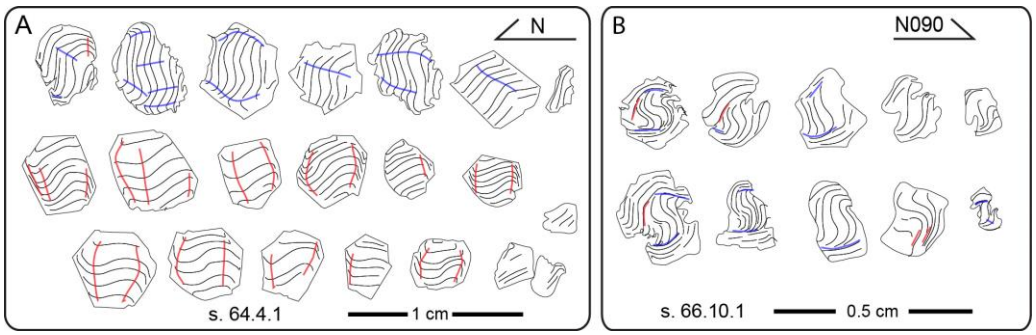

Fig. 7.13. Line tracings of inclusion trails drawn on high-resolution microphotographs of vertical thin sections oriented approximately normal to porphyroblast FIAs. Half arrows indicate the upward direction together with the normal direction indicating the horizontal, geographic direction with numbers. A) Inclusion trails in sample 64.4.1 exhibit subhorizontal (blue lines) and subvertical (red lines) axial planes, consistent with the garnets having nucleated at least twice during different crenulation forming events related to crustal shortening and collapse. B) Complex sigmoidal and spiral shaped inclusion trails in sample 66.10.1 associated with internal truncations (blue and red lines). These elements show similar preferred orientations as the axial planes in A, consistent with episodic growth pulses of individual porphyroblasts controlled by contraction-collapse cycles (e.g. Bell and Hayward, 1991). (For interpretation of the references to color in this figure legend, the reader is referred to the Web version of this article.)

7.5.2. Kinematic significance of 'S_1' inclusion trails

Williams and Platt (2017) already noted that garnet porphyroblasts occasionally host crenulated inclusion trails, which imply a polyphase character of 'D_1'. The three sets of inclusion trails distinguished in this paper suggest a superposition of three regional-scale kinematic frames further referred to as D_{1A}, D_{1B} and D_{1C} (Fig. 7.15). Aerden et al. (2022) recently recognized the same three FIA sets based on microstructural data that included 150 individual FIAs measured with XCT in 12 samples of the Sebtide Complex (the African equivalent of the Alpujárrides), another 150 individual FIAs in five samples of the Nevado-Filábride Complex complemented with 87 average FIAs for the Nevado-Filábride Complex, but only 47 individual FIAs from seven samples of the Alpujárride Complex. Our expansion of the data for the latter to 647 individual FIAs plus 25 average

FIAs from 60 samples confirms the orogen-wide character of the three FIA directions and supports a relationship with the plate motion history of the Mediterranean Alpine belt proposed by Aerden et al. (2022).

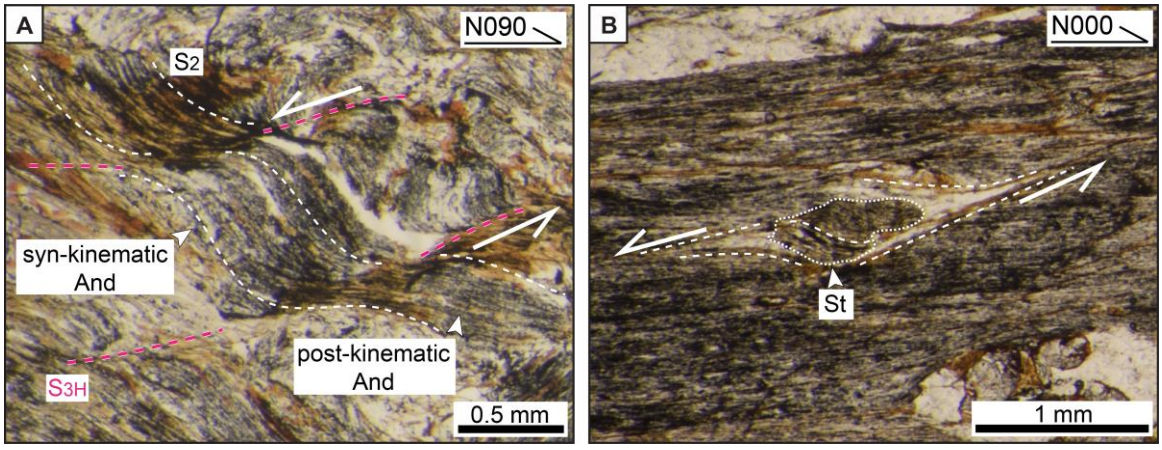

Fig. 7.14. Andalusite (A; sample 70.3.1) and staurolite (B; sample 64.6.1) porphyroblasts containing weakly sigmoidal inclusion-trails that have the same asymmetry as shear bands and strain shadows (microphotographs taken under plane polarized light; half arrows indicate the upward direction together with the normal direction indicating the horizontal, geographic direction with numbers). Note that this is consistent with a 'non-rotational' interpretation of the inclusion trails as overgrown crenulations.

These authors showed, based on Sm–Nd garnet ages and published plate-motion reconstructions (Rosenbaum et al., 2002; Vissers and Meijer, 2012; DeMets et al., 2015), that the 'red' FIA set (D_{1A}) probably formed in the latest-Eocene to early Oligocene perpendicular to NNE directed motion of Africa relative to Eurasia. Subsequent 'orange' FIAs (D_{1B}) dated between 27Ma and 22Ma in the Alpujárride-Sebtides would have developed during or after an anticlockwise rotation of the plate-motion vector to NW. The third set of 'green' FIAs (D_{1C}) was attributed to westward extrusion of the Alborán Domain in the early Miocene, approximately normal to Africa-Iberia convergence.

Aerden et al. (2022) also speculated about the polarity of subduction as suggested by the curvature sense or asymmetry of inclusion trails (see below). However, their asymmetry data were limited to 14 samples of the Sebtide Complex, six from the NFC and only four from the Alpujárride Complex. Our extension of this data to 42 Alpujárride samples now allows statistically more significant conclusions. Fig. 7.16 shows the asymmetries recorded in samples from different areas of the Alpujárride and Sebtide complexes. Of 25 samples hosting D_{1A} FIAs, 13 exhibit top-SSW asymmetries, 9 top-NNE, and 3 contain porphyroblasts showing opposite asymmetries (Figs. 7.2 and 7.3). The top-NNE asymmetries mainly correspond to the Benamocarra unit as mapped by Williams and Platt (2018) and the Intermediate Alpujárride unit (Herradura nappe). In the Upper Alpujárride units (Adra and Salobreña nappes) and the Sebtides, D_{1A} asymmetries very consistently indicate top-SSW transport thus favoring a northward dipping subduction zone (Figs. 7.16 and 7.17). The asymmetries of D_{1B} (orange) FIAs also exhibit a strong predominance (Fig. 7.16; 19 to 7) of top-S to -SE, which is consistent with generally accepted NW-dipping subduction of the African plate below the Alborán

domain in the late Oligocene to early-Miocene (Fig. 7.17). Interestingly, the asymmetry of D_{1B} FIAs recorded in two Benamocarra samples are again opposite (top-NW) to that in the underlying Upper Alpujárride unit. The third set of inclusion-trails (D_{1C}) has a top-west asymmetry in 11 samples, top-east asymmetry in 11 samples and opposite asymmetries in 3 samples. This may reflect distributed coaxial shortening in the Alpujárride complex driven by westward migration of the Alborán Domain in the Miocene without a dominant vergence.

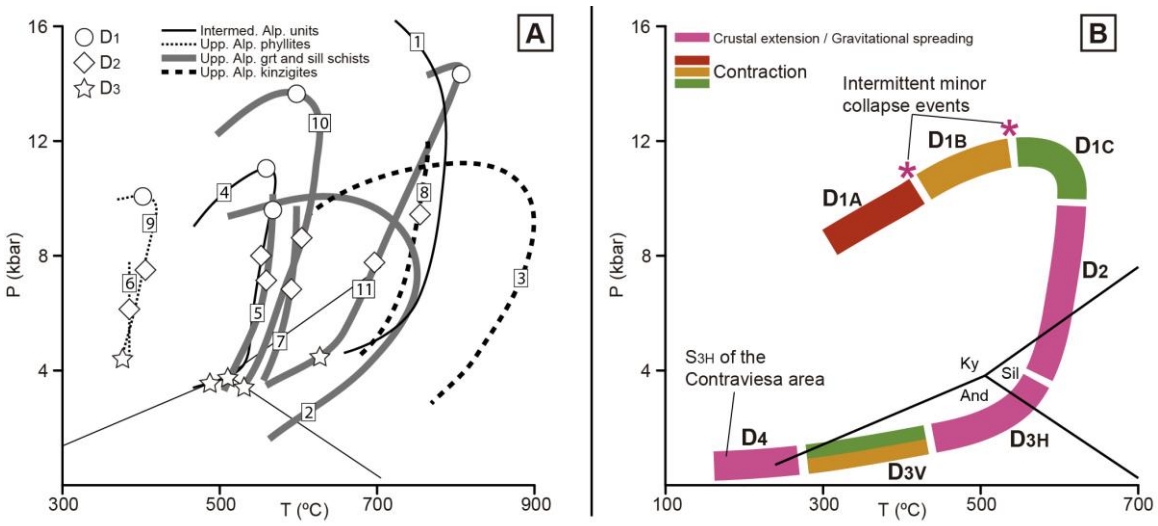

Fig. 7.15. A) P-T-t paths of different tectonic units of the Alpujárride complex. The conditions of the rocks studied in this work correspond to garnet-sillimanite schists of the Upper Alpujárride units. The paths of phyllites and kinzigites of the Upper Alpujárride units, and of the Intermediate Alpujárride units are also shown for comparison. Circles, squares and stars show the approximate location of deformation phases along the path as interpreted by the original authors. (1) Eclogites of the Ojén nappe (Tubía and Gil-Ibarguchi, 1991); (2) sillimanite schists of the Los Reales nappe near Fuengirola (Tubía, 1994); (3) kinzigites of the Los Reales nappe near Fuengirola (Tubía, 1994); (4) light colored schists of the Tejeda unit, equivalent to Intermediate Alpujárride units or Herradura nappe (Azañón and Alonso-Chaves, 1996); (5) garnet schists of the Adra nappe (Azañón et al., 1997); (6) phyllites of the Jubrique unit (Balanyá et al., 1997); (7) sillimanite schists of the Jubrique unit (Balanyá et al., 1997); (8) kinzigites of the Jubrique unit (Balanyá et al., 1997); (9) phyllites of the Salobreña nappe (Azañón et al., 1998); (10) sillimanite schists of the Salobreña nappe (Azañón et al., 1998); (11) Bentomiz unit, Upper Alpujárride nappe from the Torrox area (Alonso-Chaves and Orozco, 2007). B) Schematic P-T-t trajectory for the higher grade (sillimanite bearing) rocks studied in this work based on A. The timing of deformation events distinguished in this work are tentatively indicated using the same colors (red, orange, green) as attributed in Fig. 7.11 to differently oriented structures. Gravitational collapse stages are colored in pink. (For interpretation of the references to color in this figure legend, the reader is referred to the Web version of this article.)

The predominance of gentle FIA plunges and the bimodal steep-flat orientations of inclusion trails detected in our samples (Figs. 7.6, 7.11 and 7.13 and section 10.3.6) implies an unspecified number of alternations between crustal shortening and transient gravitational instability (collapse) during D_{1A}, D_{1B} and D_{1C}. Presumably these reflect fluctuations in a critical balance between tectonic stresses and gravity controlled, in turn, by variations in the rates of erosion, uplift, and plate convergence, the thermal and rheological evolution of the orogen and changes in boundary conditions. Intermittent

collapse phases during D_1 must have been relatively weak compared to shortening phases as they are not reflected in cyclic prograde-retrograde metamorphism. Collapse events may correspond to gravitational spreading within thrust nappes in an overall contractional setting, alternating with periods of distributed shortening. In any event, these alternations were sufficient to control episodic growth of porphyroblasts with each growth pulse being triggered by a newly developing subvertical or subhorizontal crenulations (cf. Bell and Hayward, 1991; Sanislav and Bell, 2011; Aerden and Ruiz-Fuentes, 2020). This mechanism also explains the preponderance of subhorizontal or gently plunging FIAs.

		Upper Alpujarride units and Lower Sebtides								*Intermed. Alp. units*	*Benamoc. unit*
		Jub.	Fueng.	Nerja-W	Nerja-E	Tocón	Cont.	Rif	Total		
D1A	top-NNE	1	0	0	0	1	1	1	4	2	3
	top-SSW	0	0	0	3	0	7	3	13	0	0
	both	0	0	0	0	1	0	1	2	0	1
D1B	top-NW	1	1	1	0	1	0	2	5	0	2
	top-SE	2	1	5	2	1	5	5	16	3	0
	both	0	0	0	0	1	0	0	1	0	0
D1C	top-W	1	2	3	0	0	0	2	8	2	1
	top-E	2	1	0	0	3	4	0	10	1	0
	both	0	0	0	1	0	1	0	2	0	1

Fig. 7.16. Table summarizing the asymmetries of inclusion trails from garnet, staurolite and plagioclase found in each area studied (Upper and Intermediate Alpujárrides and Benamocarra unit) and the Rif (in northern Morocco).

Two samples from the Almuñécar area (66.9.1 and 62.5.2), however, contain very steeply plunging FIAs (Fig. 7.7 and section 10.3.3) corresponding to the intersection of two steeply dipping foliations with different strikes not separated by a flat lying crenulation cleavage. In the same area, straight inclusion trails which define internal foliations with steep dips are particularly abundant (samples 66.6.1, 60.2.2, 60.3.1, 66.4.1) possibly reflecting more limited role of gravitational collapse in comparison with other areas.

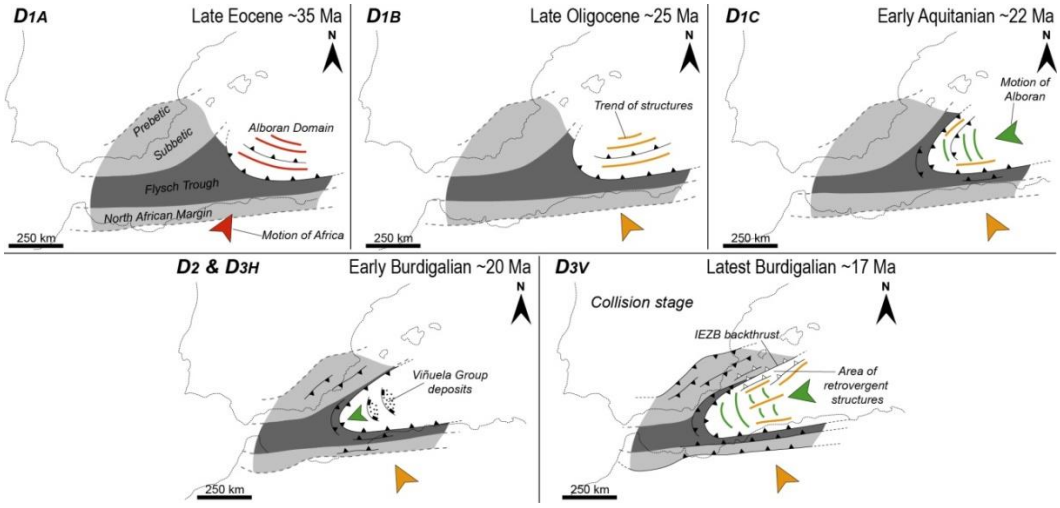

Fig. 7.17. Paleogeographic maps showing the evolution of the Alborán Domain in each phase distinguished in this study.

7.5.3. Kinematics of S_2

Even in individual thin sections, the character of the main cleavage varies from a differentiated S_2 crenulation cleavage deforming S_1 in the shortening field of D_2 to a simple schistosity that can be followed into garnet porphyroblasts and represents an S_1 that was deformed and reactivated in the extensional field of D_2. This composite character of the 'main foliation' and the fact that the process of foliation reactivation involves antithetic shearing (cf. Bell et al., 1986; Aerden, 1994) may explain partially contradictory shear-sense indicators associated with S_2. Nevertheless, most workers have concluded top-to-the-East to -NNE tectonic transport during D_2 with a component of coaxial shortening normal to S_2. The development of S_2 was accompanied by strong decompression related to opening of the western Mediterranean back-arc basin leading to sillimanite growth in the higher-grade rocks. Such an extensional origin of S_2 suggests it formed in a subhorizontal position although we have no firm data confirming this. This event (Fig. 7.17) is related with high-Temperature metamorphism dated at approximately 20 Ma (e.g. Platt and Whitehouse, 1998; Platt et al., 2005; Bessière et al., 2022), which is also the age of the oldest unconformable marine deposits on top of the Internal Domain (Viñuela Group, e.g. Aguado et al., 1990; Alonso-Chaves and Rodríguez-Vidal, 1998) and in the Alborán basin (Comas et al., 1992; Rodríguez-Fernández et al., 1999).

7.5.4. Kinematics of D_3

The tectonic significance of major N- to NW verging F_3 folds in the Alpujárride Complex and associated S_3 crenulation cleavage has been debated since long. In the Central Betics, some authors interpreted these structures as late-metamorphic N-to NE-directed folds and thrusts following D_2 extension (Cuevas, 1991; Simancas and Campos, 1993; Azañón et al., 1997; Balanyá et al., 1997; Rossetti et al., 2005; Simancas 2018). Others envisaged their development during continued crustal extension but with a changed top-N shear sense (Orozco et al., 1998, 2004, 2017; Williams and Platt, 2018). In the Fuengirola area, Tubía et al. (1993) and Tubía (1994) interpreted D_3 as a phase of ESE-WNW sinistral transtension changing to ENE-WSW sinistral transpression. Orozco et al. (1998) and Rossetti et al. (2005) locally recognized two crenulation cleavages (corresponding to our S_{3V} and S_{3H}) and Sanz de Galdeano (1989) described a superposition of two E-W and N-S folding directions in Triassic marbles of the Sierra de Tejeda (North of the Torrox area; Fig. 7.2b) both deforming an original 'main schistosity'.

Our own observations regarding D_3 can be summarized as follows (Figs. 7.15 and 7.17). In the Western and Central Alpujárrides (Jubrique, Fuengirola and Almuñécar areas), a penetrative S_{3H} is associated with synkinematic andalusite or sillimanite and is overprinted by late- to post-metamorphic S_{3V} (Fig. 7.5c, d, 7.10a, 10b). In the Contraviesa area, an opposite situation is found with steeply south-dipping S_{3V} locally overprinted by a gently dipping S_{3H} and post-metamorphic shear bands. The latter corresponding to the 'D_4' structures of previous workers. In the intermediate Torrox-Almuñécar area, S_{3H} is still the dominant crenulation cleavage but less intense as in the Jubrique schists and

locally overprinted by D_{3V}. Thus, a west-ward strain gradient associated with S_{3H} is suggested. D_{3V} has only been found pervasively developed in the Fuengirola and Contraviesa areas. In the latter, zones of intense S_{3V} and tight folding of S_2 alternate with zones with a simple steeply south dipping S_2. Cuevas (1991) interpreted the intense D_{3V} folded zones as ductile thrusts supported by quartz c-axes fabrics indicating top-NE shearing.

These heterogeneous relationships suggest that, following several alternations of crustal shortening and weak gravitational collapse stages that generated the three FIA sets preserved in garnets (D_1), a more dramatic collapse event occurred (D_2 and D_{3H}) related to opening of the western Mediterranean basin that was still followed by renewed crustal shortening responsible for S_{3V}. The late subhorizontal shear bands and detachments (D_4 of previous workers) may reflect a final phase of thrusting and gravitational spreading following uplift caused by D_{3V} (cf. Platt et al., 1983). Interestingly, several authors already interpreted D_1-D_4 in terms of alternating shortening and extension (Tubía et al., 1993; Azañón et al., 1997, 1998; Balanyá et al., 1997). Such a scenario appears confirmed and refined by our work.

The fact that 'green' and 'orange' FIAs of andalusite porphyroblasts must have formed after 'green' FIAs of garnets, and that 'green FIAs' in both minerals are surrounded by 'orange' D_3 fabrics in several samples was stated in section 4.2 as implying development of 'orange' FIAs before and after 'green' FIAs. We suggest that this reflects an alternation of two suborthogonal shortening directions related to NW motion of Africa and simultaneous westward motion of the Alborán Domain. Regional fold trends also define two sets with E-W and N–S to NW-SE trends in all investigated areas (Fig. 7.7). In the westernmost part of the Gibraltar arc the N–S set is dominant (Fig. 7.1), whereas towards the east E-W to NE-SW trends become more important (Balanyá and García-Dueñas, 1987; Balanyá, 1991; Balanyá et al., 2007).

7.5.5. Back-thrusting development

In the Tocón de Quéntar and Sierra de Baza areas, E-W trending D_{3V} folds are S-vergent, opposite to similar structures in the Almuñécar and Contraviesa areas. South-vergent structures have been previously also recognized in Sierra de Baza (Comas et al., 1979; Delgado Salazar et al., 1980), Sierra de las Estancias (Akkerman et al., 1980), Sierra de Almagro (García-Tortosa et al., 2002; Booth-Rea et al., 2005), Sierra de Carrascoy (Sanz de Galdeano et al., 1997) and in the Orihuela Mountains (Martín-Rojas et al., 2007) (see locations in Fig. 7.1). S-vergent D_3 folds are concentrated near the Internal-External Zones Boundary (IEZB), which represents the suture of the collision between the Alborán Domain and the South Iberian paleomargin. Farther to the south in our study areas, E-W trending folds are mainly north-vergent. In the northeastern part of the cordillera, the IEZB has been interpreted as a backthrust (Geel, 1973; Martín-Algarra, 1987; Jabaloy-Sánchez et al., 2007) with top-to-the-SSE/SE sense of movement (Lonergan et al., 1994). Back-thrusts have also been recognized in the Flysch Complex, Frontal Units and Maláguide Complex (Foucault, 1976; García-Dueñas and Navarro-Vilá,

1976; Rodríguez-Fernández, 1982; Martín-Algarra, 1987; Balanyá, 1991; Sanz de Galdeano et al., 1995; Geel and Roep, 1998; Fernández-Fernández et al., 2007; Martín-Algarra et al., 2009; Jabaloy-Sánchez et al., 2019a; Ruiz-Fuentes et al., 2022). The appearance of S-vergent D_{3V} folds in the Alpujárride Complex close to the IEZB can therefore be interpreted in terms of propagation of deformation associated to back-thrusting within the Alborán Domain acting as the backstop. These observations allow us to correlate D_{3V} with the beginning of the collision of Alborán with the External Domain, which accounted around the late Burdigalian (e.g. Martín-Algarra, 1987; Martín-Martín et al., 1996; Ruiz-Fuentes et al., 2022).

7.6. Conclusions

- Porphyroblasts in the Alpujárride Complex preserve a succession of three differently oriented FIA sets (WNW-ESE, E-W to NE-SW and NNW-SSE) defined by sigmoidal or spiral-shaped inclusion trails. The regional consistency of these microstructures and their preference for subhorizontal or gentle plunges, support the view that FIAs correspond to the intersections of steeply dipping and subhorizontal foliations formed during alternating crustal shortening and gravitational collapse (Bell and Johnson, 1989).
- The above implies that FIAs formed normal to crustal shortening directions and have conserved their original orientations throughout the subsequent orogenic evolution. This is shown to be consistent with the Paleogene-Neogene history of relative plate-motions between Africa, Iberia and the Alborán Domain. A major change from NNE-to NW-directed motion of Africa in the Oligocene (e.g. DeMets et al., 2015) accounts for the two earliest formed FIA sets. The third FIA is attributable to independent westward motion of the Alborán Domain since the early Miocene.
- A strong predominance of inclusion-trail asymmetries (curvature senses) associated with the first two FIA sets indicating top-SSW to top SE tectonic transport, favors a northward to NW-dipping subduction zone accommodating Africa-Iberia convergence.
- Late-metamorphic structures (assigned to D_3 and D_4 events in previous works) deforming a composite S_2 foliation in the Alpujárride Complex represent at least four different generations: two associated with steeply dipping crenulation cleavages striking broadly N–S and ENE-WSW (D_{3V}), and two subhorizontal ones generated during gravitational collapse, linked to andalusite growth (D_{3H}) and associated with brittle-ductile shear bands and detachments (D_4). These structures bear witness of dynamic interactions between tectonic stresses transmitted by Africa and the Alborán Domain and gravity.

Author statement

Alejandro Ruiz-Fuentes: conceptualization, methodology, investigation, formal analysis, writing, visualization. Domingo Aerden: conceptualization, methodology, writing.

Declaration of competing interest

The authors declare that they have no known competing financial interests or personal relationships that could have appeared to influence the work reported in this paper.

Data availability

Data will be made available on request.

Acknowledgements

We thank Etienne Skrzypek and two anonymous reviewers for constructive comments that helped improve an early version of the manuscript, and Toru Takeshita for his editorial work. We thank Ángel Perandrés-Villegas for making the thin sections studied for this work and Fátima Linares Ordóñez for the XCT scanning of samples. The research was carried out as part of a Ph.D. project of ARF financed by an FPU grant from the Spanish Ministery of Education and Science, Culture and Sports (FPU17/01874). Research expenses were covered by Spanish government grant CGL2016-80687-R AEI/FEDER, and Junta de Andalucía Projects P18-RT-3275 (AGORA), B-RNM-301-UGR18 (PAPEL) and RNM148. Funding for open access charge: Universidad de Granada / CBUA.

Appendix A. Supplementary data

Supplementary data to this article can be found online at https://doi.org/10.1016/j.jsg.2023.104823.

References

Abu Sharib, A.S.A.A., Sanislav, I.V., 2013. Polymetamorphism accompanied switching in horizontal shortening during Isan Orogeny: Example from the Eastern Fold Belt, Mount Isa Inlier, Australia. Tectonophysics 587, 146-167. https://doi.org/10.1016/j.tecto.2012.06.051

Acosta-Vigil, A., Rubatto, D., Bartoli, O., Cesare, B., Meli, S., Pedrera, A., Azor, A., Tajčmanová, L., 2014. Age of anatexis in the crustal footwall of the Ronda peridotites, S Spain. Lithos 210-211, 147-167. https://doi.org/10.1016/j.lithos.2014.08.018

Aerden, D.G.A.M., 1994. Kinematics of orogenic collapse in the Variscan Pyrenees deduced from microstructures in porphyroblastic rocks from the Lys-Caillaouas massif. Tectonophysics 238, 139-160. https://doi.org/10.1016/0040-1951(94)90053-1

Aerden, D.G.A.M., 1995. Porphyroblast non-rotation during crustal extension in the Variscan Lys-Caillaouas Massif, Pyrenees. Journal of Structural Geology 17, 709-725. https://doi.org/10.1016/0191-8141(94)00090-M

Aerden, D.G.A.M., 1998. Tectonic evolution of the Montagne Noire and a possible orogenic model for syncollisional exhumation of deep rocks, Variscan belt, France. Tectonics 17, 62-79. https://doi.org/10.1029/97TC02342

Aerden, D.G.A.M., 2004. Correlating deformation in Variscan NW-Iberia using porphyroblasts; implications for the Ibero-Armorican Arc. Journal of Structural Geology 26, 177-196. https://doi.org/10.1016/S0191-8141(03)00070-1

Aerden, D.G.A.M., Ruiz-Fuentes, A., 2020. X-ray computed micro-tomography of spiral garnets: A new test of how they form. Journal of Structural Geology 136, 104054. https://doi.org/10.1016/j.jsg.2020.104054

Aerden, D.G.A.M., Sayab, M., Bouybaouene, M.L., 2010. Conjugate-shear folding: A model for the relationships between foliations, folds and shear zones. Journal of Structural Geology 32, 1030-1045. https://doi.org/10.1016/j.jsg.2010.06.010

Aerden, D.G.A.M., Bell, T.H., Puga, E., Sayab, M., Lozano, J.A., Díaz de Federico, A., 2013. Multi-stage mountain building vs. relative plate motions in the Betic Cordillera deduced from integrated microstructural and petrological analysis of porphyroblast inclusion trails. Tectonophysics 587, 188-206. https://doi.org/10.1016/j.tecto.2012.11.025

Aerden, D.G.A.M., Ruiz-Fuentes, A., Sayab, M., Forde, A., 2021. Kinematics of subduction in the Ibero-Armorican arc constrained by 3D microstructural analysis of garnet and pseudomorphed lawsonite porphyroblasts from Île de Groix (Variscan belt). Solid Earth 12, 971-992. https://doi.org/10.5194/se-12-971-2021

Aerden, D.G.A.M., Farrell, T.P., Baxter, E.F., Stewart, E.M., Ruiz-Fuentes, A., Bouybaouene, M., 2022. Refined tectonic evolution of the Betic-Rif orogen through integrated 3-D microstructural analysis and Sm-Nd dating of garnet porphyroblasts. Tectonics 41, e2022TC007366. https://doi.org/10.1029/2022TC007366

Aguado, R., Feinberg, H., Durand-Delga, M., Martín-Algarra, A., Esteras, M., Didon, J., 1990. Nuevos datos sobre la edad de las formaciones miocenas transgresivas sobre las Zonas Internas béticas: La formación de San Pedro de Alcántara (provincia de Málaga). Revista de la Sociedad Geológica de España 3, 79-85.

Akkerman, J.H., Maier, G., Simon, O.J., 1980. On the geology of the Alpujarride complex in the western Sierra de las Estancias (Betic Cordilleras, SE Spain). Geologie en Mijnbouw 59 (4), 363-374.

Aldaya, F., 1969. Los mantos Alpujárrides al Sur de Sierra Nevada (zona bética, provincia de Granada.). Acta Geológica Hispánica IV (5), 126-130.

Aldaya, F., García-Dueñas, V., Navarro-Vilá, F., 1979. Los Mantos Alpujárrides del tercio central de las Cordilleras Béticas. Ensayo de correlación tectónica de los Alpujárrides. Acta Geológica Hispánica 14, 154-166.

Allmendinger, R. W., Cardozo, N. C., Fisher, D., 2013. Structural Geology Algorithms: Vectors & Tensors. Cambridge, England, Cambridge University Press, 289 pp.

Alonso-Chaves, F.M., Rodriguez-Vidal, J., 1998. Subsidence tectonique et sédimentation synrift associée au rifting du domaine d'Alboran au Miocène inférieur (Chaîne bétique, Espagne). Comptes Rendus de l'Académie des Sciences – Series IIA – Earth and Planetary Science 326, 51-56. https://doi.org/10.1016/S1251-8050(97)83203-X

Alonso-Chaves, F.M., Orozco, M., 2007. Evolución tectónica de las Sierras de Tejeda y Almijara: Colapso extensional y exhumación de áreas metamórficas en el Dominio de Alborán (Cordilleras Béticas). Revista de la Sociedad Geológica de España 20 (3-4), 211-228.

Alonso-Chaves, F.M., Orozco, M., 2012. El Complejo Alpujárride de La Axarquía: Zonas de cizalla dúctiles a escala cortical y pliegues recumbentes asociados. Geogaceta 52, 5-8.

Augier, R., Agard, P., Monié, P., Jolivet, L., Robin, C., Booth-Rea, G., 2005. Exhumation, doming and slab retreat in the Betic Cordillera (SE Spain): in situ 40Ar/39Ar ages and P-T-d-t paths for the Nevado-Filabride complex. Journal of Metamorphic Geology 23, 357-381. https://doi.org/10.1111/j.1525-1314.2005.00581.x

Azañón, J.M., Goffé, B., 1997. Ferro- and magnesiocarpholite assemblages as record of high-P, low-T metamorphism in the Central Alpujarrides, Betic Cordillera (SE Spain). European Journal of Mineralogy 9, 1035-1051.

Azañón, J.M., Crespo-Blanc, A., 2000. Exhumation during a continental collision inferred from the tectonometamorphic evolution of the Alpujarride Complex in the central Betics (Alboran Domain, SE Spain). Tectonics 19 (3), 549-565. https://doi.org/10.1029/2000TC900005

Azañón, J.M., García-Dueñas, V., Martínez-Martínez, J.M., Crespo-Blanc, A., 1994. Alpujarride tectonic sheets in the central Betics and similar eastern allochthonous units (SE Spain). Comptes Rendus de l'Académie des Sciences de Paris 318, 667-674.

Azañón, J.M., Crespo-Blanc, A., García-Dueñas, V., 1997. Continental collision, crustal thinning and nappe forming during the pre-Miocene evolution of the Alpujarride Complex (Alboran Domain, Betics). Journal of Structural Geology 19 (8), 1055-1071. https://doi.org/10.1016/S0191-8141(97)00031-X

Azañón, J.M., García-Dueñas, V., Goffé, B., 1998. Exhumation of high-pressure metapelites and coeval crustal extension in the Alpujarride complex (Betic Cordillera). Tectonophysics 285, 231-252. https://doi.org/10.1016/S0040-1951(97)00273-4

Balanyá, J.C., 1991. Estructura del Dominio de Alboran en la parte norte del Arco de Gibraltar. PhD Thesis, Universidad de Granada. https://digibug.ugr.es/handle/10481/50668

Balanyá, J.C., García-Dueñas, V., 1987. Les directions structurales dans le Domaine d'Alborán de part et d'autre du Détroit de Gibraltar. Comptes Rendus de l'Académie des Sciences de Paris 304, 929-933.

Balanyá, J.C., Azañón, J.M., Sánchez-Gómez, M., García-Dueñas, V., 1993. Pervasive ductile extensión, isothermal decompression and thinning of the Jubrique unit in the Paleogene

(Alpujarride Complex, western Betics Spain). Comptes Rendus de l'Académie des Sciences de Paris 316, 1595-1601.

Balanyá, J.C., García-Dueñas, V., Azañón, J.M., Sánchez-Gómez, M., 1997. Alternating contractional and extensional events in the Alpujarride nappes of the Alboran Domain (Betics, Gibraltar Arc). Tectonics 16, 226-238. https://doi.org/10.1029/96TC03871

Balanyá, J.C., García-Dueñas, V., Azañón, J.M., Sánchez-Gómez, M., 1998. Reply to "Comment on 'Alternating contractional and extensional events in the Alpujarride nappes of the Alboran Domain (Betics, Gibraltar Arc)'". Tectonics 17 (6), 977-981. https://doi.org/10.1029/1998TC900006

Balanyá, J.C., Crespo-Blanc, A., Díaz Azpiroz, M., Expósito, I., Luján, M., 2007. Structural trend line pattern and strain partitioning around the Gibraltar Arc accretionary wedge: Insights as to the mode of orogenic arc building. Tectonics 26, TC2005 https://doi.org/10.1029/2005TC001932.

Bell, T.H., 1985. Deformation partitioning and porphyroblast rotation in metamorphic rocks: a radical interpretation. Journal of Metamorphic Geology 3, 109-118. https://doi.org/10.1111/j.1525-1314.1985.tb00309.x

Bell, T.H., Johnson, S.E., 1989. Porphyroblast inclusion trails: the key to orogenesis. Journal of Metamorphic Geology 7, 279-310. https://doi.org/10.1111/j.1525-1314.1989.tb00598.x

Bell, T.H., Hayward, N., 1991. Episodic metamorphic reactions during orogenesis: the control of deformation partitioning on reaction sites and reaction duration. Journal of Metamorphic Geology 9, 619-640. https://doi.org/10.1111/j.1525-1314.1991.tb00552.x

Bell, T.H., Forde, A., 1995. On the significance of foliation patterns preserved around folds by mineral overgrowth. Tectonophysics 246, 171-181. https://doi.org/10.1016/0040-1951(94)00263-9

Bell, T.H., Welch, P.W., 2002. Prolonged Acadian orogenesis: Revelations from foliation intersection axis (FIA) controlled monazite dating of foliations in porphyroblasts and matrix. American Journal of Science 302, 549-581. https://doi.org/10.2475/ajs.302.7.549

Bell, T.H., Sapkota, J., 2012. Episodic gravitational collapse and migration of the mountain chain during orogenic roll-on in the Himalayas. Journal of Metamorphic Geology 30, 651-666. https://doi.org/10.1111/j.1525-1314.2012.00992.x

Bell, T.H., Fay, C., 2016. Holistic microstructural techniques reveal synchronous and alternating andalusite and staurolite growth during three tectonic events resulted from shifting partitioning of growth vs deformation. Lithos 262, 699-712. https://doi.org/10.1016/j.lithos.2016.06.031

Bell, T.H., Rubenach, M.J., Fleming, P.D., 1986. Porphyroblast nucleation, growth and dissolution in regional metamorphic rocks as a function of deformation partitioning during foliation development. Journal of Metamorphic Geology 4, 37-67. https://doi.org/10.1111/j.1525-1314.1986.tb00337.x

Bell, T.H., Johnson, S.E., Davis, B., Forde, A., Hayward, N., Wilkins, C., 1992. Porphyroblast inclusion-trail orientation data: eppure non son girate! Journal of Metamorphic Geology 10, 295-307. https://doi.org/10.1111/j.1525-1314.1992.tb00084.x

Bell, T.H., Forde, A., Wang, J., 1995. A new indicator of movement direction during orogenesis: measurement technique and application to the Alps. Terra Nova 7, 500-508. https://doi.org/10.1111/j.1365-3121.1995.tb00551.x

Bell, T.H., Ham, A.P., Hickey, K.A., 2003. Early formed regional antiforms and synforms that fold younger matrix schistosities: their effect on sites of mineral growth. Tectonophysics 367, 253-278. https://doi.org/10.1016/S0040-1951(03)00126-4

Bessière, E., Scaillet, S., Augier, R., Jolivet, L., Azañón, J.M., Booth-Rea, G., Romagny, A., Duval, F., 2022. 40Ar/39Ar Age Constraints on HP/LT Metamorphism in Extensively Overprinted Units: The Example of the Alpujárride Subduction Complex (Betic Cordillera, Spain). Tectonics 41, e2021TC006889. https://doi.org/10.1029/2021TC006889

Booth-Rea, G., Azañón, J.M., Goffé, B., Vidal, O., Martínez-Martínez, J.M., 2002. High-pressure, low-temperature metamorphism in Alpujarride Units of southeastern Betics (Spain). Comptes Rendus Geosciences 334, 857-865. https://doi.org/10.1016/S1631-0713(02)01787-X

Booth-Rea, G., Azañón, J.M., Martínez-Martínez, J.M., Vidal, O., García-Dueñas, V., 2005. Contrasting structural and P-T evolution of tectonic units in the southeastern Betics: Key for understanding the exhumation of the Alboran Domain HP/LT crustal rocks (western Mediterranean). Tectonics 24, TC2009 https://doi.org/10.1029/2004TC001640.

Bouillin, J.P., 1986. Le bassin maghrébin ; une ancienne limite entre l'Europe et l'Afrique a l'ouest des Alpes. Bulletin de la Société Géologique de France II (4), 547-558. https://doi.org/10.2113/gssgfbull.II.4.547

Cihan, M., Evins, P., Lisowiec, N., Blake, K., 2006. Time constraints on deformation and metamorphism from EPMA dating of monazite in the Proterozoic Robertson River Metamorphics, NE Australia. Precambrian Research 145, 1-23. https://doi.org/10.1016/j.precamres.2005.11.009

Comas, M.C., Delgado, F., Vera, J.A., 1979. Mapa y memoria de la Hoja nº 993 (Benalúa de Guadix). Mapa Geológico de España E. 1:50.000. Segunda Serie (MAGNA), Primera edición. IGME.

Comas, M.C., García-Dueñas, V., Jurado, M.J., 1992. Neogene tectonic evolution of the Alboran Sea from MCS data. Geo-Marine Letters 12, 157-164. https://doi.org/10.1007/BF02084927

Crespo-Blanc, A., Orozco, M., García-Dueñas, V., 1994. Extension versus compression during the Miocene tectonic evolution of the Betic chain. Late folding of normal fault systems. Tectonics 13, 78-88. https://doi.org/10.1029/93TC02231

Cuevas, J., 1989. Microtectónica y metamorfismo de los Mantos Alpujárrides del tercio central de las Cordilleras Béticas (entre Motril y Adra). Parte II: Las Zonas Miloníticas. Boletín Geológico y Minero 100 (5), 719-766.

Cuevas, J., 1991. Internal structure of the Adra Nappe (Alpujarride Complex, Betics, Spain). Tectonophysics 200, 199-212. https://doi.org/10.1016/0040-1951(91)90015-K

Cuevas, J., Aldaya, F., Navarro-Vilá, F., Tubía, J.M., 1986. Caractérisation de deux étapes de charriage principales dans les nappes Alpujarrides centrales (Cordillères Bétiques, Espagne). Comptes Rendus de l'Académie des Sciences de Paris 302, 1177-1180.

Cuevas, J., Navarro-Vilá, F., Tubía, J.M., 2001. Evolución estructural poliorogénica del Complejo Maláguide (Cordilleras Béticas). Boletín Geológico y Minero 11, 47-58.

DeMets, C., Iaffaldano, G., Merkouriev, S., 2015. High-resolution Neogene and Quaternary estimates of Nubia-Eurasia-North America Plate motion. Geophys. J. Int. 203, 416–427 https://doi.org/10.1093/gji/ggv277

Delgado Salazar, F., Gómez Prieto, J.A., Martín García, L., 1980. Mapa y memoria de la Hoja nº 994 (Baza). Mapa Geológico de España E. 1:50.000. Segunda Serie (MAGNA), Primera edición. IGME.

Elorza, J.J., García-Dueñas, V., 1981. Mapa y memoria de la Hoja nº 1054 (Vélez-Málaga). Mapa Geológico de España E. 1:50.000. Segunda Serie (MAGNA), Primera edición. IGME.

Esteban, J.J., Sánchez-Rodríguez, L., Seward, D., Cuevas, J., Tubía, J.M., 2004. The late thermal history of the Ronda area, southern Spain. Tectonophysics 389, 81-92. https://doi.org/10.1016/j.tecto.2004.07.050

Estévez González, C., Chamón Cobos, C., 1978. Mapa y memoria de la Hoja nº 1053/1067 (Málaga/Torremolinos). Mapa Geológico de España E. 1:50.000. Segunda Serie (MAGNA), Primera edición. IGME.

Farrell, T.P., 2019. Investigating the Tectonic Significance of Spiral Garnets from the Betic-Rif Arc of Southern Spain and Northern Morocco Using Sm-Nd Garnet Geochronology. M.Sc. thesis, Boston College, 234 pp. https://dlib.bc.edu/islandora/object/bc-ir:108592

Fay, C., Bell, T.H., Hobbs, B.E., 2008. Porphyroblast rotation versus nonrotation: Conflict resolution! Geology 36, 307-310. https://doi.org/10.1130/G24499A.1

Fernández-Fernández, E.M., Jabaloy-Sánchez, A., Nieto, F., González-Lodeiro, F., 2007. Structure of the Maláguide Complex near Vélez Rubio (Eastern Betic Cordillera, SE Spain). Tectonics 26, TC4008 https://doi.org/10.1029/2006TC002019.

Foucault, A., 1976. Complements sur la geologie de l'Ouest de la Sierra Arana et de ses environs (province de Grenade, Espagne). Bulletin de la Société Géologique de France (7), 18, 649–658. https://doi.org/10.2113/gssgfbull.S7-XVIII.3.649

Foucault, A., Paquet, J., 1971. Sur l'importance d'une tectogenèse hercynienne dans la région des Cordillères Bétiques (Sud de la Sierra Arana, Province de Grenade, Espagne). Comptes Rendus de l'Académie des Sciences de Paris 272, 2756-2758.

Fyson, W.K., 1980. Fold fabrics and emplacement of an Archean granitoid pluton, Cleft Lake, Northwest Territories. Can. J. of Earth Sc., 17. 325-332. https://doi.org/10.1139/e80-032

García-Dueñas, V., Navarro-Vilá, F., 1976. Alpujarrides, Malaguides et autres unités allochtones au Nord de la Sierra Nevada (Cordillères Bétiques, Andalousie). Bulletin de la Société Géologique de France 7-XVIII-3, 641-648. https://doi.org/10.2113/gssgfbull.S7-XVIII.3.641

García-Tortosa, F.J., López-Garrido, A.C., Sanz de Galdeano, C., 2002. Estratigrafía y estructura de la unidad de los Tres Pacos: La controversia sobre el Complejo "Almágride" en la Sierra de Almagro (Cordillera Bética, Almería, España). Revista de la Sociedad Geológica de España 15, 15-25.

Geel T., 1973. The geology of the Betic of Málaga, the Subbetic and the zone between these two units in the Vélez Rubio area (Southern, Spain). GUA Papers of Geology Ser. 1, 5, 1–185.

Geel, T., Roep, T.B., 1998. Oligocene to middle Miocene basin development in the Eastern Betic Cordilleras, SE Spain (Vélez Rubio Corridor – Espuña): reflections of West Mediterranean plate-tectonic reorganizations. Basin Research 10, 325-343. https://doi.org/10.1046/j.1365-2117.1998.00068.x

Gómez-Pugnaire, M.T., Rubatto, D., Fernández-Soler, J.M., Jabaloy, A., López-Sánchez-Vizcaíno, V., González-Lodeiro, F., Galindo-Zaldívar, J., Padrón-Navarta, J.A., 2012. Late Variscan magmatism in the Nevado-Filábride Complex: U-Pb geochronologic evidence for the pre-Mesozoic nature of the deepest Betic complex (SE Spain). Lithos 146-147, 93-111. https://doi.org/10.1016/j.lithos.2012.03.027

Guerrera, F., Martín-Algarra, A., Perrone, V., 1993. Late Oligocene-Miocene syn-/-late-orogenic successions in Western and Central Mediterranean chains from the Betic Cordillera to the Southern Apennines. Terra Nova 5, 525-544. https://doi.org/10.1111/j.1365-3121.1993.tb00302.x

Guerrera, F., Martín-Martín, M., Tramontana, M., 2021. Evolutionary geological models of the central-western peri-Mediterranean chains: a review. International Geology Review 63, 65-86 https://doi.org/10.1080/00206814.2019.1706056

Ham, A.P., Bell, T.H., 2004. Recycling of foliations during folding. Journal of Structural Geology 26, 1989-2009. https://doi.org/10.1016/j.jsg.2004.04.003

Hayward, N., 1990. Determination of early fold axis orientations in multiply deformed rocks using porphyroblast inclusion trails. Tectonophysics 179, 353-369. https://doi.org/10.1016/0040-1951(90)90301-N

Hayward, N., 1992. Microstructural analysis of the classical spiral garnet porphyroblasts of south-east Vermont - evidence for non-rotation. Journal of Metamorphic Geology 10(4), 567–587. https://doi.org/10.1111/j.1525-1314.1992.tb00106.x

Jabaloy-Sánchez, A., Fernández-Fernández, E., González-Lodeiro, F., 2007. A cross section of the eastern Betic Cordillera (SE Spain) according field data and a seismic reflection profile. Tectonophysics 433, 97-126. https://doi.org/10.1016/j.tecto.2006.11.004

Jabaloy-Sánchez, A., Padrón-Navarta, J.A., Gómez-Pugnaire, M.T., López Sánchez-Vizcaíno, V., Garrido, C.J., 2019a. Alpine Orogeny: Deformation and Structure in the Southern Iberian Margin (Betics s.l.), in: Quesada, C., Oliveira, J.T., (Eds.), The Geology of Iberia: A Geodynamic Approach, Vol. 3, Ch. 10, p. 453-486 (Alpine Cycle, Vergés, J., Kullber, J.C.,

Volume Coordinators), Regional Geology Reviews. https://doi.org/10.1007/978-3-030-11295-0_10

Jabaloy Sánchez, A., Martín-Algarra, A., Padrón-Navarta, J.A., Martín-Martín, M., Gómez-Pugnaire, M.T., López Sánchez-Vizcaíno, V., Garrido, C.J., 2019b. Lithological Successions of the Internal Zones and Flysch Trough Units of the Betic Chain, in: Quesada, C., Oliveira, J.T., (Eds.), The Geology of Iberia: A Geodynamic Approach, Vol. 3, Ch. 8, p. 377-432 (Alpine Cycle, Vergés, J., Kullber, J.C., Volume Coordinators), Regional Geology Reviews. https://doi.org/10.1007/978-3-030-11295-0_8

Johnson, C., Harbury, N., Hurford, A.J., 1997. The role of extension in the Miocene denudation of the Nevado-Filábride Complex, Betic Cordillera (SE Spain). Tectonics 16, 189-204. https://doi.org/10.1029/96TC03289

Johnson, S.E., 1992. Sequential porphyroblast growth during progressive deformation and low-P high-T (LPHT) metamorphism, Cooma Complex, Australia: The use of microstructural analysis to better understand deformation and metamorphic histories. Tectonophysics 214, 311-339. https://doi.org/10.1016/0040-1951(92)90204-J

Kirchner, K.L., Behr, W.M., Loewy, S., Stockli, D.F., 2016. Early Miocene subduction in the western Mediterranean: Constraints from Rb-Sr multimineral isochron geochronology. Geochemistry, Geophysics, Geosystems 17, 1842-1860. https://doi.org/10.1002/2015GC006208

Li, B., Massonne, H.J., 2018. Two Tertiary metamorphic events recognized in high-pressure metapelites of the Nevado-Filábride Complex (Betic Cordillera, S Spain). Journal of Metamorphic Geology 36, 603-630. https://doi.org/10.1111/jmg.12312

Lonergan, L., Platt, J.P., Gallagher, L., 1994. The Internal-External Zone Boundary in the eastern Betic Cordillera, SE Spain. Journal of Structural Geology 16, 175-188. https://doi.org/10.1016/0191-8141(94)90103-1

López Sánchez-Vizcaíno, V., Rubatto, D., Gómez-Pugnaire, M.T., Trommsdorff, V., Müntener, O., 2001. Middle Miocene high-pressure metamorphism and fast exhumation of the Nevado-Filábride Complex, SE Spain. Terra Nova 13, 327-332. https://doi.org/10.1046/j.1365-3121.2001.00354.x

Mares, V.M., 1998. Structural development of the Soldiers Cap Group in the Eastern Fold Belt of the Mt Isa Inlier: A succession of horizontal and vertical deformation events and large-scale shearing. Australian Journal of Earth Sciences 45, 373-387. https://doi.org/10.1080/08120099808728398

Martín-Algarra, A., 1987. Evolución geológica alpina del contacto entre las Zonas Internas y las Zonas Externas de la Cordillera Bética. PhD Thesis, Universidad de Granada, 1171 p. https://digibug.ugr.es/handle/10481/75699

Martín-Algarra, A., Crespo-Blanc, A., Delgado, F., Estévez, A., González-Lodeiro, F., Orozco, M., Sánchez-Gómez, M., Sanz de Galdeano, C., García-Dueñas, V., 2004. Complejo Alpujárride. Estructura. Rasgos generales, in: Vera, J.A., (Ed.) Geología de España. SGE-IGME Madrid, 416-417.

Martín-Algarra, A., Mazzoli, S., Perrone, V., Rodríguez-Cañero, R., 2009. Variscan Tectonics in the Malaguide Complex (Betic Cordillera, Southern Spain): Stratigraphic and Structural Alpine versus Pre-Alpine Constraints from the Ardales Area (Province of Málaga). II. Structure. The Journal of Geology 117, 263-284. https://doi.org/10.1086/597365

Martín-Martín, M., El Mamoune, B., Martín-Algarra, A., Martín-Pérez, J.A., 1996. The Internal-External Zone Boundary in the Eastern Betic Cordillera, SE Spain: Discussion. Journal of Structural Geology 18, 523-524.

Martín-Rojas, I., Estévez, A., Martín-Martín, M., Delgado, F., García-Tortosa, F.J., 2007. New data from Orihuela and Callosa Mountains (Betic Internal Zone, Alicante, SE Spain). Implications for the "Almágride Complex" controversy. Journal of Iberian Geology 33 (2), 311-318.

Massonne, H.J., 2014. Wealth of P-T-t information in medium-high grade metapelites: Example from the Jubrique Unit of the Betic Cordillera, S Spain. Lithos 208-209, 137-157. https://doi.org/10.1016/j.lithos.2014.08.027

Munro, M.A., Blenkinsop, T.G., 2012. MARD-A moving average rose diagram application for the geosciences. Computers & Geosciences 49, 112-120. https://doi.org/10.1016/j.cageo.2012.07.012

Nieto, F., Velilla, N., Peacor, D.R., Ortega Huertas, M., 1994. Regional retrograde alteration of sub-greenschist facies chlorite to smectite. Contrib Mineral Petrol 115, 243-252. https://doi.org/10.1007/BF00310765

Orozco, M., Alonso-Chaves, F.M., Nieto, F., 1998. Development of large north-facing folds and their relation to crustal extension in the Alboran domain (Alpujarras region, Betic Cordilleras, Spain). Tectonophysics 298, 271-295. https://doi.org/10.1016/S0040-1951(98)00188-7

Orozco, M., Álvarez-Valero, A.M., Alonso-Chaves, F.M., Platt, J.P., 2004. Internal structure of a collapsed terrain The Lújar syncline and its significance for the fold- and sheet-structure of the Alborán Domain (Betic Cordilleras, Spain). Tectonophysics 385, 85-104. https://doi.org/10.1016/j.tecto.2004.04.025

Orozco, M., Alonso-Chaves, F.M., Platt, J.P., 2017. Late extensional shear zones and associated recumbent folds in the Alpujarride subduction complex, Betic Cordillera, southern Spain. Geologica Acta 15, 51-66. DOI: 10.1344/GeologicaActa2017.15.1.5

Platt, J.P., 1998. Comment on "Alternating contractional and extensional events in the Alpujarride nappes of the Alboran Domain (Betics, Gibraltar Arc)" by Juan C. Balanyá et al. Tectonics 17 (6), 973-976. https://doi.org/10.1029/1998TC900005

Platt, J.P., Whitehouse, M.J., 1998. Early Miocene high-temperature metamorphism and rapid exhumation in the Betic Cordillera (Spain): evidence from U-Pb zircon ages. Earth and Planetary Science Letters 171, 591-605. https://doi.org/10.1016/S0012-821X(99)00176-4

Platt, J.P., van den Eeckhout, B., Janzen, E., Konert, G., Simon, O.J., Weijermars, R., 1983. The structure and tectonic evolution of the Aguilón fold-nappe, Sierra Alhamilla, Betic Cordillera, SE Spain. Journal of Structural Geology 5, 519-538. https://doi.org/10.1016/0191-8141(83)90057-3

Platt, J.P., Kelley, S.P., Carter, A., Orozco, M., 2005. Timing of tectonic events in the Alpujarride Complex, Betic Cordillera, southern Spain. Journal of the Geological Society, London 162, 451-462. https://doi.org/10.1144/0016-764903-039

Platt, J.P., Anczkiewicz, R., Soto, J.I., Kelley, S.P., Thirlwall, M., 2006. Early Miocene continental subduction and rapid exhumation in the western Mediterranean. Geology 34, 981-984. https://doi.org/10.1130/G22801A.1

Porkoláb, K., Matenco, L., Hupkes, J., Willingshofer, E., Wijbrans, J., van Schrojenstein Lantman, H., van Hinsbergen, D.J.J., 2022. Tectonic evolution of the Nevado-Filábride Complex (Sierra de los Filabres, Southeastern Spain): Insights from new structural and geochronological data. Tectonics 41, e2021TC006922. https://doi.org/10.1029/2021TC006922

Puga, E., Díaz de Federico, A., 1976. Pre-Alpine metamorphism in the Sierra Nevada Complex (Betic Cordillera Spain). Cuadernos de Geología de la Universidad de Granada 7, 161-171.

Rodríguez-Cañero, R., Jabaloy-Sánchez, A., Navas-Parejo, P., Martín-Algarra, A., 2018. Linking Palaeozoic palaeogeography of the Betic Cordillera to the Variscan Iberian Massif: new insight through the first conodonts of the Nevado-Filábride Complex. International Journal of Earth Sciences 107, 1791-1806. https://doi.org/10.1007/s00531-017-1572-8

Rodríguez-Fernández, J., 1982. El Mioceno del sector central de las Cordilleras Béticas. PhD Thesis, University of Granada, 224 p. https://digibug.ugr.es/handle/10481/32561

Rodríguez-Fernández, J., Comas, M.C., Soria, J., Martín-Pérez, J.A., Soto, J.I., 1999. The sedimentary record of the Alboran basin: An attempt at sedimentary sequence correlation and subsidence analysis, in: Zahn, R., Comas, M.C., and Klaus, A. (eds), Proceedings of the Ocean Drilling Program, Scientific Results, Vol. 161, p. 69–76.

Rosenbaum, G., Lister, G., Duboz, C., 2002. Relative motions of Africa, Iberia and Europe during Alpine orogeny. Tectonophysics 359, 117-129. https://doi.org/10.1016/S0040-1951(02)00442-0

Rossetti, F., Faccenna, C., Crespo-Blanc, A., 2005. Structural and kinematic constraints to the exhumation of the Alpujarride Complex (Central Betic Cordillera, Spain). Journal of Structural Geology 27, 199-216. https://doi.org/10.1016/j.jsg.2004.10.008

Ruiz Cruz, M.D., Sanz de Galdeano, C., Lázaro, C., 2005. Metamorphic evolution of Triassic rocks from the transition zone between the Maláguide and Alpujárride complexes (Betic Cordilleras, Spain). European Journal of Mineralogy 17, 81-91. https://doi.org/10.1127/0935-1221/2005/0017-0081

Ruiz-Fuentes, A., Cabrera-Porras, A., Martín-Algarra, A., 2022. Structural record of polyorogenic pre-Alpine and Alpine deformations within a major thrust nappe close to a suture zone (Internal-External Zones Boundary of the central Betic Cordillera, S Spain). International Geology Review https://doi.org/10.1080/00206814.2022.2129472

Sánchez-Navas, A., Oliveira-Barbosa, R.C., García-Casco, A., Martín-Algarra, A., 2012. Transformation of Andalusite to Kyanite in the Alpujarride Complex (Betic Cordillera, Southern Spain): Geologic Implications. The Journal of Geology 120, 557-574. https://doi.org/10.1086/666944

Sánchez-Navas, A., García-Casco, A., Martín-Algarra, A., 2014. Pre-Alpine discordant granitic dikes in the metamorphic core of the Betic Cordillera: tectonic implications. Terra Nova 26, 477-486. https://doi.org/10.1111/ter.12123

Sánchez-Navas, A., García-Casco, A., Mazzoli, S., Martín-Algarra, A., 2017. Polymetamorphism in the Alpujarride Complex, Betic Cordillera, South Spain. The Journal of Geology 125, 637-657. https://doi.org/10.1086/693862

Sánchez-Rodriguez, L., Gebauer, D., 2000. Mesozoic formation of pyroxenites and gabbros in the Ronda area (southern Spain), followed by Early Miocene subduction metamorphism and emplacement into the middle crust: U-Pb sensitive high-resolution ion microprobe dating of zircon. Tectonophysics 316, 19-44. https://doi.org/10.1016/S0040-1951(99)00256-5

Sanislav, I.V., 2010. Porphyroblast rotation and strain localization: Debate settled!: Comment. Geology 38(4), e204. https://doi.org/10.1130/G30522C.1

Sanislav, I.V., Bell, T.H., 2011. The inter-relationships between long-lived metamorphism, pluton emplacement and changes in the direction of bulk shortening during orogenesis. Journal of Metamorphic Geology 29, 513-536. https://doi.org/10.1111/j.1525-1314.2011.00928.x

Sanz de Galdeano, C., 1989. Estructura de las Sierras Tejeda y de Cómpeta (conjunto Alpujárride, Cordilleras Béticas). Revista de la Sociedad Geológica de España 2, 77-84.

Sanz de Galdeano, C., López-Garrido, A.C., 2003. Revisión de las unidades Alpujárrides de las sierras de Tejeda, Almijara y Guájares (sector central de la Zona Interna Bética, provincias de Granada y Málaga). Revista de la Sociedad Geológica de España 16, 135-149.

Sanz de Galdeano, C., Ruiz Cruz, M.D., 2016. Late Palaeozoic to Triassic formations unconformably deposited over the Ronda peridotites (Betic Cordilleras): Evidence for their Variscan time of crustal emplacement. Estudios Geológicos 72(1), e043. https://doi.org/10.3989/egeol.42046.368

Sanz de Galdeano, C., Delgado, F., López-Garrido, A.C., 1995. Estructura del Alpujárride y del Maláguide al NW de Sierra Nevada (Cordillera Bética). Revista de la Sociedad Geológica de España 8, 239-250.

Sanz de Galdeano, C., López-Garrido, A.C., García-Tortosa, F.J., Delgado, F., 1997. Nuevas observaciones en el Alpujarride del sector centro-occidental de la Sierra de Carrascoy (Murcia). Consecuencias paleogeográficas. Estudios Geológicos 53, 229-236. https://doi.org/10.3989/egeol.97535-6229

Sayab, M., 2005. Microstructural evidence for N-S shortening in the Mount Isa Inlier (NW Queensland, Australia): the preservation of early W-E-trending foliations in porphyroblasts revealed by independent 3D measurement techniques. Journal of Structural Geology 27, 1445-1468. https://doi.org/10.1016/j.jsg.2005.01.013

Sayab, M., Shah, S.Z., Aerden, D., 2016. Metamorphic record of the NW Himalayan orogeny between the Indian plate-Kohistan Ladakh Arc and Asia: Revelations from foliation intersection axis (FIA) controlled P-T-t-d paths. Tectonophysics 671, 110-126. https://doi.org/10.1016/j.tecto.2015.12.032

Shah, S.Z., Sayab, M., Aerden, D., Asif Khan M., 2011. Foliation intersection axes preserved in garnet porphyroblasts from the Swat area, NW Himalaya: A record of successive crustal shortening directions between the Indian plate and Kohistan-Ladakh Island Arc. Tectonophysics 509, 14-32. https://doi.org/10.1016/j.tecto.2011.05.010

Simancas, J.F., 2018. A reappraisal of the Alpine structure of the Alpujárride Complex in the Betic Cordillera: Interplay of shortening and extension in the westernmost Mediterranean. Journal of Structural Geology 115, 231-242. https://doi.org/10.1016/j.jsg.2018.08.001

Simancas, J.F., Campos, J., 1993. Compresión NNW-SSE tardi a postmetamórfica y extensión subordinada en el Complejo Alpujárride (Dominio de Alborán, Orógeno Bético). Revista de la Sociedad Geológica de España 6, 23-35.

Skrzypek, E., Schulmann, K., Stípská, P., Chopin, F., Lehmann, J., Lexa, O., Haloda, J., 2011. Tectono-metamorphic history recorded in garnet porphyroblasts: insights from thermodynamic modelling and electron backscatter diffraction análisis of inclusion trails. Journal of Metamorphic Geology 29, 473-496. https://doi.org/10.1111/j.1525-1314.2010.00925.x

Sosson, M., Morillon, A.C., Bourgois, J., Féraud, G., Poupeau, G., Saint-Marc, P., 1998. Late exhumation stages of the Alpujarride Complex (western Betic Cordilleras, Spain): new thermochronological and structural data on Los Reales and Ojen nappes. Tectonophysics 285, 253-273. https://doi.org/10.1016/S0040-1951(97)00274-6

Stallard, A., Hickey, K., 2001. Shear zone vs folding origin for spiral inclusion trails in the Canton Schist. Journal of Structural Geology 23, 1845-1864. https://doi.org/10.1016/S0191-8141(01)00031-1

Tubía, J.M., 1988. Estructura de los Alpujárrides occidentales: Cinemática y condiciones de emplazamiento de las peridotitas de Ronda. Parte I: Características litológicas. Boletín Geológico y Minero 99(II), 165-212.

Tubía, J.M., 1994. The Ronda peridotites (Los Reales nappe): an example of the relationship between lithospheric thickening by oblique tectonics and late extensional deformation within the Betic Cordillera (Spain). Tectonophysics 238, 381-398. https://doi.org/10.1016/0040-1951(94)90065-5

Tubía, J.M., Navarro-Vilá, F., 1984. Criterios para la diferenciación entre los esquistos de grado medio del Complejo Maláguide y del Manto de Los Reales al W de Málaga. La posición del contacto de corrimiento. El borde Mediterráneo Español, Granada, 33-34.

Tubía, J.M., Gil-Ibarguchi, J.I., 1991. Eclogites of the Ojén nappe: a record of subduction in the Alpujárride complex (Betic Cordilleras, southern Spain). Journal of the Geological Society, London 148, 801-804. https://doi.org/10.1144/gsjgs.148.5.0801

Tubía, J.M., Cuevas, J., Navarro-Vilá, F., Álvarez, F., Aldaya, F., 1992. Tectonic evolution of the Alpujárride Complex (Betic Cordillera, southern Spain). Journal of Structural Geology 14 (2), 193-203. https://doi.org/10.1016/0191-8141(92)90056-3

Tubía, J.M., Navarro-Vilá, F., Cuevas, J., 1993. The Maláguide-Los Reales Nappe: an example of crustal thinning related to the emplacement of the Ronda peridotites (Betic Cordillera). Physics

of the Earth and Planetary Interiors 78, 343-354. https://doi.org/10.1016/0031-9201(93)90165-6

Vissers, R.L.M., Meijer, P.T., 2012. Iberian plate kinematics and Alpine collision in the Pyrenees. Earth Science Reviews 114, 61-83. https://doi.org/10.1016/j.earscirev.2012.05.001

Williams, J.R., Platt, J.P., 2017. Superposed and refolded metamorphic isograds and superposed directions of shear during late orogenic extension in the Alborán Domain, southern Spain. Tectonics 36, 756-786. https://doi.org/10.1002/2016TC004358

Williams, J.R., Platt, J.P., 2018. A new structural and kinematic framework for the Alborán Domain (Betic-Rif arc, western Mediterranean orogenic system). Journal of the Geological Society 175, 465-496. https://doi.org/10.1144/jgs2017-086

8. Linking deformation, metamorphism and geochronology to constrain the tectonic evolution of the western Mediterranean

Alejandro Ruiz-Fuentes[1], Domingo G.A.M. Aerden[1,2], Delphine Bosch[3], Olivier Bruguier[3], Michel Corsini[4], Jean-Marc Lardeaux[4]

[1] *Departamento de Geodinámica, Universidad de Granada, Av. Fuentenueva, 18071, Granada, Spain*

[2] *Instituto Andaluz de Ciencias de la Tierra, CSIC/Universidad de Granada, Av. de las Palmeras 4, 18100, Armilla, Granada, Spain*

[3] *Géosciences Montpellier, UMR 5243, Université Montpellier 2, CC 060, place Eugène Bataillon, 34095 Montpellier cedex 5, France*

[4] *Géoazur, Université Côte d'Azur, CNRS, IRD, Observatoire de la Côte d'Azur, UMR 7329, 250, rue Albert-Einstein, 06560 Sophia Antipolis, France*

Manuscript in preparation

Abstract

Integration of microstructural, petrological and geochronological techniques has allowed the detailed characterization of timing and metamorphic features of specific deformation events in the Betic Cordillera. Pseudosection modelling, thermobarometric estimations, U-Th-Pb in-situ monazite geochronology, and Ar-Ar geochronology have been applied in samples of special interest due to the presence of well-constrained deformation fabrics and garnets with specific orientation of inclusion trails. Our study helps constrain the timing of a sequence of deformation events in the Alpujárride Complex, which occurred in a decompressional framework, from a regional-scale early Miocene event ending around 18.5 Ma coeval with the Alborán Sea opening, to a late-metamorphic event at around 17.5 Ma associated to continental collision. In the Nevado-Filábride Complex, multiple garnet generations are present in the same sample as evidenced by microstructural and chemical features, one of which has been interpreted as recording Low-Pressure/High-Temperature conditions at around 13 Ma. Age constraints for microstructural trends fossilized within porphyroblasts refine the sequence of changing shortening directions previously linked to the plate-motion interplay between the Alborán Domain, Iberia and Africa from Eocene to Middle Miocene.

Keywords: Alpujárride Complex, Nevado-Filábride Complex, Betic Cordillera, Alpine orogeny, Foliation Intersection Axes

8.1. Introduction

Geological and geophysical research in the Betic-Rif orogen during the last few decades have greatly improved our understanding of its tectonic history, particularly regarding the timing and kinematics of the belt in relation to mantle processes. Nevertheless, several controversial and interrelated questions remain debated including the age (Variscan or Alpine) and mechanism of emplacement (extensional, compressional) of mantle rocks exposed in the belt, the pre-Alpine paleogeography, the number and polarity of subduction zones, or the kinematics of polyphase deformation in the metamorphic hinterland (Nevado-Filábride and Alpujárride-Sebtide complexes).

Recently, these questions have been tackled with a new microstructural approach focusing on the geometry and orientation of porphyroblast inclusion trails combined with geochronological methods (Aerden and Sayab, 2008; Aerden et al., 2010, 2013, 2022; Ruiz-Fuentes and Aerden, 2023). This research has revealed the existence of three sets of inclusion trail in the Betic-Rif orogen and has proposed close relationships with regional-scale fold patterns and the plate-tectonic evolution of the Alpine system. The regional consistency of these inclusion-trail orientations is quite remarkable in view of the strongly curved shape of the orogen (Gibraltar Arc), although similar consistency has been documented earlier in other oroclines (Bell and Mares, 1999; Yeh and Bell, 2004; Aerden, 2004). These and other studies (e.g. Bell et al., 1992; Hayward, 1992; Aerden, 1994, 1998, 2004; Bell and Welch, 2002; Ham and Bell, 2004; Sayab, 2005; Yeh, 2007; Ali, 2010; Abu Sharib and Bell, 2011; Sanislav and Bell, 2011; Shah et al., 2011; Skrzypek et al., 2011; Bell and Sapkota, 2012; Aerden et al., 2013, 2021, 2022; Kim and Ree, 2013; Sayab et al., 2016; Ruiz-Fuentes and Aerden, 2023) illustrate the wealth of kinematic information that can be recorded by porphyroblasts and accessed with modern 3D microstructural techniques and concepts.

Particular importance is given in these works to axes of inclusion-trail curvature, alternatively referred to in the literature as axes of relative porphyroblast-matrix rotation, inclusion-trail symmetry axes (Robyr et al., 2009) or, as adopted herein, Foliation Intersection/Inflection Axes (FIA; Bell et al., 1995; Kim and Sanislav, 2017). FIA have been predicted to form either normal to the direction of bulk shortening in a rock, or normal to the direction of bulk shearing (i.e. tectonic transport) depending on the question whether inclusion trail curvature is due to matrix deformation and rotation around rotationally stable porphyroblasts (Bell, 1985; Aerden, 1995) or due to rotation of porphyroblasts induced by shearing in the matrix (Spry, 1963; Rosenfeld, 1970), respectively. Thus in both models they are a first order objective kinematic criterion requiring few further assumptions. So far, the majority of published inclusion-trail orientation data has favoured the first model (porphyroblast non-rotation) as only this model offers a plausible explanation of consistent porphyroblast orientations in multiply folded and sheared rocks.

Most FIA data has been gathered through study of multiple (between 3 and 10) differently oriented thin sections of individual samples allowing determination of an

average FIA orientation (Hayward, 1990; Aerden, 2003). In some cases, a succession of two or even three FIAs can been reconstructed using these techniques preserved in progressive porphyroblast growth stages of a sample. However, thin-section based FIA techniques are time-consuming and can run into problems where rocks contain few porphyroblasts with complex inclusion trails, or FIAs with very steep plunges, or FIAs that are defined by inclusion-trails showing inconsistent curvature senses (cf. Aerden and Ruiz-Fuentes, 2020). With the advance of X-ray computed micro-tomography (XCT) as a tool for microstructural analysis of metamorphic rocks (e.g. Huddlestone-Holmes and Ketcham, 2005, 2010; Sayab et al., 2015, 2021; Aerden and Ruiz-Fuentes, 2020) it has become possible to rapidly measure the FIAs of a large number of individual porphyroblasts in a sample, and hence to evaluate the spread of FIA orientations and detect multiple FIA sets that would be easily missed using multiple thin sections alone.

Aerden et al. (2022) and Ruiz-Fuentes and Aerden (2023) extensively applied XCT in the Betic-Rif orogen where they measured a total of 954 FIAs in 59 samples from widely scattered locations and different tectonic units. Rose diagrams for this data combined with microstructural relative-timing criteria indicate the existence of three main FIA sets in the orogen that formed at different times with the following specific trends and chronological order: WNW-ESE, NE-SW and NNW-SSE. Preliminary Sm-Nd dating of garnet porphyroblasts in 10 samples demonstrates that these FIA formed between the late Eocene and the middle Miocene (35-12 Ma). During the Miocene the formation of the two younger FIA sets appear to have alternated or to have been synchronous at different locations.

Here, we report the results of several thermobarometric (Zr-in-rutile thermometry and pseudosection modelling) and geochronological techniques (LA-ICP-MS dating of monazite and Ar-Ar dating on micas and amphibole) applied to 4 samples from the Alpujárride Complex and one from the Nevado-Filábride Complex, representative of the earlier mentioned three principle FIA sets. We use red, orange and green colours to distinguish the three FIAs in our Figures and descriptions, following the example of the original papers. Our results provide additional confirmation of the relative timing of FIA sets and absolute-age constraints. A surprisingly young age of 17.5 Ma has been found for synchronous monazite and garnet growth in one of the Alpujárride samples hosting a NE-SW trending (orange) FIA. This implies that exhumation of the complex was not yet completed at this time, and was followed by exhumation of the Nevado-Filábride starting around 13.5 Ma (Santamaría-López et al., 2019; Aerden et al., 2022) only about 4 million years later.

8.2. Geological setting

8.2.1. The Betic Cordillera

The Gibraltar Arc constitutes the western extremity of the Alpine orogenic system in the Mediterranean (Fig. 8.1). It comprises the Betic Cordillera in southern Spain and the Rif chain in northern Morocco. The Betic Cordillera is composed of a metamorphic core

(Internal Zones) and an external fold-and-thrust belt made up of Mesozoic and Cenozoic sedimentary rocks (External Zones and Flysch Complex) which represented the former South Iberian adjacent continental margin and basin environments, respectively. The Internal Zones mainly consist on a group of tectonically stacked units, which in ascending order are the Nevado-Filábride, Alpujárride and Maláguide complexes. The Nevado-Filábride on the whole or at least its lower part has been traditionally considered to represent a subducted and exhumed portion of the South Iberian crust (Guerrera et al., 1993; Platt et al., 2006; Puga et al., 2011; Gómez-Pugnaire et al., 2012; Rodríguez-Cañero et al., 2018) overthrusted by allochthonous Alpujárride and Maláguide units (Alborán Domain; Bouillin et al., 1986; Guerrera et al., 1993, 2021). However, coincident kinematics and ages of deformation recently shown in the Alpujárride and Nevado-Filábride complexes leaves open the possibility that both are derived from the same crustal domain (Aerden et al., 2022; Porkolab et al., 2022; Poulaki et al., 2023), that in the early Miocene started to collide with the Iberian microplate, leading to the destruction of the Flysch Basin and the development of the external fold-and-thrust belt. While the Nevado-Filábride and Alpujárride complexes experienced medium- to high-grade metamorphism (see details below), the uppermost Maláguide only underwent low-grade metamorphism (Nieto et al., 1994; Ruiz Cruz et al., 2005), or remained unmetamorphosed as well as several tectonic slices located at the front of the Internal Zones (Frontal Units / Dorsale Calcaire) only affected by metamorphism locally (Mazzoli et al., 2013).

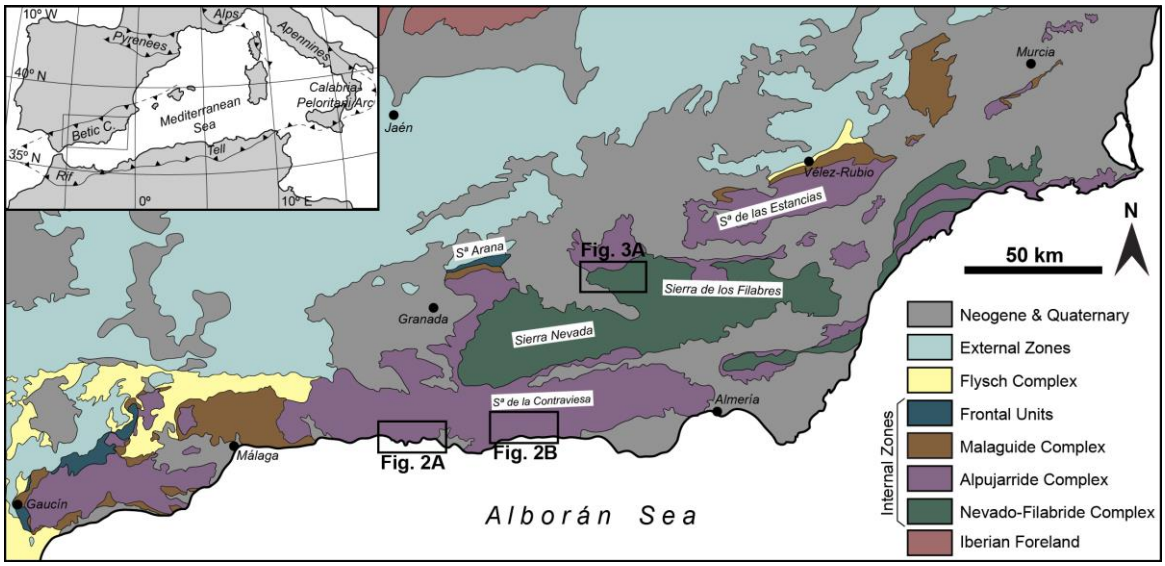

Fig. 8.1. Geological map of the Internal Zones of the Betic Cordillera (modified from Ruiz-Fuentes and Aerden, 2023).

8.2.2. Alpujárride Complex

The Alpujárride Complex is usually considered to be composed of a series of stacked lithotectonic units (Fig. 8.2), although this arrangement has been recently questioned (Williams and Platt, 2017, 2018). Different tectonic subdivisions have been proposed (e.g Aldaya et al., 1979; Simancas and Campos, 1993; Azañón et al., 1994; Alonso-Chaves and Orozco, 1998; Sanz de Galdeano and López-Garrido, 2003) that can be reduced to

three main groups of units which are the Lower-, Intermediate- and Upper Alpujárride units (Tubía et al., 1992; Martín-Algarra et al., 2004).

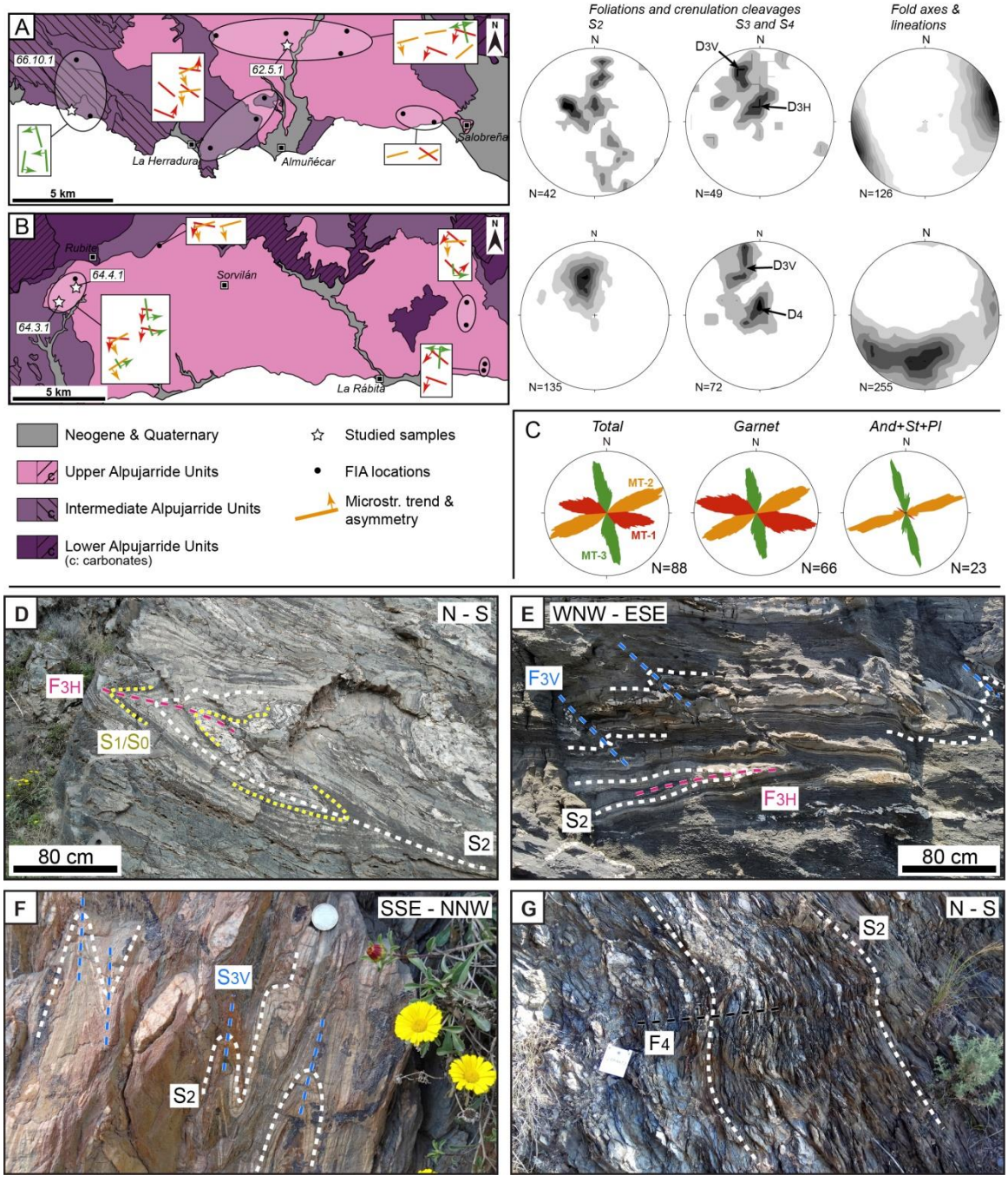

Fig. 8.2 (previous page). A and B) Geological map and equal-area and lower-hemisphere projections of structures for the Almuñécar and Contraviesa areas. Stars indicate the location of the studied samples. Coloured bars and arrows indicate the orientation and asymmetry of other FIA within the areas (see details in Ruiz-Fuentes and Aerden, 2023). Projections were made with Stereonet software (Allmendinger et al., 2013). C) FIA trends in the Alpujárride Complex determined by Ruiz-Fuentes and Aerden (2023). Data is also presented separated according to the hosting mineral for comparison. The rose diagrams are made with MARD (Munro and Blenkinsop, 2012). D) D_2 and D_{3H} fold interference east of La Herradura. E) Fold interference east of Almuñécar. D_{3V} folds overprint D_{3H}. F) D_{3V} transposition zone at the Contraviesa area. G) D_4 structures in the Contraviesa area.

The Alpujárride-type lithostratigraphic succession consists of Paleozoic migmatites, gneisses, graphite schists and quartzites, Permo-Triassic light coloured schists, quartzites and phyllites, and Triassic carbonates (Alonso-Chaves et al., 2004). Nevertheless, the type-sequence may appear incomplete or include additional lithologies. In this sense, a lack of Paleozoic rocks in the Lower Alpujárrides can be noted, or the presence of peridotites (Ronda peridotites) and granulites at the base of the Los Reales nappe (Upper Alpujárride units).

High-pressure metamorphism is recorded in the Alpujárride Complex (e.g. Azañón and Goffé, 1997; Azañón and Crespo-Blanc, 2000; Booth-Rea et al., 2002), which locally reached eclogite facies conditions (Tubía and Gil-Ibarguchi, 1991) and probably took place or at least commenced in the late-Eocene (Platt et al., 2005; Bessière et al., 2022). High-pressure metamorphism has been traditionally linked to a D_1 deformation event and S_1 foliation preserved in S_2 microlithons and porphyroblast inclusion trails, but Ruiz-Fuentes and Aerden (2023) have shown that inclusion trails correspond to a large number of different foliations that can be grouped in three sets with specific regionally consistent trends (WNW-ESE, ENE-WSW and NNW-SSE in chronological order). The corresponding deformation periods were labelled D_{1A}, D_{1B} and D_{1C} and all predate the main matrix cleavage (Fig. 8.2).

Decompression following high-pressure metamorphism may have been nearly isothermal with a slight cooling (Balanyá et al., 1997; Azañón et al., 1997, 1998; Alonso-Chaves and Orozco, 2007) or accompanied by heating (Soto and Platt, 1999; Platt et al., 2003; Booth-Rea et al., 2005). Decompression is dated as early Miocene (e.g. Zeck et al., 1992; Monié et al., 1994; Whitehouse and Platt, 2003; Bessière et al., 2022) coeval with the deposition of the earliest unconformable sediments on top of the Internal Zones and in the Alborán basin (e.g. González Donoso et al., 1982; Aguado et al., 1990; Comas et al., 1992). Decompression is generally related to development of the principle schistosity (S_2), which has been interpreted either as extensional (Azañón et al., 1997; Balanyá et al., 1997; Alonso-Chaves and Orozco, 2007; Williams and Platt, 2017, 2018; Simancas, 2018) or contractional (Tubía et al., 1992; Rossetti et al., 2005). In some areas, however, S_3 transposes S_2 and takes over the status of principle cleavage.

The late metamorphic evolution is linked to the development of at least two crenulation cleavages and fold generations, which until recently were attributed to a single D_3 event, whose extensional or contractional character also continues to be debated (Cuevas, 1991; Tubía et al., 1992; Simancas and Campos, 1993; Azañón et al., 1997; Balanyá et al., 1997, 1998; Platt, 1998; Orozco et al., 1998, 2004; Alonso-Chaves and Orozco, 2007; Williams and Platt, 2017, 2018; Simancas, 2018). Detailed overprinting relationships observed in outcrop and precisely oriented thin sections coupled to quantitative field data and petrological observations led Ruiz-Fuentes and Aerden (2023) to distinguish two sets of crenulation cleavages, an earlier subhorizontal one and a later subvertical one referred to as S_{3H} and S_{3V}. The subhorizontal (S_{3H}) crenulation cleavage is well-developed in the western and central Alpujárrides (Fig. 8.2d and e), whilst the steeply-dipping to subvertical crenulation cleavage (S_{3V}) is broadly developed in the

Contraviesa area (Fig. 8.2f) and locally in the western Alpujárrides, north of Sierra Nevada, and the Almuñécar area (Ruiz-Fuentes and Aerden, 2023). In Almuñécar, the steeply-dipping set (S_{3V}) cross-cuts S_{3H} (Fig. 8.2e) and associated D_{3H} folds thereby establishing the temporal sequence in which they formed. Late low-angle faults, shear bands and associated folds (D_4; Fig. 8.2g) postdate the above mentioned succession of structures (Cuevas et al., 1986; Cuevas, 1991; Simancas and Campos, 1993; Crespo-Blanc et al., 1994; Simancas, 2018).

8.2.3. Nevado-Filábride Complex

Several subdivisions have been proposed for the internal organization of the Nevado-Filábride Complex either involving major tectonic contacts bounding regional scale nappe units (Puga et al., 1974, 2002; García-Dueñas et al., 1988; Bakker et al., 1989; Martínez-Martínez et al., 1995, 2002) or considering a relatively continuous stratigraphic sequence (Galindo-Zaldivar et al., 1989; Gómez-Pugnaire et al., 2004, 2012; Sanz de Galdeano and López-Garrido, 2016; Santamaría-López and Sanz de Galdeano, 2018). The Nevado-Filábride lithostratigraphic sequence comprises a lower monotonous thick succession of Paleozoic graphite schists and quartzites with local intercalations of graphitic marbles (Laborda-López et al., 2015; Rodríguez-Cañero et al., 2018), corresponding to the Veleta (Puga et al., 2002) or Ragua unit (Martínez-Martínez et al., 2002). The upper series mainly include Paleozoic graphite schists with relics of pre-Alpine thermal metamorphism (Puga et al., 1975) and intercalations of gneisses, and a series of quartzites, light-coloured schists, metaevaporites, calcschists and marbles variably intercalated with mafic rocks and serpentinites, ranging in age from Permian to Jurassic (Tendero et al., 1993; Puga et al., 2011; Jabaloy-Sánchez et al., 2018; Poulaki and Stockli, 2022). These series are included in the Mulhacén complex (subdivided in Caldera, Ophiolitic and Sabinas units; Puga et al., 2002), Calar Alto and Bédar-Macael units (Martínez-Martínez et al., 2002), or as other units as stated above (e.g. Bakker et al., 1989; Gómez-Pugnaire et al., 2012; Sanz de Galdeano and López-Garrido, 2016).

The Nevado-Filábride experienced high-pressure metamorphism reaching eclogite conditions between Paleogene (Monié et al., 1991; Puga et al., 2000, 2005; Augier et al., 2005; Li and Massonne, 2018; Aerden et al., 2022; Porkoláb et al., 2022; Poulaki et al., 2023) to Lower-Middle Miocene (Platt et al., 2006; Kirchner et al., 2016), possibly encompassing two different metamorphic events (e.g. Puga et al., 2000; Li and Massonne, 2018). A large variety of P-T trajectories have been published including isothermal decompression (Augier et al., 2005; Ruiz-Cruz et al., 2015), decompression with cooling (Behr and Platt, 2012) or heating (Gómez-Pugnaire and Fernández-Soler, 1987; Santamaría-López et al., 2019) in a single loop, reheating following decompression and cooling (Bakker et al., 1989; Booth-Rea et al., 2015), or reheating and pressure increase after an earlier Alpine cycle (Puga et al., 2005; Li and Massonne, 2018). The age of high-temperature metamorphism at low pressure (7 kbar) has been estimated as ~13 Ma (Santamaría-López et al., 2019). Multiple generations of folds, shear zones and associated fabrics similar as described for the Alpujárride Complex also characterize the Nevado-Filábride Complex, including a main cleavage (S_2) and at least two younger crenulation

cleavages with subhorizontal and subvertical orientations (Aerden and Sayab, 2008; Aerden et al., 2013; Ruiz-Fuentes and Aerden, 2018). The regional geometry and distribution of these foliations in the complex requires further field work. Porphyroblast inclusion trail data and microstructural timing criteria evidence three similar sets (Fig. 8.3b) of inclusion trails as found in the Alpujárride Complex. Geochronological evidence supports a coeval development in both complexes from the late-Eocene to the early Miocene, but continuing longer in the Nevado-Filabride complex until the middle Miocene.

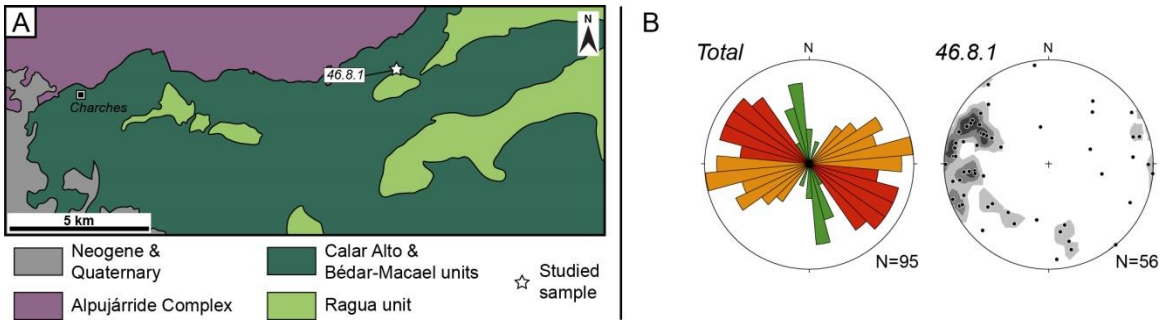

Fig. 8.3. A) Geological map of the western Sierra de los Filabres showing the location of sample 46.8.1 (modified from Martínez-Martínez et al., 1995). B) Regional-scale FIA trends in the Nevado-Filábride Complex (from Aerden et al., 2022) and individual FIAs determined in sample 46.8.1 (from Aerden and Ruiz-Fuentes, 2020).

8.3. Microstructural data and interpretation

8.3.1. Sample 66.10.1

Sample 66.10.1 (Lat: 36.74816º; Long: -3.80552º) is an amphibolitic schist from the Herradura nappe (Fig. 8.2a; Intermediate Alpujárride units) hosting 2-3 mm sized garnets with sigmoidal (45-90° curvature) to spiral-shaped (90-180° curvature) inclusion trails. Twenty-eight FIAs were measured with tightly clustered orientations around 190/20 (Fig. 8.4) making them representative of the 'green' (NNW-SSE) FIA set of Ruiz-Fuentes and Aerden (2023). These FIAs correspond to a succession of subhorizontal and N-S striking subvertical inclusion trails showing mutual truncation (Fig. 8.4). The orthogonal character and truncational relationships are best explained in terms of episodic garnet growth controlled by alternating contraction and gravitational collapse (Bell and Fay, 2016 and references cited therein; Aerden and Ruiz-Fuentes, 2020; Aerden et al., 2022; Ruiz-Fuentes and Aerden, 2023 - their Fig. 13b). The matrix cleavage (S_2) dips moderately SE in the sample and isoclinally folds an earlier S_1. S_2 is itself crenulated with subvertical, N-S striking axial planes causing gently S- to SSE-plunging L_3 crenulation axes subparallel to the measured FIAs. Fold axes and lineations measured in sample's outcrop and a second outcrop 300 m farther east exhibit a large difficult to interpret spread of orientations probably corresponding to multiple fold generations.

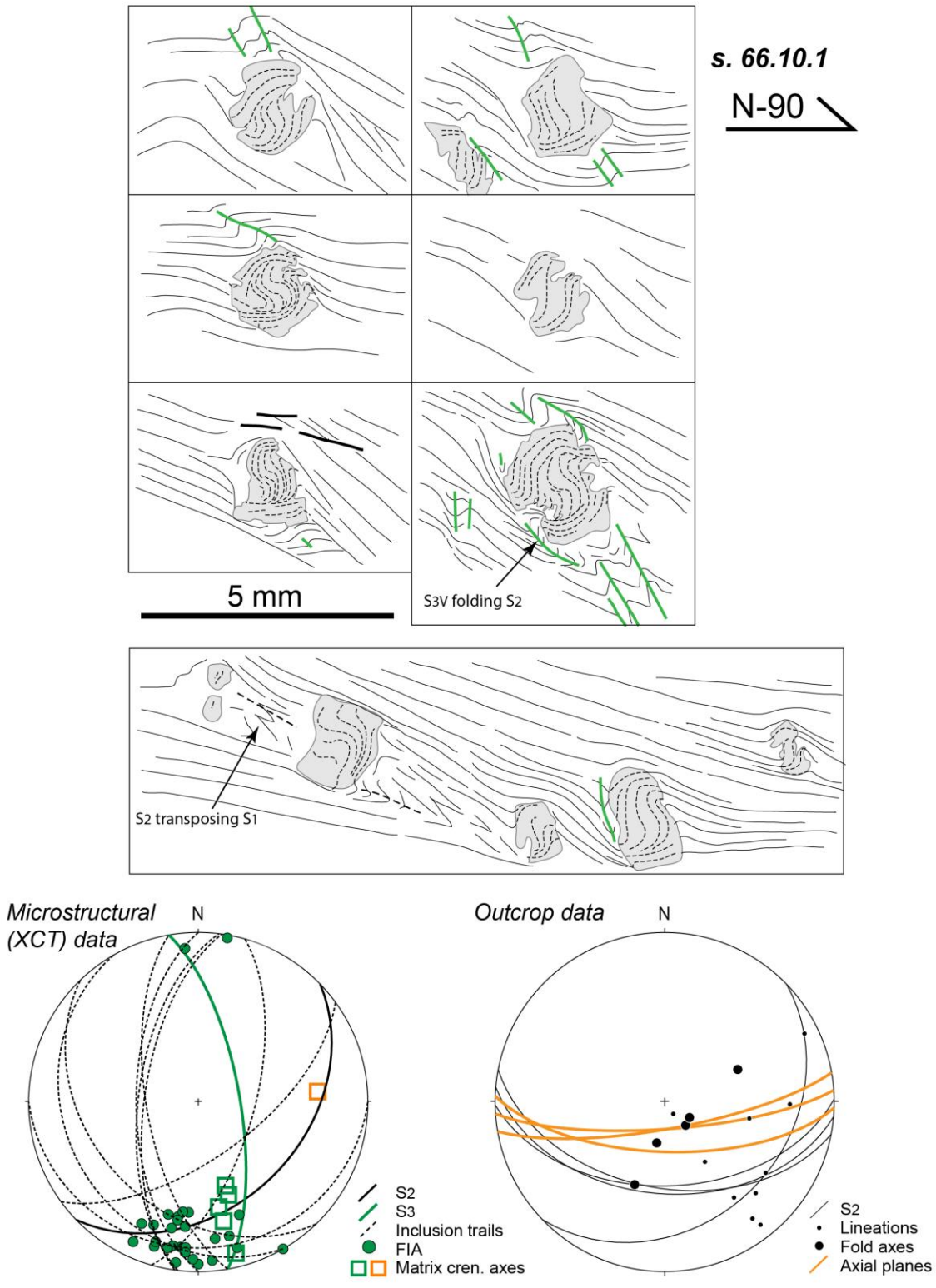

Fig. 8.4. Microstructural and outcrop data of sample 66.10.1. Projections were made with Stereonet software (Allmendinger et al., 2013).

Assuming that porphyroblast nucleation and growth is generally controlled by crenulation cleavage development and preferentially take place at the start of crenulation events (Bell and Hayward, 1991), we interpret that the development of S_2 coincided with

the final stages of an episodic garnet-growth history based on its continuity with subhorizontal inclusion trails in the rims of some porphyroblasts. This was followed by steepening of S_2 during D_3 folding without further garnet growth. The parallelism of L_3 crenulation axes and FIAs suggests that both formed during a period of E-W directed contraction alternating with stages of gravitational collapse, where S_2 represents the final and probably the regionally most significant collapse stage.

8.3.2. Sample 62.5.1

Sample 62.5.1 (Lat: 36.77957º; Long: -3.68810º) is a micaschist from the Upper Alpujárride Salobreña unit (Fig. 8.2a) containing numerous 1-2 mm sized garnets. It was studied in one horizontal and one vertical N-S striking thin section. The block of the horizontal thin section (measuring 1x3x5 cm) was analysed by XCT. Although the tomographic scan contains about 150 garnet porphyroblasts, inclusion trails are only clearly visible in some of them due to the very small size of inclusions compared to the scanning resolution used (20 µm). Those that could be measured mostly dip steeply NNE (Fig. 8.5) in porphyroblast cores and curving sigmoidally towards the horizontal in the rims resulting in gently WNW plunging FIAs (Fig. 8.5). Because of this trend, the FIAs are part of the 'red' FIA set of Ruiz-Fuentes and Aerden (2023), which was interpreted by these authors to predate the 'orange' (NE-SW) and 'green' (NNW-SSE) FIA sets. The horizontal thin section contains five garnets with well developed inclusion trails. Three have similar sigmoidal inclusion trails striking WNW-ESE in the core, changing to NE-SW in the rims (Fig. 8.5). A fourth garnet crystal exhibits spiral-shaped inclusion trails with a euhedral core overgrowing a foliation that still predates the WNW-ESE inclusion trails in the three garnets with sigmoidal trails. A fifth garnet lacks a microstructurally differentiated core and rim and passively overgrows several S_2 crenulation-cleavage planes (Fig. 8.5).

In the matrix and in outcrop, a moderately to steeply NW dipping main cleavage (S_2) is overprinted with NE-SW trending crenulations and folds assigned to the D_{3V} event of Ruiz-Fuentes and Aerden (2023). In the tomographic image, relics of older NW-SE crenulations are visible within microlithons of S_2 most probably genetically related to the FIAs, which have the same trend. A weak subhorizontal crenulation cleavage can also be recognized weakly overprinting the main cleavage which can be assigned to the late-metamorphic S_4 of Ruiz-Fuentes and Aerden (2023).

Based on these observations, we interpret the following garnet-growth history. Garnet porphyroblasts with sigmoidal inclusion trails, which appear to be the majority, nucleated when a subhorizontal crenulation cleavage (S_2) started to deform the steeply dipping WNW-ESE striking S_1 that is still preserved in the cores of these garnets. Subsequent NW-SE directed shortening (D_{3V}) folded and steepened S_2 to its current NE dipping position while triggering renewed garnet growth, both as rims around existing garnets and as new porphyroblasts that passively overgrew S_2. The garnet porphyroblasts with euhedral core observed in thin section implies that some garnets already nucleated during D_1, but most formed early syn-D_2.

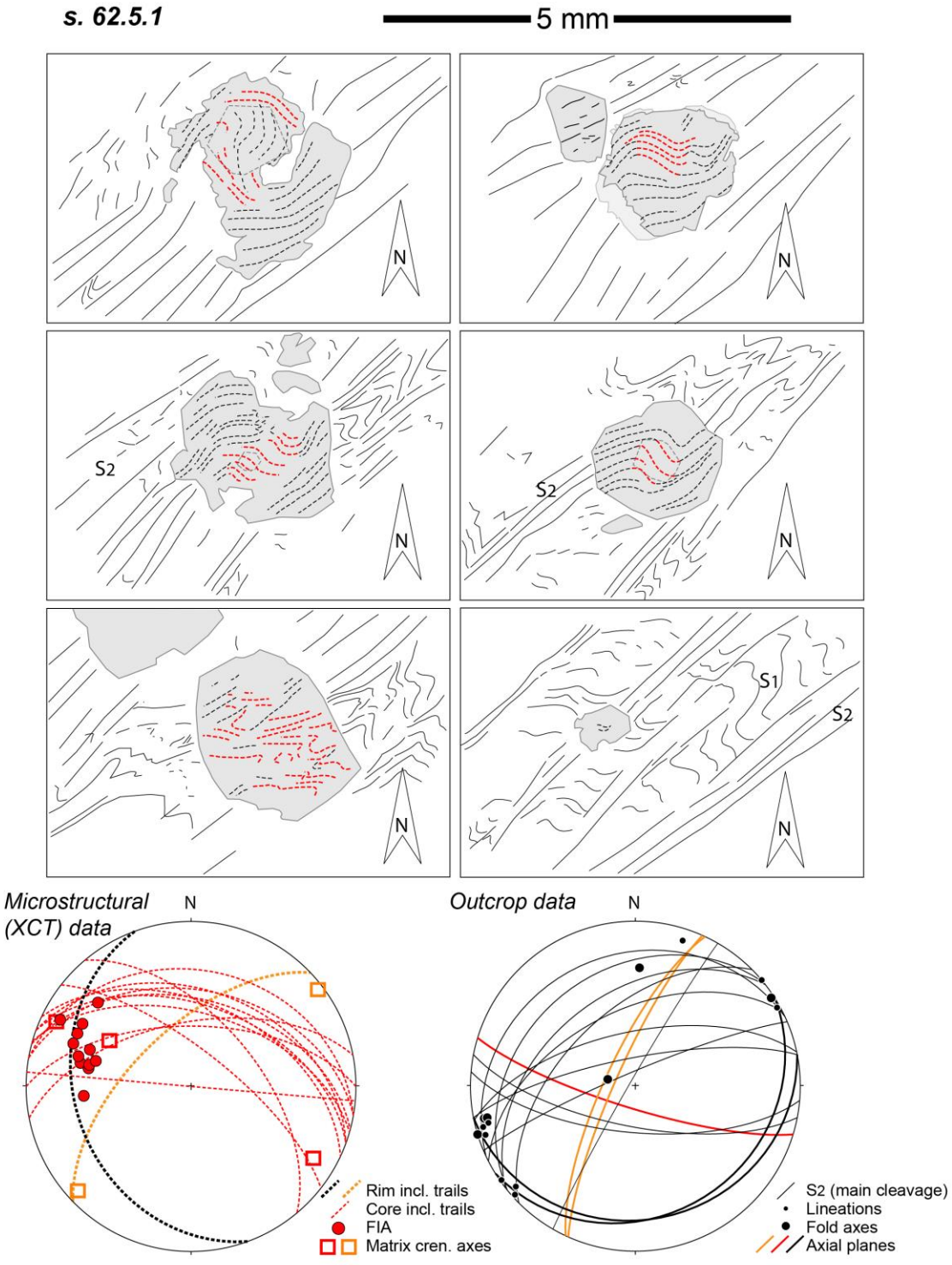

Fig. 8.5. Microstructural and outcrop data of sample 62.5.1. Projections were made with Stereonet software (Allmendinger et al., 2013).

8.3.3. Sample 64.3.1

Sample 64.3.1 (Lat: 36.78675º; Long: -3.37048º) is a micaschist from the western Sierra de la Contraviesa collected SW of Rubite (Fig. 8.2b) in the lower part of the Adra nappe (Upper Alpujárride units) according to Cuevas (1989a). In the matrix, S_2 dips moderately SE and is crenulated by a more steeply SE dipping S_{3V}.

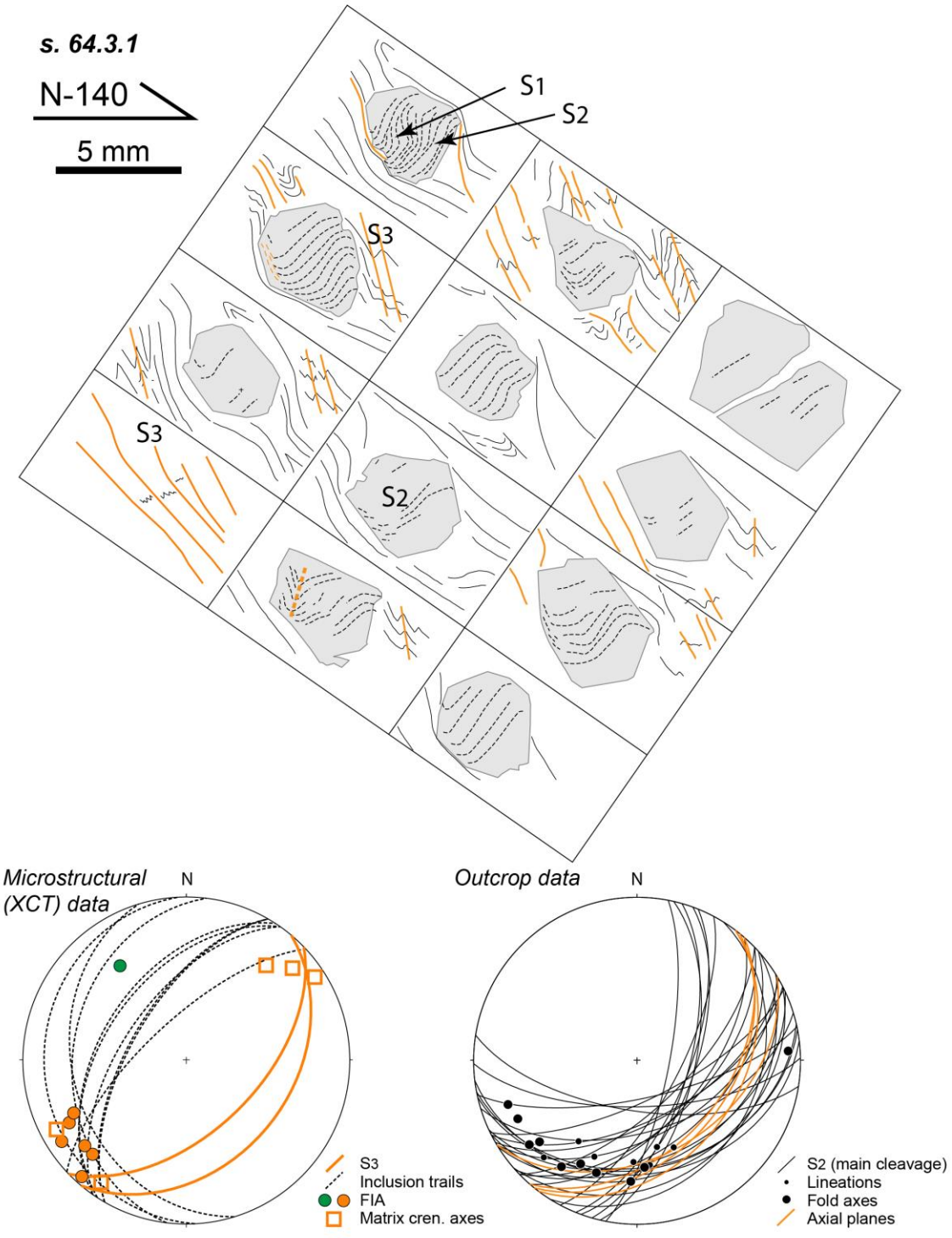

Fig. 8.6. Microstructural and outcrop data of sample 64.3.1. Projections were made with Stereonet software (Allmendinger et al., 2013).

Garnets in this sample measure 2-5 mm and have NE-SW trending FIAs sub parallel to crenulation axes in the matrix. One FIA was found with an anomalous NNW-SSE trend (Fig. 8.6). The NE-SW FIA trend corresponds to the orange FIA set of Ruiz-Fuentes and Aerden (2023). Inclusion trails are mainly straight or sigmoidal and curve from steeply NW dipping in porphyroblast towards horizontal. In some cases they continue to curve

into parallelism with S_3 in the outermost porphyroblast rims. These observations indicate that most garnets overgrew S_2 early during D_3 (cf. Bell and Hayward, 1991). Indeed, Cuevas (1989b) already mentioned the possibility that garnet was still forming during D_3 in the Adra nappe as confirmed here. However, one garnet observed in a NW-SE striking vertical thin section preserve inclusion trails of S_2 surrounding a crenulated S_1. This particular garnet can be interpreted to have grown in two stages punctuated by the onset of D_2 and later D_3.

8.3.4. Sample 64.4.1

Sample 64.4.1 (Lat: 36.79514º; Long: -3.36048º) is a micaschist from the Adra nappe located 300 metres NE of sample 64.3.1 (Fig. 8.2b). It contains 2-5 mm sized garnets and numerous smaller (0.1-2 mm) staurolite crystals. Garnet FIAs in this sample define a strong orientation maximum at 280/30 (Fig. 8.7), corresponding to the red FIA set of Ruiz-Fuentes and Aerden (2023). However, we also identified a FIA with NNW-SSE trend and subhorizontal plunge in a garnet rim, which falls in the 'green' set as defined in the same paper.

Two N-S striking vertical thin sections were studied in which two types of inclusion-trail were found (Fig. 8.7). The first type (Type-I) curve 90-120° clockwise (viewing towards the east) from gently to moderately N pitching in porphyroblast cores through the horizontal to subvertical in the rims. Type-II porphyroblasts curve more weakly clockwise from subvertical in the centre, but sharply reverse their curvature sense in the rims where they horizontally exit porphyroblasts. Such curvature reversals have been shown to either result from a staircase geometry of inclusion trails in 3D associated with a single FIA, or from two differently oriented FIAs preserved in cores and rims of porphyroblasts (Bell et al., 1995; Bell et al., 1998). The latter is in our case supported by the NNW-SSE trending FIA that was measured and subvertical N-S inclusion trails measured in the rims of two Type-II garnets in the XCT scan (Fig. 8.7).

Type-I garnets probably nucleated earlier than Type-II because the rims of the former have similar orientations as the cores of the latter, and Type-II trails are more continuous with S_2 in the matrix. The steep dip of S_2 in the matrix is a generalized feature of the Sierra de la Contraviesa due to intense D_{3V} folding (Ruiz-Fuentes and Aerden, 2023). Fold axes and lineations measured in outcrop have highly variable orientations although a spread-out down-dip maximum can be seen. The latter may correspond to early fold axes that were originally parallel to the garnet FIAs and were reoriented by D_2 and D_3. The oblique relationship between FIAs and S_2 is an additional indication for garnet in this sample having grown prior to the development of S_2 and the likely reactivation of S_2 during D_3. On the other hand, the continuity of S_2 with inclusion trails in the rims of Type-II garnets implies that the latest stages of garnet coincided with the onset of D_2.

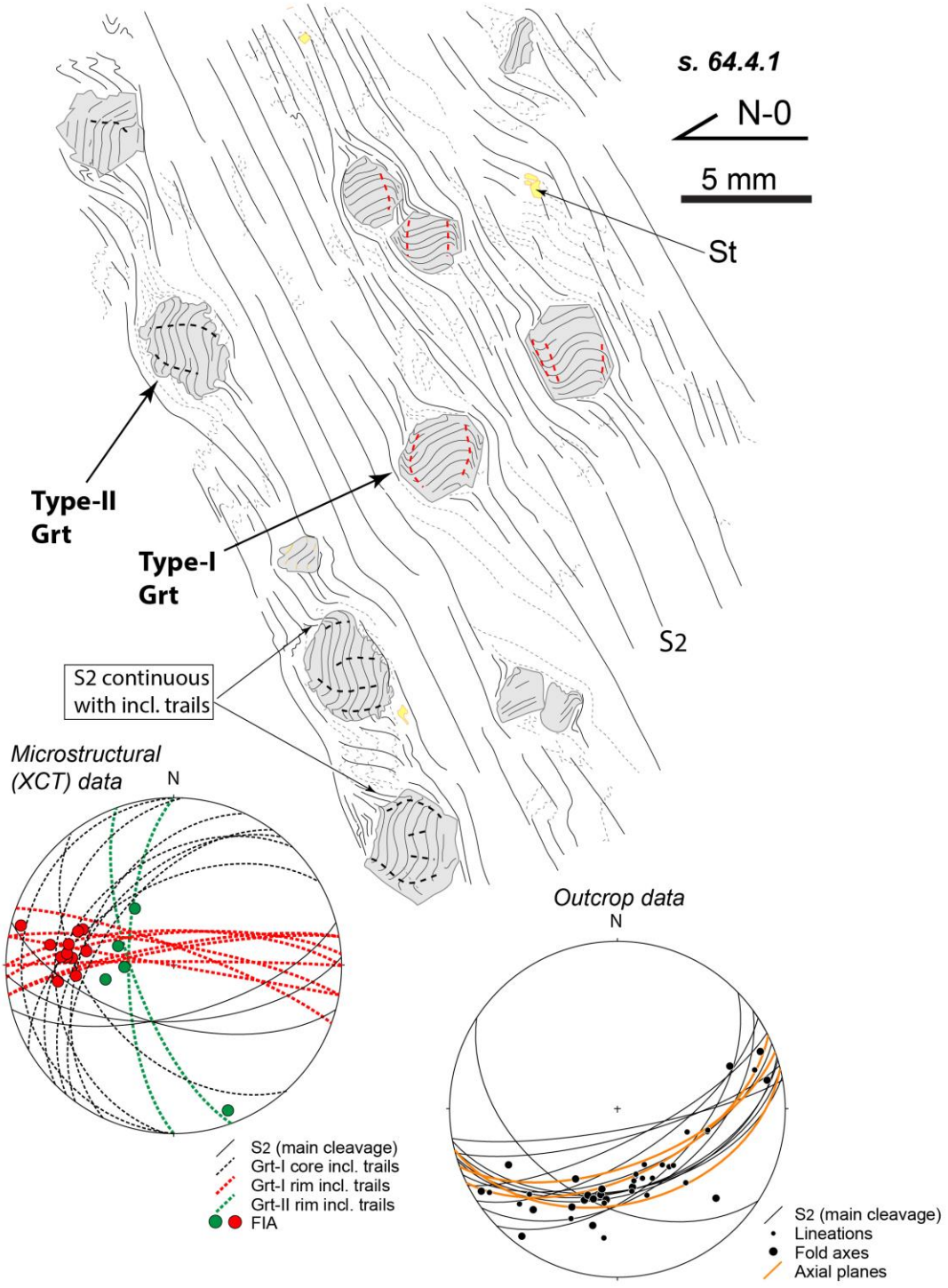

Fig. 8.7. Microstructural and outcrop data of sample 64.4.1. Projections were made with Stereonet software (Allmendinger et al., 2013).

8.3.5. Sample 46.8.1

Sample 46.8.1 is a light-grey schist from the Nevado-Filábride complex (Lat: 37.30270º; Long: -2.82784º) collected in the western Sierra de los Filabres (Fig. 8.3a) from the Permian-Triassic/Early Jurassic Tahal formation (Poulaki and Stockli, 2022), or the sedimentary sequence of the Ophiolite Unit of Lozano et al. (2018). The sample host a

large number of variably sized (1-10mm) garnets showing spiral-shaped inclusion trails. Aerden and Ruiz-Fuentes (2020) and Aerden et al. (2022) measured 65 FIAs in the sample, which exhibit three orientation maxima when plotted in a rose diagram. Significantly, these three modal maxima coincide remarkably with those defined by a large number of average FIA trends measured using the radial thin-sectioning technique of Hayward (1990) in about 80 Nevado-Filabride sample from widely scattered locations (Aerden et al., 2013, 2022).

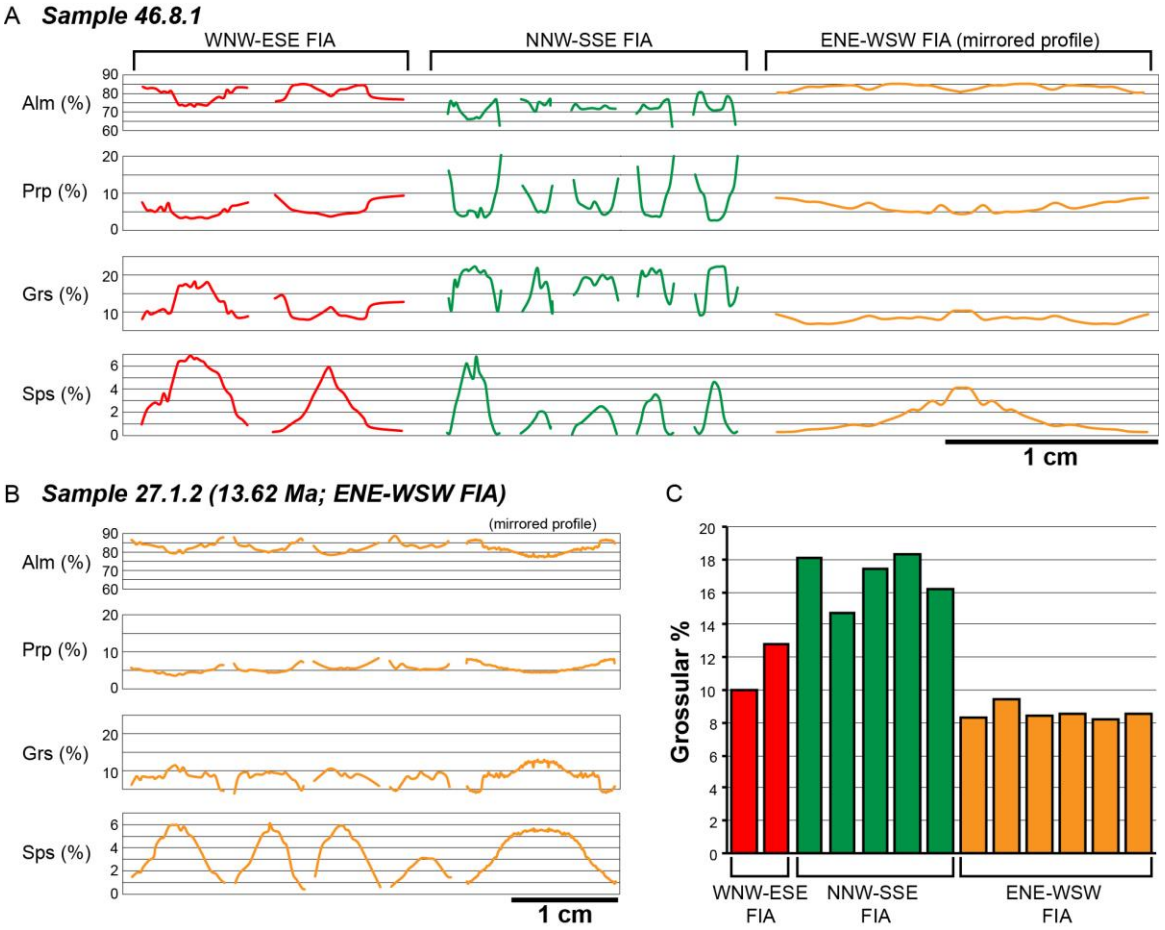

Fig. 8.8. A) Chemical profiles of garnets from sample 46.8.1 coloured according to the hosted FIA. B) Chemical profiles of garnets from sample 27.1.2 located close to 46.8.1 for comparison. C) Grossular mean percentage of each garnet from A and B.

Aerden and Ruiz-Fuentes (2020) presented the following evidence for the presence of different age groups of garnets with differently oriented FIA in sample 46.8.1. A strong correlation between FIA orientation and garnet size: red (WNW-ESE) and green (NNW-SSE) FIAs are only present in garnets measuring less than 5 mm, whereas larger garnets (5-12 mm) exclusively contain 'orange' FIAs. Secondly, green FIAs are defined by spiral inclusion trails curving in opposite directions in roughly equal proportions, whereas the curvature sense of spirals with 'red' (WNW-ESE) and 'orange' (ENE-WSW) FIAs is highly consistent, although not totally. Finally, preferred vertical and horizontal orientations of inclusion trails demonstrated in the sample and of associated internal truncation surfaces represents string evidence for episodic growth stages controlled by

alternating contraction and extension (Bell and Johnson, 1989) or a critical balance between tectonic forces and gravity.

We cut two horizontal thin sections from the XCT block as studied by Aerden and Ruiz-Fuentes (2020), which intersect several garnet porphyroblasts with known FIAs, namely, 5 small (1-2 mm) garnets with green FIAs, 2 medium sized (4mm) garnets with red FIAs, and one very large garnet (ca. 10 mm) hosting an orange FIA. Figure 8.8 shows chemical profiles through these garnets and five other large garnets from a second sample from the same outcrop (sample 27.1.2). The latter also have 'orange' FIAs and they were dated by Aerden et al. (2022) to 13.6 ± 0.7 Ma (Sm-Nd method). The chemical profiles evidence significant differences between garnets of different FIA sets. Small garnets with green FIAs have lower Alm content, very rich Prp rims and strongly Ca enriched rims (Fig. 8.8). The average composition and chemical zoning of red and orange garnets is similar for Fe, Mg and Mn, but the Ca-content is higher in the former. These differences support different P-T-X conditions of the three FIA sets and hence different growth periods.

8.4. P-T conditions

8.4.1. Pseudosection modelling

Mineralogical analyses were performed at CIC University of Granada with Cameca SX100 and JEOL JXA-iSP100 electron microprobes operating at 20 kV accelerating voltage, 20 nA beam current and 5 μm beam diameter. Mineral compositions are shown in section 10.6. Samples 62.5.1, 64.3.1 and 64.4.1 were chosen for pseudosection modelling given that they contain minor mineralogical relics or retrograde phases associated with the D_1 and D_3 events. Therefore, the bulk rock composition is representative of the effective composition which has reacted to develop the syn-D_2 main mineral assemblage. Bulk rock compositions were obtained by X-ray fluorescence at the CIC University of Granada (Table 8.1). Pseudosections have been modelled for each bulk composition with the free energy minimization software Theriak-Domino (de Capitani and Petrakakis, 2010). Geothermometers have been calculated with the aid of the GPT spreadsheet of Reche and Martínez (1996).

Sample 62.5.1 contains a syn-D_2 assemblage defined by garnet + muscovite + biotite + plagioclase + quartz. Compositions of white mica indicate the presence of only one type of mica with a high X_{Ms} component (Fig. 8.9). Biotite and plagioclase also show homogeneous compositions (Fig. 8.9). The garnet-biotite exchange thermometer was used in two garnet-biotite pairs in equilibrium to further constrain the temperature range. The calibrations of Ferry and Spear (1978), Dasgupta et al. (1991) and Bhattacharya et al. (1992) are shown in Fig. 8.10. Besides, the pressure was further precised with the plagioclase-biotite-garnet-muscovite barometer of Ghent and Stout (1981) (Fig. 8.10). These calibrations match well the conditions predicted by the pseudosection and allow us to constrain the P-T conditions to around 7-8.5 kbar and 620-680 ºC.

Table 8.1. Bulk rock compositions utilized for the calculation of the pseudosections.

Sample	62.5.1	64.3.1	64.4.1
	wt %	wt %	wt %
SiO_2	52,95	51,81	54,9
Al_2O_3	23,37	28,3	26,05
Fe_2O_3	7,38	6,71	7,63
MnO	0,11	0,07	0,05
MgO	2,05	0,99	1,09
CaO	4	0,92	0,69
Na_2O	1,66	2,94	1,37
K_2O	4,6	3,27	4,32
TiO_2	1,05	1,11	1,1
P_2O_5	0,16	0,22	0,17
Zr (ppm)	141,2	164,5	150,4
LOI	2,47	3,2	2,59
Total	99,8	99,54	99,96

The main syn-D_2 mineral assemblage in sample 64.3.1 contains garnet + staurolite + paragonite + muscovite + biotite + plagioclase + quartz. Analysis of white mica reveal two different types characterized by high X_{Ms} and X_{Pg} contents (Fig. 8.9). The P-T conditions can be constrained to 6-9 kbar and 570-640 ºC. Conditions of syn-D_3 garnets are constrained by the lower limit of the garnet stability field.

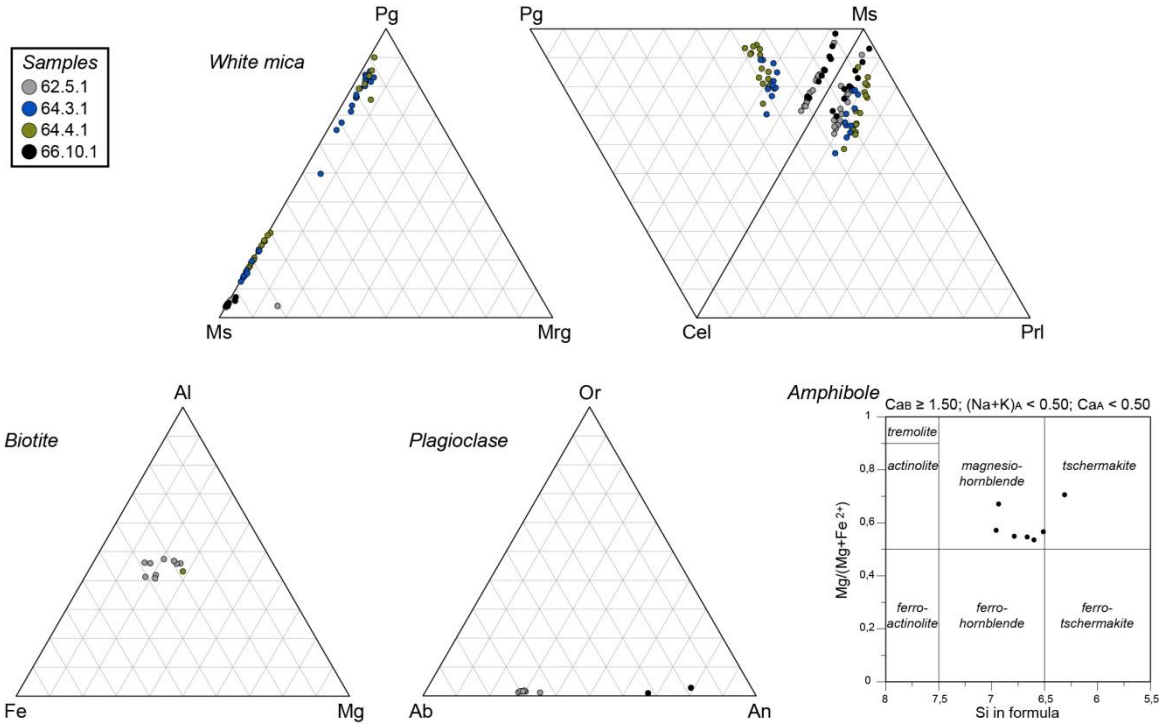

Fig. 8.9. White mica, biotite, plagioclase and amphibole analyses plotted in compositional diagrams.

D_2 in sample 64.4.1 is defined by the assemblage garnet + staurolite + muscovite + paragonite + biotite + quartz. White mica analyses (Fig. 8.9) indicate the presence of two types with high X_{Ms} and X_{Pg}, as well as in sample 64.3.1. The garnet-staurolite thermometer of Perchuk (1991) was used to precise the temperature (Fig. 8.10). The result falls close to but not within the stability field predicted by the pseudosection, which

may be due to subsequent re-equilibration of the garnet-staurolite system. These observations allow constraining the P-T conditions to 8-9.5 kbar and 600-625 ºC.

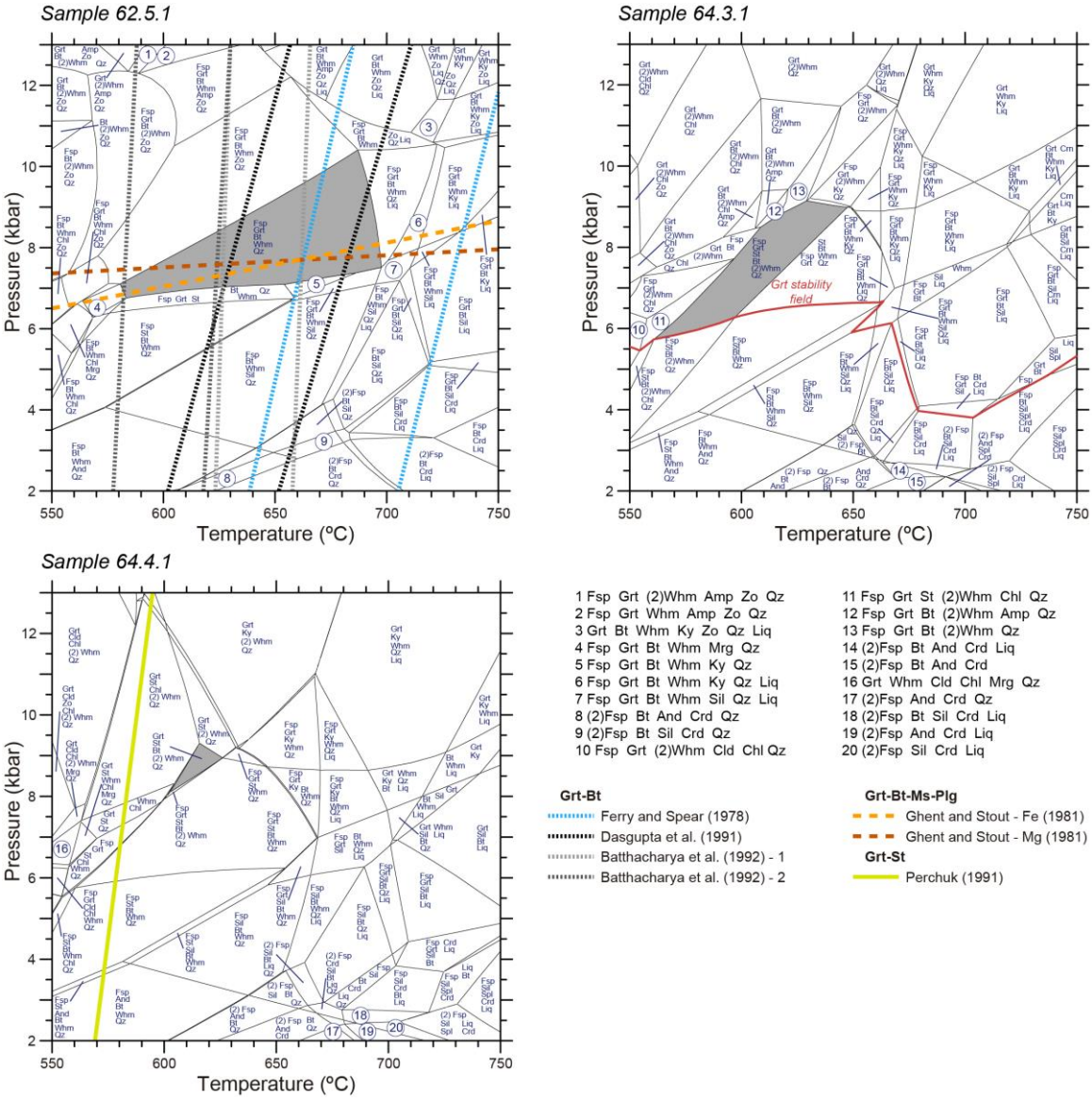

Fig. 8.10. P-T pseudosections of the studied samples. Red line in pseudosection of sample 64.3.1 indicates the limit of the garnet stability field. Thermobarometric calculations are indicated by coloured lines in pseudosections of samples 62.5.1 and 64.4.1. Shaded areas indicate the field corresponding to the mineral assemblage of each sample.

We did not obtained a satisfactory pseudosection from sample 66.10.1, probably due to the presence of a large amount of retrograde mineral phases (e.g. chlorite). Nevertheless, the main syn-D_2 assemblage (garnet + hornblende + muscovite + plagioclase + quartz) suggest amphibolite facies conditions, similar to the other samples.

8.4.2. Zr-in-rutile thermometry

Nine rutile grains were analysed in sample 46.8.1 with LA-ICP-MS at the University of Montpellier to measure the Zr content, after which we applied the thermometers of

Zack et al. (2004), Ferry and Watson (2007) and Tomkins et al. (2007). Two analysed rutile grains (ax2 and ax4) are in contact with garnets containing green (NNW-SSE) FIA, and one of these grains is partially surrounded by garnet (Fig. 8.11a) suggesting that at least the outermost garnet rim grew either synchronous or after the rutile grain. Two others rutile crystals (ax7 and ax9) lie included within the large garnet with an orange (ENE-WSW) FIA (Fig. 8.11b). Therefore, this garnet must have grown synchronous or after these inclusions. The rest of the analysed grains are part of the matrix. The results obtained with the method of Tomkins et al. (2007) are pressure dependent. The temperatures given in Table 8.2 are for a pressure of 10 kbar, but would be about 20 °C higher for 15 kbar. Rutile grain ax4, in contact with a garnet with green FIA yields the lowest temperature (512 °C) averaged between the three methods. The highest temperature (614 ºC) corresponds to one of the rutile inclusions (ax7) within the large garnet with orange FIA (Fig. 8.11b), whereas the other inclusion (ax9) in this garnet yields a much lower temperature of 537 °C. Temperatures obtained for rutile crystals of the matrix range from 539 to 609 °C.

Table 8.2. Zr-in-Rutile results from rutile crystals of sample 46.8.1. One asterisk indicates that rutile is in contact with garnets with NNW-SSE FIA. Two asterisks indicate that rutile is included within a garnet with ENE-WSW FIA. The calibration of Tomkins et al. (2007) was calculated considering a pressure of 10 kbar.

	Zr (ppm)	Zack et al. (2004)	Ferry and Watson (2007)	Tomkins et al. (2007)
ax1	68,58	530,3	538,3	548,0
ax2*	73,52	539,2	542,7	552,3
ax4*	49,59	488,9	518,3	528,4
ax5	74,88	541,6	543,9	553,5
ax7**	183,73	656,3	605,6	614,0
ax9**	66,68	526,7	536,5	546,3
ax11	73,73	539,6	542,9	552,5
ax12	76,24	543,9	545,0	554,6
ax15	152,62	632,6	592,1	600,8

The above results indicate that rutile crystallized over a range of temperatures of ca. 500-600 °C. The absence of rutile inclusions in garnets with green FIAs, except for a one partially engulfed grain lying against a garnet rim, contrasts with abundant rutile grains in the matrix and suggests that these garnets grew earlier than rutile. This, combined with the high Ca-content of garnets with 'green' FIA and a very young Sm-Nd age (13.5 Ma) for garnets with orange FIA (Aerden et al., 2022) warrants the conclusion that green FIAs nucleated earlier at lower temperatures and probably higher pressure.

8.5. In situ U-Th-Pb dating

8.5.1. Analytical method

In an attempt to constrain the timing of FIA development, in situ U-Th-Pb dating was performed in samples 64.3.1, 64.4.1 and 46.8.1, which contain monazite and xenotime grains. Mineral grains were examined at the University of Montpellier through backscattered electrons (BSE) images using a Scanning Electron Microscope (SEM). In situ U-Th-Pb analyses were performed using laser-ablation inductively coupled plasma-

mass spectrometry (LA-ICP-MS) at the University of Montpellier. Manangotry (Poitrasson et al., 2000) and Moacyr (Seydoux-Guillaume et al., 2002) standards were used to calibrate the analyses of monazite and xenotime. Raw data were reduced using the software Glitter (van Achterberg et al., 2001). Results are presented in Table 8.3 and Fig. 8.12 in Tera-Wasserburg diagrams made with Isoplot/Ex (Ludwig, 2003).

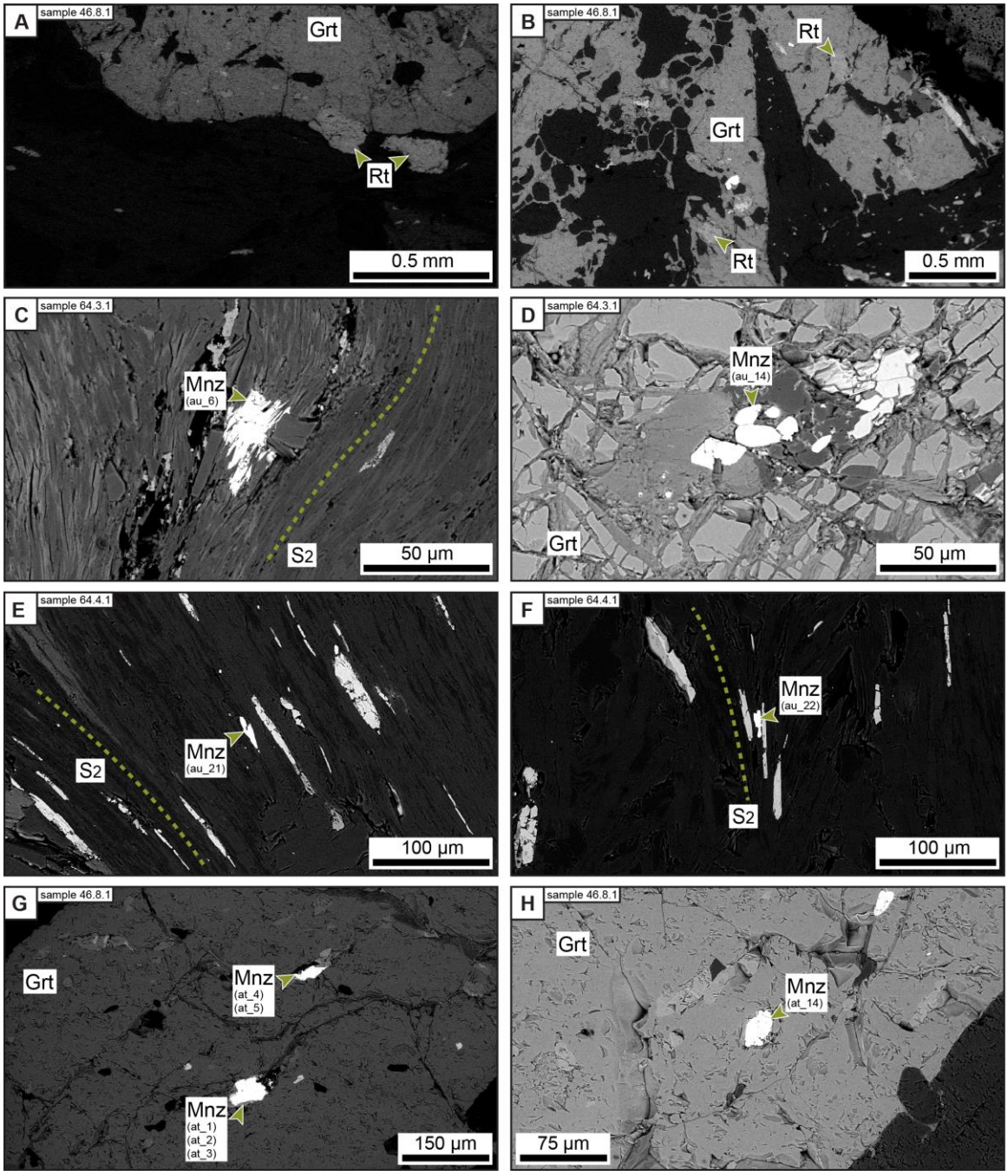

Fig. 8.11. BSE images of rutile and monazite. A) Rutile crystals in the matrix and in contact with a garnet hosting a NNW-SSE FIA (sample 46.8.1). B) Rutile crystals included within a garnet with ENE-WSW FIA (sample 46.8.1). C) Post-D_2 monazite located at the matrix of sample 64.3.1. D) Monazite crystals included within a garnet of sample 64.3.1. E and F) Syn-D_2 monazite crystals located in the matrix of sample 64.4.1. G and H) Monazite grains included within a garnet with ENE-WSW FIA (sample 46.8.1).

Table 8.3. U-Th-Pb data for monazite, xenotime, zircon and rutile from samples 64.3.1, 64.4.1 and 46.8.1.

Sample	Pb (ppm)	Th (ppm)	U (ppm)	Th/U	208Pb/ 206Pb	207Pb/ 206Pb	± (1s)	207Pb/ 235U	± (1s)	206Pb/ 238U	± (1s)	Rho	Apparent ages (Ma) 206Pb/ 238U	± (1s)	207Pb/ 206Pb	± (1s)
46.8.1																
Monazite																
at_1	201,9	45482	5736	7,93	2,39	0,1332	0,0046	0,0487	0,0015	0,00265	0,00004	0,50	17,1	0,3	2141	59
at_2	158,9	34282	4877	7,03	2,25	0,1364	0,0055	0,0479	0,0017	0,00255	0,00005	0,56	16,4	0,3	2182	68
at_3	182,9	46185	5266	8,77	2,42	0,1505	0,0115	0,0534	0,0034	0,00257	0,00011	0,67	16,5	0,7	2351	125
at_4	159,5	40258	4502	8,94	2,55	0,1308	0,0058	0,0459	0,0018	0,00254	0,00005	0,51	16,4	0,3	2108	75
at_5	210,2	48229	5734	8,41	2,42	0,1718	0,0063	0,0637	0,0019	0,00269	0,00005	0,61	17,3	0,3	2575	60
at_6	249,2	17901	2944	6,08	2,09	0,5265	0,0201	0,4494	0,0216	0,00619	0,00018	0,61	39,8	1,2	4317	55
at_7	178,7	35719	5169	6,91	2,34	0,1192	0,0083	0,0435	0,0026	0,00265	0,00009	0,56	17,1	0,6	1944	119
at_8	216,1	46143	5776	7,99	2,79	0,1343	0,0085	0,0468	0,0026	0,00253	0,00008	0,58	16,3	0,5	2154	107
at_9	247,0	31453	3790	8,30	2,36	0,4218	0,0129	0,2640	0,0100	0,00454	0,00010	0,58	29,2	0,6	3989	45
at_10	108,4	22560	3924	5,75	1,88	0,1088	0,0070	0,0366	0,0021	0,00244	0,00007	0,50	15,7	0,5	1779	113
at_11	85,2	18263	3256	5,61	1,77	0,1179	0,0067	0,0403	0,0021	0,00248	0,00006	0,47	16,0	0,4	1925	99
at_12	99,0	20058	3671	5,46	1,85	0,1169	0,0068	0,0400	0,0021	0,00248	0,00007	0,54	16,0	0,5	1909	101
at_13	213,6	53319	7647	6,97	1,85	0,1214	0,0063	0,0429	0,0019	0,00256	0,00007	0,61	16,5	0,5	1977	89
at_14	126,7	27368	3896	7,02	2,30	0,1579	0,0073	0,0558	0,0022	0,00256	0,00006	0,60	16,5	0,4	2433	76
Xenotime																
at_15	88,1	20546	5932	3,46	1,00	0,1117	0,0064	0,0295	0,0015	0,00192	0,00005	0,51	12,4	0,3	1827	100
64.3.1																
Monazite																
at_23	189,2	43837	2580	16,99	5,56	0,0928	0,0062	0,0375	0,0027	0,00293	0,00008	0,38	18,9	0,5	1484	122
at_28	130,9	26232	2761	9,50	3,31	0,1206	0,0128	0,0474	0,0056	0,00285	0,00015	0,45	18,3	1,0	1966	178
at_30	144,0	14174	1011	14,03	2,75	0,5588	0,0277	0,6734	0,0420	0,00874	0,00033	0,61	56,1	2,1	4404	71
au_1	84,5	11950	3427	3,49	1,20	0,0959	0,0063	0,0381	0,0023	0,00288	0,00008	0,46	18,5	0,5	1545	119
au_3	118,0	24102	2511	9,60	3,23	0,0880	0,0068	0,0353	0,0026	0,00291	0,00008	0,38	18,7	0,5	1383	142
au_4	109,5	22806	1893	12,05	3,93	0,1232	0,0088	0,0520	0,0034	0,00306	0,00009	0,46	19,7	0,6	2003	121
au_6	109,3	24267	2013	12,06	3,84	0,1112	0,0088	0,0446	0,0032	0,00291	0,00009	0,43	18,7	0,6	1819	137
au_7	123,3	31378	1088	28,85	7,94	0,2350	0,0500	0,1062	0,0178	0,00328	0,00043	0,78	21,1	2,8	3087	304
au_8	46,4	7911	1804	4,39	1,23	0,1598	0,0146	0,0627	0,0049	0,00285	0,00013	0,58	18,3	0,8	2453	147
au_9	152,7	32037	2606	12,29	4,09	0,0962	0,0068	0,0396	0,0026	0,00299	0,00008	0,41	19,2	0,5	1552	127
au_11	19,2	99	1150	0,09	0,32	0,1580	0,0165	0,0650	0,0060	0,00298	0,00015	0,55	19,2	1,0	2434	167
au_13	107,3	24656	1204	20,47	5,83	0,2032	0,0157	0,0940	0,0061	0,00336	0,00014	0,65	21,6	0,9	2852	120
au_14	109,4	22617	2431	9,30	3,11	0,1166	0,0102	0,0453	0,0036	0,00282	0,00011	0,50	18,2	0,7	1905	149
au_15	203,9	41585	4122	10,09	3,24	0,1031	0,0065	0,0428	0,0024	0,00301	0,00009	0,53	19,4	0,6	1680	113
au_16	123,7	22641	3587	6,31	2,06	0,0691	0,0049	0,0280	0,0019	0,00294	0,00007	0,36	18,9	0,4	902	139
64.4.1																
Monazite																
au_18	28,8	2751	878	3,13	1,29	0,1680	0,0111	0,0881	0,0092	0,00380	0,00012	0,30	24,5	0,8	2537	107
au_20	242,9	37630	7590	4,96	1,47	0,0643	0,0030	0,0294	0,0013	0,00332	0,00006	0,38	21,4	0,4	751	96
au_21	157,3	26350	4127	6,38	1,98	0,2969	0,0177	0,1855	0,0076	0,00453	0,00017	0,94	29,1	1,1	3454	89
au_22	168,3	20194	3326	6,07	2,03	0,3242	0,0170	0,2121	0,0134	0,00475	0,00017	0,56	30,5	1,1	3590	78
au_23	133,6	23878	1341	17,81	3,93	0,5087	0,0278	0,5187	0,0330	0,00740	0,00024	0,51	47,5	1,5	4267	78
au_24	96,5	10777	1578	6,83	1,98	0,3495	0,0206	0,2352	0,0119	0,00488	0,00021	0,85	31,4	1,3	3705	87

8.5.2. Results

Sample 64.3.1 contains abundant monazite grains dispersed in the matrix and included in garnet porphyroblasts. Fourteen monazite grains were analysed (15 spots), five of which are included within garnets and nine located in the matrix (Fig. 8.11c and d). The intersection with the concordia provides an age of 17.58 ± 0.37 Ma (MSWD = 1.14). Textural features of the monazite grains indicate that they formed after D_2 because they replace S_2 micas (Fig. 8.11c). The garnets were already interpreted to have grown during D_3 (see section 3.3.) so monazite and garnet probably crystallised synchronously. This situates the beginning of D_3 and the development of the orange (NW-SE) FIA in this sample around 17.6 Ma.

Sample 64.4.1 contains strongly elongated monazite grains aligned with the S_2 matrix schistosity. No monazite was found inside garnets, which in this sample predate D_2 (see section 3.4.). Six grains (6 spots) of syn-S_2 monazites (Fig. 8.11e and f) were analysed yielding an intercept age of 20.88 ± 0.66 Ma (MSWD = 0.20). The N280 trending FIAs in this sample are interpreted in section 3.4. to have formed before D_2 or 21 Ma. This confirms that the WNW-ESE FIA in this sample formed earlier than NE-SW trending FIAs dated 17.5 Ma in sample 64.3.1, located at only 300 m distance. This is further confirmation of the relative timing of red (NNW-ESE trending) versus orange (NE-SW

trending) FIA sets defined by Ruiz-Fuentes and Aerden (2023) in the Alpujárride Complex.

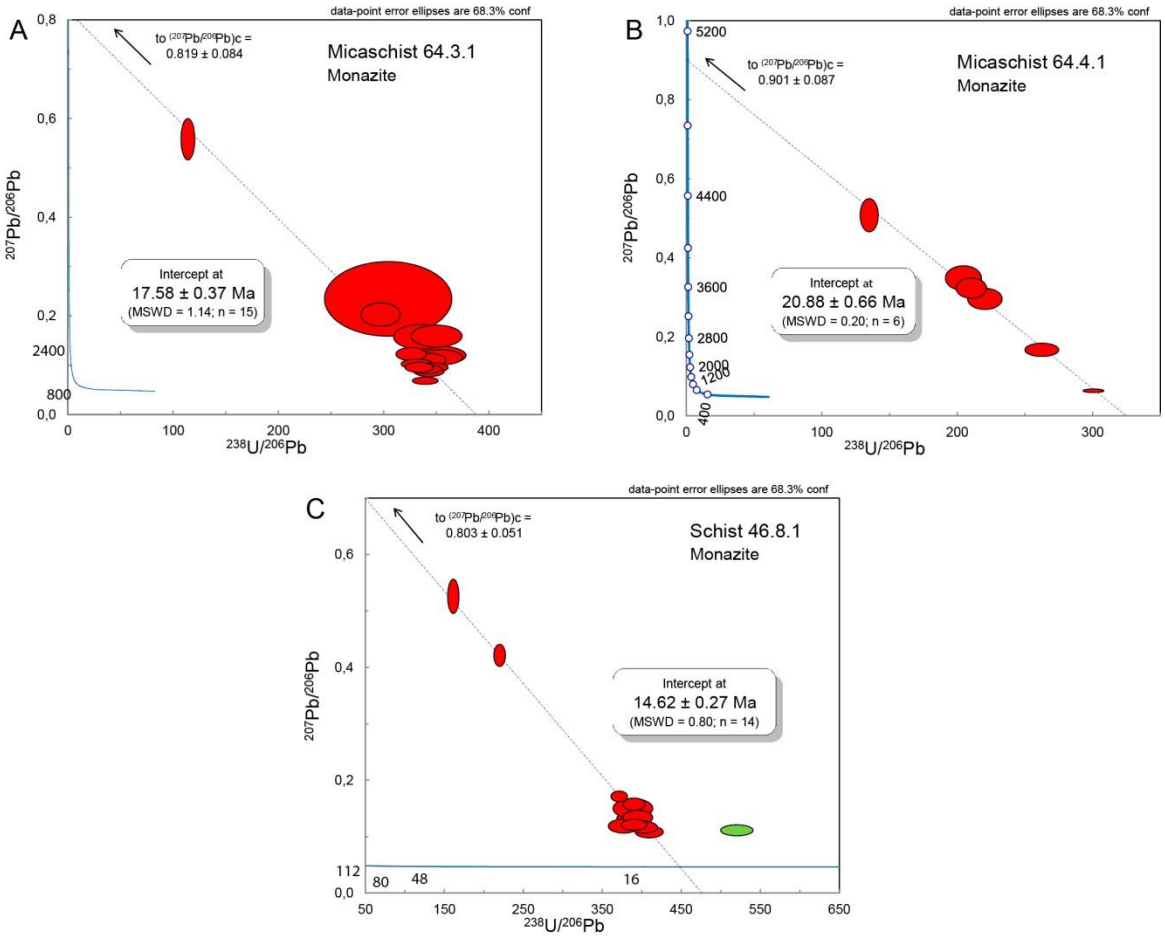

Fig. 8.12. Tera-Wasserburg diagrams of the analysed samples.

In sample 46.8.1, monazite is found widespread in the matrix and included within the big garnet with orange (ENE-WSW) FIA, but not in garnets with red (WNW-ESE) or green (NNW-SSE) FIA. Note that the same applies to rutile grains as described in section 4.2. Seven monazites (14 spots) and one xenotime grain (1 spot) were analysed (Fig. 8.11g and h). From these, six monazites are included within garnet, and one monazite and the xenotime are located in the matrix. Monazites taken alone yield an intercept age of 14.62 ± 0.27 Ma (MSWD = 0.80), while the xenotime grain shows a higher 238U/206Pb ratio, which might indicate a slightly younger age. The implied maximum crystallization age for garnets hosting these inclusions agrees well with the 13.5 ± 0.5 Ma Sm-Nd garnet age of Aerden et al. (2022). The two smaller-sized garnet populations with red and green FIA must have formed before 14.5 Ma.

8.6. Ar/Ar dating

Four samples were analyzed: 66.10.1, 62.5.1, 64.3.1 and 64.4.1 at Géosciences Montpellier. The corresponding $^{40}Ar/^{39}Ar$ age spectra are presented in Figure 8.13 and the analytical procedure, described in details in Monié et al. (2023), is given in section 10.5.

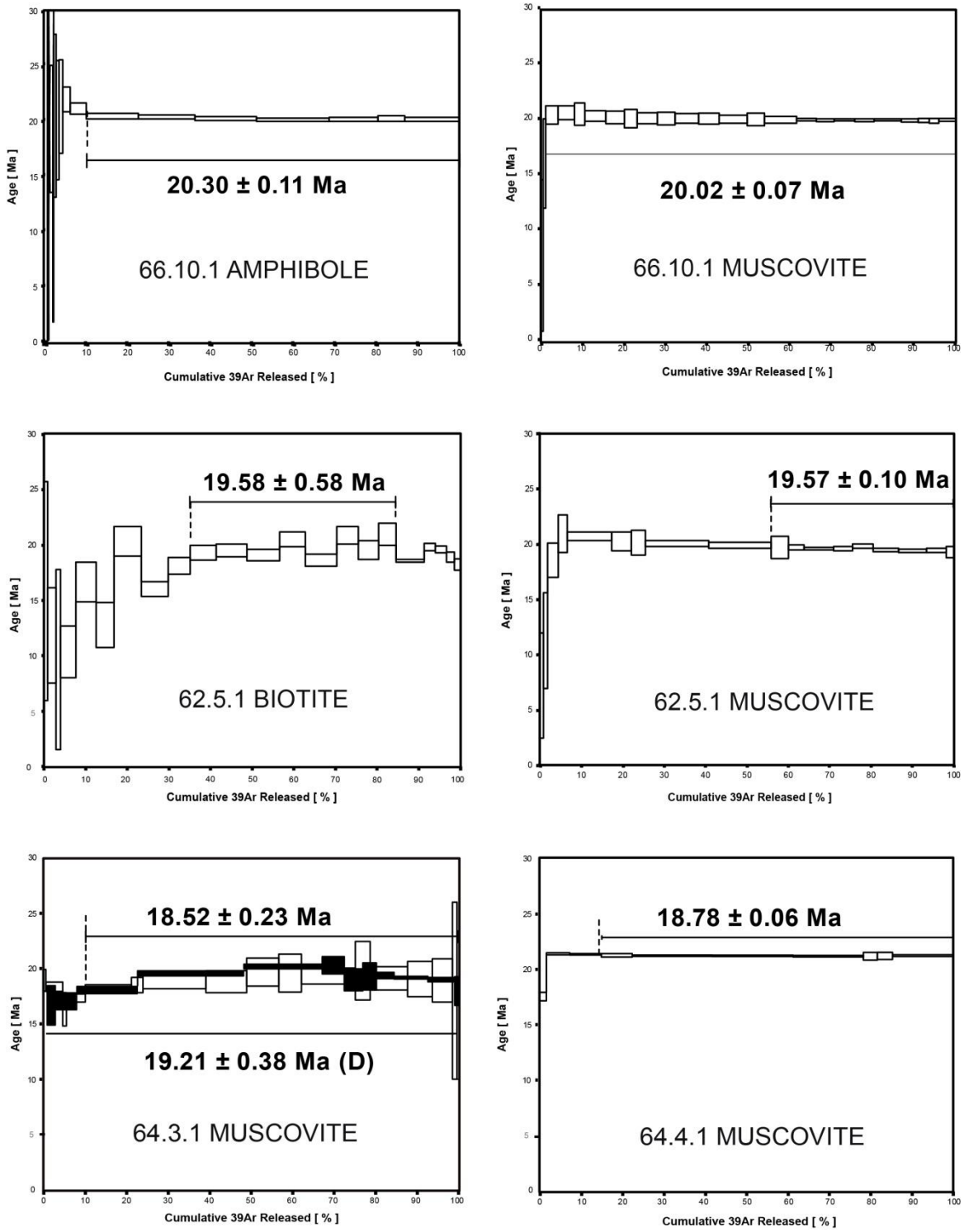

Fig. 8.13. ^{40}Ar-^{39}Ar ages obtained from the samples of the Alpujárride Complex.

In sample 66.10.1, a single amphibole grain yielded a plateau age of 20.30 ± 0.11 Ma, which corresponds to 89.79 % of ^{39}Ar released and to 7 steps. The inverse isochron for the plateau steps provides a concordant age at 20.08 ± 0.19 Ma (MSWD = 0.56; initial ^{40}Ar/^{36}Ar ratio of 303.0 ± 3.3Ma). A single muscovite grain yielded a plateau age at 20.02 ± 0.07 Ma, which corresponds to 99.01 % of ^{39}Ar released and to 22 steps. The inverse isochron for the plateau steps provides a concordant age at 19.97 ± 0.08 Ma (MSWD =

0.41; initial $^{40}Ar/^{36}Ar$ ratio of 342.2 ± 42.8 Ma). Both ages obtained on amphibole and muscovite are in the error bars.

In sample 62.5.1, a single biotite grain yielded a plateau age of 19.58 ± 0.58 Ma, which corresponds to 49.41 % of ^{39}Ar released and to 8 steps. The inverse isochron for the plateau steps provides a concordant age at 20.53 ± 3.04 Ma (MSWD = 6.8; initial $^{40}Ar/^{36}Ar$ ratio of 282.9 ± 51.6 Ma). A single muscovite grain yielded a plateau age at 19.57 ± 0.10 Ma, which corresponds to 48.08 % of ^{39}Ar released and to 9 steps. The inverse isochron for the plateau steps provides a concordant age at 19.24 ± 0.31 Ma (MSWD = 0.58; initial $^{40}Ar/^{36}Ar$ ratio of 533.5 ± 219.8 Ma). Both ages obtained on biotite and muscovite are in the error bars.

In sample 64.3.1, a single muscovite grain yielded a plateau age of 18.52 ± 0.23 Ma, which corresponds to 89.9 % of ^{39}Ar released and to 12 steps. The inverse isochron for the plateau steps provides a concordant age at 18.52 ± 0.62 Ma (MSWD = 1.86; initial $^{40}Ar/^{36}Ar$ ratio of 301.5 ± 106.8 Ma). A duplicate of single muscovite grain yielded a weighted age of 19.21 ± 0.38 Ma, which corresponds to 100 % of ^{39}Ar released and to 12 steps. The inverse isochron for the steps provides a concordant age at 19.25 ± 0.42 Ma (MSWD = 20.15; initial $^{40}Ar/^{36}Ar$ ratio of 292.9 ± 54.9 Ma). Both muscovite ages are slightly discordant, however the plateau age of 18.52 ± 0.62 Ma is of higher quality and can be considered as the most accurate age.

In sample 64.4.1, a single muscovite grain yielded a plateau age of 18.78 ± 0.06 Ma, which corresponds to 85.10 % of ^{39}Ar released and to 7 steps. The inverse isochron for the plateau steps provides a concordant age at 18.76 ± 0.09 Ma (MSWD = 0.39; initial $^{40}Ar/^{36}Ar$ ratio of 311.6 ± 40.4 Ma).

8.7. Discussion

8.7.1. Tectono-metamorphic evolution of the Alpujárride Complex

The P-T conditions obtained for the D_2 event (6-9.5 kbar and 570-680 ºC) in the Alpujárride samples are similar as previously estimated for similar rocks from the Adra and Salobreña units (Fig. 8.14a; Cuevas, 1989b; Azañón et al., 1997, 1998) and also in other Alpujárride units (Fig. 8.14a; e.g. Azañón and Alonso-Chaves, 1996; Balanyá et al., 1997; Alonso-Chaves and Orozco, 2007). Our U-Pb ages on monazite (sample 64.4.1) and Ar-Ar ages dating S_2 constrain the timing of this foliation to the 21-18.5 Ma interval, which also agrees with previous geochronological data from the Alpujárride Complex (Fig. 8.14b) obtained by U-Pb on zircon (Platt and Whitehouse, 1999; Sánchez-Rodríguez and Gebauer, 2000; Zeck and Williams, 2001; Frasca et al., 2017), Rb-Sr on mica (Zeck et al., 1989, 1992) and Ar-Ar on mica (Monié et al., 1991, 1994; Platt et al., 1998; Sosson et al., 1998; Platt et al., 2003; Bessière et al., 2022). Slightly older (Aquitanian) U-Pb zircon ages (Whitehouse and Platt, 2003; Esteban et al., 2007, 2011; Sánchez-Navas et al., 2014; Frasca et al., 2017) coincide with a Sm-Nd age for garnets in an Upper

Alpujárride sample (A7) that grew during NW-SE directed compression (Aerden et al., 2022).

Both extensional (Balanyá et al., 1997; Azañón et al., 1997, 1998; Williams and Platt, 2017, 2018; Simancas, 2018) and contractional (Tubía et al., 1992; Rossetti et al., 2005) interpretations have been proposed for the D_2 event. We favour an extensional origin because S_2 is continuous with subhorizontal inclusion trails in the rims of garnets in samples 64.3.1, 64.4.1 (type-II garnets) and 66.10.1, and because of the 21-18.5 Ma age range which matches that of the oldest transgressive sediments (Lower Burdigalian) deposited unconformably on top of the Internal Zones (Viñuela Group; González Donoso et al., 1982; Aguado et al., 1990; Alonso-Chaves and Rodríguez-Vidal, 1998) and in the Alborán basin (Comas et al., 1992; Rodríguez-Fernández et al., 1999).

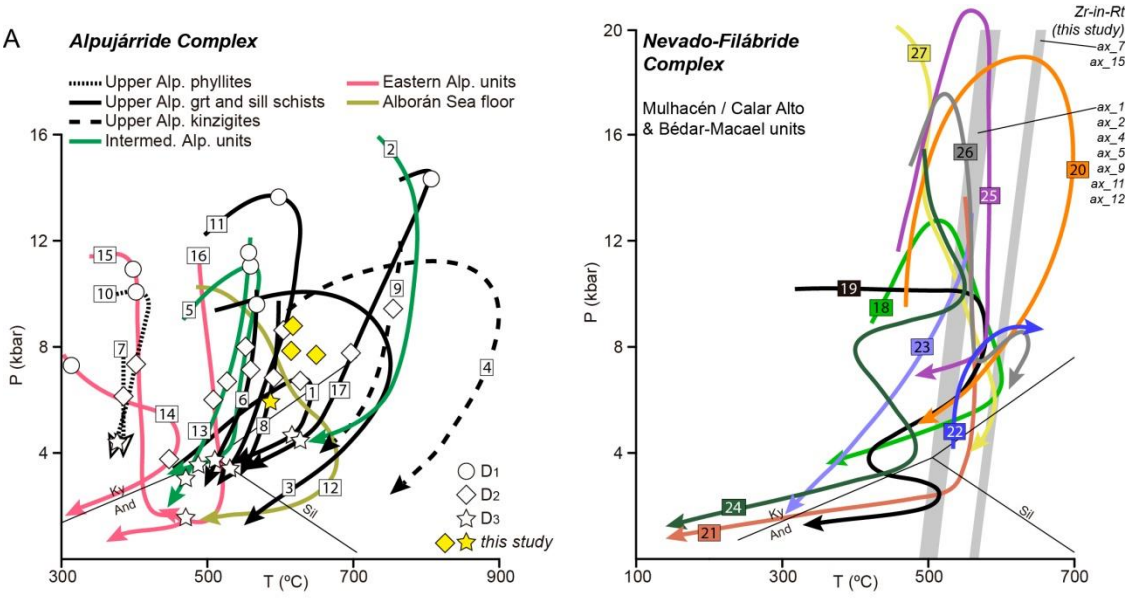

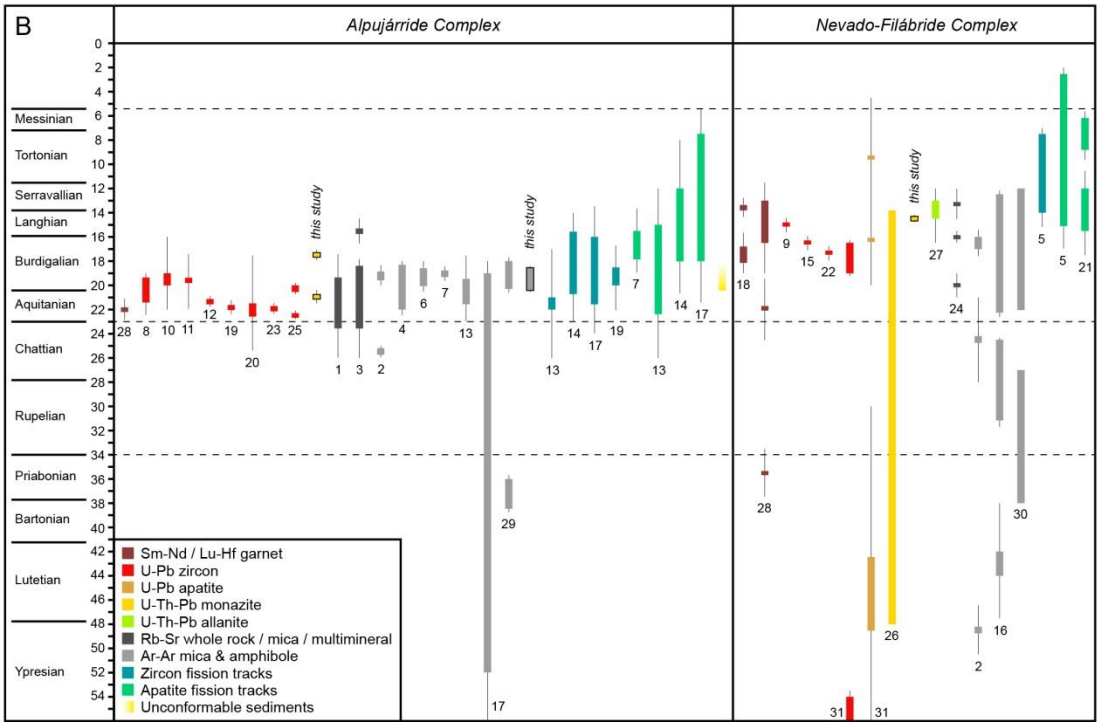

Fig. 8.14 (previous page). A) P-T-t paths determined by previous authors in the Alpujárride and Nevado-Filábride complexes. For the Alpujárride paths, white symbols indicate the estimated position of deformation events as interpreted by each author, and yellow symbols indicate the estimated position of deformation events as interpreted in this study. For the Nevado-Filábride paths, the shaded area indicates the conditions of the analysed rutile crystals according to the Tomkins et al. (2007) calibration (see Table 8.2). Alpujárride paths: (1) Cuevas, 1989b; (2) Tubía and Gil-Ibarguchi, 1991; (3 and 4) Tubía, 1994; (5) Azañón and Alonso-Chaves, 1996; (6) Azañón et al., 1997; (7, 8 and 9) Balanyá et al., 1997; (10 and 11) Azañón et al., 1998; (12) Soto and Platt, 1999; (13) Azañón and Crespo-Blanc, 2000; (14, 15 and 16) Booth-Rea et al., 2005; (17) Alonso-Chaves and Orozco, 2007. Nevado-Filábride paths: (18) Gómez-Pugnaire and Fernández-Soler, 1987; (19) Bakker et al., 1989; (20) Gómez-Pugnaire et al., 1994; (21) Augier et al., 2005; (22) Aerden et al., 2013; (23) Behr and Platt, 2012; (24) Booth-Rea et al., 2015; (25) Ruiz-Cruz et al., 2015; (26) Li and Massonne 2018; (27) Santamaría-Lopez et al., 2019. B) Geochronological data from the Alpujárride and Nevado-Filábride complexes. The data obtained in this study is indicated with bordered boxes. Radiometric ages from: (1) Zeck et al., 1989; (2) Monié et al., 1991; (3) Zeck et al., 1992; (4) Monié et al., 1994; (5) Johnson et al., 1997; (6) Platt et al., 1998; (7) Sosson et al., 1998; (8) Platt and Whitehouse, 1999; (9) Lopez Sánchez-Vizcaíno et al., 2001; (10) Sánchez-Rodríguez and Gebauer, 2000; (11) Zeck and Williams, 2001; (12) Whitehouse and Platt, 2003; (13) Platt et al., 2003; (14) Esteban et al., 2004; (15) Gómez-Pugnaire et al., 2004; (16) Augier et al., 2005; (17) Platt et al., 2005; (18) Platt et al., 2006; (19) Esteban et al., 2007; (20) Esteban et al., 2011; (21) Vázquez et al., 2011; (22) Gómez-Pugnaire et al., 2012; (23) Sánchez-Navas et al., 2014; (24) Kirchner et al., 2016; (25) Frasca et al., 2017; (26) Li and Massonne, 2018; (27) Santamaría-López et al., 2019; (28) Aerden et al., 2022; (29) Bessière et al., 2022; (30) Porkoláb et al., 2022; (31) Poulaki et al., 2023. Ages of unconformable sediments from: González Donoso et al., 1982; Aguado et al., 1990; Comas et al., 1992; Alonso-Chaves and Rodríguez-Vidal, 1998; Rodríguez-Fernández et al., 1999.

Pre-D_2 crustal shortening events in the Oligocene and even latest Eocene have been recognized and dated in the Sebtide Complex (the equivalent of the Alpujárride complex in the Rif mountains) by Homonnay et al. (2018) and Aerden et al. (2022), in the Alpujarride Complex (Platt et al., 2005; Massonne, 2014; Bessière et al., 2022) and in the Maláguide Complex (Martín-Martín et al., 1997). Other indications for a contractional setting until Aquitanian times include: i) Oligo-Aquitanian sediments in the eastern Maláguide Complex deposited in a piggy-back basin affected by blind-fault-propagation folds (Martín-Martín and Martín-Algarra, 2002); ii) a drastic increase of clastic supply during the Aquitanian in the Flysch basin, including its Mauretanian units mainly sourced from the Maláguide, indicating uplift and dismantling of the adjacent orogenic wedge (e.g. Martín-Algarra, 1987; Jabaloy-Sánchez et al., 2019). This suggests that a generalized contractional setting prevailed from Oligocene to Aquitanian times, and that the main extensional episode in the Alpujárrides may have started at the Burdigalian.

The 17.58 ± 0.37 Ma monazite age obtained in sample 64.3.1 of the Adra nappe also dates early syn-D_{3V} garnets in this sample. The steeply dipping position of S_{3V} can be associated to bulk horizontal shortening, and two criteria allow attributing D_{3V} to continental collision: i) the age coincides with a late Burdigalian start of continental collision in the Betics proposed on the basis of stratigraphic criteria (Martín-Algarra, 1987; Martín-Martín et al., 1996; Jabaloy-Sánchez et al., 2019); ii) D_{3V} structures near the Internal-External Zones Boundary (IEZB) (e.g. Martín-Rojas et al., 2007; Ruiz-Fuentes and Aerden, 2023) show similar orientation and vergences as structures associated to the IEZB itself (e.g. García-Dueñas and Navarro-Vilá, 1976; Martín-Algarra, 1987; Sanz de

Galdeano et al., 1995; Jabaloy-Sánchez et al., 2007; Martín-Algarra et al., 2009; Ruiz-Fuentes et al., 2022). Thus, our microstructural and geochronological data supports alternating crustal shortening and extension in the Betic-Rif orogen as already proposed long ago (e.g. Azañón et al., 1997; Balanyá et al., 1997).

The pseudosection of sample 64.3.1 delimits the garnet stability field to above ~6 kbar at temperatures of 550-650 ºC, or above ~4-5 kbar at 675-750 ºC. It is unlikely that the sample reached 675 ºC since no sillimanite is present, and significant heating during decompression (Fig. 8.14a) has only been determined in Alpujarride rocks from the Alborán Sea floor (Soto and Platt, 1999) and in the eastern part of the cordillera (Booth-Rea et al., 2005). Therefore, we interpret that the upper part of the shaded field in the pseudosection (Fig. 8.10) between 7-9.5 kbar and 600-650 ºC corresponds to D_2, and that D_3 developed at around 6 kbar and 570-650 ºC.

A notable difference between the Upper Alpujárride Unit exposed in the central-eastern Betics (Adra nappe) and western-central Betics (e.g. Los Reales, Sayalonga and Salobreña units) is that S_{3V} is pervasive in the first but S_{3H} is preferentially found in the west. Only in the transition between both areas, near Almuñécar, the relative timing of S_{3V} (younger) and S_{3H} (older) could be established (see section 2.2.). The metamorphic conditions of S_{3V} deduced from sample 64.3.1 cannot have been very different from those of S_{3H} since the latter is associated with andalusite and locally sillimanite (Ruiz-Fuentes and Aerden, 2023). Several explanations can be proposed for the heterogeneous development of S_{3V} and S_{3H} in the Betics. Firstly, we cannot exclude that S_{3H} was simply not recognized in the Adra nappe due to the intensity of D_{3V}. This could have parallelized S_2 and S_{3H}. Alternatively, both foliations formed synchronously in the western-central Alpujárrides and the Adra nappe, respectively, due to different stress regimes. In this case, the conditions in the Adra nappe propagated westward eventually causing S_{3H} to be overprinted by S_{3V}. Finally, it is possible that no deformation occurred within the Adra nappe while D_{3H} acted in the central and western Alpujárrides.

8.7.2. Timing of FIA sets in the Nevado-Filábride Complex

Despite the disparity of P-T-t paths proposed by different authors for the Nevado-Filábride complex (Fig. 8.14), several constraints can be identified for the metamorphic evolution of sample 46.8.1: i) garnet is not associated with retrograde deformation phases formed below 500 ºC (González-Casado et al., 1995; Augier et al., 2005; Behr and Platt, 2012; Booth-Rea et al., 2015); ii) monazite is present in the matrix and within large garnets with orange (ENE-WNW) FIA but was not found in smaller garnets hosting red (ESE-WNW) and green (NNW-SSE) FIA. This suggests that the orange FIAs formed later; iii) Aerden et al. (2022) dated three large garnets, also with orange FIA, in another sample from the same outcrop to 13.6 ± 0.7 Ma (see section 3.5.). Quartz, phengite, chloritoid and kyanite inclusions in these garnets suggest high-pressure conditions, but we do not exclude that these garnets grew at relatively low-pressures while mineral inclusions persisted metastable; iv) this possibility is raised by U-Th-Pb ages of allanite grains (12.91 ± 1.10 and 14.51 ± 2.01) obtained by Santamaria-López et al., (2019) in

two samples from the western Sierra Nevada linked by them to a late low-pressure/high temperature stage (7 kbar / 600 °C), which broadly coincides with the temperature estimated by the Zr-in-rutile (section 4.2.); v) Platt et al. (2006) on the other hand estimated pressures of 12 to 15 kbar for garnets in four Nevado-Filábride samples dated between 13.5 and 18.2 Ma (Lu-Hf ages). The above constraints lead us to conclude that high-pressure conditions probably prevailed until ca. 14 Ma in the Nevado-Filábride Complex and were followed by fast exhumation. Our new monazite ages establish that red and green FIA in sample 46.8.1 formed prior to 14.6 Ma well before the orange FIAs which formed around 13.6 Ma. This is consistent with Sm-Nd ages of Aerden et al. (2022) (Fig. 8.15) of 16-21 Ma for garnets with green FIAs in a sample collected 70 km southwest of 46.8.1 (sample 53.10.1) and 35 Ma for garnets with red FIAs from a location 25 km southwest of 46.8.1 in the lower tectonic subunit of the complex (sample B13c).

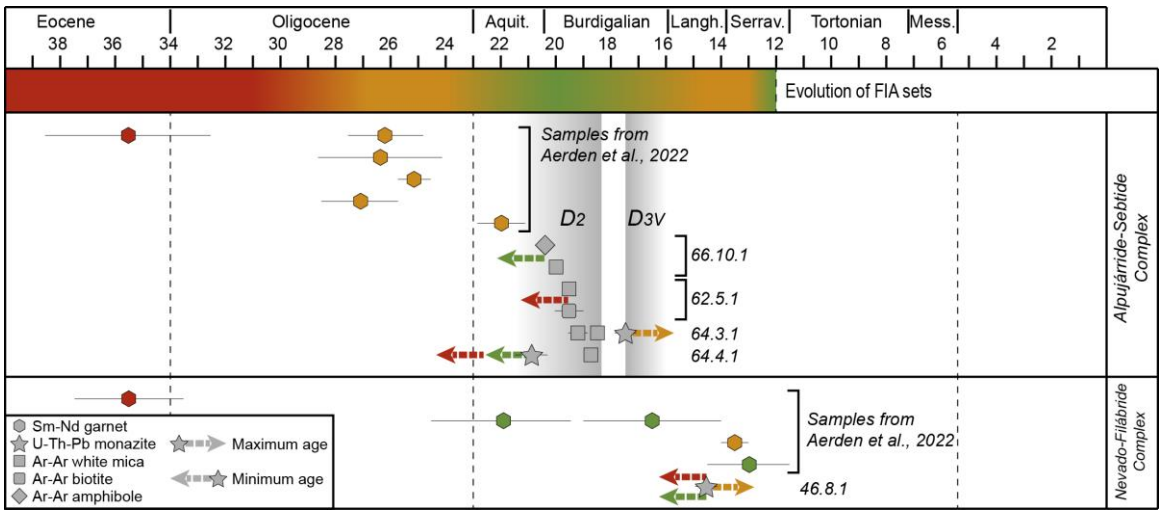

Fig. 8.15. Summary of FIA timing, colours indicate the corresponding FIA following the colour codes of Figs. 8.2 and 8.3. Garnet ages were taken from Aerden et al. (2022). Unlike direct garnet dating, monazite, mica and amphibole only allow indirect age estimation of FIAs, so the age is only interpreted as older or younger with respect to the dated mineral. Ages of deformation events in the Alpujárride Complex determined in this study are also indicated.

8.7.3. Timing of FIA sets in the Alpujárride Complex

Our results complement previous geochronological data for different FIA sets in the Gibraltar Arc as summarized in Fig. 8.15. A minimum age has been obtained for garnets with red (WNW-ESE) FIA in samples 62.5.1 and 64.4.1 as they predate ages of 20.88-19.57 Ma for S_2 in these samples, respectively. Their age might be Eocene or early Oligocene (Fig. 8.15) since garnets with equivalent FIAs have been dated as Eocene in the Sebtide, and late Oligocene ages have been obtained for garnets with orange FIA postdating the red set (Aerden et al., 2022). The formation of green (NNW-SSE) FIAs in sample 66.10.1 has been interpreted to have been closely followed by development of S_2 for which an Ar-Ar age of around 20 Ma was obtained in this sample. The continuity of inclusion trails defining green FIAs at the rims of type-II garnets in sample 64.4.1 also situate the formation of this FIA closely before S_2 in this sample (20.88 – 18.78 Ma). Garnets with orange (ENE-WSW) FIA in sample 64.3.1 and 46.8.1 have been constrained

to maximum ages of 17.58 ± 0.37 Ma and 14.62 ± 0.27 Ma in the Alpujárride and Nevado-Filábride, respectively. The age of the Nevado-Filábride sample matches well the previous age of 13.62 ± 0.69 Ma (Aerden et al., 2022) for garnets from the same outcrop and the same FIA trend as sample 46.8.1. The age of 17.58 ± 0.37 Ma of the Alpujárride sample implies a repetition of orange (ENE-WSW) FIA after the green ones had formed (NNW-SSE) as already interpreted by Ruiz-Fuentes and Aerden (2023) in the Alpujárride Complex. This appears to mark the beginning of an alternation between two orthogonal shortening directions related to simultaneous westward drifting of the Alborán Domain and NW-directed motion of Africa. This alternation is further recorded in garnets of the Nevado-Filábride until ~13 Ma (Aerden et al., 2022).

8.8. Conclusions

- The D_2 deformation event in the Alpujárride Complex took place under P-T conditions of 7-9.5 kbar and 600-680 ºC in the period 21-18.5 Ma, coeval with the beginning of the Alborán Sea opening.
- P-T conditions of subsequent compression (D_{3V}) in the Adra nappe have been constrained to 6 kbar and 570-650 ºC at an age of 17.58 ± 0.37 Ma. This age allows correlation of D_{3V} with the beginning of the collision stage between the Internal and External Zones in the Betic Cordillera.
- Relative and absolute timing evidence concerning three sets of FIA preserved in garnet, plagioclase and andalusite porphyroblasts around the Gibraltar Arc recognized previously is complemented by our combination of Ar-Ar ages for minerals associated with the principle matrix foliation and U-Th-Pb for monazite grains showing different textural relationships with respect to the matrix and porphyroblast growth stages. Garnets with red FIA in samples 62.5.1 and 64.4.1 formed before 21 Ma, the age of S_2 in the first mentioned sample. Garnets with green FIA in sample 66.10.1 grew immediately before S_2 around 20 Ma. Garnets with orange (ENE-WSW) FIA grew close to 17.5 Ma in Alpujárride sample 64.3.1 and around ~14.5 Ma in Nevado-Filábride sample 46.8.1 based on the age of cogenetic monazite inclusions. These orange FIA repeat the trend of an older set of 'orange' FIAs that predates green FIAs dated 22-27 Ma in the Sebtide complex by Aerden et al. (2022). Thus, a sequence of red, orange, green and again orange FIAs is concluded, whose geodynamic significance has already been interpreted by Aerden et al. (2022) and Ruiz-Fuentes and Aerden (2023).

Acknowledgements

We thank P. Münch and A. Iemmolo for performing the Ar-Ar analyses. ARF acknowledge financial support by an FPU grant from the Spanish Ministery of Education, Culture and Sport (FPU17/01874), and by an international mobility grant from University of Granada. Research was funded by Spanish government grant CGL2016-80687-R AEI/FEDER, and Junta de Andalucía Projects P18-RT-3275 (AGORA), B-RNM-301-UGR18 (PAPEL) and RNM148.

References

Abu Sharib, A.S.A.A., Bell, T.H., 2011. Radical changes in bulk shortening directions during orogenesis: Significance for progressive development of regional folds and thrusts. Precambrian Research 188, 1-20. https://doi.org/10.1016/j.precamres.2011.03.008

Aerden, D.G.A.M., 1994. Kinematics of orogenic collapse in the Variscan Pyrenees deduced from microstructures in porphyroblastic rocks from the Lys-Caillaouas massif. Tectonophysics 238, 139-160. https://doi.org/10.1016/0040-1951(94)90053-1

Aerden, D.G.A.M., 1995. Porphyroblast non-rotation during crustal extension in the Variscan Lys-Caillaouas Massif, Pyrenees. Journal of Structural Geology 17, 709-725. https://doi.org/10.1016/0191-8141(94)00090-M

Aerden, D.G.A.M., 1998. Tectonic evolution of the Montagne Noire and a possible orogenic model for syncollisional exhumation of deep rocks, Variscan belt, France. Tectonics 17, 62-79. https://doi.org/10.1029/97TC02342

Aerden, D., 2003. Preferred orientation of planar microstructures determined via statistical best-fit of measured intersection-lines: the 'FitPitch' computer program. Journal of Structural Geology 25, 923-934. https://doi.org/10.1016/S0191-8141(02)00119-0

Aerden, D.G.A.M., 2004. Correlating deformation in Variscan NW-Iberia using porphyroblasts; implications for the Ibero-Armorican Arc. Journal of Structural Geology 26, 177-196. https://doi.org/10.1016/S0191-8141(03)00070-1

Aerden, D., Sayab, M., 2008. From Adria- to Africa-driven orogenesis: Evidence from porphyroblasts in the Betic Cordillera, Spain. Journal of Structural Geology 30, 1272-1287. https://doi.org/10.1016/j.jsg.2008.06.009

Aerden, D.G.A.M., Ruiz-Fuentes, A., 2020. X-ray computed micro-tomography of spiral garnets: A new test of how they form. Journal of Structural Geology 136, 104054. https://doi.org/10.1016/j.jsg.2020.104054

Aerden, D.G.A.M., Sayab, M., Bouybaouene, M.L., 2010. Conjugate-shear folding: A model for the relationships between foliations, folds and shear zones. Journal of Structural Geology 32, 1030-1045. https://doi.org/10.1016/j.jsg.2010.06.010

Aerden, D.G.A.M., Bell, T.H., Puga, E., Sayab, M., Lozano, J.A., Díaz de Federico, A., 2013. Multi-stage mountain building vs. relative plate motions in the Betic Cordillera deduced from integrated microstructural and petrological analysis of porphyroblast inclusion trails. Tectonophysics 587, 188-206. https://doi.org/10.1016/j.tecto.2012.11.025

Aerden, D.G.A.M., Ruiz-Fuentes, A., Sayab, M., Forde, A., 2021. Kinematics of subduction in the Ibero-Armorican arc constrained by 3D microstructural analysis of garnet and pseudomorphed lawsonite porphyroblasts from Île de Groix (Variscan belt). Solid Earth 12, 971-992. https://doi.org/10.5194/se-12-971-2021

Aerden, D.G.A.M., Farrell, T.P., Baxter, E.F., Stewart, E.M., Ruiz-Fuentes, A., Bouybaouene, M., 2022. Refined tectonic evolution of the Betic-Rif orogen through integrated 3-D

microstructural analysis and Sm-Nd dating of garnet porphyroblasts. Tectonics 41, e2022TC007366. https://doi.org/10.1029/2022TC007366

Aguado, R., Feinberg, H., Durand-Delga, M., Martín-Algarra, A., Esteras, M., Didon, J., 1990. Nuevos datos sobre la edad de las formaciones miocenas transgresivas sobre las Zonas Internas béticas: La formación de San Pedro de Alcántara (provincia de Málaga). Revista de la Sociedad Geológica de España 3, 79-85.

Aldaya, F., García-Dueñas, V., Navarro-Vilá, F., 1979. Los Mantos Alpujárrides del tercio central de las Cordilleras Béticas. Ensayo de correlación tectónica de los Alpujárrides. Acta Geológica Hispánica 14, 154-166.

Ali, A., 2010. The tectono-metamorphic evolution of the Balcooma Metamorphic Group, north-eastern Australia: a multidisciplinary approach. Journal of Metamorphic Geology 28, 397-422. https://doi.org/10.1111/j.1525-1314.2010.00871.x

Allmendinger, R. W., Cardozo, N. C., Fisher, D., 2013. Structural Geology Algorithms: Vectors & Tensors. Cambridge, England, Cambridge University Press, 289 pp.

Alonso-Chaves, F.M., Orozco, M., 1998. El Sistema de Fallas Extensionales de La Axarquía (Sierras de Tejeda y La Almijara, Cordilleras Béticas). Geogaceta 24, 15-18.

Alonso-Chaves, F.M., Rodriguez-Vidal, J., 1998. Subsidence tectonique et sédimentation synrift associée au rifting du domaine d'Alboran au Miocène inférieur (Chaîne bétique, Espagne). Comptes Rendus de l'Académie des Sciences – Series IIA – Earth and Planetary Science 326, 51-56. https://doi.org/10.1016/S1251-8050(97)83203-X

Alonso-Chaves, F.M., Orozco, M., 2007. Evolución tectónica de las Sierras de Tejeda y Almijara: Colapso extensional y exhumación de áreas metamórficas en el Dominio de Alborán (Cordilleras Béticas). Revista de la Sociedad Geológica de España 20 (3-4), 211-228.

Alonso-Chaves, F.M., Andreo, B., Azañón, J.M., Balanyá, J.C., Booth-Rea, G., Crespo-Blanc, A., Delgado, F., Estévez, A., García-Casco, A., García-Dueñas, V., López-Garrido, A.C., Martín-Algarra, A., Orozco, M., Sánchez-Gómez, M., Sánchez-Navas, A., Sanz de Galdeano, C., Torres-Roldán, R.L., 2004. Complejo Alpujárride. Sucesiones litológicas, petrología y estratigrafía, in: Vera, J.A., (Ed.) Geología de España. SGE-IGME Madrid, 409-414.

Augier, R., Agard, P., Monié, P., Jolivet, L., Robin, C., Booth-Rea, G., 2005. Exhumation, doming and slab retreat in the Betic Cordillera (SE Spain): in situ 40Ar/39Ar ages and P-T-d-t paths for the Nevado-Filabride complex. Journal of Metamorphic Geology 23, 357-381. https://doi.org/10.1111/j.1525-1314.2005.00581.x

Azañón, J.M., Alonso-Chaves, F.M., 1996. Alpine tectono-metamorphic evolution of the Tejeda Unit, an extensionally dismembered Alpujarride Nappe (Western Betics). Comptes Rendus de l'Académie des Sciences de Paris 322, 47-54.

Azañón, J.M., Goffé, B., 1997. Ferro- and magnesiocarpholite assemblages as record of high-P, low-T metamorphism in the Central Alpujarrides, Betic Cordillera (SE Spain). European Journal of Mineralogy 9, 1035-1051.

Azañón, J.M., Crespo-Blanc, A., 2000. Exhumation during a continental collision inferred from the tectonometamorphic evolution of the Alpujarride Complex in the central Betics (Alboran Domain, SE Spain). Tectonics 19 (3), 549-565. https://doi.org/10.1029/2000TC900005

Azañón, J.M., García-Dueñas, V., Martínez-Martínez, J.M., Crespo-Blanc, A., 1994. Alpujarride tectonic sheets in the central Betics and similar eastern allochthonous units (SE Spain). Comptes Rendus de l'Académie des Sciences de Paris 318, 667-674.

Azañón, J.M., Crespo-Blanc, A., García-Dueñas, V., 1997. Continental collision, crustal thinning and nappe forming during the pre-Miocene evolution of the Alpujarride Complex (Alboran Domain, Betics). Journal of Structural Geology 19 (8), 1055-1071. https://doi.org/10.1016/S0191-8141(97)00031-X

Azañón, J.M., García-Dueñas, V., Goffé, B., 1998. Exhumation of high-pressure metapelites and coeval crustal extension in the Alpujarride complex (Betic Cordillera). Tectonophysics 285, 231-252. https://doi.org/10.1016/S0040-1951(97)00273-4

Bakker, H.E., de Jong, K., Helmers, H., Biermann, C., 1989. The geodynamic evolution of the Internal Zone of the Betic Cordilleras (south-east Spain): a model based on structural analysis and geothermobarometry. Journal of Metamorphic Geology 7, 359-381. https://doi.org/10.1111/j.1525-1314.1989.tb00603.x

Balanyá, J.C., García-Dueñas, V., Azañón, J.M., Sánchez-Gómez, M., 1997. Alternating contractional and extensional events in the Alpujarride nappes of the Alboran Domain (Betics, Gibraltar Arc). Tectonics 16, 226-238. https://doi.org/10.1029/96TC03871

Balanyá, J.C., García-Dueñas, V., Azañón, J.M., Sánchez-Gómez, M., 1998. Reply to "Comment on 'Alternating contractional and extensional events in the Alpujarride nappes of the Alboran Domain (Betics, Gibraltar Arc)'". Tectonics 17 (6), 977-981. https://doi.org/10.1029/1998TC900006

Behr, W.M., Platt, J.P., 2012. Kinematic and thermal evolution during two-stage exhumation of a Mediterranean subduction complex. Tectonics 31, TC4025. https://doi.org/10.1029/2012TC003121

Bell, T.H., 1985. Deformation partitioning and porphyroblast rotation in metamorphic rocks: a radical interpretation. Journal of Metamorphic Geology 3, 109-118. https://doi.org/10.1111/j.1525-1314.1985.tb00309.x

Bell, T.H., Johnson, S.E., 1989. Porphyroblast inclusion trails: the key to orogenesis. Journal of Metamorphic Geology 7, 279-310. https://doi.org/10.1111/j.1525-1314.1989.tb00598.x

Bell, T.H., Hayward, N., 1991. Episodic metamorphic reactions during orogenesis: the control of deformation partitioning on reaction sites and reaction duration. Journal of Metamorphic Geology 9, 619-640. https://doi.org/10.1111/j.1525-1314.1991.tb00552.x

Bell, T.H., Mares, V.M., 1999. Correlating deformation and metamorphism around orogenic arcs. American Mineralogist 84, 1727-1740. https://doi.org/10.2138/am-1999-11-1203

Bell, T.H., Welch, P.W., 2002. Prolonged Acadian orogenesis: Revelations from foliation intersection axis (FIA) controlled monazite dating of foliations in porphyroblasts and matrix. American Journal of Science 302, 549-581. https://doi.org/10.2475/ajs.302.7.549

Bell, T.H., Sapkota, J., 2012. Episodic gravitational collapse and migration of the mountain chain during orogenic roll-on in the Himalayas. Journal of Metamorphic Geology 30, 651-666. https://doi.org/10.1111/j.1525-1314.2012.00992.x

Bell, T.H., Fay, C., 2016. Holistic microstructural techniques reveal synchronous and alternating andalusite and staurolite growth during three tectonic events resulted from shifting partitioning of growth vs deformation. Lithos 262, 699-712. https://doi.org/10.1016/j.lithos.2016.06.031

Bell, T.H., Johnson, S.E., Davis, B., Forde, A., Hayward, N., Wilkins, C., 1992. Porphyroblast inclusion-trail orientation data: eppure non son girate! Journal of Metamorphic Geology 10, 295-307. https://doi.org/10.1111/j.1525-1314.1992.tb00084.x

Bell, T.H., Forde, A., Wang, J., 1995. A new indicator of movement direction during orogenesis: measurement technique and application to the Alps. Terra Nova 7, 500-508. https://doi.org/10.1111/j.1365-3121.1995.tb00551.x

Bell, T.H., Hickey, K.A., Upton, G.J.G., 1998. Distinguishing and correlating multiple phases of metamorphism across a multiply deformed region using the axes of spiral, staircase and sigmoidal inclusion trails in garnet. Journal of Metamorphic Geology 16, 767-794. https://doi.org/10.1111/j.1525-1314.1998.00170.x

Bessière, E., Scaillet, S., Augier, R., Jolivet, L., Azañón, J.M., Booth-Rea, G., Romagny, A., Duval, F., 2022. 40Ar/39Ar Age Constraints on HP/LT Metamorphism in Extensively Overprinted Units: The Example of the Alpujárride Subduction Complex (Betic Cordillera, Spain). Tectonics 41, e2021TC006889. https://doi.org/10.1029/2021TC006889

Bhattacharya, A., Mohanty, L., Maji, A., Sen, S.K., Raith, M., 1992. Non-ideal mixing in the phlogopite-annite binary: constraints from experimental data on Mg-Fe partitioning and a reformulation of the biotite-garnet geothermometer. Contrib Mineral Petrol 111, 87-93. https://doi.org/10.1007/BF00296580

Booth-Rea, G., Azañón, J.M., Goffé, B., Vidal, O., Martínez-Martínez, J.M., 2002. High-pressure, low-temperature metamorphism in Alpujarride Units of southeastern Betics (Spain). Comptes Rendus Geosciences 334, 857-865. https://doi.org/10.1016/S1631-0713(02)01787-X

Booth-Rea, G., Azañón, J.M., Martínez-Martínez, J.M., Vidal, O., García-Dueñas, V., 2005. Contrasting structural and P-T evolution of tectonic units in the southeastern Betics: Key for understanding the exhumation of the Alboran Domain HP/LT crustal rocks (western Mediterranean). Tectonics 24, TC2009. https://doi.org/10.1029/2004TC001640.

Booth-Rea, G., Martínez-Martínez, J.M., Giaconia, F., 2015. Continental subduction, intracrustal shortening, and coeval upper-crustal extensión: P-T evolution of subducted south Iberian paleomargin metapelites (Betics, SE Spain). Tectonophysics 663, 122-139. https://doi.org/10.1016/j.tecto.2015.08.036

Bouillin, J.P., Durand Delga, M., Olivier, P., 1986. Betic-Rifain and Tyrrhenian Arcs: distinctive features, genesis and development stages, in: Wezel, F.C., (Ed.), The origin of arcs, Amsterdam, Elsevier, p. 281–304.

Comas, M.C., García-Dueñas, V., Jurado, M.J., 1992. Neogene tectonic evolution of the Alboran Sea from MCS data. Geo-Marine Letters 12, 157-164. https://doi.org/10.1007/BF02084927

Crespo-Blanc, A., Orozco, M., García-Dueñas, V., 1994. Extension versus compression during the Miocene tectonic evolution of the Betic chain. Late folding of normal fault systems. Tectonics 13, 78-88. https://doi.org/10.1029/93TC02231

Cuevas, J., 1989a. Microtectónica y metamorfismo de los Alpujárrides del tercio central de las Cordilleras Béticas (entre Motril y Adra). Parte I: Litología y estructuras asociadas a D1, D2 y D3. Boletín Geológico y Minero 100 (4), 497-540.

Cuevas, J., 1989b. Microtectónica y metamorfismo de los Mantos Alpujárrides del tercio central de las Cordilleras Béticas (entre Motril y Adra). Parte II: Las Zonas Miloníticas. Boletín Geológico y Minero 100 (5), 719-766.

Cuevas, J., 1991. Internal structure of the Adra Nappe (Alpujarride Complex, Betics, Spain). Tectonophysics 200, 199-212. https://doi.org/10.1016/0040-1951(91)90015-K

Cuevas, J., Aldaya, F., Navarro-Vilá, F., Tubía, J.M., 1986. Caractérisation de deux étapes de charriage principales dans les nappes Alpujarrides centrales (Cordillères Bétiques, Espagne). Comptes Rendus de l'Académie des Sciences de Paris 302, 1177-1180.

Dasgupta, S., Sengupta, P., Guha, D., Fukuoka, M., 1991. A refined garnet – biotite Fe – Mg Exchange geothermometer and its application in amphibolites and granulites. Contrib Mineral Petrol 109, 130-137. https://doi.org/10.1007/BF00687206

de Capitani, C., Petrakakis, K., 2010. The computation of equilibrium assemblage diagrams with Theriak/Domino software. American Mineralogist 95, 1006-1016. https://doi.org/10.2138/am.2010.3354

Esteban, J.J., Sánchez-Rodríguez, L., Seward, D., Cuevas, J., Tubía, J.M., 2004. The late thermal history of the Ronda area, southern Spain. Tectonophysics 389, 81-92. https://doi.org/10.1016/j.tecto.2004.07.050

Esteban, J.J., Cuevas, J., Tubía, J.M., Liati, A., Seward, D., Gebauer, D., 2007. Timing and origin of zircon-bearing chlorite schists in the Ronda peridotites (Betic Cordilleras, Southern Spain). Lithos 99, 121-135. https://doi.org/10.1016/j.lithos.2007.06.006

Esteban, J.J., Cuevas, J., Tubía, J.M., Sergeev, S., Larionov, A., 2011. A revised Aquitanian age for the emplacement of the Ronda peridotites (Betic Cordilleras, southern Spain). Geological Magazine 148, 183-187. https://doi.org/10.1017/S0016756810000737

Ferry, J.M., Spear, F.S., 1978. Experimental Calibration of the Partitioning of Fe and Mg Between Biotite and Garnet. Contrib Mineral Petrol 66, 113-117. https://doi.org/10.1007/BF00372150

Ferry, J.M., Watson, E.B., 2007. New thermodynamic models and revised calibrations for the Ti-in-zircon and Zr-in-rutile thermometers. Contrib Mineral Petrol 154, 429-437. https://doi.org/10.1007/s00410-007-0201-0

Frasca, G., Gueydan, F., Poujol, M., Brun, J.P., Parat, F., Monié, P., Pichat, A., Mazier, S., 2017. Fast switch from extensional exhumation to thrusting of the Ronda Peridotites (South Spain). Terra Nova 29, 117-126. https://doi.org/10.1111/ter.12255

Galindo-Zaldivar, J., González-Lodeiro, F., Jabaloy, A., 1989. Progressive extensional shear structures in a detachment contact in the Western Sierra Nevada (Betic Cordilleras, Spain). Geodinamica Acta 3, 73-85. https://doi.org/10.1080/09853111.1989.11105175

García-Dueñas, V., Navarro-Vilá, F., 1976. Alpujarrides, Malaguides et autres unités allochtones au Nord de la Sierra Nevada (Cordillères Bétiques, Andalousie). Bulletin de la Société Géologique de France 7-XVIII-3, 641-648. https://doi.org/10.2113/gssgfbull.S7-XVIII.3.641

García-Dueñas, V., Martínez-Martínez, J.M., Orozco, M., Soto, J.I., 1988. Plis-nappes, cisaillements syn- à post-métamorphiques et cisaillements ductiles-fragiles en distensión dans les Nevado-Filabrides (Cordillères bétiques, Espagne). Comptes Rendus de l'Académie des Sciences de Paris 307, 1389-1395.

Ghent, E.D., Stout, M.Z., 1981. Geobarometry and Geothermometry of Plagioclase-Biotite-Garnet-Muscovite Assemblages. Contrib Mineral Petrol 76, 92-97. https://doi.org/10.1007/BF00373688

Gómez-Pugnaire, M.T., Fernández-Soler, J.M., 1987. High-pressure metamorphism in metabasites from the Betic Cordilleras (S.E. Spain) and its evolution during the Alpine orogeny. Contrib Mineral Petrol 95, 231-244.

Gómez-Pugnaire, M.T., Franz, G., López Sánchez-Vizcaíno, V., 1994. Retrograde formation of NaCl-scapolite in high pressure metaevaporites from the Cordilleras Béticas (Spain). Contrib Mineral Petrol 116, 448-461. https://doi.org/10.1007/BF00310911

Gómez-Pugnaire, M.T., Galindo-Zaldívar, J., Rubatto, D., González-Lodeiro, F., López Sánchez-Vizcaíno, V., Jabaloy, A., 2004. A reinterpretation of the Nevado-Filábride and Alpujárride Complexes (Betic Cordillera): field, petrography and U-Pb ages from orthogneisses (western Sierra Nevada, S Spain). Schweizerische Mineralogische und Petrographische Mitteilungen 84, 303-322.

Gómez-Pugnaire, M.T., Rubatto, D., Fernández-Soler, J.M., Jabaloy, A., López-Sánchez-Vizcaíno, V., González-Lodeiro, F., Galindo-Zaldívar, J., Padrón-Navarta, J.A., 2012. Late Variscan magmatism in the Nevado-Filábride Complex: U-Pb geochronologic evidence for the pre-Mesozoic nature of the deepest Betic complex (SE Spain). Lithos 146-147, 93-111. https://doi.org/10.1016/j.lithos.2012.03.027

González-Casado, J.M., Casquet, C., Martínez-Martínez, J.M., García-Dueñas, V., 1995. Retrograde evolution of quartz segregations from the Dos Picos shear zone in the Nevado-Filabride Complex (Betic chains, Spain). Evidence from fluid inclusions and quartz c-axis fabrics. Geol. Rundsch. 84, 175-186. https://doi.org/10.1007/BF00192249

González Donoso, J.M., Linares, D., Molina, E., Serrano, F., Vera, J.A., 1982. Sobre la edad de la Formación de La Viñuela (Cordilleras Béticas, provincia de Málaga). Boletín de la Real Sociedad Española de Historia Natural (Sección Geológica) 80, 255-275.

Guerrera, F., Martín-Algarra, A., Perrone, V., 1993. Late Oligocene-Miocene syn-/-late-orogenic successions in Western and Central Mediterranean chains from the Betic Cordillera to the Southern Apennines. Terra Nova 5, 525-544. https://doi.org/10.1111/j.1365-3121.1993.tb00302.x

Guerrera, F., Martín-Martín, M., Tramontana, M., 2021. Evolutionary geological models of the central-western peri-Mediterranean chains: a review. International Geology Review 63, 65-86 https://doi.org/10.1080/00206814.2019.1706056

Ham, A.P., Bell, T.H., 2004. Recycling of foliations during folding. Journal of Structural Geology 26, 1989-2009. https://doi.org/10.1016/j.jsg.2004.04.003

Hayward, N., 1990. Determination of early fold axis orientations in multiply deformed rocks using porphyroblast inclusion trails. Tectonophysics 179, 353-369. https://doi.org/10.1016/0040-1951(90)90301-N

Hayward, N., 1992. Microstructural analysis of the classical spiral garnet porphyroblasts of south-east Vermont - evidence for non-rotation. Journal of Metamorphic Geology 10(4), 567–587. https://doi.org/10.1111/j.1525-1314.1992.tb00106.x

Homonnay, E., Corsini, M., Lardeaux, J.M., Romagny, A., Münch, P., Bosch, D., Cenki-Tok, B., Ouazzani-Touhami, M., 2018. Miocene crustal extension following thrust tectonic in the Lower Sebtides units (internal Rif, Ceuta Peninsula, Spain): Implication for the geodynamic evolution of the Alboran domain. Tectonophysics 722, 507-535. https://doi.org/10.1016/j.tecto.2017.11.028

Huddlestone-Holmes, C.R., Ketcham, R.A., 2005. Getting the inside story: using computed X-ray tomography to study inclusion trails in garnet porphyroblasts. American Mineralogist 90, ea1–ea17. https://doi.org/10.2138/am.2005.1840

Huddlestone-Holmes, C.R., Ketcham, R.A., 2010. An X-ray computed tomography study of inclusion trail orientations in multiple porphyroblasts from a single sample. Tectonophysics 480, 305-320. https://doi.org/10.1016/j.tecto.2009.10.021

Jabaloy-Sánchez, A., Fernández-Fernández, E., González-Lodeiro, F., 2007. A cross section of the eastern Betic Cordillera (SE Spain) according field data and a seismic reflection profile. Tectonophysics 433, 97-126. https://doi.org/10.1016/j.tecto.2006.11.004

Jabaloy-Sánchez, A., Talavera, C., Gómez-Pugnaire, M.T., López-Sánchez-Vizcaíno, V., Vázquez-Vílchez, M., Rodríguez-Peces, M.J., Evans, N.J., 2018. U-Pb ages of detrital zircons from the Internal Betics: A key to deciphering palaeogeographic provenance and tectono-stratigraphic evolution. Lithos 318-319, 244-266. https://doi.org/10.1016/j.lithos.2018.07.026

Jabaloy Sánchez, A., Martín-Algarra, A., Padrón-Navarta, J.A., Martín-Martín, M., Gómez-Pugnaire, M.T., López Sánchez-Vizcaíno, V., Garrido, C.J., 2019. Lithological Successions of the Internal Zones and Flysch Trough Units of the Betic Chain, in: Quesada, C., Oliveira, J.T., (Eds.), The Geology of Iberia: A Geodynamic Approach, Vol. 3, Ch. 8, p. 377-432 (Alpine

Cycle, Vergés, J., Kullber, J.C., Volume Coordinators), Regional Geology Reviews. https://doi.org/10.1007/978-3-030-11295-0_8

Johnson, C., Harbury, N., Hurford, A.J., 1997. The role of extension in the Miocene denudation of the Nevado-Filábride Complex, Betic Cordillera (SE Spain). Tectonics 16, 189-204. https://doi.org/10.1029/96TC03289

Kim, H.S., Ree, J.H., 2013. Permo-Triassic changes in bulk crustal shortening direction during deformation and metamorphism of the Taebaeksan Basin, South Korea using foliation intersection/inflection axes: Implications for tectonic movement at the eastern margin of Eurasia during the Songrim (Indosinian) orogeny. Tectonophysics 587, 133-145. https://doi.org/10.1016/j.tecto.2012.08.033

Kim, H.S., Sanislav, I.V., 2017. Foliation intersection/inflection axes within porphyroblasts (FIAs): a review of advanced applications and significance. Geosciences Journal 21, 1013-1032. https://doi.org/10.1007/s12303-017-0047-z

Kirchner, K.L., Behr, W.M., Loewy, S., Stockli, D.F., 2016. Early Miocene subduction in the western Mediterranean: Constraints from Rb-Sr multimineral isochron geochronology. Geochemistry, Geophysics, Geosystems 17, 1842-1860. https://doi.org/10.1002/2015GC006208

Laborda-López, C., Aguirre, J., Donovan, S.K., 2015. Surviving metamorphism: taphonomy of fossil assemblages in marble and calc-silicate schist. Palaios 30, 668-679. https://doi.org/10.2110/palo.2015.013

Li, B., Massonne, H.J., 2018. Two Tertiary metamorphic events recognized in high-pressure metapelites of the Nevado-Filábride Complex (Betic Cordillera, S Spain). Journal of Metamorphic Geology 36, 603-630. https://doi.org/10.1111/jmg.12312

López Sánchez-Vizcaíno, V., Rubatto, D., Gómez-Pugnaire, M.T., Trommsdorff, V., Müntener, O., 2001. Middle Miocene high-pressure metamorphism and fast exhumation of the Nevado-Filábride Complex, SE Spain. Terra Nova 13, 327-332. https://doi.org/10.1046/j.1365-3121.2001.00354.x

Lozano, J.A., Puga, E., García-Casco, A., Martínez-Sevilla, F., Contreras Cortés, F., Carrasco Rus, J., Martín-Algarra, A., 2018. First evidence of prehistoric eclogite quarrying for polished tolos and their circulation on the Iberian Peninsula. Geoarchaeology 33, 364-385.

Ludwig, K.R., 2003. Mathematical–Statistical Treatment of Data and Errors for 230Th/U Geochronology. Reviews in Mineralogy and Geochemistry 52, 631–656. https://doi.org/10.2113/0520631

Martín-Algarra, A., 1987. Evolución geológica alpina del contacto entre las Zonas Internas y las Zonas Externas de la Cordillera Bética. PhD Thesis, Universidad de Granada, 1171 p. https://digibug.ugr.es/handle/10481/75699

Martín-Algarra, A., Crespo-Blanc, A., Delgado, F., Estévez, A., González-Lodeiro, F., Orozco, M., Sánchez-Gómez, M., Sanz de Galdeano, C., García-Dueñas, V., 2004. Complejo Alpujárride. Estructura. Rasgos generales, in: Vera, J.A., (Ed.) Geología de España. SGE-IGME Madrid, 416-417.

Martín-Algarra, A., Mazzoli, S., Perrone, V., Rodríguez-Cañero, R., 2009. Variscan Tectonics in the Malaguide Complex (Betic Cordillera, Southern Spain): Stratigraphic and Structural Alpine versus Pre-Alpine Constraints from the Ardales Area (Province of Málaga). II. Structure. The Journal of Geology 117, 263-284. https://doi.org/10.1086/597365

Martín-Martín, M., Martín-Algarra, A., 2002. Thrust sequence and syntectonic sedimentation in a piggy-back basin: the Oligo-Aquitanian Mula-Pliego Basin (Internal Betic Zone, SE Spain). Comptes Rendus Geoscience 334, 363-370. https://doi.org/10.1016/S1631-0713(02)01757-1

Martín-Martín, M., El Mamoune, B., Martín-Algarra, A., Martín-Pérez, J.A., 1996. The Internal-External Zone Boundary in the Eastern Betic Cordillera, SE Spain: Discussion. Journal of Structural Geology 18, 523-524. https://doi.org/10.1016/0191-8141(95)00121-S

Martín-Martín, M., El Mamoune, B., Martín-Algarra, A., Serra-Kiel, J., 1997. La formation As, datée de l'Oligocène, est impliquée dans les charriages des unités malaguides supérieures de la Sierra Espuña (zones internes bétiques, province de Murcie, Espagne). Comptes Rendus de l'Académie des Sciences de Paris 325, 861-868. https://doi.org/10.1016/S1251-8050(99)80186-4

Martín-Rojas, I., Estévez, A., Martín-Martín, M., Delgado, F., García-Tortosa, F.J., 2007. New data from Orihuela and Callosa Mountains (Betic Internal Zone, Alicante, SE Spain). Implications for the "Almágride Complex" controversy. Journal of Iberian Geology 33 (2), 311-318.

Martínez-Martínez, J.M., Soto, J.I., Balanyá, J.C., 1995. Large scale structures in the Nevado-Filabride Complex and crustal seismic fabrics of the deep seismic reflection profile ESCI-Béticas2. Revista de la Sociedad Geológica de España 8, 477-489.

Martínez-Martínez, J.M., Soto, J.I., Balanyá, J.C., 2002. Orthogonal folding of extensional detachments: Structure and origin of the Sierra Nevada elongated dome (Betics, SE Spain). Tectonics 21, 1012. https://doi.org/10.1029/2001TC001283

Massonne, H.J., 2014. Wealth of P-T-t information in medium-high grade metapelites: Example from the Jubrique Unit of the Betic Cordillera, S Spain. Lithos 208-209, 137-157. https://doi.org/10.1016/j.lithos.2014.08.027

Mazzoli, S., Martín-Algarra, A., Reddy, S.M., López Sánchez-Vizcaíno, V., Fedele, L., Noviello, A., 2013. The evolution of the footwall to the Ronda subcontinental mantle peridotites: insights from the Nieves Unit (western Betic Cordillera). Journal of the Geological Society 170, 385-402. https://doi.org/10.1144/jgs2012-105

Monié, P., Galindo-Zaldivar, J., González-Lodeiro, F., Goffe, B., Jabaloy, A., 1991. 40Ar/39Ar geochronology of Alpine tectonism in the Betic Cordilleras (southern Spain). Journal of the Geological Society 148, 289-297. https://doi.org/10.1144/gsjgs.148.2.0289

Monié, P., Torres-Roldán, R.L., García-Casco, A., 1994. Cooling and exhumation of the Western Betic Cordilleras, 40Ar/39Ar thermochronological constraints on a collapsed terrane. Tectonophysics 238, 353-379. https://doi.org/10.1016/0040-1951(94)90064-7

Munro, M.A., Blenkinsop, T.G., 2012. MARD-A moving average rose diagram application for the geosciences. Computers & Geosciences 49, 112-120. https://doi.org/10.1016/j.cageo.2012.07.012

Nieto, F., Velilla, N., Peacor, D.R., Ortega Huertas, M., 1994. Regional retrograde alteration of sub-greenschist facies chlorite to smectite. Contrib Mineral Petrol 115, 243-252. https://doi.org/10.1007/BF00310765

Orozco, M., Alonso-Chaves, F.M., Nieto, F., 1998. Development of large north-facing folds and their relation to crustal extension in the Alboran domain (Alpujarras region, Betic Cordilleras, Spain). Tectonophysics 298, 271-295. https://doi.org/10.1016/S0040-1951(98)00188-7

Orozco, M., Álvarez-Valero, A.M., Alonso-Chaves, F.M., Platt, J.P., 2004. Internal structure of a collapsed terrain The Lújar syncline and its significance for the fold- and sheet-structure of the Alborán Domain (Betic Cordilleras, Spain). Tectonophysics 385, 85-104. https://doi.org/10.1016/j.tecto.2004.04.025

Perchuk, L.L., 1991. Derivation of a thermodynamically consistent set of geothermometers and geobarometers for metamorphic and magmatic rocks, in: Perchuk, L.L. (Ed.), Progress in Metamorphic and Magmatic Petrology, p. 93-111. Cambridge University Press.

Platt, J.P., 1998. Comment on "Alternating contractional and extensional events in the Alpujarride nappes of the Alboran Domain (Betics, Gibraltar Arc)" by Juan C. Balanyá et al. Tectonics 17 (6), 973-976. https://doi.org/10.1029/1998TC900005

Platt, J.P., Whitehouse, M.J., 1999. Early Miocene high-temperature metamorphism and rapid exhumation in the Betic Cordillera (Spain): evidence from U-Pb zircon ages. Earth and Planetary Science Letters 171, 591-605. https://doi.org/10.1016/S0012-821X(99)00176-4

Platt, J.P., Soto, J.I., Whitehouse, M.J., Hurford, A.J., Kelley, S.P., 1998. Thermal evolution, rate of exhumation, and tectonic significance of metamorphic rocks from the floor of the Alboran extensional basin, western Mediterranean. Tectonics 17, 671-689. https://doi.org/10.1029/98TC02204

Platt, J.P., Argles, T.W., Carter, A., Kelley, S.P., Whitehouse, M.J., Lonergan, L., 2003. Exhumation of the Ronda peridotite and its crustal envelope: constraints from thermal modelling of a P-T-time array. Journal of the Geological Society 160, 655-676. https://doi.org/10.1144/0016-764902-108

Platt, J.P., Kelley, S.P., Carter, A., Orozco, M., 2005. Timing of tectonic events in the Alpujarride Complex, Betic Cordillera, southern Spain. Journal of the Geological Society, London 162, 451-462. https://doi.org/10.1144/0016-764903-039

Platt, J.P., Anczkiewicz, R., Soto, J.I., Kelley, S.P., Thirlwall, M., 2006. Early Miocene continental subduction and rapid exhumation in the western Mediterranean. Geology 34, 981-984. https://doi.org/10.1130/G22801A.1

Poitrasson, F., Chenery, S., Shepherd, T.J., 2000. Electron microprobe and LA-ICP-MS study of monazite hydrothermal alteration: Implications for U-Th-Pb geochronology and nuclear ceramics. Geochim. Cosmochim. Acta 64, 3283–3297.

Porkoláb, K., Matenco, L., Hupkes, J., Willingshofer, E., Wijbrans, J., van Schrojenstein Lantman, H., van Hinsbergen, D.J.J., 2022. Tectonic evolution of the Nevado-Filábride Complex (Sierra de los Filabres, Southeastern Spain): Insights from new structural and geochronological data. Tectonics 41, e2021TC006922. https://doi.org/10.1029/2021TC006922

Poulaki, E.M., Stockli, D.F., 2022. The paleotectonic evolution of the western Mediterranean: provenance insights from the internal Betics, southern Spain. Frontiers in Earth Science 10, 929502. https://doi.org/10.3389/feart.2022.929502

Poulaki, E.M., Stockli, D.F., Shuck, B.D., 2023. Pre-Subduction Architecture Controls Coherent Underplating During Subduction and Exhumation (Nevado-Filábride Complex, Southern Spain). Geochemistry, Geophysics, Geosystems 24, e2022GC010802. https://doi.org/10.1029/2022GC010802

Puga, E., Díaz de Federico, A., Fontbote, J.M., 1974. Sobre la individualización y sistematización de la unidades profundas de la Zona Bética. Estudios Geológicos 30, 543-548

Puga, E., Fontboté, J.M., Martín-Vivaldi, J.L., 1975. Kyanite Pseudomorphs after Andalusite in Polymetamorphic Rocks of the Sierra Nevada (Betic Cordillera, Southern Spain). Schweiz. Mineral. Petrogr. Mitt. 55, 227-241.

Puga, E., Nieto, J.M., Díaz de Federico, A., 2000. Contrasting P-T paths in eclogites of the Betic ophiolitic association, Mulhacén complex, southeastern Spain. The Canadian Mineralogist 38, 1137-1161. https://doi.org/10.2113/gscanmin.38.5.1137

Puga, E., Díaz de Federico, A., Nieto, J.M., 2002. Tectonostratigraphic subdivisión and petrological characterisation of the deepest complexes of the Betic zone: a review. Geodinamica Acta 15, 23-43. https://doi.org/10.1080/09853111.2002.10510737

Puga, E., Fanning, C.M., Nieto, J.M., Díaz de Federico, A., 2005. Recrystallization textures in zircon generated by ocean-floor and eclogite-facies metamorphism: a cathodoluminiscence and U-Pb SHRIMP study, with constraints from REE elements. The Canadian Mineralogist 43, 183-202. https://doi.org/10.2113/gscanmin.43.1.183

Puga, E., Fanning, M., Díaz de Federico, A., Nieto, J.M., Beccaluva, L., Bianchini, G., Díaz Puga, M.A., 2011. Petrology, geochemistry and U-Pb geochronology of the Betic Ophiolites: Inferences for Pangaea break-up and birth of the westernmost Tethys Ocean. Lithos 124, 255-272. https://doi.org/10.1016/j.lithos.2011.01.002

Reche, J., Martínez, F.J., 1996. GPT: An excel spreadsheet for thermobarometric calculations in metapelitic rocks. Computers & Geosciences 22, 775-784. https://doi.org/10.1016/0098-3004(96)00007-6

Robyr, M., Carlson, W.D., Passchier, C., Vonlanthen, P., 2009. Microstructural, chemical and textural records during growth of snowball garnet. Journal of Metamorphic Geology 27, 423–437. https://doi.org/10.1111/j.1525-1314.2009.00824.x

Rodríguez-Cañero, R., Jabaloy-Sánchez, A., Navas-Parejo, P., Martín-Algarra, A., 2018. Linking Palaeozoic palaeogeography of the Betic Cordillera to the Variscan Iberian Massif: new insight through the first conodonts of the Nevado-Filábride Complex. International Journal of Earth Sciences 107, 1791-1806. https://doi.org/10.1007/s00531-017-1572-8

Rodríguez-Fernández, J., Comas, M.C., Soria, J., Martín-Pérez, J.A., Soto, J.I., 1999. The sedimentary record of the Alboran basin: An attempt at sedimentary sequence correlation and subsidence analysis, in: Zahn, R., Comas, M.C., and Klaus, A. (eds), Proceedings of the Ocean Drilling Program, Scientific Results, Vol. 161, p. 69–76.

Rosenfeld, J.L., 1970. Rotated garnets in metamorphic rocks. Geological Society of America Special Paper, 129, 105.

Rossetti, F., Faccenna, C., Crespo-Blanc, A., 2005. Structural and kinematic constraints to the exhumation of the Alpujarride Complex (Central Betic Cordillera, Spain). Journal of Structural Geology 27, 199-216. https://doi.org/10.1016/j.jsg.2004.10.008

Ruiz Cruz, M.D., Sanz de Galdeano, C., Lázaro, C., 2005. Metamorphic evolution of Triassic rocks from the transition zone between the Maláguide and Alpujárride complexes (Betic Cordilleras, Spain). European Journal of Mineralogy 17, 81-91. https://doi.org/10.1127/0935-1221/2005/0017-0081

Ruiz-Cruz, M.D., Sanz de Galdeano, C., Santamaría, A., 2015. Petrology and thermobarometric estimates for metasediments, orthogneisses, and eclogites from the Nevado-Filábride complex in the western Sierra Nevada (Betic Cordillera, Spain). The Canadian Mineralogist 53, 1083-1107. https://doi.org/10.3749/canmin.1500037

Ruiz-Fuentes, A., Aerden, D.G.A.M., 2018. Transposition of foliations and superposition of lineations during polyphase deformation in the Nevado-Filabride complex: tectonic implications. International Journal of Earth Sciences 107, 1975-1988. https://doi.org/10.1007/s00531-017-1582-6

Ruiz-Fuentes, A., Aerden, D.G.A.M., 2023. Deciphering western Mediterranean kinematics using metamorphic porphyroblasts from the Alpujárride Complex (Betic Cordillera). Journal of Structural Geology 168, 104823. https://doi.org/10.1016/j.jsg.2023.104823

Ruiz-Fuentes, A., Cabrera-Porras, A., Martín-Algarra, A., 2022. Structural record of polyorogenic pre-Alpine and Alpine deformations within a major thrust nappe close to a suture zone (Internal-External Zones Boundary of the central Betic Cordillera, S Spain). International Geology Review https://doi.org/10.1080/00206814.2022.2129472

Sánchez-Navas, A., García-Casco, A., Martín-Algarra, A., 2014. Pre-Alpine discordant granitic dikes in the metamorphic core of the Betic Cordillera: tectonic implications. Terra Nova 26, 477-486. https://doi.org/10.1111/ter.12123

Sánchez-Rodriguez, L., Gebauer, D., 2000. Mesozoic formation of pyroxenites and gabbros in the Ronda area (southern Spain), followed by Early Miocene subduction metamorphism and emplacement into the middle crust: U-Pb sensitive high-resolution ion microprobe dating of zircon. Tectonophysics 316, 19-44. https://doi.org/10.1016/S0040-1951(99)00256-5

Sanislav, I.V., Bell, T.H., 2011. The inter-relationships between long-lived metamorphism, pluton emplacement and changes in the direction of bulk shortening during orogenesis. Journal of Metamorphic Geology 29, 513-536. https://doi.org/10.1111/j.1525-1314.2011.00928.x

Santamaría-López, A., Sanz de Galdeano, C., 2018. SHRIMP U-Pb detrital zircon dating to check subdivisions in metamorphic complexes: a case of study in the Nevado-Filábride complex

(Betic Cordillera, Spain). International Journal of Earth Sciences 107, 2539-2552. https://doi.org/10.1007/s00531-018-1613-y

Santamaría-López, A., Lanari, P., Sanz de Galdeano, C., 2019. Deciphering the tectono-metamorphic evolution of the Nevado-Filábride complex (Betic Cordillera, Spain) – A petrochronological study. Tectonophysics 767, 128158. https://doi.org/10.1016/j.tecto.2019.06.028

Sanz de Galdeano, C., López-Garrido, A.C., 2003. Revisión de las unidades Alpujárrides de las sierras de Tejeda, Almijara y Guájares (sector central de la Zona Interna Bética, provincias de Granada y Málaga). Revista de la Sociedad Geológica de España 16, 135-149.

Sanz de Galdeano, C., López-Garrido, A., 2016. The nevado-filábride complex in the western part of Sierra de los Filabres (Betic Internal Zone), structure and lithologic succession. Boletín Geológico y Minero 127, 823-836. DOI: 10.21701/bolgeomin.127.4.005

Sanz de Galdeano, C., Delgado, F., López-Garrido, A.C., 1995. Estructura del Alpujárride y del Maláguide al NW de Sierra Nevada (Cordillera Bética). Revista de la Sociedad Geológica de España 8, 239-250.

Sayab, M., 2005. Microstructural evidence for N-S shortening in the Mount Isa Inlier (NW Queensland, Australia): the preservation of early W-E-trending foliations in porphyroblasts revealed by independent 3D measurement techniques. Journal of Structural Geology 27, 1445-1468. https://doi.org/10.1016/j.jsg.2005.01.013

Sayab, M., Suuronen, J.P., Hölttä, P., Aerden, D., Lahtinen, R., Kallonen, A.P., 2015. High-resolution X-ray computed microtomography: A holistic approach to metamorphic fabric analyses. Geology 43, 55-58. https://doi.org/10.1130/G36250.1

Sayab, M., Shah, S.Z., Aerden, D., 2016. Metamorphic record of the NW Himalayan orogeny between the Indian plate-Kohistan Ladakh Arc and Asia: Revelations from foliation intersection axis (FIA) controlled P-T-t-d paths. Tectonophysics 671, 110-126. https://doi.org/10.1016/j.tecto.2015.12.032

Sayab, M., Aerden, D., Kuva, J., Hassan, W.U., 2021. Tectonic evolution of the Karakoram metamorphic complex (NW Himalayas) reflected in the 3D structures of spiral garnets: Insights from X-ray computed micro-tomography. Geoscience Frontiers 12, 101113. https://doi.org/10.1016/j.gsf.2020.11.010

Seydoux-Guillaume, A.M., Paquette, J.L., Wiedenbeck, M., Montel, J.M., Heinrich, W., 2002. Experimental resetting of the U–Th–Pb systems in monazite. Chemical Geology 191, 165-181. https://doi.org/10.1016/S0009-2541(02)00155-9

Shah, S.Z., Sayab, M., Aerden, D., Asif Khan M., 2011. Foliation intersection axes preserved in garnet porphyroblasts from the Swat area, NW Himalaya: A record of successive crustal shortening directions between the Indian plate and Kohistan-Ladakh Island Arc. Tectonophysics 509, 14-32. https://doi.org/10.1016/j.tecto.2011.05.010

Simancas, J.F., 2018. A reappraisal of the Alpine structure of the Alpujárride Complex in the Betic Cordillera: Interplay of shortening and extension in the westernmost Mediterranean. Journal of Structural Geology 115, 231-242. https://doi.org/10.1016/j.jsg.2018.08.001

Simancas, J.F., Campos, J., 1993. Compresión NNW-SSE tardi a postmetamórfica y extensión subordinada en el Complejo Alpujárride (Dominio de Alborán, Orógeno Bético). Revista de la Sociedad Geológica de España 6, 23-35.

Skrzypek, E., Schulmann, K., Stípská, P., Chopin, F., Lehmann, J., Lexa, O., Haloda, J., 2011. Tectono-metamorphic history recorded in garnet porphyroblasts: insights from thermodynamic modelling and electron backscatter diffraction análisis of inclusion trails. Journal of Metamorphic Geology 29, 473-496. https://doi.org/10.1111/j.1525-1314.2010.00925.x

Sosson, M., Morillon, A.C., Bourgois, J., Féraud, G., Poupeau, G., Saint-Marc, P., 1998. Late exhumation stages of the Alpujarride Complex (western Betic Cordilleras, Spain): new thermochronological and structural data on Los Reales and Ojen nappes. Tectonophysics 285, 253-273. https://doi.org/10.1016/S0040-1951(97)00274-6

Soto, J.I., Platt, J.P., 1999. Petrological and Structural Evolution of High-Grade Metamorphic Rocks from the Floor of the Alboran Sea Basin, Western Mediterranean. Journal of Petrology 40, 21-60. https://doi.org/10.1093/petroj/40.1.21

Spry. A., 1963. Origin and significance of snowball structure in garnet. Journal of Petrology, 4, 211-222. https://doi.org/10.1093/petrology/4.2.211

Tendero, J.A., Martín-Algarra, A., Puga, E., Díaz de Federico, A., 1993. Lithostratigraphie des métasédiments de l'association ophiolitique Nevado-Filabride (SE Espagne) et mise en évidence d'objets ankéritiques évoquant des foraminifères planctoniques du Crétacé : conséquences paléogéographiques. Comptes Rendus de l'Académie des Sciences de Paris 316, 1115-1122.

Tomkins, H.S., Powell, R., Ellis, D.J., 2007. The pressure dependence of the zirconium-in-rutile thermometer. Journal of Metamorphic Geology 25, 703-713. https://doi.org/10.1111/j.1525-1314.2007.00724.x

Tubía, J.M., 1994. The Ronda peridotites (Los Reales nappe): an example of the relationship between lithospheric thickening by oblique tectonics and late extensional deformation within the Betic Cordillera (Spain). Tectonophysics 238, 381-398. https://doi.org/10.1016/0040-1951(94)90065-5

Tubía, J.M., Gil-Ibarguchi, J.I., 1991. Eclogites of the Ojén nappe: a record of subduction in the Alpujárride complex (Betic Cordilleras, southern Spain). Journal of the Geological Society, London 148, 801-804. https://doi.org/10.1144/gsjgs.148.5.0801

Tubía, J.M., Cuevas, J., Navarro-Vilá, F., Álvarez, F., Aldaya, F., 1992. Tectonic evolution of the Alpujárride Complex (Betic Cordillera, southern Spain). Journal of Structural Geology 14 (2), 193-203. https://doi.org/10.1016/0191-8141(92)90056-3

van Achterberg, E., Ryan, C.G., Jackson, S.E., Griffin, W.L., 2001. Data reduction software for LA-ICP-MS: appendix, in: Sylvester, P.J. (Ed.), Laser Ablation-ICP-Mass Spectrometry in the Earth Sciences: Principles and Applications. In: Short Course Ser., Mineral. Assoc. Can., vol.29, Ottawa, Ontario, Canada, pp. 239–243.

Vázquez, M., Jabaloy, A., Barbero, L., Stuart, F.M., 2011. Deciphering tectonic- and erosion-driven exhumation of the Nevado-Filábride Complex (Betic Cordillera, Southern Spain) by

low temperature thermochronology. Terra Nova 23, 257-263. https://doi.org/10.1111/j.1365-3121.2011.01007.x

Whitehouse, M.J., Platt, J.P., 2003. Dating high-grade metamorphism—constraints from rare-earth elements in zircon and garnet. Contrib Mineral Petrol 145, 61-74. https://doi.org/10.1007/s00410-002-0432-z

Williams, J.R., Platt, J.P., 2017. Superposed and refolded metamorphic isograds and superposed directions of shear during late orogenic extension in the Alborán Domain, southern Spain. Tectonics 36, 756-786. https://doi.org/10.1002/2016TC004358

Williams, J.R., Platt, J.P., 2018. A new structural and kinematic framework for the Alborán Domain (Betic-Rif arc, western Mediterranean orogenic system). Journal of the Geological Society 175, 465-496. https://doi.org/10.1144/jgs2017-086

Yeh, M.W., 2007. Deformation sequence of Baltimore gneiss domes, USA, assessed from porphyroblast Foliation Intersection Axes. Journal of Structural Geology 29, 881-897. https://doi.org/10.1016/j.jsg.2006.12.003

Yeh, M.W., Bell, T.H., 2004. Significance of dextral reactivation of an E-W transfer fault in the formation of the Pennsylvania orocline, central Appalachians. Tectonics 23, TC5009. https://doi.org/10.1029/2003TC001593

Zack, T., Moraes, R., Kronz, A., 2004. Temperature dependence of Zr in rutile: empirical calibration of a rutile thermometer. Contrib Mineral Petrol 148, 471-488. https://doi.org/10.1007/s00410-004-0617-8

Zeck, H.P., Williams, I.S., 2001. Hercynian Metamorphism in Nappe Core Complexes of the Alpine Betic-Rif Belt, Western Mediterranean—a SHRIMP Zircon Study. Journal of Petrology 42, 1373-1385. https://doi.org/10.1093/petrology/42.7.1373

Zeck, H.P., Albat, F., Hansen, B.T., Torres-Roldán, R.L., García-Casco, A., Martín-Algarra, A., 1989. A 21 ± 2 Ma age for the termination of the ductile Alpine deformation in the internal zone of the Betic Cordilleras, South Spain. Tectonophysics 169, 215-220. https://doi.org/10.1016/0040-1951(89)90196-0

Zeck, H.P., Monié, P., Villa, I.M., Hansen, B.T., 1992. Very high rates of cooling and uplift in the Alpine belt of the Betic Cordilleras, southern Spain. Geology 20, 79-82. https://doi.org/10.1130/0091-7613(1992)020<0079:VHROCA>2.3.CO;2

Part III

9. Conclusions.

10. Appendix.

9. Conclusions

9.1. Concluding remarks

This Ph.D. Thesis aims to constrain the tectonic evolution of the Betic Cordillera taking into account the information provided by porphyroblast inclusion trails from the metamorphic complexes of the orogen. To achieve this objective, a methodology to routinely measure inclusion trails from XCT scans has been developed and applied in samples from the Nevado-Filábride and Alpujárride complexes. The obtained data has been integrated with structural observations at micro- and outcrop-scale in a regional tectonic framework. The main conclusions obtained from this Ph.D. Thesis are presented below.

Application of XCT for studying inclusion trails

The use of XCT to measure FIAs, inclusion-trail planes or porphyroblast shapes represents a significant step forward in utilizing these structures for reconstructing the tectonic evolution of deformed terranes. The technique allows such data to be collected for individual porphyroblasts, where earlier thin-section based methods could only provide an average FIA at best. Moreover, these earlier FIA methods can be challenging when dealing with samples hosting multiple FIA sets with diverse orientations, or a single FIA set expressed by inclusion trails with opposite asymmetries. Despite its benefits, however, the XCT technique is not a replacement of conventional optical microscopy of thin sections, because of its limited ability to identify and distinguish different mineral phases and limited spatial resolution for reasonable scanning times and workable file sizes.

The XCT technique has been applied to evaluate competing genetic models of sigmoidal- and spiral-shaped inclusion trails in garnet porphyroblasts (snowball garnets) present in two samples from the Variscan Iberian Massif and the Nevado-Filábride Complex (Chapter 4). The 3D data obtained in these rocks for FIA, porphyroblast shapes and shape-orientations, porphyroblast sizes, inclusion-trail curvature senses, and inclusion-trail orientations all favour a 'non-rotational' origin of these microstructures. In particular, the preferred vertical and horizontal orientations displayed by these microstructural elements are as predicted by this model, and refutes significant porphyroblast rotations.

Nevado-Filábride Complex

The internal structure of the Nevado-Filábride Complex (Chapter 5 and 6) is characterized by the existence of two sets of crenulation cleavages. The older set (S_3) dips more steeply as the main (S_2) cleavage, whereas the younger set (S_4) dips more gently to

subhorizontal. Both crenulation cleavages locally transpose the regional main schistosity (S_2). Several regional-scale F_3 folds have been interpreted from vergence switches of small-scale folds and associated changes in the attitude of the main foliation. Several D_4 high-strain zones characterized by intense S_4 and S-C structures have been recognized in the lower part of the Nevado-Filábride Complex, which partially coincide with the contact between the Veleta/Ragua and Mulhacén/Calar Alto units as traced by previous workers. Although this supports the existence of such a contact, its map geometry and precise location still require profound revision, at least in some areas. In some areas (west of Mulhacen peak, for example) the Veleta-Mulhacén / Ragua-Calar Alto contact appears to be parallel to a steeply dipping S_2 instead of S_4 suggesting an origin early syn- to pre-D_2, followed by modification and displacement of the contact by D_4 shear zones.

XCT analysis of several Nevado-Filábride samples, including some from previously little studied areas in the eastern Nevado-Filabride Complex (section 10.2), further confirm the presence of three main FIA sets in the Mulhacén nappe associated with complex (polyphase) inclusion-trails. In the Veleta nappe, however, garnets typically exhibit simple (straight) inclusion trails that according to radiometric ages predate the three FIA sets of the Mulhacén nappe. This new microstructural and geochronological evidence demonstrates that the enigmatic "D_1" event of earlier workers related to the prograde metamorphic path, in fact corresponds to an intricate polyphase deformation history.

Alpujárride Complex

Three regionally consistent FIA sets with similar trends and relative timing as in the Nevado-Filábride (WNW-ESE, ENE-WSW and NNW-SSE in chronological order) have been demonstrated in the Alpujárride Complex (Chapter 7). However, the intermediate ENE-WSW FIA set not only formed before but also after the NNW-SSE set. A strong predominance of gently plunging to subhorizontal FIAs has been found in the complex (see also section 10.3.3), which combined with subvertical and subhorizontal preferred orientations of inclusion trails (see also section 10.3.6) and independent shear-sense indicators provide strong evidence for a 'non-rotational' origin of these microstructures. According to this model, FIAs represent the intersections of steeply and gently dipping foliations formed during alternating stages of crustal shortening and gravitational collapse. Consequently, the three main FIA sets newly discovered in the Alpujárride Complex should reflect a succession of different crustal shortening directions perpendicular to those FIA sets. This prediction has been found to be consistent with the Paleogene-Neogene plate-motion kinematics of Iberia, Africa and the Alborán Domain. A major swing from NNE- to NW-directed Africa-Iberia convergence, known to have occurred during the Oligocene from paleomagnetic data, matches the chronology and orientations of the WNW-ESE and ENE-WSW FIA sets. Moreover, the predominant inclusion-trails asymmetries associated with these sets imply top-to-the-SSW and –SE tectonic transport, or NNE to NW dipping subduction. The younger NNW-SSE FIA is attributable to independent westward displacement of the Alborán Domain, approximately orthogonal to the direction of simultaneous Iberia-Africa convergence.

Garnet FIAs in the Alpujárride Complex correspond to the traditional D_1 and D_2 events of earlier workers. They are post-dated by several sets of crenulation cleavages and shear bands that developed during late metamorphic stages. A subhorizontal S_{3H} crenulation cleavage associated with andalusite and locally sillimanite is well-developed in the western and central Alpujárrides. It is locally overprinted by a younger steeply dipping S_{3V} crenulation cleavage. The latter is particularly strong in the Sierra de la Contraviesa and southern Almuñécar areas. D_{3V} folds and crenulation axes exhibit bimodal N-S and ENE-WSW trends that mimic the trends of the two younger FIA sets, despite having formed much later. These coincident orientations probably reflect a long-lived dynamic interference of NW-SE directed Iberia-Africa convergence and simultaneous westward migration of the Alborán Domain, causing alternations in time and in space of two roughly perpendicular shortening directions. These structures are post-dated by brittle-ductile shear bands and subhorizontal low-angle faults (D_4), which either represent thrusts, low-angle normal faults or a mixture of both.

Timing and conditions of deformation

The conditions and timing of D_2 in the Alpujárride Complex have been estimated as 7-9.5 kbar/600-680 ºC in the period of 21-18.5 Ma (Chapter 8), coinciding with the opening of the Alborán Sea. Geochronological evidence situates the WNW-ESE FIA set well before the D_2 event, whereas the NNW-SSE set developed immediately prior to it or even partially simultaneously. D_{3V} in the Adra nappe is estimated to have taken place at 6 kbar/570-650 ºC around 17.5 Ma, which allows this deformation to be linked to the continental collision between the Internal and External Zones of the Betic Cordillera. Garnet growth during this stage created new ENE-WSW FIAs after the NNW-SSE FIA set that had already formed, with the same trend as the FIA set that immediately preceded the NNW-SSE set.

In the Nevado-Filábride, a maximum age of ~14.5 Ma has been obtained for the ENE-WSW FIA set, which confirms previous geochronological evidence indicating a repetition of this FIA generation (after the NNW-SSE FIA set) also in this complex. The similar FIA sequences of the Nevado-Filábride and Alpujárride complexes imply a broadly similar kinematic evolution. However, the different initial paleogeographic and structural positions of both complexes are reflected in different timings of the main deformations events. Prograde metamorphism (D_{1A}, D_{1B} and D_{1C}) and initial decompression (D_2) of the Alpujárrides took place from Eocene to lower Burdigalian times and was still followed by several late-metamorphic deformation phases (D_{3H}, D_{3V} and D_4) from the middle-upper Burdigalian to Langhian related to exhumation of the complex. These exhumation-related deformations overlap in time with the latest stages of prograde metamorphism (D_1) and initial decompression (D_2) of the Nevado-Filábrides recorded by garnet growth until ~13 Ma, which are post-dated by late-metamorphic structures (D_3 and D_4) of Serravallian to early Tortonian age.

Final remarks

A wealth of new kinematic and metamorphic data from porphyroblasts presented in this Ph.D. Thesis reveal a complex polyphase tectonic evolution of the Betic Cordillera. This confirms the key role played by porphyroblasts in the study of orogenic belts thanks to their remarkable capacity to preserve a succession of different tectonic fabrics with their original orientations. This allows detailed reconstructions of polyphase kinematics predating deformations related to the exhumation of metamorphic rocks, and to link this history to P-T-t paths. The new microstructural approach followed in this thesis exemplified in the Betic Cordillera, offers new perspectives for tectonic reconstructions in other orogenic belts as well.

Forthcoming research

From the results of this Ph.D. Thesis, several issues arise that can be addressed in the future to further constrain the tectonic evolution of the Betic Cordillera:

- Detailed mapping of the Veleta-Mulhacén/Ragua-Calar Alto tectonic contact, focusing on the specific fabrics associated with it is necessary in order to better understand the internal structure of the Nevado-Filábrides.
- The FIA sequence in the Nevado-Filábrides has been primarily determined from samples taken from the Mulhacén nappe due to the scarcity and smaller size of garnets in the Veleta nappe. A significant difference between both nappe units is that garnets in the Veleta nappe usually feature simple inclusion trails, whereas those of the Mulhacén nappe are typically complex with well differentiated core and rim zones. Additionally, it is important to consider a different age of garnets from the Veleta and Mulhacén nappes. Garnets from the Veleta nappe have been dated much older (~35 Ma) than those from the Mulhacén nappe (~20-13 Ma). This raises questions about whether certain FIA sets developed preferentially in one nappe over the other, potentially due to deformation partitioning and strain localization, or due to a distinct metamorphic evolution of both nappes.
- In the Alpujárrides, the Guadaiza, Ojén and Yunquera units located under the Ronda peridotites were preliminary investigated but porphyroblasts with appropriate inclusion trails for FIA determination were not found. To gain insights into the kinematics of peridotite emplacement and exhumation, study of additional porphyroblastic samples is necessary to obtain a representative number of FIAs also in these units. These FIA can then be compared with those of the Los Reales nappe above the peridotites and equivalent Upper Alpujárride rocks (Chapter 7).
- To improve the accuracy of the timing of deformation events in the Alpujárride Complex, additional ages of D_{3V} and D_{3H} should be obtained. This will also provide a test for the temporal relationship between both structural generations that has been interpreted from overprinting relationships. To gain better insight into the timing of early deformation events associated with prograde metamorphism, it is necessary to further constrain the age of pre-D_2 garnets hosting different FIA sets. This can be done by dating monazite inclusions or by directly dating the garnets themselves.

9.2. Conclusiones

El objetivo de esta tesis era constreñir la evolución tectónica de la Cordillera Bética teniendo en cuenta la información proporcionada por las foliaciones internas de porfiroblastos procedentes de los complejos metamórficos del orógeno. Para lograr este objetivo, una metodología para medir de manera rutinaria estas foliaciones internas a partir de escaneos de XCT ha sido desarrollada y aplicada en muestras de los complejos Nevado-Filábride y Alpujárride. Los datos obtenidos se han integrado en el marco tectónico regional con observaciones estructurales a escala de afloramiento y microscópica. Las principales conclusiones de la tesis se presentan a continuación.

Aplicación de XCT para estudiar foliaciones internas de porfiroblastos

El uso de XCT para medir FIAs, planos de foliaciones internas o formas de porfiroblastos representa un significativo paso adelante en la utilización de estas estructuras para reconstruir la evolución tectónica de terrenos deformados. La técnica permite obtener dichos datos de porfiroblastos individuales, mientras que métodos basados en láminas delgadas solo proporcionan un valor medio de FIA. Además, estos métodos previos pueden ser problemáticos al tratar con muestras con múltiples sets de FIA con diferentes orientaciones, o un solo set definido por inclusiones con asimetrías opuestas. A pesar de sus beneficios, la técnica XCT no reemplaza la microscopía óptica de láminas delgadas, debido a su limitada capacidad de diferenciar fases minerales y su limitada resolución espacial para tiempos de escaneo y tamaños de archivo razonables.

La técnica XCT se ha aplicado para evaluar modelos genéticos de foliaciones internas sigmoidales y en espiral en porfiroblastos de granate (granates en bola de nieve) presentes en dos muestras procedentes del Macizo Ibérico Varisco y el Complejo Nevado-Filábride (Capítulo 4). Los datos 3D obtenidos en estas rocas de FIA, formas de porfiroblastos y orientación de la forma, tamaño de porfiroblastos, sentido de curvatura de foliaciones internas, y orientaciones de foliaciones internas, favorecen un origen no-rotacional de estas microestructuras. En particular, las orientaciones preferentes verticales y horizontales mostradas por estos elementos microestructurales son como las predichas por este modelo, y refutan rotaciones significativas de porfiroblastos.

Complejo Nevado-Filábride

La estructura interna del Complejo Nevado-Filábride (Capítulos 5 y 6) se caracteriza por la existencia de dos sets de clivajes de crenulación. El set más antiguo (S_3) presenta mayor buzamiento que el clivaje principal (S_2), mientras que el set más joven (S_4) es subhorizontal. Ambos clivajes de crenulación transponen localmente la esquistosidad principal regional (S_2). Varios pliegues F_3 de escala regional han sido interpretados a partir de cambios de vergencia de pligues de pequeña escala, asociados a cambios en la orientación de la foliación principal. Varias zonas de alta deformación D_4 caracterizadas por una intensa S_4 y estructuras S-C han sido reconocidas en la parte baja del Complejo Nevado-Filábride, y coinciden parcialmente con el contacto entre las unidades

Veleta/Ragua y Mulhacén/Calar Alto propuesto por autores previos. Aunque esto apoya la existencia de tal contacto, su geometría y localización requieren ser revisadas, al menos en algunas zonas. En algunas áreas (al oeste del pico Mulhacén, por ejemplo) el contacto Veleta-Mulhacén / Ragua-Calar Alto parece ser paralelo a una S_2 con fuerte buzamiento en lugar de a S_4, lo que sugiere un origen del contacto previo a, o durante D_2, posteriormente modificado y desplazado por zonas de cizalla asociadas a D_4.

El análisis mediante XCT de varias muestras Nevado-Filábrides, incluyendo algunas de áreas poco estudiadas en la parte este del complejo (sección 10.2), confirma la presencia de tres principales sets de FIAs en el manto del Mulhacén asociados con foliaciones internas complejas (polifásicas). En el manto del Veleta, los granates típicamente muestran foliaciones internas simples (rectas) que de acuerdo con las edades radiométricas preceden los tres sets de FIA del manto del Mulhacén. Esta evidencia microestructural y geocronológica demuestra que el enigmático evento "D_1" de autores previos relacionado con el metamorfismo prograd, se corresponde con una intrincada historia de deformación polifásica.

Complejo Alpujárride

Tres sets de FIA consistentes a escala regional con direcciones y relaciones temporales similares a las del Nevado-Filábride (WNW-ESE, ENE-WSW y NNW-SSE en orden cronológico) han sido obtenidos en el Complejo Alpujárride (Capítulo 7). Sin embardo, el set intermedio ENE-WSW no solo se formó antes sino también después del NNW-SSE. Se ha encontrado una fuerte predominancia de FIAs subhorizontales en el complejo (ver también sección 10.3.3), lo que combinado con las orientaciones preferentes subverticales y subhorizontales de foliaciones internas (ver también sección 10.3.6), e indicadores independientes de sentido de cizalla, evidencian un origen no-rotacional de estas microestructuras. Según este modelo, los FIA representan intersecciones de foliaciones con altos y bajos valores de buzamiento, formadas durante etapas alternantes de acortamiento cortical y colapso gravitacional. Así, los tres sets de FIA del Complejo Alpujárride deberían reflejar una sucesión de diferentes direcciones de acortamiento, perpendiculares a dichos sets. Esta predicción es consistente con los movimientos de placas de Iberia, África y el Dominio de Alborán durante el Paleógeno-Neógeno. Un giro mayor de NNE a NW en la dirección de convergencia entre África e Iberia, establecido durante el Oligoceno a partir de datos paleomagnéticos, coincide con la cronología y orientación de los sets WNW-ESE y ENE-WSW. Además, las asimetrías predominantes asociadas con estos sets implican transporte tectónico de techo hacia SSW y SE, o una subducción que buza hacia NNE y NW. El set NNW-SSE se atribuye al desplazamiento independiente hacia el W del Dominio de Alborán, aproximadamente perpendicular a la dirección de la convergencia simultánea entre África e Iberia.

Los FIAs de granates en el Complejo Alpujárride corresponden a los eventos D_1 y D_2 de autores previos. Varios sets de clivajes de crenulación y bandas de cizalla se desarrollaron con posterioridad a ellos durante las etapas tardimetamórficas. Un clivaje de crenulación subhorizontal S_{3H} asociado con andalucita y localmente sillimanita está bien

desarrollado en los Alpujárrides occidentales y centrales. Es localmente cortado por un clivaje de crenulación S_{3V} muy inclinado más joven. Este último se desarrolla con intensidad en la Sierra de la Contraviesa y la parte sur de la zona de Almuñécar. Los pliegues y ejes de crenulación D_{3V} muestran direcciones bimodales N-S y ENE-WSW, que coinciden con las direcciones de los dos sets de FIA más jóvenes, a pesar de haberse formado más tarde. Estas orientaciones similares probablemente reflejan una interferencia entre la convergencia NW-SE de Iberia y África y la simultánea migración hacia el oeste del Dominio de Alborán, causando alternancias en el tiempo y el espacio de dos direcciones de acortamiento aproximadamente perpendiculares. Estas estructuras son cortadas por bandas de cizalla de carácter dúctil-frágil y fallas de bajo ángulo (D_4) que podrían ser cabalgamientos, fallas normales de bajo ángulo o una mezcla de ambos.

Edad y condiciones de la deformación

Las condiciones y la edad de D_2 en el Complejo Alpujárride han sido estimadas en 7-9.5 kbar/600-680 ºC en el periodo de 21-18.5 Ma (Capítulo 8), coincidiendo con la apertura del Mar de Alborán. Evidencias geocronológicas sitúan el FIA WNW-ESE mucho antes del evento D_2, mientras que el set NNW-SSE se desarrolló inmediatamente antes o parcialmente simultáneo a este. Las condiciones de D_{3V} en el manto de Adra se estiman en 6 kbar/570-650 ºC en torno a 17.5 Ma, lo que permite vincularlo a la colisión continental entre las Zonas Internas y Externas de la Cordillera Bética. El crecimiento de granate durante esta etapa generó nuevos FIAs ENE-WSW, más jóvenes que el set NNW-SSE, pero con la misma dirección que el set que precede al set NNW-SSE.

En el Nevado-Filábride, una edad máxima de ~14.5 Ma ha sido obtenida para el set ENE-WSW, lo que confirma evidencias geocronológicas previas que indicaban la repetición de este FIA (después del NNW-SSE) también en este complejo. La similitud en las secuencias de FIA del Nevado-Filábride y Alpujárride implican una evolución cinemática similar en líneas generales. Sin embargo, las diferentes posiciones paleogeográficas y estructurales de ambos complejos se ven reflejadas en la diferente edad de los principales eventos de deformación. El metamorfismo prograd (D_{1A}, D_{1B} and D_{1C}) y descompresión inicial (D_2) en el Alpujárride tuvo lugar desde el Eoceno al Burdigaliense inferior, seguido por varias fases de deformación tardimetamórficas (D_{3H}, D_{3V} and D_4) asociadas a la exhumación del complejo en el Burdigaliense medio-superior y Langhiense. Estas deformaciones asociadas a la exhumación se solapan en el tiempo con las últimas etapas de metamorfismo prograd (D_1) y descompresión inicial (D_2) del Nevado-Filábride tal y como indican las edades de crecimiento de granate hasta ~13 Ma. Estructuras tardimetamórficas se desarrollan con posterioridad durante el Serravalliense y Tortoniese inferior.

Comentarios finales

La gran cantidad de nuevos datos cinemáticos y metamórficos obtenidos a partir de porfiroblastos presentados en esta tesis revelan una compleja evolución tectónica polifásica en la Cordillera Bética. Esto confirma el rol clave que juegan los porfiroblastos

en el estudio de cinturones orogénicos gracias a su notable capacidad de preservar una sucesión de diferentes fábricas tectónicas con sus orientaciones originales. Esto permite realizar reconstrucciones detalladas de cinemáticas polifásicas que preceden a deformaciones asociadas con la exhumación de rocas metamórficas, y unir esta historia a trayectorias P-T-t. El nuevo enfoque microestructural seguido en esta tesis, ejemplificado en la Cordillera Bética, ofrece nuevas perspectivas para reconstrucciones tectónicas en otros cinturones orogénicos.

Perspectivas futuras

De los resultados de esta tesis, surgen varias cuestiones que pueden ser abordadas en el futuro para seguir avanzando en el conocimiento de la evolución tectónica de la Cordillera Bética:

- Mejorar la cartografía del contacto Veleta-Mulhacén/Ragua-Calar Alto, haciendo énfasis en las fábricas específicas asociadas con él, es necesario para entender mejor la estructura interna del Complejo Nevado-Filábride.
- La secuencia de FIAs en el Nevado-Filábride ha sido principalmente determinada a partir de muestras del manto del Mulhacén debido a la escasez y pequeño tamaño de granates en el manto del Veleta. Una diferencia significativa entre ambos mantos es que los granates del manto del Veleta normalmente tienen foliaciones internas simples, mientras que en el manto del Mulhacén suelen ser complejas con zonas de núcleo y borde bien diferenciadas. Además, es importante considerar la diferente edad de los granates del Veleta y del Mulhacén. Los granates del manto del Veleta han sido datados como más antiguos (~35 Ma) que los del manto del Mulhacén (~20-13 Ma). De aquí surge la cuestión sobre si ciertos sets de FIA se han desarrollado preferentemente en un manto respecto al otro, potencialmente debido a la partición y localización de la deformación, o a consecuencia de una diferente evolución metamórfica de ambos mantos.
- En el Alpujárride, las unidades de Guadaiza, Ojén y Yunquera, localizadas bajo las peridotitas de Ronda, fueron preliminarmente investigadas pero no se encontraron porfiroblastos con foliaciones internas apropiadas para determinar FIAs. El estudio de muestras adicionales para obtener un número representativo de FIAs en estas unidades podría dar información acerca de la cinemática asociada al emplazamiento y exhumación de las peridotitas, al poder comparar esos FIAs con los ya determinados en el manto de Los Reales y Alpujárrides Superiores equivalentes (Capítulo 7).
- Para mejorar la precisión de las edades de los eventos de deformación en el Complejo Alpujárride, habría que obtener edades adicionales de D_{3V} y D_{3H}. Esto también proporcionaría un test acerca de la relación temporal entre ambas generaciones de estructuras interpretada a partir de relaciones de corte. Para mejorar las edades de deformación asociadas con el metamorfismo prograd, es necesario constreñir las edades de granates pre-D_2 que incluyan diferentes sets de FIA. Esto puede ser realizado mediante datación de inclusiones de monacita en los granates, o datando los propios granates directamente.

10. Appendix

10.1. Supplementary Material of Chapter 4

Tables listing the data that are plotted in the various stereograms and rose diagrams in this paper.

V	Volume of best-fit ellipsoid
d	Diametre of a sphere with same volume as best-fit ellipsoid
tr	trend
pl	plunge
L	length
X	long axes best-fit ellipsoid
Y	intermediate axes best-fit ellipsoid
Z	short axes best-fit ellipsoid
FIA	Foliation-Intersection Axis
FIA set	FIA set of Ruiz Fuentes & Aerden (2018) assigned to
Asym.	Clockwise (C) or anticlockwise (A) followed by viewing direction

sample 49.10															
	V (mm3)	d (mm)	X			Y			Z			FIA		Asym.	
			tr	pl	L(mm)	tr	pl	L(mm)	tr	pl	L(mm)	tr	pl		
1	0,5	1,0	349	64	1,25	192	24	1,05	98	9	0,76	90	15	A	E
2	0,6	1,1	106	25	1,29	309	63	1,04	200	9	0,91	60	30	A	NE
3	0,8	1,1	356	7	1,28	257	53	1,09	91	37	1,05	45	20	A	NE
4	2,0	1,6	328	21	2,36	193	62	1,32	65	18	1,23	45	25	A	NE
5	2,1	1,6	161	33	1,93	293	46	1,56	53	25	1,36	55	25	A	NE
6	4,1	2,0	159	30	2,99	26	50	1,96	264	24	1,35	65	25	A	NE
7	2,5	1,7	354	9	2,36	92	44	1,57	255	45	1,28	290	30	A	NE
8	3,2	1,8	332	3	2,10	63	6	1,97	220	83	1,49	235	22	A	NE
9	2,5	1,7	143	15	2,12	344	74	1,83	234	6	1,23	10	5	A	NE
10	3,0	1,8	168	32	2,32	5	57	1,86	263	8	1,32	77	10	A	NE
11	6,7	2,3	158	21	3,44	271	45	2,11	52	37	1,77	90	15	A	E
12	5,7	2,2	156	34	2,81	36	37	2,40	274	35	1,63	70	35	A	NE
13	5,3	2,2	210	68	2,72	27	22	2,20	117	1	1,69	42	12	A	NE
14	7,2	2,4	157	22	3,15	65	6	2,40	321	67	1,81	230	10	A	NE
15	5,3	2,2	140	42	2,67	246	17	2,06	352	43	1,85	55	15	A	NE
16	7,4	2,4	279	88	3,07	168	1	2,30	78	2	2,00	72	27	A	NE
17	8,3	2,5	152	13	4,05	261	55	2,35	54	32	1,67	245	40	A	NE
18	7,1	2,4	149	38	3,25	324	52	2,24	57	3	1,86	240	0	A	NE
19	7,7	2,4	171	50	3,25	75	5	2,26	341	39	2,00	267	0	A	NE
20	7,7	2,4	216	31	2,90	63	56	2,41	313	13	2,09	52	50	A	NE
21	8,2	2,5	270	52	3,09	179	1	2,37	89	38	2,13	35	32	A	NE
22	7,9	2,5	2	66	3,33	134	17	2,23	229	17	2,05	40	3	A	NE
23	8,0	2,5	135	15	2,98	40	17	2,65	265	67	1,93	192	5	A	NE
24	9,5	2,6	127	58	3,38	242	15	2,44	340	28	2,19	242	7	A	NE
25	10,7	2,7	161	24	4,18	325	65	2,47	68	6	1,98	260	5	A	NE
26	11,8	2,8	204	85	3,47	45	5	2,92	315	2	2,22	55	18	A	NE
27	15,0	3,1	187	62	3,84	89	5	2,90	356	28	2,56	80	17	A	NE
28	11,4	2,8	332	74	3,34	203	11	2,85	111	13	2,29	193	0	A	NE
29	13,8	3,0	267	45	3,35	2	4	3,00	96	45	2,62	57	30	A	NE
30	12,3	2,9	130	52	3,71	334	36	2,73	235	11	2,32	258	12	A	NE
31	17,1	3,2	154	11	4,49	55	38	3,18	257	50	2,29	65	30	A	NE
32	18,2	3,3	165	20	4,53	64	26	3,06	287	56	2,51	270	6	A	E
33	19,6	3,3	202	68	4,14	355	20	3,06	88	9	2,95	80	18	A	NE
34	21,0	3,4	284	69	4,03	47	12	3,44	141	17	2,89	48	6	A	NE
35	23,6	3,6	306	73	4,95	108	16	3,11	199	5	2,93	77	22	A	NE
36	27,0	3,7	252	86	4,71	35	4	3,56	125	3	3,08	50	13	A	NE
37	27,1	3,7	149	65	5,23	44	7	3,41	311	24	2,90	240	3	A	NE
38a	23,8	3,6	282	73	4,47	19	2	3,54	110	17	2,88	20	5	A	NE
38b	9,8	2,7	293	73	3,53	128	17	2,42	37	4	2,19	35	14	A	NE
39	35,2	4,1	222	84	4,99	336	2	3,69	66	5	3,65	55	10	A	NE

sample 46.8																
	V (mm3)	d (mm)	X			Y			Z			FIA		Asym		FIA set
			tr	pl	L	tr	pl	L	tr	pl	L	tr	pl			
1	18,4	3,3	63	61	5,23	277	24	3,06	180	14	2,20	115	15	A		2
2	4,8	2,1	43	56	2,37	140	5	2,09	234	34	1,85					
3	4,3	2,0	280	9	2,18	188	11	2,01	49	76	1,88	35	27	C	NE	5
4	4,2	2,0	103	2	2,24	10	54	2,00	194	36	1,80	170	35	A	SE	4
5	4,8	2,1	92	24	2,19	306	62	2,14	188	14	1,94					
6	4,3	2,0	163	49	2,26	35	28	2,01	289	27	1,80	295	40	A	SE	2
7	9,3	2,6	117	4	3,85	213	55	2,60	24	34	1,77					
8	6,5	2,3	299	31	3,15	71	48	2,31	193	25	1,70					
9	4,1	2,0	290	16	2,19	49	59	2,09	192	26	1,72	140	0	A	SE	2
10	4,7	2,1	155	22	2,27	305	65	2,01	60	11	1,97	210	35	A	NE	5
11	8,4	2,5	38	45	3,73	206	45	2,63	302	6	1,64					
12	15,9	3,1	292	24	5,04	42	38	3,14	178	42	1,92	295	35	A	SE	2
13	6,8	2,4	327	19	4,24	61	11	2,14	181	68	1,44					
14	4,6	2,1	107	2	2,39	16	4	2,02	224	85	1,81					
15	4,8	2,1	320	67	2,44	200	12	2,07	105	19	1,82					
16	9,1	2,6	30	17	3,87	295	13	2,47	170	68	1,83	290	10	A	SE	2
17	5,1	2,1	301	27	2,53	48	30	2,10	178	48	1,82	40	35	C	NE	5
18	7,0	2,4	58	77	4,44	287	9	1,81	195	10	1,68	70	55	A	NE	3
19	26,6	3,7	55	43	5,73	320	5	3,32	225	46	2,67	260	37	A	NE	3
20	21,7	3,5	71	11	5,32	310	70	2,83	164	17	2,76	300	17	A	SE	2
21	5,2	2,1	3	40	2,30	105	14	2,18	211	46	1,96	165	40	C	SE	4
22	26,3	3,7	61	39	6,07	158	8	3,42	258	50	2,42	285	30	A	SE	2
23	6,3	2,3	5	54	2,56	129	22	2,39	231	27	1,96	192	45	C	NE	5
24	8,9	2,6	211	26	4,83	116	11	2,59	5	61	1,36					
25	16,6	3,2	74	9	4,88	335	43	3,72	174	45	1,75					
26	5,9	2,2	83	40	2,71	183	12	2,17	286	48	1,91	165	17	C	SE	4
27	6,0	2,3	257	15	2,49	349	7	2,30	103	74	2,00	100	47	C	SE	3
29	7,5	2,4	288	9	3,07	96	81	2,31	198	2	2,03	275	10	A	SE	3
30	9,3	2,6	69	4	4,68	160	21	2,21	328	69	1,72					
31	20,0	3,4	76	32	5,57	330	24	2,67	210	48	2,57	298	17	A	SE	2
32	33,7	4,0	80	11	5,66	172	10	3,66	304	75	3,11	295	30	A	SE	2
33	12,8	2,9	284	22	3,81	125	67	2,85	17	7	2,26	300	25	A	SE	2
34	14,9	3,1	295	46	4,76	198	7	2,59	101	44	2,32					
35	12,5	2,9	314	60	6,30	63	11	4,78	159	28	0,79					
36	8,2	2,5	2	40	2,84	167	49	2,44	265	7	2,26	220	40	C	NE	5
37	9,4	2,6	220	15	2,82	345	65	2,60	124	20	2,45					
38	19,6	3,3	84	3	4,99	354	4	3,46	211	85	2,17	295	32	A	SE	2
39	23,4	3,5	181	50	5,06	290	15	3,64	32	36	2,42	275	12	A	SE	3
40	15,8	3,1	57	35	3,99	291	40	2,89	172	30	2,63	290	50	A	SE	2
41	9,2	2,6	264	40	2,94	106	48	2,59	4	11	2,30	323	5	A	SE	2
42	8,0	2,5	345	63	2,60	85	5	2,51	177	27	2,33	175	10	C	SE	4
43	9,2	2,6	354	9	2,98	86	15	2,45	234	72	2,40	265	30	A	NE	3
44	42,8	4,3	66	39	7,78	293	40	5,70	179	26	1,84	348	60	A	SE	4
45	14,4	3,0	283	3	4,39	18	55	3,19	191	35	1,96	295	15	A	SE	2
46	33,7	4,0	277	31	6,07	58	53	3,71	175	19	2,86	265	20	A	NE	3
47	14,4	3,0	253	18	3,36	345	8	3,13	100	70	2,61	352	5	C	SE	4
48	13,3	2,9	112	21	3,41	7	34	3,31	228	49	2,26					
49	31,8	3,9	200	51	7,01	100	7	3,52	5	38	2,46	283	10	A	SE	2
50	79,2	5,3	215	39	8,29	113	14	4,74	7	48	3,85	85	20	A	NE	3
51	28,0	3,8	297	20	6,41	38	27	4,29	175	55	1,95					
52	36,3	4,1	89	7	9,16	197	68	3,11	356	21	2,43	90	5	A	E	3
53	42,4	4,3	282	21	5,72	33	44	5,09	174	38	2,78	280	10	A	SE	3
54	34,5	4,0	78	8	6,17	324	72	4,30	170	17	2,48					
55	44,0	4,4	295	26	6,61	203	4	4,74	105	64	2,68					
56	39,6	4,2	285	40	6,34	57	39	4,76	170	26	2,50					
57	73,1	5,2	100	11	6,56	9	8	5,13	243	77	4,15	315	20	A	SE	2
58	21,9	3,5	243	45	3,94	43	43	3,58	143	10	2,96					

59	35,3	4,1	158	46	4,78	251	3	4,41	344	44	3,20	58	7	A	NE	5
60	61,8	4,9	171	4	5,56	80	4	5,16	301	84	4,12	235	30	A	NE	5
61	63,7	5,0	18	40	6,67	111	4	5,00	205	50	3,65	235	35	A	NE	5
62	166,3	6,8	248	14	9,59	349	38	6,36	142	49	5,21	250	15	A	NE	3
63	49,2	4,5	19	11	5,55	111	8	4,67	234	76	3,63	260	15	A	NE	3
64	80,7	5,4	74	12	6,32	333	41	5,27	178	46	4,62	73	10	A	NE	3
65	79,7	5,3	196	5	6,43	91	70	5,60	288	19	4,23	263	30	A	NE	3
66	62,4	4,9	90	7	8,79	299	82	3,81	181	4	3,56					
67	66,7	5,0	335	14	7,43	70	20	4,61	212	65	3,72	225	12	A	NE	5
68	63,2	4,9	31	11	5,98	124	12	4,98	260	73	4,05	285	17	A	SE	2
69	66,7	5,0	153	4	6,05	63	1	5,08	325	86	4,15	307	20	A	SE	2
70	149,6	6,6	77	26	9,59	267	64	5,84	169	4	5,10	72	16	A	NE	3
71	186,4	7,1	79	35	11,04	263	55	6,47	170	2	4,98	95	0	A	NE	3
72	116,0	6,1	33	47	6,67	142	17	6,17	246	38	5,38	245	7	A	NE	5
73	97,0	5,7	105	11	7,23	14	5	5,94	258	78	4,31	245	10	A	NE	5
74	139,6	6,4	337	49	8,74	107	29	6,09	213	26	5,01	250	3	A	NE	3
76	184,4	7,1	76	22	10,30	314	52	9,71	179	29	3,52					
77	235,6	7,7	255	81	9,72	82	9	7,34	351	1	6,30	270	2	A	E	3
78	427,5	9,3	263	5	12,48	168	39	8,39	359	50	7,79	260	8	A	NE	3
79	48,9	4,5	88	7	6,82	352	37	4,36	187	52	3,14	265	25	A	NE	3
79	48,9	4,5	88	7	6,82	352	37	3,73	187	52	3,14	165	25	A	SE	4
80		13,8	not measured									60	0	A	NE	5
81		7,6	not measured									270	5	A	E	3
82		9,6	not measured									270	10	A	E	3
83		2,8	not measured									110	65	C	SE	2
84		4,4	not measured									110	0	A	SE	2
85		2,0	not measured									137	10	C	SE	2
86		2,0	not measured									2	60	C	S	4
87		1,9	not measured									137	30	A	SE	2
88		1,9	not measured									287	45	A	E	2

10.2. Additional inclusion-trail data from 7 samples of the Nevado-Filábride Complex

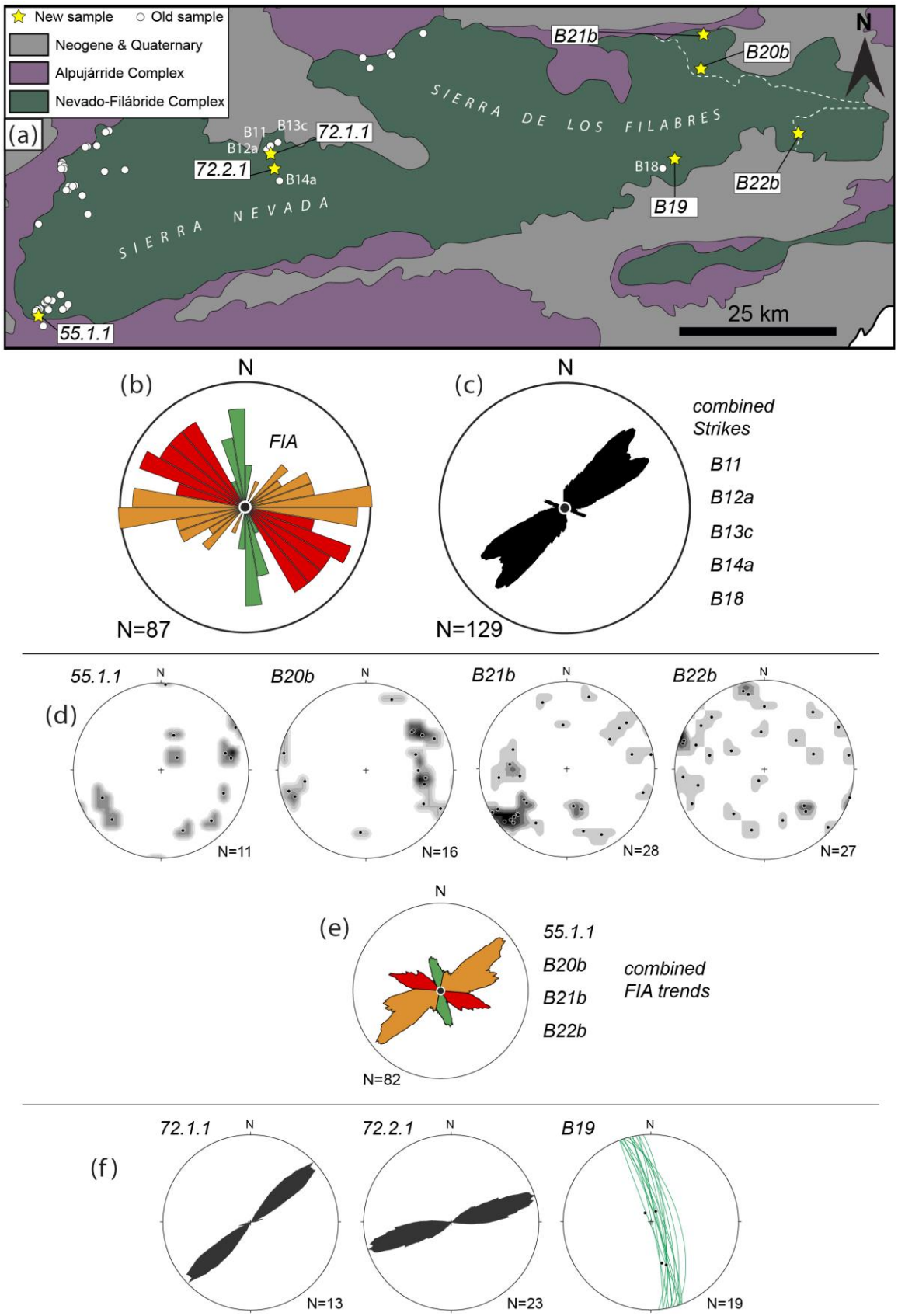

Fig. 10.2.1 (previous page). (a) Map of the Nevado-Filábride Complex showing the location of newly analysed samples (yellow stars). (b) Rose diagram of Aerden et al. (2022) for average FIA trends in 67 samples whose locations are shown as white dots in the map. The three FIA sets of these authors are given different colours. (c) Moving-average rose diagram for the strike of straight inclusion trails measured in 5 samples of graphitic schist by Aerden et al. (2013). (d) Extra FIAs measured in four newly studied samples (yellow star locations). (e) Moving-average rose diagram for all new FIAs combined. The modal maxima match those of the rose diagram in (a). Therefore, the new data support the distinction of Aerden et al's (2022) three FIA sets. (f) New inclusion-trail strikes measured in two samples of the Veleta/Ragua-unit (72.1.1 and 72.2.1), and one sample (B19) of the Montenegro Fm. (lower part of the Calar-Alto unit). The data of the Veleta/Ragua samples match inclusion-trail strikes measured previously in 5 similar rocks plotted in (c). Inclusion trails planes in samples B19 were measured in 3D using XCT. They are vertical with NNW-SSE strike and can be tentatively linked to the NNW-SSE FIA set coloured green in (b).

Three main FIA sets with specific orientations (WNW-ESE, ENE-WSW and NNW-SSE; Fig. 10.2.1a) have been distinguished in the Nevado-Filábride Complex through the works of Aerden et al. (2013, 2022), Ruiz-Fuentes and Aerden (2018) and Aerden and Ruiz-Fuentes (2020). Based on microstructural relative-timing criteria and limited Sm-Nd garnet ages (4 samples) the chronological order of these FIA sets was interpreted as: (1) WNW-ESE, (2) ENE-WNW, (3) NNW-SSE, followed by a repetition of the younger two FIA sets, that is, (4) ENE-WNW, and (5) NNW-SSE.

These findings have been strengthened by the identification of three similar FIA sets in the Alpujárride Complex (Ruiz-Fuentes and Aerden, 2023) and equivalent rocks of the Sebtide in North Morocco (Aerden et al., 2022). Relative-timing criteria and Sm-Nd garnet ages in these complexes are consistent with the FIA sequence deduced earlier in the Nevado-Filábride Complex, but initially no evidence was found for a repetition of FIA trends. This was not surprising considering that garnet growth in the Nevado-Filábride lasted several million years longer until ca. 13 Ma. However, the new U-Th-Pb monazite ages and Ar-Ar mica ages for 4 Alpujárride samples reported in Chapter 8 demonstrate a late repetition of the ENE-WNW trending FIA set in the Alpujárride Complex around 17.5 Ma (see Chapter 8), after the NNW-SSE FIA set had formed.

The oldest FIA set (WNW-ESE) in all three complexes is thought to have developed around 35 Ma (Aerden et al., 2022) in rocks that already contained a pre-existing cleavage of early-Alpine or Variscan age. This primitive foliation is preserved in the deeper levels of the Veleta/Ragua unit as simple inclusion trails within small garnets and consistently strikes NE-SW in different samples (Fig. 10.2.1c). Aerden et al. (2013) and Ruiz-Fuentes and Aerden (2018) originally inferred a relationship with a few NNE-SSW trending FIA determined with the FitPitch program (Aerden, 2003). However, further study of the corresponding samples with XCT by Aerden et al. (2022) showed that the FitPitch FIAs were not accurate and no further evidence was found for an extra FIA set predating the WNW-ESE set.

I have collected additional inclusion-trail data from 7 Nevado-Filábride samples which are presented in this Appendix section and briefly discussed. The newly studied samples

are mostly from the eastern Sierra de los Filabres since the large majority of published FIA data come from the western and central Nevado-Filábride.

South-western Sierra Nevada:

Sample 55.1.1 is from south-western Sierra Nevada located at the Mulhacén/Calar Alto unit, very near the contact with the overlying Alpujárride Complex. It contains 1.5-3 mm sized garnets with mainly sigmoidal inclusion trails. Garnet FIAs in this sample have variable plunges and do not have well-defined orientation maxima, although a broad preference for trends of about N065/N245 can be noticed. Asymmetries of FIAs around this trend indicate both top-to-the-NNW and –SSE senses of shear.

Eastern Sierra Nevada (Puerto de la Ragua):

Samples 72.1.1 and 72.2.1 from the Veleta/Ragua unit contain garnets of around 1 mm and sub-mm in size which contain relatively straight inclusion trails. Strikes of inclusion trails in these samples are similar (NE-SW) as reported by Aerden et al. (2013) for other samples from this unit.

Eastern Sierra de los Filabres:

Sample B19 is located in the Montenegro Fm. of the Calar Alto unit. Garnets in sample B19 have around 1 mm of diameter and mainly have straight inclusion trails that are systematically oriented vertical with NNW-SSE strike. Only four garnets were found with subvertical FIAs.

Sample B20b is located in the Bédar-Macael unit. It contains garnets of variable size from 1 cm to 1 mm with mainly sigmoidal but also spiral inclusion trails. It has gently plunging FIAs with two distinct WNW-ESE and ENE-WSW trend maxima. Local shear senses deduced from asymmetry of inclusion trails indicate top-to-the-SSW for the WNW-ESE FIAs, and top-to-the-SSE for the ENE-WSW FIAs, considering porphyroblast non-rotation.

Sample B21b is also located in the Bédar-Macael unit. The sample hosts garnets of variable size from around 3 mm to sub-mm, which contain mainly spiral but also sigmoidal inclusion trails. It contains the same two groups of FIA as sample B20b and an additional NNW-SSE-trending group. Local shear senses considering porphyroblast non-rotation indicate top-to-the-SSW and –NNE for the WNW-ESE set, top-to-the-NNW for the ENE-WSW set, and both shear senses (top-to-the-WSW and- ENE) for the NNW-SSE set.

Sample B22b is located at the base of the Bédar-Macael unit, only a few meters away from the limit with the underlying Calar Alto unit. It contains sub-mm to 3 mm sized garnets with well-developed sigmoidal and spiral inclusion trails. FIAs in sample B22b are greatly dispersed, similar as described for sample 55.1.1. Some clustering can, nevertheless, be noticed around N290. A significant proportion of FIAs are subvertical or steeply plunging.

In summary, the new data generally support the existence of three main FIA sets all across the ca. 100km long Nevado-Filábride tectonic window. However, FIAs measured in two samples (55.1.1 and B22b) show an unusually large scatter that might reflect differential porphyroblast rotations. It is noteworthy in this respect, that both samples are located very close to major tectonic contacts between the Calar-Alto and Bédar-Macael unit (white stipple line in the map of Fig. 10.2.1a) and the contact with the Alpujárride Complex.

References

Aerden, D., 2003. Preferred orientation of planar microstructures determined via statistical best-fit of measured intersection-lines: the 'FitPitch' computer program. Journal of Structural Geology 25, 923-934. https://doi.org/10.1016/S0191-8141(02)00119-0

Aerden, D.G.A.M., Ruiz-Fuentes, A., 2020. X-ray computed micro-tomography of spiral garnets: A new test of how they form. Journal of Structural Geology 136, 104054. https://doi.org/10.1016/j.jsg.2020.104054

Aerden, D.G.A.M., Bell, T.H., Puga, E., Sayab, M., Lozano, J.A., Díaz de Federico, A., 2013. Multi-stage mountain building vs. relative plate motions in the Betic Cordillera deduced from integrated microstructural and petrological analysis of porphyroblast inclusion trails. Tectonophysics 587, 188-206. https://doi.org/10.1016/j.tecto.2012.11.025

Aerden, D.G.A.M., Farrell, T.P., Baxter, E.F., Stewart, E.M., Ruiz-Fuentes, A., Bouybaouene, M., 2022. Refined tectonic evolution of the Betic-Rif orogen through integrated 3-D microstructural analysis and Sm-Nd dating of garnet porphyroblasts. Tectonics 41, e2022TC007366. https://doi.org/10.1029/2022TC007366

Ruiz-Fuentes, A., Aerden, D.G.A.M., 2018. Transposition of foliations and superposition of lineations during polyphase deformation in the Nevado-Filabride complex: tectonic implications. Int. J. Earth Sci. 107, 1975–1988. https://doi.org/10.1007/s00531-017-1582-6

Ruiz-Fuentes, A., Aerden, D.G.A.M., 2023. Deciphering western Mediterranean kinematics using metamorphic porphyroblasts from the Alpujárride Complex (Betic Cordillera). Journal of Structural Geology 168, 104823. https://doi.org/10.1016/j.jsg.2023.104823

10.3. Supplementary Material of Chapter 7

10.3.1. Measuring FIAs and crenulation axes with X-ray Computed Tomography

X-ray computed tomography (XCT) scanning was performed at the University of Granada with an Xradia 510 (Versa Zeiss) microtomographer at resolutions of 4.35-20.27 μm, using 140kV voltage and 1201-3201 projections. Thin-section sized blocks typically measuring 5 x 3 x 2 cm were scanned after sticking a metallic orientation arrow on them to facilitate reorientation of the generated image stack. Image stacks were processed and studied with the Fiji distribution (Schindelin et al., 2012) of the software ImageJ (Schneider et al., 2012). If needed, XCT scans were re-oriented in such a way that the X, Y and Z reference axes of the image stack coincide with geographic coordinate axes. From there, the following workflow was followed to measure FIAs:

- Segmentation of high X-ray attenuation particles (which includes garnets) using the Threshold tool.
- Segmentation by size in order to eliminate small particles with similar X-ray attenuation values as garnet. This is achieved using the 3D Simple Segmentation tool included in the 3D plugin suite (Ollion et al., 2013) of Fiji.
- Obtaining the coordinates of garnet centers using the Particle Analyser tool of the BoneJ plugin suite (Doube et al., 2010).
- FIAs were measured using the Volume Viewer tool, which allows viewing slices of any orientation through garnets. The procedure is analogous to the radial thinsectioning technique of Hayward (1990) and Bell et al. (1995). First, a vertical slice is rotated around a vertical axis to constrain the FIA trend based on a flip in inclusion-trail curvature asymmetry between slices striking on both sides of the FIA. Then the FIA plunge is determined by rotating an initially horizontal slice around a horizontal axis lying normal to the previously deduced FIA trend. In rare cases of samples containing steeply plunging FIAs, a slightly different approach was taken consisting of rotating a slice twice about two perpendicular horizontal axes. The FIA then corresponds to the intersection of two steeply dipping planes identified by asymmetry flips.
- Fold axes visible in XCT scans marked by layers with contrasting X-ray attenuation values were measured by recording the spatial coordinates of two or more points located on the fold axes and applying simple trigonometry.

10.3.2. Sample locations, corresponding nappe unit name and their regional equivalence according to Azañón and Crespo-Blanc (2000) and Martín-Algarra et al. (2004).

Area	Samples	Local nappe-unit name	Equivalence Azañon and Crespo Blanc (2000) / Martín-Algarra et al. (2004)	
Jubrique-Fuengirola	70.6.1, 71.6.1, 71.4.1, 71.3.1, 71.2.1, 71.1.1, 71.11.1, 61.1.1, 70.3.1, 61.5.1, 70.1.1, 71.16.1, 71.16.2, 71.15.1	Los Reales nappe (Tubía, 1988)	Adra-Salobreña	Upper Alp.
Almuñécar-Torrox	68.6.1, 68.5.1, 68.7.2, 68.4.1	Benamocarra unit (Aldaya et al., 1979; Elorza and García-Dueñas, 1981)	Adra unit	Upper Alp.
	67.10.1, 67.10.2, 68.3.1, 67.7.1, 67.3.1, 68.2.1, 67.1.1	Sayalonga unit (Aldaya et al., 1979; Elorza and García-Dueñas, 1981)	Salobreña unit	Upper Alp.
	66.10.1, 66.9.1, 66.11.1, 66.8.1, 66.6.1, 60.2.1, 60.2.2, 60.3.1	Herradura nappe (Avidad and García-Dueñas, 1972)	Herradura unit	Intermediate Alp.
	62.4.1, 62.5.1, 62.5.2, 62.6.1, 60.7.1, 60.8.1, 66.3.1, 66.4.1	Salobreña nappe (Avidad and García-Dueñas, 1972)	Salobreña unit	Upper Alp.
	58.1.1, 60.10.1	Guájares nappe (Avidad and García-Dueñas, 1972; Avidad Castañeda et al., 1978)	Adra unit	Upper Alp.
Tocón de Quéntar	63.9.1, 63.8.1, 63.6.1, 63.3.1, 63.3.2	La Plata nappe (García-Dueñas and Navarro-Vilá, 1976)	Adra unit	Upper Alp.
	63.1.3	Hernán Valle nappe (Comas et al., 1979)	Adra unit	Upper Alp.
Contraviesa	64.3.1, 64.3.2, 64.4.1, 64.5.1, 59.10.1, 59.10.2, 65.2.2, 65.3.2, 65.7.1, 65.10.2	Adra nappe (Aldaya, 1969; Aldaya et al., 1979)	Adra unit	Upper Alp.
	64.6.1	Murtas nappe (Aldaya, 1969; Aldaya et al., 1979)	Salobreña unit	Intermediate Alp.

10.3.3. Equal-area stereograms for FIAs defined by sigmoidal and spiral-shaped inclusion trails (contoured dots) and straight inclusion trails (great circles and rose diagrams) measured with XCT. Each dot represents the FIA of a single garnet.

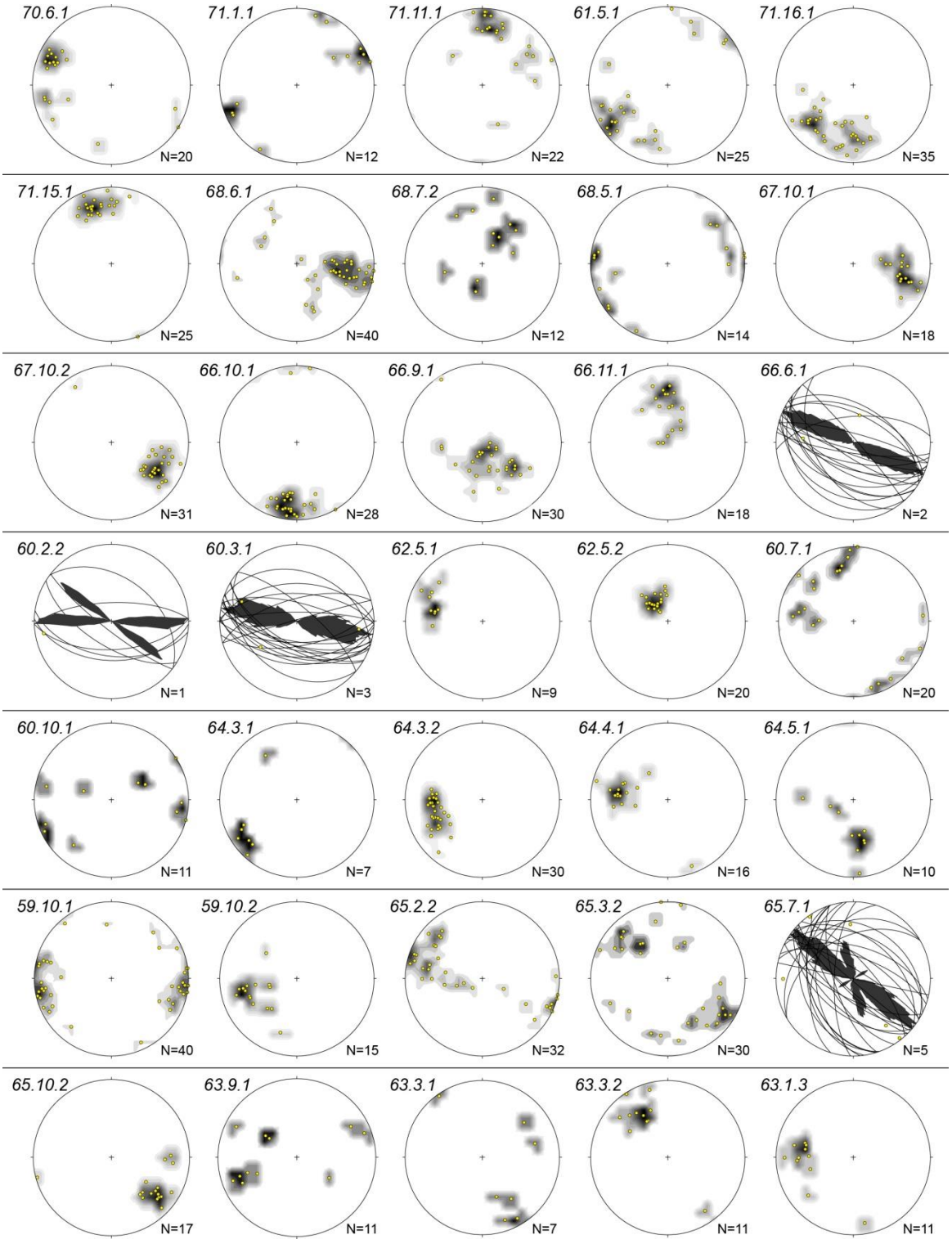

10.3.4. Moving-average rose diagrams for the strike of straight inclusion trails measured in horizontal thin sections. Inclusion trails in sample 66.4.1 were also measured in 3D using XCT (great circles).

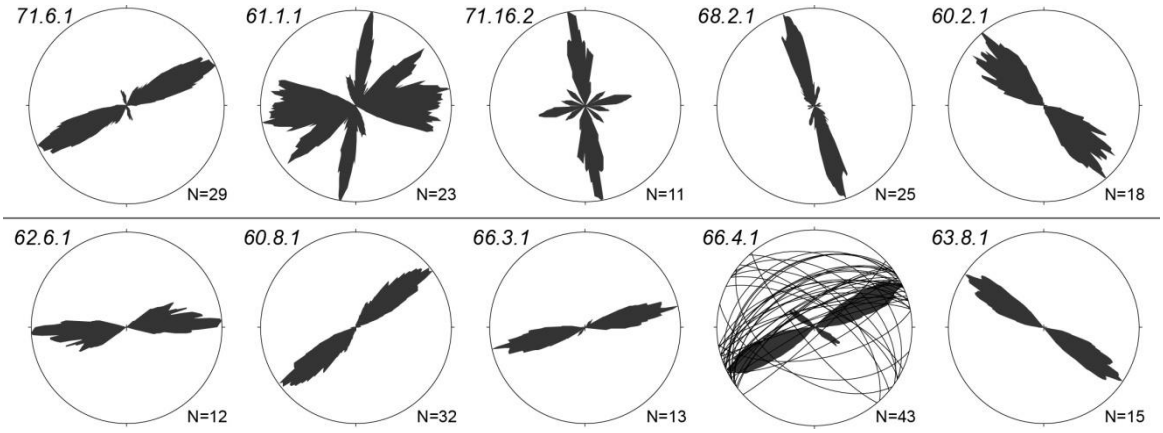

10.3.5. Summary of microstructural data. FIAs with asterisks were determined using radial thin section sets (method of Hayward, 1990), all others with XCT.

Area	Sample	Mineral	Average FIA trends		Modal maxima of inclusion-trail strikes			Matrix Folds & Lineations	
Jubrique-	70.6.1	Grt	072	115				81/000	
Fuengirola	71.6.1	Pl			063	163			
	71.4.1	And	* 075					09/352	
	71.3.1	And	* 075					05/015	
	71.2.1	And	* 060						
	71.1.1	Grt	020	068				08/346	
	71.11.1	Grt	005	059					
	61.1.1	And			009	066	093	06/267	
	70.3.1	And	* 165					20/085	
	61.5.1	Grt	018	056				10/092	
	71.16.1	Grt	001	046					
	71.16.2	St			072	172			
	70.1.1	St	* 000					12/274	
	71.15.1	Grt	163						
Almuñécar-	68.6.1	Grt	097	159				10/017	
Torrox	68.7.2	Grt	041	170					
	68.5.1	Grt	052	096					
	68.4.1	And	* 105						
	68.3.1	Pl	* 015					08/265	
	67.10.1	Grt	102					07/012	
	67.10.2	Grt	119					06/008	
	67.7.1	And & St	* 165						
	67.3.1	And	* 150					02/082	
	68.2.1	St & Pl			163				
	67.1.1	And & St	* 165						
	66.10.1	Grt	008					50/161	
	66.9.1	Grt	Vertical						
	66.11.1	Grt	176					05/133	
	66.8.1	Grt	* 165						
	66.6.1	Grt	113					32/264	39/184
	62.4.1	St	* 075					08/049	
	60.2.1	Grt			132				
	60.2.2	Grt	082	125				30/073	
	60.3.1	Grt	067	099				20/251	
	62.5.1	Grt	112					15/053	23/314
	62.5.2	Grt	Vertical					15/252	
	62.6.1	St			082			06/077	
	60.8.1	Grt			051			09/214	
	60.7.1	Grt	107	167				21/172	
	66.3.1	St			075				
	66.4.1	Grt	065	125				11/065	
	60.10.1	Grt	063	102				00/174	14/301
	58.1.1	Grt	* 060					14/122	
Tocón de	63.9.1	Grt	068	115				07/169	
Quéntar	63.8.1	St			124			19/170	
	63.6.1	Grt	* 075						
	63.3.1	Grt	064	148					
	63.3.2	Grt	151						
	63.1.3	Grt	100	170					
Contraviesa	64.3.1	Grt	056	145				18/044	
	64.3.2	Grt	063	094				28/214	
	64.4.1	Grt	100	162				13/165	
	64.5.1	Grt	095	172				52/152	
	59.10.1	Grt	077	100				34/167	
	59.10.2	Grt	075					26/177	
	64.6.1	Grt & St	* 045					11/170	
	65.2.2	Grt	109					23/236	62/169
	65.3.2	Grt	130	176				58/189	15/259
	65.7.1	Grt	135	175				51/222	
	65.10.2	Grt	087	130					

10.3.6. Inclusion trail pitches measured in sections oriented normal to FIA in samples containing a single or very dominant FIA set.

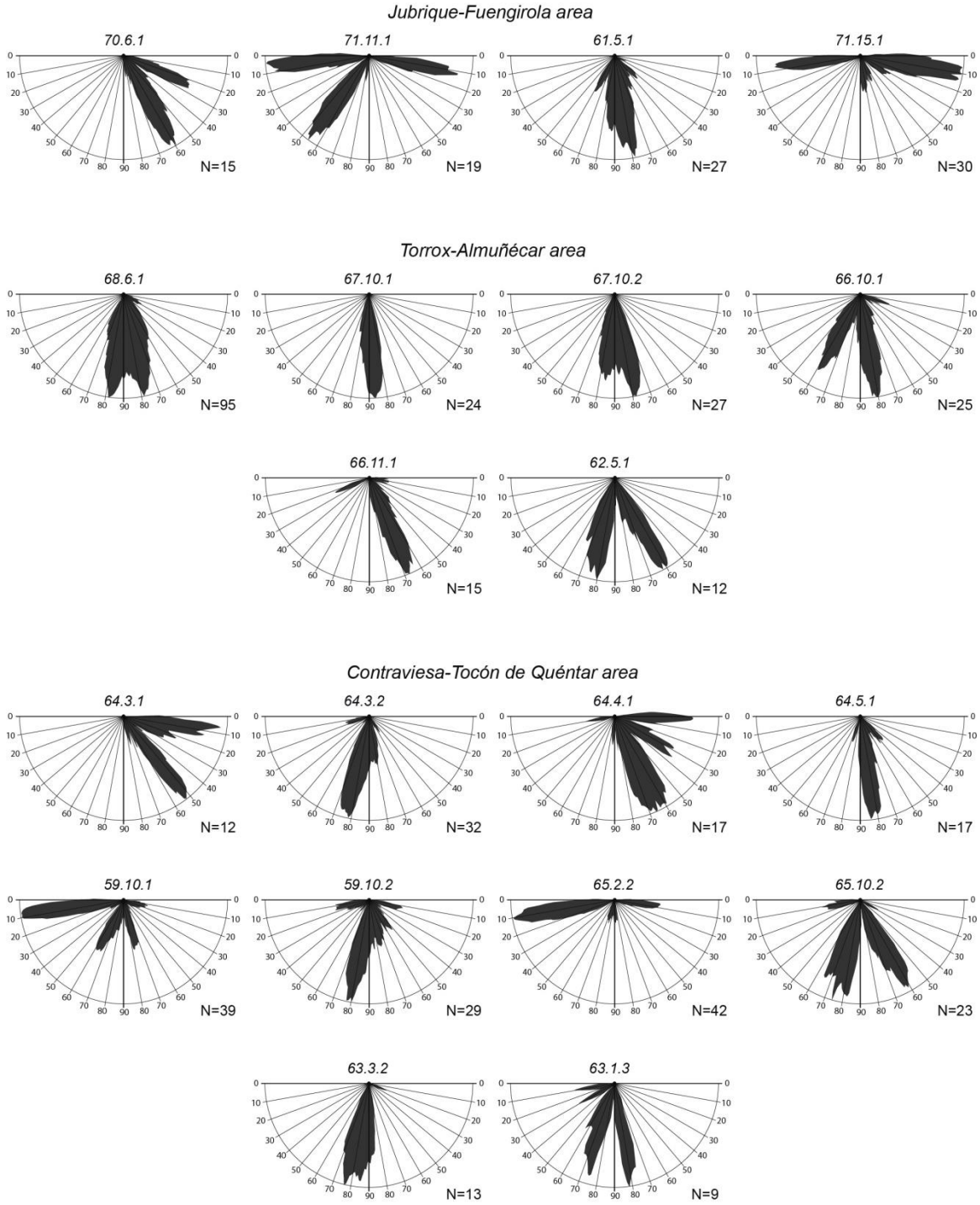

References

Aldaya, F., 1969. Los mantos Alpujárrides al Sur de Sierra Nevada (zona bética, provincia de Granada.). Acta Geológica Hispánica IV (5), 126-130.

Aldaya, F., García-Dueñas, V., Navarro-Vilá, F., 1979. Los Mantos Alpujárrides del tercio central de las Cordilleras Béticas. Ensayo de correlación tectónica de los Alpujárrides. Acta Geológica Hispánica 14, 154-166.

Avidad, J., García-Dueñas, V., 1972. Mapa de la Hoja nº 1055 (Motril). Mapa Geológico de España E. 1:50.000. Segunda Serie (MAGNA), Primera edición. IGME.

Avidad Castañeda, J., García-Dueñas, V., Gallegos, J.A., González Donoso, J.M., 1978. Mapa de la Hoja nº 1041 (Dúrcal). Mapa Geológico de España E. 1:50.000. Segunda Serie (MAGNA), Primera edición. IGME.

Azañón, J.M., Crespo-Blanc, A., 2000. Exhumation during a continental collision inferred from the tectonometamorphic evolution of the Alpujarride Complex in the central Betics (Alboran Domain, SE Spain). Tectonics 19 (3), 549-565. https://doi.org/10.1029/2000TC900005

Bell, T.H., Forde, A., Wang, J., 1995. A new indicator of movement direction during orogenesis: measurement technique and application to the Alps. Terra Nova 7, 500-508. https://doi.org/10.1111/j.1365-3121.1995.tb00551.x

Comas, M.C., Delgado, F., Vera, J.A., 1979. Mapa y memoria de la Hoja nº 993 (Benalúa de Guadix). Mapa Geológico de España E. 1:50.000. Segunda Serie (MAGNA), Primera edición. IGME.

Doube, M., Klosowski, M.M., Arganda-Carreras, I., Cordelières, F.P., Dougherty, R.P., Jackson, J.S., Schmid, B., Hutchinson, J.R., Shefelbine, S.J., 2010. BoneJ: Free and extensible bone image analysis in ImageJ. Bone 47, 1076-1079. https://doi.org/10.1016/j.bone.2010.08.023

Elorza, J.J., García-Dueñas, V., 1981. Mapa y memoria de la Hoja nº 1054 (Vélez-Málaga). Mapa Geológico de España E. 1:50.000. Segunda Serie (MAGNA), Primera edición. IGME.

García-Dueñas, V., Navarro-Vilá, F., 1976. Alpujarrides, Malaguides et autres unités allochtones au Nord de la Sierra Nevada (Cordillères Bétiques, Andalousie). Bulletin de la Société Géologique de France 7-XVIII-3, 641-648. https://doi.org/10.2113/gssgfbull.S7-XVIII.3.641

Hayward, N., 1990. Determination of early fold axis orientations in multiply deformed rocks using porphyroblast inclusion trails. Tectonophysics 179, 353-369. https://doi.org/10.1016/0040-1951(90)90301-N

Martín-Algarra, A., Crespo-Blanc, A., Delgado, F., Estévez, A., González-Lodeiro, F., Orozco, M., Sánchez-Gómez, M., Sanz de Galdeano, C., García-Dueñas, V., 2004. Complejo Alpujárride. Estructura. Rasgos generales, in: Vera, J.A., (Ed.) Geología de España. SGE-IGME Madrid, 416-417.

Ollion, J., Cochennec, J., Loll, F., Escudé, C., Boudier, T., 2013. TANGO: a generic tool for high-throughput 3D image analysis for studying nuclear organization. Bioinformatics 29, 1840-1841. https://doi.org/10.1093/bioinformatics/btt276

Schindelin, J., Arganda-Carreras, I., Frise, E., Kaynig, V., Longair, M., Pietzsch, T., Preibisch, S., Rueden, C., Saalfeld, S., Schmid, B., Tinevez, J.Y., White, D.J., Hartenstein, V., Eliceiri, K., Tomancak, P., Cardona, A., 2012. Fiji: an open-source platform for biological-image analysis. Nature Methods 9, 676-682. https://doi.org/10.1038/nmeth.2019

Schneider, C.A., Rasband, W.S., Eliceiri, K.W., 2012. NIH Image to ImageJ: 25 years of image analysis. Nature Methods 9, 671-675. https://doi.org/10.1038/nmeth.2089

Tubía, J.M., 1988. Estructura de los Alpujárrides occidentales: Cinemática y condiciones de emplazamiento de las peridotitas de Ronda. Parte I: Características litológicas. Boletín Geológico y Minero 99(II), 165-212.

10.4. Alpujárride Complex sample list

Summary of the methods applied to each sample: TS (thin section), XCT (X-ray Computed Tomography), VTS (vertical thin sections), HTS (horizontal thin section), GC/TB (geochronology and thermobarometry).

Sample	Long.	Lat.	TS	XCT	VTS	HTS	GC/TB	Brief description
58.1.1	-3,72559º	36,95853º	■		■			Grt-graphite schist
59.10.1	-3,30801º	36,81464º	■	■				Grt-schist
59.10.2	-3,30801º	36,81464º	■	■				Grt-schist
59.11.1	-3,32370º	36,81628º	■					Grt-schist
60.2.1	-3,70479º	36,74471º	■			■		Grt-St-Sill-quartzschist
60.2.2	-3,70479º	36,74471º	■	■				Grt-St-Sill-quartzschist
60.3.1	-3,69936º	36,75328º	■	■				Grt-St-quartzschist
60.4.1	-3,69589º	36,75079º	■					Quartzite
60.6.1	-3,66755º	36,83706º	■					Phyllite
60.7.1	-3,65466º	36,78496º	■	■				Grt-graphite schist
60.8.1	-3,65816º	36,77547º	■			■		Grt-graphite schist
60.10.1	-3,55372º	36,81918º	■	■				Grt-graphite schist
61.1.1	-4,77831º	36,51005º	■			■		And-schist
61.1.2	-4,77831º	36,51005º	■					Grt-quartzschist
61.2.1	-4,71291º	36,54678º	■					Kinzigite
61.3.1	-4,85060º	36,58447º	■					Migmatite
61.4.1	-4,64679º	36,51257º	■					Grt-graphite schist
61.5.1	-4,63913º	36,50690º	■	■	■			Grt-And-schist
62.1.1	-3,62841º	36,84894º	■					Grt-quartzite
62.2.1	-3,62016º	36,82566º	■					Grt-quartzite
62.3.1	-3,72795º	36,78048º	■					Grt-graphite schist
62.3.2	-3,72795º	36,78048º	■					Grt-graphite schist
62.4.1	-3,72764º	36,78349º	■		■			Grt-St-graphite schist
62.5.1	-3,68810º	36,77957º	■	■			■	Grt-Pl-schist
62.5.2	-3,68810º	36,77957º	■	■				Grt-Pl-schist
62.6.1	-3,68899º	36,78312º	■			■		St-graphite quartzschist
63.1.1	-3,01642º	37,40011º	■					Graphite quartzschist
63.1.2	-3,01642º	37,40011º	■					Quartzite
63.1.3	-3,01642º	37,40011º	■	■				Grt-quartzschist
63.2.1	-3,33414º	37,27345º	■					And-graphite schist
63.3.1	-3,33312º	37,27340º	■	■				Grt-graphite quartzschist
63.3.2	-3,33312º	37,27340º	■	■				Grt-graphite quartzschist
63.4.1	-3,33143º	37,2723º	■					And-graphite schist
63.5.1	-3,37307º	37,26938º	■					Graphite quartzschist
63.5.2	-3,37307º	37,26938º	■					Graphite quartzschist
63.6.1	-3,37188º	37,2688º	■		■			Grt-And-graphite schist
63.7.1	-3,36977º	37,27145º	■					Graphite quartzschist
63.8.1	-3,37303º	37,26746º	■			■		Grt-St-And-graphite schist
63.9.1	-3,39129º	37,23487º	■	■				Grt-And-graphite quartzschist
63.10.1	-3,53114º	37,08038º	■					Grt-graphite schist
64.1.1	-3,39237º	36,78464º	■					Phyllite
64.2.1	-3,39829º	36,79032º						Quartzite
64.2.2	-3,39829º	36,79032º	■					Quartzite
64.3.1	-3,37048º	36,78675º	■	■			■	Grt-St-Pl-schist
64.3.2	-3,37048º	36,78675º	■	■				Grt-schist
64.4.1	-3,36048º	36,79514º	■	■			■	Grt-St-schist
64.5.1	-3,36106º	36,79760º	■	■				Grt-St-schist
64.6.1	-3,27618º	36,85497º	■		■			Grt-St-graphite schist
64.6.2	-3,27618º	36,85497º	■					Grt-St-graphite schist
65.1.1	-3,22158º	36,75047º	■					Grt-graphite schist
65.1.2	-3,22158º	36,75047º	■					Grt-graphite schist
65.2.1	-3,10616º	36,75413º	■					Grt-graphite schist
65.2.2	-3,10616º	36,75413º	■	■				Grt-quartzschist
65.3.1	-3,10582º	36,75584º						Quartz vein

65.3.2	-3,10582º	36,75584º	■	■				Grt-graphite schist
65.3.3	-3,10582º	36,75584º						Quartz vein
65.3.4	-3,10582º	36,75584º						Quartz vein
65.3.5	-3,10582º	36,75584º						Quartz vein
65.4.1	-3,11011º	36,75660º						Quartz vein
65.4.2	-3,11011º	36,75660º	■					Grt-graphite schist
65.5.1	-3,11983º	36,76265º	■					Grt-graphite schist
65.6.1	-3,11603º	36,77142º						Quartz vein
65.7.1	-3,11806º	36,77419º	■	■				Grt-quartzschist
65.10.1	-3,11722º	36,78664º						Grt-quartzschist
65.10.2	-3,11722º	36,78664º	■	■				Grt-graphite quartzschist
66.1.1	-3,50741º	36,77942º	■					Phyllite
66.1.2	-3,50741º	36,77942º						Phyllite
66.2.1	-3,46886º	36,69553º	■					Phyllite
66.2.2	-3,46886º	36,69553º	■					Quartzite
66.3.1	-3,62292º	36,74721º	■			■		Grt-St-graphite schist
66.4.1	-3,60664º	36,74518º	■	■				Grt-graphite schist
66.5.1	-3,72699º	36,73519º	■					Mafic quartzite
66.6.1	-3,73059º	36,73178º	■	■				Grt-Sill-quartzschist
66.7.1	-3,71997º	36,73688º	■					Mafic quartzite
66.8.1	-3,80516º	36,77155º	■		■			Grt-schist
66.9.1	-3,80277º	36,74899º	■	■				Grt-schist
66.10.1	-3,80552º	36,74816º	■	■			■	Grt-schist
66.11.1	-3,79875º	36,74647º	■	■				Grt-graphite schist
66.12.1	-3,61001º	36,77742º						And-schist
67.1.1	-3,93126º	36,79275º	■		■			St-And-graphite quartzschist
67.1.2	-3,93126º	36,79275º	■					Grt-graphite quartzschist
67.2.1A	-3,93436º	36,78067º	■					And-graphite schist
67.2.1B	-3,93436º	36,78067º	■					And-graphite schist
67.3.1	-3,95885º	36,77555º	■		■			Sill-And-graphite schist
67.4.1	-3,96324º	36,80320º	■					Grt-graphite schist
67.5.1	-3,97142º	36,82831º	■					Graphite quartzschist
67.6.1	-3,99074º	36,81862º	■					St-And-graphite schist
67.7.1	-4,00554º	36,80340º	■		■			St-And-graphite schist
67.8.1	-4,00908º	36,82077º	■					Grt-And-graphite schist
67.8.2	-4,00908º	36,82077º	■					Grt-graphite schist
67.9.1	-4,04738º	36,81811º	■					Grt-quartzite
67.10.1	-4,02909º	36,84067º	■	■				Grt-graphite quartzschist
67.10.2	-4,02909º	36,84067º	■	■				Grt-graphite quartzschist
67.11.1	-4,06240º	36,87246º						Schist
67.11.2	-4,06240º	36,87246º						Schist
68.1.1	-3,90763º	36,74361º						And-graphite schist
68.2.1	-3,93260º	36,73938º	■			■		Grt-St-Pl-quartzschist
68.3.1	-4,03029º	36,78642º	■		■			Grt-St-Pl-Sill-And-graphite schist
68.4.1	-4,16639º	36,78779º	■		■			Grt-And-graphite schist
68.5.1	-4,19914º	36,81511º	■	■				Grt-graphite schist
68.5.2	-4,19914º	36,81511º	■					Grt-And-graphite schist
68.5.3	-4,19914º	36,81511º						Quartz vein
68.6.1A	-4,24493º	36,82318º	■	■				Grt-graphite schist
68.6.1B	-4,24493º	36,82318º						Grt-graphite schist
68.7.1	-4,22349º	36,75811º	■					Grt-And-graphite schist
68.7.2A	-4,22349º	36,75811º	■	■				Grt-graphite schist
68.7.2B	-4,22349º	36,75811º						Grt-graphite schist
69.1.1	-3,34506º	36,82098º	■					Phyllite
69.1.2	-3,34506º	36,82098º	■					Phyllite
69.3.1	-3,27466º	36,79413º	■					Quartzschist
69.4.1	-3,25577º	36,79788º	■					Graphite quartzschist
69.5.1	-3,25148º	36,79726º	■					Grt-graphite quartzschist
69.7.1	-3,21260º	36,81376º	■					Grt-graphite schist
69.8.1	-3,20888º	36,83476º	■					Graphite quartzschist
69.9.1	-3,20754º	36,84718º	■					Graphite quartzschist
69.12.1	-3,19855º	36,87683º	■					Phyllite
70.1.1	-4,55947º	36,58116º	■		■			And-St-graphite schist
70.2.1	-4,54992º	36,59270º	■					Sill-And-graphite schist
70.3.1	-4,68584º	36,53091º	■		■			Sill-And-graphite schist
70.4.1	-5,01988º	36,54158º	■					And-graphite quartzschist
70.5.1	-5,25636º	36,44813º	■					Grt-graphite schist

70.5.2	-5,25636º	36,44813º	■					Grt-graphite schist
70.6.1	-5,25497º	36,44660º	■	■				Grt-graphite schist
71.1.1	-5,22087º	36,56712º	■	■				Grt-And-graphite schist
71.2.1	-5,22162º	36,56740º	■		■			And-graphite schist
71.3.1	-5,22325º	36,56546º	■		■			And-graphite schist
71.4.1	-5,22555º	36,56629º	■		■			And-graphite schist
71.5.1	-5,17884º	36,56043º	■					Peridotite
71.6.1	-5,22168º	36,54472º	■			■		Pl-Sill-And-graphite schist
71.7.1	-5,22185º	36,5423º	■					Grt-Sill-And-graphite quartzschist
71.8.1	-5,22530º	36,53621º	■					Sill-And-graphite schist
71.9.1	-5,22619º	36,54405º	■					Graphite schist
71.10.1	-5,16713º	36,62094º	■					Graphite schist
71.11.1	-5,15519º	36,62048º	■	■				Grt-Sill-And-graphite quartzschist
71.12.1	-5,14371º	36,61488º	■					Grt-St-Sill-gneiss
71.13.1	-5,13796º	36,61565º	■					Sill-gneiss
71.14.1	-4,93777º	36,72667º	■					Grt-Sill-gneiss
71.14.2	-4,93777º	36,72667º	■					Grt-Sill-gneiss
71.14.3	-4,93777º	36,72667º	■					Grt-Sill-gneiss
71.15.1	-4,75289º	36,89385º	■	■				Grt-graphite quartzschist
71.16.1	-4,67174º	36,58239º	■	■				Grt-graphite quartzschist
71.16.2	-4,67174º	36,58239º	■			■		Grt-St-Sill-graphite quartzschist
71.17.1	-4,67249º	36,58012º	■					Grt-And-graphite schist
73.8.1	-3,33488º	37,27343º	■					Quartzite
78.4.1	-4.67176°	36.58232°	■					And-graphite schist
78.5.1	-4.67220°	36.58472°	■					Sill-And-graphite schist
79.8.1	-5.23906°	36.56444°	■					Graphite schist
79.14.1	-5.23056°	36.53897°	■					Grt-Pl-And-graphite schist
86.4.1	-4.66077°	36.58761°	■					Sill-And-gneiss
86.6.1	-4.70728°	36.58768°	■					Migmatite
87.1.1	-3.65058°	36.74500°	■					Sill-graphite quartzschist
87.1.2	-3.65058°	36.74500°	■					St-And-graphite quartzschist
87.1.3	-3.65058°	36.74500°	■					Grt-graphite quartzschist
87.1.4	-3.65058°	36.74500°	■					Grt-St-And-graphite schist
87.2.1	-3.71902°	36.73261°	■					Mafic quartzite

10.5. Supplementary Material of Chapter 8

$^{40}Ar/^{39}Ar$ analytical method

Samples were prepared and analysed following the procedure described in Monié et al. (2023). They were crushed and sieved and a 100–200 μm grain size was retained for micas and amphibole separation. The grains were leached with HNO3 (1N) for a few minutes and then repeatedly cleaned ultrasonically in distilled water and alcohol. Grains were finally selected under a binocular microscope. Samples were packed in aluminum foil for irradiation in the core of the Triga Mark II nuclear reactor of Pavia (Italy) with several aliquots of the Taylor Creek sanidine standard (28.619 ± 0.034 Ma in Renne et al., 2011) as flux monitor. Argon isotopic interferences on K and Ca were determined by irradiation of KF and CaF_2 pure salts from which the following correction factors were obtained: $(^{40}Ar/^{39}Ar)K$ = 0.00945 ± 0.00077, $(^{38}Ar/^{39}Ar)K$ = 0.02950± 0.0094, $(^{39}Ar/^{37}Ar)Ca$ = 0.0006135 ± 0.000088 and $(^{36}Ar/^{37}Ar)Ca$ = 0.0002591 ± 0.000017. $^{40}Ar/^{39}Ar$ step-heating analyses were performed at Géosciences Montpellier (France). The gas extraction and purification line consist of (a) an IR-CO_2 laser of 100 kHz used at 3-15% power to heat samples during 60 seconds, (b) a lenses system for beam focusing, (c) a steel chamber maintained at 10^{-8} - 10^{-9} bar, with a copper holder in which 2 mm-diameter blind holes were milled, and (d) two Zr-Al getters for purification of gases. Argon isotopes are analyzed with an Argus VI multi-collection mass spectrometer (with 4 faradays for masses ^{40}Ar-^{37}Ar and ion counting on ^{36}Ar). One minute was allowed for equilibration before analysis. Mass discrimination of machines is followed daily. Mass discrimination was monitored daily using an automated air pipette and ranged between 0,99944 ± 0.00029 and 1.000876 ± 0.0003 per dalton. Aliquots of 5-10 micas were distributed in holes of the copper holder and were step heated. Blank analyses were performed every three sample analyses. Raw data of each step and blank were processed and ages were calculated using the ArArCALC-software (Koppers, 2002). Isotopic ratios were corrected for irradiation interferences and air contamination using a mean air value $(^{40}Ar/^{36}Ar)_{atm}$ of 298.56 ± 0.31 (Lee et al., 2006; Renne et al., 2009). Plateau ages are calculated from at least three consecutive ^{39}Ar release steps comprising up to 50% of total $^{39}Ar_K$ released and overlapping at the 2σ confidence level (Fleck et al., 1977).

$^{40}Ar/^{39}Ar$ results

Sample 66.10.1 amphibole

Results	40(a)/36(a) ± 2σ	40(r)/39(k) ± 2σ	Age ± 2σ (Ma)	MSWD	39Ar(k) (%,n)	K/Ca ± 2σ
Age Plateau		5,52400 ± 0,02658 ± 0,48%	20,30 ± 0,11 ± 0,55%	1,63 13%	89,79 7	0,123 ± 0,007
		Full External Error ± 0,19		2,15	2σ Confidence Limit	
		Analytical Error ± 0,10		1,2772	Error Magnification	
Total Fusion Age		5,48943 ± 0,05839 ± 1,06%	20,17 ± 0,22 ± 1,09%		18	0,106 ± 0,000
		Full External Error ± 0,27				
		Analytical Error ± 0,21				
Normal Isochron	302,98 ± 3,26 ± 1,08%	5,46491 ± 0,04868 ± 0,89%	20,08 ± 0,19 ± 0,93%	0,56 73%	89,79 7	
		Full External Error ± 0,24		2,26	2σ Confidence Limit	
		Analytical Error ± 0,18		1,0000	Error Magnification	
				15	Number of Iterations	
				0,0000506126	Convergence	
Inverse Isochron	302,97 ± 3,27 ± 1,08%	5,46523 ± 0,04875 ± 0,89%	20,08 ± 0,19 ± 0,93%	0,56 73%	89,79 7	
		Full External Error ± 0,24		2,26	2σ Confidence Limit	
		Analytical Error ± 0,18		1,0000	Error Magnification	
				3	Number of Iterations	
				0,0000124600	Convergence	
				29%	Spreading Factor	

Sample 66.10.1 muscovite

Results	40(a)/36(a) ± 2σ	40(r)/39(k) ± 2σ	Age ± 2σ (Ma)	MSWD	39Ar(k) (%,n)	K/Ca ± 2σ
Age Plateau		5,45413 ± 0,01047 ± 0,19%	20,02 ± 0,07 ± 0,34%	0,60 92%	99,01 22	3,08 ± 0,36
		Full External Error ± 0,16		1,62	2σ Confidence Limit	
		Analytical Error ± 0,04		1,0000	Error Magnification	
Total Fusion Age		5,46471 ± 0,02659 ± 0,49%	20,06 ± 0,11 ± 0,56%		24	4,29 ± 0,06
		Full External Error ± 0,18				
		Analytical Error ± 0,10				
Normal Isochron	326,86 ± 42,33 ± 12,95%	5,44494 ± 0,01730 ± 0,32%	19,99 ± 0,08 ± 0,42%	0,39 99%	99,01 22	
		Full External Error ± 0,17		1,63	2σ Confidence Limit	
		Analytical Error ± 0,06		1,0000	Error Magnification	
				1	Number of Iterations	
				0,0000019372	Convergence	
Inverse Isochron	342,17 ± 42,81 ± 12,51%	5,44042 ± 0,01753 ± 0,32%	19,97 ± 0,08 ± 0,42%	0,41 99%	99,01 22	
		Full External Error ± 0,17		1,63	2σ Confidence Limit	
		Analytical Error ± 0,06		1,0000	Error Magnification	
				4	Number of Iterations	
				0,0000513012	Convergence	
				19%	Spreading Factor	

Sample 62.5.1 biotite

Results	40(a)/36(a) ± 2σ	40(r)/39(k) ± 2σ	Age ± 2σ (Ma)	MSWD	39Ar(k) (%,n)	K/Ca ± 2σ
Age Plateau		5,32361 ± 0,15678	19,58 ± 0,58	6,03	49,41	1,28 ± 0,32
		± 2,95%	± 2,94%	0%	8	
		Full External Error	± 0,59	2,07	2σ Confidence Limit	
		Analytical Error	± 0,57	2,4552	Error Magnification	
Total Fusion Age		4,95203 ± 0,07275	18,22 ± 0,27		22	2,28 ± 0,07
		± 1,47%	± 1,49%			
		Full External Error	± 0,30			
		Analytical Error	± 0,27			
Normal Isochron	287,07 ± 52,36	5,49894 ± 0,85613	20,22 ± 3,13	6,68	49,41	
	± 18,24%	± 15,57%	± 15,48%	0%	8	
		Full External Error	± 3,13	2,15	2σ Confidence Limit	
		Analytical Error	± 3,13	2,5839	Error Magnification	
				15	Number of Iterations	
				0,0000433317	Convergence	
Inverse Isochron	282,90 ± 51,58	5,58361 ± 0,83223	20,53 ± 3,04	6,80	49,41	
	± 18,23%	± 14,90%	± 14,82%	0%	8	
		Full External Error	± 3,05	2,15	2σ Confidence Limit	
		Analytical Error	± 3,04	2,6072	Error Magnification	
				7	Number of Iterations	
				0,0002612012	Convergence	
				17%	Spreading Factor	

Sample 62.5.1 muscovite

Results	40(a)/36(a) ± 2σ	40(r)/39(k) ± 2σ	Age ± 2σ (Ma)	MSWD	39Ar(k) (%,n)	K/Ca ± 2σ
Age Plateau		5,33683 ± 0,02327	19,57 ± 0,10	1,85	44,08	3,8 ± 1,0
		± 0,44%	± 0,52%	6%	9	
		Full External Error	± 0,17	2,00	2σ Confidence Limit	
		Analytical Error	± 0,08	1,3589	Error Magnification	
Total Fusion Age		5,37659 ± 0,03566	19,71 ± 0,14		18	8,0 ± 0,7
		± 0,66%	± 0,72%			
		Full External Error	± 0,20			
		Analytical Error	± 0,13			
Normal Isochron	380,93 ± 169,60	5,30125 ± 0,06753	19,44 ± 0,25	0,98	44,08	
	± 44,52%	± 1,27%	± 1,30%	44%	9	
		Full External Error	± 0,29	2,07	2σ Confidence Limit	
		Analytical Error	± 0,25	1,0000	Error Magnification	
				1	Number of Iterations	
				0,0000267910	Convergence	
Inverse Isochron	533,52 ± 219,80	5,24558 ± 0,08471	19,24 ± 0,31	0,58	44,08	
	± 41,20%	± 1,61%	± 1,63%	77%	9	
		Full External Error	± 0,34	2,07	2σ Confidence Limit	
		Analytical Error	± 0,31	1,0000	Error Magnification	
				3	Number of Iterations	
				0,0000141963	Convergence	
				5%	Spreading Factor	

Sample 64.3.1 muscovite

Results	40(a)/36(a) ± 2σ	40(r)/39(k) ± 2σ	Age ± 2σ (Ma)	MSWD	39Ar(k) (%,n)	K/Ca ± 2σ
Age Plateau		5,04576 ± 0,06149 ± 1,22%	18,52 ± 0,23 ± 1,24%	1,63	89,90	0,1 ± 0,9
			Full External Error ± 0,27	8%	12	
			Analytical Error ± 0,22	1,85	2σ Confidence Limit	
				1,2757	Error Magnification	
Total Fusion Age		5,14364 ± 0,08448 ± 1,64%	18,88 ± 0,31 ± 1,66%		18	7,2 ± 3,9
			Full External Error ± 0,34			
			Analytical Error ± 0,31			
Normal Isochron	242,90 ± 102,88 ± 42,36%	5,11524 ± 0,15711 ± 3,07%	18,77 ± 0,58 ± 3,07%	1,43	89,90	
			Full External Error ± 0,59	16%	12	
			Analytical Error ± 0,57	1,89	2σ Confidence Limit	
				1,1951	Error Magnification	
				100	Number of Iterations	
				0,0009244296	Convergence	
Inverse Isochron	301,46 ± 106,84 ± 35,44%	5,04552 ± 0,16791 ± 3,33%	18,52 ± 0,62 ± 3,32%	1,86	89,90	
			Full External Error ± 0,63	5%	12	
			Analytical Error ± 0,61	1,89	2σ Confidence Limit	
				1,3650	Error Magnification	
				3	Number of Iterations	
				0,0000101356	Convergence	
				23%	Spreading Factor	

Sample 64.3.1 muscovite

Results	40(a)/36(a) ± 2σ	40(r)/39(k) ± 2σ	Age ± 2σ (Ma)	MSWD	39Ar(k) (%,n)	K/Ca ± 2σ
Age Plateau		5,23430 ± 0,10378 ± 1,98%	19,21 ± 0,38 ± 1,99%	18,67	100,00	0,53 ± 0,26
			Full External Error ± 0,41	0%	12	
			Analytical Error ± 0,38	1,85	2σ Confidence Limit	
				4,3214	Error Magnification	
Total Fusion Age		5,22617 ± 0,03532 ± 0,68%	19,18 ± 0,14 ± 0,73%		12	2,24 ± 0,64
			Full External Error ± 0,20			
			Analytical Error ± 0,13			
Normal Isochron	248,68 ± 64,94 ± 26,11%	5,27561 ± 0,11604 ± 2,20%	19,36 ± 0,43 ± 2,21%	31,91	100,00	
			Full External Error ± 0,45	0%	12	
			Analytical Error ± 0,42	1,89	2σ Confidence Limit	
				5,6492	Error Magnification	
				1	Number of Iterations	
				0,0000167915	Convergence	
Inverse Isochron	292,94 ± 54,89 ± 18,74%	5,24524 ± 0,11503 ± 2,19%	19,25 ± 0,42 ± 2,20%	20,15	100,00	
			Full External Error ± 0,45	0%	12	
			Analytical Error ± 0,42	1,89	2σ Confidence Limit	
				4,4892	Error Magnification	
				4	Number of Iterations	
				0,0000157329	Convergence	
				67%	Spreading Factor	

Sample 64.4.1 muscovite

Results	40(a)/36(a) ± 2σ	40(r)/39(k) ± 2σ	Age ± 2σ (Ma)	MSWD	39Ar(k) (%,n)	K/Ca ± 2σ
Age Plateau		5,11187 ± 0,00888 ± 0,17%	18,78 ± 0,06 ± 0,33%	0,39 88% 2,15 1,0000	85,10 7 2σ Confidence Limit Error Magnification	19,1 ± 5,1
			Full External Error ± 0,15 Analytical Error ± 0,03			
Total Fusion Age		5,10165 ± 0,00893 ± 0,18%	18,74 ± 0,06 ± 0,33%		10	53,5 ± 4,3
			Full External Error ± 0,15 Analytical Error ± 0,03			
Normal Isochron	311,76 ± 40,63 ± 13,03%	5,10534 ± 0,02155 ± 0,42%	18,76 ± 0,09 ± 0,50%	0,40 85% 2,26 1,0000 1 0,0000000329	85,10 7 2σ Confidence Limit Error Magnification Number of Iterations Convergence	
			Full External Error ± 0,17 Analytical Error ± 0,08			
Inverse Isochron	311,57 ± 40,42 ± 12,97%	5,10561 ± 0,02148 ± 0,42%	18,76 ± 0,09 ± 0,50%	0,39 86% 2,26 1,0000 4 0,0000614192 4%	85,10 7 2σ Confidence Limit Error Magnification Number of Iterations Convergence Spreading Factor	
			Full External Error ± 0,17 Analytical Error ± 0,08			

References

Fleck, R.J., Sutter, J.F., Elliot, D.H., 1977. Interpretation of discordant 40Ar/39Ar age-spectra of mesozoic tholeiites from Antarctica. Geochimica et Cosmochimica Acta 41, 15-32.

Koppers, A.A.P., 2002. ArArCALCFsoftware for 40Ar/39Ar age calculations. Computers & Geosciences 28, 605–619.

Lee, J-Y, Marti, K., Severinghaus, J.P., Kawamura, K., Yoo, H.S., Lee, J.B., Kim, J.S., 2006. A redetermination of the isotopic abundances of atmospheric Ar. Geochimica et Cosmochimica Acta 70, 4507–4512.

Monié, P., Münch, P., Milesi, G., Bonno, M., Iemmolo, A., 2023. 40Ar/39Ar geochronology of crustal deformation. Comptes Rendus Géoscience 356(S2), 1-29.

Renne, P.R., Balco, G., Ludwig, K.R., Mundil, R., Min, K., 2011. Response to the comment by W.H. Schwarz et al. on “Joint determination of 40K decay constants and 40Ar/40K for the Fish Canyon sanidine standard, and improved accuracy for 40Ar/39Ar geochronology” by P.R. Renne et al. (2010): Geochimica et Cosmochimica Acta 75, 5097–5100. doi:10.1016/j.gca.2011.06.021

10.6. EPMA results

Amphibole microprobe analyses (Alpujárride Complex).

Mineral	Amp	Amp	Amp	Amp	Amp	Amp	Amp	Amp
Sample	66.10.1	66.10.1	66.10.1	66.10.1	66.10.1	66.10.1	66.10.1	66.10.1
Analysis	p17	p18	p38	91*	92*	93*	94*	96*
SiO_2	45,10	47,66	44,15	47,20	41,78	42,09	43,36	42,77
TiO_2	0,66	0,80	0,33	0,44	0,42	0,73	0,28	0,46
Al_2O_3	10,09	7,66	9,83	7,35	9,91	10,18	7,59	9,62
FeO	18,42	17,63	19,28	16,89	21,23	19,72	15,62	19,42
MnO	0,46	0,51	0,47	0,59	0,49	0,54	0,56	0,50
MgO	9,86	11,12	9,69	11,84	8,09	10,12	10,69	9,55
CaO	11,98	12,36	12,27	11,47	11,81	10,67	14,63	11,69
Na_2O	0,93	0,91	1,12	1,00	0,95	0,93	1,03	0,98
K_2O	1,23	0,67	1,05	0,33	1,58	0,95	0,33	1,18
Cr_2O_3	0,01	0,01	0,01					
BaO				0,00	0,00	0,01	0,00	0,01
ZnO				0,02	0,05	0,03	0,05	0,05
Sum	98,73	99,33	98,20	97,13	96,31	95,97	94,14	96,22
Si	6,66	6,96	6,60	6,93	6,46	6,31	6,79	6,51
Ti	0,07	0,09	0,04	0,05	0,05	0,08	0,03	0,05
Al iv	1,34	1,04	1,40	1,07	1,54	1,69	1,21	1,49
Al vi	0,42	0,27	0,33	0,21	0,27	0,11	0,19	0,24
Fe^{2+}	1,80	1,81	1,87	1,27	2,09	0,94	2,04	1,66
Fe^{3+}	0,47	0,34	0,54	0,80	0,66	1,53	0,00	0,81
Mn	0,06	0,06	0,06	0,07	0,06	0,07	0,07	0,06
Mg	2,17	2,42	2,16	2,59	1,87	2,26	2,49	2,17
Ca	1,90	1,93	1,96	1,81	1,96	1,71	2,45	1,91
Na	0,27	0,26	0,32	0,28	0,28	0,27	0,31	0,29
K	0,23	0,13	0,20	0,06	0,31	0,18	0,07	0,23
Cr	0,00	0,00	0,00	0,00	0,00	0,00	0,00	0,00
Ba	0,00	0,00	0,00	0,00	0,00	0,00	0,00	0,00
Zn	0,00	0,00	0,00	0,00	0,01	0,00	0,01	0,01
OH	2,00	2,00	2,00	2,00	2,00	2,00	2,00	2,00
Sum	17,39	17,32	17,49	17,15	17,55	17,17	17,67	17,42
$(Ca+Na)_B$	2,00	2,00	2,00	2,00	2,00	1,99	2,45	2,00
Na_B	0,10	0,07	0,04	0,19	0,04	0,27	0,00	0,09
$(Na+K)_A$	0,39	0,32	0,49	0,15	0,55	0,18	0,38	0,42
$Mg/(Mg+Fe^{2+})$	0,55	0,57	0,54	0,67	0,47	0,71	0,55	0,57

Biotite microprobe analyses (Alpujárride Complex).

Mineral	Bt	Bt	Bt	Bt	Bt	Bt	Bt	Bt	Bt	Bt
Sample	62.5.1	62.5.1	62.5.1	62.5.1	62.5.1	62.5.1	62.5.1	62.5.1	62.5.1	64.4.1
Analysis	p9	p10	p26	p27	p28	p29	p30	p31	68*	p9
SiO_2	36,35	35,87	36,93	36,51	36,38	35,10	36,03	33,85	34,51	36,64
TiO_2	2,24	2,37	1,84	2,30	1,71	1,47	2,11	1,86	1,87	1,14
Al_2O_3	18,56	18,01	20,41	20,21	21,09	21,68	19,98	20,88	17,88	19,16
FeO	23,17	23,66	17,38	17,96	18,57	20,60	22,53	24,43	24,79	17,76
MnO	0,05	0,11	0,11	0,15	0,09	0,12	0,12	0,13	0,13	0,00
MgO	7,33	7,45	9,25	8,80	8,53	7,46	5,92	5,51	6,21	9,97
CaO	0,04	0,05	0,08	0,05	0,07	0,10	0,01	0,07	0,08	0,24
Na_2O	0,13	0,15	0,15	0,17	0,20	0,17	0,15	0,18	0,11	0,36
K_2O	9,15	8,96	9,06	9,19	9,20	9,23	9,28	9,00	8,87	7,59
Cr_2O_3	0,04	0,05	0,02	0,03	0,01	0,02	0,02	0,03		0,00
BaO									0,03	
ZnO									0,01	
Sum	97,05	96,67	95,20	95,35	95,84	95,94	96,15	95,93	94,49	92,87
Si	2,75	2,74	2,76	2,74	2,72	2,66	2,74	2,62	2,72	2,80
Ti	0,13	0,14	0,10	0,13	0,10	0,08	0,12	0,11	0,11	0,07
Al	1,66	1,62	1,80	1,79	1,86	1,93	1,79	1,90	1,66	1,72
FeTot	1,47	1,51	1,09	1,13	1,16	1,30	1,44	1,58	1,64	1,13
Mn	0,00	0,01	0,01	0,01	0,01	0,01	0,01	0,01	0,01	0,00
Mg	0,83	0,85	1,03	0,98	0,95	0,84	0,67	0,64	0,73	1,14
Ca	0,00	0,00	0,01	0,00	0,01	0,01	0,00	0,01	0,01	0,02
Na	0,02	0,02	0,02	0,02	0,03	0,02	0,02	0,03	0,02	0,05
K	0,88	0,87	0,86	0,88	0,88	0,89	0,90	0,89	0,89	0,74
Cr	0,00	0,00	0,00	0,00	0,00	0,00	0,00	0,00	0,00	0,00
Ba	0,00	0,00	0,00	0,00	0,00	0,00	0,00	0,00	0,00	0,00
Zn	0,00	0,00	0,00	0,00	0,00	0,00	0,00	0,00	0,00	0,00
Sum	7,74	7,76	7,68	7,69	7,71	7,75	7,70	7,78	7,79	7,67
XFe	0,64	0,64	0,51	0,53	0,55	0,61	0,68	0,71	0,69	0,50
XMg	0,36	0,36	0,49	0,47	0,45	0,39	0,32	0,29	0,31	0,50

Chlorite microprobe analyses (Alpujárride Complex).

Mineral	Chl	Chl	Chl	Chl	Chl	Chl	Chl
Sample	66.10.1	66.10.1	66.10.1	66.10.1	66.10.1	66.10.1	66.10.1
Analysis	15	16	19	35	36	37	46
SiO_2	27,923	28,467	27,683	31,054	27,108	27,636	29,043
TiO_2	0,101	0,031	0,123	0,284	0,097	0,048	0,044
Al_2O_3	18,94	18,038	19,556	17,433	19,511	19,25	18,193
FeO	24,044	22,084	23,595	19,757	22,566	22,807	21,667
MnO	0,332	0,344	0,365	0,347	0,367	0,386	0,366
MgO	15,996	17,696	16,749	19,639	17,102	17,41	18,018
CaO	0,117	0,076	0,079	0,186	0,044	0,081	0,108
Na_2O	0,092	0,056	0,057	0,07	0,044	0,087	0,108
K_2O	0,236	0,057	0,06	0,536	0,085	0,074	0,095
Cr_2O_3	0,014	0,015	0,007	0	0	0,005	0,007
Sum	87,795	86,864	88,274	89,306	86,924	87,784	87,649
Si	2,92	2,97	2,86	3,10	2,84	2,87	2,99
Ti	0,01	0,00	0,01	0,02	0,01	0,00	0,00
Al iv	1,08	1,03	1,14	0,90	1,16	1,13	1,01
Al vi	1,25	1,19	1,25	1,16	1,25	1,22	1,20
FeTot	2,10	1,93	2,04	1,65	1,98	1,98	1,87
Mn	0,03	0,03	0,03	0,03	0,03	0,03	0,03
Mg	2,49	2,75	2,58	2,93	2,67	2,69	2,77
Ca	0,01	0,01	0,01	0,02	0,00	0,01	0,01
Na	0,02	0,01	0,01	0,01	0,01	0,02	0,02
K	0,03	0,01	0,01	0,07	0,01	0,01	0,01
Cr	0,00	0,00	0,00	0,00	0,00	0,00	0,00
Sum	9,94	9,93	9,94	9,89	9,96	9,97	9,92

Garnet microprobe analyses (Alpujárride Complex).

Mineral	Grt	Grt	Grt	Grt	Grt	Grt	Grt	Grt	Grt	Grt
Sample	64.4.1	64.4.1	64.4.1	64.4.1	64.4.1	64.4.1	64.4.1	64.4.1	64.4.1	64.4.1
Analysis	1*	2*	3*	4*	5*	6*	7*	8*	13*	14*
SiO_2	37,17	37,18	37,06	37,04	36,95	37,02	36,91	36,71	36,86	36,82
TiO_2	0,10	0,09	0,11	0,10	0,12	0,13	0,14	0,13	0,13	0,10
Al_2O_3	20,76	20,67	20,61	20,52	20,48	20,53	20,37	20,15	20,25	20,45
FeO	35,55	36,27	35,96	36,02	35,78	36,20	35,74	35,30	34,78	35,86
MnO	0,27	0,28	0,25	0,28	0,38	0,71	1,04	1,30	1,60	1,24
MgO	2,58	2,43	2,38	2,30	2,08	1,85	1,66	1,60	1,48	1,65
CaO	3,92	3,67	3,89	3,80	4,14	3,96	4,30	4,26	4,43	4,00
Na_2O	0,01	0,03	0,01	0,03	0,02	0,01	0,03	0,04	0,01	0,02
K_2O	0,01	0,00	0,02	0,01	0,02	0,02	0,02	0,03	0,02	0,02
Cr_2O_3										
BaO	0,00	0,00	0,00	0,00	0,00	0,00	0,00	0,00	0,00	0,01
ZnO	0,01	0,02	0,03	0,02	0,01	0,00	0,03	0,01	0,00	0,00
Sum	100,38	100,66	100,31	100,13	99,99	100,44	100,23	99,54	99,58	100,16
Si	2,98	2,98	2,98	2,99	2,98	2,98	2,98	2,99	3,00	2,98
Ti	0,01	0,01	0,01	0,01	0,01	0,01	0,01	0,01	0,01	0,01
Al	1,96	1,95	1,95	1,95	1,95	1,95	1,94	1,93	1,94	1,95
Fe2+	2,32	2,35	2,34	2,36	2,34	2,37	2,33	2,32	2,32	2,35
Fe3+	0,07	0,08	0,08	0,07	0,07	0,07	0,08	0,08	0,04	0,08
Mn	0,02	0,02	0,02	0,02	0,03	0,05	0,07	0,09	0,11	0,08
Mg	0,31	0,29	0,29	0,28	0,25	0,22	0,20	0,19	0,18	0,20
Ca	0,34	0,32	0,34	0,33	0,36	0,34	0,37	0,37	0,39	0,35
Na	0,00	0,01	0,00	0,00	0,00	0,00	0,00	0,01	0,00	0,00
K	0,00	0,00	0,00	0,00	0,00	0,00	0,00	0,00	0,00	0,00
Cr	0,00	0,00	0,00	0,00	0,00	0,00	0,00	0,00	0,00	0,00
Ba	0,00	0,00	0,00	0,00	0,00	0,00	0,00	0,00	0,00	0,00
Zn	0,00	0,00	0,00	0,00	0,00	0,00	0,00	0,00	0,00	0,00
Sum	8,00	8,00	8,00	8,00	8,00	8,00	8,00	8,00	8,00	8,00
XFe	88,24	88,98	89,13	89,51	90,33	91,44	92,11	92,28	92,81	92,19
Alm	77,74	78,98	78,59	79,07	78,67	79,45	78,40	77,98	77,44	78,83
Prp	10,36	9,78	9,58	9,26	8,42	7,44	6,72	6,53	6,00	6,68
Grs	11,29	10,61	11,26	11,02	12,03	11,47	12,50	12,48	12,88	11,65
Sps	0,60	0,63	0,57	0,65	0,88	1,63	2,39	3,01	3,68	2,84

Mineral	Grt	Grt	Grt	Grt	Grt	Grt	Grt	Grt	Grt	Grt	Grt
Sample	64.4.1	64.4.1	64.4.1	64.4.1	64.4.1	64.4.1	64.4.1	64.4.1	64.4.1	64.4.1	64.4.1
Analysis	15*	16*	17*	18*	19*	20*	21*	22*	23*	24*	25*
SiO_2	36,88	36,61	36,77	37,14	36,96	37,15	36,88	37,06	37,07	36,86	36,86
TiO_2	0,18	0,11	0,16	0,09	0,12	0,10	0,13	0,10	0,09	0,09	0,12
Al_2O_3	20,27	20,28	20,30	20,57	20,47	20,60	20,34	20,55	20,54	20,48	20,50
FeO	35,76	36,13	36,34	36,41	35,49	35,48	35,48	36,13	35,96	35,93	36,08
MnO	1,02	0,73	0,32	0,30	0,32	0,30	1,28	0,18	0,25	0,35	0,36
MgO	1,68	1,83	2,26	2,44	2,48	2,56	1,60	2,42	2,28	2,48	2,21
CaO	4,33	3,88	3,59	3,46	4,05	4,14	4,76	3,76	4,06	3,92	4,04
Na_2O	0,03	0,01	0,01	0,01	0,00	0,00	0,02	0,02	0,02	0,00	0,02
K_2O	0,02	0,01	0,02	0,00	0,02	0,02	0,02	0,01	0,02	0,02	0,01
Cr_2O_3											
BaO	0,00	0,00	0,00	0,00	0,00	0,00	0,00	0,00	0,00	0,00	0,00
ZnO	0,02	0,03	0,00	0,00	0,01	0,00	0,01	0,00	0,02	0,01	0,03
Sum	100,18	99,61	99,78	100,44	99,92	100,36	100,52	100,23	100,32	100,13	100,23
Si	2,98	2,98	2,98	2,99	2,98	2,98	2,97	2,98	2,98	2,97	2,97
Ti	0,01	0,01	0,01	0,01	0,01	0,01	0,01	0,01	0,01	0,01	0,01
Al	1,93	1,94	1,94	1,95	1,95	1,95	1,93	1,95	1,95	1,94	1,95
Fe2+	2,33	2,37	2,37	2,37	2,31	2,30	2,28	2,35	2,33	2,31	2,33
Fe3+	0,09	0,09	0,09	0,07	0,08	0,08	0,11	0,08	0,08	0,11	0,10
Mn	0,07	0,05	0,02	0,02	0,02	0,02	0,09	0,01	0,02	0,02	0,02
Mg	0,20	0,22	0,27	0,29	0,30	0,31	0,19	0,29	0,27	0,30	0,27
Ca	0,37	0,34	0,31	0,30	0,35	0,36	0,41	0,32	0,35	0,34	0,35
Na	0,00	0,00	0,00	0,00	0,00	0,00	0,00	0,00	0,00	0,00	0,00
K	0,00	0,00	0,00	0,00	0,00	0,00	0,00	0,00	0,00	0,00	0,00
Cr	0,00	0,00	0,00	0,00	0,00	0,00	0,00	0,00	0,00	0,00	0,00
Ba	0,00	0,00	0,00	0,00	0,00	0,00	0,00	0,00	0,00	0,00	0,00
Zn	0,00	0,00	0,00	0,00	0,00	0,00	0,00	0,00	0,00	0,00	0,00
Sum	8,00	8,00	8,00	8,00	8,00	8,00	8,00	8,00	8,00	8,00	8,00
XFe	91,99	91,44	89,69	89,03	88,60	88,23	92,22	89,02	89,51	88,58	89,75
Alm	78,27	79,51	79,65	79,52	77,57	77,10	76,75	78,98	78,48	77,78	78,47
Prp	6,81	7,44	9,16	9,80	9,98	10,28	6,47	9,74	9,19	10,02	8,96
Grs	12,58	11,37	10,45	9,99	11,72	11,94	13,84	10,89	11,76	11,40	11,74
Sps	2,34	1,68	0,74	0,69	0,73	0,68	2,95	0,40	0,57	0,80	0,83

Mineral	Grt	Grt	Grt	Grt	Grt	Grt	Grt	Grt	Grt	Grt	Grt
Sample	64.4.1	64.4.1	64.4.1	64.4.1	64.4.1	64.4.1	64.4.1	64.4.1	64.4.1	64.4.1	64.4.1
Analysis	26*	27*	28*	29*	30*	31*	32*	33*	34*	p2	p4
SiO_2	36,63	36,68	37,10	36,68	36,43	36,52	36,94	36,95	37,15	37,48	38,10
TiO_2	0,13	0,13	0,15	0,16	0,13	0,15	0,10	0,08	0,08	0,16	0,16
Al_2O_3	20,31	20,19	20,46	20,19	20,31	20,04	20,49	20,65	20,74	21,74	22,01
FeO	36,00	35,54	35,30	35,16	35,10	35,65	36,30	35,32	35,93	35,64	35,41
MnO	0,49	0,85	1,01	1,48	1,38	0,91	0,33	0,29	0,42	0,43	0,26
MgO	2,03	1,74	1,67	1,53	1,51	1,77	2,23	2,69	2,46	2,09	2,32
CaO	4,13	4,47	4,77	4,63	4,60	4,35	3,80	4,04	3,79	4,11	4,50
Na_2O	0,00	0,01	0,00	0,00	0,02	0,01	0,01	0,00	0,01	0,12	0,03
K_2O	0,02	0,02	0,02	0,01	0,01	0,02	0,01	0,02	0,01	0,03	0,00
Cr_2O_3										0,03	0,01
BaO	0,00	0,01	0,00	0,00	0,00	0,00	0,00	0,00	0,00		
ZnO	0,00	0,02	0,01	0,00	0,01	0,03	0,01	0,00	0,01		
Sum	99,74	99,67	100,49	99,85	99,49	99,46	100,22	100,03	100,60	101,83	102,80
Si	2,97	2,98	2,99	2,98	2,97	2,97	2,98	2,97	2,98	2,96	2,98
Ti	0,01	0,01	0,01	0,01	0,01	0,01	0,01	0,01	0,00	0,01	0,01
Al	1,94	1,93	1,94	1,93	1,95	1,92	1,95	1,96	1,96	2,03	2,03
Fe2+	2,34	2,32	2,31	2,29	2,29	2,32	2,36	2,28	2,33	2,31	2,31
Fe3+	0,11	0,09	0,07	0,09	0,10	0,11	0,09	0,09	0,08	0,05	0,00
Mn	0,03	0,06	0,07	0,10	0,10	0,06	0,02	0,02	0,03	0,03	0,02
Mg	0,25	0,21	0,20	0,19	0,18	0,21	0,27	0,32	0,29	0,25	0,27
Ca	0,36	0,39	0,41	0,40	0,40	0,38	0,33	0,35	0,33	0,35	0,38
Na	0,00	0,00	0,00	0,00	0,00	0,00	0,00	0,00	0,00	0,02	0,00
K	0,00	0,00	0,00	0,00	0,00	0,00	0,00	0,00	0,00	0,00	0,00
Cr	0,00	0,00	0,00	0,00	0,00	0,00	0,00	0,00	0,00	0,00	0,00
Ba	0,00	0,00	0,00	0,00	0,00	0,00	0,00	0,00	0,00	0,00	0,00
Zn	0,00	0,00	0,00	0,00	0,00	0,00	0,00	0,00	0,00	0,00	0,00
Sum	8,00	8,00	8,00	8,00	8,00	8,00	8,00	8,00	8,00	8,00	8,00
XFe	90,48	91,66	92,03	92,53	92,60	91,52	89,78	87,63	88,77	90,33	89,55
Alm	78,54	77,89	77,26	76,88	77,11	77,90	79,21	76,80	78,22	78,72	77,69
Prp	8,26	7,08	6,69	6,21	6,16	7,22	9,01	10,84	9,90	8,42	9,07
Grs	12,06	13,06	13,75	13,49	13,52	12,78	11,02	11,70	10,93	11,88	12,66
Sps	1,13	1,97	2,30	3,41	3,20	2,10	0,76	0,66	0,95	0,97	0,58

Mineral	Grt	Grt	Grt	Grt	Grt	Grt	Grt	Grt	Grt	Grt	Grt
Sample	64.4.1	64.4.1	64.4.1	64.4.1	64.4.1	64.4.1	64.4.1	64.3.1	64.3.1	64.3.1	64.3.1
Analysis	p6	p14	p16	p18	p28	p30	p32	73*	74*	75*	76*
SiO_2	38,33	37,92	38,10	38,02	37,77	38,13	38,11	36,89	37,05	36,88	36,88
TiO_2	0,20	0,14	0,16	0,10	0,20	0,15	0,12	0,08	0,09	0,11	0,14
Al_2O_3	22,13	21,58	21,49	21,65	21,42	21,83	21,93	20,44	20,44	20,26	20,29
FeO	34,61	34,59	35,04	34,88	34,80	35,45	34,81	35,78	35,97	35,92	35,67
MnO	0,16	1,95	1,02	0,30	1,41	0,36	0,34	0,39	0,31	0,38	0,55
MgO	2,87	1,42	1,70	2,60	1,61	2,41	2,74	2,65	2,44	2,21	2,02
CaO	4,46	4,41	4,96	4,22	4,89	4,25	4,16	3,69	3,95	4,25	4,34
Na_2O	0,03	0,04	0,04	0,04	0,04	0,07	0,03	0,02	0,02	0,02	0,01
K_2O	0,00	0,00	0,00	0,01	0,01	0,01	0,01	0,02	0,02	0,02	0,02
Cr_2O_3	0,02	0,03	0,02	0,03	0,01	0,01	0,03				
BaO								0,00	0,00	0,00	0,00
ZnO								0,00	0,00	0,03	0,02
Sum	102,80	102,08	102,53	101,84	102,15	102,66	102,26	99,96	100,30	100,07	99,96
Si	2,98	3,00	3,00	3,00	2,99	2,98	2,99	2,97	2,98	2,98	2,98
Ti	0,01	0,01	0,01	0,01	0,01	0,01	0,01	0,00	0,01	0,01	0,01
Al	2,03	2,01	1,99	2,01	2,00	2,01	2,03	1,94	1,94	1,93	1,93
Fe2+	2,25	2,29	2,31	2,30	2,28	2,31	2,28	2,31	2,32	2,31	2,32
Fe3+	0,00	0,00	0,00	0,00	0,02	0,01	0,00	0,11	0,10	0,11	0,09
Mn	0,01	0,13	0,07	0,02	0,09	0,02	0,02	0,03	0,02	0,03	0,04
Mg	0,33	0,17	0,20	0,31	0,19	0,28	0,32	0,32	0,29	0,27	0,24
Ca	0,37	0,37	0,42	0,36	0,41	0,36	0,35	0,32	0,34	0,37	0,38
Na	0,00	0,01	0,01	0,01	0,01	0,01	0,00	0,00	0,00	0,00	0,00
K	0,00	0,00	0,00	0,00	0,00	0,00	0,00	0,00	0,00	0,00	0,00
Cr	0,00	0,00	0,00	0,00	0,00	0,00	0,00	0,00	0,00	0,00	0,00
Ba	0,00	0,00	0,00	0,00	0,00	0,00	0,00	0,00	0,00	0,00	0,00
Zn	0,00	0,00	0,00	0,00	0,00	0,00	0,00	0,00	0,00	0,00	0,00
Sum	8,00	8,00	8,00	8,00	8,00	8,00	8,00	8,00	8,00	8,00	8,00
XFe	87,12	93,18	92,04	88,27	92,35	89,15	87,69	87,88	88,79	89,69	90,53
Alm	75,90	77,29	77,08	77,14	76,61	77,74	76,74	77,66	78,01	77,81	77,96
Prp	11,22	5,66	6,67	10,25	6,35	9,46	10,77	10,71	9,85	8,95	8,15
Grs	12,53	12,63	13,97	11,94	13,88	12,00	11,74	10,73	11,44	12,37	12,62
Sps	0,35	4,42	2,28	0,67	3,16	0,80	0,75	0,90	0,70	0,87	1,27

Mineral	Grt	Grt	Grt	Grt	Grt	Grt	Grt	Grt	Grt	Grt	Grt
Sample	64.3.1	64.3.1	64.3.1	64.3.1	64.3.1	64.3.1	64.3.1	64.3.1	64.3.1	64.3.1	64.3.1
Analysis	77*	78*	79*	80*	81*	82*	83*	84*	89*	90*	91*
SiO_2	36,99	36,73	36,71	37,07	36,93	37,03	36,91	37,19	37,13	36,99	36,40
TiO_2	0,24	0,12	0,12	0,10	0,11	0,10	0,11	0,08	0,11	0,08	0,11
Al_2O_3	20,32	20,02	20,19	20,47	20,34	20,40	20,31	20,60	21,07	20,48	19,87
FeO	35,70	35,37	35,51	35,43	35,89	35,89	35,42	35,54	33,45	35,86	34,96
MnO	0,86	0,92	0,97	0,72	0,62	0,48	0,30	0,41	1,62	0,34	1,25
MgO	1,76	1,70	1,77	1,88	1,86	2,06	2,37	2,55	1,89	2,62	1,61
CaO	4,55	4,85	4,53	4,48	4,37	4,24	4,33	4,01	4,30	3,95	4,67
Na_2O	0,03	0,01	0,01	0,03	0,02	0,01	0,02	0,01	0,25	0,01	0,00
K_2O	0,02	0,02	0,01	0,03	0,01	0,02	0,02	0,02	0,02	0,01	0,02
Cr_2O_3											
BaO	0,00	0,00	0,00	0,01	0,00	0,00	0,00	0,00	0,01	0,00	0,01
ZnO	0,01	0,00	0,00	0,01	0,02	0,01	0,01	0,02	0,00	0,02	0,02
Sum	100,48	99,73	99,82	100,22	100,17	100,25	99,79	100,43	99,85	100,34	98,92
Si	2,98	2,98	2,98	2,99	2,98	2,99	2,98	2,98	2,99	2,97	2,98
Ti	0,01	0,01	0,01	0,01	0,01	0,01	0,01	0,00	0,01	0,00	0,01
Al	1,93	1,92	1,93	1,95	1,94	1,94	1,93	1,95	2,00	1,94	1,92
Fe2+	2,32	2,29	2,30	2,32	2,34	2,34	2,30	2,30	2,21	2,29	2,29
Fe3+	0,09	0,11	0,10	0,07	0,09	0,08	0,10	0,08	0,05	0,11	0,11
Mn	0,06	0,06	0,07	0,05	0,04	0,03	0,02	0,03	0,11	0,02	0,09
Mg	0,21	0,21	0,21	0,23	0,22	0,25	0,28	0,31	0,23	0,31	0,20
Ca	0,39	0,42	0,39	0,39	0,38	0,37	0,37	0,34	0,37	0,34	0,41
Na	0,00	0,00	0,00	0,00	0,00	0,00	0,00	0,00	0,04	0,00	0,00
K	0,00	0,00	0,00	0,00	0,00	0,00	0,00	0,00	0,00	0,00	0,00
Cr	0,00	0,00	0,00	0,00	0,00	0,00	0,00	0,00	0,00	0,00	0,00
Ba	0,00	0,00	0,00	0,00	0,00	0,00	0,00	0,00	0,00	0,00	0,00
Zn	0,00	0,00	0,00	0,00	0,00	0,00	0,00	0,00	0,00	0,00	0,00
Sum	8,00	8,00	8,00	8,00	8,00	8,00	8,00	8,00	8,00	8,00	8,00
XFe	91,63	91,76	91,50	91,13	91,26	90,41	88,96	88,28	90,69	87,98	92,11
Alm	77,76	76,85	77,37	77,80	78,39	78,31	77,14	77,26	75,71	77,23	76,78
Prp	7,10	6,90	7,18	7,57	7,51	8,31	9,57	10,25	7,77	10,55	6,57
Grs	13,17	14,14	13,21	12,99	12,68	12,28	12,59	11,56	12,72	11,45	13,74
Sps	1,96	2,11	2,24	1,64	1,42	1,10	0,69	0,92	3,79	0,77	2,91

Mineral	Grt	Grt	Grt	Grt	Grt	Grt	Grt	Grt	Grt	Grt	Grt
Sample	64.3.1	64.3.1	64.3.1	64.3.1	64.3.1	64.3.1	64.3.1	64.3.1	66.10.1	66.10.1	66.10.1
Analysis	92*	93*	p2	p4	p6	p21	p23	p25	76*	77*	78*
SiO_2	37,12	36,90	38,19	37,59	38,16	38,20	38,24	38,11	36,97	36,70	36,61
TiO_2	0,10	0,06	0,10	0,15	0,07	0,13	0,12	0,26	0,10	0,12	0,13
Al_2O_3	20,34	20,53	21,40	20,63	21,50	21,46	21,29	21,47	20,23	20,11	20,04
FeO	35,93	35,89	34,02	34,02	35,08	35,41	35,56	35,26	32,37	32,81	33,45
MnO	0,47	0,61	1,83	1,75	0,55	0,80	0,55	0,77	1,76	1,47	1,83
MgO	2,04	2,49	1,57	1,57	2,62	1,98	2,10	2,53	1,75	1,71	1,61
CaO	4,22	3,65	4,32	4,91	3,93	4,20	4,36	3,73	6,83	6,59	5,84
Na_2O	0,00	0,02	0,08	0,13	0,06	0,46	0,03	0,02	0,02	0,04	0,02
K_2O	0,02	0,02	0,00	0,01	0,00	0,01	0,00	0,00	0,02	0,05	0,04
Cr_2O_3			0,01	0,02	0,04	0,03	0,01	0,04			
BaO	0,00	0,00							0,00	0,00	0,00
ZnO	0,00	0,01							0,00	0,02	0,00
Sum	100,24	100,19	101,52	100,79	102,02	102,67	102,26	102,19	100,03	99,63	99,57
Si	2,99	2,97	3,04	3,01	3,00	2,99	3,01	3,00	2,97	2,97	2,97
Ti	0,01	0,00	0,01	0,01	0,00	0,01	0,01	0,02	0,01	0,01	0,01
Al	1,93	1,95	2,00	1,95	1,99	1,98	1,98	1,99	1,92	1,92	1,92
Fe2+	2,35	2,31	2,26	2,25	2,31	2,22	2,34	2,32	2,05	2,07	2,14
Fe3+	0,07	0,11	0,00	0,03	0,00	0,10	0,00	0,00	0,13	0,15	0,13
Mn	0,03	0,04	0,12	0,12	0,04	0,05	0,04	0,05	0,12	0,10	0,13
Mg	0,25	0,30	0,19	0,19	0,31	0,23	0,25	0,30	0,21	0,21	0,19
Ca	0,36	0,31	0,37	0,42	0,33	0,35	0,37	0,31	0,59	0,57	0,51
Na	0,00	0,00	0,01	0,02	0,01	0,07	0,01	0,00	0,00	0,01	0,00
K	0,00	0,00	0,00	0,00	0,00	0,00	0,00	0,00	0,00	0,01	0,00
Cr	0,00	0,00	0,00	0,00	0,00	0,00	0,00	0,00	0,00	0,00	0,00
Ba	0,00	0,00	0,00	0,00	0,00	0,00	0,00	0,00	0,00	0,00	0,00
Zn	0,00	0,00	0,00	0,00	0,00	0,00	0,00	0,00	0,00	0,00	0,00
Sum	8,00	8,00	8,00	8,00	8,00	8,00	8,00	8,00	8,00	8,00	8,00
XFe	90,56	88,54	92,40	92,30	88,24	90,59	90,47	88,65	90,71	90,94	91,64
Alm	78,56	77,89	76,96	75,54	77,37	77,75	78,24	77,78	69,09	70,24	72,07
Prp	8,19	10,08	6,33	6,30	10,32	8,08	8,25	9,96	7,07	7,00	6,58
Grs	12,18	10,63	12,53	14,17	11,10	12,32	12,28	10,54	19,81	19,36	17,12
Sps	1,07	1,40	4,18	3,98	1,22	1,85	1,23	1,72	4,03	3,41	4,23

Mineral	Grt	Grt	Grt	Grt	Grt	Grt	Grt	Grt	Grt	Grt	Grt
Sample	66.10.1	66.10.1	66.10.1	66.10.1	66.10.1	66.10.1	66.10.1	66.10.1	66.10.1	66.10.1	66.10.1
Analysis	79*	80*	81*	82*	83*	84*	85*	86*	87*	88*	p2
SiO_2	36,93	36,73	36,74	36,79	37,07	36,91	37,89	36,73	36,89	37,09	37,95
TiO_2	0,14	0,12	0,12	0,11	0,13	0,19	0,19	0,13	0,12	0,12	0,22
Al_2O_3	20,23	20,06	20,10	20,13	20,24	20,02	20,47	20,09	20,27	20,31	21,42
FeO	33,03	33,23	32,99	32,63	32,27	32,50	30,50	32,64	32,41	32,00	32,39
MnO	1,91	1,85	1,43	1,57	2,01	2,13	3,11	2,11	1,90	2,18	2,30
MgO	1,53	1,56	1,68	1,75	1,73	1,59	1,74	1,57	1,70	1,76	1,72
CaO	6,29	6,38	6,48	6,72	6,59	6,59	6,77	6,31	6,64	6,55	6,25
Na_2O	0,03	0,01	0,05	0,02	0,01	0,03	0,07	0,02	0,01	0,02	0,06
K_2O	0,02	0,02	0,03	0,03	0,01	0,01	0,16	0,02	0,01	0,01	0,01
Cr_2O_3											0,03
BaO	0,00	0,00	0,00	0,00	0,00	0,01	0,00	0,00	0,00	0,00	
ZnO	0,01	0,02	0,01	0,02	0,01	0,03	0,01	0,00	0,01	0,03	
Sum	100,11	99,99	99,63	99,77	100,09	100,02	100,90	99,63	99,98	100,07	102,37
Si	2,98	2,97	2,97	2,97	2,98	2,98	3,02	2,98	2,97	2,98	2,98
Ti	0,01	0,01	0,01	0,01	0,01	0,01	0,01	0,01	0,01	0,01	0,01
Al	1,92	1,91	1,92	1,92	1,92	1,90	1,92	1,92	1,92	1,93	1,98
Fe2+	2,12	2,10	2,09	2,06	2,07	2,07	1,98	2,09	2,07	2,06	2,09
Fe3+	0,11	0,15	0,14	0,14	0,10	0,12	0,05	0,12	0,12	0,10	0,04
Mn	0,13	0,13	0,10	0,11	0,14	0,15	0,21	0,15	0,13	0,15	0,15
Mg	0,18	0,19	0,20	0,21	0,21	0,19	0,21	0,19	0,20	0,21	0,20
Ca	0,54	0,55	0,56	0,58	0,57	0,57	0,58	0,55	0,57	0,56	0,53
Na	0,00	0,00	0,01	0,00	0,00	0,00	0,01	0,00	0,00	0,00	0,01
K	0,00	0,00	0,00	0,00	0,00	0,00	0,02	0,00	0,00	0,00	0,00
Cr	0,00	0,00	0,00	0,00	0,00	0,00	0,00	0,00	0,00	0,00	0,00
Ba	0,00	0,00	0,00	0,00	0,00	0,00	0,00	0,00	0,00	0,00	0,00
Zn	0,00	0,00	0,00	0,00	0,00	0,00	0,00	0,00	0,00	0,00	0,00
Sum	8,00	8,00	8,00	8,00	8,00	8,00	8,00	8,00	8,00	8,00	8,00
XFe	92,01	91,79	91,20	90,74	90,88	91,56	90,58	91,67	90,98	90,68	91,23
Alm	71,16	70,77	70,84	69,64	69,39	69,56	66,63	70,31	69,47	69,01	70,38
Prp	6,18	6,33	6,84	7,11	6,96	6,41	6,93	6,39	6,89	7,09	6,77
Grs	18,27	18,63	19,00	19,62	19,05	19,14	19,40	18,42	19,28	18,92	17,70
Sps	4,40	4,28	3,32	3,63	4,60	4,90	7,04	4,88	4,36	4,97	5,15

Mineral	Grt	Grt	Grt	Grt	Grt	Grt	Grt	Grt	Grt	Grt	Grt
Sample	66.10.1	66.10.1	62.5.1	62.5.1	62.5.1	62.5.1	62.5.1	62.5.1	62.5.1	62.5.1	62.5.1
Analysis	p4	p6	45*	46*	47*	48*	49*	50*	51*	52*	53*
SiO_2	38,24	37,96	37,20	37,03	37,01	36,92	36,72	36,74	37,02	36,71	37,59
TiO_2	0,17	0,18	0,11	0,13	0,11	0,15	0,16	0,16	0,13	0,14	0,14
Al_2O_3	21,36	21,55	20,76	20,50	20,52	20,45	20,26	20,36	20,35	20,29	21,13
FeO	32,81	32,11	33,55	33,39	33,68	33,49	33,07	33,21	32,98	32,74	32,10
MnO	1,62	1,77	0,59	1,11	1,25	1,54	1,63	1,72	1,74	1,65	1,46
MgO	1,66	1,63	1,88	1,50	1,52	1,35	1,23	1,17	1,07	1,11	1,21
CaO	6,54	7,01	6,32	6,45	5,98	6,26	6,56	6,65	6,81	7,16	7,44
Na_2O	0,06	0,01	0,00	0,00	0,00	0,02	0,01	0,00	0,01	0,00	0,01
K_2O	0,01	0,00	0,01	0,02	0,01	0,01	0,02	0,01	0,01	0,01	0,02
Cr_2O_3	0,02	0,02									
BaO			0,00	0,00	0,00	0,00	0,00	0,00	0,00	0,00	0,00
ZnO			0,00	0,00	0,01	0,01	0,02	0,00	0,02	0,00	0,01
Sum	102,48	102,23	100,44	100,14	100,09	100,20	99,67	100,02	100,15	99,83	101,09
Si	3,00	2,98	2,98	2,98	2,98	2,98	2,98	2,97	2,99	2,97	2,99
Ti	0,01	0,01	0,01	0,01	0,01	0,01	0,01	0,01	0,01	0,01	0,01
Al	1,98	2,00	1,96	1,95	1,95	1,94	1,94	1,94	1,94	1,94	1,98
Fe2+	2,14	2,09	2,18	2,17	2,20	2,17	2,15	2,14	2,15	2,11	2,12
Fe3+	0,01	0,02	0,07	0,08	0,07	0,09	0,09	0,10	0,07	0,11	0,02
Mn	0,11	0,12	0,04	0,08	0,09	0,10	0,11	0,12	0,12	0,11	0,10
Mg	0,19	0,19	0,22	0,18	0,18	0,16	0,15	0,14	0,13	0,13	0,14
Ca	0,55	0,59	0,54	0,56	0,52	0,54	0,57	0,58	0,59	0,62	0,63
Na	0,01	0,00	0,00	0,00	0,00	0,00	0,00	0,00	0,00	0,00	0,00
K	0,00	0,00	0,00	0,00	0,00	0,00	0,00	0,00	0,00	0,00	0,00
Cr	0,00	0,00	0,00	0,00	0,00	0,00	0,00	0,00	0,00	0,00	0,00
Ba	0,00	0,00	0,00	0,00	0,00	0,00	0,00	0,00	0,00	0,00	0,00
Zn	0,00	0,00	0,00	0,00	0,00	0,00	0,00	0,00	0,00	0,00	0,00
Sum	8,00	8,00	8,00	8,00	8,00	8,00	8,00	8,00	8,00	8,00	8,00
XFe	91,68	91,66	90,65	92,32	92,36	93,05	93,55	93,81	94,34	94,01	93,65
Alm	71,54	69,96	72,94	72,75	73,76	72,88	72,13	71,96	71,99	70,82	70,72
Prp	6,49	6,37	7,53	6,05	6,10	5,45	4,97	4,75	4,32	4,51	4,80
Grs	18,37	19,73	18,19	18,65	17,28	18,15	19,13	19,34	19,70	20,86	21,19
Sps	3,60	3,94	1,34	2,54	2,85	3,53	3,77	3,94	3,99	3,80	3,29

Mineral	Grt	Grt	Grt	Grt	Grt	Grt	Grt	Grt	Grt	Grt	Grt
Sample	62.5.1	62.5.1	62.5.1	62.5.1	62.5.1	62.5.1	62.5.1	62.5.1	62.5.1	62.5.1	62.5.1
Analysis	54*	55*	56*	57*	58*	59*	60*	61*	62*	63*	64*
SiO_2	36,56	36,70	37,11	36,93	36,86	36,87	37,25	36,99	36,84	36,82	37,08
TiO_2	0,13	0,12	0,12	0,16	0,13	0,13	0,17	0,14	0,14	0,15	0,12
Al_2O_3	20,10	20,34	20,57	20,41	20,43	20,34	20,28	20,38	20,31	20,37	20,53
FeO	33,61	33,54	33,66	33,81	33,73	33,77	32,77	33,25	33,17	33,47	33,87
MnO	1,49	1,17	1,01	1,12	1,44	1,69	1,62	1,61	1,45	1,19	1,18
MgO	1,37	1,51	1,56	1,49	1,40	1,26	1,12	1,27	1,32	1,43	1,45
CaO	6,30	6,33	6,25	6,22	6,08	6,02	7,20	6,37	6,66	6,39	6,24
Na_2O	0,00	0,00	0,00	0,01	0,01	0,02	0,01	0,01	0,01	0,00	0,01
K_2O	0,02	0,02	0,02	0,02	0,01	0,02	0,01	0,02	0,02	0,02	0,02
Cr_2O_3											
BaO	0,00	0,00	0,00	0,00	0,00	0,00	0,00	0,00	0,00	0,00	0,00
ZnO	0,01	0,01	0,00	0,02	0,00	0,03	0,01	0,00	0,02	0,01	0,01
Sum	99,59	99,75	100,30	100,19	100,09	100,15	100,44	100,04	99,95	99,85	100,52
Si	2,97	2,97	2,98	2,98	2,98	2,98	3,00	2,99	2,98	2,98	2,98
Ti	0,01	0,01	0,01	0,01	0,01	0,01	0,01	0,01	0,01	0,01	0,01
Al	1,92	1,94	1,95	1,94	1,94	1,94	1,92	1,94	1,93	1,94	1,94
Fe2+	2,16	2,16	2,19	2,18	2,18	2,19	2,13	2,17	2,14	2,17	2,19
Fe3+	0,13	0,11	0,07	0,09	0,09	0,10	0,07	0,07	0,10	0,09	0,09
Mn	0,10	0,08	0,07	0,08	0,10	0,12	0,11	0,11	0,10	0,08	0,08
Mg	0,17	0,18	0,19	0,18	0,17	0,15	0,13	0,15	0,16	0,17	0,17
Ca	0,55	0,55	0,54	0,54	0,53	0,52	0,62	0,55	0,58	0,55	0,54
Na	0,00	0,00	0,00	0,00	0,00	0,00	0,00	0,00	0,00	0,00	0,00
K	0,00	0,00	0,00	0,00	0,00	0,00	0,00	0,00	0,00	0,00	0,00
Cr	0,00	0,00	0,00	0,00	0,00	0,00	0,00	0,00	0,00	0,00	0,00
Ba	0,00	0,00	0,00	0,00	0,00	0,00	0,00	0,00	0,00	0,00	0,00
Zn	0,00	0,00	0,00	0,00	0,00	0,00	0,00	0,00	0,00	0,00	0,00
Sum	8,00	8,00	8,00	8,00	8,00	8,00	8,00	8,00	8,00	8,00	8,00
XFe	92,87	92,22	92,13	92,42	92,81	93,50	94,09	93,41	93,07	92,64	92,63
Alm	72,54	72,71	73,41	73,37	73,36	73,48	71,16	72,74	71,93	72,90	73,42
Prp	5,57	6,13	6,27	6,02	5,68	5,11	4,47	5,13	5,35	5,79	5,84
Grs	18,45	18,46	18,02	18,05	17,65	17,53	20,68	18,45	19,38	18,57	18,04
Sps	3,44	2,70	2,29	2,56	3,31	3,88	3,69	3,68	3,33	2,73	2,70

Mineral	Grt	Grt	Grt	Grt	Grt	Grt	Grt	Grt	Grt	Grt	Grt
Sample	62.5.1	62.5.1	62.5.1	62.5.1	62.5.1	62.5.1	62.5.1	62.5.1	62.5.1	62.5.1	62.5.1
Analysis	65*	66*	67*	p2	p4	p6	p7	p8	p12	p14	p16
SiO_2	36,98	36,95	36,88	37,64	37,71	38,23	38,22	37,41	38,34	37,91	38,40
TiO_2	0,13	0,13	0,13	0,17	0,22	0,08	0,12	0,08	0,20	0,14	0,33
Al_2O_3	20,39	20,45	20,38	21,70	21,54	21,89	22,23	21,86	21,16	21,80	21,66
FeO	33,35	33,94	33,61	33,11	32,61	32,84	32,57	33,05	32,27	33,45	32,59
MnO	1,11	1,18	1,44	1,19	1,15	0,66	0,65	0,66	1,69	0,98	0,56
MgO	1,51	1,51	1,40	1,53	1,54	2,82	2,22	2,59	1,18	1,68	1,89
CaO	6,61	6,25	6,59	6,76	7,25	5,65	6,69	5,39	7,29	6,30	7,05
Na_2O	0,02	0,01	0,00	0,01	0,01	0,05	0,02	0,04	0,00	0,03	0,00
K_2O	0,02	0,02	0,02	0,00	0,00	0,00	0,03	0,03	0,00	0,00	0,00
Cr_2O_3				0,02	0,02	0,02	0,04	0,03	0,02	0,02	0,02
BaO	0,00	0,00	0,00								
ZnO	0,02	0,00	0,02								
Sum	100,13	100,43	100,46	102,12	102,04	102,24	102,79	101,14	102,15	102,30	102,51
Si	2,98	2,97	2,96	2,96	2,97	2,98	2,97	2,96	3,02	2,98	3,00
Ti	0,01	0,01	0,01	0,01	0,01	0,00	0,01	0,00	0,01	0,01	0,02
Al	1,94	1,94	1,93	2,01	2,00	2,01	2,04	2,04	1,97	2,02	2,00
Fe2+	2,15	2,17	2,13	2,14	2,11	2,13	2,11	2,14	2,13	2,19	2,13
Fe3+	0,10	0,11	0,13	0,04	0,04	0,01	0,01	0,05	0,00	0,01	0,00
Mn	0,08	0,08	0,10	0,08	0,08	0,04	0,04	0,04	0,11	0,07	0,04
Mg	0,18	0,18	0,17	0,18	0,18	0,33	0,26	0,30	0,14	0,20	0,22
Ca	0,57	0,54	0,57	0,57	0,61	0,47	0,56	0,46	0,62	0,53	0,59
Na	0,00	0,00	0,00	0,00	0,00	0,01	0,00	0,01	0,00	0,00	0,00
K	0,00	0,00	0,00	0,00	0,00	0,00	0,00	0,00	0,00	0,00	0,00
Cr	0,00	0,00	0,00	0,00	0,00	0,00	0,00	0,00	0,00	0,00	0,00
Ba	0,00	0,00	0,00	0,00	0,00	0,00	0,00	0,00	0,00	0,00	0,00
Zn	0,00	0,00	0,00	0,00	0,00	0,00	0,00	0,00	0,00	0,00	0,00
Sum	8,00	8,00	8,00	8,00	8,00	8,00	8,00	8,00	8,00	8,00	8,00
XFe	92,24	92,33	92,70	92,27	92,10	86,64	89,12	87,52	93,87	91,76	90,61
Alm	72,22	73,10	71,92	72,11	70,84	71,59	71,09	72,63	71,04	73,42	71,52
Prp	6,08	6,08	5,67	6,04	6,08	11,04	8,68	10,36	4,64	6,59	7,41
Grs	19,16	18,11	19,12	19,19	20,51	15,89	18,78	15,50	20,56	17,80	19,83
Sps	2,54	2,71	3,29	2,66	2,56	1,47	1,44	1,51	3,76	2,18	1,24

Garnet microprobe analyses (Nevado-Filábride Complex).

Mineral	Grt	Grt	Grt	Grt	Grt	Grt	Grt	Grt	Grt	Grt	Grt
Sample	46.8.1	46.8.1	46.8.1	46.8.1	46.8.1	46.8.1	46.8.1	46.8.1	46.8.1	46.8.1	46.8.1
Analysis	1*	2*	3*	4*	5*	6*	7*	8*	9*	10*	11*
SiO_2	37,34	36,96	36,85	36,22	36,15	36,58	36,27	36,37	36,67	36,34	36,46
TiO_2	0,03	0,07	0,10	0,04	0,09	0,06	0,10	0,07	0,06	0,08	0,14
Al_2O_3	20,84	20,55	20,53	20,22	20,11	20,42	20,11	20,35	20,53	20,36	20,47
FeO	32,62	34,62	35,36	38,20	38,45	38,37	38,17	37,19	36,31	35,40	35,24
MnO	0,20	0,13	0,18	0,36	0,52	0,67	0,99	1,47	2,02	2,41	2,52
MgO	3,57	2,38	1,85	1,40	1,27	1,22	1,16	1,15	1,05	0,95	0,93
CaO	5,25	4,93	5,17	3,30	2,96	2,87	2,86	3,09	3,50	3,84	3,97
Na_2O	0,02	0,02	0,01	0,00	0,02	0,03	0,01	0,04	0,04	0,03	0,03
K_2O	0,02	0,03	0,03	0,01	0,02	0,01	0,01	0,02	0,02	0,02	0,02
Cr_2O_3											
BaO	0,00	0,00	0,00	0,00	0,00	0,00	0,00	0,01	0,00	0,01	0,02
ZnO	0,03	0,01	0,02	0,01	0,02	0,00	0,02	0,01	0,00	0,00	0,01
Sum	99,90	99,71	100,11	99,77	99,61	100,24	99,68	99,76	100,20	99,43	99,81
Si	2,98	2,98	2,97	2,96	2,96	2,98	2,97	2,97	2,98	2,98	2,98
Ti	0,00	0,00	0,01	0,00	0,01	0,00	0,01	0,00	0,00	0,00	0,01
Al	1,96	1,95	1,95	1,95	1,94	1,96	1,94	1,96	1,97	1,97	1,97
Fe2+	2,08	2,25	2,28	2,47	2,50	2,52	2,51	2,45	2,40	2,35	2,34
Fe3+	0,09	0,09	0,10	0,14	0,13	0,09	0,10	0,09	0,07	0,08	0,07
Mn	0,01	0,01	0,01	0,02	0,04	0,05	0,07	0,10	0,14	0,17	0,17
Mg	0,42	0,29	0,22	0,17	0,16	0,15	0,14	0,14	0,13	0,12	0,11
Ca	0,45	0,43	0,45	0,29	0,26	0,25	0,25	0,27	0,30	0,34	0,35
Na	0,00	0,00	0,00	0,00	0,00	0,00	0,00	0,01	0,01	0,00	0,00
K	0,00	0,00	0,00	0,00	0,00	0,00	0,00	0,00	0,00	0,00	0,00
Cr	0,00	0,00	0,00	0,00	0,00	0,00	0,00	0,00	0,00	0,00	0,00
Ba	0,00	0,00	0,00	0,00	0,00	0,00	0,00	0,00	0,00	0,00	0,00
Zn	0,00	0,00	0,00	0,00	0,00	0,00	0,00	0,00	0,00	0,00	0,00
Sum	8,00	8,00	8,00	8,00	8,00	8,00	8,00	8,00	8,00	8,00	8,00
XFe	83,07	88,71	91,12	93,53	94,16	94,45	94,65	94,60	94,97	95,30	95,39
Alm	70,15	75,71	77,01	83,62	84,74	85,01	84,47	82,69	80,78	79,13	78,63
Prp	14,30	9,64	7,51	5,78	5,25	4,99	4,78	4,72	4,27	3,90	3,80
Grs	15,10	14,35	15,06	9,76	8,78	8,43	8,43	9,15	10,27	11,35	11,70
Sps	0,45	0,31	0,42	0,84	1,23	1,57	2,32	3,44	4,68	5,62	5,88

Mineral	Grt	Grt	Grt	Grt	Grt	Grt	Grt	Grt	Grt	Grt	Grt
Sample	46.8.1	46.8.1	46.8.1	46.8.1	46.8.1	46.8.1	46.8.1	46.8.1	46.8.1	46.8.1	46.8.1
Analysis	12*	13*	14*	15*	16*	17*	18*	19*	20*	21*	22*
SiO_2	36,36	36,09	36,26	36,25	36,28	36,36	36,94	36,93	36,48	36,89	36,45
TiO_2	0,21	0,17	0,05	0,07	0,05	0,07	0,07	0,07	0,04	0,07	0,06
Al_2O_3	20,36	20,05	20,12	20,08	20,22	20,37	20,49	20,57	20,44	20,64	20,36
FeO	36,64	37,05	37,82	37,96	37,87	36,04	35,40	32,42	35,19	33,70	34,35
MnO	1,83	1,53	1,05	0,91	0,64	0,31	0,18	0,10	0,07	0,62	1,10
MgO	1,04	1,10	1,14	1,19	1,39	2,05	2,33	3,99	3,10	1,46	1,13
CaO	3,27	3,20	3,02	2,90	3,05	4,37	4,64	5,07	3,82	6,72	6,05
Na_2O	0,02	0,02	0,02	0,01	0,01	0,00	0,01	0,01	0,01	0,01	0,02
K_2O	0,02	0,01	0,01	0,02	0,01	0,02	0,01	0,02	0,02	0,02	0,02
Cr_2O_3											
BaO	0,00	0,00	0,00	0,00	0,00	0,00	0,00	0,00	0,00	0,00	0,00
ZnO	0,01	0,02	0,00	0,01	0,02	0,01	0,02	0,02	0,00	0,00	0,01
Sum	99,75	99,24	99,49	99,40	99,55	99,59	100,09	99,20	99,18	100,13	99,55
Si	2,97	2,97	2,97	2,98	2,97	2,95	2,97	2,96	2,95	2,97	2,96
Ti	0,01	0,01	0,00	0,00	0,00	0,00	0,00	0,00	0,00	0,00	0,00
Al	1,96	1,94	1,95	1,94	1,95	1,95	1,94	1,94	1,95	1,96	1,95
Fe2+	2,44	2,44	2,49	2,51	2,48	2,30	2,28	2,04	2,24	2,17	2,22
Fe3+	0,07	0,10	0,10	0,10	0,11	0,14	0,11	0,14	0,15	0,10	0,12
Mn	0,13	0,11	0,07	0,06	0,04	0,02	0,01	0,01	0,01	0,04	0,08
Mg	0,13	0,13	0,14	0,15	0,17	0,25	0,28	0,48	0,37	0,17	0,14
Ca	0,29	0,28	0,27	0,26	0,27	0,38	0,40	0,43	0,33	0,58	0,53
Na	0,00	0,00	0,00	0,00	0,00	0,00	0,00	0,00	0,00	0,00	0,00
K	0,00	0,00	0,00	0,00	0,00	0,00	0,00	0,00	0,00	0,00	0,00
Cr	0,00	0,00	0,00	0,00	0,00	0,00	0,00	0,00	0,00	0,00	0,00
Ba	0,00	0,00	0,00	0,00	0,00	0,00	0,00	0,00	0,00	0,00	0,00
Zn	0,00	0,00	0,00	0,00	0,00	0,00	0,00	0,00	0,00	0,00	0,00
Sum	8,00	8,00	8,00	8,00	8,00	8,00	8,00	8,00	8,00	8,00	8,00
XFe	95,06	94,77	94,68	94,52	93,61	90,28	89,05	81,05	85,68	92,54	94,17
Alm	81,87	82,35	83,90	84,39	83,77	78,01	76,69	68,93	75,88	73,16	74,98
Prp	4,26	4,54	4,71	4,90	5,71	8,40	9,43	16,12	12,69	5,90	4,64
Grs	9,62	9,51	8,94	8,59	9,02	12,88	13,48	14,72	11,26	19,52	17,81
Sps	4,25	3,60	2,46	2,12	1,50	0,71	0,40	0,23	0,17	1,42	2,56

Mineral	Grt	Grt	Grt	Grt	Grt	Grt	Grt	Grt	Grt	Grt	Grt
Sample	46.8.1	46.8.1	46.8.1	46.8.1	46.8.1	46.8.1	46.8.1	46.8.1	46.8.1	46.8.1	46.8.1
Analysis	23*	24*	25*	26*	27*	28*	29*	30*	31*	32*	33*
SiO_2	36,35	36,31	36,62	36,48	36,36	36,34	36,49	36,68	36,74	36,80	36,57
TiO_2	0,07	0,08	0,11	0,10	0,11	0,07	0,09	0,10	0,06	0,05	0,04
Al_2O_3	20,31	20,37	20,34	20,19	20,04	20,32	20,28	20,39	20,54	20,71	20,46
FeO	32,94	31,72	30,93	30,40	30,65	30,85	30,62	31,72	32,37	33,55	34,54
MnO	1,47	1,96	2,57	2,68	2,10	2,93	2,39	2,16	1,90	0,85	0,34
MgO	0,99	0,94	1,04	1,30	1,21	0,87	1,48	0,90	0,97	1,28	2,12
CaO	7,13	7,60	7,77	7,61	8,07	7,61	7,41	7,63	7,02	6,74	5,25
Na_2O	0,03	0,03	0,03	0,03	0,02	0,02	0,04	0,00	0,02	0,02	0,01
K_2O	0,02	0,02	0,02	0,02	0,02	0,02	0,02	0,02	0,02	0,02	0,02
Cr_2O_3											
BaO	0,00	0,00	0,00	0,00	0,00	0,00	0,02	0,00	0,00	0,00	0,00
ZnO	0,00	0,02	0,00	0,01	0,03	0,00	0,02	0,00	0,00	0,00	0,01
Sum	99,29	99,05	99,44	98,82	98,61	99,01	98,85	99,60	99,64	100,01	99,35
Si	2,96	2,96	2,97	2,97	2,97	2,96	2,97	2,97	2,98	2,97	2,96
Ti	0,00	0,00	0,01	0,01	0,01	0,00	0,01	0,01	0,00	0,00	0,00
Al	1,95	1,96	1,94	1,94	1,93	1,95	1,94	1,95	1,96	1,97	1,95
Fe2+	2,11	2,04	1,99	1,96	1,97	1,98	1,97	2,05	2,11	2,17	2,22
Fe3+	0,14	0,12	0,11	0,11	0,13	0,12	0,12	0,10	0,08	0,10	0,12
Mn	0,10	0,14	0,18	0,18	0,15	0,20	0,16	0,15	0,13	0,06	0,02
Mg	0,12	0,11	0,13	0,16	0,15	0,11	0,18	0,11	0,12	0,15	0,26
Ca	0,62	0,66	0,68	0,66	0,71	0,66	0,65	0,66	0,61	0,58	0,46
Na	0,00	0,00	0,00	0,01	0,00	0,00	0,01	0,00	0,00	0,00	0,00
K	0,00	0,00	0,00	0,00	0,00	0,00	0,00	0,00	0,00	0,00	0,00
Cr	0,00	0,00	0,00	0,00	0,00	0,00	0,00	0,00	0,00	0,00	0,00
Ba	0,00	0,00	0,00	0,00	0,00	0,00	0,00	0,00	0,00	0,00	0,00
Zn	0,00	0,00	0,00	0,00	0,00	0,00	0,00	0,00	0,00	0,00	0,00
Sum	8,00	8,00	8,00	8,00	8,00	8,00	8,00	8,00	8,00	8,00	8,00
XFe	94,62	94,70	94,03	92,53	93,01	94,97	91,63	94,96	94,74	93,36	89,66
Alm	71,42	69,05	67,00	66,01	66,31	67,12	66,53	69,07	71,15	73,17	75,15
Prp	4,06	3,87	4,26	5,33	4,98	3,56	6,07	3,67	3,95	5,20	8,67
Grs	21,07	22,49	22,79	22,43	23,81	22,49	21,83	22,28	20,51	19,68	15,40
Sps	3,44	4,60	5,95	6,23	4,90	6,83	5,57	4,98	4,39	1,95	0,78

Mineral	Grt	Grt	Grt	Grt	Grt	Grt	Grt	Grt	Grt	Grt	Grt
Sample	46.8.1	46.8.1	46.8.1	46.8.1	46.8.1	46.8.1	46.8.1	46.8.1	46.8.1	46.8.1	46.8.1
Analysis	34*	35*	45*	46*	47*	48*	49*	50*	51*	52*	53*
SiO_2	36,87	37,21	36,70	36,53	36,64	36,76	36,39	36,37	36,74	37,00	36,79
TiO_2	0,03	0,04	0,02	0,04	0,07	0,03	0,05	0,03	0,04	0,13	0,03
Al_2O_3	20,64	20,86	20,59	20,50	20,39	20,51	20,44	20,50	20,56	20,66	20,52
FeO	35,36	29,79	35,28	34,81	32,36	34,57	33,91	35,55	34,12	32,99	34,33
MnO	0,07	0,08	0,07	0,31	0,65	0,88	0,82	0,27	0,33	0,04	0,36
MgO	3,09	5,08	3,00	2,17	1,26	1,28	1,29	2,88	2,95	3,39	2,00
CaO	3,69	5,84	3,67	5,15	7,92	5,97	6,49	3,53	4,70	5,32	5,79
Na_2O	0,01	0,01	0,01	0,01	0,00	0,01	0,01	0,01	0,01	0,01	0,02
K_2O	0,01	0,02	0,02	0,02	0,02	0,02	0,03	0,02	0,02	0,02	0,02
Cr_2O_3											
BaO	0,00	0,00	0,00	0,01	0,00	0,00	0,00	0,00	0,00	0,00	0,00
ZnO	0,03	0,02	0,00	0,02	0,01	0,03	0,00	0,03	0,02	0,02	0,04
Sum	99,80	98,96	99,37	99,57	99,32	100,06	99,42	99,19	99,49	99,60	99,88
Si	2,97	2,96	2,97	2,95	2,97	2,97	2,96	2,95	2,96	2,96	2,96
Ti	0,00	0,00	0,00	0,00	0,00	0,00	0,00	0,00	0,00	0,01	0,00
Al	1,96	1,95	1,96	1,95	1,95	1,95	1,96	1,96	1,95	1,95	1,95
Fe2+	2,27	1,85	2,27	2,22	2,08	2,23	2,17	2,27	2,17	2,10	2,19
Fe3+	0,11	0,13	0,11	0,13	0,11	0,10	0,13	0,14	0,13	0,11	0,12
Mn	0,00	0,01	0,01	0,02	0,04	0,06	0,06	0,02	0,02	0,00	0,02
Mg	0,37	0,60	0,36	0,26	0,15	0,15	0,16	0,35	0,35	0,41	0,24
Ca	0,32	0,50	0,32	0,45	0,69	0,52	0,56	0,31	0,41	0,46	0,50
Na	0,00	0,00	0,00	0,00	0,00	0,00	0,00	0,00	0,00	0,00	0,00
K	0,00	0,00	0,00	0,00	0,00	0,00	0,00	0,00	0,00	0,00	0,00
Cr	0,00	0,00	0,00	0,00	0,00	0,00	0,00	0,00	0,00	0,00	0,00
Ba	0,00	0,00	0,00	0,00	0,00	0,00	0,00	0,00	0,00	0,00	0,00
Zn	0,00	0,00	0,00	0,00	0,00	0,00	0,00	0,00	0,00	0,00	0,00
Sum	8,00	8,00	8,00	8,00	8,00	8,00	8,00	8,00	8,00	8,00	8,00
XFe	85,95	75,42	86,31	89,45	93,20	93,53	93,31	86,67	85,95	83,81	90,13
Alm	76,59	62,56	76,89	75,27	70,21	75,32	73,66	77,09	73,51	70,82	74,14
Prp	12,52	20,39	12,20	8,87	5,12	5,21	5,28	11,85	12,01	13,68	8,12
Grs	10,74	16,85	10,74	15,13	23,16	17,43	19,15	10,43	13,72	15,41	16,90
Sps	0,15	0,19	0,17	0,73	1,51	2,04	1,92	0,62	0,76	0,10	0,84

Mineral	Grt	Grt	Grt	Grt	Grt	Grt	Grt	Grt	Grt	Grt	Grt
Sample	46.8.1	46.8.1	46.8.1	46.8.1	46.8.1	46.8.1	46.8.1	46.8.1	46.8.1	46.8.1	46.8.1
Analysis	54*	55*	56*	57*	58*	59*	60*	61*	62*	63*	64*
SiO_2	36,05	35,96	36,90	36,53	36,80	37,12	37,01	35,95	36,16	36,10	36,13
TiO_2	0,05	0,06	0,02	0,07	0,07	0,04	0,06	0,09	0,06	0,04	0,06
Al_2O_3	20,28	20,14	20,63	20,45	20,68	20,91	20,78	20,12	20,31	20,26	20,35
FeO	32,96	33,23	33,22	33,16	33,56	32,90	33,71	36,25	36,11	37,04	37,57
MnO	0,49	0,72	0,90	1,09	0,99	0,72	0,06	1,75	1,70	1,15	1,28
MgO	1,61	1,43	1,91	1,11	1,13	1,61	3,47	1,05	1,19	1,65	1,15
CaO	6,92	6,88	6,23	7,27	6,77	6,88	4,86	3,69	3,60	2,86	2,93
Na_2O	0,01	0,04	0,00	0,02	0,00	0,02	0,00	0,01	0,00	0,02	0,02
K_2O	0,03	0,02	0,02	0,02	0,03	0,02	0,02	0,03	0,02	0,02	0,01
Cr_2O_3											
BaO	0,00	0,00	0,00	0,01	0,00	0,00	0,00	0,01	0,00	0,00	0,00
ZnO	0,00	0,01	0,01	0,02	0,00	0,00	0,01	0,00	0,00	0,03	0,01
Sum	98,40	98,49	99,84	99,74	100,03	100,22	99,98	98,94	99,14	99,16	99,52
Si	2,95	2,94	2,97	2,96	2,97	2,98	2,95	2,96	2,97	2,96	2,96
Ti	0,00	0,00	0,00	0,00	0,00	0,00	0,00	0,01	0,00	0,00	0,00
Al	1,95	1,94	1,96	1,95	1,97	1,98	1,95	1,95	1,97	1,96	1,97
Fe2+	2,10	2,10	2,14	2,11	2,18	2,14	2,12	2,38	2,39	2,42	2,47
Fe3+	0,15	0,17	0,10	0,13	0,09	0,07	0,13	0,12	0,09	0,12	0,11
Mn	0,03	0,05	0,06	0,07	0,07	0,05	0,00	0,12	0,12	0,08	0,09
Mg	0,20	0,17	0,23	0,13	0,14	0,19	0,41	0,13	0,15	0,20	0,14
Ca	0,61	0,60	0,54	0,63	0,59	0,59	0,42	0,33	0,32	0,25	0,26
Na	0,00	0,01	0,00	0,00	0,00	0,00	0,00	0,00	0,00	0,00	0,00
K	0,00	0,00	0,00	0,00	0,00	0,00	0,00	0,00	0,00	0,00	0,00
Cr	0,00	0,00	0,00	0,00	0,00	0,00	0,00	0,00	0,00	0,00	0,00
Ba	0,00	0,00	0,00	0,00	0,00	0,00	0,00	0,00	0,00	0,00	0,00
Zn	0,00	0,00	0,00	0,00	0,00	0,00	0,00	0,00	0,00	0,00	0,00
Sum	8,00	8,00	8,00	8,00	8,00	8,00	8,00	8,00	8,00	8,00	8,00
XFe	91,48	92,32	90,29	94,06	94,13	91,72	83,68	94,86	94,24	92,30	94,60
Alm	71,58	71,73	72,07	71,58	73,43	71,95	71,78	80,51	80,43	81,96	83,53
Prp	6,67	5,97	7,75	4,52	4,58	6,49	14,00	4,36	4,91	6,84	4,77
Grs	20,61	20,60	18,11	21,37	19,72	19,91	14,08	11,00	10,66	8,50	8,71
Sps	1,15	1,70	2,07	2,52	2,27	1,64	0,14	4,12	3,99	2,70	3,00

Mineral	Grt	Grt	Grt	Grt	Grt	Grt	Grt	Grt	Grt	Grt	Grt
Sample	46.8.1	46.8.1	46.8.1	46.8.1	46.8.1	46.8.1	46.8.1	46.8.1	46.8.1	46.8.1	46.8.1
Analysis	65*	66*	67*	68*	69*	70*	71*	72*	73*	74*	75*
SiO_2	36,19	36,10	36,35	36,18	36,11	36,09	36,10	36,09	36,11	36,28	36,32
TiO_2	0,05	0,09	0,07	0,06	0,05	0,06	0,06	0,04	0,06	0,07	0,07
Al_2O_3	20,31	20,24	20,29	20,35	20,29	20,33	20,18	20,45	20,15	20,26	20,30
FeO	37,88	37,89	38,04	38,30	37,54	38,43	38,80	38,46	38,65	37,67	37,11
MnO	0,95	0,95	0,74	0,52	0,35	0,40	0,29	0,24	0,22	0,14	0,13
MgO	1,23	1,21	1,27	1,41	1,81	1,45	1,64	1,85	1,88	2,06	2,15
CaO	3,11	2,97	3,02	2,92	3,25	2,76	2,49	2,49	2,51	2,95	3,43
Na_2O	0,01	0,02	0,02	0,01	0,01	0,01	0,00	0,01	0,02	0,01	0,01
K_2O	0,02	0,01	0,01	0,01	0,03	0,00	0,02	0,01	0,02	0,01	0,01
Cr_2O_3											
BaO	0,00	0,00	0,00	0,00	0,00	0,00	0,00	0,00	0,00	0,00	0,00
ZnO	0,01	0,02	0,00	0,01	0,01	0,01	0,03	0,03	0,00	0,00	0,01
Sum	99,76	99,49	99,79	99,78	99,44	99,54	99,60	99,67	99,61	99,45	99,54
Si	2,96	2,96	2,97	2,95	2,95	2,95	2,95	2,94	2,95	2,96	2,95
Ti	0,00	0,01	0,00	0,00	0,00	0,00	0,00	0,00	0,00	0,00	0,00
Al	1,96	1,96	1,95	1,96	1,95	1,96	1,95	1,97	1,94	1,95	1,95
Fe2+	2,46	2,48	2,50	2,49	2,41	2,51	2,51	2,48	2,48	2,44	2,38
Fe3+	0,12	0,12	0,10	0,13	0,15	0,12	0,14	0,14	0,16	0,13	0,14
Mn	0,07	0,07	0,05	0,04	0,02	0,03	0,02	0,02	0,01	0,01	0,01
Mg	0,15	0,15	0,15	0,17	0,22	0,18	0,20	0,23	0,23	0,25	0,26
Ca	0,27	0,26	0,26	0,26	0,28	0,24	0,22	0,22	0,22	0,26	0,30
Na	0,00	0,00	0,00	0,00	0,00	0,00	0,00	0,00	0,00	0,00	0,00
K	0,00	0,00	0,00	0,00	0,00	0,00	0,00	0,00	0,00	0,00	0,00
Cr	0,00	0,00	0,00	0,00	0,00	0,00	0,00	0,00	0,00	0,00	0,00
Ba	0,00	0,00	0,00	0,00	0,00	0,00	0,00	0,00	0,00	0,00	0,00
Zn	0,00	0,00	0,00	0,00	0,00	0,00	0,00	0,00	0,00	0,00	0,00
Sum	8,00	8,00	8,00	8,00	8,00	8,00	8,00	8,00	8,00	8,00	8,00
XFe	94,28	94,37	94,18	93,54	91,65	93,43	92,63	91,67	91,54	90,67	90,14
Alm	83,47	83,95	84,16	84,31	82,03	84,89	85,15	84,38	84,23	82,45	80,73
Prp	5,06	5,01	5,20	5,82	7,47	5,97	6,77	7,66	7,79	8,49	8,83
Grs	9,24	8,82	8,91	8,65	9,66	8,20	7,41	7,40	7,47	8,73	10,14
Sps	2,23	2,23	1,73	1,23	0,83	0,94	0,68	0,56	0,51	0,33	0,31

Mineral	Grt	Grt	Grt	Grt	Grt	Grt	Grt	Grt	Grt	Grt	Grt
Sample	46.8.1	46.8.1	46.8.1	46.8.1	46.8.1	46.8.1	46.8.1	46.8.1	46.8.1	46.8.1	46.8.1
Analysis	p37	p38	p39	p40	p41	p42	p43	p44	p44b	p44c	p45
SiO_2	39,63	38,42	38,19	37,41	38,14	37,81	38,59	38,05	41,41	39,21	36,61
TiO_2	0,03	0,05	0,05	0,06	0,06	0,05	0,07	0,04	0,05	0,06	0,05
Al_2O_3	22,49	21,64	21,74	21,75	21,72	21,73	21,86	21,99	23,85	22,53	21,16
FeO	31,60	32,55	33,15	32,90	32,21	32,64	32,54	34,52	34,39	29,06	31,48
MnO	0,08	0,54	1,04	1,27	1,39	1,59	1,38	0,29	0,04	0,11	0,32
MgO	4,56	1,69	1,14	1,04	0,97	0,98	1,02	2,28	3,48	5,28	3,70
CaO	5,08	7,46	6,89	7,11	7,64	7,27	7,43	5,13	4,24	6,48	5,32
Na_2O	0,00	0,04	0,03	0,06	0,03	0,06	0,05	0,05	0,02	0,01	0,07
K_2O	0,00	0,01	0,01	0,01	0,01	0,00	0,00	0,01	0,01	0,01	0,02
Cr_2O_3	0,02	0,00	0,01	0,02	0,01	0,03	0,00	0,01	0,01	0,00	0,03
BaO											
ZnO											
Sum	103,48	102,39	102,24	101,61	102,17	102,15	102,94	102,36	107,48	102,74	98,76
Si	3,02	3,01	3,01	2,96	3,00	2,98	3,02	2,98	3,06	2,99	2,94
Ti	0,00	0,00	0,00	0,00	0,00	0,00	0,00	0,00	0,00	0,00	0,00
Al	2,02	2,00	2,02	2,03	2,02	2,02	2,01	2,03	2,08	2,02	2,00
Fe2+	2,02	2,13	2,18	2,14	2,12	2,13	2,13	2,25	2,13	1,85	2,00
Fe3+	0,00	0,00	0,00	0,04	0,00	0,02	0,00	0,01	0,00	0,00	0,12
Mn	0,00	0,04	0,07	0,09	0,09	0,11	0,09	0,02	0,00	0,01	0,02
Mg	0,52	0,20	0,13	0,12	0,11	0,12	0,12	0,27	0,38	0,60	0,44
Ca	0,42	0,63	0,58	0,60	0,64	0,61	0,62	0,43	0,34	0,53	0,46
Na	0,00	0,01	0,01	0,01	0,01	0,01	0,01	0,01	0,00	0,00	0,01
K	0,00	0,00	0,00	0,00	0,00	0,00	0,00	0,00	0,00	0,00	0,00
Cr	0,00	0,00	0,00	0,00	0,00	0,00	0,00	0,00	0,00	0,00	0,00
Ba	0,00	0,00	0,00	0,00	0,00	0,00	0,00	0,00	0,00	0,00	0,00
Zn	0,00	0,00	0,00	0,00	0,00	0,00	0,00	0,00	0,00	0,00	0,00
Sum	8,00	8,00	8,00	8,00	8,00	8,00	8,00	8,00	8,00	8,00	8,00
XFe	79,55	91,54	94,20	94,59	94,91	94,87	94,71	89,44	84,72	75,54	81,84
Alm	68,24	71,29	73,55	72,50	71,38	71,85	71,87	75,89	74,66	61,99	68,40
Prp	17,54	6,59	4,53	4,15	3,83	3,89	4,02	8,96	13,47	20,07	15,18
Grs	14,05	20,93	19,58	20,46	21,68	20,69	21,02	14,50	11,78	17,71	15,68
Sps	0,17	1,20	2,34	2,90	3,11	3,57	3,10	0,64	0,09	0,23	0,74

Mineral	Grt	Grt	Grt	Grt	Grt	Grt	Grt	Grt	Grt	Grt	Grt
Sample	46.8.1	46.8.1	46.8.1	46.8.1	46.8.1	46.8.1	46.8.1	46.8.1	46.8.1	46.8.1b	46.8.1b
Analysis	p46	p47	p48	p49	p50	p51	p52	p52b	p52c	p17	p18
SiO_2	38,30	38,24	38,09	38,24	38,02	38,29	37,94	38,52	39,30	37,24	37,52
TiO_2	0,06	0,25	0,06	0,10	0,17	0,05	0,04	0,14	0,05	0,04	0,05
Al_2O_3	21,74	21,86	21,57	21,53	21,70	21,67	21,53	21,93	22,50	21,39	21,20
FeO	35,99	36,13	32,73	31,82	31,89	32,50	35,27	34,18	29,24	35,99	35,47
MnO	0,07	0,32	1,20	2,07	1,80	0,69	0,30	0,10	0,15	0,43	0,94
MgO	2,81	2,38	0,80	0,71	0,76	1,23	2,31	3,12	5,29	1,90	1,39
CaO	3,23	3,49	7,25	7,72	7,83	7,71	4,15	4,53	6,01	2,69	3,39
Na_2O	0,04	0,04	0,06	0,07	0,05	0,02	0,03	0,03	0,02	0,01	0,03
K_2O	0,00	0,01	0,00	0,00	0,00	0,01	0,01	0,00	0,00	0,00	0,00
Cr_2O_3	0,00	0,00	0,01	0,01	0,02	0,02	0,00	0,02	0,01	0,01	0,03
BaO											
ZnO											
Sum	102,24	102,73	101,77	102,27	102,24	102,19	101,56	102,57	102,57	99,71	100,01
Si	3,01	3,00	3,02	3,01	3,00	3,01	3,00	3,00	3,00	3,02	3,04
Ti	0,00	0,01	0,00	0,01	0,01	0,00	0,00	0,01	0,00	0,00	0,00
Al	2,01	2,02	2,01	2,00	2,01	2,01	2,01	2,01	2,02	2,04	2,02
Fe2+	2,36	2,37	2,17	2,10	2,10	2,14	2,34	2,23	1,87	2,44	2,40
Fe3+	0,00	0,00	0,00	0,00	0,00	0,00	0,00	0,00	0,00	0,00	0,00
Mn	0,00	0,02	0,08	0,14	0,12	0,05	0,02	0,01	0,01	0,03	0,06
Mg	0,33	0,28	0,09	0,08	0,09	0,14	0,27	0,36	0,60	0,23	0,17
Ca	0,27	0,29	0,61	0,65	0,66	0,65	0,35	0,38	0,49	0,23	0,29
Na	0,01	0,01	0,01	0,01	0,01	0,00	0,01	0,00	0,00	0,00	0,00
K	0,00	0,00	0,00	0,00	0,00	0,00	0,00	0,00	0,00	0,00	0,00
Cr	0,00	0,00	0,00	0,00	0,00	0,00	0,00	0,00	0,00	0,00	0,00
Ba	0,00	0,00	0,00	0,00	0,00	0,00	0,00	0,00	0,00	0,00	0,00
Zn	0,00	0,00	0,00	0,00	0,00	0,00	0,00	0,00	0,00	0,00	0,00
Sum	8,00	8,00	8,00	8,00	8,00	8,00	8,00	8,00	8,00	8,00	8,00
XFe	87,77	89,49	95,81	96,19	95,93	93,66	89,56	85,99	75,61	91,39	93,47
Alm	79,60	79,99	73,29	70,61	70,73	71,79	78,39	74,87	62,84	83,19	82,05
Prp	11,09	9,39	3,21	2,80	3,00	4,86	9,13	12,19	20,27	7,84	5,73
Grs	9,16	9,89	20,78	21,94	22,24	21,81	11,81	12,72	16,56	7,97	10,03
Sps	0,15	0,72	2,72	4,66	4,04	1,55	0,67	0,22	0,34	1,00	2,19

Mineral	Grt	Grt	Grt	Grt	Grt	Grt	Grt	Grt	Grt	Grt	Grt
Sample	46.8.1b	46.8.1b	46.8.1b	46.8.1b	46.8.1b	46.8.1b	46.8.1b	46.8.1b	46.8.1b	46.8.1b	46.8.1b
Analysis	p19	p20	p21	p22	p23	p24	p25	p26	p27	p28	p29
SiO_2	37,20	37,22	37,18	37,40	37,06	37,31	37,14	37,10	37,15	37,52	37,52
TiO_2	0,05	0,10	0,24	0,09	0,04	0,03	0,06	0,08	0,05	0,06	0,06
Al_2O_3	21,22	21,22	21,11	21,19	20,90	21,21	21,23	21,28	20,92	21,28	21,37
FeO	35,63	35,54	34,59	34,69	34,06	34,81	31,44	31,34	31,06	31,17	30,86
MnO	1,12	1,25	1,20	1,61	1,30	1,77	2,77	2,82	2,83	3,05	2,92
MgO	1,37	1,26	1,60	1,30	1,85	1,29	0,88	0,84	0,90	0,82	0,84
CaO	3,14	3,31	3,53	3,55	3,14	3,35	5,60	5,64	5,77	5,46	5,99
Na_2O	0,02	0,02	0,03	0,03	0,01	0,03	0,05	0,04	0,04	0,06	0,06
K_2O	0,00	0,00	0,00	0,00	0,00	0,00	0,00	0,00	0,00	0,00	0,00
Cr_2O_3	0,01	0,03	0,02	0,02	0,01	0,02	0,02	0,01	0,01	0,01	0,02
BaO											
ZnO											
Sum	99,75	99,95	99,49	99,88	98,37	99,81	99,18	99,15	98,73	99,44	99,63
Si	3,02	3,02	3,02	3,03	3,04	3,03	3,02	3,02	3,04	3,05	3,04
Ti	0,00	0,01	0,01	0,01	0,00	0,00	0,00	0,00	0,00	0,00	0,00
Al	2,03	2,03	2,02	2,03	2,02	2,03	2,04	2,04	2,02	2,04	2,04
Fe2+	2,42	2,41	2,35	2,35	2,34	2,36	2,14	2,13	2,12	2,12	2,09
Fe3+	0,00	0,00	0,00	0,00	0,00	0,00	0,00	0,00	0,00	0,00	0,00
Mn	0,08	0,09	0,08	0,11	0,09	0,12	0,19	0,19	0,20	0,21	0,20
Mg	0,17	0,15	0,19	0,16	0,23	0,16	0,11	0,10	0,11	0,10	0,10
Ca	0,27	0,29	0,31	0,31	0,28	0,29	0,49	0,49	0,51	0,48	0,52
Na	0,00	0,00	0,00	0,01	0,00	0,00	0,01	0,01	0,01	0,01	0,01
K	0,00	0,00	0,00	0,00	0,00	0,00	0,00	0,00	0,00	0,00	0,00
Cr	0,00	0,00	0,00	0,00	0,00	0,00	0,00	0,00	0,00	0,00	0,00
Ba	0,00	0,00	0,00	0,00	0,00	0,00	0,00	0,00	0,00	0,00	0,00
Zn	0,00	0,00	0,00	0,00	0,00	0,00	0,00	0,00	0,00	0,00	0,00
Sum	8,00	8,00	8,00	8,00	8,00	8,00	8,00	8,00	8,00	8,00	8,00
XFe	93,59	94,04	92,37	93,74	91,18	93,82	95,25	95,42	95,10	95,50	95,35
Alm	82,44	82,09	80,10	80,33	79,78	80,61	73,15	73,00	72,37	72,95	71,76
Prp	5,65	5,20	6,61	5,36	7,71	5,31	3,65	3,50	3,73	3,44	3,50
Grs	9,30	9,79	10,48	10,54	9,43	9,94	16,69	16,83	17,24	16,38	17,86
Sps	2,62	2,92	2,80	3,77	3,08	4,14	6,51	6,66	6,67	7,23	6,88

Mineral	Grt	Grt	Grt	Grt	Grt	Grt	Grt	Grt	Grt	Grt	Grt
Sample	46.8.1b	46.8.1b	46.8.1b	46.8.1b	46.8.1b	46.8.1b	46.8.1b	46.8.1b	46.8.1b	46.8.1b	46.8.1b
Analysis	p30	p31	p32	p33	p34	p35	p36	p37	p38	p39	p40
SiO_2	37,10	37,28	37,36	37,28	37,63	37,66	36,41	37,19	37,19	37,05	37,60
TiO_2	0,05	0,07	0,10	0,07	0,22	0,03	0,07	0,01	0,05	0,03	0,03
Al_2O_3	20,91	21,21	21,22	21,04	21,34	21,29	20,78	21,21	21,38	21,47	21,53
FeO	31,39	31,33	31,27	31,23	32,00	33,36	33,32	35,05	34,61	35,98	36,08
MnO	2,93	2,85	2,80	2,63	2,52	2,35	1,81	1,65	1,47	0,80	0,60
MgO	0,87	0,90	0,85	0,83	0,95	1,10	1,40	1,26	1,63	1,68	1,82
CaO	5,43	5,55	5,78	5,95	5,20	4,31	4,25	3,22	3,44	2,89	2,86
Na_2O	0,04	0,04	0,05	0,03	0,04	0,04	0,04	0,00	0,03	0,02	0,02
K_2O	0,00	0,00	0,00	0,00	0,00	0,00	0,00	0,01	0,00	0,01	0,00
Cr_2O_3	0,01	0,02	0,02	0,03	0,02	0,02	0,03	0,00	0,01	0,01	0,02
BaO											
ZnO											
Sum	98,73	99,24	99,44	99,09	99,92	100,15	98,09	99,59	99,79	99,94	100,53
Si	3,04	3,03	3,03	3,04	3,04	3,04	3,00	3,03	3,01	3,00	3,02
Ti	0,00	0,00	0,01	0,00	0,01	0,00	0,00	0,00	0,00	0,00	0,00
Al	2,02	2,03	2,03	2,02	2,03	2,03	2,02	2,04	2,04	2,05	2,04
Fe2+	2,15	2,13	2,12	2,13	2,16	2,25	2,30	2,39	2,34	2,44	2,43
Fe3+	0,00	0,00	0,00	0,00	0,00	0,00	0,00	0,00	0,00	0,00	0,00
Mn	0,20	0,20	0,19	0,18	0,17	0,16	0,13	0,11	0,10	0,06	0,04
Mg	0,11	0,11	0,10	0,10	0,11	0,13	0,17	0,15	0,20	0,20	0,22
Ca	0,48	0,48	0,50	0,52	0,45	0,37	0,38	0,28	0,30	0,25	0,25
Na	0,01	0,01	0,01	0,01	0,01	0,01	0,01	0,00	0,00	0,00	0,00
K	0,00	0,00	0,00	0,00	0,00	0,00	0,00	0,00	0,00	0,00	0,00
Cr	0,00	0,00	0,00	0,00	0,00	0,00	0,00	0,00	0,00	0,00	0,00
Ba	0,00	0,00	0,00	0,00	0,00	0,00	0,00	0,00	0,00	0,00	0,00
Zn	0,00	0,00	0,00	0,00	0,00	0,00	0,00	0,00	0,00	0,00	0,00
Sum	8,00	8,00	8,00	8,00	8,00	8,00	8,00	8,00	8,00	8,00	8,00
XFe	95,29	95,15	95,40	95,50	94,98	94,46	93,03	93,98	92,26	92,31	91,76
Alm	73,24	73,00	72,68	72,66	74,58	77,19	77,32	81,34	79,74	82,73	82,79
Prp	3,62	3,72	3,51	3,42	3,94	4,53	5,80	5,21	6,69	6,89	7,43
Grs	16,22	16,57	17,22	17,73	15,52	12,76	12,64	9,57	10,15	8,50	8,40
Sps	6,92	6,71	6,60	6,19	5,95	5,51	4,24	3,88	3,43	1,87	1,38

Mineral	Grt	Grt	Grt	Grt	Grt	Grt
Sample	46.8.1b	46.8.1b	46.8.1b	46.8.1b	46.8.1b	46.8.1b
Analysis	p41	p42	p43	p44	p45	p46
SiO_2	37,38	37,00	37,01	37,07	37,17	37,29
TiO_2	0,05	0,06	0,08	0,07	0,05	0,06
Al_2O_3	21,34	20,97	21,07	21,09	21,27	21,11
FeO	35,71	35,57	35,59	35,60	35,72	35,86
MnO	0,39	0,86	0,82	0,65	0,63	0,43
MgO	1,89	1,48	1,53	1,63	1,67	1,73
CaO	2,96	2,99	3,21	3,26	3,17	3,13
Na_2O	0,01	0,02	0,02	0,02	0,00	0,01
K_2O	0,01	0,00	0,00	0,00	0,00	0,00
Cr_2O_3	0,01	0,02	0,02	0,02	0,02	0,00
BaO						
ZnO						
Sum	99,74	98,96	99,35	99,41	99,70	99,63
Si	3,03	3,03	3,02	3,02	3,02	3,03
Ti	0,00	0,00	0,00	0,00	0,00	0,00
Al	2,04	2,02	2,02	2,02	2,03	2,02
Fe2+	2,42	2,44	2,43	2,42	2,42	2,44
Fe3+	0,00	0,00	0,00	0,00	0,00	0,00
Mn	0,03	0,06	0,06	0,05	0,04	0,03
Mg	0,23	0,18	0,19	0,20	0,20	0,21
Ca	0,26	0,26	0,28	0,28	0,28	0,27
Na	0,00	0,00	0,00	0,00	0,00	0,00
K	0,00	0,00	0,00	0,00	0,00	0,00
Cr	0,00	0,00	0,00	0,00	0,00	0,00
Ba	0,00	0,00	0,00	0,00	0,00	0,00
Zn	0,00	0,00	0,00	0,00	0,00	0,00
Sum	8,00	8,00	8,00	8,00	8,00	8,00
XFe	91,37	93,12	92,90	92,44	92,32	92,09
Alm	82,53	82,91	82,28	82,13	82,34	82,65
Prp	7,80	6,13	6,29	6,72	6,85	7,10
Grs	8,76	8,93	9,52	9,63	9,35	9,23
Sps	0,91	2,04	1,92	1,53	1,46	1,01

Ilmenite microprobe analyses (Alpujárride Complex).

Mineral	Ilm	Ilm	Ilm	Ilm	Ilm	Ilm	Ilm	Ilm	Ilm	Ilm	Ilm
Sample	64.4.1	64.4.1	64.4.1	64.4.1	64.4.1	64.4.1	64.4.1	64.4.1	64.4.1	64.4.1	64.4.1
Analysis	p1	p3	p5	p13	p15	p17	p27	p29	p31	31/	33/
SiO_2	0,00	0,00	0,00	0,00	0,00	0,00	0,00	0,00	0,00	0,74	0,00
TiO_2	52,67	51,21	52,06	52,67	52,23	52,34	52,86	51,88	51,72	51,67	53,25
Al_2O_3	0,01	0,03	0,01	0,01	0,00	0,01	0,00	0,02	0,05	0,56	0,03
FeO	47,08	48,34	48,00	46,53	47,51	47,52	47,55	47,34	47,54	45,13	45,43
MnO	0,05	0,07	0,05	0,35	0,21	0,08	0,17	0,05	0,13	0,09	0,10
MgO	0,37	0,45	0,56	0,30	0,25	0,22	0,19	0,44	0,09	0,10	0,13
CaO	0,07	0,30	0,06	0,08	0,09	0,08	0,06	0,09	0,10	0,02	0,03
Na_2O	0,03	0,01	0,04	0,03	0,05	0,07	0,03	0,02	0,05	0,22	0,00
K_2O	0,00	0,00	0,01	0,00	0,01	0,00	0,01	0,00	0,01	0,26	0,11
Cr_2O_3	0,01	0,02	0,01	0,01	0,02	0,01	0,02	0,03	0,03	0,03	0,02
Sum	100,28	100,41	100,78	100,00	100,37	100,33	100,89	99,85	99,72	98,80	99,09
Si	0,00	0,00	0,00	0,00	0,00	0,00	0,00	0,00	0,00	0,02	0,00
Ti	0,99	0,96	0,97	1,00	0,98	0,99	0,99	0,98	0,98	0,98	1,02
Al	0,00	0,00	0,00	0,00	0,00	0,00	0,00	0,00	0,00	0,02	0,00
Fe2+	0,97	0,94	0,95	0,97	0,96	0,97	0,98	0,96	0,97	0,96	0,97
Fe3+	0,01	0,07	0,05	0,01	0,03	0,03	0,02	0,04	0,04	0,00	0,00
Mn	0,00	0,00	0,00	0,01	0,00	0,00	0,00	0,00	0,00	0,00	0,00
Mg	0,01	0,02	0,02	0,01	0,01	0,01	0,01	0,02	0,00	0,00	0,00
Ca	0,00	0,01	0,00	0,00	0,00	0,00	0,00	0,00	0,00	0,00	0,00
Na	0,00	0,00	0,00	0,00	0,00	0,00	0,00	0,00	0,00	0,01	0,00
K	0,00	0,00	0,00	0,00	0,00	0,00	0,00	0,00	0,00	0,01	0,00
Cr	0,00	0,00	0,00	0,00	0,00	0,00	0,00	0,00	0,00	0,00	0,00
Sum	2,00	2,00	2,00	2,00	2,00	2,00	2,00	2,00	2,00	2,00	2,00
Ilm	99,17	96,02	97,22	98,90	97,86	98,41	98,84	98,06	97,90	99,80	99,77
Pph	0,11	0,14	0,10	0,77	0,44	0,17	0,36	0,11	0,29	0,20	0,23
Hem	0,71	3,83	2,68	0,34	1,69	1,42	0,80	1,83	1,81	0,00	0,00

Mineral	Ilm	Ilm	Ilm	Ilm	Ilm	Ilm	Ilm	Ilm	Ilm	Ilm	Ilm
Sample	64.3.1	64.3.1	64.3.1	64.3.1	64.3.1	64.3.1	64.3.1	64.3.1	66.10.1	66.10.1	62.5.1
Analysis	p1	p3	p5	p20	p22	p24	63/	64/	p3	p5	30/
SiO_2	0,00	0,00	0,00	0,00	0,46	0,08	0,00	0,17	0,00	0,00	0,51
TiO_2	51,81	44,48	61,47	46,22	45,14	49,64	52,15	55,10	25,69	43,65	52,98
Al_2O_3	0,06	0,03	0,04	0,06	0,74	0,11	0,04	0,15	0,11	0,02	0,48
FeO	44,12	53,66	34,90	51,41	44,97	47,12	45,55	39,88	66,23	50,98	43,49
MnO	0,08	0,17	0,11	0,55	0,53	1,01	0,52	0,51	1,48	0,14	1,81
MgO	0,01	0,24	0,03	0,01	0,10	0,02	0,06	0,04	0,00	0,02	0,06
CaO	0,06	0,12	0,11	0,08	0,22	0,17	0,01	0,03	0,20	0,20	0,01
Na_2O	0,00	0,03	0,08	0,13	0,07	0,04	0,00	0,06	0,00	0,01	0,01
K_2O	0,00	0,00	0,00	0,01	0,00	0,01	0,06	0,04	0,01	0,01	0,31
Cr_2O_3	0,03	0,04	0,07	0,03	0,02	0,06	0,03	0,06	0,13	0,04	0,00
Sum	96,16	98,78	96,80	98,48	92,26	98,25	98,42	96,05	93,84	95,07	99,65
Si	0,00	0,00	0,00	0,00	0,01	0,00	0,00	0,00	0,00	0,00	0,01
Ti	1,02	0,85	1,22	0,88	0,92	0,96	1,01	1,09	0,51	0,86	1,00
Al	0,00	0,00	0,00	0,00	0,02	0,00	0,00	0,00	0,00	0,00	0,01
Fe2+	0,97	0,83	0,77	0,86	0,90	0,93	0,98	0,88	0,47	0,85	0,92
Fe3+	0,00	0,31	0,00	0,24	0,12	0,08	0,00	0,00	0,98	0,27	0,00
Mn	0,00	0,00	0,00	0,01	0,01	0,02	0,01	0,01	0,03	0,00	0,04
Mg	0,00	0,01	0,00	0,00	0,00	0,00	0,00	0,00	0,00	0,00	0,00
Ca	0,00	0,00	0,00	0,00	0,01	0,00	0,00	0,00	0,01	0,01	0,00
Na	0,00	0,00	0,00	0,01	0,00	0,00	0,00	0,00	0,00	0,00	0,00
K	0,00	0,00	0,00	0,00	0,00	0,00	0,00	0,00	0,00	0,00	0,01
Cr	0,00	0,00	0,00	0,00	0,00	0,00	0,00	0,00	0,00	0,00	0,00
Sum	2,00	2,00	2,00	2,00	2,00	2,00	2,00	2,00	2,00	2,00	2,00
Ilm	99,83	84,00	99,69	86,82	92,70	93,58	98,86	98,72	47,12	86,10	95,96
Pph	0,17	0,38	0,31	1,20	1,26	2,22	1,14	1,28	3,30	0,32	4,04
Hem	0,00	15,62	0,00	11,98	6,04	4,20	0,00	0,00	49,58	13,58	0,00

Chloritoid, staurolite and epidote microprobe analyses (Alpujárride Complex).

Mineral	Cld	Cld	St	St	St	Ep	Ep
Sample	64.4.1	64.4.1	64.4.1	64.4.1	64.4.1	66.10.1	66.10.1
Analysis	p7	p8	35*	37*	38*	p45	p50
SiO_2	24,50	25,37	27,69	27,84	27,80	37,88	36,52
TiO_2	0,00	0,01	0,46	0,65	0,43	0,09	4,62
Al_2O_3	41,23	38,71	52,51	52,10	52,64	24,48	23,24
FeO	25,20	25,19	14,79	14,40	14,61	10,86	11,41
MnO	0,15	0,09	0,03	0,02	0,02	0,17	0,05
MgO	2,41	2,54	1,54	1,55	1,61	0,06	0,04
CaO	0,08	0,57	0,00	0,00	0,00	22,92	22,58
Na_2O	0,02	0,04	0,01	0,01	0,01	0,05	0,02
K_2O	0,00	0,02	0,01	0,01	0,01	0,03	0,09
Cr_2O_3	0,04	0,02				0,00	0,04
BaO			0,00	0,01	0,00		
ZnO			0,22	0,32	0,17		
Sum	93,63	92,54	97,25	96,91	97,29	96,53	98,60
Si	2,00	2,10	7,78	7,84	7,79	3,09	2,94
Ti	0,00	0,00	0,10	0,14	0,09	0,01	0,28
Al	3,97	3,78	17,38	17,29	17,39	2,36	2,21
FeTot	1,72	1,75	3,47	3,39	3,43	0,74	0,77
Mn	0,01	0,01	0,01	0,00	0,00	0,01	0,00
Mg	0,29	0,31	0,65	0,65	0,67	0,01	0,00
Ca	0,01	0,05	0,00	0,00	0,00	2,00	1,95
Na	0,00	0,01	0,00	0,00	0,00	0,01	0,00
K	0,00	0,00	0,01	0,00	0,00	0,00	0,01
Cr	0,00	0,00	0,00	0,00	0,00	0,00	0,00
Ba	0,00	0,00	0,00	0,00	0,00	0,00	0,00
Zn	0,00	0,00	0,05	0,07	0,04	0,00	0,00
Sum	8,01	8,01	29,44	29,39	29,42	8,23	8,18

Plagioclase microprobe analyses (Alpujárride Complex).

Mineral	Pl	Pl	Pl	Pl	Pl	Pl	Pl	Pl	Pl	Pl
Sample	62.5.1	62.5.1	62.5.1	62.5.1	62.5.1	62.5.1	62.5.1	62.5.1	66.10.1	66.10.1
Analysis	32	33	34	35	27/	28/	69*	70*	p43	89*
SiO_2	61,53	61,46	60,86	61,45	61,24	59,14	60,56	60,38	50,68	46,30
TiO_2	0,01	0,01	0,00	0,01	0,01	0,00	0,09	0,00	0,03	0,16
Al_2O_3	24,83	24,46	24,87	24,56	24,77	25,62	24,49	24,33	31,28	32,74
FeO	0,08	0,07	0,07	0,10	0,05	0,08	0,12	0,06	0,29	0,73
MnO	0,00	0,00	0,00	0,00	0,00	0,04	0,02	0,01	0,01	0,03
MgO	0,00	0,00	0,00	0,00	0,00	0,00	0,00	0,00	0,14	0,31
CaO	6,09	5,84	6,27	6,00	5,99	7,23	6,12	6,12	13,67	15,62
Na_2O	8,08	8,15	7,90	8,04	8,13	7,42	7,85	8,00	3,60	1,98
K_2O	0,27	0,21	0,26	0,28	0,29	0,20	0,32	0,27	0,16	0,46
Cr_2O_3	0,00	0,00	0,00	0,00	0,00	0,00			0,00	
BaO							0,00	0,00		0,02
ZnO							0,02	0,01		0,00
Sum	100,89	100,22	100,23	100,44	100,49	99,72	99,59	99,17	99,86	98,35
Si	2,71	2,73	2,70	2,72	2,71	2,64	2,71	2,71	2,31	2,16
Ti	0,00	0,00	0,00	0,00	0,00	0,00	0,00	0,00	0,00	0,01
Al	1,29	1,28	1,30	1,28	1,29	1,35	1,29	1,29	1,68	1,80
FeTot	0,00	0,00	0,00	0,00	0,00	0,00	0,00	0,00	0,01	0,03
Mn	0,00	0,00	0,00	0,00	0,00	0,00	0,00	0,00	0,00	0,00
Mg	0,00	0,00	0,00	0,00	0,00	0,00	0,00	0,00	0,01	0,02
Ca	0,29	0,28	0,30	0,28	0,28	0,35	0,29	0,29	0,67	0,78
Na	0,69	0,70	0,68	0,69	0,70	0,64	0,68	0,70	0,32	0,18
K	0,01	0,01	0,01	0,02	0,02	0,01	0,02	0,02	0,01	0,03
Cr	0,00	0,00	0,00	0,00	0,00	0,00	0,00	0,00	0,00	0,00
Ba	0,00	0,00	0,00	0,00	0,00	0,00	0,00	0,00	0,00	0,00
Zn	0,00	0,00	0,00	0,00	0,00	0,00	0,00	0,00	0,00	0,00
Sum	5,00	5,00	5,00	5,00	5,00	5,00	5,00	5,00	5,00	5,00
Ab	69,54	70,77	68,46	69,69	69,91	64,28	68,62	69,22	31,97	18,18
An	28,95	28,01	30,05	28,73	28,47	34,60	29,56	29,23	67,11	79,04
Or	1,51	1,22	1,49	1,58	1,63	1,12	1,82	1,55	0,92	2,79

White mica microprobe analyses (Alpujárride Complex).

Mineral	Wm	Wm	Wm	Wm	Wm	Wm	Wm	Wm	Wm	Wm	Wm
Sample	64.4.1	64.4.1	64.4.1	64.4.1	64.4.1	64.4.1	64.4.1	64.4.1	64.4.1	64.4.1	64.4.1
Analysis	p10	p11	p12	p47	p48	p49	p50	p51	p52	p1b	p2b
SiO_2	46,95	46,67	47,02	47,48	48,36	46,34	46,81	47,32	47,71	46,01	47,72
TiO_2	0,33	0,31	0,31	0,26	0,27	0,26	0,32	0,28	0,29	0,30	0,08
Al_2O_3	36,44	36,29	34,79	33,32	32,04	36,37	35,91	33,61	33,34	36,57	40,18
FeO	1,42	1,32	2,09	3,00	2,79	1,60	1,85	2,16	2,51	1,26	0,53
MnO	0,01	0,02	0,00	0,00	0,01	0,00	0,02	0,00	0,00	0,00	0,00
MgO	0,57	0,54	0,80	1,19	1,58	0,49	0,72	1,15	1,34	0,45	0,11
CaO	0,05	0,03	0,02	0,02	0,04	0,03	0,01	0,03	0,03	0,02	0,29
Na_2O	1,92	1,86	1,44	1,11	1,00	1,79	1,68	1,20	1,06	1,94	5,64
K_2O	8,04	7,92	8,36	8,72	8,74	8,16	8,26	8,41	8,61	8,05	2,00
Cr_2O_3	0,00	0,02	0,03	0,03	0,03	0,01	0,02	0,02	0,03	0,02	0,01
BaO											
ZnO											
Sum	95,73	94,99	94,86	95,13	94,86	95,05	95,59	94,16	94,93	94,61	96,57
Si	3,08	3,08	3,12	3,16	3,22	3,06	3,08	3,16	3,17	3,05	3,01
Ti	0,02	0,02	0,02	0,01	0,01	0,01	0,02	0,01	0,01	0,02	0,00
Al iv	0,92	0,92	0,88	0,84	0,78	0,94	0,92	0,84	0,83	0,95	0,99
Al vi	1,89	1,90	1,84	1,78	1,74	1,90	1,87	1,81	1,78	1,91	2,00
FeTot	0,08	0,07	0,12	0,17	0,16	0,09	0,10	0,12	0,14	0,07	0,03
Mn	0,00	0,00	0,00	0,00	0,00	0,00	0,00	0,00	0,00	0,00	0,00
Mg	0,06	0,05	0,08	0,12	0,16	0,05	0,07	0,11	0,13	0,04	0,01
Ca	0,00	0,00	0,00	0,00	0,00	0,00	0,00	0,00	0,00	0,00	0,02
Na	0,24	0,24	0,19	0,14	0,13	0,23	0,21	0,16	0,14	0,25	0,69
K	0,67	0,67	0,71	0,74	0,74	0,69	0,69	0,72	0,73	0,68	0,16
Cr	0,00	0,00	0,00	0,00	0,00	0,00	0,00	0,00	0,00	0,00	0,00
Ba	0,00	0,00	0,00	0,00	0,00	0,00	0,00	0,00	0,00	0,00	0,00
Zn	0,00	0,00	0,00	0,00	0,00	0,00	0,00	0,00	0,00	0,00	0,00
Sum	6,96	6,95	6,95	6,96	6,94	6,97	6,96	6,94	6,94	6,97	6,91
Pg	0,26	0,26	0,21	0,16	0,15	0,25	0,24	0,18	0,16	0,27	-
Ms	0,08	0,09	0,11	0,12	0,12	0,08	0,09	0,13	0,13	0,07	-
Cel	0,56	0,55	0,55	0,55	0,49	0,59	0,58	0,52	0,52	0,60	-
Prl	0,08	0,08	0,12	0,16	0,22	0,06	0,08	0,16	0,17	0,05	-

Mineral	Wm	Wm	Wm	Wm	Wm	Wm	Wm	Wm	Wm	Wm	Wm
Sample	64.4.1	64.4.1	64.4.1	64.4.1	64.4.1	64.4.1	64.4.1	64.4.1	64.4.1	64.4.1	64.4.1
Analysis	p3b	37/	p4b	p5b	p6b	p7b	p8b	p9b	44/	45/	46/
SiO_2	46,33	46,48	47,03	47,82	46,92	47,24	46,26	47,44	45,23	46,87	46,05
TiO_2	0,08	0,12	0,24	0,29	0,07	0,29	0,28	0,27	0,14	0,08	0,09
Al_2O_3	40,17	39,49	34,03	33,40	39,94	33,86	36,35	34,59	40,21	40,53	39,28
FeO	0,52	0,81	2,66	2,53	0,51	2,08	1,41	1,61	0,63	0,46	1,25
MnO	0,02	0,00	0,00	0,00	0,01	0,00	0,00	0,00	0,00	0,01	0,00
MgO	0,07	0,16	1,03	1,33	0,06	1,19	0,52	0,88	0,12	0,06	0,10
CaO	0,41	0,38	0,01	0,02	0,19	0,02	0,09	0,04	1,03	0,40	0,41
Na_2O	5,99	5,35	1,32	1,09	6,35	1,18	2,13	1,38	5,52	6,28	5,71
K_2O	1,44	2,20	8,64	8,79	0,91	8,58	7,72	8,36	1,87	1,28	1,71
Cr_2O_3	0,01	0,01	0,02	0,02	0,01	0,02	0,01	0,02	0,03	0,00	0,02
BaO											
ZnO											
Sum	95,03	95,01	94,97	95,28	94,96	94,46	94,77	94,59	94,76	95,98	94,60
Si	2,97	2,99	3,13	3,17	3,00	3,15	3,06	3,15	2,92	2,97	2,98
Ti	0,00	0,01	0,01	0,01	0,00	0,01	0,01	0,01	0,01	0,00	0,00
Al iv	1,03	1,01	0,87	0,83	1,00	0,85	0,94	0,85	1,08	1,03	1,02
Al vi	2,01	1,99	1,80	1,78	2,01	1,81	1,90	1,85	1,99	2,01	1,98
FeTot	0,03	0,04	0,15	0,14	0,03	0,12	0,08	0,09	0,03	0,02	0,07
Mn	0,00	0,00	0,00	0,00	0,00	0,00	0,00	0,00	0,00	0,00	0,00
Mg	0,01	0,02	0,10	0,13	0,01	0,12	0,05	0,09	0,01	0,01	0,01
Ca	0,03	0,03	0,00	0,00	0,01	0,00	0,01	0,00	0,07	0,03	0,03
Na	0,74	0,67	0,17	0,14	0,79	0,15	0,27	0,18	0,69	0,77	0,72
K	0,12	0,18	0,73	0,74	0,07	0,73	0,65	0,71	0,15	0,10	0,14
Cr	0,00	0,00	0,00	0,00	0,00	0,00	0,00	0,00	0,00	0,00	0,00
Ba	0,00	0,00	0,00	0,00	0,00	0,00	0,00	0,00	0,00	0,00	0,00
Zn	0,00	0,00	0,00	0,00	0,00	0,00	0,00	0,00	0,00	0,00	0,00
Sum	6,94	6,93	6,97	6,95	6,92	6,95	6,97	6,93	6,96	6,94	6,95
Pg	-	-	0,19	0,16	-	0,17	0,29	0,20	-	-	-
Ms	-	-	0,09	0,12	-	0,12	0,07	0,11	-	-	-
Cel	-	-	0,57	0,54	-	0,55	0,56	0,52	-	-	-
Prl	-	-	0,13	0,17	-	0,15	0,06	0,15	-	-	-

Mineral	Wm	Wm	Wm	Wm	Wm	Wm	Wm	Wm	Wm	Wm	Wm
Sample	64.4.1	64.3.1	64.3.1	64.3.1	64.3.1	64.3.1	64.3.1	64.3.1	64.3.1	64.3.1	64.3.1
Analysis	36*	p16	p17	p18	p19	p26	p27	p28	p29	p30	p31
SiO_2	46,08	46,23	47,02	45,54	43,81	47,65	46,98	48,10	47,90	47,05	46,30
TiO_2	0,30	0,11	0,11	0,10	0,16	0,29	0,27	0,29	0,27	0,13	0,10
Al_2O_3	36,13	39,40	38,53	37,52	34,55	32,55	33,78	32,64	32,77	38,72	39,30
FeO	1,44	0,99	1,61	1,24	3,23	2,93	2,81	2,60	2,93	0,90	0,88
MnO	0,01	0,00	0,00	0,01	0,00	0,00	0,02	0,00	0,01	0,00	0,00
MgO	0,50	0,08	0,24	0,19	0,77	1,40	1,04	1,40	1,39	0,35	0,22
CaO	0,04	0,43	0,36	0,45	0,60	0,04	0,01	0,03	0,01	0,35	0,40
Na_2O	2,12	5,48	4,54	4,57	2,99	1,01	1,15	0,94	1,02	4,61	5,12
K_2O	8,09	1,41	3,03	2,42	4,09	9,03	8,91	8,95	9,17	3,49	2,49
Cr_2O_3		0,03	0,02	0,02	0,04	0,05	0,04	0,01	0,03	0,03	0,03
BaO	0,19										
ZnO	0,02										
Sum	94,92	94,15	95,46	92,06	90,24	94,95	95,03	94,97	95,51	95,62	94,84
Si	3,06	2,99	3,03	3,03	3,03	3,18	3,13	3,20	3,18	3,02	2,99
Ti	0,01	0,01	0,01	0,00	0,01	0,01	0,01	0,01	0,01	0,01	0,01
Al iv	0,94	1,01	0,97	0,97	0,97	0,82	0,87	0,80	0,82	0,98	1,01
Al vi	1,88	2,00	1,95	1,97	1,85	1,75	1,79	1,76	1,75	1,96	1,98
FeTot	0,08	0,05	0,09	0,07	0,19	0,16	0,16	0,14	0,16	0,05	0,05
Mn	0,00	0,00	0,00	0,00	0,00	0,00	0,00	0,00	0,00	0,00	0,00
Mg	0,05	0,01	0,02	0,02	0,08	0,14	0,10	0,14	0,14	0,03	0,02
Ca	0,00	0,03	0,02	0,03	0,04	0,00	0,00	0,00	0,00	0,02	0,03
Na	0,27	0,69	0,57	0,59	0,40	0,13	0,15	0,12	0,13	0,57	0,64
K	0,68	0,12	0,25	0,21	0,36	0,77	0,76	0,76	0,78	0,29	0,21
Cr	0,00	0,00	0,00	0,00	0,00	0,00	0,00	0,00	0,00	0,00	0,00
Ba	0,01	0,00	0,00	0,00	0,00	0,00	0,00	0,00	0,00	0,00	0,00
Zn	0,00	0,00	0,00	0,00	0,00	0,00	0,00	0,00	0,00	0,00	0,00
Sum	6,99	6,90	6,91	6,89	6,93	6,97	6,98	6,94	6,97	6,93	6,93
Pg	0,28	-	-	-	0,50	0,15	0,16	0,14	0,14	-	-
Ms	0,03	-	-	-	0,19	0,10	0,09	0,12	0,09	-	-
Cel	0,60	-	-	-	0,21	0,56	0,60	0,53	0,57	-	-
Prl	0,06	-	-	-	0,03	0,18	0,13	0,20	0,18	-	-

Mineral	Wm	Wm	Wm	Wm	Wm	Wm	Wm	Wm	Wm	Wm	Wm
Sample	64.3.1	64.3.1	64.3.1	64.3.1	64.3.1	64.3.1	64.3.1	64.3.1	64.3.1	64.3.1	64.3.1
Analysis	p32	p33	p34	p35	p36	p37	p38	p39	p40	p41	p42
SiO_2	47,77	46,81	46,46	46,39	46,75	46,49	45,57	47,17	46,16	47,25	46,40
TiO_2	0,27	0,07	0,26	0,07	0,26	0,08	0,10	0,30	0,11	0,09	0,09
Al_2O_3	33,01	40,37	34,09	40,23	32,81	39,65	39,34	32,39	40,35	40,03	39,54
FeO	2,79	0,64	2,70	0,60	2,53	0,80	0,90	3,62	0,96	1,16	0,69
MnO	0,00	0,00	0,00	0,01	0,00	0,00	0,00	0,00	0,01	0,02	0,00
MgO	1,25	0,09	0,94	0,06	1,11	0,11	0,11	1,29	0,11	0,12	0,11
CaO	0,04	0,39	0,01	0,34	0,02	0,36	0,47	0,09	0,60	0,23	0,41
Na_2O	1,09	6,08	1,42	6,15	1,14	5,92	5,78	1,05	5,82	5,94	5,76
K_2O	8,73	1,54	8,86	1,34	8,93	1,58	1,78	8,75	1,49	1,53	1,71
Cr_2O_3	0,05	0,02	0,05	0,02	0,04	0,03	0,03	0,03	0,02	0,01	0,02
BaO											
ZnO											
Sum	94,99	96,01	94,77	95,21	93,59	95,00	94,09	94,68	95,63	96,37	94,74
Si	3,18	2,97	3,11	2,97	3,16	2,99	2,97	3,17	2,95	2,99	2,99
Ti	0,01	0,00	0,01	0,00	0,01	0,00	0,00	0,02	0,01	0,00	0,00
Al iv	0,82	1,03	0,89	1,03	0,84	1,01	1,03	0,83	1,05	1,01	1,01
Al vi	1,77	2,00	1,80	2,01	1,78	1,99	1,98	1,73	1,99	1,99	1,99
FeTot	0,16	0,03	0,15	0,03	0,14	0,04	0,05	0,20	0,05	0,06	0,04
Mn	0,00	0,00	0,00	0,00	0,00	0,00	0,00	0,00	0,00	0,00	0,00
Mg	0,12	0,01	0,09	0,01	0,11	0,01	0,01	0,13	0,01	0,01	0,01
Ca	0,00	0,03	0,00	0,02	0,00	0,02	0,03	0,01	0,04	0,02	0,03
Na	0,14	0,75	0,18	0,76	0,15	0,74	0,73	0,14	0,72	0,73	0,72
K	0,74	0,13	0,76	0,11	0,77	0,13	0,15	0,75	0,12	0,12	0,14
Cr	0,00	0,00	0,00	0,00	0,00	0,00	0,00	0,00	0,00	0,00	0,00
Ba	0,00	0,00	0,00	0,00	0,00	0,00	0,00	0,00	0,00	0,00	0,00
Zn	0,00	0,00	0,00	0,00	0,00	0,00	0,00	0,00	0,00	0,00	0,00
Sum	6,95	6,95	7,00	6,94	6,97	6,94	6,96	6,98	6,94	6,93	6,93
Pg	0,16	-	0,20	-	0,16	-	-	0,15	-	-	-
Ms	0,12	-	0,06	-	0,08	-	-	0,11	-	-	-
Cel	0,53	-	0,62	-	0,58	-	-	0,55	-	-	-
Prl	0,18	-	0,11	-	0,16	-	-	0,17	-	-	-

Mineral	Wm	Wm	Wm	Wm	Wm	Wm	Wm	Wm	Wm	Wm	Wm
Sample	64.3.1	64.3.1	64.3.1	64.3.1	64.3.1	64.3.1	64.3.1	64.3.1	64.3.1	64.3.1	66.10.1
Analysis	p43	p44	85/	86/	87/	88/	85*	86*	87*	88*	p39
SiO_2	48,24	46,21	46,34	46,75	46,79	46,65	45,89	45,94	46,61	45,90	46,38
TiO_2	0,23	0,09	0,23	0,26	0,10	0,09	0,10	0,09	0,07	0,09	0,21
Al_2O_3	30,70	39,58	35,01	35,40	40,11	40,82	38,61	38,70	39,72	38,71	33,55
FeO	3,06	1,24	1,78	1,83	0,71	0,60	0,93	0,79	0,56	0,72	2,62
MnO	0,00	0,00	0,02	0,00	0,00	0,02	0,00	0,00	0,00	0,00	0,02
MgO	1,74	0,25	0,65	0,65	0,14	0,08	0,15	0,15	0,08	0,12	0,93
CaO	0,03	0,34	0,04	0,06	0,40	0,65	0,39	0,34	0,34	0,36	0,05
Na_2O	0,85	5,99	1,66	1,67	5,56	6,19	5,72	5,88	6,40	6,02	0,31
K_2O	8,99	1,66	8,45	8,38	2,33	1,37	2,35	2,06	1,65	2,42	10,37
Cr_2O_3	0,02	0,02	0,01	0,03	0,02	0,01					0,02
BaO							0,03	0,03	0,02	0,04	
ZnO							0,00	0,01	0,01	0,01	
Sum	93,84	95,37	94,19	95,01	96,14	96,47	94,18	94,00	95,45	94,38	94,46
Si	3,26	2,97	3,10	3,10	2,98	2,95	2,99	3,00	2,98	2,99	3,13
Ti	0,01	0,00	0,01	0,01	0,00	0,00	0,00	0,00	0,00	0,00	0,01
Al iv	0,74	1,03	0,90	0,90	1,02	1,05	1,01	1,00	1,02	1,01	0,87
Al vi	1,70	1,97	1,86	1,86	1,99	2,00	1,96	1,97	1,98	1,96	1,80
FeTot	0,17	0,07	0,10	0,10	0,04	0,03	0,05	0,04	0,03	0,04	0,15
Mn	0,00	0,00	0,00	0,00	0,00	0,00	0,00	0,00	0,00	0,00	0,00
Mg	0,18	0,02	0,06	0,06	0,01	0,01	0,01	0,01	0,01	0,01	0,09
Ca	0,00	0,02	0,00	0,00	0,03	0,04	0,03	0,02	0,02	0,03	0,00
Na	0,11	0,75	0,21	0,21	0,69	0,76	0,72	0,74	0,79	0,76	0,04
K	0,77	0,14	0,72	0,71	0,19	0,11	0,20	0,17	0,13	0,20	0,89
Cr	0,00	0,00	0,00	0,00	0,00	0,00	0,00	0,00	0,00	0,00	0,00
Ba	0,00	0,00	0,00	0,00	0,00	0,00	0,00	0,00	0,00	0,00	0,00
Zn	0,00	0,00	0,00	0,00	0,00	0,00	0,00	0,00	0,00	0,00	0,00
Sum	6,95	6,97	6,98	6,97	6,95	6,96	6,98	6,97	6,98	7,00	6,99
Pg	0,12	-	0,23	0,23	-	-	-	-	-	-	0,04
Ms	0,11	-	0,06	0,07	-	-	-	-	-	-	0,06
Cel	0,49	-	0,60	0,58	-	-	-	-	-	-	0,75
Prl	0,26	-	0,10	0,10	-	-	-	-	-	-	0,13

Mineral	Wm	Wm	Wm	Wm	Wm	Wm	Wm	Wm	Wm	Wm	Wm
Sample	66.10.1	66.10.1	66.10.1	66.10.1	66.10.1	66.10.1	66.10.1	66.10.1	66.10.1	62.5.1	62.5.1
Analysis	p40	p42	p47	p48	p49	p51	p52	p53	p54	36	37
SiO_2	46,36	45,84	46,74	45,52	45,78	47,63	46,92	46,71	46,24	48,27	47,59
TiO_2	0,27	0,25	0,24	0,22	0,15	0,27	0,33	0,27	0,33	0,26	0,30
Al_2O_3	34,69	34,29	32,31	35,41	37,10	30,98	32,65	30,11	32,80	32,02	34,15
FeO	2,41	2,84	2,69	1,90	1,90	3,39	3,16	3,87	3,38	2,20	1,35
MnO	0,00	0,03	0,01	0,04	0,00	0,01	0,00	0,02	0,00	0,00	0,01
MgO	0,81	0,66	1,38	0,73	0,46	1,71	1,27	1,58	1,02	1,72	1,08
CaO	0,04	0,04	0,04	0,24	0,19	0,00	0,01	0,01	0,01	0,04	0,01
Na_2O	0,30	0,37	0,29	0,42	0,53	0,28	0,31	0,35	0,29	0,29	0,36
K_2O	10,49	10,52	10,40	10,25	10,38	10,40	10,68	10,31	10,49	10,27	10,54
Cr_2O_3	0,03	0,03	0,03	0,01	0,01	0,00	0,04	0,00	0,03	0,02	0,02
BaO											
ZnO											
Sum	95,39	94,85	94,12	94,74	96,51	94,67	95,36	93,23	94,58	95,09	95,40
Si	3,10	3,09	3,17	3,06	3,02	3,22	3,15	3,22	3,13	3,22	3,16
Ti	0,01	0,01	0,01	0,01	0,01	0,01	0,02	0,01	0,02	0,01	0,01
Al iv	0,90	0,91	0,83	0,94	0,98	0,78	0,85	0,78	0,87	0,78	0,84
Al vi	1,83	1,81	1,75	1,86	1,90	1,69	1,74	1,67	1,75	1,74	1,83
FeTot	0,13	0,16	0,15	0,11	0,10	0,19	0,18	0,22	0,19	0,12	0,07
Mn	0,00	0,00	0,00	0,00	0,00	0,00	0,00	0,00	0,00	0,00	0,00
Mg	0,08	0,07	0,14	0,07	0,05	0,17	0,13	0,16	0,10	0,17	0,11
Ca	0,00	0,00	0,00	0,02	0,01	0,00	0,00	0,00	0,00	0,00	0,00
Na	0,04	0,05	0,04	0,06	0,07	0,04	0,04	0,05	0,04	0,04	0,05
K	0,89	0,90	0,90	0,88	0,87	0,90	0,92	0,91	0,91	0,87	0,89
Cr	0,00	0,00	0,00	0,00	0,00	0,00	0,00	0,00	0,00	0,00	0,00
Ba	0,00	0,00	0,00	0,00	0,00	0,00	0,00	0,00	0,00	0,00	0,00
Zn	0,00	0,00	0,00	0,00	0,00	0,00	0,00	0,00	0,00	0,00	0,00
Sum	6,99	7,01	7,00	7,00	7,01	7,00	7,02	7,02	7,01	6,96	6,96
Pg	0,04	0,05	0,04	0,06	0,07	0,04	0,04	0,05	0,04	0,04	0,05
Ms	0,06	0,04	0,06	0,05	0,05	0,07	0,04	0,05	0,05	0,09	0,06
Cel	0,78	0,80	0,72	0,81	0,85	0,66	0,75	0,67	0,75	0,64	0,72
Prl	0,10	0,09	0,17	0,06	0,02	0,22	0,15	0,22	0,13	0,22	0,16

Mineral	Wm	Wm	Wm	Wm	Wm	Wm	Wm	Wm	Wm	Wm	Wm
Sample	62.5.1	62.5.1	62.5.1	62.5.1	62.5.1	62.5.1	62.5.1	62.5.1	62.5.1	62.5.1	62.5.1
Analysis	38	39	40	41	42	43	44	45	46	47	48
SiO_2	48,14	48,09	45,35	47,90	48,41	47,53	46,91	48,05	47,49	48,65	46,15
TiO_2	0,28	0,27	0,27	0,21	0,24	0,30	0,29	0,26	0,28	0,27	0,24
Al_2O_3	32,64	31,28	35,86	31,60	30,61	34,43	33,72	31,33	32,48	31,62	32,09
FeO	2,09	2,68	1,15	2,24	2,87	1,24	1,70	2,54	2,04	2,51	2,41
MnO	0,03	0,01	0,00	0,03	0,01	0,00	0,00	0,00	0,01	0,01	0,01
MgO	1,57	1,85	0,74	1,82	2,10	1,00	1,05	1,70	1,32	1,68	1,32
CaO	0,01	0,01	0,04	0,01	0,01	0,05	0,03	0,01	0,06	0,07	2,28
Na_2O	0,33	0,27	0,45	0,30	0,28	0,35	0,36	0,29	0,30	0,28	0,33
K_2O	10,38	10,27	10,52	10,32	10,18	10,54	10,53	10,44	10,39	10,30	9,98
Cr_2O_3	0,02	0,03	0,02	0,00	0,01	0,03	0,03	0,02	0,03	0,02	0,02
BaO											
ZnO											
Sum	95,48	94,77	94,40	94,44	94,72	95,47	94,61	94,62	94,38	95,41	94,85
Si	3,20	3,23	3,05	3,22	3,25	3,15	3,15	3,23	3,20	3,24	3,12
Ti	0,01	0,01	0,01	0,01	0,01	0,02	0,01	0,01	0,01	0,01	0,01
Al iv	0,80	0,77	0,95	0,78	0,75	0,85	0,85	0,77	0,80	0,76	0,88
Al vi	1,76	1,71	1,88	1,73	1,68	1,84	1,81	1,72	1,77	1,72	1,68
FeTot	0,12	0,15	0,06	0,13	0,16	0,07	0,10	0,14	0,11	0,14	0,14
Mn	0,00	0,00	0,00	0,00	0,00	0,00	0,00	0,00	0,00	0,00	0,00
Mg	0,16	0,19	0,07	0,18	0,21	0,10	0,11	0,17	0,13	0,17	0,13
Ca	0,00	0,00	0,00	0,00	0,00	0,00	0,00	0,00	0,00	0,00	0,17
Na	0,04	0,04	0,06	0,04	0,04	0,04	0,05	0,04	0,04	0,04	0,04
K	0,88	0,88	0,90	0,89	0,87	0,89	0,90	0,90	0,89	0,88	0,86
Cr	0,00	0,00	0,00	0,00	0,00	0,00	0,00	0,00	0,00	0,00	0,00
Ba	0,00	0,00	0,00	0,00	0,00	0,00	0,00	0,00	0,00	0,00	0,00
Zn	0,00	0,00	0,00	0,00	0,00	0,00	0,00	0,00	0,00	0,00	0,00
Sum	6,97	6,97	7,00	6,98	6,98	6,96	6,98	6,98	6,97	6,96	7,04
Pg	0,05	0,04	0,06	0,04	0,04	0,05	0,05	0,04	0,04	0,04	-
Prl	0,08	0,08	0,04	0,07	0,09	0,06	0,05	0,07	0,06	0,08	-
Ms	0,66	0,63	0,84	0,65	0,60	0,72	0,74	0,65	0,68	0,62	-
Cel	0,20	0,23	0,05	0,22	0,25	0,15	0,15	0,23	0,20	0,24	-

Mineral	Wm	Wm	Wm	Wm
Sample	62.5.1	62.5.1	62.5.1	62.5.1
Analysis	49	50	51	72*
SiO_2	47,66	48,30	48,47	47,56
TiO_2	0,30	0,26	0,27	0,26
Al_2O_3	33,75	30,96	32,69	34,15
FeO	1,96	3,01	1,95	1,38
MnO	0,00	0,00	0,01	0,00
MgO	1,13	1,80	1,41	0,97
CaO	0,03	0,01	0,02	0,03
Na_2O	0,35	0,25	0,31	0,39
K_2O	10,39	10,37	10,35	10,81
Cr_2O_3	0,02	0,01	0,01	
BaO				0,12
ZnO				0,01
Sum	95,57	94,97	95,47	95,69
Si	3,16	3,24	3,22	3,15
Ti	0,02	0,01	0,01	0,01
Al iv	0,84	0,76	0,78	0,85
Al vi	1,80	1,69	1,77	1,82
FeTot	0,11	0,17	0,11	0,08
Mn	0,00	0,00	0,00	0,00
Mg	0,11	0,18	0,14	0,10
Ca	0,00	0,00	0,00	0,00
Na	0,04	0,03	0,04	0,05
K	0,88	0,89	0,88	0,91
Cr	0,00	0,00	0,00	0,00
Ba	0,00	0,00	0,00	0,00
Zn	0,00	0,00	0,00	0,00
Sum	6,96	6,98	6,95	6,98
Pg	0,05	0,04	0,04	0,05
Prl	0,07	0,08	0,08	0,03
Ms	0,70	0,63	0,64	0,75
Cel	0,16	0,24	0,22	0,15